DOC.20070913.0001

QA: QA

ANL-EBS-MD-000005 REV 04

August 2007

Stress Corrosion Cracking of Waste Package Outer Barrier and Drip Shield Materials

Prepared for:
U.S. Department of Energy
Office of Civilian Radioactive Waste Management
Office of Repository Development
1551 Hillshire Drive
Las Vegas, Nevada 89134-6321

Prepared by:
Sandia National Laboratories
OCRWM Lead Laboratory for Repository Systems
1180 Town Center Drive
Las Vegas, Nevada 89144

Under Contract Number
DE-AC04-94AL85000

DISCLAIMER

This report was prepared as an account of work sponsored by an agency of the United States Government. Neither the United States Government nor any agency thereof, nor any of their employees, nor any of their contractors, subcontractors or their employees, makes any warranty, express or implied, or assumes any legal liability or responsibility for the accuracy, completeness, or any third party's use or the results of such use of any information, apparatus, product, or process disclosed, or represents that its use would not infringe privately owned rights. Reference herein to any specific commercial product, process, or service by trade name, trademark, manufacturer, or otherwise, does not necessarily constitute or imply its endorsement, recommendation, or favoring by the United States Government or any agency thereof or its contractors or subcontractors. The views and opinions of authors expressed herein do not necessarily state or reflect those of the United States Government or any agency thereof.

QA: QA

Stress Corrosion Cracking of Waste Package Outer Barrier and Drip Shield Materials

ANL-EBS-MD-000005 REV 04

August 2007

Model Signature Page/Change History

Complete only applicable items.

1. Total Pages: 378

2. Type of Mathematical Model

☒ Process Model ☐ Abstraction Model ☐ System Model

Describe Intended Use of Model

To be used as an input to license application activities, such as the development of the Total System Performance Assessment Model /Analysis for the License Application, MDL-WIS-PA-000005, to provide technical bases for assessing waste package and drip shield degradation due to potential stress corrosion cracking under exposure conditions anticipated in the repository.

3. Title

Stress Corrosion Cracking of Waste Package Outer Barrier and Drip Shield Materials

4. DI (including Revision No. and Addendum No.):

ANL-EBS-MD-000005 REV 04

	Printed Name	Signature	Date
5. Originator	Fred Hua and Gerald Gordon		8/31/07
6. Independent Technical Reviewer for	Jean Younker	Ming Zhu	9/6/07
7. Checker	Tiangan Lian		9/6/07
8. QCS/Lead Lab QA Reviewer	Brian Mitcheltree		9/6/07
9. Responsible Manager/Lead	Neil Brown		9/7/07
10. Responsible Manager	Cliff Howard For Paul R Dixon		9-7-07

11. Remarks

Change History

12. Revision No. and Addendum No.	13. Description of Change
00	Initial Issue
00/01	This model report has been changed to include "no backfill" design and more data in support of analysis in the Waste Package Degradation PMR ICN 01 (WP PMR) and SR-CR. Vertical bars in the right margin of the text indicate the changes made in this ICN.
01	Final Copy of REV 01 ICN 00. The entire document has been revised. Changes are too extensive to be identified by vertical bars at the right margin of each page.
01/01	Final Copy of REV 01 ICN 01. Changes are results of corrective actions required to close out Condition Reports, CR 773, CR 787, CR 792, CR 1150, CR 1138, CR 1173, and CR 1177, related to REV 01 ICN 00. Changes from REV 01 ICN 00 are too extensive to be identified by vertical bars at the right margin of each page.

	revision also corrects the following DTNs: L021105312215.023 to LL021105312251.023 (identified in CR 664C and TER-03-0043); and LL03041252251.57 to LL030412512251.057 (also identified in CR 664C). Input DIRS 118611, TIC 247505 (Development and Use of Predictive Model of Crack Propagation in 304/316L, A533B/A508 and Inconel 600/182 Alloys in 288°C Water) was revised from Technical Information to Direct Input, qualified (identified in CR 79B).
03	This revision (REV 03):· • Updates the experimental basis for the current SCC initiation threshold stress criterion for the Alloy 22 outer barrier from 90% to 90% to 105% of yield strength · • Updates the experimental basis for the current SCC initiation threshold stress criterion for Titanium Grade 7 from 50% to 80% of yield strength · • Establishes SCC initiation threshold stress criterion of 50% yield strength for Titanium Grades 28 and 29· • Provides SCC crack growth rate results for Titanium Grades 7, 28, and 29· • Models seismic crack density for titanium alloys and restructures waste package seismic crack density model· • Incorporates the new stress and stress intensity factor profile analysis performed by Structural Integrity Associates for as-welded, laser-peened and plasticity-burnished naval long waste package closure weld· • Incorporates recent SCC crack growth rate results for Alloy 22 waste package materials and revises the *n* value (repassivation slope) and/or the K_{ISCC} values· • Summarizes the current understanding of the low-temperature creep behavior of titanium alloys· • Addresses the following Condition Reports: — CR 6703 - Improper unit conversion in the SCC report [DIRS 172203]. All unit conversions are transparently documented (Table 6-10, 6-11, 6-13 and 6-14). — CR 6664 - Transparency of engineered barrier degradation parameters in process-level reports and TSPA. Transparency of engineered barrier degradation parameters in the process-level report significantly improved throughout the document. — CR 6656 - Parameter values in the WAPDEG report could not be fully traced to their source reports and DTNs. Parameter values in the WAPDEG report are no longer used in this revision. These parameters are developed in this revision to the report (Section 6.5) and are documented in output DTN: MO0702PASTRESS.002. — CR 6693 - Defensibility of the Engineered Barrier Degradation reports. Defensibility of this Engineered Barrier Degradation report is significantly improved by adding new test data and rationales, improving the transparency and traceability and strengthening the uncertainty analyses throughout the report. — CR 6853 - Titanium creep. Lower-temperature creep behavior of titanium alloys including Titanium Grades 7 and 29 is discussed in Section 6.8.7. — CR 9202 - Thickness reduction for corrosion. 90% and 105% of yield strength as lower and upper bounds are documented in this report's output DTN: MO0702PASTRESS.002.
04	This revision (Rev 04) addresses all comments from DOE dated 06/18/2007. In this revision, all the project vendor data (e.g. GE GRC and Structural Integrity Associates) used as direct input, previously residing in RIS, are now residing in TDMS with DTN numbers. CR 11015 against Rev 03 of this report is also addressed by a thorough checking during preparation of Rev 04 of this report. Changes are too extensive to be identified by vertical bars at the right margin of each page.

CONTENTS

Page

ACRONYMS xix

1. PURPOSE 1-1
   1.1 PURPOSE AND BACKGROUND 1-1
   1.2 MODEL OVERVIEW 1-2

2. QUALITY ASSURANCE 2-1

3. USE OF SOFTWARE 3-1

4. INPUTS 4-1
   4.1 DIRECT INPUT 4-1
      4.1.1 Qualification of Outside Sources 4-24
   4.2 CRITERIA 4-25
   4.3 CODES AND STANDARDS 4-26

5. ASSUMPTIONS 5-1

6. MODEL DISCUSSION 6-1
   6.1 GENERAL DESCRIPTION OF SCC MODELING 6-1
      6.1.1 General Description of SCC of Alloy 22 6-1
      6.1.2 General Description of SCC of Titanium Alloys 6-3
   6.2 SCC CRACK INITIATION FOR ALLOY 22 6-3
      6.2.1 Laboratory Testing for Alloy 22 SCC Crack Initiation 6-5
      6.2.2 SCC Crack Initiation Threshold Stress Criterion for Alloy 22 6-14
   6.3 DISCUSSION OF MECHANICAL METALLURGY CONCEPTS 6-16
      6.3.1 Uniaxial Data versus Multiaxial Stress 6-16
      6.3.2 Density of Incipient Cracks 6-17
      6.3.3 Incipient Crack Size 6-18
      6.3.4 Manufacturing Flaws 6-19
      6.3.5 Crack Aspect Ratio 6-25
   6.4 THE BASE-CASE SLIP DISSOLUTION–FILM RUPTURE MODEL FOR ALLOY 22 6-25
      6.4.1 Introduction 6-25
      6.4.2 Slip Dissolution–Film Rupture Mechanism 6-26
      6.4.3 Model Quantification 6-30
      6.4.4 Adaptation of Slip Dissolution-Film Rupture Model to Alloy 22 6-33
      6.4.5 Threshold Stress Intensity Factor (K_{ISCC}) 6-41
      6.4.6 Alternative Model: The Coupled Environmental Fracture Model for Alloy 22 6-44
   6.5 EVALUATION OF THE STRESS INTENSITY FACTOR 6-45
      6.5.1 Definition of Stress Intensity Factor 6-46
      6.5.2 Solutions for K_I 6-47

CONTENTS (Continued)

Page

6.5.3 Calculations of Stress and Stress Intensity Factors for Waste Package Closure Welds 6-47
6.5.4 Impact of Corrosion on Stress and Stress Intensity Factor Profiles 6-75
6.5.5 Mitigation of Weld Residual Stress 6-80
6.5.6 Uncertainty and Variability of Residual Stress and Stress Intensity Factor 6-101
6.6 ESTIMATE OF LENGTH AND INTERCRACK SPACING OF RADIAL THROUGH-WALL CRACKING AND CRACK OPENING 6-113
6.6.1 Estimated Length and Intercrack Spacing of Radial Through-Wall Cracking 6-113
6.6.2 Estimate of the Size of Crack Opening 6-113
6.7 SEISMIC CRACK DENSITY MODEL FOR WASTE PACKAGE 6-114
6.7.1 Nature of Seismic Deformation and Crack Growth 6-115
6.7.2 General Approach to Modeling Seismic Crack Density 6-118
6.7.3 Primary Conceptual Model for Crack Area Density: Hexagonal Geometry 6-119
6.7.4 Alternative Conceptual Model for Crack Area Density: Circular Geometry 6-128
6.8 SCC OF TITANIUM DRIP SHIELD MATERIALS 6-131
6.8.1 A Brief Introduction to Titanium Alloys 6-132
6.8.2 SCC Susceptibility of Relevant Titanium Alloys 6-135
6.8.3 SCC Crack Initiation for Drip Shield Materials 6-138
6.8.4 SCC Crack Propagation in Drip Shield Materials 6-160
6.8.5 Modeling Seismic Crack Density for Drip Shield Materials 6-173
6.8.6 SCC Crack "Plugging" 6-180
6.8.7 Lower-Temperature Creep of Titanium Alloys 6-182
6.9 FEATURES, EVENTS AND PROCESSES 6-193

7. MODEL VALIDATION 7-1
7.1 INTENDED PURPOSE OF THE ALLOY 22 SDFR MODEL 7-1
7.1.1 Confidence-Building during Model Development to Establish Scientific Basis and Accuracy for Intended Use 7-1
7.1.2 Confidence-Building after Model Development to Support the Scientific Basis of the Model 7-3
7.2 VALIDATION ACTIVITIES AND ASSOCIATED CRITERIA USED TO DETERMINE THAT THE REQUIRED LEVEL OF CONFIDENCE HAS BEEN OBTAINED 7-5
7.3 COMPARISON OF ACTIVITIES PERFORMED TO GENERATE CONFIDENCE IN THE MODEL WITH MODEL VALIDATION CRITERIA 7-6
7.3.1 Activities Performed for Validating the SDFR Model Using Peer-Reviewed Literature 7-6
7.3.2 Activity Performed for Validating the SDFR Model Applicable to Alloy 22 Using Independently Obtained Experimental Data 7-8

CONTENTS (Continued)

Page

7.3.3 Corroboration of SDFR Model with Available Alternative Conceptual Models 7-14
7.3.4 Activities Performed to Demonstrate the Technical Basis for the Selection of the Threshold Stress Intensity Factor and the Threshold Stress Parameter for SCC Initiation 7-14
7.4 DISCUSSION OF SCC PARAMETERS FOR DRIP SHIELD MATERIALS 7-17
7.4.1 Intended Purpose of the Parameters 7-17
7.4.2 Identification and Documentation of Validation Activities and Associated Criteria to be Used to Determine that the Required Level of Confidence Has Been Obtained for the Drip Shield Seismic Crack Density Model 7-18
7.4.3 Documentation of Activities to be Performed to Generate Confidence in the Model during Model Development 7-19
7.4.4 Other Confidence Building Activities 7-22
7.5 VALIDATION OF SEISMIC CRACK DENSITY MODELS FOR WASTE PACKAGE AND DRIP SHIELD MATERIALS 7-23
7.5.1 Validation Activities for the Waste Package Outer Barrier Seismic Crack Density Model 7-24
7.5.2 Validation Activities for the Drip Shield Seismic Crack Density Model 7-31

8. CONCLUSIONS 8-1
8.1 CONCLUSIONS 8-1
8.1.1 Conclusions of the SCC Initiation Threshold Stress for Alloy 22 8-1
8.1.2 Conclusions of the Slip Dissolution-Film Rupture Model for Alloy 22 8-2
8.1.3 Conclusions on Evaluation of Stress and Stress Intensity Factor Distributions in As-Welded and Plasticity-Burnished Waste Package Closure Weld Lids 8-4
8.1.4 Conclusions of Seismic Crack Density Model for Alloy 22 8-7
8.1.5 Conclusions for Potential SCC Analyses for Titanium Alloys 8-8
8.1.6 Conclusions of Seismic Crack Density Model for Titanium Alloys 8-10
8.2 COMPLIANCE WITH YMP ACCEPTANCE CRITERIA 8-12
8.2.1 System Description and Demonstration of Multiple Barriers 8-12
8.2.2 Degradation of Engineered Barriers 8-14
8.3 SUMMARY OF MODEL AND ANALYSES OUTPUT AND PARAMETERS USED 8-21
8.4 TSPA DATA INPUT PACKAGE FOR SCC OF WASTE PACKAGE OUTER BARRIER AND DRIP SHIELD MATERIALS 8-46
8.4.1 TSPA Parameter(s) Identification and Description 8-47
8.4.2 TSPA Implementation 8-48
8.4.3 Statement and Justification of Uncertainty Treatment 8-53

9. INPUTS AND REFERENCES 9-1
9.1 DOCUMENTS CITED 9-1
9.2 CODES, STANDARDS, REGULATIONS, AND PROCEDURES 9-14

CONTENTS (Continued)

Page

9.3 SOURCE DATA, LISTED BY DATA TRACKING NUMBER 9-15
9.4 OUTPUT DATA..... 9-16
9.5 SOFTWARE CODES..... 9-17

APPENDIX A – DATA QUALIFICATION PLAN A-1

APPENDIX B – MATHCAD CALCULATION FOR *n* VALUES IN TABLE 6-6 .....B-1

APPENDIX C – NORMAL DISTRIBUTION HYPOTHESIS TEST FOR *n* VALUES C-1

APPENDIX D – UNCERTAINTY ANALYSIS OF PEENED STRESS DATA D-1

FIGURES

Page

1-1. Flow Diagram of Alloy 22 Stress Corrosion Cracking Lifetime Modeling Approach 1-3

4-1. Time to Failure versus Applied Stress Ratio in 15% BSW Solution at 105°C 4-8
4-2. Failure Stress versus Time to Failure for GE GRC Run 1 Keno Specimens 4-8
4-3. Time to Failure versus Fraction of Yield Strength for Titanium Specimens in 15% BSW Solution at 105°C 4-9

6-1. Polished and Etched Metallographic Cross Section of GE Specimen #157 of Alloy 22 after over 25,000 hours (approximately 2.9 years) at 93 ksi (641 MPa) in Diluted BSW Solution Showing No Evidence of SCC Initiation 6-8
6-2. 165°C SCW Exposed Alloy 22 Single and Double U-bend Specimens 6-10
6-3. Alloy 22 Double U-Bend Specimens Exposed for 17 Months in 105°C BSW at LTCTF 6-11
6-4. Ratio of the Stress Intensity Factor ($K(\theta)$) of a Crack Making an Angle (θ) with the Stress Direction to the Factor ($K(90°)$) of a Crack Oriented Perpendicular to the Stress Direction as a Function of the Angle (θ), for a Crack with an Arbitrary Stress and Crack Length 6-24
6-5. Schematic Oxidation Charge Density versus Time for a Strained Crack Tip and Unstrained Crack Sides in the Slip Dissolution-Film Rupture Mechanism 6-27
6-6. Schematic of Oxidation Current Density versus Time Following Repeated Oxide Rupture Events 6-29
6-7. Crack Growth Rate (Presented by Observed Data Points and Predicted Curve) versus Crack Tip Strain Rate for Sensitized Stainless Steel Type 304 in Oxygenated 288°C Water 6-32
6-8. Temperature Dependence of Sensitized Stainless Steel Type 304 and Alloy 600 Under Comparable Stress Intensity Factor and Environmental Conditions 6-34
6-9. Crack Growth Rate versus Stress Intensity Factor for Alloy 22 Based on the SDFR Model 6-41
6-10. Comparison of Predicted Crack Growth Rates for Stainless Steel Type 304 6-45
6-11. Sketch of (a) Current License Application Design for Waste Package Final Closure Weld Region (b) Waste Package Closure Welds Configuration that SIA Used for Its Finite-Element Analysis 6-50
6-12. Axisymmetric Model of Naval Long Waste Package, with Thick Sleeve Where the Directions of x, y, and z Are Those of the Three Component Stresses, S_x (radial), S_y (axial), and S_z (hoop) 6-52
6-13. Finite-Element Details in the Fillet Weld and Closure Weld Regions 6-53
6-14. Assignment of Weld Passes in the Fillet Weld and Closure Weld 6-53
6-15. Thermal Boundary Conditions (a) and Structural Boundary Conditions (b) in the Finite-Element Analysis 6-54
6-16. Single-Edge Cracked Plate 6-55
6-17. Elliptical Crack in Infinite Plate 6-55

FIGURES (Continued)

Page

6-18. Through-Wall Section in the Outer Lid Closure Weld 6-56
6-19. Stress Distribution in Naval Long Waste Package Closure Lid Weld at Normal Operating Temperature (257°F or 125°C) 6-60
6-20. Stress Distribution at Room Temperature in Naval Long Waste Package Closure Lid Weld at Room Temperature (70°F or 21°C) 6-61
6-21. Outer Lid Outside Surface Residual Stress Distribution, Thick Upper Portion of Sleeve, at Normal Condition Temperature 6-62
6-22. Outer Lid Outside Surface Residual Stress Distribution, Thick Upper Portion of Sleeve, at Room Temperature 6-63
6-23. Flaw Orientation for Lid Welds 6-64
6-24. Hoop Stresses in Outer Lid of CRM–21-PWR Design at 125°C 6-66
6-25. Selected Cross Sections for CRM-21-PWR Waste Package Design 6-67
6-26. Outer Lid Circumferential Flaw Geometric Correction Factor 6-67
6-27. Through-Wall Stress Distributions in Section A-A of the As-Welded Naval Long Waste Package Outer Closure Lid at Normal Condition Temperature 6-69
6-28. Through-Wall Stress Distributions in Section B-B of the As-Welded Naval Long Waste Package Outer Closure Lid at Normal Condition Temperature 6-70
6-29. Through-Wall Stress Intensity Factor Distributions in Section A-A of the As-Welded Naval Long Waste Package Outer Closure Lid at Normal Condition Temperature 6-72
6-30. Through-Wall Stress Intensity Factor Distributions in Section B-B of the As-Welded Naval Long Waste Package Outer Closure Lid at Normal Condition Temperature 6-73
6-31. Comparison of the Through-Wall Hoop (Sz) Stress Intensity Factor Distributions Using ELL in Sections A-A and B-B of the As-Welded Naval Long Waste Package Outer Closure Lid at Normal Condition Temperature 6-75
6-32. Finite-Element Model Used To Evaluate Effect of Corrosion 6-77
6-33. Effect of Corrosion on Radial Stress in Waste Package Outer Lid 6-78
6-34. Effect of Corrosion on Hoop Stress in Waste Package Outer Lid 6-78
6-35. Stress Intensity Factor for Full-Circumference Flaw in the 25-mm Waste Package Outer Lid 6-79
6-36. Stress Intensity Factor for Radial Elliptical Crack in the 25-mm Waste Package Outer Lid 6-80
6-37. Mitigation of Weld Stress in Alloy 22 with Laser Peening 6-82
6-38. Curve-Fitted Through-Wall Stress Profile, Section A-A, Normal Condition Temperature with Laser Peening 6-84
6-39. Curve-Fitted Through-Wall Stress Profile, Section B-B, Normal Condition Temperature with Laser Peening 6-84
6-40. Curve-Fitted Through-Wall Stress Profile, Section A-A, Normal Condition Temperature with Plasticity Burnishing 6-86
6-41. Curve-Fitted Through-Wall Stress Profile, Section B-B, Normal Condition Temperature with Plasticity Burnishing 6-87

FIGURES (Continued)

Page

6-42. Stress Intensity Factor Distribution in Section A-A, Normal Condition Temperature, Laser-Peened 6-89
6-43. Stress Intensity Factor Distribution in Section B-B, Normal Condition Temperature, Laser-Peened 6-90
6-44. Comparison of the Through-Wall Hoop Stress Intensity Factor Distributions using Elliptical Crack Geometry in Sections A-A and B-B of the Laser-Peened Naval Long Waste Package Outer Closure Lid at Normal Condition Temperature 6-92
6-45. Stress Intensity Factor Distribution in Section A-A, Normal Condition Temperature, Plasticity-Burnished 6-94
6-46. Stress Intensity Factor Distribution in Section B-B, Normal Condition Temperature, Plasticity-Burnished 6-94
6-47. Comparison of the Through-Wall Hoop Stress Intensity Factor Distributions Using Elliptical Crack Geometry in Sections A-A and B-B of the Plasticity-Burnished Naval Long Waste Package Outer Closure Lid at Normal Condition Temperature 6-96
6-48. Comparison of Radial Stress, S_x, (a) and Hoop Stress, S_z, (b) in Waste Package Outer Lid with and without Plasticity Burnishing 6-98
6-49. Stress Intensity Factors due to (a) Radial Stress and (b) Hoop Stress with and without Plasticity Burnishing 6-99
6-50. Comparison of Plasticity Burnishing and Laser Peening for Effect of Stress Mitigation 6-100
6-51. Variation of Hoop Stress versus Depth for As-Welded Waste Package Outer Closure Lid 6-104
6-52. Hoop Stress versus Depth for Plasticity-Burnished Waste Package Outer Closure Lid with Variability as a Function of Angle 6-105
6-53. Variation of Stress Intensity Factor versus Depth for As-Welded Waste Package Outer Closure Lid 6-106
6-54. Stress Intensity Factor versus Depth for Plasticity-Burnished Waste Package Outer Closure Lid with Variability as a Function of Angle 6-107
6-55. Variation and Uncertainty of Hoop Stress ($\theta = 0$) versus Depth for As-Welded Waste Package Outer Closure Lid 6-108
6-56. Hoop Stress ($\theta = 0$) versus Depth for Plasticity-Burnished Waste Package Outer Closure Lid with Uncertainty as a Function of Yield Strength 6-109
6-57. Variation of Stress Intensity Factor ($\theta = 0$) versus Depth for As-Welded Waste Package Outer Closure Lid 6-110
6-58. Stress Intensity Factor ($\theta = 0$) versus Depth for Plasticity-Burnished Waste Package Outer Closure Weld Lid with Uncertainty as a Function of Yield Strength 6-111
6-59. Measured Stress (Using 1-Inch Ring Core Method) versus Depth for Alloy 22 Laser-Peened 1-Inch-Thick Gas Tungsten Arc Welding Welded Plate 6-112
6-60. Measured Stress (Using 1-Inch Ring-Core Method) versus Depth for Alloy 22 Plasticity-Burnished 1-in-thick Gas Tungsten Arc Welding Welded Plate 6-112

FIGURES (Continued)

Page

6-61. Typical Examples of (a) Transgranular Stress Corrosion Cracking and (b) Intergranular SCC in Stainless Steel 6-116
6-62. Parallel Rows of Parallel Cracks Whose Centers are Arranged in a Hexagonal Array (with Row Spacing Equal to the Wall Thickness, *t*) 6-122
6-63. Parallel Rows of Randomly Oriented Cracks with Centers Arranged in a Hexagonal Array (with Row Spacing Equal to Wall Thickness, *t*) 6-122
6-64. Parallel Rows of Parallel Flaws (with Row Spacing Equal to (√3/2) Wall Thickness) 6-124
6-65. Hollow Cylinder of Inner Radius *a* and Outer Radius *b* Subject to Internal Pressure p_i and External Pressure p_o 6-129
6-66. Relationship between Relevant Titanium Alloys 6-135
6-67. Failure Stress versus Time to Failure for GE GRC Keno Test Run 1 Specimens 6-142
6-68. Comparison of Air Creep Rupture Times with Minimum Failure Times in 105°C to 125°C Brine Environments 6-144
6-69. Fracture Morphology for As-Received Titanium Grade 7 Keno Specimen Fracture Surfaces at 105°C: (a) Air and (b) Aqueous Exposure 6-145
6-70. Welded Titanium Grade 12 U-bend Specimen after Five Years Exposure at LTCTF, (A) Side View Top and (B) Apex View 6-148
6-71. Maximum Remaining Tensile Stress versus Exposure Time for Each Titanium Grades 7 and 16 U-Bend Test Specimens Exposed to a Range of Brines without Observed SCC Initiation 6-150
6-72. Maximum Remaining U-Bend Tensile Stress at Each Exposure Interval versus Exposure Time 6-152
6-73. Comparison of Air Creep Rupture Failure Times with Time-on-Test in 60°C to 125°C Brines Without Stress Corrosion Crack Initiation and Maximum Remaining Tensile Stress at Each U-Bend Exposure Interval versus Exposure Time 6-153
6-74. Time-to-Failure versus Percent Yield Strength for Titanium Specimens in 15% BSW Solution at 105°C 6-158
6-75. Elevation of Crevice and Stress Corrosion Temperature Threshold Limits for Alpha-Beta Titanium Alloys (Including Titanium Grade 29) in Aqueous Chloride Media 6-159
6-76. (a) Crack Length and Temperature versus Time Plot of the Stress Corrosion Crack Length and Temperature versus Time Plot of the Stress Corrosion Cracking Response of Specimen c143 (As-Received Titanium Grade 7) at 110°C in a Concentrated Mixed-Salt Environment with 5 psi Over-Pressure of Laboratory Air and (b) Direct Current Potential Drop Indicated Crack Length versus Time for Titanium Grade 7 Tested in 105°C Air at 30 MPa√m 6-162
6-77. Crack Length and Temperature versus Time Plot of the SCC Response of Specimen c148 6-163
6-78. Crack Length versus Time for Titanium Grades 28 (a) and 29 (b) 6-167
6-79. Measured Crack Growth Rate versus Stress Intensity Factor for Titanium Grades 29 (a) and 28 (b) in SCW Solution at 150°C 6-169

FIGURES (Continued)

Page

6-80. Crack Length versus Time for Titanium Grade 29 6-170
6-81. Effect of Sustained-Load Cracking Compared to SCC on K_I in Ti-8Al-1Mo-1V Mill-Annealed Sheet 6-173
6-82. Comparison of 1,000-Hour Creep Response for Titanium Grade 2 with Titanium Grades 5 and 9 Over a Range of Applied Stresses and Temperatures 6-185
6-83. Time to Failure versus Applied Stress for Titanium Grades 2 and 7 Tested in Air at 100°C to 105° 6-187
6-84. Steady-State Creep Rate versus Applied Stress Ratio for Titanium Grades 2 and 7 at Room Temperature and 100°C to 105°C. 6-188
6-85. Comparison of Secondary Creep Rates versus Applied Stress for Titanium Grades 2 and 7 with Titanium Grades 5 and 24 at Room Temperature 6-189
6-86. Comparison of Steady-State Creep Rates of Titanium Grades 2 and 7 with Titanium Grade 5 versus applied stress at 100°C to 260°C. 6-190
6-87. Comparison of Approximate Primary Creep Strains versus Applied Stress for Titanium Grades 2 and 7 at Room Temperature and at 100°C to 105°C and for Titanium Grades 5, 24, And 29 at Room Temperature 6-191
6-88. Crack Length (Indicated by Direct Current Potential Drop) versus Time for Titanium Grade 7 Test in 110°C Air at 30 MPa√m 6-192
6-89 Displacement versus Time for a Round Tensile Specimen of Titanium Grade 29 Tested at a Constant Load Of 63.7 ksi in 150°C Air 6-193

7-1. Frequency Distributions of the Ratio of Calculated to Observed Crack Growth Rates for Stainless Steel Type 304 7-7
7-2. Comparison of the SDFR Prediction Model and Measured Data for Alloy 22 7-13
7-3. Photomacrographs Showing the Apex Region of Two Double U-bend Specimens Exposed to 105°C BSW for 17 Months 7-20
7-4. SEM Micrograph of a Stress Corrosion Crack, Showing Intergranular Attack and Intragranular Stress Cracking 7-35

8-1. Comparison of Air Creep Rupture Failure Times with Time on Test in 60°C to 125°C Brines Without Stress Corrosion Crack Initiation 8-28
8-2. Variation of Hoop Stress versus Depth for As-Welded Waste Package Closure Weld Lid 8-37
8-3. Hoop Stress versus Depth for Plasticity-Burnished Waste Package Outer Closure Lid with Variability as Function of Angle 8-38
8-4. Variation of SIF versus Depth for As-Welded Waste Package Outer Closure Weld Lid 8-39
8-5. Stress Intensity Factor versus Depth for Plasticity-Burnished Waste Package Outer Closure Lid with Variability as Function of Angle 8-40
8-7. Hoop Stress ($\theta = 0$) versus Depth for Plasticity-Burnished Waste Package Outer Closure Lid with Uncertainty as Function of Yield Strength 8-42
8-8. Variation of SIF ($\theta = 0$) versus Depth for As-Welded Waste Package Outer Closure Weld Lid 8-43

FIGURES (Continued)

Page

8-9. Stress Intensity Factor (θ = 0) versus Depth for Plasticity-Burnished Waste Package Outer Closure Weld Lid with Uncertainty as a Function of Yield Strength 8-44

D-1. Fractile Plot of Stress Values D-1
D-2. Probability Plot of Stress Values D-2

TABLES

Page

4-1. Summary of Input Data 4-3
4-2. Measured Crack Growth Rates for Alloy 22 Specimens 4-10
4-3. Coefficients of Stress Profiles for the As-Welded, Laser-Peened, and Plasticity-Burnished Naval Long Waste Package Design 4-11
4-4. Stress Intensity Factor Profiles for the Naval Long As-Welded Waste Package Outer Lid 4-12
4-5. Stress Intensity Factor Profiles for the Naval Long Plasticity-Burnished Waste Package Outer Lid 4-14
4-6. Stress Intensity Factor Profiles for the Naval Long Laser-Peened Waste Package Outer Lid 4-17
4-7. Input Data for Yield Strength, Modulus of Elasticity, and Other Parameters 4-20
4-8. Comparison of Constant-Load Failure Times in Diluted BSW Brine with Those in Air for Titanium Grade 7 4-21
4-9. Summary of LTCTF Titanium Grades 7 and 16 U-Bend Specimen Maximum Remaining Stress Levels 4-22
4-10. Five-Year General Corrosion Rates for Alloy 22 4-23

6-1. Chemical Composition (wt %) of the Alloy 22 Specimens Tested at LTCTF with Heat Numbers 6-9
6-2. Slow Strain Rate Test Results for Annealed Alloy 22 (Strain Rate 1.66×10^{-6} s^{-1}) 6-13
6-3. SCC Initiation Threshold Stress Criteria of Alloy 22 6-15
6-4. Estimation by Interpolation of Alloy 22 Yield Strength at 105°C and 125°C from Yield Strength Values at Other Temperatures 6-16
6-5. Measured Crack Growth Rates (mm/s) in 288°C Oxygenated Water Due to Drop in Corrosion Potential 6-35
6-6. Summary of Source Data for Alloy 22 SDFR Model Quantification 6-37
6-7. Distribution of the Parameter *n* 6-40
6-8. Distribution of the Threshold Stress Intensity Factor, K_{ISCC}, for Alloy 22 6-43
6-9. Stress versus Depth of Proposed Stress Mitigation Treatments 6-59
6-10. Unit Conversion Factors from English Units to Metric Units 6-68
6-11. Stress Coefficients for the As-Welded Naval Long Waste Package Outer Lid 6-71
6-12. Stress and Stress Intensity Factor Profiles for the As-Welded Naval Long Waste Package Outer Lid 6-73
6-13. Stress Coefficients for the Laser-Peened Naval Long Waste Package Outer Lid 6-85
6-14. Stress Coefficients for the Plasticity-Burnished Naval Long Waste Package Outer Lid 6-88
6-15. Stress and Stress Intensity Factor Profiles for the Laser-Peened Naval Long Waste Package Outer Lid 6-91
6-16. Stress and Stress Intensity Factor Profiles for the Plasticity-Burnished Naval Long Waste Package Outer Lid 6-95
6-17. Crack Characteristics for Hexagonal Geometry 6-126
6-18. Crack Characteristics for Circular Geometry 6-130

TABLES (Continued)

Page

6-19. ASTM Specifications for Chemical Compositions (wt %) of Relevant Titanium Alloys 6-132
6-20. ASTM Specifications of Mechanical Properties of Relevant Titanium Alloys 6-134
6-21. Heat and Composition of Materials Tested at GE GRC 6-135
6-22. Input Data for Yield Strength of Titanium Grade 7 6-138
6-23. Input Data for Yield Strength of Titanium Grades 5, 28, and 29 6-139
6-24. Yield Strength of Titanium Grade 7 Material Used in GE GRC Keno Test Measured by GE GRC in 125°C Air 6-140
6-25. Comparison of Constant-Load Failure Times for Titanium Grade 7 in Diluted BSW Brine with Those of Titanium Grades 2 and 7 in Air 6-143
6-26. Yield Strength of Titanium Grade 7 Used in LTCTF U-Bend Test 6-146
6-27. Estimate by Interpolation of Titanium Grade 7 Yield Strength at 60°C and 90°C from Yield Strength Values at Other Temperatures 6-147
6-28. Chemical Composition of Titanium Alloy U-Bend Specimens Test in LTCTF 6-147
6-29. Summary of LTCTF Titanium Grades 7 and 16 U-Bend Specimen Maximum Remaining Stress Levels 6-150
6-30. Data Used to Construct Figure 6-73 6-154
6-31. Example of Interpolation of Titanium Grade 7 Yield Strength at 115°C from Yield Strength Values at Other Temperatures. 6-157
6-32. Summary of Threshold Stress Criteria for SCC Initiation 6-160
6-33. Measured Crack Growth Rates for Titanium Grades 7, 28, and 29 Compact Tension Specimens 6-165
6-34. Crack Growth Rate versus Stress Intensity Factor for Titanium Grade 28 6-167
6-35. Crack Growth Rate versus Stress Intensity Factor for Titanium Grade 29 6-168
6-36. Summary of Threshold Stress Intensity Factor Results for Relevant Titanium Alloys 6-172
6-37. Crack Characteristics for Hexagonal Geometry 6-178
6-38. Crack Characteristics for Circular Geometry 6-180
6-39. Creep Data Used to Construct Figure 6-82 6-186
6-40. FEPs Discussed in this Report 6-193

7-1. Supporting (Corroborating) Information Used to Validate the SDFR Model 7-4
7-2. Nominal Chemical Composition of Several Nickel–Chromium-Based Alloys (wt %) 7-8
7-3. Summary of LTCTF Crack Growth Rates in Compact Tension Specimens 7-12
7-4. Comparison of Predicted and Measured Crack Growth Rates for Alloy 22 7-13
7-5. New Titanium Specimens Added to KENO Test on June 8, 2006 7-20

8-1. Summary of Model Outputs 8-21
8-2. Output Data for Yield Strength and Modulus of Elasticity for Alloy 22 and Titanium Grade 7 8-26
8-3. SCC Initiation Threshold Stress Criteria of Alloy 22 8-28
8-4. SCC Initiation Threshold Stress Criteria of Titanium Alloys 8-29
8-5. Distribution of the Parameter *n* 8-29

TABLES (Continued)

Page

8-6. Distribution of the Threshold Stress Intensity Factor, K_{ISCC}, for Alloy 22 8-29
8-7. Stress Coefficients for the As-Welded Naval Long Waste Package Outer Lid..... 8-31
8-8. Stress Coefficients for the Laser-Peened Naval Long Waste Package Outer Lid 8-31
8-9. Stress Coefficients for the Plasticity-Burnished Naval Long Waste Package Outer Lid 8-32
8-10. Stress and SIF Profiles for the As-Welded Naval Long Waste Package Outer Lid 8-33
8-11. Stress and SIF Profiles for the Laser-Peened Naval Long Waste Package Outer Lid 8-34
8-12. Stress and SIF Profiles for the Plasticity-Burnished Naval Long Waste Package Outer Lid 8-36
8-13. Crack Characteristics for Alloy 22 for Hexagonal Geometry 8-45
8-14. Crack Characteristics for Drip Shield for Hexagonal Geometry 8-46
8-15. TSPA Parameter Information/Specification 8-47

D-1. Descriptive Statistics of Data D-2

INTENTIONALLY LEFT BLANK

ACRONYMS

ACM	alternative conceptual model
AECL	Atomic Energy of Canada Limited
ASM	American Society of Metals
ASME	American Society of Mechanical Engineers
ASTM	American Society of Testing and Materials
AWS	American Welding Society
BSC	Bechtel SAIC Company
BSW	basic saturated water
BWR	boiling water reactor
CEF	coupled environmental fracture
CPB	controlled plasticity burnishing
CRWMS	Civilian Radioactive Waste Management System
DOE	U.S. Department of Energy
DTN	data tracking number
EBS	Engineered Barrier System
ELI	extra-low interstitial
ELL	elliptical crack geometry
FEP	features, events, or processes
GE GRC	General Electric Global Research Center
GTAW	gas tungsten arc welding
HIC	hydrogen-induced cracking
HLW	high-level radioactive waste
LLNL	Lawrence Livermore National Laboratory
LRO	long-range ordering
LTCTF	Long-Term Corrosion Test Facility
LWR	light water reactor
M&O	Management and Operating Contractor
NACE	National Association of Corrosion Engineers
NDE	nondestructive examination
NRC	U.S. Nuclear Regulatory Commission
OCRWM	Office of Civilian Radioactive Waste Management
PWR	pressurized water reactor
QA	quality assurance

ACRONYMS (Continued)

SAW	simulated acidified water
SCC	stress corrosion cracking
SCDM	seismic crack density model
SCE	saturated calomel electrode
SCW	simulated concentrated water
SD	standard deviation
SDW	simulated dilute water
SDFR	slip dissolution–film rupture
SECP	single-edge cracked plate
SEM	scanning electron microscope
SFE	stacking fault energies
SHE	standard hydrogen electrode
SIA	Structural Integrity Associates
SIF	stress intensity factor
SLC	sustained load cracking
SNF	spent nuclear fuel
SNL	Sandia National Laboratories
SSRT	slow strain rate test
STN	software tracking number
TCP	tetrahedrally close-packed
TSPA	total system performance assessment
TWP	technical work plan
UNS	unified numbering system
VA	validation activities
YMP	Yucca Mountain Project
YS	yield strength
$YS_{(T)}$	yield strength at temperature T

1. PURPOSE

1.1 PURPOSE AND BACKGROUND

Stress corrosion cracking (SCC) is one of the most common corrosion-related causes for premature breach of metal structural components. SCC is the initiation and propagation of cracks in structural components due to three factors that must be present simultaneously (Jones 1992 [DIRS 169906], Section 8.1): metallurgical susceptibility, critical environment, and sustained tensile stresses. The purpose of this report is to provide an evaluation of the potential for SCC of the Engineered Barrier System (EBS) components (i.e., the waste package outer barrier and drip shield) under repository relevant exposure conditions. For the waste package outer barrier and drip shield, the critical environment is taken as any aqueous environment contacting the metal surfaces. This is conservative because SCC usually requires an aqueous environment that is corrosive to the the waste package and drip shield materials.

The waste package outer barrier contributes to waste isolation by keeping water away from the waste for its lifetime and, when breached, by reducing both the contact of water with the waste and the radionuclide release rate from the waste. The drip shield barrier contributes to waste isolation by keeping seepage waters and falling rocks away from the waste package for its lifetime and, when breached by SCC, by reducing the contact of water with the waste package.

An SCC breach of the waste package outer barrier and drip shield materials would initiate and propagate tight, sometimes branching, cracks that might be induced by the combination of an aggressive environment and tensile stresses developed in the drip shields or the waste packages. The Stainless Steel Type 316 inner structural cylinder of the waste package is excluded from the SCC evaluation because the total system performance assessment (TSPA) does not take credit for the inner cylinder as part of the performance barrier.

This document provides a detailed description of the process-level models that can be applied to assess the performance of Alloy 22 (UNS N06022) (for the waste package outer barrier) and titanium alloys (Titanium Grades 7 for the drip shield plate, 29 for the structural support, and 28 for the Titanium Grades 7/29 weld-filler metal) subjected to SCC effects. Plasticity-burnishing (more generically referred to as low plasticity burnishing) or other residual stress mitigation techniques were considered as a means of mitigating SCC in the waste package final closure lid weld. In the current design for license application, plasticity burnishing has been adopted as the stress mitigation method.

This report is prepared in compliance with *Technical Work Plan for Postclosure Engineered Barrier Degradation Modeling* (SNL 2007 [DIRS 178849]). As directed by the technical work plan (TWP), abstraction models (i.e., the seismic crack density models (SCDMs)), were developed to model the crack area density (defined as the crack opening area per unit of seismically damaged area) of the waste package outer barrier and the drip shield subjected to seismic activity. This activity was conducted by the Performance Assessment Department of Waste Package Corrosion and Early Failure. The estimates of crack area density resulting from the modeling activities, along with the abstraction models, provide information to address *Yucca Mountain Review Plan, Final Report* (NRC 2003 [DIRS 163274]) acceptance criteria.

1.2 MODEL OVERVIEW

Stress corrosion cracking is the initiation and propagation of cracks in metal components under stress in corrosive environments. For SCC to occur, three factors must exist simultaneously: material susceptibility, critical environment, and a sustained tensile stress. Although Alloy 22, the material used for the waste package outer barrier, is highly corrosion resistant, SCC might occur under certain combinations of these three factors. A lifetime-modeling approach was developed to assess the degradation of the waste package outer barrier due to this potential for stress corrosion cracking. The treatment of the Alloy 22 waste package outer barrier material susceptibility to stress corrosion cracking under the repository environment and the coexisting stress conditions is addressed in this document in Sections 6.2 through 6.7.

Since the waste package is solution-annealed to remove welding residual stresses, only the waste package closure weld flaws will act as possible initiation sites for potential SCC. Therefore, only the waste package closure weld flaws are considered in this report. For the drip shield, weld flaws are not addressed because the drip shield is thermally stress-relieved before emplacement.

Figure 1-1 illustrates how the lifetime-modeling approach considers crack initiation and the stress threshold that defines crack initiation (Section 6.2), mechanical metallurgical concepts (Section 6.3), the base case of the slip dissolution-film rupture (SDFR) model (Section 6.4), stress and stress intensity factor conditions that drive crack initiation and propagation (Section 6.5), threshold stress intensity factor (K_{ISCC}) (Section 6.4.5) that defines propagation of initiated incipient cracks and manufacturing flaws, and the crack-growth model (based on the SDFR theory) that determines the crack growth rate (Section 6.4.4). SCC and residual stresses are modeled only for Alloy 22 closure welds. The seismic crack densities are modeled for both Alloy 22 waste package and drip shield.

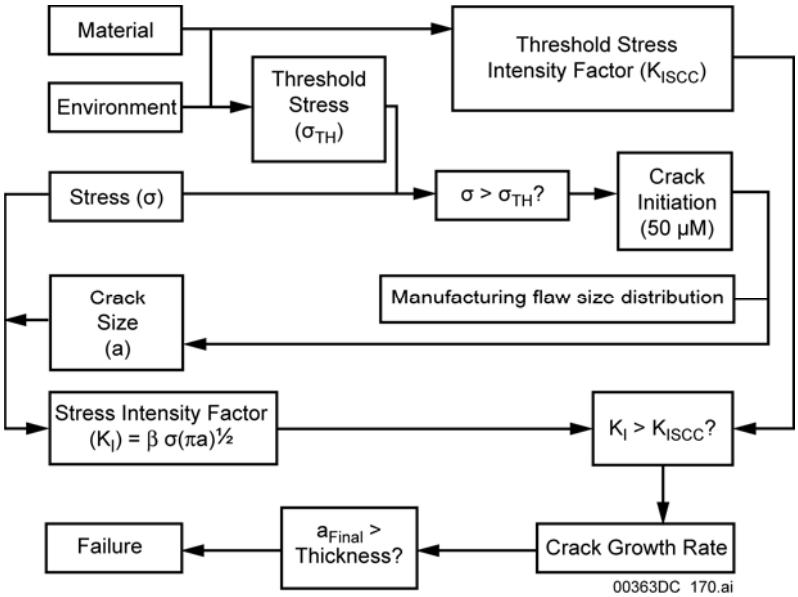

NOTE: When an indicated value of σ, K_I, or a_{Final} is less than the indicated parameter value, the corresponding crack initiation, crack growth, or breach (lifetime) does not occur.

Figure 1-1. Flow Diagram of Alloy 22 Stress Corrosion Cracking Lifetime Modeling Approach

In addition, an estimated length and intercrack spacing of radial through-wall cracks is provided in Section 6.6.1, and an estimate of the size of crack openings for through-wall cracks is given in Section 6.6.2. These analyses were conducted based on established engineering methods and practices, and no new models were developed. Therefore, no model validation is required. Section 6.8 provides technical bases for potential SCC in the drip shield. The general mechanical and chemical properties of the relevant and analogue titanium alloys (Titanium Grades 2, 7, and 16; Titanium Grades 5, 23, 28, and 29) and their susceptibilities to SCC are briefly introduced in Sections 6.8.1 and 6.8.2, respectively. Section 6.8.3 discusses the initiation criteria for SCC in Titanium Grades 7 and 28/29. The SCC initiation threshold stress criteria are established in Section 6.8.3.1.3 for Titanium Grade 7 and in Section 6.8.3.2.3 for Titanium Grades 28/29. The crack growth of Titanium Grades 7 and 28/29 is discussed in Section 6.8.4. Section 6.8.5 develops the seismic crack density model (SCDM) for the titanium drip shield material. The titanium SCC crack "plugging" and low-temperature creep phenomena of titanium alloys are discussed in Sections 6.8.6 and 6.8.7, respectively.

Technical Work Plan for Postclosure Engineered Barrier Degradation Modeling (SNL 2007 [DIRS 178849], Section 2.3.2) states that the drip shield SCC modeling warrants a low level of confidence (Level I). These drip shield SCC-related subjects will be validated in Sections 7.4 and 7.5.2 by using the validation activities specified in *Technical Work Plan for Postclosure Engineered Barrier Degradation Modeling* (SNL 2007 [DIRS 178849], Section 2.3.2).

However, of the drip shield-related subjects discussed in Section 6.8, only the SCDM is developed as a model. No model development is conducted in the following activities: (1) the drip shield crack growth rate (Section 6.8.4) is a measured parameter; (2) the low-temperature creep section (Section 6.8.7) summarizes the literature observations on the subject; and (3) the SCC crack initiation threshold stress criteria are experimentally derived parameters. This is also true for the SCC crack "plugging" section (Section 6.8.6). However, for purposes of defensibility, explicit confidence-building activities were conducted for these subjects. For the drip shield, the SCC initiation threshold stresses (for Titanium Grades 7, 28, and 29) (Section 6.8.3), and threshold stress intensity factors (for Titanium Grades 7, 28, and 29) (Sections 6.8.4.2.2 and 6.8.4.2.4) are discussed in Section 7.4 to provide additional confidence. The SCDM will be validated in Section 7.5.2.

In Section 8, the SCC modeling approach provides the elements necessary to perform a lifetime prediction of the waste package outer barrier subjected to stress corrosion cracking. "Lifetime" is defined as the time for an initiated crack to grow through a wall. These elements are listed in Section 8 as (1) conclusions (Section 8.1), (2) compliance with Yucca Mountain Project (YMP) acceptance criteria (Section 8.2), and (3) model outputs (Section 8.3). For the TSPA, this report feeds parameters related to: (1) SCC initiation for the waste package; (2) stress and stress-intensity factor profiles of waste package, and (3) the SDFR model for the waste package. Section 8.4 summarizes the TSPA data input package provided by this report. Brief descriptions are provided for identification and description of TSPA parameter(s) (Section 8.4.1), TSPA implementation (Section 8.4.2) and justification of uncertainty treatment (Section 8.4.3).

The models developed in this report for potential SCC of waste package and drip shield materials are limited to being applicable only in the repository relevant environments. The seismic crack density models developed for the waste package and drip shields are applicable for seismic events and instances where residual stress results in exceedance of the yield stress criteria.

2. QUALITY ASSURANCE

All waste package configurations and drip shields have been determined to be important to waste isolation and are classified as "Safety Category" in *Q-List* (SNL 2006 [DIRS 175539], Table A-1) and in *Safety Classification of SSCs and Barriers* (BSC 2005 [DIRS 174836], Section 6.4.2).

This report has been developed per SCI-PRO-006, *Models*, as per *Technical Work Plan for Postclosure Engineered Barrier Degradation Modeling* (SNL 2007 [DIRS 178849]). The inputs to this report are documented according to SCI-PRO-004, *Managing Technical Product Inputs*. The methods used to control the electronic management of data as required by IM-PRO-002, *Control of the Electronic Management of Information*, were accomplished in accordance with the TWP. The process for control of the electronic management of information on evaluation of work activities, processes, or process functions outlined in Section 5.0 of IM-PRO-002, is followed to ensure accuracy, completeness, and security of electronic information and data used in preparation of this report.

Preparation of the TWP and this report are subject to the requirements of the U.S. Department of Energy (DOE) *Quality Assurance Requirements and Description* (DOE 2007 [DIRS 182051]).

INTENTIONALLY LEFT BLANK

3. USE OF SOFTWARE

No software or computer codes qualified and controlled in accordance with IM-PRO-003, *Software Management,* were used in developing this report. The computer software-generated data on through-thickness residual stress and stress intensity factor profiles at the waste package outer closure welds were obtained by procurement from a qualified vendor. These data, presented in DTN: MO0708RTSWRS06.000 [DIRS 182558], file *BSC-03Q-301-R2.pdf*, were developed using computer software internally qualified by the vendor (SIA, San Jose, California) in compliance with the Structural Integrity Associates Quality Assurance Program, which was approved by the YMP Office of Quality Assurance.

Microsoft Excel 97 was used to perform support calculations and graphics. Microsoft Excel 97 is a standardized commercial spreadsheet program designed to assist in routine calculations and graphics. Microsoft Excel 97 is a commercial off-the-shelf software program exempt from software qualification in accordance with Section 2.1 of IM-PRO-003. Furthermore, according to IM-PRO-003, Section 2.1, the use of Excel for graphical representation is exempt, as are the calculations using built-in mathematical functions. When Excel is used for calculations (Section 6.4.4), information required for an independent person to reproduce the work (including the formula or algorithm used, and listing of inputs or outputs) is provided. The calculations using Microsoft Excel 97 can be independently performed on any platform capable of running this commercial software program, including Windows 95, 98, 2000, and NT.

MathCad 2001i was used in Section 6.4 to perform computations for this report. The program provides built-in mathematical functions that can be used to automate the calculation process. It also includes a graphics package to assist in data presentation. The computations performed in this report using MathCad 2001i use only standard functions and produce results independent of the software program used. MathCad 2001i is a commercial off-the-shelf software program exempt from software qualification in accordance with Section 2.1 of IM-PRO-003. Furthermore, the use of MathCad 2001i for graphical representation is exempt per Section 2.1 of IM-PRO-003, as are calculations using built-in mathematical functions. When MathCad 2001i is used for calculations (Section 6.4), information required for an independent person to reproduce the work (including formula or algorithm used, and listing of inputs or outputs) is provided.

INTENTIONALLY LEFT BLANK

4. INPUTS

4.1 DIRECT INPUT

The input data for the development of parameters or other databases, or both, used in the models or analyses in this document are summarized in Table 4-1. The data source, the data tracking number (DTN) if available, and a description of how the data are used in the model development are also described in Table 4-1. The uncertainties of the input data are discussed throughout the relevant subsections in Section 6. The details of the input data that are used in the model development and discussions are listed in Table 4-2 through Table 4-10 and shown in Figure 4-1 through Figure 4-3. Direct inputs used to develop the models are not used to validate the models.

Model input data have been selected and managed in accordance with SCI-PRO-004, *Managing Technical Product Inputs*. Some of the developed data were obtained from established fact. In addition, some inputs received in English units are presented as is, although all output units in Section 8.3 are in metric units. To ensure transparency, some direct input data in this section have been rearranged from the original data.

Input data shown in Figure 4-1 and Figure 4-2 are used in Section 6.8.3 for determination of the threshold stresses for crack initiation for Titanium Grade 7. Input data shown in Figure 4-3 are used in Section 6.8.3 as Figure 6-74 for analysis of SCC threshold stress criterion for Titanium Grades 28 and 29. The data to estimate the time to failure for these materials are taken from the figures that are contained in the reports referenced therein.

The term "yield strength" (YS) and its value(s) are frequently used in this document. However, the yield strength value(s) referred to in Section 6.2, where the SCC crack initiation is discussed based on test data, are experimentally measured data while in Section 6.5, where the stress and stress intensity factor distributions are evaluated, the at-temperature yield strength ($YS_{(T)}$) is normally used. Because the finite-element analysis was performed at the "normal" operating temperature, 125°C, in Section 6.5, the term, $YS_{(125°C)}$, and its value interpolated to other temperatures are frequently used.

Section 6.8.3 discusses the results obtained at the General Electric Global Research Center (GE GRC) (DTN: MO0705SCCIGM06.000 [DIRS 180869], file: *GE-GRC-Final_Sept-2006-Rev3.doc*, Table 8) and the Lawrence Livermore National Laboratory (LLNL) Long-Term Corrosion Test Facility (LTCTF) using their Titanium Grade 7 yield strength values. However, this document uses yield strength values specified in *2001 ASME Boiler and Pressure Vessel Code (includes 2002 addenda)* (ASME 2001 [DIRS 158115], Section II, Part D, Table Y-1, pp. 632 to 634) for modeling.

The data provide reasonable and appropriate measures of the mechanical properties of the Alloy 22 and titanium alloys used in construction of the waste package outer barrier and drip shield. Section 6.5 evaluates stress and stress intensity factor distribution and their uncertainties and variabilities using the yield strength of Alloy 22 at 125°C.

Conversions from English units to metric units are accomplished using conversion factors from *Metals Handbook* (Boyer and Gall 1997 [DIRS 155318], pp. 1-55 and 1-57). In particular, the English unit, ksi, has been converted to the metric unit, MPa, according to 1 ksi = 6.894757 MPa (Boyer and Gall 1997 [DIRS 155318], p. 1-57) and the English unit, inches, has been converted to the metric unit, mm, according to 1 inch = 2.54×10^{-2} m (Boyer and Gall 1997 [DIRS 155318], p. 1-55), which is equal to 25.4 mm. These conversion factors are considered established fact in accordance with SCI-PRO-004, *Managing Technical Product Inputs*, because they are information accepted by the scientific and engineering community as established fact obtained from a source that scientists would use in their standard work practices.

It should be noted that—as will be indicated in Section 6.8.1—as far as the mechanical properties are concerned, the drip shield-relevant titanium alloys discussed in this report can be divided into two groups, the lower strength alloys such as Titanium Grades 2, 7, and 16; and the higher strength alloys such as Titanium Grades 5, 23, 24, and 29. Also, as will be seen from Table 6-19 and Table 6-20, it is clear that the slightly lower yield strength of Titanium Grade 29 as compared with its non-ruthenium analogue, Titanium Grade 5, is due to its lower oxygen content (0.13 wt % as compared with 0.20 wt %), rather than to the presence of ruthenium, because the yield strength of Titanium Grade 24 is identical to that of Titanium Grade 5 (both are 0.20 wt % oxygen). Similarly, adding palladium to Titanium Grade 2, yielding Titanium Grades 7 or 16, does not alter the mechanical properties of Titanium Grade 2. Based on this, Titanium Grades 2, 7, and 16 are reasonably treated as approximately equivalent materials, aside from corrosion behavior, as are Titanium Grades 5, 23, 24, and 29. Similarly, Titanium Grade 28 is considered as identical to Titanium Grade 9.

Table 4-1. Summary of Input Data

Data Name	Data Source	DTN	Description
For Alloy 22			
Crack Initiation Measurements for Alloy 22 and Titanium Grade 7 Specimens	*Stress Corrosion Crack Initiation & Growth Measurements in Environments Relevant to High Level Nuclear Waste Packages* (DTN: MO0705SCCIGM06.000 [DIRS 180869], file *GE-GRC-Final_Sept-2006-Rev3.doc*, Figure 21)	MO0705SCCIGM06.000 [DIRS 180869]	Input data are shown in Figure 4-1. Input data are used in Section 6.2 for determination of the threshold stresses for crack initiation for Alloy 22.
Measured Crack Growth Rates for Alloy 22 Specimens	*Stress Corrosion Crack Initiation & Growth Measurements in Environments Relevant to High Level Nuclear Waste Packages* (DTN: MO0707SCCIGMER.000 [DIRS 182202]) Stress Corrosion Crack Growth and Initiation Measurements for C-22 and Ti-7, GE GRC 121202. Submittal date: 01/08/2003 [DIRS 161253] (DTN: MO0705SCCIGM06.000 [DIRS 180869])	MO0707SCCIGMER.000 [DIRS 182202] LL021105312251.023 [DIRS 161253] MO0705SCCIGM06.000 [DIRS 180869]	Input data are listed in Table 4-2. Input data are used in Section 6.4.4 for determination of the repassivation slope *n* of the slip dissolution–film rupture model.
V_{gc}, General Corrosion Rates for Alloy 22	LTCTF Corrosion Rate Calculations for Five-Year Exposed Alloy C22 Specimens Cleaned Under TIP-CM-51. Submittal date: 5/28/2003	LL030412512251.057 [DIRS 163712]	Corrosion rate calculations for Alloy 22 after more than five years of exposure. Input data are listed in Table 4-10. Input data are used in Section 6.4.5 for discussion on the threshold stress intensity factor (K_{ISCC}).
Coefficients of Stress Profiles, A_0, A_1, A_2, and A_3	Calculation package: *Weld Residual Stress and Fracture Mechanics Study of Outer Lid Closure Weld of Naval Long Waste Package Configuration* (DTN: MO0708RTSWRS06.000 [DIRS 182558], file *BSC-03Q-301-R2.pdf*)	N/A	Input data are listed in Table 4-3. Input data are used in Section 6.5.3 for stress profiles in as-welded, laser-peened, and plasticity-burnished Alloy 22 closure lids.

Table 4-1. Summary of Input Data (Continued)

Data Name	Data Source	DTN	Description
Stress Intensity Factor Profiles	Calculation package: *Weld Residual Stress and Fracture Mechanics Study of Outer Lid Closure Weld of Naval Long Waste Package Configuration* (DTN: MO0708RTSWRS06.000 [DIRS 182558], file *NdStrs-R2.xls*	N/A	Input data are listed in Table 4-4, Table 4-5and Table 4-6. Input data are used in Section 6.5.3 for evaluation of stress and stress intensity factors for waste package closure welds.
Circumferential Variation in Weld Residual Stress	Structural Integrity Associates Calculation Files 2004, Calculation TRW-06Q-304 [DIRS 171792], p. 4	MO0409GGSIACAL.000 [DIRS 171792]	Input data (5 ksi about the mean stress) are used in Section 6.5.6 for uncertainty analysis.
Yield Strength for Alloy 22	Physical and Chemical Characteristics of Alloy 22	MO0003RIB00071.000 [DIRS 148850] (Relevant data from Alloy Digest 1985 [DIRS 178194], p. 2, Table 3)	This is the data for 0.028-in to 0.125-in (0.71-mm to 3.2-mm) -thick sheet. Input data are listed in Table 4-7. For conservatism purposes, the higher values are used in Sections 6.2 and 6.5 for Alloy 22 SCC crack initiation stress threshold criteria and evaluation of residual stress and stress intensity factor distribution and uncertainty analysis.
Yield Strength for Alloy 22	Physical and Chemical Characteristics of Alloy 22	MO0003RIB00071.000 [DIRS 148850] (Relevant data from Haynes International 1988 [DIRS 101995], p. 15)	This is the data set for 0.25-in to 0.75-in (6.4-mm to 19.1-mm) -thick plate. Input data are listed in Table 4-7 and are used in Section 6.7 for SCDM.
E (Modulus of Elasticity) for Alloy 22	Physical and Chemical Characteristics of Alloy 22	MO0003RIB00071.000 [DIRS 148850] (Relevant data from Hastelloy Alloy C-22. (Haynes International 1988 [DIRS 101995], p. 15)	This is the data set for 0.028-in to 0.125-in (0.71-mm to 3.2-mm) -thick sheet. Input data are listed in Table 4-7 and are used in Sections 6.2 and 6.5.6 for Alloy 22 SCC and model uncertainty analysis.
Initial Size of Incipient Cracks	"Development and Use of a Predictive Model of Crack Propagation in 304/316L, A533B/A508 and Inconel 600/182 Alloys in 288°C Water" (Ford and Andresen 1988 [DIRS 118611]).	N/A	Qualified in Section 6.2.1. Input data (0.05-mm incipient flaw size) used in Section 6.2 for discussion of SCC initiation threshold stress criterion for Alloy 22.

Table 4-1. Summary of Input Data (Continued)

Data Name	Data Source	DTN	Description
For Titanium Alloys			
Crack Initiation Measurements for Alloy 22 and Titanium Grade 7 Specimens	DTN: MO0705SCCIGM06.000 [DIRS 180869], file *GE-GRC-Final_Sept-2006-Rev3.doc*, Figure 21	MO0705SCCIGM06.000 [DIRS 180869]	Input data are shown in Figure 4-1. Input data are used in Section 6.8.3 for determination of the threshold stresses for crack initiation for Titanium Grade 7.
Time to Failure versus Percent Yield Strength for Titanium Specimens in 15% BSW Solution at 105°C.	DTN: MO0705SCCIGM06.000 [DIRS 180869], file *GE-GRC-Final_Sept-2006-Rev3.doc*, Figure 22	MO0705SCCIGM06.000 [DIRS 180869]	Input data are shown in Figure 4-3. Input data are used in Section 6.8.3 as Figure 6-74 for analysis of SCC threshold stress criterion for Titanium Grades 28 and 29.
Time to failure vs applied stress for Titanium Grade 7 in air.	DTN: MO0705SCCIGM06.000 [DIRS 180869], file *GE-GRC-Final_Sept-2006-Rev3.doc*, Figures 27 and 29.	MO0705SCCIGM06.000 [DIRS 180869]	Input data are used in Section 6.8.3 for determination of the threshold stresses for crack initiation for Titanium Grade 7.
Failure Stress versus Time to Failure for Titanium, Alloy 22, and Stainless Steels	*Stress Corrosion Crack Initiation & Growth Measurements in Environments Relevant to High Level Nuclear Waste Packages*	DTN: LL021105312251.023 [DIRS 161253], Figure 2-5.	SCC initiation measurements for Alloy 22 and Titanium Grade 7. Input data are shown in Figure 4-2. Input data are used in Section 6.8.3 for determination of the threshold stresses for crack initiation for Titanium Grade 7.
Yield Strength for Titanium Grade 7	*2001 ASME Boiler and Pressure Vessel Code (includes 2002 addenda)* (ASME 2001 [DIRS 158115], Section II, Part D, Table Y-1, pp. 632 to 634)	N/A	Input data are listed in Table 4-7 and are used in Sections 6.8.3 and 6.8.5 for discussing drip shield SCC initiation threshold stress criterion and seismic crack density.
Yield Strength for Titanium Grade 7	DTN: MO0707SCCIGMER.000 [DIRS 182202], Table 2-4	MO0707SCCIGMER.000 [DIRS 182202]	Input data are listed in Table 4-7 and are used in Sections 6.8.3 and 6.8.5 for discussing drip shield SCC initiation threshold stress criterion
Yield Strength for Titanium Grade 7	Physical and Chemical Characteristics of Ti Grade 7 and 16. Submittal date: 03/13/2000 [DIRS 152926]	MO0003RIB00073.000 [DIRS 152926]	Input data are listed in Table 4-7 and are used in Sections 6.8.3 and 6.8.5 for discussing drip shield SCC initiation threshold stress criterion
E (Modulus of Elasticity) for Titanium Grade 7	Physical and Chemical Characteristics of Ti Grade 7 and 16. Submittal date: 03/13/2000 [DIRS 152926]	MO0003RIB00073.000 [DIRS 152926]	Input data are listed in Table 4-7 and are used in Section 6.8.5 for modeling seismic crack density of drip shield.

Table 4-1. Summary of Input Data (Continued)

Data Name	Data Source	DTN	Description
Yield Strength for Titanium Grades 23 and 29	*Standard Specification for Titanium and Titanium Alloy Strip, Sheet, and Plate*. (ASTM B 265-02 [DIRS 162726])	N/A	Input data are listed in Table 4-7 and are used in Sections 6.8.3.2 for discussing drip shield SCC initiation threshold stress criterion
Yield Strength for Titanium Grades 23 and 29[a]	"Selection of Titanium Alloys for Design." (Donachie 2002 [DIRS 178207], Table 7)	N/A	Input data are listed in Table 4-7 and are used in Sections 6.8.3.2 for discussing drip shield SCC initiation threshold stress criterion
Yield Strength for Titanium Grade 29	DTN: MO0705SCCIGM06.000 [DIRS 180869], file *GE-GRC-Final_Sept-2006-Rev3.doc*	MO0705SCCIGM06.000 [DIRS 180869]	Input data are listed in Table 4-7 and are used in Sections 6.8.3.2 for discussing drip shield SCC initiation threshold stress criterion
Yield Strength for Titanium Grade 28	ASTM B 265-02 [DIRS 162726]	N/A	Input data are listed in Table 4-7 and are used in Sections 6.8.3.2 for discussing drip shield SCC initiation threshold stress criterion
Constant Load Failure Times in Diluted BSW Brine and in Air	DTN: MO0707SCCIGMER.000 [DIRS 182202], Tables 2-2 to 2-4, and 2-7, Figures 6-3 to 6-6) *Preliminary Analysis of the Creep Behaviour of Nuclear Fuel-Waste Container Materials* (Dutton et al. 1996 [DIRS 175817], Table 1, Figure 13).	MO0707SCCIGMER.000 [DIRS 182202]	Input data are shown in Table 4-8 and are used in Section 6.8.3 for analysis of SCC threshold stress criterion for Titanium Grade 7.
LTCTF Titanium Grades 7 and 16 U-Bend Specimen Remaining Stress Levels	Report: 1181-13258-R2. DTN: MO0708XRAYDRST.000 [DIRS 182572], Appendix, pp.. 23 to 71	N/A	Input data are shown in Table 4-9 and are used in Section 6.8.3 for analysis of SCC threshold stress criterion for Titanium Grade 7.

Table 4-1. Summary of Input Data (Continued)

Data Name	Data Source	DTN	Description
Measured Crack Growth Rates for Titanium Grades 7/28/29 Contact Tension Specimens	DTN: MO0707SCCIGMER.000 [DIRS 182202], Table 1-7 DTN: MO0705SCCIGM06.000 [DIRS 180869], file *GE-GRC-Final_Sept-2006-Rev3.doc*, Table 3	MO0707SCCIGMER.000 [DIRS 182202] MO0705SCCIGM06.000 [DIRS 180869]	Input data are used in Section 6.8.4 as Table 6-33 for analysis of SCC crack growth for Titanium Grades 7, 28, and 29.

NOTES: [a] In Donachie 2002 [DIRS 178207], Table 7, only the yield strength values of Ti-6Al-4V (Titanium Grade 5) are listed. However, Titanium Grades 23 and 29 are extra low interstitial variants for Titanium Grade 5 (Ti-6Al-4V) that result in a small reduction in room temperature yield strength (10 ksi or 8%). Because of the same alloying element compositions, the reduction in yield strength with temperature should be equivalent.

Some of the yield strength input data are with the English units in the input sources. The English unit, ksi, has been converted to the metric unit, MPa, according to 1 ksi = 6.894757 MPa (Boyer and Gall 1997 [DIRS 155318], p. 1-57).

BSW = basic saturated water.

As indicated in Section 1.2, of the drip shield-related subjects discussed in Section 6.8, only the seismic crack density model (SCDM) is considered a model. The following subjects are not considered models: (1) the drip shield SCC crack growth rat e (Section 6.8.4) is a measured parameter; (2) the low-temperature creep section (Section 6.8.7) summarizes the literature observations on the subject; and (3) the SCC crack initiation threshold stress criteria (these are considered as the experimentally derived parameters). These parameters are developed and validated for defensibility only. Therefore, the data used for developing these parameters are not necessarily qualified as those used for model development.

As indicated in the readme file of DTN: MO0708RTSWRS06.000 [DIRS 182558], "*NdStrs-R2.xls*" is mislabeled as "*NdStrs-R1.xls*." The correct filename, "*NdStrs-R2.xls*," is used throughout this report, although there is no difference between "*NdStrs-R1.xls*" and "*NdStrs-R2.xls*."

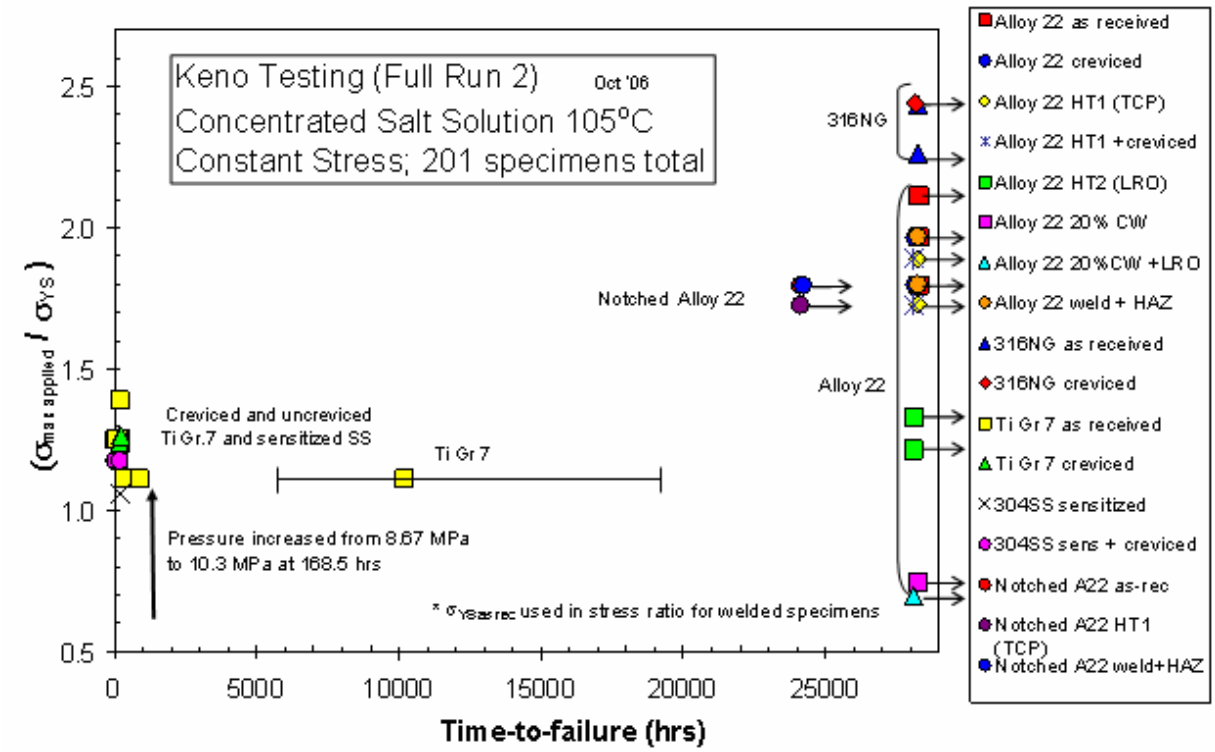

Source: DTN: MO0705SCCIGM06.000 [DIRS 180869], file *GE-GRC-Final_Sept-2006-Rev3.doc*, Figure 21.

Figure 4-1. Time to Failure versus Applied Stress Ratio in 15% BSW Solution at 105°C

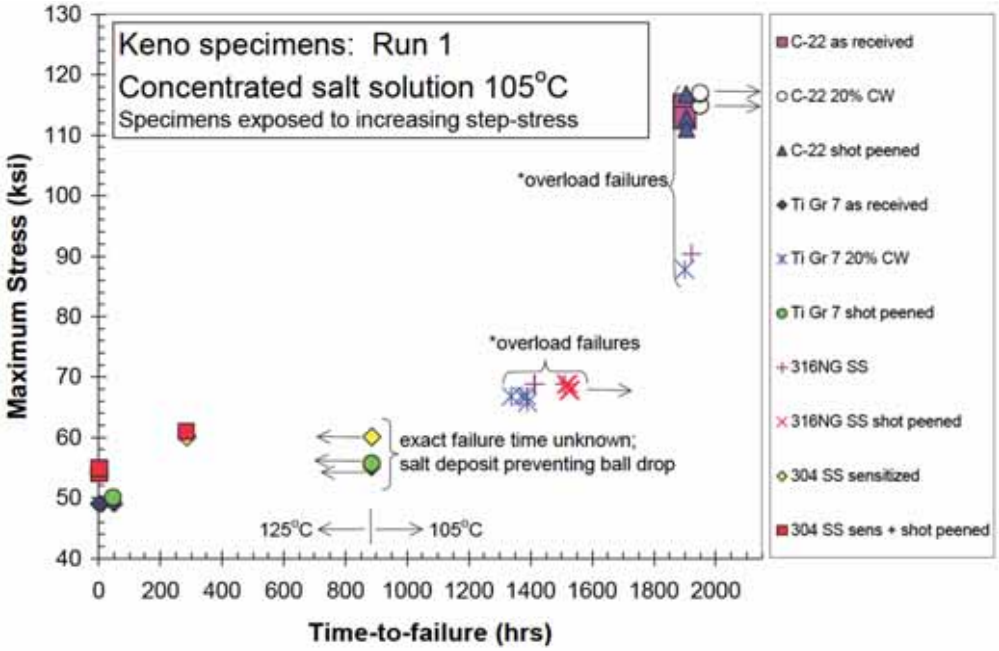

Source: DTN: LL021105312251.023 [DIRS 161253], Figure 2-5.

NOTES: Stress was incrementally increased during testing. The maximum applied stress (which equals the failure stress) is plotted.

Figure 4-2. Failure Stress versus Time to Failure for GE GRC Run 1 Keno Specimens

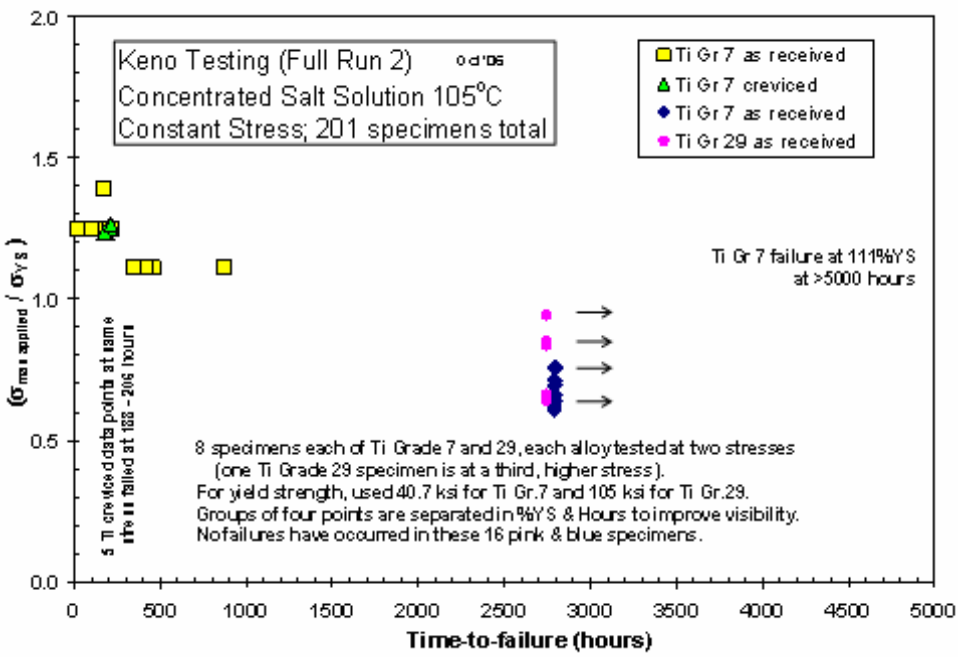

Source: DTN: MO0705SCCIGM06.000 [DIRS 180869], file *GE-GRC-Final_Sept-2006-Rev3.doc*, Figure 22.

Figure 4-3. Time to Failure versus Fraction of Yield Strength for Titanium Specimens in 15% BSW Solution at 105°C

Table 4-2. Measured Crack Growth Rates for Alloy 22 Specimens

Specimen	Test Environment (Specimen Condition)	Cyclic Frequency	Maximum Load Hold Time (hrs)(s)	Stress Intensity Factor (MPa(√m))	Crack Growth Rate (mm/s)[a]	Source
C153	110°C BSW (20% Cold-worked)	0.001 Hz @ R= 0.7	CL[b]	30	5.0×10^{-10}	DTN: LL021105312251.023 [DIRS 161253], p. 11
C144	110°C BSW (Mill-annealed)	0.001 Hz @ R= 0.7	1 (3,000)	30	$< 10^{-11}$ mm/s [c]	DTN: LL021105312251.023 [DIRS 161253], p. 7
C152	110°C BSW (Mill-annealed)	0.001 Hz @ R= 0.7	1 (3,000) 2.5 (9,000) 24 (85,400)	45 45 45	7×10^{-9} 2.2×10^{-9} 4.0×10^{-10}	DTN: LL021105312251.023 [DIRS 161253], pp. 10 to 11
C200	110°C BSW (Mill-annealed + Aged 700°C/175h)	0.001 Hz @ R= 0.5	1 (3,000) 2.5 (9,000) 24 (85,400) CL[b]	24.2 24.2 24.2 24.2	1.3×10^{-7} 4.6×10^{-8} 6.6×10^{-9} 6.0×10^{-10}	DTN: MO0707SCCIGMER.000 [DIRS 182202], Figures 1-67 to 1-68
C263	150°C simulated concentrated water (SCW) (As-welded)	0.001 Hz @ R= 0.7	1 (3,000) 2.5 (9,000) 24 (85,400)	40 40 40	3×10^{-9} 1.2×10^{-9} 1.2×10^{-9}	DTN:MO0705SCCIGM06.000 [DIRS 180869], file *GE-GRC-Final_Sept-2006-Rev3.doc*, Tables 2a to 2b
C264	150°C SCW (As-welded)	0.001 Hz @ R= 0.7	1 (3,000) 2.5 (9,000) 24 (85,400)	40 40 40	1.3×10^{-9} 1.3×10^{-9} $< 1.3 \times 10^{-9}$	
C265	150°C SCW (As-welded + tetrahedrally close-packed (TCP))	0.001 Hz @ R= 0.5	1 (3,000)	40	2×10^{-9}	
C266	150°C SCW (As-welded + long-range ordering (LRO))	0.001 Hz @ R= 0.5	1 (3,000)	40	3×10^{-9}	

NOTES: [a] Growth rates obtained at sustained constant load or at hold times of about 1 hour to 24 hours (3,000 s to 85,400 s).

[b] CL = constant load.

[c] Test results indicated that either cracking appeared to cease or growth rate seemed to arrest, indicating growth rates less than 10^{-11} mm/s, the growth-rate detection threshold.

[d] TCP heat treatment = 650°C for 200 hours.

[e] LRO heat treatment = 550°C for 10 hours.

Table 4-3. Coefficients of Stress Profiles for the As-Welded, Laser-Peened, and Plasticity-Burnished Naval Long Waste Package Design

Stress Coefficient	A_0 (ksi)	A_1 (ksi/in)	A_2 (ksi/in^2)	A_3 (ksi/in^3)	Source in Reference
As-Welded Naval Long Waste Package Outer Lid Section A-A, Radial Stress S_x	−11.151	279.64	−765.46	520.13	Sheet "AAStrsFit"
As-Welded Naval Long Waste Package Outer Lid Section A-A, Hoop Stress S_z	42.164	142.49	−374.62	254.87	Sheet "AAStrsFit"
As-Welded Naval Long Waste Package Outer Lid Section B-B, Radial Stress S_x	−3.9316	196.58	−565.89	388.99	Sheet "BBStrFit"
As-Welded Naval Long Waste Package Outer Lid Section B-B, Hoop Stress S_z	45.955	90.001	−245.2	161.57	Sheet "BBStrFit"
Laser-Peened Naval Long Waste Package Outer Lid Section A-A, Radial Stress S_x	−46.621	497.32	−1,150.9	726.37	Sheet "A-AThrWLPStrsPlt"
Laser-Peened Naval Long Waste Package Outer Lid Section A-A, Hoop Stress S_z	−35.651	607.56	−1,187	686.08	Sheet "A-AThrWLPStrsPlt"
Laser-Peened Naval Long Waste Package Outer Lid Section B-B, Radial Stress S_x	−41.029	430.6	−987.87	617.8	Sheet "B-BLPStrsPlt"
Laser-Peened Naval Long Waste Package Outer Lid Section B-B, Hoop Stress S_z	−32.73	570.96	−1,097.5	618.7	Sheet "B-BLPStrsPlt"
Plasticity-Burnished Naval Long Waste Package Outer Lid Section A-A, Radial Stress S_x	−90.179	772.46	−1,646.7	994.72	Sheet "A-ACPBPlt"
Plasticity-Burnished Naval Long Waste Package Outer Lid Section A-A, Hoop Stress S_z	−75.293	853.48	−1,626	922.37	Sheet "A-ACPBPlt"
Plasticity-Burnished Naval Long Waste Package Outer Lid Section B-B, Radial Stress S_x	−82.228	695.42	−1,470.7	881.5	Sheet "B-BCPB"
Plasticity-Burnished Naval Long Waste Package Outer Lid Section B-B, Hoop Stress S_z	−72.008	817.86	−1,542	859.56	Sheet "B-BCPB"

Source: DTN: MO0708RTSWRS06.000 [DIRS 182558], file *NdStrs-R2.xls*.

NOTES: A_0, A_1, A_2 and A_3 are the stress coefficients which will be discussed in Section 6.5.
Data are rearranged; specific worksheets within the source file are as indicated in the last column.
Some rows are highlighted to differentiate data for as-welded, laser-peened, and plasticity burnished conditions as an added transparency.

Table 4-4. Stress Intensity Factor Profiles for the Naval Long As-Welded Waste Package Outer Lid

Single-Edge Cracked Plate					Elliptical Crack Growth				
Distance from Outer Surface (mm)	A–A*		B–B*		Distance from Outer Surface (mm)	A–A		B–B	
	Radial	Hoop	Radial	Hoop		Radial	Hoop	Radial	Hoop
	K–Sx (MPa√m)	K–Sz (MPa√m)	K–Sx (MPa√m)	K–Sz (MPa√m)		K–Sx (MPa√m)	K–Sz (MPa√m)	K–Sx (MPa√m)	K–Sz (MPa√m)
Column Q Cell 10 to Cell 59	Column R Cell 10 to Cell 59	Column S Cell 10 to Cell 59	Column T Cell 10 to Cell 59	Column U Cell 10 to Cell 59	Column W Cell 10 to Cell 59	Column X Cell 10 to Cell 59	Column Y Cell 10 to Cell 59	Column Z Cell 10 to Cell 59	Column AA Cell 10 to Cell 59
0.4064	−2.2679	11.6577	−0.5488	12.5377	0.4064	−1.3570	11.2274	−0.4521	12.0789
0.8128	−2.2901	17.1560	−0.1187	18.2334	0.8128	−1.8229	16.3747	−0.1454	17.4132
1.2192	−1.7449	21.8009	0.6122	22.9263	1.2192	−1.7296	20.6275	0.5272	21.7084
1.6256	−0.8637	26.0498	1.5272	27.1368	1.6256	−0.9171	24.4393	1.3621	25.4811
2.0320	0.2410	30.0653	2.5644	31.0562	2.0320	0.0926	27.9742	2.2987	28.9231
2.4384	1.4985	33.9234	3.6824	34.7768	2.4384	1.2306	31.3100	3.2975	32.1289
2.8448	2.8147	38.2028	4.8662	38.9175	2.8448	2.4418	34.6315	4.3363	35.3007
3.2512	4.2080	42.6716	6.1083	43.2337	3.2512	3.7016	37.8956	5.3950	38.3989
3.6576	5.6749	47.1741	7.3935	47.5646	3.6576	4.9860	41.0731	6.4552	41.3976
4.0640	7.1989	51.7155	8.7107	51.9188	4.0640	6.2731	44.1727	7.5027	44.3103
4.4704	8.7668	56.2986	10.0515	56.3016	4.4704	7.5447	47.2003	8.5258	47.1464
4.8768	10.3682	60.9251	11.4087	60.7167	4.8768	8.7859	50.1596	9.5147	49.9128
5.2832	12.0423	65.9632	12.8333	65.5339	5.2832	9.9890	53.1682	10.4735	52.7323
5.6896	13.7863	71.4552	14.3235	70.7963	5.6896	11.1489	56.2437	11.3998	55.6239
6.0960	15.5413	77.0431	15.8149	76.1464	6.0960	12.2533	59.2771	12.2768	58.4770
6.5024	17.2938	82.7200	17.2974	81.5799	6.5024	13.2946	62.2685	13.0995	61.2934
6.9088	19.0311	88.4797	18.7613	87.0919	6.9088	14.2662	65.2181	13.8634	64.0743
7.3152	20.7408	94.3156	20.1975	92.6776	7.3152	15.1628	68.1262	14.5653	66.8208
7.7216	22.5402	100.5963	21.7118	98.6936	7.7216	15.9883	71.0425	15.2110	69.5831
8.1280	24.7409	108.1385	23.5736	105.9186	8.1280	16.7588	74.0742	15.8189	72.4684
8.5344	26.9850	115.8554	25.4598	113.3017	8.5344	17.4490	77.0775	16.3620	75.3331
8.9408	29.2656	123.7396	27.3649	120.8387	8.9408	18.0569	80.0523	16.8387	78.1774
9.3472	31.5760	131.7875	29.2834	128.5229	9.3472	18.5808	82.9990	17.2481	81.0020
9.7536	33.9100	139.9926	31.2103	136.3488	9.7536	19.0201	85.9181	17.5901	83.8071

Table 4-4. Stress Intensity Factor Profiles for the Naval Long As-Welded Waste Package Outer Lid (Continued)

Single-Edge Cracked Plate					Elliptical Crack Growth				
	A–A*		B–B*			A–A		B–B	
	Radial	Hoop	Radial	Hoop		Radial	Hoop	Radial	Hoop
Distance from Outer Surface (mm)	K–Sx (MPa√m)	K–Sz (MPa√m)	K–Sx (MPa√m)	K–Sz (MPa√m)	Distance from Outer Surface (mm)	K–Sx (MPa√m)	K–Sz (MPa√m)	K–Sx (MPa√m)	K–Sz (MPa√m)
Column Q Cell 10 to Cell 59	Column R Cell 10 to Cell 59	Column S Cell 10 to Cell 59	Column T Cell 10 to Cell 59	Column U Cell 10 to Cell 59	Column W Cell 10 to Cell 59	Column X Cell 10 to Cell 59	Column Y Cell 10 to Cell 59	Column Z Cell 10 to Cell 59	Column AA Cell 10 to Cell 59
10.1600	36.2618	148.3493	33.1411	144.3132	10.1600	19.3746	88.8104	17.8644	86.5936
10.5664	38.2561	159.5894	34.9801	155.2786	10.5664	19.6747	91.8087	18.0997	89.4909
10.9728	40.1446	171.0316	36.7322	166.4494	10.9728	19.8921	94.7872	18.2693	92.3757
11.3792	41.9080	182.6629	38.3827	177.8148	11.3792	20.0282	97.7469	18.3744	95.2484
11.7856	43.5280	194.4677	39.9170	189.3625	11.7856	20.0849	100.6890	18.4165	98.1098
12.1920	44.9869	206.4352	41.3218	201.0817	12.1920	20.0643	103.6150	18.3976	100.9608
12.5984	46.2679	218.5522	42.5840	212.9624	12.5984	19.9697	106.5266	18.3199	103.8023
13.0048	48.1026	234.2217	44.4082	228.3407	13.0048	19.8018	109.3852	18.1798	106.5930
13.4112	50.0290	251.2966	46.3416	245.1024	13.4112	19.5644	112.2171	17.9830	109.3603
13.8176	51.7880	268.6451	48.1372	262.1411	13.8176	19.2622	115.0390	17.7348	112.1193
14.2240	53.3637	286.2541	49.7825	279.4424	14.2240	18.9007	117.8531	17.4393	114.8719
14.6304	54.7413	304.1114	51.2662	296.9953	14.6304	18.4855	120.6618	17.1007	117.6191
15.0368	55.9084	322.2049	52.5784	314.7899	15.0368	18.0229	123.4693	16.7241	120.3629
15.4432	58.8299	346.5300	55.4147	338.5568	15.4432	17.4711	126.1197	16.2699	122.9517
15.8496	63.7225	377.3965	59.9305	368.5585	15.8496	16.8311	128.6086	15.7393	125.3802
16.2560	68.6858	408.8971	64.4753	399.1305	16.2560	16.1578	131.0953	15.1815	127.8020
16.6624	73.7252	441.0250	69.0521	430.2652	16.6624	15.4602	133.5852	14.6034	130.2195
17.0688	78.8497	473.7782	73.6669	461.9525	17.0688	14.7476	136.0818	14.0120	132.6369
17.4752	84.0719	507.1556	78.3286	494.1882	17.4752	14.0300	138.5927	13.4152	135.0577
17.8816	90.7634	549.5402	84.3115	535.1530	17.8816	13.3747	141.0079	12.8516	137.3554
18.2880	101.4317	618.0596	93.9639	601.5792	18.2880	12.9212	143.1078	12.4023	139.2751
18.6944	111.8743	687.7614	103.3809	669.0943	18.6944	12.5225	145.2363	11.9918	141.2024
19.1008	122.0826	758.6258	112.5545	737.6731	19.1008	12.1929	147.4021	11.8349	143.1430
19.5072	132.0579	830.6363	121.4848	807.2925	19.5072	11.9474	149.6130	12.3031	145.1000

Table 4-4. Stress Intensity Factor Profiles for the Naval Long As-Welded Waste Package Outer Lid (Continued)

Single-Edge Cracked Plate					Elliptical Crack Growth				
Distance from Outer Surface (mm)	A–A*		B–B*		Distance from Outer Surface (mm)	A–A		B–B	
	Radial	Hoop	Radial	Hoop		Radial	Hoop	Radial	Hoop
	K–Sx (MPa√m)	K–Sz (MPa√m)	K–Sx (MPa√m)	K–Sz (MPa√m)		K–Sx (MPa√m)	K–Sz (MPa√m)	K–Sx (MPa√m)	K–Sz (MPa√m)
Column Q Cell 10 to Cell 59	Column R Cell 10 to Cell 59	Column S Cell 10 to Cell 59	Column T Cell 10 to Cell 59	Column U Cell 10 to Cell 59	Column W Cell 10 to Cell 59	Column X Cell 10 to Cell 59	Column Y Cell 10 to Cell 59	Column Z Cell 10 to Cell 59	Column AA Cell 10 to Cell 59
19.9136	141.8068	903.7852	130.1766	877.9349	19.9136	11.8017	151.8777	12.7591	147.0790
20.3200	151.3480	978.0648	138.6421	949.5850	20.3200	11.7723	154.2017	13.2028	149.0866

Source: DTN: MO0708RTSWRS06.000 [DIRS 182558], file *NdStrs-R2.xls,* Sheet "Ksolu_As Welded."

NOTES: Data are rearranged (and rounded to the fourth digits after the decimal point).
Data sources are as indicated in the column headings.
* A–A and B−B are section locations where the finite element analyses were performed as defined in Figure 6-18.

Table 4-5. Stress Intensity Factor Profiles for the Naval Long Plasticity-Burnished Waste Package Outer Lid

Single-Edge Cracked Plate					Elliptical Crack Growth				
Distance from Outer Surface (mm)	A−A*		B−B*		Distance from Outer Surface (mm)	A−A		B−B	
	Radial	Hoop	Radial	Hoop		Radial	Hoop	Radial	Hoop
	K−Sx (MPa√m)	K−Sz (MPa√m)	K−Sx (MPa√m)	K−Sz (MPa√m)		K−Sx (MPa√m)	K−Sz (MPa√m)	K−Sx (MPa√m)	K−Sz (MPa√m)
Column P Cell 10 to Cell 59	Column Q Cell 10 to Cell 59	Column R Cell 10 to Cell 59	Column S Cell 10 to Cell 59	Column T Cell 10 to Cell 59	Column P Cell 10 to Cell 59	Column W Cell 10 to Cell 59	Column X Cell 10 to Cell 59	Column Y Cell 10 to Cell 59	Column Z Cell 10 to Cell 59
0.4064	−22.1504	−17.9483	−20.2201	−17.1605	0.4064	−11.3747	−9.4403	−10.3742	−9.0280
0.8128	−28.9782	−22.6622	−26.4855	−21.6590	0.8128	−15.8672	−13.0870	−14.4749	−12.5147
1.2192	−32.7419	−24.5417	−29.9656	−23.4422	1.2192	−19.1668	−15.7063	−17.4891	−15.0183
1.6256	−34.7772	−24.7639	−31.875	−23.6359	1.6256	−21.8264	−17.7655	−19.9207	−16.9861
2.0320	−35.6553	−23.8426	−32.7327	−22.7318	2.0320	−24.0641	−19.4500	−21.9682	−18.5951
2.4384	−35.6987	−22.0731	−32.831	−21.0119	2.4384	−25.9937	−20.8568	−23.7353	−19.8904
2.8448	−35.9412	−20.2774	−33.1145	−19.2622	2.8448	−27.7556	−18.7051	−25.3504	−17.7697
3.2512	−36.0260	−18.1813	−33.2564	−17.2205	3.2512	−29.3531	−16.1168	−26.8161	−15.2615
3.6576	−35.7654	−15.6533	−33.0844	−14.7613	3.6576	−30.7901	−13.1794	−28.1388	−12.4154

Table 4-5. Stress Intensity Factor Profiles for the Naval Long Plasticity-Burnished Waste Package Outer Lid (Continued)

Single-Edge Cracked Plate					Elliptical Crack Growth				
	A−A*		B−B*			A−A		B−B	
	Radial	Hoop	Radial	Hoop		Radial	Hoop	Radial	Hoop
Distance from Outer Surface (mm)	K−Sx (MPa√m)	K−Sz (MPa√m)	K−Sx (MPa√m)	K−Sz (MPa√m)	Distance from Outer Surface (mm)	K−Sx (MPa√m)	K−Sz (MPa√m)	K−Sx (MPa√m)	K−Sz (MPa√m)
Column P Cell 10 to Cell 59	Column Q Cell 10 to Cell 59	Column R Cell 10 to Cell 59	Column S Cell 10 to Cell 59	Column T Cell 10 to Cell 59	Column P Cell 10 to Cell 59	Column W Cell 10 to Cell 59	Column X Cell 10 to Cell 59	Column Y Cell 10 to Cell 59	Column Z Cell 10 to Cell 59
4.0640	−35.2177	−12.7494	−32.6512	−11.9382	4.0640	−29.3330	−9.9714	−27.2066	−9.3069
4.4704	−34.4280	−9.5133	−31.9976	−8.7931	4.4704	−27.7050	−6.5568	−25.7696	−5.9973
4.8768	−33.4314	−5.9794	−31.1554	−5.3591	4.8768	−25.9604	−2.9886	−24.2237	−2.5375
5.2832	−32.4658	−2.2008	−30.3444	−1.6837	5.2832	−24.2628	0.6173	−22.7187	0.9620
5.6896	−31.5443	1.8491	−29.5766	2.2602	5.6896	−22.6467	4.2344	−21.2863	4.4758
6.0960	−30.4821	6.1848	−28.6796	6.4831	6.0960	−21.0234	7.9070	−19.8444	8.0456
6.5024	−29.3075	10.7787	−27.6789	10.9587	6.5024	−19.4190	11.6084	−18.4166	11.6455
6.9088	−28.0475	15.6038	−26.5989	15.6612	6.9088	−17.8559	15.3153	−17.0235	15.2534
7.3152	−26.7285	20.6344	−25.4632	20.5656	7.3152	−16.3534	19.0077	−15.6825	18.8492
7.7216	−25.3834	26.0005	−24.3077	25.7980	7.7216	−14.9554	22.6634	−14.4339	22.4124
8.1280	−23.9144	32.1659	−23.0577	31.8056	8.1280	−13.7238	26.2705	−13.3358	25.9316
8.5344	−22.2286	38.7572	−21.6109	38.2264	8.5344	−12.5857	29.8352	−12.3199	29.4116
8.9408	−20.3356	45.7646	−19.9761	45.0511	8.9408	−11.5510	33.3463	−11.3956	32.8415
9.3472	−18.2453	53.1787	−18.1618	52.2700	9.3472	−10.6281	36.7941	−10.5702	36.2114
9.7536	−15.9670	60.9899	−16.1767	59.8734	9.7536	−9.8234	40.1706	−9.85017	39.5132
10.1600	−13.5098	69.1883	−14.0291	67.8518	10.1600	−9.1423	43.4690	−9.2403	42.7402
10.5664	−14.3984	75.7990	−14.932	74.3510	10.5664	−8.6057	46.7415	−8.76137	45.9433
10.9728	−15.3892	82.6203	−15.9242	81.0597	10.9728	−8.1949	49.9358	−8.39517	49.0706
11.3792	−16.5174	89.6163	−17.0377	87.9426	11.3792	−7.9119	53.0484	−8.14361	52.1183
11.7856	−17.8178	96.7504	−18.3036	94.9643	11.7856	−7.7572	56.0768	−8.0075	55.0834
12.1920	−19.3252	103.9864	−19.7534	102.0892	12.1920	−7.7304	59.0194	−7.98665	57.9640
12.5984	−21.0734	111.2875	−21.4174	109.2818	12.5984	−7.8296	61.8761	−8.07986	60.7590
13.0048	−23.8915	119.6266	−24.091	117.5015	13.0048	−7.9894	64.7048	−8.22727	63.5239
13.4112	−27.1471	128.5514	−27.1727	126.2999	13.4112	−8.2501	67.4665	−8.46617	66.2202
13.8176	−30.5892	137.7290	−30.4211	135.3434	13.8176	−8.6281	70.1443	−8.81213	68.8312

Table 4-5. Stress Intensity Factor Profiles for the Naval Long Plasticity-Burnished Waste Package Outer Lid (Continued)

Single-Edge Cracked Plate					Elliptical Crack Growth				
Distance from Outer Surface (mm)	A−A*		B−B*		Distance from Outer Surface (mm)	A−A		B−B	
	Radial	Hoop	Radial	Hoop		Radial	Hoop	Radial	Hoop
	K−Sx (MPa√m)	K−Sz (MPa√m)	K−Sx (MPa√m)	K−Sz (MPa√m)		K−Sx (MPa√m)	K−Sz (MPa√m)	K−Sx (MPa√m)	K−Sz (MPa√m)
Column P Cell 10 to Cell 59	Column Q Cell 10 to Cell 59	Column R Cell 10 to Cell 59	Column S Cell 10 to Cell 59	Column T Cell 10 to Cell 59	Column P Cell 10 to Cell 59	Column W Cell 10 to Cell 59	Column X Cell 10 to Cell 59	Column Y Cell 10 to Cell 59	Column Z Cell 10 to Cell 59
14.2240	−34.2502	147.1219	−33.8658	144.5957	14.2240	−9.1176	72.7415	−9.26025	71.3592
14.6304	−38.1612	156.6950	−37.5349	154.0215	14.6304	−9.7115	75.2627	−9.80459	73.8078
15.0368	−42.3504	166.4143	−41.4547	163.5881	15.0368	−10.4019	77.7130	−10.4384	76.1814
15.4432	−46.1692	180.0773	−45.1276	176.9654	15.4432	−11.1588	80.0499	−11.1324	78.4372
15.8496	−49.0951	198.4291	−48.0871	194.8655	15.8496	−11.9855	82.2619	−11.8901	80.5633
16.2560	−51.6230	217.8863	−50.6955	213.8140	16.2560	−12.8962	84.3998	−12.7273	82.6085
16.6624	−53.7461	238.4456	−52.9479	233.8052	16.6624	−13.8787	86.4731	−13.6336	84.5809
17.0688	−55.4523	260.1082	−54.8351	254.8360	17.0688	−14.9191	88.4922	−14.5967	86.4895
17.4752	−56.7241	282.8795	−56.3432	276.9073	17.4752	−16.0027	90.4686	−15.604	88.3443
17.8816	−58.3282	311.7154	−58.2379	304.8905	17.8816	−16.8258	92.6432	−16.3809	90.3732
18.2880	−61.9365	357.0449	−62.1685	349.0343	18.2880	−16.7580	95.5196	−16.3565	93.0524
18.6944	−65.2746	404.2907	−65.8661	394.9934	18.6944	−16.6184	98.4483	−16.2746	95.7651
19.1008	−68.3805	453.3914	−69.3684	442.6997	19.1008	−16.3841	101.4484	−16.1156	98.5278
19.5072	−71.2807	504.2920	−72.7032	492.0916	19.5072	−16.0310	104.5400	−15.8583	101.3589
19.9136	−73.9883	556.9519	−75.886	543.1196	19.9136	−15.5335	107.7446	−15.4803	104.2780
20.3200	−76.5027	611.3402	−78.9212	595.7421	20.3200	−14.8649	111.0842	−14.9582	107.3050

Source: DTN: MO0708RTSWRS06.000 [DIRS 182558], file *NdStrs-R2.xls*, Sheet "Ksolu_CPB."

NOTE: Data are rearranged (and rounded to the fourth digits after the decimal point). Data sources are as indicated in the column headings.

* A−A and B−B are section locations where the finite element analyses were performed as defined in Figure 6-18.

Table 4-6. Stress Intensity Factor Profiles for the Naval Long Laser-Peened Waste Package Outer Lid

Single-edge Cracked Plate					Elliptical Crack Growth				
Distance from Outer Surface (mm)	A−A*		B−B*		Distance from Outer Surface (mm)	A−A		B−B	
	Radial	Hoop	Radial	Hoop		Radial	Hoop	Radial	Hoop
	K−Sx (MPa√m)	K-Sz (MPa√m)	K−Sx (MPa√m)	K−Sz (MPa√m)		K−Sx (MPa√m)	K−Sz (MPa√m)	K−Sx (MPa√m)	K−Sz (MPa√m)
Column P Cell 10 to Cell 59	Column Q Cell 10 to Cell 59	Column R Cell 10 to Cell 59	Column S Cell 10 to Cell 59	Column T Cell 10 to Cell 59	Column P Cell 10 to Cell 59	Column W Cell 10 to Cell 59	Column X Cell 10 to Cell 59	Column Y Cell 10 to Cell 59	Column Z Cell 10 to Cell 59
0.4064	−11.2007	−7.9715	−9.8752	−7.2836	0.4064	−5.8542	−4.4149	−5.1539	−4.0496
0.8128	−14.2933	−9.2656	−12.6279	−8.4082	0.8128	−8.1291	−6.0412	−7.1593	−5.5359
1.2192	−15.7016	−8.9762	−13.9052	−8.0604	1.2192	−9.7739	−7.1517	−8.6113	−6.5468
1.6256	−16.1516	−7.7268	−14.3430	−6.8162	1.6256	−11.0779	−7.4927	−9.7638	−6.6227
2.0320	−15.9606	−5.8016	−14.2192	−4.9388	2.0320	−12.1552	−5.6960	−10.7176	−4.8741
2.4384	−15.3119	−3.3696	−13.6939	−2.5850	2.4384	−13.0663	−3.4512	−11.5254	−2.7050
2.8448	−14.7222	−0.7810	−13.2229	−0.0738	2.8448	−13.5542	−0.9200	−12.1672	−0.2639
3.2512	−14.0206	2.0682	−12.6548	2.6888	3.2512	−12.4780	1.8571	−11.2601	2.4109
3.6576	−13.1241	5.2136	−11.9160	5.7339	3.6576	−11.2454	4.8365	−10.2141	5.2780
4.0640	−12.0680	8.6201	−11.0368	9.0285	4.0640	−9.9050	7.9693	−9.0716	8.2918
4.4704	−10.8798	12.2599	−10.0412	12.5468	4.4704	−8.4959	11.2155	−7.8668	11.4149
4.8768	−9.5806	16.1109	−8.9477	16.2680	4.8768	−7.0507	14.5414	−6.6278	14.6158
5.2832	−8.2572	20.2598	−7.8347	20.2819	5.2832	−5.6473	17.9097	−5.4239	17.8614
5.6896	−6.9171	24.7385	−6.7087	24.6205	5.6896	−4.3040	21.3088	−4.2710	21.1410
6.0960	−5.5081	29.4384	−5.5210	29.1742	6.0960	−2.9872	24.7318	−3.1390	24.4463
6.5024	−4.0501	34.3394	−4.2889	33.9240	6.5024	−1.7128	28.1613	−2.0416	27.7606
6.9088	−2.5622	39.4217	−3.0287	38.8515	6.9088	−0.4944	31.5821	−0.9907	31.0697
7.3152	−1.0629	44.6663	−1.7565	43.9387	7.3152	0.6565	34.9809	0.0035	34.3607
7.7216	0.4953	50.2800	−0.4350	49.3851	7.7216	1.7220	38.3600	0.9249	37.6365
8.1280	2.3223	56.8355	1.1089	55.7410	8.1280	2.6828	41.7465	1.7557	40.9243
8.5344	4.2697	63.7308	2.7587	62.4245	8.5344	3.5585	45.0972	2.5141	44.1806
8.9408	6.3293	70.9577	4.5071	69.4273	8.9408	4.3433	48.4048	3.1950	47.3982
9.3472	8.4932	78.5081	6.3473	76.7416	9.3472	5.0328	51.6630	3.7945	50.5706
9.7536	10.7538	86.3737	8.2727	84.3593	9.7536	5.6236	54.8667	4.3094	53.6928

Table 4-6. Stress Intensity Factor Profiles for the Naval Long Laser-Peened Waste Package Outer Lid (Continued)

Single-edge Cracked Plate					Elliptical Crack Growth				
Distance from Outer Surface (mm)	A−A*		B−B*		Distance from Outer Surface (mm)	A−A		B−B	
	Radial	Hoop	Radial	Hoop		Radial	Hoop	Radial	Hoop
	K−Sx (MPa√m)	K-Sz (MPa√m)	K−Sx (MPa√m)	K−Sz (MPa√m)		K−Sx (MPa√m)	K−Sz (MPa√m)	K−Sx (MPa√m)	K−Sz (MPa√m)
Column P Cell 10 to Cell 59	Column Q Cell 10 to Cell 59	Column R Cell 10 to Cell 59	Column S Cell 10 to Cell 59	Column T Cell 10 to Cell 59	Column P Cell 10 to Cell 59	Column W Cell 10 to Cell 59	Column X Cell 10 to Cell 59	Column Y Cell 10 to Cell 59	Column Z Cell 10 to Cell 59
10.1600	13.1039	94.5469	10.2770	92.2726	10.1600	6.1133	58.0116	4.7373	56.7603
10.5664	13.7515	102.6353	10.7861	100.1939	10.5664	6.5083	61.1760	5.0830	59.8494
10.9728	14.2954	110.9337	11.2080	108.3249	10.9728	6.8024	64.2839	5.3416	62.8854
11.3792	14.7097	119.4135	11.5201	116.6389	11.3792	6.9952	67.3333	5.5127	65.8656
11.7856	14.9688	128.0471	11.6999	125.1077	11.7856	7.0876	70.3229	5.5968	68.7885
12.1920	15.0477	136.8049	11.7261	133.7050	12.1920	7.0810	73.2522	5.5949	71.6529
12.5984	14.9221	145.6615	11.5772	142.4046	12.5984	6.9778	76.1216	5.5087	74.4585
13.0048	14.6054	156.3774	11.2361	152.9326	13.0048	6.8080	78.9566	5.3650	77.2286
13.4112	14.1379	167.9505	10.7568	164.3034	13.4112	6.5553	81.7403	5.1487	79.9465
13.8176	13.4958	179.7861	10.1276	175.9314	13.8176	6.2151	84.4664	4.8553	82.6061
14.2240	12.6556	191.8558	9.3279	187.7890	14.2240	5.7928	87.1381	4.4892	85.2091
14.6304	11.5957	204.1332	8.3386	199.8499	14.6304	5.2946	89.7593	4.0555	87.7588
15.0368	10.2965	216.5918	7.1422	212.0877	15.0368	4.7274	92.3344	3.5599	90.2582
15.4432	10.0934	233.7074	6.8421	228.8110	15.4432	4.0826	94.7842	2.9961	92.6296
15.8496	11.3370	256.0711	7.7392	250.5769	15.8496	3.3592	97.0997	2.3629	94.8632
16.2560	12.7956	279.3797	8.8174	273.2306	16.2560	2.5801	99.3667	1.6782	97.0416
16.6624	14.4752	303.6290	10.0805	296.7656	16.6624	1.7555	101.5929	0.9505	99.1708
17.0688	16.3858	328.8178	11.5362	321.1775	17.0688	0.8967	103.7866	0.1891	101.2577
17.4752	18.5424	354.9494	13.1956	346.4630	17.4752	0.0157	105.9568	−0.5960	103.3100
17.8816	21.3185	388.0784	15.3445	378.5514	17.8816	−0.7147	108.2263	−1.2546	105.4375
18.2880	25.2713	440.7778	18.3960	429.7597	18.2880	−0.9354	110.8524	−1.4741	107.8717
18.6944	29.2202	495.1496	21.4365	482.5448	18.6944	−1.0945	113.5226	−1.6465	110.3304
19.1008	33.1436	551.1489	24.4444	536.8529	19.1008	−1.1742	116.2510	−1.7566	112.8248

Table 4-6. Stress Intensity Factor Profiles for the Naval Long Laser-Peened Waste Package Outer Lid (Continued)

Single-edge Cracked Plate					Elliptical Crack Growth				
Distance from Outer Surface (mm)	A−A*		B−B*		Distance from Outer Surface (mm)	A−A		B−B	
	Radial	Hoop	Radial	Hoop		Radial	Hoop	Radial	Hoop
	K−Sx (MPa√m)	K-Sz (MPa√m)	K−Sx (MPa√m)	K−Sz (MPa√m)		K−Sx (MPa√m)	K−Sz (MPa√m)	K−Sx (MPa√m)	K−Sz (MPa√m)
Column P Cell 10 to Cell 59	Column Q Cell 10 to Cell 59	Column R Cell 10 to Cell 59	Column S Cell 10 to Cell 59	Column T Cell 10 to Cell 59	Column P Cell 10 to Cell 59	Column W Cell 10 to Cell 59	Column X Cell 10 to Cell 59	Column Y Cell 10 to Cell 59	Column Z Cell 10 to Cell 59
19.5072	37.0294	608.7348	27.4061	592.6368	19.5072	−1.1554	119.0541	−1.7886	115.3708
19.9136	40.8767	667.8757	30.3174	649.8568	19.9136	−1.0181	121.9496	−1.7258	117.9817
20.3200	44.6951	728.5505	33.1826	708.4801	20.3200	−0.7417	124.9527	−1.5507	120.6705

Source: DTN: MO0708RTSWRS06.000 [DIRS 182558], file *NdStrs-R2.xls*, Sheet "Ksolu_Peening."

NOTE: Data are rearranged (and rounded to the fourth digits after the decimal point). Data sources are as indicated in the column headings.

* A−A and B−B are section locations where the finite element analyses were performed as defined in Figure 6-18.

Table 4-7. Input Data for Yield Strength, Modulus of Elasticity, and Other Parameters

Input Name	Input Source	DTN	Input Value or Equation
Yield Strength for Alloy 22	Hastelloy Alloy C-22. Filing Code: Ni-317 (Alloy Digest 1985 [DIRS 178194], p. 2, Table 3)	MO0003RIB00071.000 Physical and Chemical Characteristics of Alloy 22. Submittal date: 03/13/2000 [DIRS 148850]	403 MPa at room temperature (21°C) (70°F, 294 K) 371 MPa at 93°C (200°F, 366 K) 303 MPa at 204°C (400°F, 477 K)
Yield Strength for Alloy 22	Hastelloy Alloy C-22. (Haynes International 1988 [DIRS 101995], p. 15)	MO0003RIB00071.000 Physical and Chemical Characteristics of Alloy 22. Submittal date: 03/13/2000 [DIRS 148850]	372 MPa (54 ksi) at room temperature (21°C) (70°F, 294 K) 338 MPa (49 ksi) at 93°C (200°F, 366 K) 283 MPa (41 ksi) at 204°C (400°F, 477 K)
Modulus of Elasticity for Alloy 22	Hastelloy Alloy C-22. (Haynes International 1988 [DIRS 101995], p. 14)	MO0003RIB00071.000 Physical and Chemical Characteristics of Alloy 22. Submittal date: 03/13/2000 [DIRS 148850].	206 GPa at room temperature (21°C) (70°F, 294 K) 203 GPa 93°C (200°F, 366 K) 196 GPa at 204°C (400°F, 477 K)
Yield Strength for Titanium Grade 7 (UNS R52400)	*2001 ASME Boiler and Pressure Vessel Code (includes 2002 addenda)* (ASME 2001 [DIRS 158115], Section II, Part D, Table Y-1, pp. 632 to 634)	N/A	276 MPa (40 ksi) at room temperature (21°C) (70°F, 294 K) 176 MPa (25.6 ksi) at 149°C (300°F, 422 K)
Yield Strength for Titanium Grade 7	*Stress Corrosion Crack Initiation & Growth Measurements in Environments Relevant to High Level Nuclear Waste Packages* (DTN: MO0707SCCIGMER.000 [DIRS 182202], Table 2-4, p. 171)	MO0707SCCIGMER.000 [DIRS 182202]	248 MPa (36 ksi) measured in 125°C air
Yield Strength for Titanium Grade 7	Physical and Chemical Characteristics of Ti Grades 7 and 16. Submittal date: 03/13/2000 [DIRS 152926]	MO0003RIB00073.000 [DIRS 152926]	362 MPa (52.5 ksi) at room temperature (21°C) (70°F, 294 K)* 145 MPa (21 ksi) at 204°C (400°F, 477 K) * 107 MPa (15.5) at 316°C (600°F, 589K)*
Modulus of Elasticity for Titanium Grade 7	Physical and Chemical Characteristics of Titanium Grades 7 and 16	MO0003RIB00073.000 [DIRS 152926] (Relevant data from ASME 1995b, Table TM-5, p. 617).	107 GPa (15.5×10^3 ksi) at 294 K (70°F, 21°C) 101 GPa (15×10^3 ksi) at 422 K (300°F, 149°C) 97 GPa (14×10^3 ksi) at 477 K (400°F, 204°C)
Yield Strength for Titanium Grades 23 and 29	ASTM B 265-02 [DIRS 162726], Table 1, p. 2	N/A	759 MPa at room temperature (21°C) (70°F, 294 K)

Table 4-7. Input Data for Yield Strength, Modulus of Elasticity, and Other Parameters (Continued)

Input Name	Input Source	DTN	Input Value or Equation
Yield Strength for Titanium Grades 23 and 29**	Donachie 2002 [DIRS 178207], Table 7	N/A	87% of 759 MPa at 93°C (200°F, 366 K) 70% of 759 MPa at 204°C (400°F, 477 K)
Yield Strength for Titanium Grade 29	DTN: MO0705SCCIGM06.000 [DIRS 180869], file *GE-GRC-Final_Sept-2006-Rev3.doc*, Table 8	MO0705SCCIGM06.000 [DIRS 180869]	724 MPa (105 ksi) 105°C (221°F, 378 K)
Yield Strength for Titanium Grade 28	ASTM B 265-02 [DIRS 162726], Table 1, p. 2	N/A	483 MPa at room temperature (21°C) (70°F, 294 K)

NOTES: Some of the yield strength input data use English units in the input sources. The English unit, ksi, has been converted to the metric unit, MPa, according to 1 ksi = 6.894757 MPa (Boyer and Gall 1997 [DIRS 155318], p. 1-57).

*Yield strength values listed are the average of the values listed in DTN: MO0003RIB00073.000 [DIRS 152926]. The room temperature value (362 MPa) is fully consistent with the actual measured yield strength value for the Ti Grade 7 material tested at LTCTF (Foreman 1998 [DIRS 178278], p. 2).

**Donachie 2002 [DIRS 178207], Table 7, lists only the yield strength values of Ti-6Al-4V (Titanium Grade 5). However, Titanium Grades 23 and 29 are extra-low interstitial variants for Titanium Grade 5 (Ti-6Al-4V) that result in a small reduction in room temperature yield strength (10 ksi or 8%). Because of the same alloying element compositions, the reduction in yield strength with temperature is expected to be equivalent.

Table 4-8. Comparison of Constant-Load Failure Times in Diluted BSW Brine with Those in Air for Titanium Grade 7

Test Run	Material Condition	Applied Stress[a] MPa (ksi)	Percent of At-Temperature Yield Strength[b]	Failure Time Range (hrs)	Specimen #[c]
Keno 1	20% Cold-worked	462 (67.0)	92	1,337 to 1,922	GE-6, 16, 26, 36, 46, 49
Keno 1	Annealed	338 (49.0)	136	0.7 to 50	GE-2, 12, 22, 32, 42, 47
Keno 2	Annealed	345 (50.0)	139	170	GE-16, 73, 132, 42, 51
Keno 2	Annealed	310 (45.0)	125	20 to 220	GE-15, 72, 131, 41, 50, 109, 167, 168, 110, 17, 74, 133, 43, 52
Keno 2	Annealed	276 (40.0)	111	342 to 10,182	GE-14, 71, 130, 40, 98, 108
Air -GE	Annealed-GE (long)	310	125	10.1	GE-Creep 1
Air -GE	Annealed-GE (long)	350	141	1.6	GE-Creep 2
Air -GE	Annealed-GE (long)	328	132	6.2	GE-Creep 3
Air -GE	Annealed-GE (long)	276	111	493	GE-Creep 4

Table 4-8. Comparison of Constant-Load Failure Times in Diluted BSW Brine with Those in Air for Titanium Grade 7 (Continued)

Test Run	Material Condition	Applied Stress[a] MPa (ksi)	Percent of At-Temperature Yield Strength[b]	Failure Time Range (hrs)	Specimen #[c]
Air -GE	Annealed-GE (long)	326	131	1.2	GE-Creep 5
Air -GE	Annealed-GE (short)	285	115	143	GE-Creep 6
Air-AECL[d]	Annealed-AECL[d]	222 (32.2)	95	350[e]	AECL-C-1
Air-AECL[d]	Annealed-AECL[d]	187 (27.1)	80	24, 140	AECL-C-3

Sources: GE Keno test data are from DTN: MO0707SCCIGMER.000 [DIRS 182202], Tables 2-2 to 2-4, and 2-7.
GE air creep data AIR-GE 1-4 are from DTN: MO0707SCCIGMER.000 [DIRS 182202], Figures 6-3 to 6-6.
GE air creep data AIR GE 5-6 are from DTN: MO0705SCCIGM06.000 [DIRS 180869], Figures 27 and 29.

Air-AECL data are from Dutton et al. 1996 [DIRS 175817], Table 1, Figure 13.

NOTES: [a]Some of the applied stress input data are given with English units in the input sources. The English unit, ksi, has been converted to the metric unit, MPa, according to 1 ksi = 6.894757 MPa (Boyer and Gall 1997 [DIRS 155318], p. 1-57).
[b]The at-temperature yield strength is 248 MPa in 125°C air, as shown in Table 6-24 (DTN: MO0707SCCIGMER.000 [DIRS 182202], Table 2-4).
[c] GE Keno Run specimen numbers are listed in DTN: MO0707SCCIGMER.000 [DIRS 182202], Tables 2-2 and 2-7.
[d]AECL = Atomic Energy of Canada Limited; AECL data are for Titanium Grade 2.
[e]Failure time estimated from Dutton et al. 1996 [DIRS 175817], Figure 13.

Some rows are highlighted to differentiate data for different categories as an added transparency.

Table 4-9. Summary of LTCTF Titanium Grades 7 and 16 U-Bend Specimen Maximum Remaining Stress Levels

Time (yrs)	Test Temperature (°C)	Specimen ID	Maximum Stress (MPa)	Maximum of Maximum Stress (MPa)
5.5	RT	FUA 141	192	—
5.5	RT	FUE 142	360	360
5.5	RT	NUA 181	375	375
5.5	RT	NUE 182	370	370
0.5	60	FUA 122	287	287
2.5	60	NUA 148	188	—
1	60	FUA 124	209	209
2.3	60	FUA 126	60	—
5	60	FUA 128	145	145
0.5	90	FUE 134	181	—
1	90	FUE 136	192	—
2.4	60	NUE 136	197	—
2.3	90	FUE 138	121	—
2.5	90	NUA 178	232	232
2.5	90	NUE 166	65	—
5	90	FUE 140	113	—

Table 4-9 Summary of LTCTF Titanium Grades 7 and 16 U-Bend Specimen Maximum Remaining Stress Levels (Continued)

Time (yrs)	Test Temperature (°C)	Specimen ID	Maximum Stress (MPa)	Maximum of Maximum Stress (MPa)
0.01	RT	Titanium Grade 7 RT Yield Strength	362	362

Source: DTN: MO0708XRAYDRST.000 [DIRS 182572], Appendix pp. 23 to 71.

NOTES: RT = room temperature.

For each U-bend specimen, Lambda Technologies made X-ray measurements at three locations. For each specimen, the highest measured stress value was intended to be selected. For a given specimen, if the highest value was inadvertently not selected, the results would only be more conservative.

Table 4-10. Five-Year General Corrosion Rates for Alloy 22

Sample	Corrosion Rate (nm/yr)	Sample	Corrosion Rate (nm/yr)
DCA 019	9.40	DCA 175	0.82
DCA 020	8.22	DCA 176	0.81
DCA 021	8.63	DCA 177	46.67
DCA 022	6.36	DCA 178	8.40
DCA 023	9.75	DCA 179	5.24
DCA 024	22.52	DCA 180	5.28
DCA 049	12.04	DCB 019	10.24
DCA 050	17.29	DCB 020	6.94
DCA 051	15.75	DCB 022	5.84
DCA 052	5.76	DCB 023	6.89
DCA 053	8.30	DCB 049	16.07
DCA 054	6.40	DCB 050	14.51
DCA 079	3.06	DCB 052	4.29
DCA 080	3.10	DCB 053	5.92
DCA 081	4.19	DCB 079	2.00
DCA 082	9.52	DCB 080	7.88
DCA 083	7.23	DCB 082	19.58
DCA 084	14.71	DCB 083	13.61
DCA 109	5.81	DCB 109	4.32
DCA 110	11.60	DCB 110	2.01
DCA 111	5.77	DCB 112	9.05
DCA 112	3.11	DCB 113	10.86
DCA 113	10.56	DCB 139	0.00
DCA 114	10.91	DCB 140	2.85
DCA 139	4.71	DCB 142	2.03
DCA 140	3.54	DCB 143	5.69
DCA 141	2.74	DCB 175	0.41
DCA 142	6.27	DCB 176	2.08
DCA 143	5.89	DCB 178	1.25
DCA 144	8.27	DCB 179	0.41

Source: DTN: LL030412512251.057 [DIRS 163712].

4.1.1 Qualification of Outside Sources

This section presents planning and documentation for the data qualification of unqualified external source data used as direct input in this report. Data qualification is performed in accordance with SCI-PRO-006, *Models*. The method used for qualification of all external sources of data is the "technical assessment method." The rationale for using this method is that there is no record of the Quality Assurance Plan under which the data were collected in the original sources. Qualification process attributes used in the technical assessment of the external sources are selected from the list provided in Attachment 4 of SCI-PRO-001 *Qualification of Unqualified Data*.

External Data Qualification for:

- *Alloy Digest 1985. Hastelloy Alloy C-22. Filing Code: Ni-317. Orange, New Jersey: Alloy Digest. TIC: 239931 [DIRS 178194].*
- *Haynes International 1988. Hastelloy Alloy C-22. Kokomo, Indiana: Haynes International. TIC: 239938 [DIRS 101995].*

Per SCI-PRO-006, data that are obtained from outside sources but are not established facts must be shown to be suitable for the specific application. When appropriately justified, these data are considered qualified for use within the technical product.

The method, for qualification for all external sources of data, is the Method 5, "technical assessment method." The rationale for using this method is that there is no record of the Quality Assuarance Plan under which the data were collected in the original sources. These evaluations were performed independently from the data collection or data reduction process and by a subject matter expert. For Method 5, one "actions to be taken" is considered: c) confirmation that the data have been used in similar applications.

Qualification process attributes used in the technical assessment of each external source are selected from the list provided in Attachment 4 of SCI-PRO-001. Particularly, the following criterion is used to qualify (1) Alloy Digest 1985. Hastelloy Alloy C-22. Filing Code: Ni-317. Orange, New Jersey: Alloy Digest. TIC: 239931 [DIRS 178194] and (2) Haynes International 1988. Hastelloy Alloy C-22. Kokomo, Indiana: Haynes International. TIC: 239938 [DIRS 101995]:

- Data must have been used for other similar investigations requiring verification processes

As indicated in DTN: MO0003RIB00071.000 [DIRS 148850], both Alloy Digest 1985 [DIRS 178194] and Haynes International 1988 [DIRS 101995] are accepted by the Project and used as Q data. Therefore, both Alloy Digest 1985 [DIRS 178194] and Haynes International 1988 [DIRS 101995] are considered qualified for use within this technical product.

External Data Qualification for:

- *Dutton, R.; Leitch, B.W.; Crosthwaite, J.L.; and Kasprick, G.R. 1996. Preliminary Analysis of the Creep Behaviour of Nuclear Fuel-Waste Container Materials. AECL-11495. Pinawa, Manitoba, Canada: Atomic Energy of Canada Limited. TIC: 232683 [DIRS 175817].*

Per SCI-PRO-006, data obtained from outside sources that are not established facts must be demonstrated to be suitable for the specific application. When appropriately justified, these data are considered qualified for use within the technical product. These evaluations were performed independently from the data-collection or data-reduction process by a subject matter expert. For Method 5, one "action to be taken" is considered: b) Determination that confidence in the data acquisition or developmental results is warranted.

The following evaluation criteria mentioned in SCI-PRO-006 are used to justify the direct use of information from *Preliminary Analysis of the Creep Behaviour of Nuclear Fuel-Waste Container Materials* (Dutton et al. 1996 [DIRS 175817]):

- Reliability of the data source—The information used in this report is based on experimental results published in an Atomic Energy of Canada Limited (AECL) report (AECL-11495). AECL is a prestigious nuclear technology and services company providing services to nuclear utilities worldwide. The data used in this report were obtained by AECL in support of the Canadian Nuclear Fuel Waste Management Program, which was funded by AECL and Ontario Hydro (a nuclear power plant vendor) under the auspices of the CANDU Owner's Group.

- Qualifications of personnel or organizations generating data—The information was generated and published by R. Dutton, who is respected in the scientific community for his scholarly research on titanium metal and its alloys. Based on the qualifications of the researcher and the reputation of the organization generating data (i.e., AECL), the use of this information in this document is appropriate.

Based on this assessment, *Preliminary Analysis of the Creep Behaviour of Nuclear Fuel-Waste Container Materials* (Dutton et al. 1996 [DIRS 175817], Figure 13) is qualified for intended use within this report.

4.2 CRITERIA

According to *Technical Work Plan for Postclosure Engineered Barrier Degradation Modeling* (SNL 2007 [DIRS 178849]), Section 3.2, Table 3-1), the following acceptance criteria are applicable to this report:

1. *System Description and Demonstration of Multiple Barriers* (NRC 2003 [DIRS 163274], Section 2.2.1.1.3; PRD-002/T-014, PRD-002/T-016):

    - AC1–Identification of Barriers is Adequate
    - AC2–Description of the Capability of Identified Barrier is Acceptable
    - AC3–Technical Basis for Barrier Capability is Adequately Presented.

2. *Degradation of Engineered Barriers* (NRC 2003 [DIRS 163274], Section 2.2.1.3.1.3; PRD-002/T-015):

   - AC1–System Description and Model Integration are Adequate
   - AC2–Data are Sufficient for Model Justification
   - AC3–Data Uncertainty is Characterized and Propagated Through the Model Abstraction
   - AC4–Model Uncertainty is Characterized and Propagated Through the Model Abstraction
   - AC5–Model Abstraction Output is Supported by Objective Comparisons.

The criteria as they relate to the waste package and drip shield barriers are addressed in Section 8.2, which discusses locations in the report that address individual acceptance criteria related to the two primary criteria.

4.3 CODES AND STANDARDS

The following codes or standards were used to generate this report:

- 10 CFR 63 [DIRS 180319]. Energy: Disposal of High-Level Radioactive Wastes in a Geologic Repository at Yucca Mountain, Nevada
- ASTM B 575-94 (Reapproved 1997) [DIRS 100497]. *Standard Specification for Low-Carbon Nickel-Molybdenum-Chromium, Low-Carbon Nickel-Chromium-Molybdenum, and Low-Carbon Nickel-Chromium-Molybdenum-Tungsten Alloy Plate, Sheet, and Strip*
- ASTM G 30-94 [DIRS 137688]. *Standard Practice for Making and Using U-Bend Stress-Corrosion Test Specimens*
- ASTM E 399-90 [DIRS 117480]. *Standard Test Method for Plane-Strain Fracture Toughness of Metallic Materials*
- ASTM G 129-00 [DIRS 171563]. *Standard Practice for Slow Strain Rate Testing to Evaluate the Susceptibility of Metallic Materials to Environmentally Assisted Cracking*
- ASTM G 49-85 (Reapproved 2000) [DIRS 171562]. *Standard Practice for Preparation and Use of Direct Tension Stress-Corrosion Test Specimens*
- ASTM B 265-02 [DIRS 162726]. *Standard Specification for Titanium and Titanium Alloy Strip, Sheet, and Plate*
- ASTM G 38-01 [DIRS 177289]. *Standard Practice for Making and Using C-Ring Stress-Corrosion Test Specimens*.

5. ASSUMPTIONS

Per SCI-PRO-006, this section includes a description of the assumption(s) used, in the absence of direct confirming data or evidence, to perform the model activity, to perform analyses and model development, and if necessary, to develop their abstractions for potential SCC of waste package and drip shield in the postclosure repository environments. Discussions of model assumptions (other than those made in the absence of direct confirming data or evidence, documented in Section 5) and the impact of key assumptions on model output will be documented in Section 6 thoughout the model development (SCI-PRO-006).

Assumption:

SCC initiation and growth in structural components made of Alloy 22 and Titanium Grades 7, 28, and 29 are treated as independent of environmental variables including brine composition and temperature.

Rationale:

SCC is the initiation and propagation of cracks in structural components due to three factors that are present simultaneously (Jones 1992 [DIRS 169906], Section 8.1): metallurgical susceptibility, critical environment, and sustained tensile stresses. Not including the environmental effect is a conservative approach to SCC modeling.

For Alloy 22, it has been shown that for a broad range of relevant and accelerated test environments, SCC initiation in slow strain rate tests has only been observed in 1M NaF (not a relevant brine) and in carbonate/bicarbonate containing brines including simulated concentrated water (SCW) (Section 6.2.1.3 and Table 6-2) and at temperatures above about 50°C (Shukla et al. 2006 [DIRS 177461]; Chiang et al. 2005 [DIRS 178444]). Shukla et al. (2006 [DIRS 177461]) developed an SCC initiation model based on an extensive test program that covered a broad range of test environments. As will be discussed in Section 6.2, they concluded that brines containing bicarbonate and chloride ions at pH values between 7 and 11 are essential for SCC initiation of Alloy 22, and they only observed initiation at anodically applied potentials greater than the open circuit potential. This is consistent with extensive Project test results described in Section 6.2.1 that indicate SCC initiation is not observed under open-circuit conditions in oxygenated carbonate/bicarbonate brines including SCW brine at temperatures ranging from below boiling up to 160°C. This is also consistent with SCC growth rate tests in aerated 150°C SCW brine (Table 6-6). The crack growth rates obtained on as-welded Alloy 22 at a very high stress-intensity factor (40MPa√m) under a near-sustained, 24-hour hold time at maximum load are extremely low (i.e., 1.2×10^{-9} mm/s). Since extensive Alloy 22 test results on U-bends, slow strain rate test results, and fatigue precracked compact tension specimens are available for the apparently most aggressive relevant brine, SCW, over a broad range of test temperatures (22°C to 160°C), test times (up to 3.2 years to 5 years), and stress levels (Sections 6.2.1 and Table 6-6), it is conservative to assume SCC initiation and growth in Alloy 22 is independent of environment. Similarly, as described in Section 6.8.3.1.2, SCW brine is also highly aggressive for SCC initiation in titanium alloys as evidenced by the observed SCC initiation in welded Titanium Grade 12 U-bend specimens exposed to 90°C SCW but not to simulated acidified water (SAW) or simulated dilute water (SDW) brines for up to five years.

Thus, it is conservative to also assume no environmental dependence for the drip shield titanium alloys, Titanium Grades 7, 28 and 29.

Confirmation Status: This is a conservative assumption and does not require further confirmation.

Use in Model and Analyses: This assumption is used throughout this report.

6. MODEL DISCUSSION

6.1 GENERAL DESCRIPTION OF SCC MODELING

One of the most common corrosion-related causes for early failure (breach) of metal structural components is stress corrosion cracking (SCC). SCC is the initiation and propagation of cracks in structural components due to three factors that are present simultaneously (Jones 1992 [DIRS 169906], Section 8.1): metallurgical susceptibility, critical environment, and sustained tensile stresses.

Discussion of SCC in this document is restricted to that which affects the waste package outer barrier and the drip shield materials. The waste package outer barrier is made of Alloy 22 and the drip shield plate material, weld filler metal and structural support material are made of Titanium Grades 7, 28, and 29, respectively. The stainless steel waste package inner structural cylinder is not modeled, as the total system performance assessment (TSPA) does not take credit for corrosion resistance of the stainless steel inner vessel of the waste package or the transportation, aging, and disposal canister.

Alloy 22, the material used for the waste package outer barrier, is a highly corrosion-resistant material. While SCC has not been observed under expected repository environments, it is modeled or treated as susceptible to stress corrosion cracking under the test conditions that simulate the Yucca Mountain environment (Sections 6.2 and 6.4) and the coexisting stress conditions induced by welding in the closure welds of the waste package final closure lids (Section 6.5). Analysis of the potential SCC behavior of Titanium Grades 7, 28, and 29 is discussed in Section 6.8.

6.1.1 General Description of SCC of Alloy 22

In this document, a lifetime-modeling approach is developed to assess the degradation of the Alloy 22 waste package outer barrier due to potential stress corrosion cracking. As indicated by the flow diagram shown in Figure 1-1, lifetime modeling considers crack initiation and preexisting manufacturing flaws (Section 6.2), the stress conditions (that drive the crack initiation and propagation) (Section 6.5), the potential crack initiation stress threshold (Section 6.2.2), the threshold stress intensity factor (that defines propagation of initiated incipient cracks and manufacturing flaws) (Section 6.4.5), and the crack growth model (based on the SDFR theory) that determines the crack growth rate (Section 6.4). As is summarized in Section 8, the stress corrosion cracking model considers all the elements needed to assess the effects of potential SCC on the Alloy 22 waste package outer barrier performance.

Stress corrosion cracking has historically been separated into “initiation” and “propagation” phases (Jones and Ricker 1987 [DIRS 118672], p. 146). For lifetime modeling, initiation is associated with microscopic crack formation at defect sites such as mechanical flaws. Coalescence of these microscopically small cracks will lead to SCC initiation on an otherwise “smooth” surface. SCC can also initiate at surface flaws or defects resulting from manufacturing processes (e.g., welding). Crack initiation (including the threshold stress for crack initiation) and manufacturing defects are discussed in Section 6.2.

To account for crack propagation, the SDFR model is adopted as the base-case model to provide mathematical formulas for the prediction of crack growth rate. The SDFR model relates the crack advance (or propagation), subsequent to crack initiation at the bare metal surface, to the metal oxidation that occurs when the protective film at the crack tip is ruptured. In literature, there are other mechanistic approaches to understanding the SCC mechanism. For example, Galvele (1987 [DIRS 178480]) proposed the enhanced surface mobility model using simple metallurgical principles and the assumption that high surface mobility is present in the process. The crack velocity is related to surface mobility and stress concentration at the crack tip. An excellent overview of SCC crack propagation mechanisms and models can be found in *Corrosion* (ASM 1987 [DIRS 103753], pp. 159 to 163). The SDFR stress corrosion cracking model is adopted because of its success in describing SCC of nickel alloys and stainless steels and its use by the nuclear industry in quantifying SCC damage in stainless steel and nickel-alloy components. The SDFR stress corrosion cracking model is described in Section 6.4.

It is also possible that a crack may reach an "arrest" state after it enters the propagation phase. A threshold stress intensity factor (K_{ISCC}), below which cracks will no longer propagate, exists that provides a criterion for determining if an initiated crack or preexisting flaw will reach the arrest state. The threshold stress intensity factor is based on the theory that below a threshold value (K_{ISCC}) of the stress intensity factor, K_I, no growth occurs for a given crack. On the other hand, some researchers believe that a threshold K_{ISCC} does not really exist and that at low K_I values standard laboratory tests are not long enough to determine low(er) values of crack propagation rate (Andresen et al. 2004 [DIRS 178449]). K_{ISCC} is discussed in Section 6.4.5. Determination of the weld-induced stress and K_I profiles through the waste package wall are described in Section 6.5. The threshold stress, threshold stress intensity factor, and other parameters associated with the SDFR crack growth model are determined from experimental data developed for environments relevant to those to which the waste package and drip shield may be exposed in the repository.

An alternative conceptual model (ACM), the coupled environmental fracture (CEF) model, was developed for the case where the internal and external environments are coupled by the need to conserve charge in the system. The CEF model represents an alternative approach to the base-case SDFR model for the prediction of the crack growth rate. It is considered only for the purpose of validation of the base-case model. The CEF model and the technical basis for screening out this model are discussed in Section 6.4.6. The base-case SDFR and the alternative CEF models were initially developed to account for SCC of sensitized Stainless Steel Type 304 (i.e., stainless steel exposed to higher temperatures that make the grain boundaries more susceptible to corrosion). An evaluation of other SCC models for sensitized stainless steel indicates a weaker theoretical basis for these models (Macdonald and Urquidi-Macdonald 1991 [DIRS 162702]). Therefore, no additional alternative conceptual models for SCC are considered in this document.

The seismic crack density model of the waste package estimates the crack opening area on a waste package damaged by a seismic event. The cracks within the damaged area are assumed to be caused as a result of stresses induced by a seismic event. In order to assess the potential for radionuclide release through these cracks, it is necessary to assess the possible number of cracks in the damaged area and the opening areas of these cracks.

The seismic scenario requires three inputs to represent the effective area of a network of cracks:

(1) Total damaged area on the waste package, A_D

(2) Crack density in the damaged area on the surface of the barrier, ρ_{SCC}

(3) Crack opening area of an individual crack, A_{SCC}.

The damage abstractions for the seismic scenario will define the total damaged area on the barrier. The total area of the crack network, $A_{SCC,\ NET}$, is then the product of the seismically damaged area, A_D (SNL 2007 [DIRS 176828], Section 6.7), the crack density, ρ_{SCC} (the number of cracks per unit area); and the crack opening area of an individual crack, A_{SCC} (area/crack) (i.e., $A_{SCC,\ NET} = A_D\ (\rho_{SCC}\ A_{SCC})$) (Herrera 2004 [DIRS 168133], Section 6.1).

The factor ($\rho_{SCC}\ A_{SCC}$) is the crack area density or crack area per unit of seismically damaged area (i.e., the fraction of the seismically damaged area) through which radionuclides can be released. The factor ($\rho_{SCC}\ A_{SCC}$) can be viewed as a scaling factor applied to the seismically damaged area to obtain the total area of the crack network, $A_{SCC,\ NET}$. Section 6.7.3 provides estimates of the crack area density.

6.1.2 General Description of SCC of Titanium Alloys

Section 6.8 discusses the treatment of SCC of drip shield materials, including crack growth rate, initiation threshold stresses, and threshold stress intensity factors for Titanium Grades 7, 28, and 29; seismic crack density of potential stress corrosion cracks in the drip shield materials, and low-temperature creep of titanium alloys. Not all drip shield related subjects discussed in Section 6.8 are "models." For instance, the SCC crack growth rate (Section 6.8.4) is a measured parameter only, and the low-temperature creep section (Section 6.8.7) only summarizes observations on the subject in the literature. This is true for the SCC crack "plugging" section (Section 6.8.6). Therefore, only the representation of seismic crack density constitutes model development (Section 6.8.5). The SCC initiation threshold stresses (Section 6.8.3) and threshold stress intensity factors (Section 6.8.4.2.2 and Section 6.8.4.2.4) are criteria developed to address the potential for SCC.. Therefore, these criteria and parameters are discussed in Sections 7.4 only as additional confidence-building activities to support defensibility. The seismic crack density model for the drip shield is validated in Section 7.5.2. *Technical Work Plan for Postclosure Engineered Barrier Degradation Modeling* (SNL 2007 [DIRS 178849], Section 2.3.2) states that the drip shield SCC modeling warrants a low level of confidence (Level I).

6.2 SCC CRACK INITIATION FOR ALLOY 22

This section discusses the issues of crack initiation and manufacturing flaws. In the absence of cyclic stresses for a given alloy and associated metallurgical condition, under certain environmental conditions, SCC will not initiate on a "smooth" surface, if the surface stress is below a threshold value (defined as the threshold stress) (ASM International 1987 [DIRS 103753], Vol. 13, p. 276). A "smooth" surface is one without sharp defects such as notches and weld flaws. These sharp defects can generate a significant stress intensity factor.

For lifetime modeling, it is appropriate to consider that initiation is associated with microscopic crack formation at defect sites such as mechanical flaws. Coalescence of these microscopically small cracks will lead to SCC initiation on an otherwise "smooth" surface. Initial SCC can also initiate at surface flaws or defects resulting from manufacturing processes (e.g., welding).

Shukla et al. (2006 [DIRS 177461]) recently developed an empirical model with respect to SCC initiation in Alloy 22 that assumes there is a unique potential, E_{SCC}, above which SCC initiation can occur under a range of environmental conditions, when:

$$E_{corr} - E_{SCC} \geq 0$$

and

$$\frac{[Cl^-]}{[HCO_3^-] + [CO_3^{2-}]} > 0.12$$

and

$$[Cl^-] > 0.09M$$

The model incorporates a corrosion potential submodel also developed by Shukla et al. (2006 [DIRS 177461]), who determined E_{SCC} based on slow strain rate test (SSRT) experiments covering a range of environments and applied potentials, including chloride brines with a range of carbonate, bicarbonate, and chloride concentrations. Shukla et al. (2006 [DIRS 177461]) determined that bicarbonate and chloride ions are essential for SCC initiation of Alloy 22, which only occurs under anodically polarized conditions and not under open-circuit potential conditions.

Speciation calculations indicated that sufficient bicarbonate is only possible in solutions with pH values ranging from 7 to 11. Under these conditions, an anodic peak is observed in cyclic polarization curves and the peak potential is directly correlated with SCC susceptibility. Further, Shukla et al. (2006 [DIRS 177461]) stated that the corrosion potential could only exceed E_{SCC} in low pH solutions (pH less than 6), whereas SSRT showed no signs of SCC at these lower pH values due to the absence of bicarbonate ions. Therefore, according to this model, SCC initiation of Alloy 22 is not possible in the repository. This assertion is consistent with the lack of SCC initiation under open-circuit potential conditions observed in YMP-sponsored testing described in Section 6.2.1. However, as described in Section 6.4.4.2, SCC initiated by cyclic loading of fatigue precracked fracture mechanics specimens exhibits subsequent constant-load crack growth when tested in 110°C aerated basic saturated water (BSW) and 150°C aerated simulated concentrated water (SCW) (bicarbonate-containing basic brines) under open-circuit conditions. Shukla et al. (2006 [DIRS 177461]) did not evaluate the effect of nitrate in these solutions on the open-circuit potential and SCC susceptibility, although nitrate is normally present in YMP-relevant brines. However, Chiang et al. (2005 [DIRS 178444]) studied the contribution of each anion in SCW independently on the polarization and cracking susceptibility of Alloy 22. They determined that the offending anion was bicarbonate and that nitrate did not have any effect on SCC susceptibility. Recent work by Dunn et al. (2006 [DIRS 177469]) shows that a thick oxide layer forms on Alloy 22 samples at 95°C in solutions with chloride and bicarbonate

at high-anodic potentials. The oxide layer has reduced chromium content, which appears to correlate with SCC susceptibility.

6.2.1 Laboratory Testing for Alloy 22 SCC Crack Initiation

6.2.1.1 Constant-Load Tests

General Electric Global Research Center (GE GRC) initially tested 185 Alloy 22, Titanium Grade 7, and Stainless Steel Types 304 and 316 constant-load specimens in 105°C diluted BSW (DTN: MO0409GE835924.000 [DIRS 171564]; DTN: MO0707SCCIGMER.000 [DIRS 182202], Table 2-3; DTN: MO0705SCCIGM06.000 [DIRS 180869], file *GE-GRC-Final_Sept-2006-Rev3.doc*, file *GE-GRC-Final_Sept-2006-Rev3.doc*, Figure 21). Among these specimens, which covered a range of metallurgical conditions, 120 were fabricated from Alloy 22, 23 from Titanium Grade 7, 24 from Stainless Steel Type 316 (Nuclear Grade), and 18 from Stainless Steel Type 304 (DTN: MO0707SCCIGMER.000 [DIRS 182202], Table 2-3). Subsequently, a number of specimens were replaced with titanium specimens. The total number of the specimens tested was 201.

Test Conditions

Figure 4-1 (DTN: MO0705SCCIGM06.000 [DIRS 180869], file *GE-GRC-Final_Sept-2006-Rev3.doc*, Figure 21) updates the crack initiation measurements obtained under constant-load conditions in diluted BSW at 105°C as reported in DTN: MO0409GE835924.000 [DIRS 171564], and by DTN: MO0707SCCIGMER.000 [DIRS 182202]. These constant-load tests were performed in general conformance to ASTM G 49-85 [DIRS 171562] but were slightly modified as indicated in DTN: LL021105312251.023 ([DIRS 161253]), Section 2.2). In Figure 4-1, the crack initiation stress measurements are presented as applied stress ratio (the ratio of applied stress to the at-temperature yield strength) versus time-to-failure (or total exposure time without failure for specimens subjected to over 28,000 hours (approximately 3.2 years) of exposure). The measured values for at-temperature yield strength will be described in relevant sections.

The composition of BSW, a concentrated salt solution, is shown in DTN: LL021105312251.023 ([DIRS 161253], Sections 2.2 and 2.5). The target test solution composition, used to obtain the data in Figure 4-1, is 0.27M Na_2CO_3, 0.35M KCl, 0.41M NaCl, 0.013M NaF, 0.43M $NaNO_3$, 0.03M Na_2SO_4, and 0.04M $Na_2SiO_3 \cdot 9H_2O$. This composition represents a solution diluted to yield approximately 15% of the concentration of BSW and is used to simulate the chemistry of one of the concentrated Yucca Mountain groundwaters. At 105°C, the pH of this diluted BSW solution is reported as 10.3 (DTN: LL021105312251.023 [DIRS 161253], p. 99, Table 2-1).

The results shown in Figure 4-1, together with the previously reported test results shown in Figure 4-2 (DTN: LL021105312251.023 [DIRS 161253], Figure 2-5), confirm that Alloy 22 possesses excellent resistance to stress corrosion cracking. As can be seen from Figure 4-1, failure has not been observed after test times of over 28,000 hours (approximately 3.2 years) (over 20,000 hours (approximately 2.3 years) for notched specimens) for any of the 120 Alloy 22 specimens covering a variety of metallurgical conditions, including the as-welded condition. The applied stress ratios were up to about 2.03 times the interpolated 105°C yield strength value

(Table 6-4) and 2.1 times the measured 125°C yield strength value of the as-received material (324 MPa). This stress ratio corresponds to an applied stress of about 95% of the 125°C measured ultimate tensile strength (104 ksi or 717 MPa) (DTN: LL021105312251.023 [DIRS 161253], Table 2-4). The yield and ultimate tensile strengths of the as-received +20% cold-worked Alloy 22 are measured at 125°C as 125 ksi (862 MPa) and 133 ksi (917 MPa), respectively (DTN: LL021105312251.023 [DIRS 161253], Figure 2-4). The yield strength value at 125°C, rather than the value at 105°C, was used to calculate the stress to yield strength ratio, since 125°C is the representative long-term waste package temperature used in subsequent analyses for weld residual stresses and stress intensity factors (Section 6.5).

Metallurgical Variables of Testing Materials

The 120 constant-load Alloy 22 test specimens reported in Figure 4-1 include "smooth"-surface specimens and notched specimens with the notches located in either weld metal or in the weld heat-affected zone (DTN: LL021105312251.023 [DIRS 161253], Figures 2-19 to 2-22 for notch details). These specimens represent a range of different microstructures or metallurgical conditions, including the:

1. Annealed condition (solution annealed at a high temperature and rapidly cooled)
2. As-welded condition including weld metal and heat-affected zone
3. Annealed-plus-thermally aged condition (i.e., heated in a temperature range where potentially deleterious precipitates can form) that produces extensive formation of a tetrahedrally close-packed (TCP) phase (700°C for 175 hours)
4. Annealed-plus-thermally aged condition to produce long-range ordering (LRO) (520°C for 1,000 hours)
5. Cold-worked condition (20% cold-worked) with and without thermal aging at 700°C for 175 hours.

The various constant-load test conditions evaluated are provided in Figure 4-1. A more-detailed description and a series of optical and scanning electron microscope photomicrographs of the various microstructures are presented in DTN: LL021105312251.023 [DIRS 161253].

Aging and Phase Stability of Waste Package Outer Barrier (BSC 2004 [DIRS 171924], Section 8) concluded "…the formation of TCP or ordered oP6 phases in Alloy 22 base metal and welds (which are deemed to be similar to base metal) will not be a concern for conditions of less than 300°C for a period of 500 years followed by temperatures less than 200°C for a period of 9,500 years, conditions that bound the repository time-temperature profiles." The results reported in Figure 4-1 are consistent with *Aging and Phase Stability of Waste Package Outer Barrier* (BSC 2004 ([DIRS 171924]) conclusions that the thermal aging conditions evaluated in these constant-load tests are highly conservative.

To maintain this conservative position, the GE GRC constant-load test matrix was designed to represent TCP and LRO conditions. Based on *Aging and Phase Stability of Waste Package Outer Barrier* (BSC 2004 [DIRS 171924], Figure 91), the TCP heat treatment (700°C for

175 hours) results in a 100% grain boundary coverage fraction. From Table 10 of the *Aging and Phase Stability of Waste Package Outer Barrier* (BSC 2004 ([DIRS 171924]), a similar LRO heat treatment at a temperature of 550°C for 1,000 hours results in an increase in Alloy 22 microhardness from an as-received value of 217 Hv to an as-aged value of 329 Hv. This increase in hardness is consistent with the measured increase in yield strength (DTN: LL021105312251.023 [DIRS 161253], Table 2-4). As reported in the DTN: LL021105312251.023 ([DIRS 161253], Table 2-4), the yield strength of Alloy 22 plate material increased from 47 ksi (324 MPa) for the as-received material to 70 ksi (483 MPa) for the LRO heat-treated material.

Test Results

Figure 4-1 summarizes the stress corrosion crack initiation measurements obtained under constant-load conditions in diluted BSW at 105°C as reported in DTN: MO0409GE835924.000 [DIRS 171564], and by DTNs: MO0707SCCIGMER.000 [DIRS 182202] and MO0705SCCIGM06.000 [DIRS 180869], file *GE-GRC-Final_Sept-2006-Rev3.doc*, Figure 21. The minimum failure stress (or maximum, long-term applied stress without SCC failure) can be obtained from the constant-load test results shown in that figure. The levels of the maximum, long-term applied stress without SCC failure produced an applied stress/yield strength ratio of about 2.1 for as-received (mill-annealed) Alloy 22 and about 2.0 for as-welded Alloy 22. The lack of SCC initiation was confirmed using dye penetrant and metallographic examination of an as-received Alloy 22 test specimen after over 25,000 hours (approximately 2.9 years) of testing at 93 ksi (641 MPa) as shown in Figure 6-1. The applied stress/yield strength ratio for this particular case is about 1.9. As can be seen from Figure 4-1, the highest applied stress/yield strength ratio tested without failure was 2.11. As reported by DTN: MO0707SCCIGMER.000 ([DIRS 182202], Table 2-3), six specimens were tested at 100 ksi (approximately 689 MPa) applied stress, which is above 2.11 times the yield strength measured at 125°C (47 ksi or 324 MPa), with no SCC failure observed.

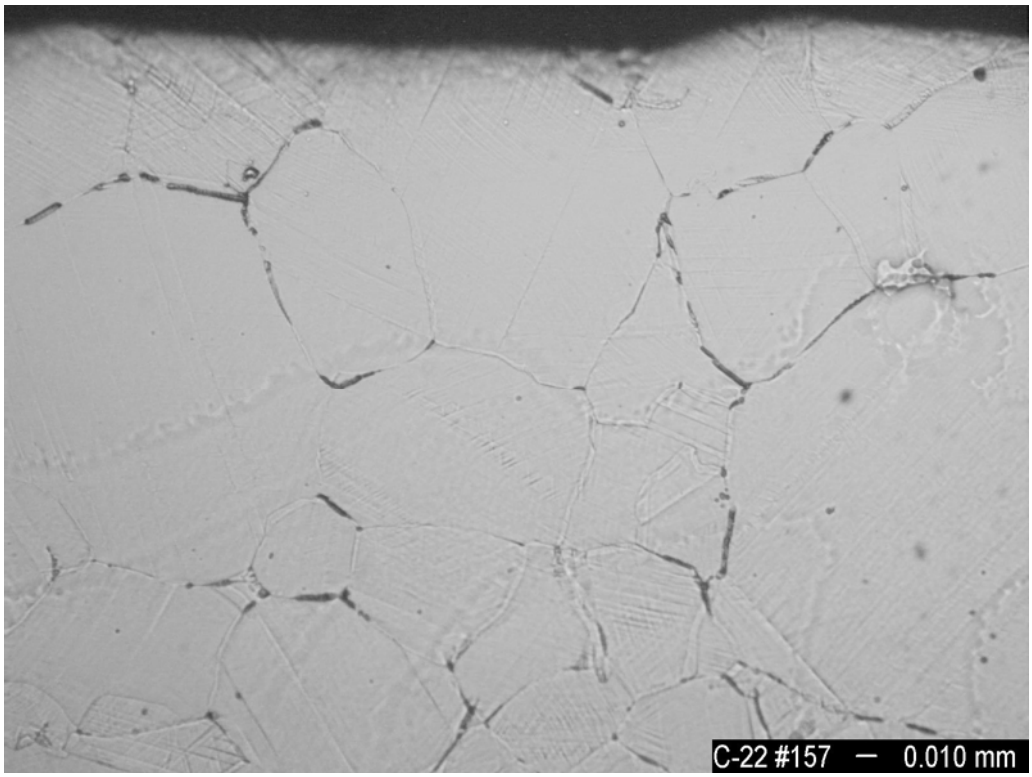

Source: DTN: MO0707SCCIGMER.000 [DIRS 182202], Figure 2-27.

Figure 6-1. Polished and Etched Metallographic Cross Section of GE Specimen #157 of Alloy 22 after over 25,000 hours (approximately 2.9 years) at 93 ksi (641 MPa) in Diluted BSW Solution Showing No Evidence of SCC Initiation

6.2.1.2 U-Bend SCC Initiation Tests

6.2.1.2.1 Alloy 22 Tests in Long Term Corrosion Test Facility

Alloy 22 U-bend specimens were exposed at the Lawrence Livermore National Laboratory (LLNL) Long-Term Corrosion Test Facility (LTCTF) to a range of relevant aerated-brine environments at 60°C and 90°C for times up to five years (Fix et al. 2003 [DIRS 162700], p. 1).

Test Conditions

The LTCTF testing program produced single U-bend specimens using wrought sheets and welded sheets. In the welded specimens, the weld was across the apex of the bend. The weld process was gas metal arc welding using matching filler metal, and the seam had full penetration. The chemical compositions of the sheet material and the filler metal used for the fabrication of the LTCTF U-bend specimens are shown in Table 6-1, as are the SSRT specimen chemical compositions. Section 6.2.1.3 discusses the SSRT results.

Table 6-1. Chemical Composition (wt %) of the Alloy 22 Specimens Tested at LTCTF with Heat Numbers

Element	Single U-Bend (Heat 2277-0-3264)	Weld Filler Metal (Heat 2277-4-3263)	SSRT (Heat 2277-8-3126)
Carbon	0.004	0.002	0.004
Cobalt	1.14	0.89	1.03
Chromium	21.3	21.6	21.70
Iron	4.4	3.6	3.59
Manganese	0.29	0.32	0.27
Molybdenum	13.4	13.5	13.26
Nickel	~56	~56	~56
Phosphorus	0.01	0.009	0.006
Sulfur	<0.002	0.003	0.001
Vanadium	0.17	0.15	0.14
Tungsten	2.9	2.9	2.80

Source: Fix et al. 2003 [DIRS 162700], Table 2.

NOTE: SSRT = slow strain rate test.

The U-bend specimens chosen for laboratory testing contained residual stresses due to permanent deformation and the restraint applied to the specimen "legs" using insulated bolts. The specimens were tested in the as-machined condition, which corresponded to a root mean square roughness of 32 μ-in. The specimens were degreased in acetone before testing. The U-bend specimens were prepared using strips 3/4-in wide (approximately 19 mm) and 1/16-in thick (approximately 1.6 mm) according to ASTM G 30-94 [DIRS 137688]. The resulting specimens had a constant nominal separation between both legs or ends, of 0.5 in (approximately 13 mm) secured by a bolt electrically insulated from the specimen through ceramic zirconia washers. The total plastic deformation in the external outer fiber of Alloy 22 was approximately 12% (Fix et al. 2003 [DIRS 162700]).

Test Results

The high resistance of Alloy 22 to SCC initiation demonstrated by the constant-load tests described in Section 6.2.1.1 is corroborated by results of high magnification visual examination of a number of Alloy 22 U-bend specimens fabricated and tested per ASTM G 30-94 ([DIRS 137688]). No evidence of stress corrosion cracking initiation has been observed in these LTCTF U-bend specimens after about five years of exposure in 60°C and 90°C SDW, SCW, and simulated acidified water (SAW) brines. The brine compositions used in these experiments are listed in DTN: LL040803112251.117 [DIRS 171362]. Fifty-two specimens were removed from six of the testing tanks, and cleaned and examined optically at up to 100 times magnification using a stereomicroscope (Fix et al. 2003 [DIRS 162700]). Six of these specimens were later disassembled, examined in the scanning electron microscope, and subsequently mounted for metallographic sectioning. No evidence of environmentally assisted cracking was observed while the U-bend specimens remained under stress after the five-year exposure period.

6.2.1.2.2 GE GRC Alloy 22 Single and Double U-Bends Exposed in Aerated 165°C SCW

Based on the constant-load test results described previously (Sections 6.2.1.1 and 6.2.1.2.1) and the SSRT results to be described in Section 6.2.1.3, Alloy 22 has been shown to be extremely resistant, if not immune, to SCC initiation in a range of concentrated chloride-containing brines with pH values varying from about 3 to 12. To further accelerate the potential for SCC initiation, an additional selection of U-bend specimens were exposed in an autoclave in brine under more aggressive conditions.

Test Conditions

A set of single and double (creviced) U-bends were exposed in an autoclave in aerated SCW basic brine at a temperature of 165°C, which is well above the brine boiling point of the test solution (about 105°C)) (DTN: MO0707SCCIGMER.000 [DIRS 182202], Section 4.0). The SCW brine was found to be the most aggressive relative to SCC initiation based on the series of SSRTs performed in a broad range of environments as described below in Section 6.2.1.3. This brine falls in the range of environments leading to potential SCC susceptibility for Alloy 22 as indicated by the SCC initiation model discussed in Section 6.2 (Shukla et al. 2006 [DIRS 177461]). The single U-bend specimens (Figure 6-2(a)) were fabricated from approximately 1-in-thick welded Alloy 22 plate material with the weld located at the specimen apex. In addition to the as-welded condition, the test matrix covered a range of simulated thermal aging heat treatment conditions that produced either TCP or LRO phases. The specimens tested and conditions covered are summarized in Table 6-2. In addition to the single U-bends, ten double U-bend specimens (Figure 6-2(b)) were fabricated from about 1-in-thick Alloy 22 plate in the as-received (mill annealed) condition (DTN: MO0707SCCIGMER.000 [DIRS 182202], Table 4-2).

(a) Single U-bend (b) Double U-bend

Source: DTN: MO0707SCCIGMER.000 [DIRS 182202], Figures 4-2 and 4-3.

Figure 6-2. 165°C SCW Exposed Alloy 22 Single and Double U-bend Specimens

Test Results

The single and double U-bend specimens were exposed for 17,241 total hours (approximately 2 years) with periodic removals to perform stereomicroscopic inspections and to retighten the specimen leg bolts to compensate for any stress relaxation that may have occurred. The double

U-bends were disassembled for inspection after 14,756 hours (approximately 1.7 years) exposure. The specimens were then reassembled to continue the test. In all cases, no evidence of SCC initiation was observed. The specimens were covered with a thin, milky deposit that was identified by attenuated total-relectance infrared spectra-analysis as being rich in silica and alumina (DTN: MO0707SCCIGMER.000 [DIRS 182202], Section 4.0). Although silica is a constituent of the SCW brine, the source of alumina is likely the ceramic spacer sleeve present on the double U-bend specimens as there was evidence of some dissolution of the ceramic sleeves (DTN: MO0707SCCIGMER.000 [DIRS 182202], Section 4.0).

6.2.1.2.3 Other U-bend Tests

To further corroborate the high degree of resistance to SCC initiation indicated by the SSRTs, two Alloy 22 U-bend specimens (one annealed and one as-welded) were exposed for 28 days to 90°C SCW while polarized to +400 $mV_{(SSC)}$, a condition under which incipient stress corrosion cracking was observed during SSRTs (Fix et al. 2003 [DIRS 162700]). While these tests are relatively short term, the specimens are under +400 $mV_{(SSC)}$ polarization to accelerate the breakdown of the passive film. The posttest stereomicroscopic examination of these U-bend specimens revealed no evidence of stress corrosion initiation.

In addition to the GE GRC single and double U-bends exposed in 165°C SCW brine, additional double U-bends were exposed at the LLNL LTCTF for 17 months in aerated 105°C BSW brine with no evidence of SCC initiation, as shown in Figure 6-3 (DTN: LL030102212251.005 [DIRS 178276]).

Source: DTN: LL030102212251.005 [DIRS 178276].

Figure 6-3. Alloy 22 Double U-Bend Specimens Exposed for 17 Months in 105°C BSW at LTCTF

6.2.1.3 Slow Strain Rate Test

Additional corroboration supporting very high resistance of Alloy 22 SCC initiation is provided by a series of slow strain rate tests (SSRTs) performed at LLNL in general conformance to ASTM G 129-00 [DIRS 171563] over a range of potentially relevant and accelerated environments (Estill et al. 2002 [DIRS 167274]; King et al. 2004 [DIRS 170981]).

Test Conditions

These SSRT specimens were made from mill-annealed Alloy 22. The alloy heat and chemical composition of the SSRT specimens are listed in Table 6-1. The SSRTs were conducted in test solutions described in Table 6-2 at 22°C to 120°C with a strain rate of $1.66 \times 10^{-6}\ s^{-1}$. Because the SSRT specimen is subjected to continuously increasing strain until failure, the test does not generally give a direct measure of the threshold stress for SCC initiation. Even though SCC may initiate during the test, it is usually not evident at that precise point in the test. However, the absence of SCC in this test is consistent with the material being a SCC-resistant material with a high threshold stress.

The SSRT results for Alloy 22 specimens tested at E_{corr} and above (i.e., anodically polarized) are summarized in Table 6-2. Table 6-2 contains a consolidated compilation of the results obtained by Estill et al. (2002 [DIRS 167274], Table 6) and King et al. (2004 [DIRS 170981], Table 2). The test data cover a broad range of relevant and potentially accelerating environments, with and without lead additions and/or with and without anodic polarization.

Test Results

Examination of the results summarized in Table 6-2 confirms the expected high degree of stress corrosion cracking resistance at open-circuit potentials in the environments evaluated, including approximately 8.5 M (saturated) $CaCl_2$-type brines (pH of approximately 6) at 120°C, as well as 1% lead chloride solutions (pH of approximately 4) at 95°C. In two cases, SCC initiation was or may have been observed. In the first case, SCC initiation was observed in SCW with an applied potential of 200 $mV_{(SSC)}$ to 400 $mV_{(SSC)}$. This potential is significantly more noble than the corresponding open-circuit corrosion potential, which was in the range of −241 $mV_{(SSC)}$ to −76 $mV_{(SSC)}$. SCC initiation at applied anodic potential of >300 mV in this environment is consistent with the model for Alloy 22 initiation previously developed by the Center for Nuclear Waste Regulatory Analyses (CNWRA) (Shukla et al. 2006 [DIRS 177461]). This is discussed briefly by Dunn et al. (2005 [DIRS 178104]).

SCC initiation was also observed in 1M NaF at 90°C and polarized to +400 $mV_{(SSC)}$; the corresponding E_{corr} was –244 $mV_{(SSC)}$.

Table 6-2. Slow Strain Rate Test Results for Annealed Alloy 22 (Strain Rate 1.66×10^{-6} s^{-1})

Specimen ID	Test Environment	Temperature (°C)	E_{corr} (mV versus SSC)	$E_{Applied}$ (mV versus SSC)	Time to Failure of Specimen (hrs)	Maximum Stress (MPa)	Reduction in Area (%)	Observation
012	Air	22	None	None	124	786	74	Ductile necking
040	Air	22	None	None	123	813	70	Ductile necking
098	1M NaCl at pH = 6.9	90	−104	+400	74[a]	660	76	No SCC
123	4M NaCl at pH = 6.2	98	−323	+349	127	762	80	No SCC
091	1M NaF at pH = 9.2	85	133	E_{corr}	112	756	67	No SCC
130	1M NaF at pH = 7.6	90	−244	+400	112	727	67	Incipient SCC
004	8.5M $CaCl_2$ at pH ~ 6	120	−140 to −180	E_{corr}	127	752	71	No SCC
013	1% $PbCl_2$ at pH ~ 4 Aerated	95	—	E_{corr}	126	765	72	No SCC
015	SAW at pH ~ 3	63	−7 to +360	E_{corr}	118	758	79	No SCC
016	SAW at pH ~ 3 + 0.005% $Pb(NO_3)_2$	76	−6 to +370	E_{corr}	124	772	74	No SCC
017	SAW at pH ~ 3 + 0.005% $Pb(NO_3)_2$	76	0 to +350	E_{corr}	125	772	74	No SCC
003	SAW at pH ~ 3 + 0.005% $Pb(NO_3)_2$	95	−90 to +400	E_{corr}	118	752	85	No SCC
127	BSW at pH ~ 13 − $[NO_3 + SO_4]$[b]	98	−240 to −220	E_{corr}	123	745	72	No SCC
124	BSW at pH ~ 13 − $[NO_3 + SO_4]$[b]	105	−330	+100	120	745	78	No SCC
122	BSW at pH ~ 13 − $[NO_3 + SO_4]$[b]	98	−245	+200	122	752	72	No SCC
120	BSW at pH ~ 13	105	−323	+400	99	745	74	No SCC
119	BSW at pH ~ 13	105	−301	+400	118	745	75	No SCC
115	BSW at pH ~ 13 − $[NO_3]$[b]	105	−335	+400	115	752	77	No SCC
129	BSW at pH ~ 13 − $[SO_4^{2-}]$[b]	105	−314	+400	119	731	82	No SCC
125	SSW at pH ~ 6	100	−154	+400	113	717	71	No SCC
020	SCW at pH ~ 9 to 10	22	−109	+400	116	800	85	No SCC
133	SCW at pH ~ 9 to 10	22	−128	+400	124	798	80	No SCC
032	SCW at pH ~ 9 to 10	50	−129	+400	110	757	75	Incipient SCC
134	SCW at pH ~ 9 to 10	65	−217	+400	97	684	59	SCC
112	SCW at pH ~ 9 to 10	73	−93	+400	91	697	71	SCC
021	SCW at pH ~ 9 to 10	73	−172	+400	90	665	64	SCC
033	SCW at pH ~ 9 to 10	86	−169	+400	76	642	44	SCC
113	SCW at pH ~ 9 to 10	75	−200	+317	116	765	63	Incipient SCC
030	SCW at pH ~ 9 to 10	85	−182	+300	98	725	65	SCC
020	SCW at pH ~ 9 to 10	22	−109	+291	116	800	85	No SCC
023	SCW at pH ~ 9 to 10	73	−224	+200	DNB	DNB	72	Incipient SCC
025	SCW at pH ~ 9 to 10	73	−172	+200	116	776	80	Incipient SCC
029	SCW at pH ~ 9 to 10	89	−144	+200	112	678	73	Incipient SCC
026	SCW at pH ~ 9 to 10	73	−241	+100	120	764	79	No SCC
037	SCW at pH ~ 9 to 10	22	−76	E_{corr}	DNB	DNB	32	No SCC
034	SCW at pH ~ 9 to 10	90	−143	E_{corr}	129	712	80	No SCC

Sources: Estill et al. 2002 [DIRS 167274]; King et al. 2004 [DIRS 170981].

NOTES: BSW = basic saturated water; DNB = did not break—equipment stoppage; SAW = simulated acidified water; SCC = stress corrosion cracking; SCW = simulated concentrated water; SSW = simulated saturated water.

[a] Short time to failure due to crevice corrosion at coating interface.

[b] BSW without the presence of nitrate or sulfate, or both.

SCW is a bicarbonate-containing, concentrated (approximately 1,000-fold) version of J-13 groundwater with a pH value of approximately 9 to 10. The pure 1M NaF with a pH = 7.6 is used as an accelerated test and is not directly relevant to the repository environment. Clearly, these SSRT results are consistent with the very low susceptibility of Alloy 22 to SCC. Even under these highly accelerated conditions (SCW at 90°C and at the high applied potential of 400 $mV_{(SSC)}$), the stress at which the onset of SCC was first detected, using a sensitive acoustic emission monitoring technique, corresponded to an applied stress of 605 MPa, about 156% of the room temperature yield strength of the Alloy 22 plate material (Fix et al. 2003 [DIRS 162700]). Although this high-SCC-onset stress (and correspondingly high strain value) does not necessarily equal the crack initiation stress under the highly accelerated conditions, the test results are nevertheless consistent with the fact that the threshold initiation stress for SCC is very high for Alloy 22 as concluded by other test methods described in Sections 6.2.1.1 and 6.2.1.2.

With respect to the SSRTs, a given strain rate (more precisely, the cross-head speed) is imposed on the test specimen. Once SCC initiates, the crack growth rate is partially governed by the imposed strain rate, which is much faster than the measured crack growth rates for Alloy 22 obtained by using compact tension specimens per ASTM E 399-90 [DIRS 117480]. Therefore, the SSRT data are not used to generate crack growth rates in development of the stress corrosion crack growth rate model (Section 6.4.4). However, the SSRT results for the case where lead additions were evaluated are discussed in Section 6.4.4.

6.2.2 SCC Crack Initiation Threshold Stress Criterion for Alloy 22

The constant-load and U-bend test results mentioned previously are for exposures up to five years. Results available in the literature for other nickel-base alloys (Alloy X-750 and Inconel 718) indicate that, depending on the applied stress level, SCC initiation may not occur at applied stress ratios of ≤1.0 times yield strength until times as long as 8 to 14 years on test (Gordon 1999 [DIRS 178145]). At above-yield strength stress ratios, SCC initiation was observed after about two to three years of exposure. However, unlike Alloy 22, these results are for age-hardenable nickel alloys tested under higher-temperature light water reactor (LWR) coolant conditions at temperatures of 288°C. Because of the age-hardening nature of these alloys, it is likely that microstructural changes can occur at 288°C, leading to increasing SCC susceptibility with exposure time.

Further, in the case of Alloy 22 that has not been age hardened, the reported GE GRC results discussed in Section 6.2.1.1 include constant-load Keno specimens tested for over three years at applied stresses as high as 2.1 times yield strength (approximately 95% of the ultimate tensile strength measured at 125°C) with no evidence of SCC initiation. The test results obtained at LTCTF also show that U-bend specimens held at or over yield strength stresses for up to five years did not exhibit SCC initiation.

Therefore, in order to derive a defensible threshold stress criterion value for the waste package outer barrier, an appropriate extrapolation scheme is necessary. For Alloy 22, the threshold stress criterion associated with the initiation of SCC can be established by applying an appropriate safety factor to the maximum long-term applied stress without failure. Results obtained from the constant-load tests described in Figure 4-1 can be used because the conditions

can be shown to be conservative relative to the expected repository environment and failure was not observed.

The maximum long-term applied stress without failure obtained from the constant-load (primary stress) test results is 2.1 times yield strength as discussed in Section 6.2.1.1. An acceptable stress safety factor of 2.0 has often been used in general engineering practice. For example, the American Society of Mechanical Engineers (ASME) (ASME 1969 [DIRS 162446], p. 20) uses a reduction factor of 2.0 on the runout stress (endurance limit or maximum, long-term applied stress without failure) for defining fatigue lifetime cycles. Using a similar factor of 2.0, the SCC threshold stress initiation criterion for Alloy 22 can be defined as 1.05 $YS_{(T)}$ (at-temperature yield strength). Further, to conservatively reflect uncertainty, a range from 0.9 $YS_{(T)}$ to 1.05 $YS_{(T)}$ with a uniform distribution between these values is selected for use in TSPA (Table 6-3). The nominal yield strength values of Alloy 22 are listed in Table 4-7, and, where appropriate, ASME code minimum values may be conservatively used.

Table 6-3. SCC Initiation Threshold Stress Criteria of Alloy 22

Material	Threshold Stress Criterion
Alloy 22	Uniformly distributed between 0.9 × $YS_{(T)}$ and 1.05 × $YS_{(T)}$

Source: This report.

NOTE: $YS_{(T)}$ = at-temperature yield strength.

For modeling purposes such as incorporation into TSPA model abstractions, the yield strength value at the normal operating temperature of 125°C is used in Section 6.5 for evaluation of residual stress and stress intensity factor distributions in the waste package closure weld. Although GE GRC experimentally determined the yield strength of Alloy 22 at 125°C as 324 MPa, for general application purpose, the yield strength of Alloy 22 at 125°C is interpolated from the data contained in *Physical and Chemical Characteristics of Alloy 22* DTN: MO0003RIB00071.000 [DIRS 148850]. Both Alloy Digest (1985 [DIRS 178194], p. 2, Table 3) and Haynes International (1988 [DIRS 101995], p. 15) are listed in DTN: MO0003RIB00071.000 [DIRS 148850]. However, Alloy Digest (1985 [DIRS 178194]) gives higher yield strength values (for thinner plate) than the value given by Haynes International (1988 [DIRS 101995]) for thicker plate. The higher yield-strength value is used for the finite element analyses of weld residual stresses and stress intensity factors since it results in higher, and therefore, more conservative calculated residual stress values. The interpolated yield strength value at 125°C ($YS_{(125°C)}$) is shown in Table 6-4 as 351 MPa with 90% of $YS_{(125°C)}$) as 316 MPa. As a comparison, Table 6-4 also shows the interpolated yield strength of Alloy 22 at 105°C. The difference between the yield strength values at 125°C and 105°C is minor (within a few MPa).

The temperature of 125°C is chosen to be conservative because the higher the temperature, the lower the yield strength. The waste package stresses are calculated by design using 150°C mechanical properties (SNL 2007 [DIRS 179567], Table 4-1, Parameter No. 03-07A). However, calculated weld residual stresses are higher at lower temperatures (DTN: MO0708RTSWRS06.000 [DIRS 182558], file *BSC-03Q-301-R2.pdf*, Figures 16 and 17). Therefore, it is conservative to use a lower-temperature yield-strength value because it will result

in higher weld residual stresses. Using the 125°C applied stress/yield strength ratio when considering the SCC initiation threshold stress is also consistent with the stress and stress intensity factor distributions discussed in Section 6.5 where the finite element analyses for weld residual stress and stress intensity factors are performed for room temperature and 125°C. In fact, GE GRC initiated its Keno test campaign in 125°C brine (DTN: MO0707SCCIGMER.000 [DIRS 182202], Section 2.2). The test temperature was lowered to 105°C (just below the boiling point of the brine) because of the experimental difficulties at 125°C. The difference in yield strength due to temperature difference between of 125°C and 105°C is minor (by only a few MPa or about 3%) as can be seen from Table 6-4.

Table 6-4. Estimation by Interpolation of Alloy 22 Yield Strength at 105 °C and 125°C from Yield Strength Values at Other Temperatures

Temperature			Yield Strength (ksi)	Conversion Factor	Yield Strength (MPa)
K	°F	°C			
294	70	21	58.5	1 ksi = 6.894759 MPa	403
366	200	93	53.8		371
477	400	204	43.9		303
398	257	125	50.9		351
378	221	105	52.7		363
90% of $YS_{(RT)}$ = 52.65 ksi or 363 MPa					
90% of $YS_{(125°C)}$ = 45.81 ksi or 316 MPa					
105% of $YS_{(RT)}$ = 61.43 ksi or 423 MPa					
105% of $YS_{(125°C)}$ = 53.45 ksi or 369 MPa					

Source: The yield-strength data are from first row of Table 4-7. For instance, the yield strength at 125°C ($YS_{(125°C)}$) is interpolated from the yield strength values at 93°C and 204°C according to the following relationship:

$$YS_{(125^o C)} = YS_{(93^o C)} + \left[\frac{125^o C - 93^o C}{204^o C - 93^o C}\right] \times (YS_{(204^o C)} - YS_{(93^o C)})$$

6.3 DISCUSSION OF MECHANICAL METALLURGY CONCEPTS

Before discussing crack growth rate modeling, some mechanical metallurgy concepts should be clarified as they are frequently used in the modeling processes. These concepts include the relationship between uniaxial stress and multiaxial stress, density of incipient cracks, and incipient crack size.

6.3.1 Uniaxial Data versus Multiaxial Stress

As described earlier, the development of a threshold stress criterion is based primarily on uniaxial test data plus results obtained on U-bend specimens under a biaxial stress state. In contrast, design calculations that determine the integrity of components under expected loading conditions generally result in stress outputs described in terms of multiaxial stress components. The application of the multiaxial stress condition (e.g., using a result from a three-dimensional finite element model) to assess the potential for crack initiation and through-wall crack propagation in a component is consistent with the failure theory used by the ASME, which uses

the Tresca criteria (maximum shear stress theory) as the failure basis and allows for comparison of multiaxial stresses with allowable stresses that were generated from uniaxial test results (Bernstein 1988 [DIRS 164860], p. 436).

For example, the prediction of stress–strain behavior in sophisticated elastic–plastic analyses (i.e., at high stress and strain values where permanent deformation occurs) typically uses the equivalent effective stress–strain approach and uniaxial material stress–strain data to assess multiaxial stress conditions. In order to apply the uniaxial stress-strain information to multiaxial conditions, principal stresses are used. This approach considers that a combination of stresses can be equivalent to a uniaxial condition. Even in a uniaxial stress–strain test (where failure typically occurs along the 45-degree plane, in pure shear), the cross sections that are not perpendicular to the load line are in a multiaxial stress condition that is equivalent to the uniaxial condition. These multiaxial stress states can be observed using Mohr's circle (Timoshenko and Goodier 1951 [DIRS 122064], p. 14). Thus, the use of uniaxial stress-strain curves for multiaxial loading conditions is acceptable when used in combination with principal stresses determined from the stress analyses.

Slip is highly localized, microscopic strain that can lead to a surface offset or step where its plane intersects the surface and, possibly ruptures the passive film present at the surface. SCC initiation can be treated as microscopic crack formation due to the repetitive process of passive film rupture at slip sites followed by a dissolution transient (indicated by a current increase) until passivation recurs (indicated by a current decay) (Section 6.4). According to Averbach (1968 [DIRS 164859], pp. 449 to 455), these microcrack formations are due to the plastic flow in the local state; yielding occurs by slip or twin formation; and these slip or twin formations occur in the plane that is subjected (and perpendicular) to the maximum stress.

By analogy to the theories and criteria used in structural type evaluations, initiation test data under the uniaxial test condition could be used to determine the initiation threshold under the triaxial stress state. The data can be used because the slip and twin formations occur perpendicularly to the maximum stress plane.

Use of a threshold stress intensity factor is another established method of predicting crack propagation behavior. Stress intensity factor is defined as a function of the stresses in Section 6.5.1. In this case, crack propagation will not occur if the stress intensity factor remains below a threshold value (K_{ISCC}) (Section 6.4.5). The stress intensity factor is a direct function of the stress perpendicular to the crack plane. Thus, it is a function only of the stress perpendicular to a specific plane and comparable to uniaxial test data (for the same stress at the specific plane location).

In conclusion, the use of uniaxial test data to predict crack initiation and failure for a multiaxially loaded component is consistent with engineering practice and appropriate for the application of defining SCC initiation criteria for the waste package outer barrier.

6.3.2 Density of Incipient Cracks

In a commercial metal alloy, there is a relatively high density of potential incipient surface cracks associated with microscopic discontinuities (e.g., precipitates, grain boundaries, passive

film rupture sites, etc.). In the performance assessment, the surface of the waste package is divided into many subdivisions, referred to as patches. In any given surface location where the principal tensile stress above the threshold value exists, multiple cracks may initiate and grow together, but only one becomes predominant. As will be discussed in Section 6.6.1, the minimum spacing between parallel through-wall radial cracks must be greater than the plate thickness to ensure the stress (and resultant stress intensity factor) will be sufficient to drive a crack through-wall (SIA 2002 [DIRS 161933]). In other words, those cracks with the spacing smaller than the plate thickness will not develop into the through-wall cracks.

6.3.3 Incipient Crack Size

Environmental cracking has historically been separated into "initiation" and "propagation" phases (Jones and Ricker 1987 [DIRS 118672], p. 146). The particular crack depth defining the boundary between the two phases is somewhat arbitrary. For the purpose of lifetime modeling, however, when the stress exceeds the stress corrosion cracking threshold stress, the initiation crack size (associated with microscopic crack formation at defect sites such as mechanical flaws) is taken as 0.05 mm as developed by Ford and Andresen (1988 [DIRS 118611], p. 798; Andresen 1991 [DIRS 166965], Figures 39 to 41). Thereafter, the crack may either reach the arrest state or enter the "propagation" phase as long as the crack tip stress intensity factor exceeds the threshold K_{ISCC} value. Incipient crack size is one of the intrinsic properties of a material related to its susceptibility to SCC.

Demonstration that the initial size (0.05 mm or 50 μm) is suitable for intended use is based on the data evaluation criteria specified in the data qualification plan in Appendix A, which requires that one or more of the following factors (SCI-PRO-001*, Qualification of Unqualified Data,* Attachment 3) be used:

- Method 1: Equivalent QA Program—GE GRC researchers Ford and Andresen (1988 [DIRS 118611]), have more than 20-year experience in the field of SCC and highly regarded reputations, within the US and internationally. The GE GRC has a QA program equivalent to the YMP QA program, and that program has been accepted by the YMP.

- Method 2: Corroborating Data—Corroborating data is available in NRC NUREG/CR-5864 (Harris et al. 1992 [DIRS 168053], p. 3-8), where the size of initiating cracks was measured as 10^{-3} in (approximately 0.0254 mm or 25.4 microns). Compared to this value, the use of 0.05 mm (or 50 microns) as the crack size for incipient cracks is clearly conservative because the value of 0.05 mm is much greater than the actual size of incipient cracks.

- Method 5: Technical Assessment—The initial size (0.05 mm) is based on expert observation documented in a technical paper (Ford and Andresen 1988 [DIRS 118611]) published in a refereed and peer-reviewed publication (i.e., *Proceedings of the Third International Symposium on Environmental Degradation of Materials in Nuclear Power Systems—Water Reactors*, published by the Metallurgical Society, Warrendale, Pennsylvania). In addition to the data used by Ford and Andresen (1988 [DIRS 118611]), the initiation flaw size of 0.05 mm (or 50 microns) was also used as the

upper range of the initiated crack size by Ford (1996 [DIRS 167203], p. 377), another technical paper published in a refereed and peer-reviewed journal (i.e., *Corrosion*, published by the National Association of Corrosion Engineers (NACE) International, Houston, Texas). These scientific activities and prior use of the data are considered equivalent to an effective technical assessment.

6.3.4 Manufacturing Flaws

6.3.4.1 Flaw Size and Flaw Density Distribution

Since the waste package is solution-annealed to remove welding residual stresses, only the waste package closure weld flaws will act as possible initiation sites for potential SCC. Therefore, only the waste package closure weld flaws are considered in this report. More detailed discussions on weld-flaw size and flaw-density distributions are quantified in *Analysis of Mechanisms for Early Waste Package/Drip Shield Failure* (SNL 2007 [DIRS 178765], Section 6.3.1).

The welding process for the waste package final closure is gas tungsten arc welding (GTAW) (SNL 2007 [DIRS 179567]). Selection of this process is fully consistent with the recommendations that resulted from an expert evaluation of a range of potential closure welding processes (Lundin 2002 [DIRS 161780]). This evaluation concluded that the cold-wire-feed GTAW process should be selected for the waste package final closure weld process to be implemented in a hot cell. The GTAW process was recommended primarily for its ability to provide high quality closure weld joints with optimum control of the welding variables. The process produces welds that can be readily inspected by automated and remote methods (Lundin 2002 [DIRS 161780]). According to Lundin (2002 [DIRS 161780]):

> The choice of the GTAW (gas tungsten arc welding) process also naturally limits and defines the size and other characteristics of the discontinuities that can be induced during welding. Further, the weld face is optimally contoured for ready inspection by remote visual methodologies. The discontinuities generated by GTAW are well defined and include lack of penetration, lack of fusion, porosity, and microfissuring. It is also possible to form defects such as tungsten inclusions, caused by the flaking of the tungsten electrode. The extent of any of the discontinuities noted above will be related to a single weld pass and do not have a tendency to propagate between passes during welding. Thus, they are of a nature, which naturally limits their size and orientation within the weld. Since the possible generation of discontinuities during welding is limited to the types indicated above, they are readily amenable to detection by remote and automated inspection using eddy current, ultrasonic and visual methods. With a prior knowledge of the type and orientation of any discontinuities, the non-destructive examination (NDE) processes most capable for detection and sizing of the discontinuities can be defined.

The volumetric ultrasonic inspection method is employed on the outer lid weld region of the waste package outer barrier as the primary flaw-detection method for postweld inspections. There should be no significant undiscovered subsurface defects for these welds. Additionally,

eddy current or surface wave-type ultrasonic inspections are planned for evaluating the weld surface to detect and repair any surface breaking defects. Lack of fusion defects is, by definition, oriented in the direction of the weld bead. The tungsten inclusion and porosity defects tend to be smaller rounded defects that have no effective directionality.

Consistent with the previous discussion, the expected type, size, and orientation of the defects that can result from the GTAW process are supported by a recent weld defect evaluation study in which 16 full-diameter CRM-21-PWR waste package Alloy 22 closure weld mockup ring specimens were fabricated using a prototypical GTAW process under conditions that simulated the hot cell-type access restrictions (Smith 2003 [DIRS 163114], Section 2.3). Weld defects present in these rings were examined by various NDE techniques, including liquid penetrant and eddy current surface examinations and volumetric radiographic and ultrasonic examinations (Smith 2003 [DIRS 163114], Section 3). These were followed by metallographic destructive examination (Smith 2003 [DIRS 163114], Section 4). Information gathered from these weld mockup experiments was used to develop a summary of weld flaw density, orientation, and size distribution applicable to the closure welds of the waste package (SNL 2007 [DIRS 178765], Section 6.3.1).

As stated in *Total System Performance Assessment Data Input Package for Requirements Analysis for DOE SNF/HLW and Navy SNF Waste Package Overpack Physical Attributes Basis for Performance Assessment* (SNL 2007 [DIRS 179567]), the flaw detection and repair-size criterion is 1/16 in or 1.6 mm as compared to the somewhat more sensitive 1-mm ultrasonic inspection defect-detection threshold used for the weld mockup study. The 1-mm ultrasonic inspection defect-detection threshold was confirmed by metallographic examinations, which verified the presence of seven defects (SNL 2007 [DIRS 179567]) detected by ultrasonic testing and confirmed by metallography. The ultrasonic dimensions were consistent with, or slightly overestimated, the metallographically measured dimensions (SNL 2007 [DIRS 179567]).

Imperfections uncovered by metallographic examinations but not detected by ultrasonic inspections were gas bubbles, the majority of which were less than 0.003 in (approximately 0.08 mm) in diameter (SNL 2007 [DIRS 178765], Section 6.3.1). Gas bubbles are spherical (SNL 2007 [DIRS 178765], Section 6.3.1) and are not sharp cracks that can propagate due to stress corrosion cracking (Andresen and Ford 1985 [DIRS 162528], p. 20). Crack initiation on the bubble surface due to stress concentration is ruled out, as weld-induced tensile stress at and near the waste package surface will be mitigated. All flaws found in the mockup specimens were in the weld metal and root of the weld. The flaws were characterized as lack of fusion and were oriented parallel to the hoop-stress direction in each case (Smith 2003 [DIRS 163114], Sections 5.1 and 7). Based on the results of this 16-weld mockup ring study, the defect size and orientation distributions were determined and reported (SNL 2007 [DIRS 178765], Section 6.3.1).

The initial weld flaw size distribution is exponentially distributed with an upper-bound truncation due to the weld thickness. The size-distribution parameter is uncertain and described by a gamma distribution (SNL 2007 [DIRS 178765], Section 6.3.1.2). Flaws are uniformly distributed spatially and their occurrence frequency is represented by a Poisson distribution. The mean flaw density (Poisson distribution parameter) of the closure weld region is uncertain and described by a gamma distribution (SNL 2007 [DIRS 178765], Section 6.3.1.3). These weld

flaw characteristics are representative of those to be expected in the noninspected weld. An ultrasonic inspection is performed in the shop for fabrication welds and in the site closure cell for waste package final closure lid welds to detect and repair the flaws that would affect the waste package performance. Consideration of this fact is modeled by use of a probability of nondetection curve to derive post-inspection flaw size and density distributions (SNL 2007 [DIRS 178765], Section 6.3.1).

6.3.4.2 Embedded Flaws

As general corrosion proceeds, embedded flaws can become surface-breaking flaws. Consideration of preexisting surface-breaking flaws only may not be sufficiently conservative. As an alternative conservative approach, the fraction of flaws considered for propagation is increased by adding a fraction of the flaws embedded within the entire thickness region of the weld in the performance assessment. The fraction of the surface-breaking flaws is increased by adding the fraction of flaws embedded within the one-quarter- (0.25) thickness region of the weld surface. This is conservative as, based on the higher measured mean general corrosion rate for creviced specimens of 7.23 nm/yr (Section 6.4.5), it will take more than 860,000 years to remove the one-quarter (0.25) thickness of the surface of the final closure lid. Additionally, it is likely that, in addition to embedded flaws becoming surface-breaking due to general corrosion, some flaws will become less sharp (lowering the stress intensity factor) or be removed entirely due to the same general corrosion process.

6.3.4.3 Radial versus Circumferential Cracks in Waste Package Closure Welds

For analysis purposes, the Alloy 22 waste package cylinder is considered equivalent to a thin-walled pipe. The schematic relationship between the circumferential and radial cracks that are oriented on the waste package lid with respect to the final closure weld is shown later in Figure 6-23.

The weld flaw description and orientation distribution obtained from the 16-ring study (SNL 2007 [DIRS 178765], Section 6.3.1) is consistent with the results obtained by Shcherbinskii and Myakishev (1970 [DIRS 149953]). Shcherbinskii and Myakishev (1970 [DIRS 149953]) described a statistical treatment of weld flaw orientations based on analysis of a significant set of data of ultrasonic flaw orientation measurements. They concluded that the planar-type weld flaw detected ultrasonically tends to be predominately oriented in the direction of the weld centerline. More than 98% of the defects fall within ±16 degrees of the weld center line in the case of steam pipe welds (e.g., the tails of the distributions fall to less than 2% probability as the azimuth approaches 90 degrees) (Shcherbinskii and Myakishev 1970 [DIRS 149953], Figure 1). A similar conclusion, drawn from the data for plate welds (Shcherbinskii and Myakishev 1970 [DIRS 149953], Figure 2), indicates that the statistical distribution of defects with respect to the orientation angle approximated by a centered normal distribution with a maximum standard deviation of 5 degrees yields a probability of 99% that the defects are located within about ±13 degrees.

These data suggest that only less than 1% of these flaws have a potential to undergo SCC as radial cracks. There is an obvious typographical error in the results of Shcherbinskii and Myakishev (1970 [DIRS 149953], Figures 1 and 2). This reference is an English translation of

the Russian publication. The frequencies given as 1.8 Hz and 2.5 Hz in these figures should read 1.8 MHz and 2.5 MHz, which are typical values used in ultrasonic testing. However, this apparent mistranslation has no effect on the conclusion drawn from this paper.

As discussed above, manufacturing defects, especially the weld flaws, are likely oriented along the weld direction. Once initiated, the cracks tend to propagate following the direction perpendicular to the maximum principal stresses, whether the cracks are propagating due to fatigue or stress corrosion. In structures where shear stress is not significant (i.e., thin-wall pipes or plates), the maximum principal stresses are the same as the three directional component stresses. Thin-wall pipes are usually defined by a radius-to-wall thickness ratio greater than 10. For an axisymmetric structure or model, there is no shear stress in the in-plane direction. The hoop (circumferential) stress is usually the most dominant stress component and the stress in the through-wall direction (which will drive laminations) is usually the lowest among the three stress components. A typical example is a cylindrical shell subjected to internal pressure loading.

Due to the orthogonality effect of stresses, once an oblique-oriented crack (measured with respect to the direction of loading) turns into the direction perpendicular to the maximum stress, the stresses in other directions have little effect in turning the crack from that direction. Thus, the oblique-oriented flaws turning to become perpendicular to the maximum stress cannot be ruled out. However, once this occurs, the orientation will not change. Likewise, a radial flaw, which is already oriented perpendicular to the maximum (hoop) stress, will remain radially oriented.

In addition, cracks tend to propagate in the direction that offers the least resistance. If a crack initiates at the bottom of the weld, near or in the heat-affected zone, it tends to propagate in the heat-affected zone, parallel to the fusion line between the weld and base metal instead of turning into the base metal at an oblique angle. Therefore, any crack, initiated and oriented in any direction at its very early stage, would adjust its direction and tend to align and propagate in the hoop or circumferential orientation, whichever results in the largest stress intensity factor.

Based on the weld-flaw orientation measurement data provided by Shcherbinskii and Myakishev (1970 [DIRS 149953]), there is a strong dependence of the weld flaw orientation on the direction of welding. This is consistent with the expectation that most defects are associated with the application of the weld metal and would tend to be oriented along the interface of deposited beads. Although it is unlikely that flaws are observed at significant oblique angles to the weld travel direction, this circumstance cannot be entirely ruled out. Depending on the quality of the welds and welding procedures, a more-uniform distribution with regards to angular orientation may be obtained. However, processes tightly controlled by the ASME and the American Welding Society (AWS), as well as NDE processes, will be in place when the waste package closure weld is produced. If flaws were present that made a significant oblique angle with the direction of the weld placement, it would not be surprising to see the flaw direction turn towards the radial direction.

The potential for flaws turning or not turning towards the radial direction can be studied by determining the stress intensity factor for a crack in a plate with an angle, θ, to the direction of the load, subjected to a constant stress. As an example, for an arbitrary stress and crack length, the ratio of the stress intensity factor for a flaw at an angle, θ, with the direction of the load to the

stress intensity factor oriented perpendicular to the stress direction (maximum stress intensity factor) can provide some insight to the expected behavior of flaws. Figure 6-4 shows this ratio with respect to the angle that the flaw makes with the direction of the load. The analyses in the figure are based on the solutions presented in *The Stress Analysis of Cracks Handbook* (Tada et al. 2000 [DIRS 167756], p. 127). The ratio of the stress intensity factor for a circumferential flaw oriented at a small angle to the load direction subjected to hoop stress to that of a radial flaw oriented perpendicular to the load is very low (0.03 and 0.05 for flaws oriented 5 and 10 degrees to the load direction, respectively). This demonstrates a very low driving force for the crack to change from circumferentially to radially oriented. This same circumferential flaw would be oriented close to 90 degrees (perpendicular) to the radial stress. Figure 6-4 shows that the ratio of the stress intensity factors is at least 95% of a flaw perpendicular to the load direction (θ = 90°). Thus, there is a significant driving force to keep the flaw in its circumferential direction. Combined with the presence of the heat-affected zone, it is unlikely that these flaws would become radial.

Combining the test results regarding flaw orientation from Shcherbinskii and Myakishev (1970 [DIRS 149953]) and the stress intensity factor ratio discussed above, it is concluded that the probability of an expected circumferentially oriented flaw becoming radial is very small. Only flaws that are oriented at angles greater than approximately 45 degrees with the load direction have the potential to turn in the radial direction, and the probability that such flaws exist is very unlikely. Essentially all flaws are oriented towards the direction of the welding (circumferentially). An investigation of the stress intensity factor for flaws at oblique angles to the load direction supports the conclusion that flaws oriented to within approximately ±15 degrees of the loading direction will not be subjected to sufficient driving force to cause the flaws to turn radial. Also supporting this conclusion is the fact that the flaw would need to turn away from the path of least resistance, the heat-affected zone, to grow into the base or weld metal. If a flaw were to occur and be oriented at an angle greater than ±15 degrees from the load direction, the flaw orientation might change such that the flaw would become radially oriented. However, as noted earlier, the probability of such flaws occurring is small relative to flaws oriented within ±15 degrees of the welding direction. This is consistent with the cracks observed in pipelines where the cracks generally propagate along the weld direction (in the direction of the axis or longitudinally) due to the pressure-induced hoop stresses.

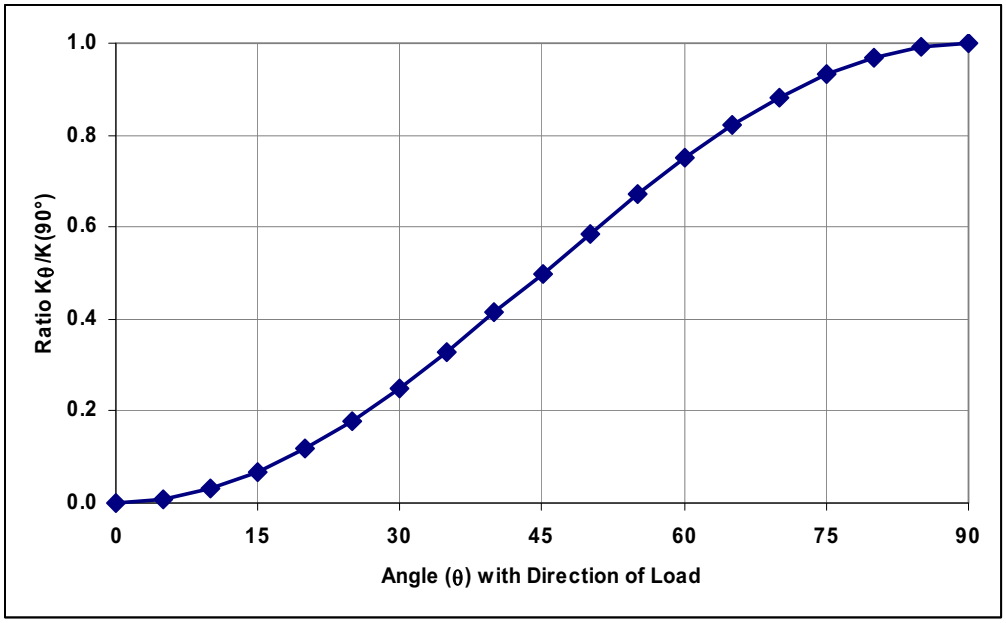

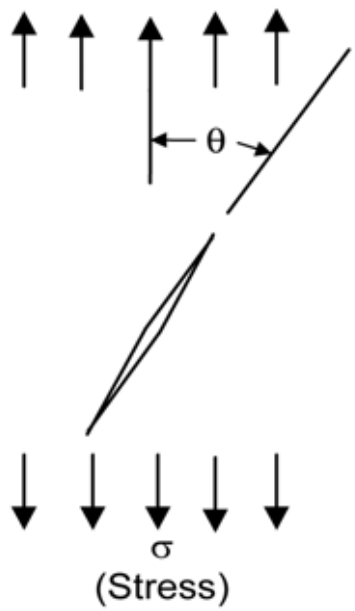

Source: Based on solutions presented by Tada et al. 2000 [DIRS 167756], p. 127.

Figure 6-4. Ratio of the Stress Intensity Factor ($K(\theta)$) of a Crack Making an Angle (θ) with the Stress Direction to the Factor ($K(90°)$) of a Crack Oriented Perpendicular to the Stress Direction as a Function of the Angle (θ), for a Crack with an Arbitrary Stress and Crack Length

In summary, radially oriented flaws are important to the SCC analysis for waste package lifetime calculations because the hoop stress, which drives the radially oriented cracks, is the dominant stress component. However, almost all of the flaws are more or less in the direction of the weld, and only flaws that are oriented at angles greater than about 45 degrees with the weld direction may turn in the radial direction. As discussed earlier, about 98% to 99% of the flaws are within about ±13 to ±16 degrees of the weld centerline. Thus, it is conservative to recommend that

radially oriented flaws (those with a 45-degree or greater angle from the direction of the weld) comprise approximately 0.5% of the flaws. A slightly more-conservative value (0.8%) is recommended for this parameter in *Analysis of Mechanisms for Early Waste Package/Drip Shield Failure* (SNL 2007 [DIRS 178765], Section 6.3.1.5).

6.3.5 Crack Aspect Ratio

The crack aspect ratio relates crack length to depth and is an important input for determining crack opening area once a crack propagates through-wall. Treatment of the crack length for either a manufacturing defect or an incipient crack is based on the following assumptions:

- Surface flaws are semielliptical with depth *a* and length *2c* (as shown in Figure 6-17, where 2c is given as "l").
- The crack aspect ratio (γ) is the ratio of one-half of crack length (*c)* to the crack depth (*a*) (i.e., $\gamma = c/a$). A semicircular crack has an aspect ratio of 1 ($\gamma = 1$).
- A crack maintains its aspect ratio during its growth until the depth reaches the wall thickness. At this point, the shape instantaneously becomes rectangular.
- The crack aspect ratio is 1 for radial cracks in the closure weld.
- The probability that the crack aspect ratio, γ, is greater than 1 for circumferential cracks is given by an exponential distribution based on one of the formulations provided by Harris et al. (1981 [DIRS 118624], Equation 2-10, p. 29):

$$P(\gamma > 1) = e^{-(\gamma-1)/\lambda} \qquad \text{(Eq. 1)}$$

  where λ is the standard deviation of γ and has a value of 0.7. From Equation 1, the mean and median values (γ_{mean} and γ_{50}) and the standard deviation (γ_{sd}) of γ can be obtained by the following formulas:

$$\gamma_{mean} = 1 + \lambda = 1.7$$

$$\gamma_{50} = 1 + \lambda \ln 2 = 1.485$$

$$\gamma_{sd} = \lambda = 0.7.$$

  A gamma or Weibull distribution with a shape factor of one is equivalent to an exponential distribution.

6.4 THE BASE-CASE SLIP DISSOLUTION–FILM RUPTURE MODEL FOR ALLOY 22

6.4.1 Introduction

A SCC model has been developed by Ford and Andresen (Andresen and Ford 1985 [DIRS 162528]; Ford and Andresen 1988 [DIRS 118611]) and has been successfully applied to

stainless steel and nickel-based alloys (Andresen and Ford 1994 [DIRS 118581]). In this report, a set of parameters is developed based on that model that is appropriate for use in performance assessment of Alloy 22.

A crack propagation rate model for Alloy 22 can be developed from a fundamental understanding of the cracking mechanism. The formulation of such a fundamentally based model of crack propagation requires the choice of a working hypothesis for the cracking mechanism and the evaluation of the parameters of importance in the mechanism. For the systems of interest, the SDFR mechanism has been chosen. As indicated in Section 6.3.1, slip is highly localized, microscopic strain that can lead to a surface offset or step where the slip plane intersects the surface and, thus, can rupture the passive film present at the surface. This cracking mechanism has been successfully applied to model SCC of stainless steel, low-alloy steel, and nickel-based alloys in LWR environments (Ford and Andresen 1988 [DIRS 118611], pp. 789 to 800; Andresen and Ford 1994 [DIRS 118581], pp. 61 to 70).

To account for crack propagation, the SDFR model is adopted as the base-case model to provide mathematical formulas for the prediction of crack growth rate. The SDFR model relates the advance (or propagation) of cracks, subsequent to crack initiation at the bare metal surface, to the metal oxidation that occurs when the protective film at the crack tip is ruptured.

6.4.2 Slip Dissolution–Film Rupture Mechanism

In accordance with the SDFR model, crack advance is faradaically (i.e., based on Faraday's Law) related to the metal oxidation that occurs when the protective film at the crack tip is ruptured. Two articles by Ford and Andresen (Ford and Andresen 1988 [DIRS 118611], Figure 2; Andresen and Ford 1994 [DIRS 118581], Figure 1) schematically show the change in oxidation current and charge densities with time following the rupture of a protective film at the crack tip. In Figure 6-5, $\overline{V}_T$ is the average crack growth rate at the tip, V_S is the crack growth rate at the crack side, M and ρ are atomic weight and density of the crack tip metal, respectively, F is Faraday's constant, n is the number of electrons involved in the oxidation of a metal atom, Q_f is the oxidation charge density per film rupture, $\dot{\varepsilon}$ is the strain rate at the crack tip, and ε_f is the fracture strain of the film. The initial oxidation rate (and, hence, crack advance rate) is rapid, typically controlled by activation or diffusion kinetics as the exposed metal rapidly dissolves. Availability of the balancing cathodic reduction current is also necessary, but is generally not limiting in hot water environments. However, in most (if not all) hot water cracking systems, a protective oxide reforms at the bared surface, and the rate of total oxidation (and crack tip advance) slows with time. Thus, crack advance can only be maintained if the film rupture process is repetitive. Therefore, for a given crack tip environment, corrosion potential, and metallurgical condition, crack growth is controlled by the change in oxidation charge density with time and the frequency of film rupture at the strained crack tip. The latter parameter is determined by the fracture strain of the film, ε_f, and the strain rate at the crack tip, $\dot{\varepsilon}$.

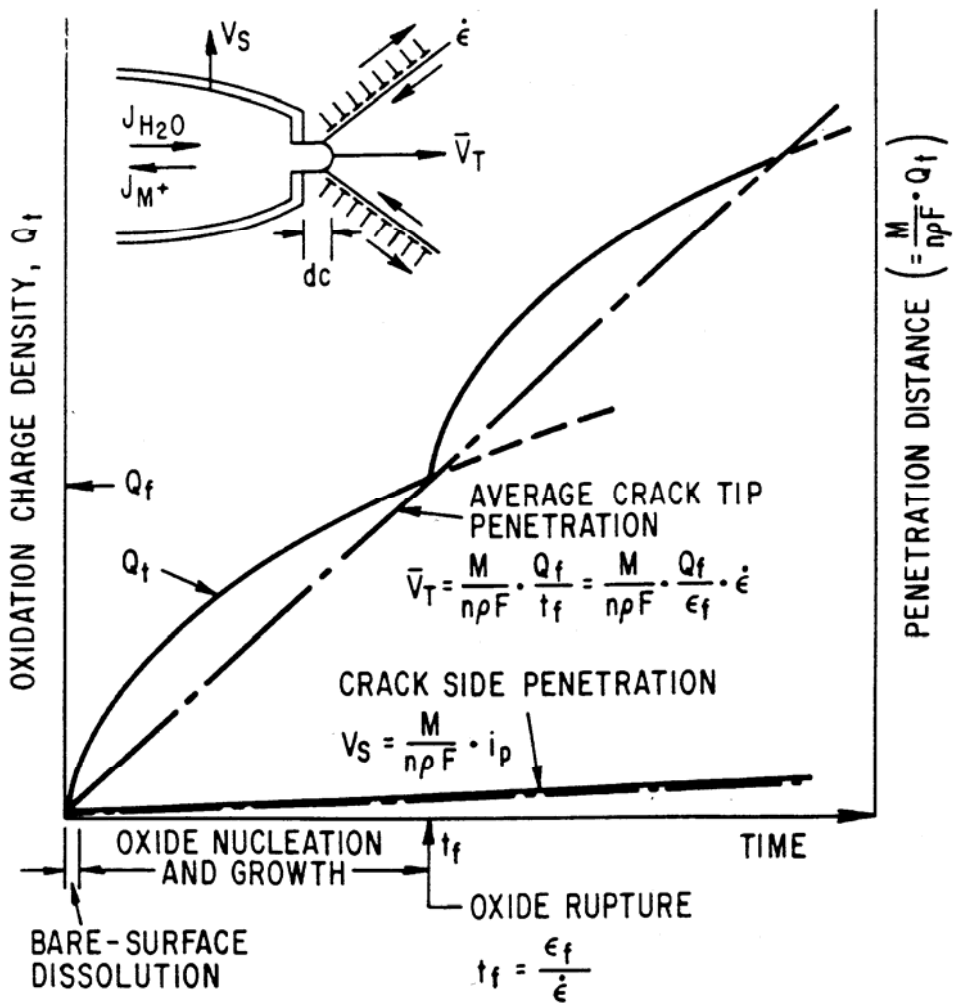

Source: Ford and Andresen 1988 [DIRS 118611], Figure 2; Andresen and Ford 1994 [DIRS 118581], Figure 1.

Figure 6-5. Schematic Oxidation Charge Density versus Time for a Strained Crack Tip and Unstrained Crack Sides in the Slip Dissolution-Film Rupture Mechanism

By invoking Faraday's law, the average environmental crack growth rate, V_t, can be related to the strain rate at the crack tip, $\dot{\varepsilon}$ ($\dot{\varepsilon}_{ct}$ in Equation 2) by the following equation (Ford 1996 [DIRS 167203], Equation 1; Ford and Andresen 1988 [DIRS 118611], Figure 2, p. 790; Andresen and Ford 1994 [DIRS 118581], Figure 1, p. 62):

$$V_t = \frac{M}{z\rho F}\frac{Q_f}{\varepsilon_f}\dot{\varepsilon}_{ct} \qquad \text{(Eq. 2)}$$

where M, ρ = atomic weight and density of the crack tip metal
F = Faraday's constant
z = number of electrons involved in the oxidation of a metal atom (i.e., *n* in Figure 6-5)
Q_f = oxidation charge density per film rupture
ε_f = fracture strain of the film.

The time, t_f, to reach the fracture strain, ε_f, is:

$$t_f = \varepsilon_f / \dot{\varepsilon}_{ct} \qquad \text{(Eq. 3)}$$

Figure 6-6 shows the schematic of oxidation current density versus time following repeated oxide rupture events. Repassivation current transients exhibit an initially high bare surface dissolution current density, i_0, at an initial short time, t_0. Thereafter, oxide growth (or thickening) leads to decay in the oxidation current density, which often follows a power law relationship (Ford 1996 [DIRS 167203], Equation 3):

$$i_t = i_o \left[\frac{t}{t_o} \right]^{-n} \qquad \text{(Eq. 4)}$$

Because of this power law relationship, Equation 2 can be reformulated as follows (Andresen and Ford 1994 [DIRS 118581], Equation 1, p. 62):

$$V_t = A(\dot{\varepsilon}_{ct})^n \qquad \text{(Eq. 5)}$$

where, for a given environment, *A* and *n* are material constants that can be measured from the repassivation response. The repassivation slope, *n*, is the slope on a log–log plot of (i_t/i_0) versus (t/t_o) from Equation 4.

If a bare surface condition is maintained at the crack tip (i.e., $\varepsilon_f/\dot{\varepsilon}_{ct} < t_0$, or $t_f < t_0$, hence, $i_t = i_0$), a "maximum" crack growth rate should result. Integration of Equation 4 leads to:

$$Q_f = \int_0^{t_f} i_t dt = i_o(t_f) = i_o \left(\varepsilon_f / \dot{\varepsilon}_{ct} \right) \qquad \text{(Eq. 6)}$$

Substitution of Equation 6 into Equation 2 yields the predicted maximum environmental crack growth rate:

$$V_{\max} = \frac{M}{z\rho F} i_o \qquad \text{(Eq. 7)}$$

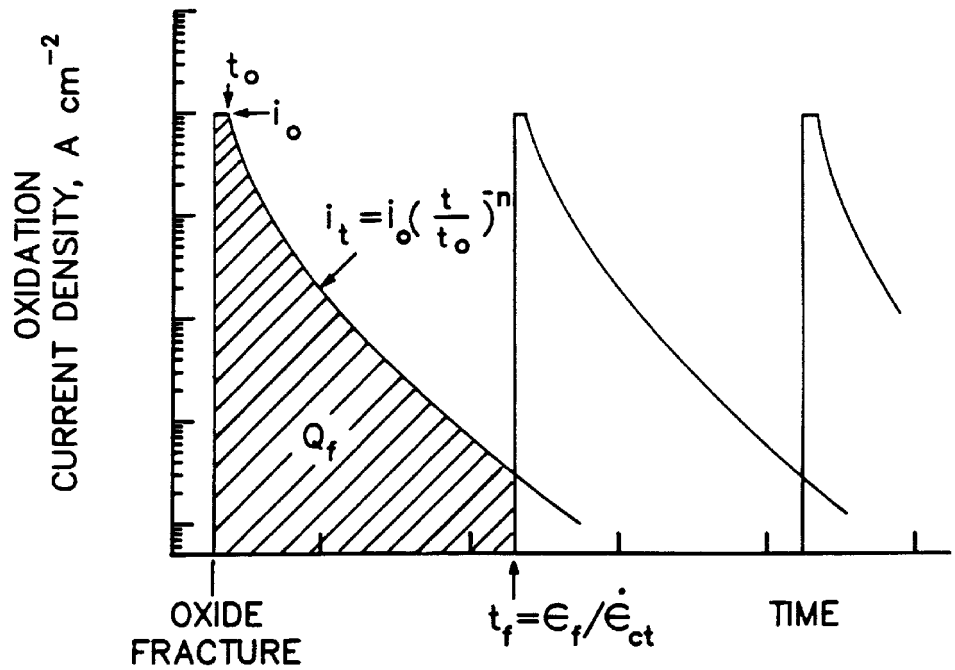

Source: Schematic based on discussion in text.

Figure 6-6. Schematic of Oxidation Current Density versus Time Following Repeated Oxide Rupture Events

This expression for the maximum environmental crack growth rate is the quantitative basis for the early observations relating the maximum oxidation current density on a straining surface to the maximum crack growth rate. These early correlations were obtained primarily for alloys in concentrated environments (e.g., boiling $MgCl_2$, 9M NaOH solutions, etc.) under dynamic straining conditions. By comparison, in environments more relevant to the conditions at Yucca Mountain, it is expected that (a) the passivation rate is high (e.g., in less-aggressive chemistries or for lower-susceptibility materials) and, thus, *n* (in Equation 4) will be large; (b) the onset of repassivation is rapid (i.e., t_0 is short); and (c) under constant-load or displacement conditions, the periodicity of oxide rupture, $\varepsilon_f/\dot{\varepsilon}_{ct}$, is much greater than t_0. Consequently, the oxidation charge rate, Q, is given by the following equation:

$$Q_f = \int_0^{t_f} i_t dt = \frac{i_o t_o^n}{(1-n)\left(\varepsilon_f / \dot{\varepsilon}_{ct}\right)^{n-1}} \qquad \text{(Eq. 8)}$$

Under these circumstances, a bare surface will not be maintained at the crack tip, and the crack propagation rate (Ford 1996 [DIRS 167203], Equation 5) is given by the substitution of Equation 8 into Equation 2:

$$V_t = \frac{M}{z\rho F} \frac{i_o t_o^n}{(1-n)\varepsilon_f^n} (\dot{\varepsilon}_{ct})^n \qquad \text{(Eq. 9)}$$

This is an expanded version of Equation 5 and relates the parameters A and n to the specific oxidation rates (Equation 4) and the fracture strain of the oxide at the crack tip:

$$A = \frac{M}{z\rho F} \frac{i_o t_o^n}{(1-n)\varepsilon_f^n} \qquad \text{(Eq. 10)}$$

6.4.3 Model Quantification

As the repassivation current follows a power law response (Equation 4), the faradaic relationship between the oxidation rate following oxide rupture and crack advance increment per time (growth rate, V_t), coupled with the relationship between crack tip strain rate, $\dot{\varepsilon}$, and periodicity of oxide rupture, distills to the expression shown in Equation 9.

Evaluation of the crack advance mechanism leads to the conclusion that the film rupture–slip oxidation mechanism represents a justifiable model that is capable of being quantitatively evaluated for hot water systems. The mechanism is justifiable because almost all engineering alloys depend on the presence of a stable oxide film to act as a kinetic barrier to rapid dissolution–oxidation, especially in hot water. It is quantifiable, because predictions result directly from measurements of repassivation kinetics, typically obtained by rapidly straining wires of base alloy or synthetic (e.g., representative of the grain boundary) composition (Figure 6-5).

According to Andresen and Ford (1994 [DIRS 118581], p. 62), the model can be quantified by evaluating the following processes: (1) the steady-state and transient compositions of the environment at the crack tip as a function of the conditions in the bulk (external) solution; (2) the oxidation rates for the material or environmental system expected at a strained crack tip; and (3) the oxide fracture strain and the crack tip strain rate, defined in terms of engineering parameters such as the stress intensity factor. For practical application, empirical approaches have been used for the model quantification processes.

The initial application of the SDFR model was on the quantitative prediction of cracking in austenitic Stainless Steel Types 304 and 316 in 288°C high-purity boiling water reactor (BWR) water (Ford and Andresen 1988 [DIRS 118611]). The quantification processes for the model are summarized as follows:

Step 1 Measurements of n are obtained from repassivation tests as the repassivation current follows a power law response (Equation 4). Those tests typically involve rapidly straining wires to increase the anodic passive current density, and subsequently measuring the decay of the passive current density with time.

Step 2 Once n is known, the value of A is determined from Equation 10, which relates the parameters A and n to the specific oxidation rates and the fracture strain of the oxide at the crack tip.

An alternative procedure, however, has also been used to quantify the model parameters. Based on this procedure, A is directly determined from n empirically. The empirical determination of A is based on stress corrosion crack growth tests that measure the crack growth rate, V_t, at specific

crack tip strain rate, $\dot{\varepsilon}$. The value of A is calculated in accordance with Equation 5 for each set of n, V_t, and $\dot{\varepsilon}$. Curve fitting is then used to develop the empirical relationship between A and n.

An empirical relationship between A and n (with A in $cm \cdot s^{(n-1)}$ and n being dimensionless) of:

$$A = 7.8 \times 10^{-3}\ n^{3.6} \qquad \text{(Eq. 11)}$$

was provided by Ford and Andresen (1988 [DIRS 118611], p. 791) for Stainless Steel Type 304 in 288°C water.

Substitution of Equation 11 into Equation 5 leads to:

$$V_t = 7.8 \times 10^{-3}\ n^{3.6}\ (\dot{\varepsilon}_{ct})^n \qquad \text{(Eq. 12)}$$

where V_t is in cm/s and $\dot{\varepsilon}$ is in s^{-1}.

For sensitized Stainless Steel Type 304 in 288°C water, Figure 6-7 indicates that Equation 12 with n = 0.55 and $A = 8.5 \times 10^{-4}$ is a good prediction model for observed crack growth rate versus crack tip strain rate relationships.

For Alloy 22, independent experimental measurement of A and n is preferred but not available. Therefore, the relationship between A and n (Equation 11) is used for application of the SDFR mechanism to SCC in Alloy 22 (although, as seen in Section 6.4.4.4, an n-value distribution more appropriate for Alloy 22 is developed). Further rationale for applicability of the SDFR model to Alloy 22 is given in the Section 6.4.4.4.

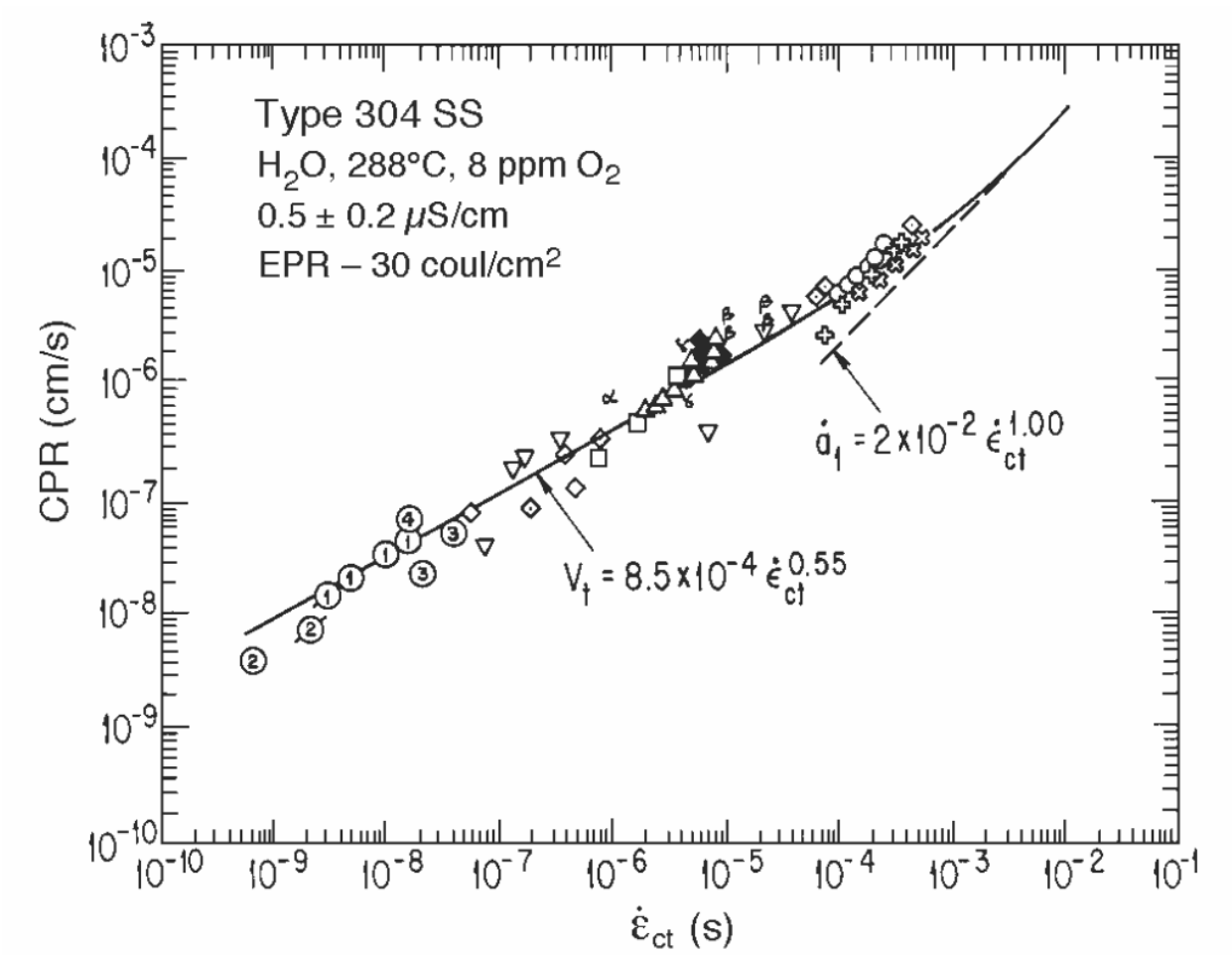

Source: Ford 1996 [DIRS 167203], Figure 12.

Figure 6-7. Crack Growth Rate (Presented by Observed Data Points and Predicted Curve) versus Crack Tip Strain Rate for Sensitized Stainless Steel Type 304 in Oxygenated 288°C Water

The crack tip strain rate, $\dot{\varepsilon}_{ct}$, in Equation 12, is related to the engineering stress parameters (such as the stress intensity factor) via formulations developed by Ford and Andresen (1988 [DIRS 118611], Table 1). According to Ford and Andresen (1988 [DIRS 118611], p. 791), the formulations provided are semi-empirical relationships to normalize the effects of a wide range of stressing conditions on the environmentally assisted crack propagation rates. For constant load, the relationship is:

$$\dot{\varepsilon}_{ct} = 4.1 \times 10^{-14} K_I^4 \qquad \text{(Eq. 13)}$$

where the stress intensity factor K_I is in MPa√m.

For constant load, substituting Equation 13 in Equation 5 leads to the following alternative crack growth rate equation:

$$V_t = \overline{A}(K_I)^{\overline{n}} \quad \text{(Eq. 14)}$$

where

$$\overline{A} = A\left(4.1x10^{-14}\right)^n \quad \text{(Eq. 15)}$$

$$\overline{n} = 4n \quad \text{(Eq. 16)}$$

6.4.4 Adaptation of Slip Dissolution-Film Rupture Model to Alloy 22

6.4.4.1 Background and Rationale

Andresen and Ford (1994 [DIRS 118581], p. 62) applied the SDFR model to stainless steels, low-alloy and carbon steels, nickel alloys, and irradiated stainless steels. Ford and Andresen (1988 [DIRS 118611], p. 789) also used the SDFR model for Alloy 600 and Alloy 182 (chromium-containing nickel-based alloys similar to Alloy 22 except for the addition of molybdenum and tungsten to the latter) using the *A* versus *n* relationship of Stainless Steel Type 304 in 288°C water. They concluded that this formulation of the SDFR model was statistically valid for Alloys 600 and 182 over a range of anionic impurity concentrations (Ford and Andresen 1988 [DIRS 118611], Figure 10). It is well known that adding molybdenum improves SCC resistance of nickel-based alloys (Jones 1992 [DIRS 169906], Section 8.4.3). Tungsten behaves similarly to molybdenum in improving the corrosion resistance of nickel-based alloys. Addition of 3% to 4% of tungsten in combination with 13% to 16% molybdenum (similar range as in Alloy 22) in nickel–chromium-based materials results in alloys with outstanding resistance to localized corrosion (ASM 1987 [DIRS 103753], p. 641). Therefore, adding molybdenum and tungsten to nickel–chromium-based alloys has a positive impact on the resistance of the alloys to SCC and provides further conservatism in the approach.

Subsequently, Andresen (1991 [DIRS 166965], Figure 37) used the SDFR model for the higher chromium-content nickel-based alloy, Alloy 82 (UNS N06082), and determined that the measured stress corrosion cracking growth rates agreed reasonably well with model-predicted rates. Alloy 82 (UNS N06082), which contains 18% to 22% chromium, overlaps Alloy 22 (20% to 22.5% chromium) (DTN: MO0003RIB00071.000 [DIRS 148850], p. 2) in chromium content. Analyses indicate that the inner, protective corrosion films that form in the passive potential range on chromium-containing nickel-based alloys with chromium content greater than about 15% contain a very thin passive film layer of primarily Cr_2O_3 (with some nickel content) at the oxide–alloy interface (Pensado et al. 2002 [DIRS 166944], p. 2-2). Such a thin, passive Cr_2O_3 film is likely to possess similar repassivation kinetics and mechanical properties (e.g., fracture strain) over the range of nickel–chromium-based alloys of interest. This is consistent with the fact that the model is shown to apply or to give reasonable predictive results for a range of nickel-based alloys with chromium contents spanning the Alloy 22 compositional range. Further, there is general statistical agreement between the observed temperature dependency of SCC growth rate for sensitized Stainless Steel Type 304 and nickel–chromium-based Alloy 600 over the temperature range of most interest (approximately 50°C to 200°C), when compared

under comparable stress intensity factor and environmental conditions (Andresen 1993 [DIRS 166966], Figures 15 and 16). For example, Figure 6-8 shows that crack growth rates for sensitized Stainless Steel Type 304 and Alloy 600 follow the same temperature dependency with reasonably similar crack growth rates over a temperature range from about 25°C to 275°C, which is broader than the temperature range of most interest to the YMP (approximately 50°C to 200°C).

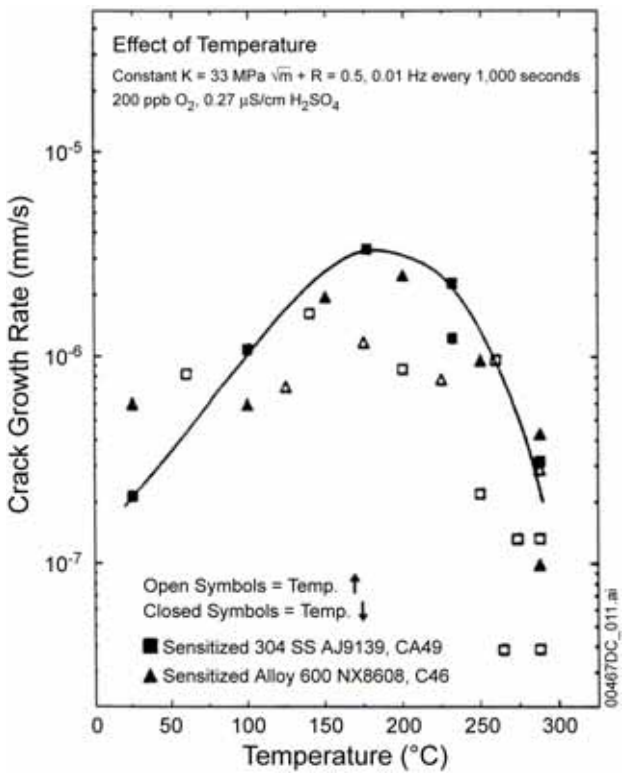

Source: Andresen 1993 [DIRS 166966], Figure 15.

Figure 6-8. Temperature Dependence of Sensitized Stainless Steel Type 304 and Alloy 600 Under Comparable Stress Intensity Factor and Environmental Conditions

Additional confidence in the applicability of this model to Alloy 22 can be gained from observation of the response of Alloy 22 under similar LWR coolant conditions. Test results from GE GRC (DTN: MO0402GEA22SCC.000 [DIRS 167911]) indicate the crack growth rate response of Alloy 22 exposed to 288°C pure water (2 ppm O_2) is broadly consistent with the crack growth rate response of other nickel-based alloys, such as Alloys 600 and 182 (Andresen et al. 2002 [DIRS 166967]) and austenitic stainless steel (Andresen et al. 2002 [DIRS 167762]). The measured crack growth rates show a similar dependency on parameters like corrosion potential and water purity (sulfate). In all test cases, the change in corrosion potential from ~ +0.2 V_{SHE} (where SHE stands for "standard hydrogen electrode") to ~ –0.5 V_{SHE} (due to a change from 2 ppm O_2 to H_2-deaerated water) causes a drop of at least one order of magnitude in the crack growth rate, as indicated by Table 6-5. Also, as expected, under repository-type oxidizing conditions (i.e., at 0.2 V_{SHE}) Alloy 22 shows crack growth rates an order of magnitude lower than those of other materials under identical test conditions, demonstrating its superiority as a structural material under conditions where SCC is a concern.

Table 6-5. Measured Crack Growth Rates (mm/s) in 288°C Oxygenated Water Due to Drop in Corrosion Potential

Alloy	Stress Intensity Factor MPa√m	Corrosion Potential +0.2 V_{SHE}	Corrosion Potential -0.5 V_{SHE}	Reference
Alloy 22	27.5 [25 ksi (√in)]	2.3×10^{-8}	4.0×10^{-9}	DTN: MO0402GEA22SCC.000 [DIRS 167911], Figure 3
Alloy 182	28.4	3.0×10^{-7}	6.0×10^{-9}	Andresen et al. 2002 [DIRS 166967], Figure 7
Alloy 600	30.0	3.3×10^{-7}	3.7×10^{-8}	Andresen et al. 2002 [DIRS 166967], Figure 8
Unsensitized Stainless Steel Type 316L	27.5 [25 ksi (√in)]	4.1×10^{-7}	$>2.0 \times 10^{-8}$	Andresen et al. 2002 [DIRS 167762], Figure 5

As indicated earlier in this section, in addition to the expected similarities in composition and mechanical properties, the expected micro-deformation modes of the alloys per se should be comparable for this class of alloys (i.e., austenitic Stainless Steel Types 304, 304L, 316, and 316L) and nickel–chromium-based alloys (e.g., Alloys 600 and 22). This is based on examination of literature values for stacking fault energies (SFE) (Gordon 2004 [DIRS 167027]). A low SFE value promotes coplanar dislocation arrays promoting local stress buildups that can more easily rupture the passive surface film at slip offsets, whereas high SFE values promote dislocation tangles that tend to diffuse local stress buildups. These alloys all possess a face-centered cubic-crystallographic lattice structure and have similar relatively low values of estimated SFE ranging from about 20 ergs/cm^2 to 30 ergs/cm^2 for Stainless Steel Types 304L and 316L to about 80 ergs/cm^2 for Alloy 600. The estimated SFE value for Alloy 22 is about 65 ergs/cm^2. This range is relatively low compared to the published values of about 340 ergs/cm^2 for pure nickel or nickel alloys with much lower chromium contents (Gordon 2004 [DIRS 167027], Table 1). Lower values of SFE can promote microstress and resulting microstrain buildups at the surface region that may accelerate SCC initiation. However, the relatively high local deformation at a stressed crack or weld flaw tip is likely to lead to relatively high local strains regardless of SFE. Thus, this will tend to overwhelm any effect of SFE on SCC propagation.

Based on these observations, there is ample reason to conclude that SCC of nickel-based Alloy 22 occurs by the same fundamental mechanism characterized by the slip dissolution-film rupture SCC model (i.e., the relationship among V_t, $\dot{\varepsilon}_{ct}$, A, and n, which is described by Equation 5).

The n parameter in the model has been experimentally benchmarked for Alloy 22 based on data obtained in a range of relevant repository brine environments for Yucca Mountain as described in the rest of this section.

6.4.4.2 Crack Growth Rate Data

To express A in units of mm-s$^{(n-1)}$, Equation 11 (the relationship between A and n) becomes:

$$A = 7.8 \times 10^{-2}\, n^{3.6} \qquad \text{(Eq. 17)}$$

where A is in mm-s$^{(n-1)}$ and n is dimensionless (note in Equation 11 the unit of A is cm-s$^{(n-1)}$).

For the constant-load condition, the relationship between the crack tip strain rate ($\dot{\varepsilon}_{ct}$) and stress intensity factor (K_I) is established as Equation 13, with V_t in mm/s and K_I in MPa√m in Equation 14, Equation 15 becomes:

$$\overline{A} = 7.8 \times 10^{-2} n^{3.6} (4.1 \times 10^{-14})^{n} \qquad \text{(Eq. 15′)}$$

Substitution of A (Equation 17) and $\dot{\varepsilon}_{ct}$ (Equation 13) into Equation 5 leads to:

$$V_t = 7.8 \times 10^{-2} n^{3.6} (4.1 \times 10^{-14})^{n} (K_I)^{4n} \qquad \text{(Eq. 18)}$$

where V_t is in mm/s and K_I in MPa√m.

For Alloy 22 under constant-load condition, the parameter n can be determined from Equation 18 based on crack growth rates measured at various levels of applied stress intensity factor, K_I.

The stress corrosion crack growth rate measurements from the GE GRC (DTNs: LL021105312251.023 [DIRS 161253]; MO0705SCCIGM06.000 [DIRS 180869], file *GE-GRC-Final_Sept-2006-Rev3.doc*) are used for the quantification of parameters for the SDFR model to be used for Alloy 22. The test data were developed from eight Alloy 22 fatigue precracked compact tension specimens listed in Table 6-6. Four specimens (C144, C152, C153, and C200) were tested at 110°C in a concentrated, aerated, BSW environment, with a target composition and solution pH of 13.4 at room temperature, as listed in DTN: LL021105312251.023 ([DIRS 161253], pp. 3 and 6). The other four specimens (C263, C264, C265, and C266) were tested at 150°C in aerated SCW, also a concentrated basic brine solution with a target composition listed in DTN: MO0705SCCIGM06.000 ([DIRS 180869], file *GE-GRC-Final_Sept-2006-Rev3.doc*, Section 1.1). The compact tension specimens (loaded per ASTM E 399-90 [DIRS 117480]) used for the crack growth rate measurements were fabricated from Alloy 22 plate (about 1 in thick (25.4 mm)) in a range of microstructural conditions and included base metal and welds fabricated using the GTAW process (DTN: MO0705SCCIGM06.000 [DIRS 180869], file *GE-GRC-Final_Sept-2006-Rev3.doc*, Table 1-1).

Table 6-6. Summary of Source Data for Alloy 22 SDFR Model Quantification

Specimen	Test Conditions	Hold Time (hrs)	Tested Stress Intensity Factor (MPa√m)	Measured Crack Growth Rate (mm/s)	Source	Calculated *n* Value[b]
C153	110°C BSW (20% Cold-worked)	Constant load	30	5.0×10^{-10}	DTN: LL021105312251.023 [DIRS 161253], p. 11	1.119
C144	110°C BSW (Mill-annealed)	1	30	10^{-11}[a]	DTN: LL021105312251.023 [DIRS 161253], p. 7	1.392
C152	110°C BSW (Mill-annealed)	24	45	4.0×10^{-10}	DTN: LL021105312251.023 [DIRS 161253], p. 10	1.281
C200	110°C BSW (Mill-annealed + Aged 700°C/175 h)	Constant load	24.2	6.0×10^{-10}	DTN: MO0707SCCIGMER.000 [DIRS 182202], Figures 1-67 and 1-68	1.041
C263	150°C SCW (As-welded)	24	40	1.2×10^{-9}	DTN: MO0705SCCIGM06.000 [DIRS 180869], file *GE-GRC-Final_Sept-2006-Rev3.doc*, Tables 2a and 2b	1.151
C264	150°C SCW (As-welded)	2.5	40	1.3×10^{-9}	DTN: MO0705SCCIGM06.000 [DIRS 180869], file *GE-GRC-Final_Sept-2006-Rev3.doc*, Tables 2a and 2b	1.145
C265	150°C SCW (As-welded + TCP)	1	40	2.0×10^{-9}	DTN: MO0705SCCIGM06.000 [DIRS 180869], file *GE-GRC-Final_Sept-2006-Rev3.doc*, Tables 2a and 2b	1.111
C266	150°C SCW (As-welded + LRO)	1	40	3.0×10^{-9}	DTN: MO0705SCCIGM06.000 [DIRS 180869], file *GE-GRC-Final_Sept-2006-Rev3.doc*, Tables 2a and 2b	1.080

NOTES: [a] Crack growth rate of 10^{-11} is used to represent test results where cracking appeared to cease propagating (i.e., the growth rate seemed to approach zero).
[b] Calculated from Equation 18.

The specimens were subjected to cyclic loading to initiate crack growth and followed by constant loading conditions with various hold times (DTN: MO0707SCCIGMER.000 [DIRS 182202], Section 1.1). The set of data from DTNs: LL021105312251.023 [DIRS 161253], MO0707SCCIGMER.000 [DIRS 182202], Figures 1-67 and 1-68, and MO0705SCCIGM06.000 [DIRS 180869], file *GE-GRC-Final_Sept-2006-Rev3.doc*, Tables 2a and 2b, were used as input for establishing values of *n* for Alloy 22 and are summarized in Table 4-2. Table 6-6 contains a conservative subset of Table 4-2 values, and Table 6-6 also contains the calculated *n* values. These data were selected according to criteria established by Ford and Andresen (1988 [DIRS 118611], Figure 6) and Ford (1996 [DIRS 167203]), who have determined that the values of *n* generally lie between 0.3 and 1. A low value of *n* implies an aggressive environment or a poorly resistant alloy to SCC. The values of *n* listed in Table 6-6 are greater than unity, which indicates that Alloy 22 is highly resistant to SCC propagation in the tested environments.

Although Equation 18 is strictly applicable to the constant load condition, it is conservative to use shorter hold-time data where constant load results are not available or where they are deemed less reliable. Where data are available for a range of maximum load hold times, the longest hold time or constant load values are used, as these values are most representative of the normal waste package sustained stress state. In addition, longer hold times result in a greater contribution from SCC as compared to corrosion fatigue. The specimens listed in Table 6-6 represent a range of metallurgical conditions (mill-annealed, cold-worked, as-welded, and thermally aged), and include starter flaws located in base metal as well as in weld metal.

Specimens C200, C265, and C266 were thermally aged at 700°C for 175 hours for C200, at 650°C for 200 hours for C265, and at 550°C for 10 hours for C266. These first two aging conditions result in significant tetrahedrally close packed (TCP) phase precipitation and the latter in significant long range ordering (LRO) that greatly exceeds the extent expected during the waste package closure weld thermal exposure. According to *Aging and Phase Stability of Waste Package Outer Barrier* (BSC 2004 [DIRS 171924], Section 8), material aging is not a concern for the waste package at temperatures below 300°C for up to 500 years and below 200°C for the next 9,500 years. These thermally aged specimens are conservatively included in the calculations of *n* values in Section 6.4.4.4. The specimen test environments include 110°C aerated BSW and 150°C aerated SCW. Based on a series of Alloy 22 SSRTs conducted over a range of applied potentials and test environments (Section 6.2.1.3), it is evident that SCW is among the most aggressive environments relative to SCC susceptibility. It is also evident from examination of Table 6-6 that crack growth rates are a factor of approximately two to three higher for weld metal than for base metal and approximately three higher for the thermally aged weld metal. However, the welded specimens were tested at a higher temperature, which may account for the somewhat higher measured crack growth rates.

Table 6-6 notes that a crack growth rate of 10^{-11} mm/s is used to represent the test results which indicated that cracks appeared to cease propagating (i.e., the growth rate seemed to approach zero). The choice of 10^{-11} mm/s is judged to be near the lower limit of practical growth rate measurement based on the observation that good statistical confidence in growth rate exists when the crack growth increment is at least 10 times the limiting resolution of the technique (Andresen et al. 2002 [DIRS 166967], p. 4). The lower limit of crack growth increment cited by Andresen et al. (2002 [DIRS 166967], p. 4) is 1 μm. To gain statistical confidence using a 10-μm crack

extension, a rate of 10^{-11} mm/s would require a test time of about 30 years, which is relatively impractical.

6.4.4.3 Effect of Lead

As indicated by Pan et al. (2002 [DIRS 165536], Section 3.1) and described in more detail by Barkatt et al. (2000 [DIRS 154496]), SCC was observed in one of several Alloy 22 U-bend specimens exposed in 250°C concentrated groundwater purposely contaminated with 0.5% lead at pH 0.5. Therefore, to evaluate the potential effect of lead under more relevant conditions, crack growth rate measurements (DTN: LL021105312251.023 [DIRS 161253], pp. 10 and 11) were also obtained for specimen C152 after the addition of 1,000 ppm of lead (added as $Pb(NO_3)_2$) to the autoclave with the BSW test solution. The lead addition was made after 8,670 hours (approximately 1 year) of testing in 110°C BSW solution (DTN: LL021105312251.023 [DIRS 161253], composition, p. 3; with solution pH = 13.4 at room temperature, p. 6). Because of the relatively high pH of this solution, most of the lead becomes insoluble in the test solution because of the lead carbonate, lead sulfate, and possibly lead oxide precipitation. Based on a detailed comparison of crack growth rates before and after the lead addition, in all cases the growth rate after the lead addition was the same or somewhat lower. Thus, lead has little effect on the repassivation parameter, *n*, which is obtained from the crack growth rates. The test conditions varied over a significant range of loading conditions and growth rates. In addition to these higher pH brine stress corrosion crack growth rate results, there are also SCC-initiation test results obtained using SSRTs, at 76°C to 95°C in low pH, SAW brine solution (pH or approximately 3) with and without 0.005% lead nitrate additions (Section 6.2.1, Table 6-2). These results also show no effect of lead on SCC susceptibility; thus, there appears to be no basis for concern that lead will affect SCC susceptibility in relevant concentrated brine environments over a broad range of pH values.

6.4.4.4 *n* Value Distribution

To characterize the uncertainty for the *n* value, it can be determined from the *n* values in the last column of Table 6-6 that the mean value of *n*, n_{MEAN}, is 1.165 and the standard deviation (SD), n_{SD}, is 0.115, by using Excel functions AVERAGE and STDEV, respectively. For TSPA applications, the *n* should be sampled from a truncated (at ±2 SD) normal distribution with a mean of 1.165 and upper and lower bounds of 1.395 and 0.935, respectively, as shown in Table 6-7. In Section 6.4.5.3, the range of *n* values is used to establish a corresponding range of K_{ISCC} values. The reasonableness of selecting a ±SD on the *n* parameter and the corresponding K_{ISCC} is also discussed in Section 6.4.5.3. The analysis for supporting the selection of normal distribution is given in Appendix C.

Table 6-7. Distribution of the Parameter *n*

	Standard Deviation	*n* Value (n_{MEAN} ± *i*SD, *i* = 1 and 2)	Cumulative Probability
n_{MEAN} = 1.165	-2	0.935	0.000
n_{SD} = 0.115	-1	1.050	0.142
	0	1.165	0.500
	1	1.280	0.858
	2	1.395	1.000

NOTE: Generated using Excel function NORMDIST; mean, upper-bound, lower-bound, standard deviation (output DTN: MO0702PASTRESS.002, *Model Output DTN.doc*, Table 8-5).

The base-case SDFR SCC model developed for Alloy 22, represented by Equation 18, is graphically illustrated in Figure 6-9 for *n* values at 0.935 (the lower bound), 1.165 (mean), and 1.395 (the upper bound), as well as the graphical representation of Equation 18 for sensitized Stainless Steel Type 304 (with *n* = 0.55, Section 6.4.3). Excellent resistance to SCC for Alloy 22 is illustrated in Figure 6-9, where even the higher crack growth rates exhibited by the top curve of Alloy 22 with *n* = 0.935 are about two orders of magnitude lower than the crack growth rates associated with the Stainless Steel Type 304 curve.

In summary, the eight data points listed in Table 6-6 were used to obtain a mean value and a range for the *n* parameter of the model. The model prediction is shown in Figure 6-9 over the range of stress intensity factor values (15 MPa√m to 55 MPa√m), and the individual data points are also included in Figure 6-9 along with ±2σ limits for the *n* parameter. The ±2σ limits are not for the eight data points.

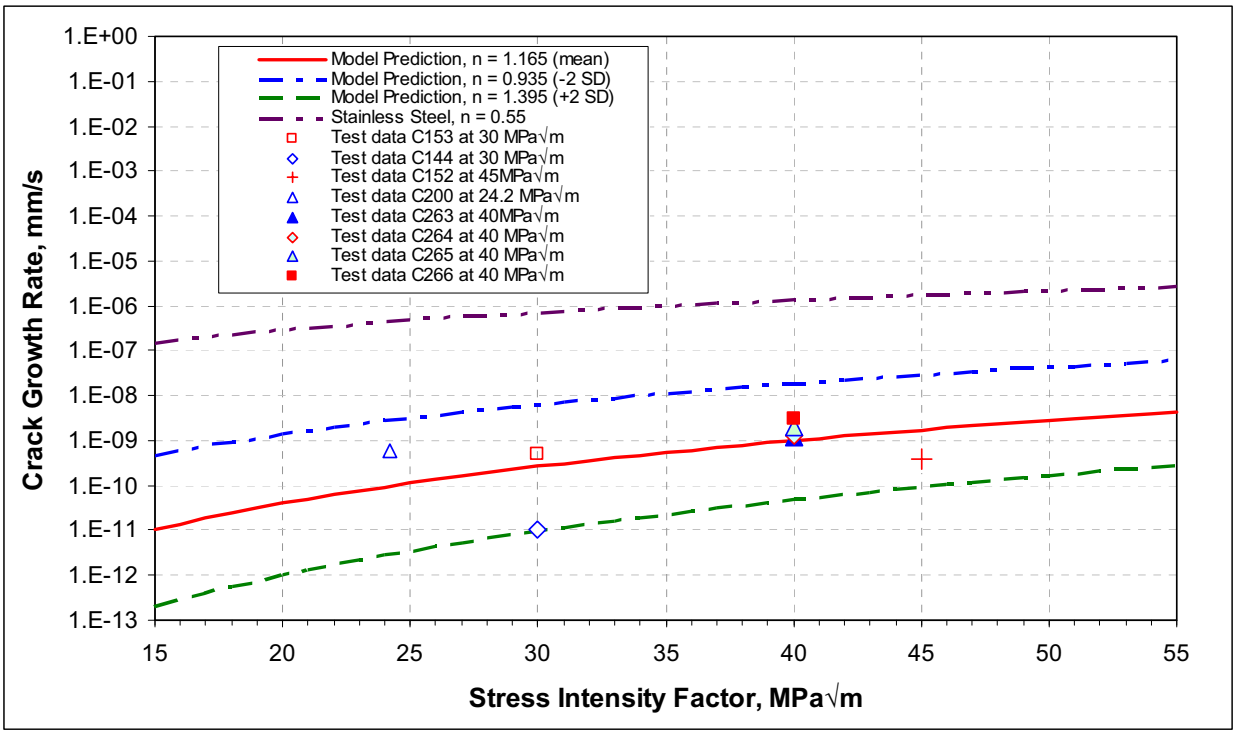

Source: Plot generated from Equation 18 using Alloy 22 *n* values from Table 6-7, and stainless steel *n* values from Section 6.4.3. Data points for specimens C153, C144, C152, C200, C263, C264, C265, and C266 are from Table 6-6 and the data sources referenced therein. Output DTN: MO0705CREEPSCC.000, *SDFRvData.xls.*

Figure 6-9. Crack Growth Rate versus Stress Intensity Factor for Alloy 22 Based on the SDFR Model

6.4.5 Threshold Stress Intensity Factor (K_{ISCC})

6.4.5.1 Concept of K_{ISCC}

The threshold stress intensity factor (K_{ISCC}) is a critical value of stress intensity factor (K_I) below which any preexisting crack will not grow or is in an arrest state. Preexisting cracks are usually caused by manufacturing processes (especially welding) (Section 6.3.4) or crack initiation (Section 6.2).

The concept of threshold stress intensity factor (K_{ISCC}) has been commonly used to assess the susceptibility of material to stress corrosion cracking. The description of this concept can be found in work by Jones and Ricker (1987 [DIRS 118672], pp. 145 to 163) and Sprowls (1987 [DIRS 118702], pp. 245 to 282). To assess the susceptibility of a material to SCC by using the concept of K_{ISCC}, it is necessary to obtain values of: (1) stress intensity factor K_I as a function of crack size correspondent to the stress state at and near the crack site, and (2) the threshold stress intensity factor K_{ISCC} of the material.

6.4.5.2 Threshold Stress Intensity Factor for Alloy 22

The calculations of stress intensity factor for the waste package closure welds in the outer lid of the waste package are described in Section 6.5. The threshold stress intensity factor can

normally be determined experimentally. Because of the extremely low growth rates observed for Alloy 22, however, a very long test time is required to experimentally obtain the value of K_{ISCC} for Alloy 22. In addition, there are other experimental difficulties involved. For instance, Roy et al. (1998 [DIRS 118696]) documented an attempt to obtain an experimentally measured K_{1SCC} for Alloy 22 using double cantilever beam-type fracture mechanics specimens. However, review of these data revealed that the data were invalid, as described by Dunn et al. (1999 [DIRS 154481], Section 2.2.3, p. 2-5). There were discrepancies between the American Society of Testing and Materials (ASTM) procedure and the test results reported by Roy et al. (1998 [DIRS 118696]). The tests did not comply with the recommended test procedure for these double cantilever beam (DCB) specimens. The initial crack length used appears to be too short, and the specimen crack length-to-thickness ratio of 0.31 was below the ASTM recommended range of 0.45 to 0.55 (ASTM E 399-90 [DIRS 117480]). Thus, these results are not used to develop the threshold stress intensity factor for Alloy 22.

6.4.5.3 Crack-Blunting Criterion for Alloy 22 K_{ISCC}

Because of the extremely low SCC growth rates and the need for unacceptably long test times, an alternative approach, involving a more conservative crack-blunting criterion, is used to define the threshold stress intensity factor. Based on this criterion (Andresen and Ford 1994 [DIRS 118581], p. 62), crack blunting occurs when the corrosion rate of the crack sides approaches the oxidation rate at the crack tip (i.e., the sharp crack will degenerate to a blunt pit). It follows that a stress corrosion crack will not grow if the general corrosion rate at the crack sides exceeds the crack tip growth rate. Allowing V_{gc} to be the general corrosion rate, the threshold stress intensity factor, K_{ISCC}, can be calculated by replacing V_t in Equation 14 with V_{gc} as shown in Equation 19.

$$K_{ISCC} = (V_{gc} / \overline{A})^{1/\overline{n}} \qquad \text{(Eq. 19)}$$

where $V_{gc} = V_t$ per the crack-blunting criterion. In Equation 19, the unit of A is mm-s$^{(n-1)}$ (see note to Equation 17); therefore, the unit of mm/s should be used for V_{gc}.

The mean general corrosion rate, which can be calculated from Table 4-10, is used to represent $V_{gc.}$ Observation of Table 4-10 indicates that the general corrosion rate associated with sample DCA 177 is an outlier, as it is a factor of about six higher than the mean value. If this outlier is removed from the data set, the mean general corrosion rate is 7.23 nm/yr. If the one zero value in Table 4-10 were also removed, the mean rate would increase very slightly. However, an increase in mean rate would result in a higher K_{ISCC} value, which is less conservative. When used in Equation 19, the unit of V_{gc} should be converted to centimeters per second (cm/s). Values for $\overline{A}$ and $\overline{n}$ can be determined from Equations 15, 16, and 17 for a given value of n'. The values of threshold stress intensity factor (K_{ISCC}) for Alloy 22 thus calculated are shown in Table 6-8, corresponding to the n values shown in Table 6-7.

The threshold stress intensity factor is applied to incipient flaws (once the threshold stress for initiation is exceeded) and weld flaws. At each time step, the stress intensity factor, K_I, at a growing crack tip or defect tip is compared with the K_{ISCC} value. As discussed in Section 6.1, at the point that the K_I value drops below K_{ISCC}, the crack will arrest.

For Alloy 22, it is recognized that, at the lower stress intensity values (minus two sigma on the mean) in Table 6-8, the indicated K_{ISCC} may not be realistic. The implication is that the K_{ISCC} values at the lower limits are highly conservative, considering the high degree of resistance to SCC initiation and crack growth of Alloy 22. Also, the mean value (6.62 MPa√m) (obtained when the crack growth rate equals the general corrosion rate) and the 2-standard deviation value of 15.38 MPa√m are conservatively obtained based on test data from much higher stress intensity factor values (30 MPa√m to 45 MPa√m) at which maintaining crack growth under static loading conditions is difficult to accomplish.

At the low bound (-2 standard deviations), K_{ISCC} is 1.96MPa√m. Although this value may intuitively seem very low for Alloy 22, values for other corrosion-resistant chromium–iron–nickel-containing alloys (such as the sensitized stainless steels) have reported values as low as 3 MPa√m for an alloy containing 15.5% chromium and 21% nickel in aerated 22% NaCl at 105°C (Jones 1992 [DIRS 178458], Chapter 5, Figure 5) and 7 MPa√m for Stainless Steel Type 304L in 42% magnesium chloride brine at 130°C (Jones 1992 [DIRS 178458], Chapter 4, Figure 7). These very low K_{ISCC} values were obtained using relatively short-term tests because the crack growth rates were high. However, even at the K_I values tested for Alloy 22 (within the range of approximately 30 MPa√m to 45 MPa√m), the crack growth rates measured are approaching the experimental measurement limit of detectibility. Therefore, it is impractical to experimentally directly measure K_{ISCC} based on much lower crack growth rates for Alloy 22 (as compared to those of stainless steels) in a time period on the order of a few years. In contrast, the real situation involves thousands of years. Therefore, it is a reasonable approach to use the truncated value at −2 standard deviations as a conservative estimate of the K_{ISCC} lower bound. The lower bound is chosen because it approaches zero. The approach is reasonable and conservative because the −2-standard deviation value is comparable to the measured lower bound values for other less SCC-resistant alloys as discussed above.

Table 6-8. Distribution of the Threshold Stress Intensity Factor, K_{ISCC}, for Alloy 22

	Standard Deviation (SD)	***n* Value(n_{Mean} ± *i*SD, *i* = 0, 1, and 2)**	**'K_{ISCC}' Value (MPa√m)**
n_{Mean} = 1.165	-2	0.935	1.96
n_{SD} = 0.115	-1	1.050	3.83
V_{gcMean} = 7.23 nm/yr	0	1.165	6.62
	1	1.280	10.45
	2	1.395	15.38

Source: Output DTN: MO0702PASTRESS.002, file *Model Output DTN.doc*, Table 8-6.

NOTE: Generated using Excel function NORMDIST; mean, upper bound, lower bound, standard deviation.

6.4.6 Alternative Model: The Coupled Environmental Fracture Model for Alloy 22

An ACM is based on simplifications that are different from those employed in the base model. An important reason for considering an ACM is to help build confidence that the changes in modeling decisions or simplifications will not change conclusions regarding subsystem and total system performance. Conceptual model uncertainty results from sparse observational data and a lack of available information to corroborate or refute plausible alternative interpretations of the subsystem and the processes occurring within the subsystem.

In addition to the base-case SDFR model, which provides a formula for prediction of the crack growth rate, an ACM, the coupled environmental fracture (CEF) model (Macdonald and Urquidi-Macdonald 1991 [DIRS 162702]; Macdonald et al. 1994 [DIRS 162701]), was developed based on the theory that the internal and external environments are coupled by the need to conserve charge in the system. Thus, as oxygen reduction on the external surface consumes the positive current emanating from the crack mouth, the solution of Laplace's equation for the external environment yields a boundary condition for solving Laplace's equation for the internal crack environment. The reduction of oxygen on the external surfaces is described in terms of a general Butler-Volmer equation that incorporates mass transport and charge transport phenomena. In this way, the model incorporates the effects of oxygen concentration, flow rate, and the conductivity of the external environment as well as accounting for effect of stress on crack growth. The CEF model represents an alternative approach for the prediction of the crack growth rate. It is considered in this report only to corroborate the conservative predictions of the base-case model.

The CEF model is a physico-electrochemical model developed for intergranular SCC in sensitized Stainless Steel Type 304 in simulated LWR environments to explain and explore the effects of various environmental and mechanical variables on the kinetics of crack propagation. The goals are: (1) to derive a physically realistic model that unifies the electrochemical, chemical, and mechanical aspects of the propagation of cracks through sensitized Stainless Steel Type 304, and (2) to use this model to explore how the rate of crack propagation depends on various environmental variables, including oxygen concentration, conductivity, and mechanical (stress intensity) parameters. Macdonald and Urquidi-Macdonald (1991 [DIRS 162702]) and Macdonald et al. (1994 [DIRS 162701]) discuss the mathematical development of the model.

The SDFR model and the CEF model are similar in several ways. Both were developed for intergranular SCC in sensitized Stainless Steel Type 304 simulated LWR environments. Both use Faraday's law to develop the equation for the crack growth rate. The departure point starts as the SDFR model takes an empirical approach to develop a functional form to express the crack growth rate in terms of, explicitly, the crack tip strain rate and two parameters (i.e., A and n) while the CEF model stays with a deterministic approach. The CEF model is more a theoretical model and the SDFR model is a mixed theoretical and empirical model.

The SDFR model and the CEF model predict the crack growth rate for SCC. However, it was discovered that the CEF model has the tendency of underestimating the crack growth rate, as compared to the SDFR model when both models were applied to predict the crack growth rate for Stainless Steel Type 304 in a BWR environment. Figure 6-10 illustrates this nonconservatism. Comparison with experimental data summarized by Ford and Andresen (1988

[DIRS 118611], Figure 22) for crack propagation rate versus stress intensity factor for sensitized Stainless Steel Type 304 in fully aerated, high-purity water at elevated temperature indicated that the crack growth rate predicted by the CEF model (i.e., 3.2×10^{-9} cm/s at 20 MPa√m) (Macdonald and Urquidi-Macdonald 1991 [DIRS 162702], p. 78) tends to be at the lower end of the range cited by Ford and Andresen (1988 [DIRS 118611], Figure 22). For this reason, the CEF model was not included for further evaluation but was used only to corroborate the conservative crack growth-rate predictions of the base-case SDFR model.

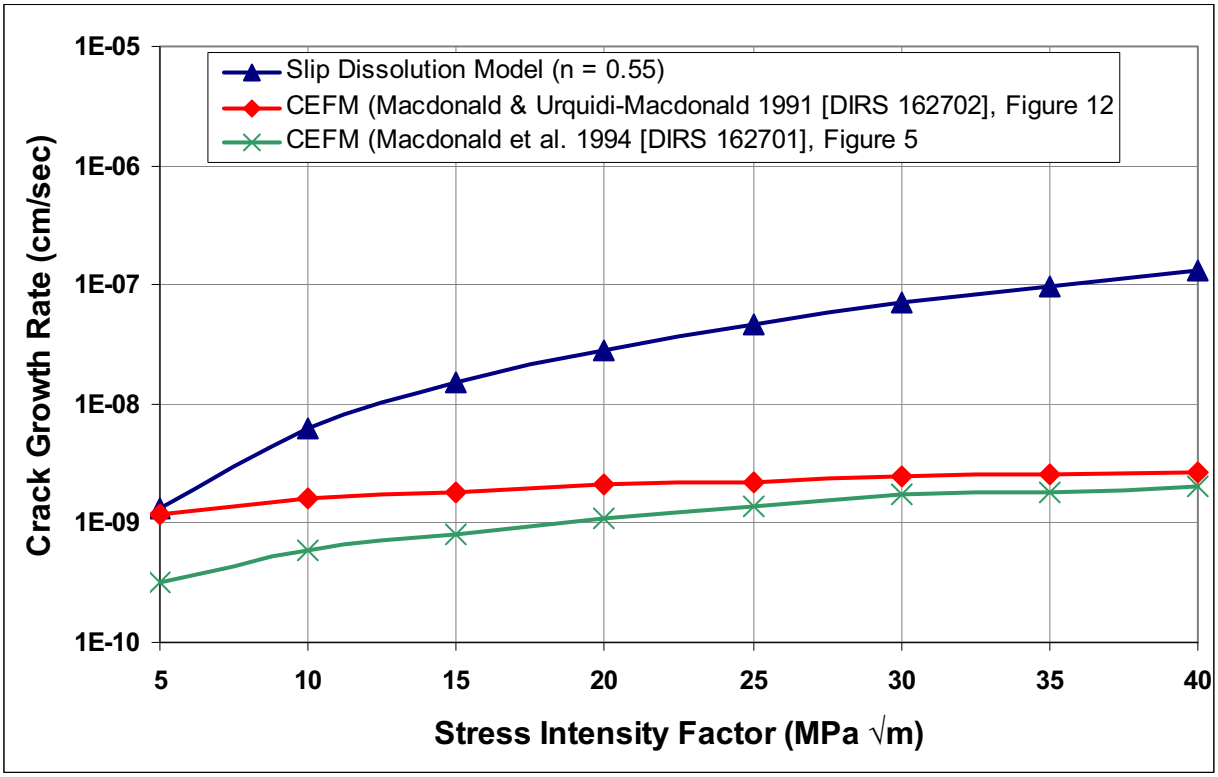

Sources: Plot generated from data by Ford and Andresen (1988 [DIRS 118611], Figure 6), Macdonald and Urquidi-Macdonald (1991 [DIRS 162702], Figure 12), and Macdonald et al. (1994 [DIRS 162701], Figure 5).

Figure 6-10. Comparison of Predicted Crack Growth Rates for Stainless Steel Type 304

6.5 EVALUATION OF THE STRESS INTENSITY FACTOR

The evaluation of stress and the stress intensity factor for the waste package outer closure weld was performed by SIA (2002 [DIRS 161933]; 2003 [DIRS 162457]; DTN: MO0708RTSWRS06.000 [DIRS 182558]). An additional analysis performed by SIA (2003 [DIRS 162457]) was for the CRM-21-PWR waste package configuration (Bokhari 2003 [DIRS 162429]), which is slightly different from the current waste package configurations for license application including the naval long waste package (SNL 2007 [DIRS 179567]). The closure weld design and trunnion configuration are similar to those for the CRM-21-PWR waste package, but the naval long waste package has a larger diameter than the CRM-21-PWR waste package. (BSC 2005 [DIRS 173492]; 2005 [DIRS 174923]; SNL 2007 [DIRS 179567]). In addition, there are other deviations between the waste package design that SIA (2002

[DIRS 161933]; 2003 [DIRS 162457]; DTN: MO0708RTSWRS06.000 [DIRS 182558]) used to perform the finite-element analysis and the current waste package design for license application.

- First, the analyses performed by SIA are for the waste package designs with middle closure lid including the most recent analysis for naval long waste package design (DTN: MO0708RTSWRS06.000 [DIRS 182558], file *BSC-03Q-301-R2.pdf*). The earlier analysis by SIA (2003 [DIRS 162457]) for CRM-21-PWR was also for a waste package design with middle lid. Based on a recent Technical Management Review Board decision (BSC 2006 [DIRS 178479], however, the waste package middle closure lid has been removed from the waste package.

- Secondly, the earlier analysis performed by SIA was for as-welded and laser-peened waste package closure welds, while the most recent analysis by SIA includes the results for as-welded, laser-peened, and plasticity burnished waste package closure welds. The stress mitigation method used in the earlier revision of this report (BSC 2004 [DIRS 172203]) was based on laser peening. The current waste package closure weld design specifies plasticity burnishing as the final closure lid weld stress mitigation method. Plasticity burnishing is included in the most recent analysis report prepared by SIA (DTN: MO0708RTSWRS06.000 [DIRS 182558]).

The impact of these deviations will be assessed in the rest of this section. It should also be pointed out that although the current waste package final closure weld stress mitigation is plasticity burnishing, the results of laser peening are also presented in this section as corroborative information where appropriate.

This section discusses the fundamental aspects of the stress and stress intensity factor analysis, the methods used by SIA, and the numerical results obtained. The majority of the results described in this section are listed in Table 4-3 through Table 4-6 as direct inputs and can be used as is as the model output. However, the data presented in Table 4-3 through Table 4-6 are rearranged from the source data in DTN: MO0708RTSWRS06.000 [DIRS 182558], file *BSC-03Q-301-R2.pdf*), for the purpose of transparency and unit conversion. The reorganized stress coefficient data are presented in Table 6-11, Table 6-13, and Table 6-14. The reorganized stress and stress intensity factor distribution data are presented in Table 6-12 and Table 6-16. The details of the conversion are also presented in Table 6-11, Table 6-13, and Table 6-14.

6.5.1 Definition of Stress Intensity Factor

The stress intensity factor, K_I, is defined as a function of stress (σ) and crack depth size (a), as shown in Equation 20:

$$K_I(a, \sigma) = \beta\, \sigma\, (\pi a)^{1/2} \qquad \text{(Eq. 20)}$$

where β is a geometry factor dependent on the size and shape of the crack and the configuration of the structural component, σ is the tensile stress distribution through the wall thickness of the structural component, and a is the crack depth size. The unit of stress intensity factor is MPa√m. Depending on the original source, a different representation, MPa($m^{0.5}$) is also used in some of the figures in this report.

6.5.2 Solutions for K_I

Closed-form solutions for the geometry factor, β, are possible only in some simple cases of uniform tensile stress and simple geometry. For example, in considering the classical problem of a single-edge cracked plate with thickness, h, it has been shown that β can be expressed by the following formula (Ewalds and Wanhill 1984 [DIRS 118602], p. 49):

$$\beta = 1.12 - 0.231\left(\frac{a}{h}\right) + 10.55\left(\frac{a}{h}\right)^2 - 21.72\left(\frac{a}{h}\right)^3 + 30.95\left(\frac{a}{h}\right)^4$$

In most practical cases where stresses are nonuniformly distributed across the thickness, the stress intensity factor has to be calculated by numerical algorithms, such as the finite element method. Rice (1968 [DIRS 147983], p. 381) has shown that a path-independent J-integral taken over an arbitrary contour surrounding the crack tip is proportional to the square of the crack tip stress intensity factor, K_I. According to Chan et al. (1970 [DIRS 147968], p. 8), an estimate of the crack tip stress intensity factor can be obtained by numerically evaluating the J-integral for the finite element solution over a path surrounding the crack tip.

Although finite element programs can be used to evaluate the stress intensity factor, the effort is usually very time consuming because a series of elaborate finite-element analyses must be completed for numerous crack sizes starting from 0 through the thickness of the containment wall.

A simplified solution has been developed by using fracture mechanics to evaluate the parameter $(K_I)_{PCCRACK,}$ the stress intensity factor (Section 6.5.3.3.3). Then a geometry correction factor, G, which is usually a function of the crack size, a, is evaluated from the results of finite-element analysis. Finally, the true stress intensity factor (K_I) is derived from $(K_I)_{PCCRACK}$ and G.

6.5.3 Calculations of Stress and Stress Intensity Factors for Waste Package Closure Welds

Only weld-induced residual stress in the final closure welds of the waste package outer barrier is considered for performance assessment. Section 6.5.3.1 rationalizes the approach that only weld-induced residual stress in the final closure welds of the waste package outer barrier is considered for performance assessment. Section 6.5.3.2 briefly describes the current waste package closure weld design for license application which formed the basis for the SIA analysis. Stress analysis based on the current design is presented in Section 6.5.3.3. Calculations of stress intensity factors for the current waste package closure welds are presented in Section 6.5.3.3.3.

6.5.3.1 Residual Stress in Final Closure Welds of Waste Package

SCC resulting from seismic damage is modeled in the *Seismic Consequence Abstraction* (SNL 2007 [DIRS 176828], Section 6.7) for both Alloy 22 and the drip shield. It is recommended that, in the absence of seismic response, only weld-induced residual stress in the final closure welds of the waste package outer barrier be considered for performance assessment for the following reasons:

1. Rockfall impact-induced residual stresses in the waste package are precluded due to the presence of the emplaced drip shield located between the drift wall and the waste package outer Alloy 22 corrosion resistant barrier. The primary potential failure mode for the drip shield is SCC resulting from either rockfall- or seismic-induced deformation-related stresses, as discussed in Section 6.8.5. According to Section 6.8, the sources of SCC in the Titanium Grade 7 drip shield are (1) weld-induced residual stress; (2) plastic residual stress caused by seismic events; and (3) residual stress produced by rockfalls. The weld-induced residual stress is eliminated by annealing. The threshold stress for crack initiation in drip shield developed in Section 6.8.3 is used as the through-wall crack propagation criterion for seismic-induced SCC. An analysis of the consequence of residual stress produced by rockfalls is presented in Section 6.8.5.1. Drip shield seismic SCC is discussed in Section 6.8.5. The seismic crack density model discussed in Section 6.8.5 indicates that SCC resulting from rockfall will result in very tight crack openings. The Stainless Steel Type 316 inner barrier of the waste package will also be excluded from the SCC evaluation because the TSPA will not take credit for the waste package inner vessel. This leaves the waste package outer barrier the only subject of importance to residual stress.

2. Sustained postclosure stresses in the waste package Alloy 22 outer corrosion barrier, including internal pressure stresses and contact stresses between waste package and pallet, are limited by design. These stresses are well below the 0.9 to 1.05 times yield strength SCC initiation criterion (BSC 2004 [DIRS 169766], Tables 2, 21, 22, and 23; SNL 2007 [DIRS 179354], Table 4-1). Therefore, only the closure weld regions, where residual stresses exist, are potentially susceptible to SCC initiation and propagation. The weld regions are susceptible to SCC because: (1) welding can produce high-tensile residual stress in the weld area; (2) there is a much higher density of preexisting flaws due to fabrication and welding in the welds than in the base metal; and (3) welding could result in segregation and nonequilibrium brittle phases, the occurrence of which could enhance the susceptibility of materials to SCC. In the current design, all the welds, with the exception of the final closure welds, are subjected to solution heat treatment to relieve the residual stress when the entire Alloy 22 corrosion barrier is heat-treated before the loading of the waste. Low-probability seismic events may lead to plastic deformation that may have the potential of leading to plastic upsets. The resultant sustained residual stresses may initiate cracks and drive them through the wall. Breach criteria (crack opening area) for cracking initiated by seismic events have been developed for the waste package material and are described in Section 6.7. The breach criteria are based on a threshold stress, which is discussed in Section 6.2. Therefore, in the absence of seismic activity,

weld residual stress is the only type of stress of concern for the waste package outer barrier.

6.5.3.2 Naval Long Waste Package Closure Lid Design for License Application

One of six waste package configurations for license application is the naval long waste package. The dimensions and closure weld design of the current naval long waste package are described in *Total System Performance Assessment Data Input Package for Requirements Analysis for DOE SNF/HLW and Navy SNF Waste Package Overpack Physical Attributes Basis for Performance Assessment* (SNL 2007 [DIRS 179567]).

The SCC analysis was completed on the previous revision of the naval long waste package (with middle lid) as described in *Naval Long Waste Package Configuration* (BSC 2006 [DIRS 174922]; 2006 [DIRS 174923]). The naval long waste package was selected, at the time, as representative of the predominant number of waste packages. At the time, the previous naval long waste package had a larger diameter than the CRM-21-PWR waste package (BSC 2004 [DIRS 166894], Section 5.3.1; Bokhari 2003 [DIRS 162429], Attachment 1, Figure 1), although the closure weld design and sleeve configuration were the same as that for the CRM-21-PWR waste package (BSC 2005 [DIRS 173492]).

The important dimensions of the previous naval long waste package (with middle lid) are summarized as follows:

- Middle lid thickness = 1/2 in (13 mm)
- Outer lid thickness = 1 in (25.4 mm)
- Outer barrier outer diameter = 74.08 in (1,881.5 mm)
- Outer barrier inner diameter = 72.08 in (1,830.7 mm)
- Upper sleeve outer diameter (thick sleeve portion) = 77.28 in (1,962.9 mm).

The weld details of the closure weld in the outer lid and the calculation that demonstrates the stress reduction benefit of low plasticity burnishing (Section 6.5.5) are addressed in *Total System Performance Assessment Data Input Package for Requirements Analysis for DOE SNF/HLW and Navy SNF Waste Package Overpack Physical Attributes Basis for Performance Assessment* (SNL 2007 [DIRS 179567]).

For comparison, the schematic sketches of the final closure weld lid area of the naval long waste package design without middle lid for license application (schematically drawn based on the description provided in *Total System Performance Assessment Data Input Package for Requirements Analysis for DOE SNF/HLW and Navy SNF Waste Package Overpack Physical Attributes Basis for Performance Assessment* (SNL 2007 [DIRS 179567])) and the waste package closure lid region configuration, naval long with middle lid, used by SIA for its finite-element analysis (DTN: MO0708RTSWRS06.000 [DIRS 182558], file *BSC-03Q-301-R2.pdf*), are shown in Figure 6-11a and Figure 6-11b, respectively.

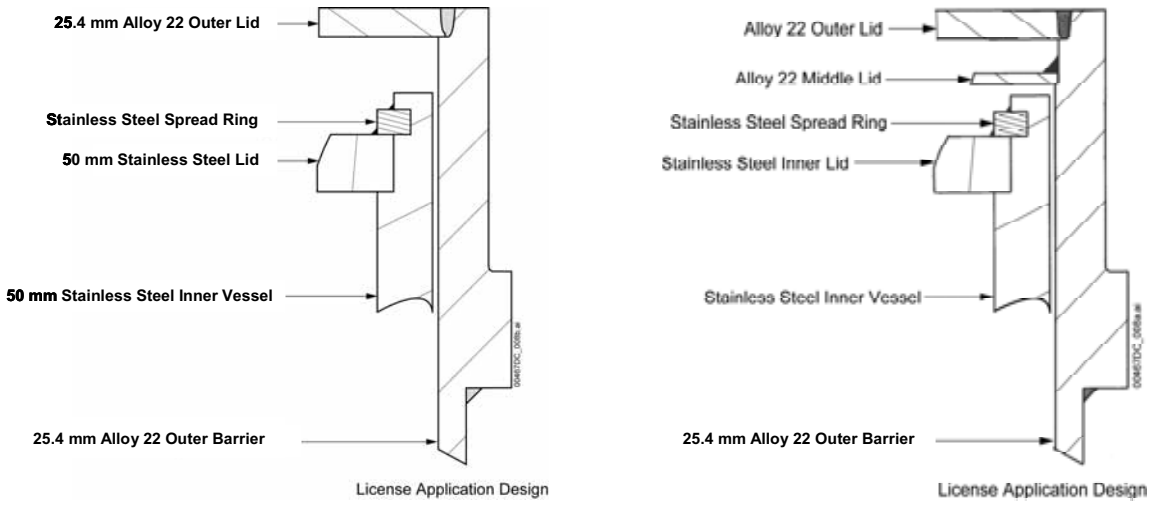

(a) (b)

Sources: (a) Schematic representation of the design described in SNL 2007 [DIRS 179567].
(b) The waste package configuration used by SIA for finite-element analysis, DTN: MO0708RTSWRS06.000 [DIRS 182558], file *BSC-03Q-301-R2.pdf*.

NOTE: Not to scale.

Figure 6-11. Sketch of (a) Current License Application Design for Waste Package Final Closure Weld Region (b) Waste Package Closure Welds Configuration that SIA Used for Its Finite-Element Analysis

For TSPA purposes, the profiles of stress and stress intensity factor due to weld residual stress in waste package closure welds are needed for the naval long waste package outer closure weld lid (without the middle lid) subjected to plasticity burnishing stress mitigation. The SIA finite-element analysis results (DTN: MO0708RTSWRS06.000 [DIRS 182558], file *BSC-03Q-301-R2.pdf*) are based on the previous naval long waste package outer closure weld lid (with the middle lid) subjected to laser peening and plasticity burnishing.

The impact of removal of the middle lid on the analysis results performed by SIA, which was for the closure weld of waste package with the middle lid, was evaluated by SIA (DTN: MO0708RTSWRS06.000 [DIRS 182558], p. 8). This evaluation includes the middle lid and the fillet weld with welding residual stress. Including the middle lid in the model could impact the analysis either by contributing to stiffness when the closure weld is applied or by the impact of the middle lid fillet weld on the initial condition for the closure weld. However, the contribution of the middle lid to stiffness of the structure when the closure weld is applied is not significant because the trunnion already provides significant constraint. Also, the impact of the middle lid fillet weld on the closure lid results is not expected to be significant because the welding of the closure weld will relieve the fillet weld-induced residual stress (DTN: MO0708RTSWRS06.000 [DIRS 182558], file *BSC-03Q-301-R2.pdf*).

Based on an analytical study, if a middle lid and fillet weld are present (but no residual stress is caused by the fillet weld), the residual stress magnitude and distribution in the outer lid closure weld (due to the closure weld itself) are essentially similar to the case where the middle lid fillet weld residual stress is included. Therefore, including a middle lid in the analysis does not

significantly alter the results for the closure weld of the waste package without the middle lid (DTN: MO0708RTSWRS06.000 [DIRS 182558], file *BSC-03Q-301-R2.pdf*). Further, the application of plasticity burnishing essentially replaces the prior stresses in the outer several millimeters of the final closure lid weld region with a new stress distribution imposed by the burnishing process.

6.5.3.3 Stress Analysis

6.5.3.3.1 Basics of SIA Finite-Element Analysis Approach

The SIA weld residual-stress calculations (DTN: MO0708RTSWRS06.000 [DIRS 182558], file *BSC-03Q-301-R2.pdf*) are based on the methodology documented by Rybicki et al. (1977 [DIRS 178214]) and Rybicki and Stonesifer (1979 [DIRS 178216]). The residual stress due to welding is controlled by the welding parameters, thermal transients, temperature-dependent material properties, and elastic–plastic stress reversals. The analytical technique uses finite-element analysis to simulate the multipass weld process. In order to reduce computational time, the lumped-weld bead pass approach, as documented by Rybicki et al. (1977 [DIRS 178214]) and Rybicki and Stonesifer (1979 [DIRS 178216]), was used in the evaluation performed by SIA (DTN: MO0708RTSWRS06.000 [DIRS 182558]).

An Axisymmetric Model

An axisymmetric model was used in the evaluation for the weld residual stress in the outer lid closure weld. As this is an axisymmetric model, the upper trunnion sleeve can only be modeled with one thickness. Because of the higher constraint resulting from a thicker outer wall, it is conservative to model the thicker section of the trunnion sleeve. Therefore, the trunnion was modeled using a uniform thickness equivalent to that for the thick portion. The axisymmetric model is shown in Figure 6-12.

Finite-Element Details

The finite-element details in the weld region are shown in Figure 6-13**.** The definition of the lumped weld passes is shown in Figure 6-14. For the fillet weld in the middle lid, five lumped weld passes were modeled. As the final as-welded bead deposit map is not available for the full penetration weld in the outer lid, it is assumed that eight lumped weld passes are in the V-groove and the final cap layer is beyond the outer lid outside surface. Therefore, the final cap layer is not included in the model. The elements in the outer lid, the fillet weld, and the closure weld were eliminated at the start of the analysis. The deposition of the weld bead was modeled by activating the corresponding bead pass elements with an element heat generation rate. The elements in the outer lid were active alive upon the start of the closure weld.

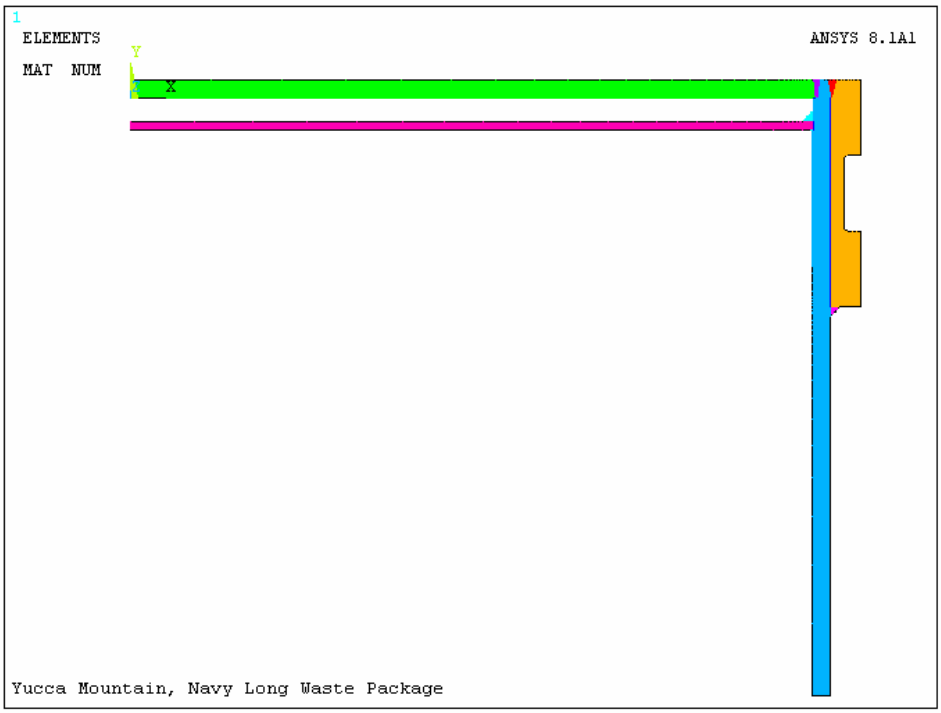

Source: DTN: MO0708RTSWRS06.000 [DIRS 182558], file *BSC-03Q-301-R2.pdf*, Figure 5.

NOTE: The trunnion sleeve pictured in orange (far right-ha nd side) has been changed and is now a uniform thickness consistent with the thick portion of the sleeve.

Figure 6-12. Axisymmetric Model of Naval Long Waste Package, with Thick Sleeve Where the Directions of x, y, and z Are Those of the Three Component Stresses, S_x (radial), S_y (axial), and S_z (hoop)

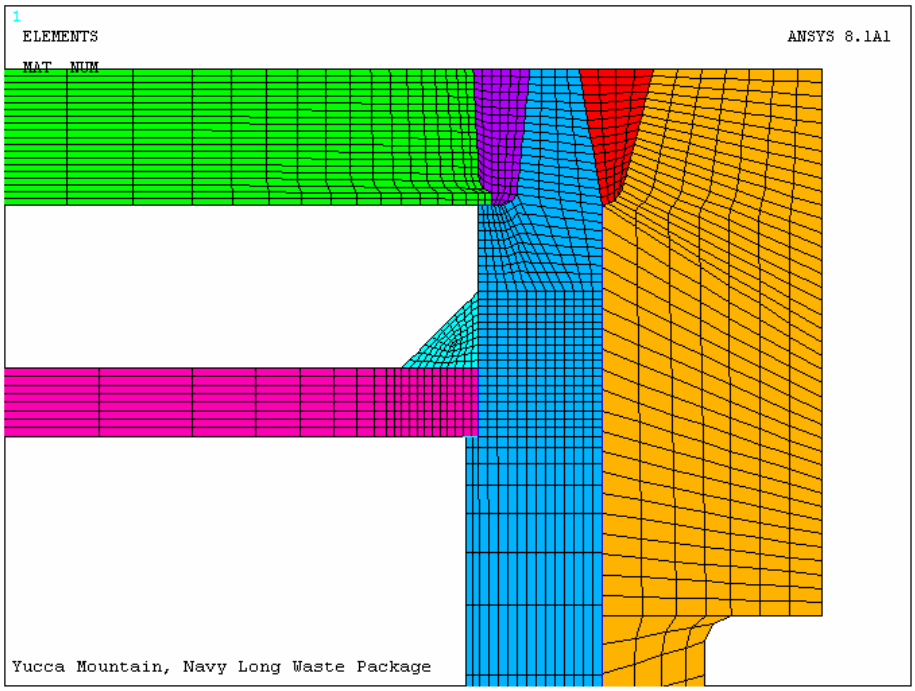

Source: DTN: MO0708RTSWRS06.000 [DIRS 182558], file *BSC-03Q-301-R2.pdf*, Figure 6.

Figure 6-13. Finite-Element Details in the Fillet Weld and Closure Weld Regions

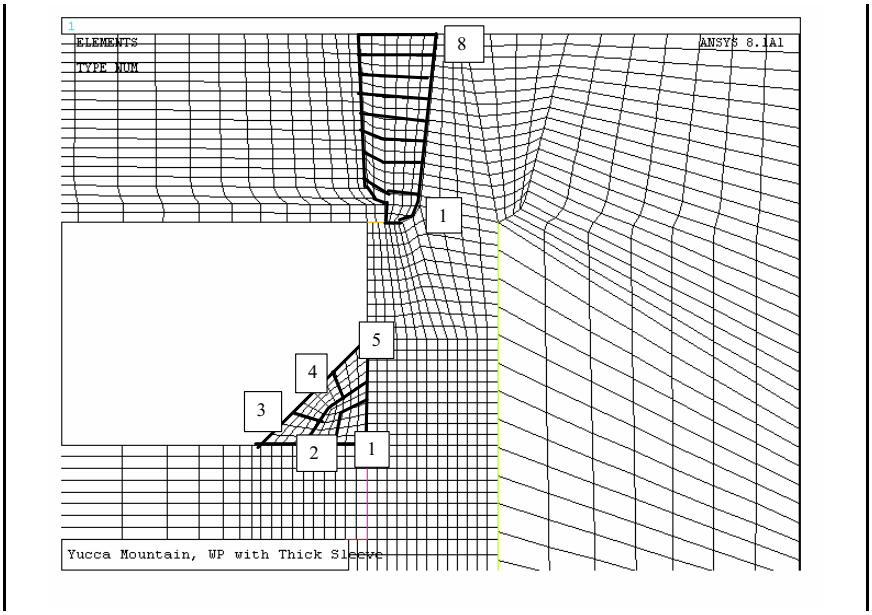

Source: DTN: MO0708RTSWRS06.000 [DIRS 182558], file *BSC-03Q-301-R2.pdf*, Figure 7.

Figure 6-14. Assignment of Weld Passes in the Fillet Weld and Closure Weld

Thermal and Structural Boundaries

For the thermal boundary conditions, the inside and outside surface heat transfer coefficients were assumed to be 1 Btu/hr-ft^2-°F and 5 Btu/hr-ft^2-°F, respectively, as shown in Figure 6-15a. For the structural boundary conditions, roller constraints were assumed at the longitudinal axis (center of the outer lid) and bottom of the model (cut locater of the outer barrier) as shown in Figure 6-15b.

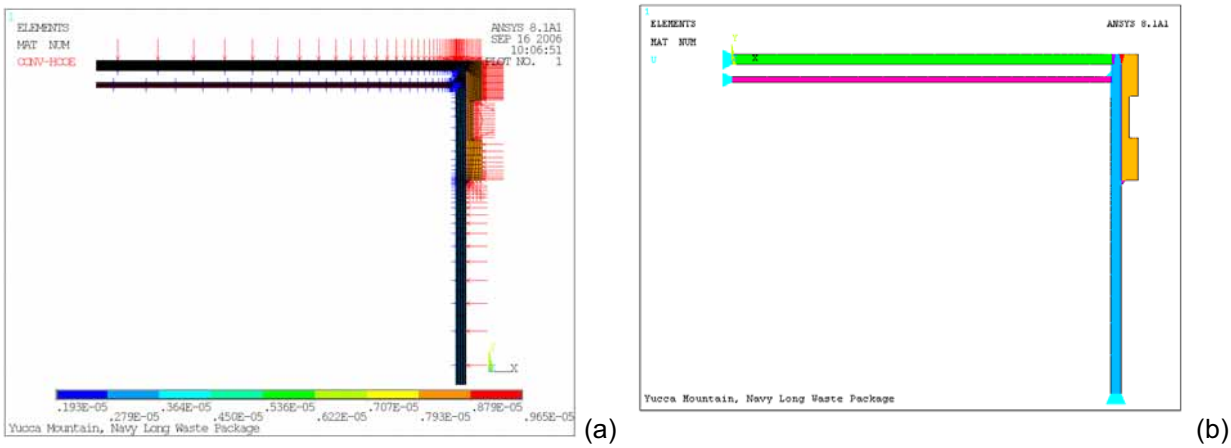

Sources: (a) DTN: MO0708RTSWRS06.000 [DIRS 182558], file *BSC-03Q-301-R2.pdf*, Figure 8.
(b) DTN: MO0708RTSWRS06.000 [DIRS 182558], file *BSC-03Q-301-R2.pdf*, Figure 9.

Figure 6-15. Thermal Boundary Conditions (a) and Structural Boundary Conditions (b) in the Finite-Element Analysis

Crack Geometries

Two crack models were used for the fracture mechanics evaluation of the stress and stress intensity factor profiles. The first is a single-edge cracked plate (SECP) illustrated in Figure 6-16. The second is an elliptical surface crack in an infinite plate with crack aspect ration of a/l = 0.1 as shown in Figure 6-16 from "Risk-Informed Requirements for Class 1, 2, and 3 Piping, Method B, Section XI, Division 1" in *1995 Code Cases, Nuclear Components* (ASME 1995 [DIRS 169771]). The SECP and elliptical crack models are used to simulate the radial crack in the weld subjected to the hoop stress (S_z) and the circumferential crack in the weld subjected to radial stress (S_x), respectively. In other words, a radially oriented flaw would be potentially driven by hoop stress. A circumferentially oriented flaw would be driven by radial stress. The flaw orientation for lid welds is discussed in more detail in Section 6.5.3.3.3 (Figure 6-23) in relation to stress intensity factor profiles.

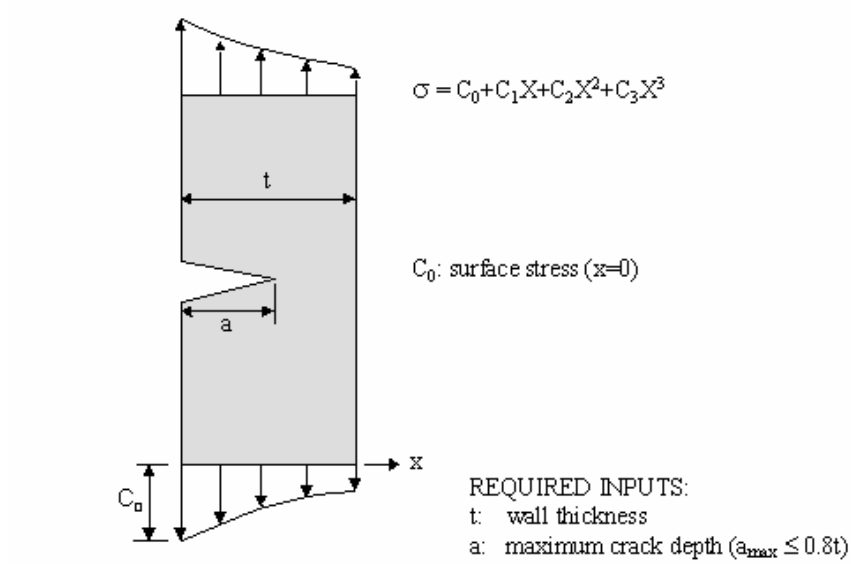

Source: DTN: MO0708RTSWRS06.000 [DIRS 182558], file *BSC-03Q-301-R2.pdf*, Figure 12.

Figure 6-16. Single-Edge Cracked Plate

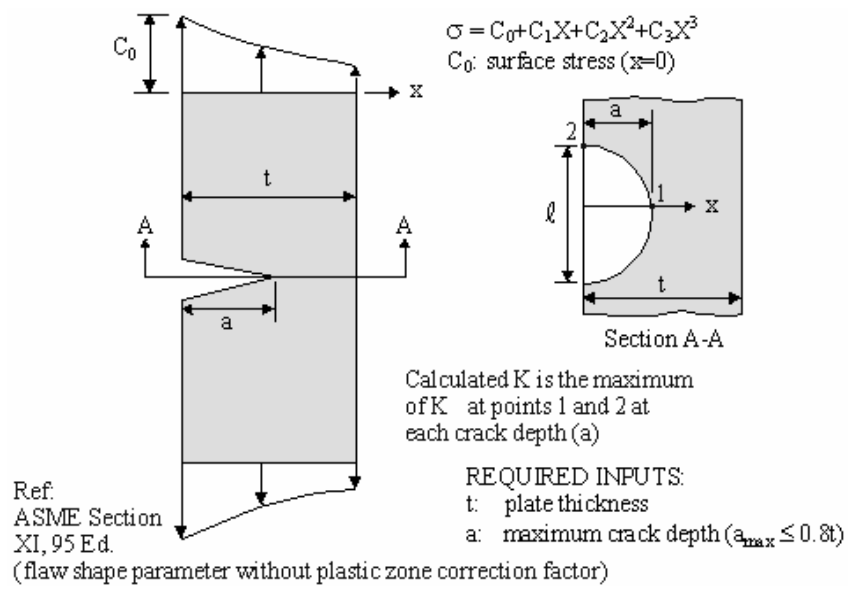

Source: DTN: MO0708RTSWRS06.000 [DIRS 182558], file *BSC-03Q-301-R2.pdf*, Figure 13.

Figure 6-17. Elliptical Crack in Infinite Plate

Selection of Through-Wall Sections

The through-wall sections for fracture mechanics evaluation are identified as Sections A-A and B-B in Figure 6-18. Section A-A is through the root of the outer lid closure weld and perpendicular to the outside surface of the outer lid. Section B-B is through the inside edge of the weld. Although, for the completion of the data presentation, Sections A-A and B-B results are presented here, only the data obtained for Section A-A are used in Section 6.5.6 for

uncertainty and variability analysis because, as indicated in Figure 6-31 (Section 6.5.3.4.2), Figure 6-45 (Section 6.5.5.2.3) and Figure 6-47 (Section 6.5.5.2.4), the stress intensity factor distribution along Sections A-A and B-B are virtually identical for as-welded, laser-peened, and plasticity-burnished waste package closure welds.

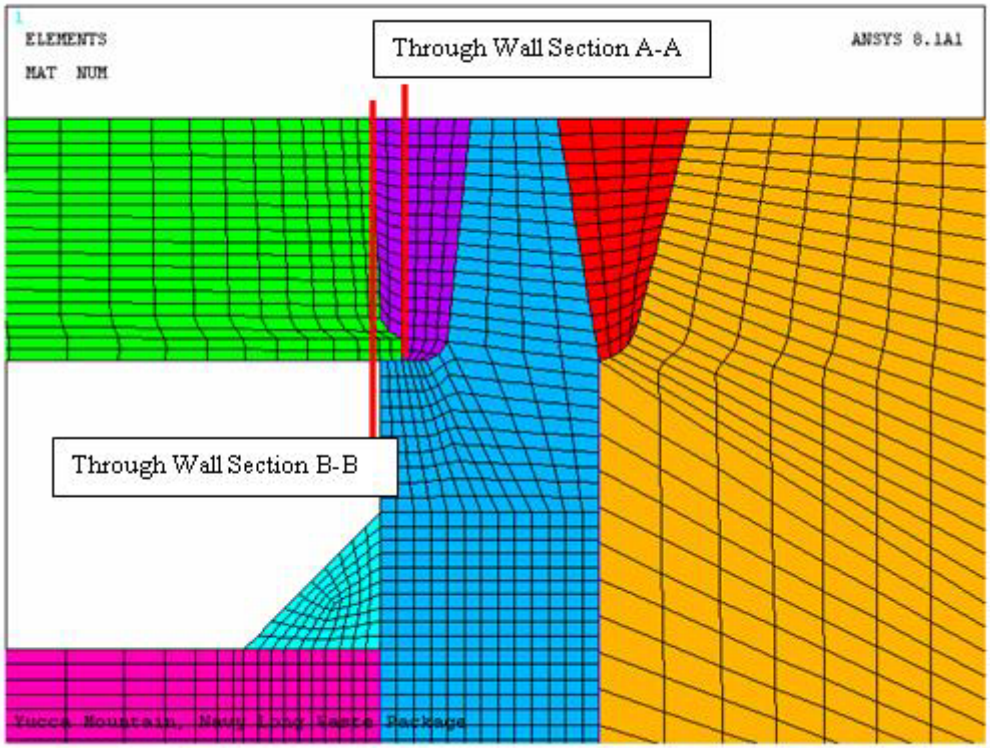

Source: DTN: MO0708RTSWRS06.000 [DIRS 182558], file *BSC-03Q-301-R2.pdf*, Figure 11.

Figure 6-18. Through-Wall Section in the Outer Lid Closure Weld

The through-wall stresses at Sections A-A and B-B Figure 6-18 are extracted from the finite-element analysis results only for the normal condition temperature (i.e., 125°C). The directions of x, y, and z used in the finite element model are shown in Figure 6-13.

The through-wall stress distributions are curve-fitted to a third-order polynomial for use in the crack model.

Assumptions Used in the SIA Finite-Element Analysis

In the SIA analysis (DTN: MO0708RTSWRS06.000 [DIRS 182558], file *BSC-03Q-301-R2.pdf*), the following assumptions were made:

- Material is homogeneous and isotropic
- Normal condition temperature is 257°F (125°C)
- Poisson's ratio of Alloy 22 is temperature independent
- Torch point heat source in the welding was modeled as volumetric heat source

- Heat input for fillet weld is 37.5 kJ/in
- Heat efficiency of the welding is 80%
- Yield strength and modulus of elasticity at or above 2,500°F (1,371°C) are negligible and were assigned small values to provide solution convergence
- Heat transfer coefficients in the thermal analyses are temperature independent, consistent with assumption of an average heat transfer
- There is no latent heat of weld beads
- A ten-second ramp-up and ramp-down cycle was used for welding heat generation
- No heat transfer occurs across the gap between the trunnion sleeve and the outer barrier, the gap between the middle lid and the outer barrier, and the gap between the outer lid and the outer barrier
- Material properties of the weld metal are the same as the base metal
- Yield strength of the weld metal and base metal are equal
- Elastic-plastic stress-strain behavior of Alloy 22 is bilinear kinematic
- Tangent modulus of Alloy 22 is similar to that of low alloy steel.

Material Properties

The material properties are important to the determination of the final weld residual stress. The material properties used in this evaluation for Alloy 22 are identical to those discussed in detail in *Evaluation of the CRM-21 PWR and Viability Availability Waste Package* (SIA 2003 [DIRS 162457]). For thermal analysis, the material properties used are thermal conductivity, specific heat, and density. For stress analysis, the material properties used are coefficient of thermal expansion, modulus of elasticity, Poisson's ratio, density, and yield strength.

Thermal Analysis

A thermal analysis of the waste package closure was performed to simulate the temperature history caused by each weld pass. Each weld pass will result in a different temperature field because as passes are applied, more material is added, residual stress from previous passes is being incorporated, and the relative location of the weld heat input changes with respect to the lid thickness.

Welding Simulation

The effect of each weld pass was simulated through heat generated in the finite elements, which represent the weld pass, and then the heat was transferred to the adjoining parts of the waste package. The heat generation rate (12,268 joules/in) used in the finite-element thermal analysis (SIA 2003 [DIRS 162457], p. 1-8) meets the project design requirement of less than 45kJ/in (SNL 2007 [DIRS 179567], Table 4-1, Parameter No. 03-15).

For the axisymmetric representation of the three-dimensional problem, it is desirable to convert the nonaxisymmetric heat input into an equivalent axisymmetric heat input, which is representative of what a typical point on the circumference of the weld would experience. This translates to an impulse heat input (i.e., a large amount of heat input over a short time), which is

represented by a triangular-shaped pulse for two seconds (ramp up in one second and ramp down in one second) followed by a cooling period. The length of cooling period after the deposit of weld beads is determined by the time required for the weld torch to travel around the circumference of the closure weld.

Weld Residual Stress Analysis

The stress analysis is performed for all individually modeled weld passes. For example, if six weld passes are modeled, six thermal stress analyses are performed. The analysis of weld pass 1 uses the temperature history for weld pass 1 thermal analysis. The analysis of weld pass 2 uses the weld pass 2 thermal analysis and the residual stress due to weld pass 1 as the initial condition. This process continues until all weld passes are analyzed. The final solution (at ambient conditions) is the room temperature weld residual stress.

Stress Mitigation

According to the current waste package final closure weld design, the stress mitigation of the outer lid closure weld will be by plasticity burnishing (SNL 2007 [DIRS 179354]), which imparts a layer of compressive residual stress to a minimum depth of 3 mm (0.12 in.) (SNL 2007 [DIRS 179567]). Based upon previous analyses using a compressive depth of 1.9 mm, a minimum mitigated depth of 4.6 mm (0.1811 in.) (BSC 2004 [DIRS 171499]) is achieved for tensile stress levels less than 90% of yield strength (BSC 2004 [DIRS 171499]). As described in *Waste Package Closure System Description Document* (BSC 2004 [DIRS 171499]), the performance acceptance criterion for stress mitigation is:

> Tensile stress from welding in the area near the intersection of the outer lid and outer barrier shall be mitigated by imparting a layer of compressive residual stress to a minimum depth of 1.9 mm (0.0748 in) and limiting tensile stress to 90 percent of yield strength to a minimum depth of 4.6 mm (0.1811 in).

According to the results of controlled plasticity burnishing (CPB) in *Controlled Plasticity Burnishing (CPB) for Developing a Very Deep Layer of Compressive Residual Stresses in Rectangular Specimens of Alloy 22 for Yucca Mountain Nuclear Waste Package Closure Weld* (Woolf 2003 [DIRS 178059]), the through-wall stress profile at the closure weld is adjusted to produce the near-surface compressive stresses that transition below surface to the as-welded tensile residual stresses. The approach adopted in an earlier version of this document (BSC 2004 [DIRS 172203]) for laser peening is to adjust the surface stress of the original through-wall residual stress profile to a chosen compressive stress (-40 ksi) to a depth of 1.5 mm (0.06 in) without considering the self-equilibrium condition of the residual stress. This approach is considered acceptable, as the general impact on the section stress caused by the CPB is small compared to the closure weld. The stress mitigation from the proposed CPB in Woolf's report (2003 [DIRS 178059]) is presented in Table 6-9, along with that for laser peening from the previous version of this document (BSC 2004 [DIRS 172203]).

Table 6-9. Stress versus Depth of Proposed Stress Mitigation Treatments

Controlled Plasticity Burnishing[a]		Laser Peening[b]	
Depth (in)	Stress (ksi) (Radial and Tangential)	Depth (in)	Stress (ksi)
0.05	−85	0.06	-40
0.15	−50	—	—
0.25	−40	—	—

Sources: [a]Woolf 2003 [DIRS 178059].
[b]BSC 2004 [DIRS 172203].

6.5.3.3.2 Finite-Element Model

Determining the weld residual stress requires a thermal analysis to determine the temperature history caused by the welding process and a subsequent weld residual stress analysis. This problem has been solved using finite-element analysis methods. Although the determination of weld residual stress for the waste package welds is a three-dimensional problem, it has been found that the use of two-dimensional axisymmetric modeling of the problem provides a reasonable estimate of the behavior (Chan et al. 1970 [DIRS 147968], p. 3). Thus, the waste package closure weld models were treated as being two-dimensionally axisymmetric about the waste package axial centerline.

Using a similar analysis method and material parameters, reasonable agreement between experimentally measured and calculated through-wall residual stress distributions was obtained previously by SIA for a 16-in-long linear weld produced in a 1-in-thick by 12-in-wide Alloy 22 plate (SIA 2003 [DIRS 178078], Section 7.0). This weld was very similar in geometry to the current outer lid closure weld. For this similar case, the finite-element model gave very reasonable results compared to the residual stress measurements at the locations of most interest near the weld. The finite-element model for the naval long waste package closure weld design (with middle lid) is shown in Figure 6-14. The weld geometry and immediate neighboring material for the outer lid are modeled in detail with sufficiently small elements to capture the large thermal and strain gradients associated with the weld pass application. The element sizes become larger with distance from the weld as the field variable gradients are significantly lower.

For the naval long waste package closure weld with middle lid, the stress distributions due to welding and temperature are shown in Figure 6-19 and Figure 6-20 for normal operating temperature (257°F or 125°C) and room temperature (70°F or 21°C), respectively. As can be seen from Figure 6-19 and Figure 6-20, the maximum, minimum, and severe stress gradients are concentrated in the closure and fillet welds at both temperatures. In both cases, the axial stresses do not significantly contribute to the driving force for crack growth.

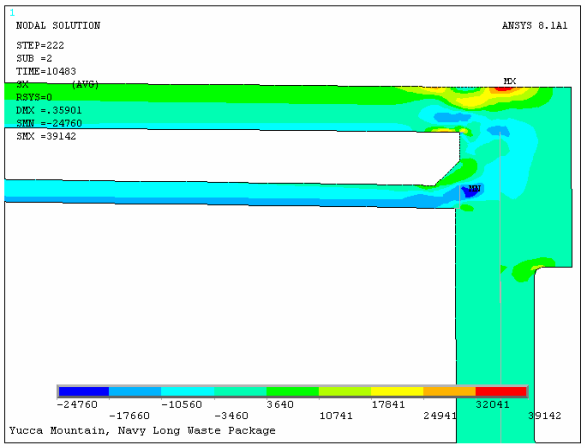

(a) Radial Stress

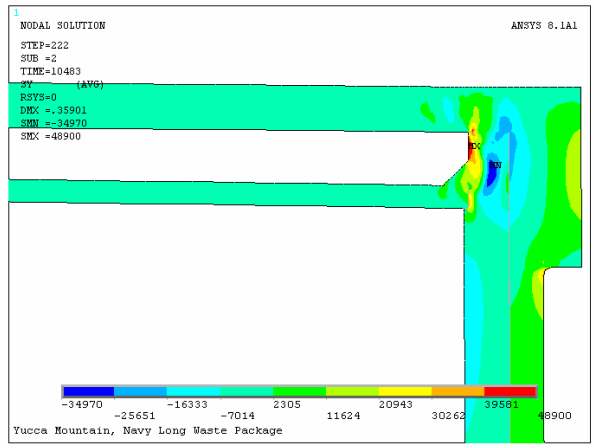

(b) Axial Stress

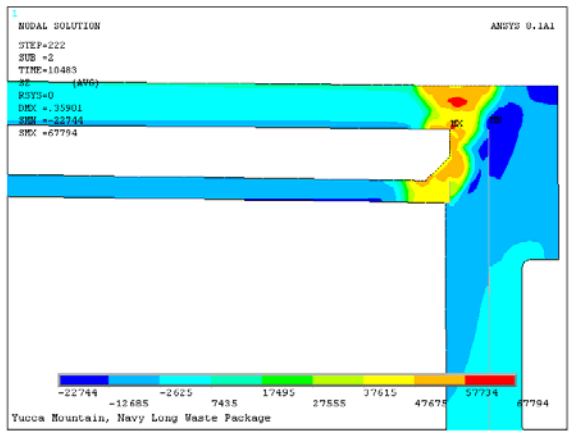

(c) Hoop Stress

Source: DTN: MO0708RTSWRS06.000 [DIRS 182558], file *BSC-03Q-301-R2.pdf*, Figure 14.

Figure 6-19. Stress Distribution in Naval Long Waste Package Closure Lid Weld at Normal Operating Temperature (257°F or 125°C)

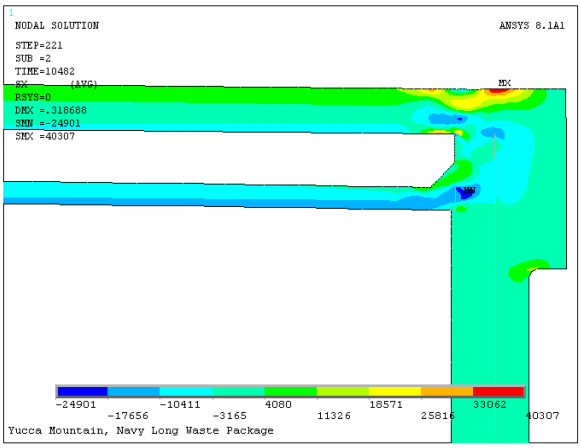

(a) Radial Stress

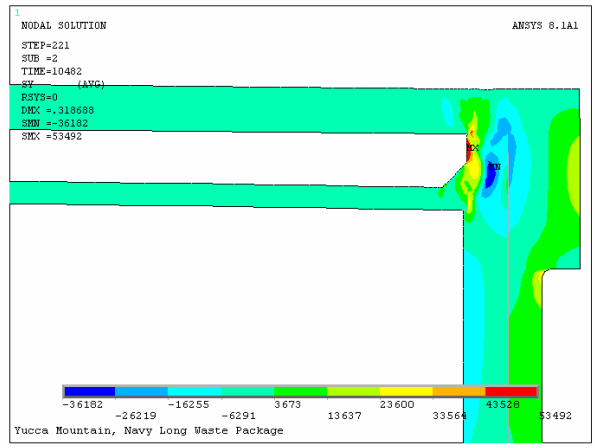

(b) Axial Stress

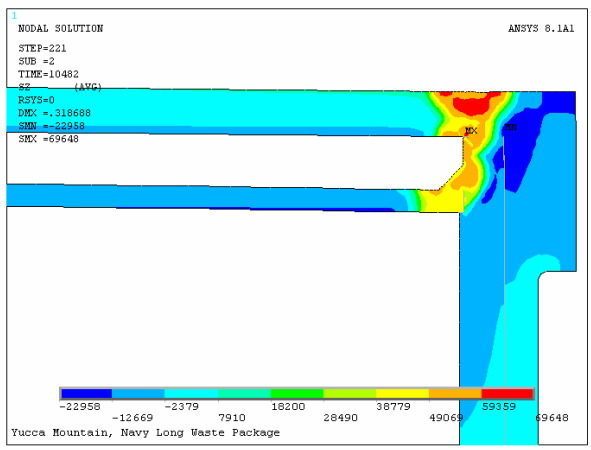

(c) Hoop Stress

Source: DTN: MO0708RTSWRS06.000 [DIRS 182558], file *BSC-03Q-301-R2.pdf*, Figure 15.

Figure 6-20. Stress Distribution at Room Temperature in Naval Long Waste Package Closure Lid Weld at Room Temperature (70°F or 21°C)

The stresses on the top surface of the model (including the outer lid, outer barrier, and trunnion sleeve) at the operating temperature of 257°F (125°C) and at room temperature are presented in Figure 6-21 and Figure 6-22, respectively. The outside surface stress distribution in Figure 6-21 includes the residual stress and the normal operating condition thermal stress.

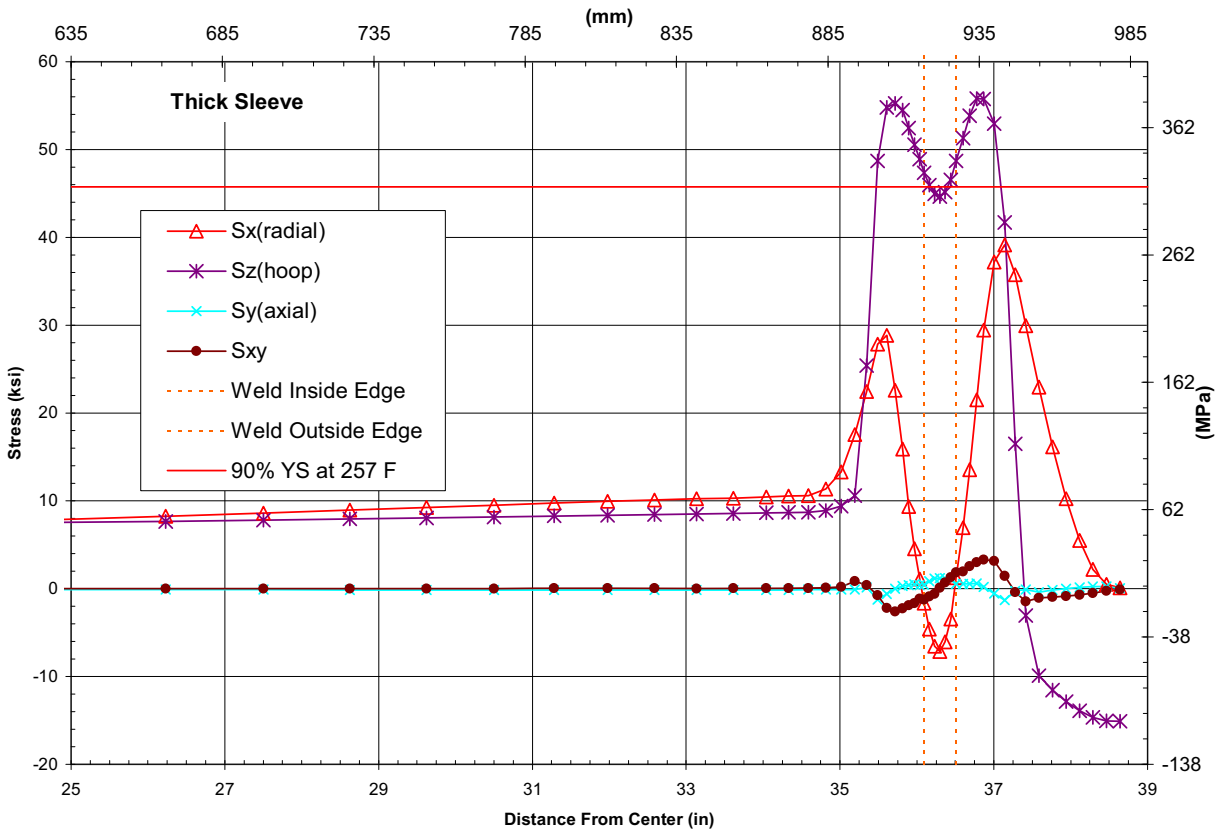

Source: Modified from DTN: MO0708RTSWRS06.000 [DIRS 182558], file *BSC-03Q-301-R2.pdf*, Figure 16.

Figure 6-21. Outer Lid Outside Surface Residual Stress Distribution, Thick Upper Portion of Sleeve, at Normal Condition Temperature

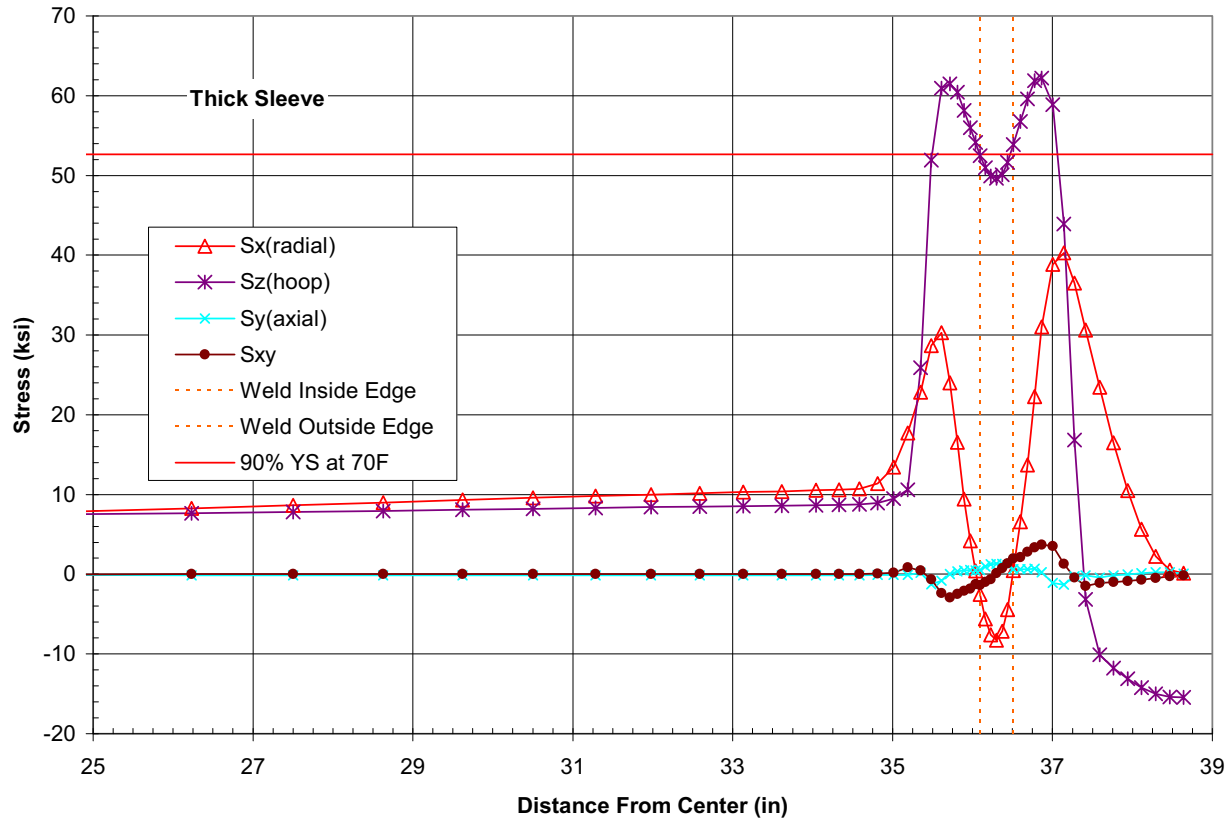

Source: Modified from DTN: MO0708RTSWRS06.000 [DIRS 182558], file *BSC-03Q-301-R2.pdf*, Figure 17.

Figure 6-22. Outer Lid Outside Surface Residual Stress Distribution, Thick Upper Portion of Sleeve, at Room Temperature

At the normal condition temperature of 257°F (125°C), the yield strength of Alloy 22 is interpolated from the Alloy 22 yield strength values in Table 4-7, as presented in Table 6-4. There are two Alloy 22 yield strength values in Table 4-7. As indicated in Table 4-1, the yield strength values from "Hastelloy Alloy C-22" (Alloy Digest 1985 [DIRS 178194], p. 2, Table 3) for 0.028-in- to 0.125-in-thick (0.71-mm- to 3.2-mm-) sheet are used in this section. Both Alloy Digest (1985 [DIRS 178194], p. 2, Table 3) and Haynes International (1988 [DIRS 101995], p. 15) are listed in DTN: MO0003RIB00071.000 [DIRS 148850], Physical and Chemical Characteristics of Alloy 22. However, Alloy Digest (1985 [DIRS 178194]) gives higher yield strength values (for thinner plate) than the value given by Haynes International (1988 [DIRS 101995]) for thicker plate. The higher yield strength value is used for the finite-element analyses of weld residual stresses and stress intensity factors since it results in higher and, therefore, more-conservative calculated residual stress values. The interpolated yield strength of Alloy 22 at 125°C is 50.9 ksi (351 MPa) (see Table 6-4). The threshold stress criterion (i.e., the 90% of the $YS_{(125°C)}$) is, therefore, 45.75 ksi (316 MPa). At room temperature, 90% of the $YS_{(RT)}$ (58.5 ksi or 403 MPa) is 52.65 ksi (363 MPa). These values are also summarized in Table 6-4.

At 125°C (Figure 6-21), in the regions close to the weld, the hoop residual stress (S_z) is higher than the 90% $YS_{(125°C)}$ criterion (316 MPa). The other stresses (radial S_x, and axial S_y) are well below the 90% $YS_{(125°C)}$ (316 MPa) everywhere on the top outside surface of the lid. At room temperature, Figure 6-22 shows that the hoop stress is also higher than the 90% $YS_{(RT)}$ criterion (363 MPa) at and near the closure weld. The hoop stress at 21°C is higher than that at 125°C; this is because at 21°C there is a lack of the effect of compressive thermal stress. It is evident from Figure 6-21 and Figure 6-22 that the weld-related residual hoop stresses drop off rapidly normal to the weld centerline and approach the unwelded base plate values within about 1 in (25.4 mm) on either side of the weld. The radial stress drop-off is less symmetric than the hoop stress because of the higher constraint present on the outboard side of the weld due to the relatively thick trunnion sleeve.

6.5.3.3.3 Stress Intensity Factor Profile Calculations

This section provides the basis for using the SECP crack geometry for analyzing radial stress and stress intensity factor profiles while using the elliptical crack geometry (ELL) for analyzing hoop stress and stress intensity factor profiles in the rest of Section 6.5.

For the Alloy 22 waste package outer barrier closure weld regions, the flaw orientations most likely susceptible to crack propagation are those of circumferential flaws (parallel to weld) and of radially oriented flaws (perpendicular to weld). Figure 6-23 schematically illustrates the flaw orientations with respect to the weld. As indicated in Section 6.5.3.3.1, a radially oriented flaw would be potentially driven by hoop stress. A circumferentially oriented flaw would be driven by radial stress.

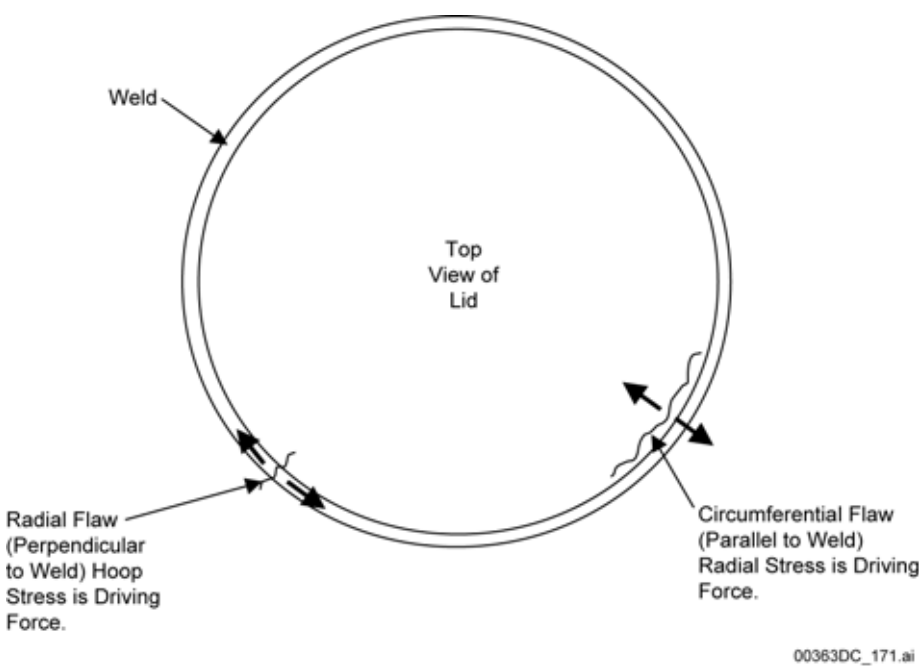

Source: Created for illustrative purposes only.

Figure 6-23. Flaw Orientation for Lid Welds

A general form of the stress intensity factor is expressed by Equation 20. As indicated in Section 6.5.2, β is a geometry factor dependent on the size and shape of the crack and the configuration of the structural component, a, the crack depth, and σ is the stress distribution through the wall thickness of the structural component. Closed-form solutions of Equation 20 are possible only in some simple cases of uniform tensile stress and simple geometry.

Although finite-element analyses can be used to evaluate the stress intensity factor (Section 6.5.2), the effort is usually quite time-consuming because a series of elaborate finite-element analyses must be completed for numerous crack sizes starting from 0 through the thickness of the containment wall. A simplified solution procedure was developed by using fracture mechanics to evaluate the parameter $(K_I)_{PCCRACK}$ for a given stress distribution. Then a geometry correction factor, G, as a function of the crack size, a, was developed by curve fitting from comparing the simplified solutions with the results of finite-element analysis for only a limited number of crack sizes. Given the geometry correction factor, the true stress intensity factor, K_I, for any crack size can be derived from $(K_I)_{PCCRACK}$ and G, without going through the finite-element analysis. This is achieved by using the relationship shown in Equation 21:

$$K_I = G\left(K_I\right)_{PCCRACK} \qquad \text{(Eq. 21)}$$

For a circumferential flaw, $(K_I)_{PCCRACK}$ was derived from an infinite SECP with an infinitely long flaw. For a radial flaw, $(K_I)_{PCCRACK}$ was derived from an elliptical surface crack in an infinite plate with a crack aspect ratio of 1 (a semicircular crack). In either case, the stress distribution was calculated by using a third-order polynomial of the type represented by Equation 22:

$$\sigma = A_0 + A_1x + A_2x^2 + A_3x^3 \qquad \text{(Eq. 22)}$$

where x is the distance from the outer surface of the closure lid and A_0, A_1, A_2, and A_3 are coefficients of the third-order polynomial fit of the through-wall stress distribution (or profile).

The model of a circular crack in an infinite plate is a better representation of a limited-length radial crack in the closure weld than an infinite edge crack in an infinite SECP. It is judged that a radial crack in the closure weld would not grow into a long semielliptical crack due to the rapid decay of hoop stress in the radial distance away from the weld and base metal interface. This is well demonstrated in earlier work performed by SIA for the CRM–21-PWR waste package design as indicated in Figure 6-24 (SIA 2003 [DIRS 162457]). The "1-1," "2-2," and "3-3" notations in Figure 6-24 are cross section identifications corresponding to those indicated in Figure 6-25 (SIA 2003 [DIRS 162457], Figure 2-22).

The stress intensity factor for an infinite SECP with an infinitely long flaw is expressed in Equation 23 (Buchalet and Bamford 1976 [DIRS 118597], Equation 2, p. 388):

$$(K_I)_{SECP} = \sqrt{(\pi a)}\left[A_0F_1 + \left(\frac{2a}{\pi}\right)A_1F_2 + \left(\frac{a^2}{2}\right)A_2F_3 + \frac{4a^3}{3\pi}A_3F_4\right] \qquad \text{(Eq. 23)}$$

where F_0, F_1, F_2, and F_3 are magnification factors and A_0, A_1, A_2, and A_3 are coefficients of the third-order polynomial fit of the through-wall stress distribution (or profile) as indicated in Equation 22.

The magnification factors F_0, F_1, F_2, and F_3 are functions of the crack depth (a) versus thickness (h) ratio (a/h). They are graphically presented by Buchalet and Bamford (1976 [DIRS 118597], Figure 6) and used to calculate the stress intensity factor.

The SECP stress intensity factor is for the ideal geometry and must be modified by the geometry correction factor (G) to consider the actual geometry. For example, in earlier work performed by SIA for the CRM–21-PWR waste package design, Figure 6-26 shows, for a circumferential flaw, the G-factor distribution in the closure weld of the CRM–21-PWR waste package outer lid as a result of a curve fit based on the exact G values calculated at four discrete points corresponding to crack-versus-thickness ratios of 0.2, 0.3, 0.4, and 0.6 (SIA 2003 [DIRS 162457], Figure 3-11). For shallow flaws, Figure 6-26 indicates the correction factor is near 1. For deeper flaws, the correction becomes more significant, and, therefore, using the SECP solution would be more conservative. For a radial flaw, the simplified solution obtained from a fracture mechanics crack model that contains a semicircular surface flaw in a flat plate is judged to be close to the final solution. Therefore, the geometrical correction factor approaches unity for the case of radial cracks. Because the correction factor reduces the calculated stress intensity factor values due to relaxation of constraint as the crack deepens, it is conservative to ignore this factor, as is done in DTN: MO0708RTSWRS06.000 [DIRS 182558], file *BSC-03Q-301-R2.pdf* and in this document.

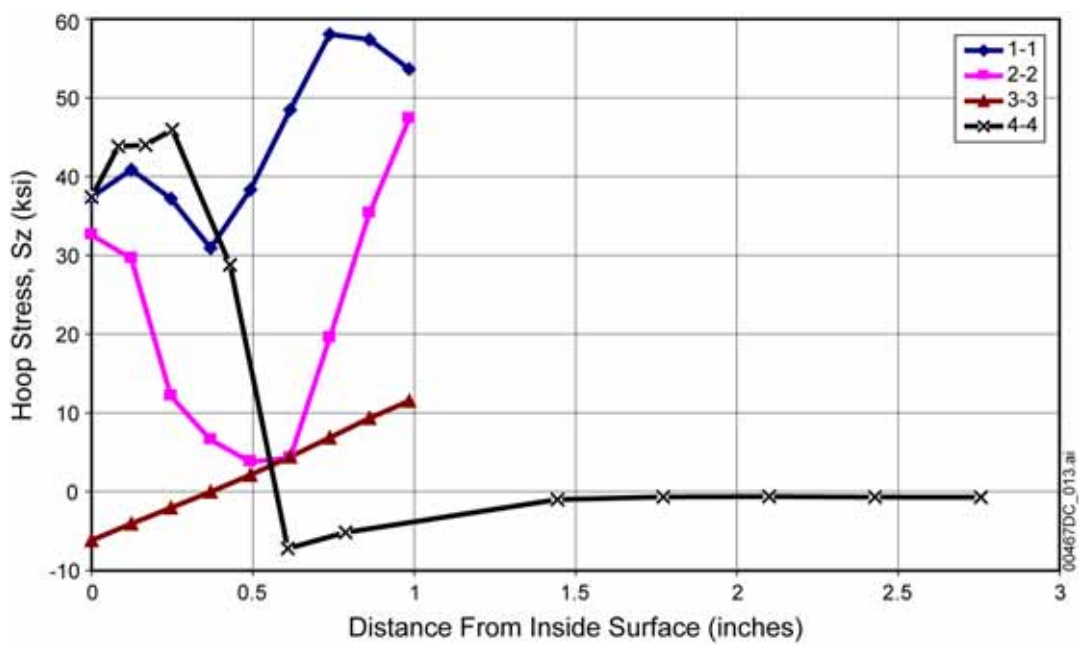

Source: SIA 2003 [DIRS 162457], Figure 2-22.

Figure 6-24. Hoop Stresses in Outer Lid of CRM–21-PWR Design at 125°C

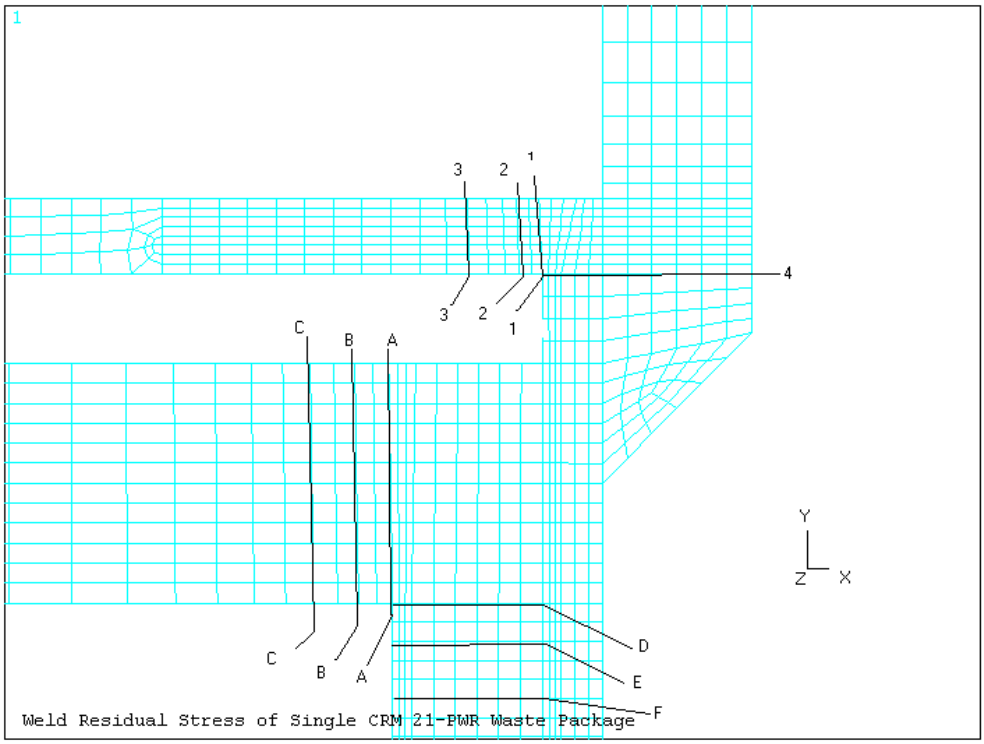

Source: SIA 2003 [DIRS 162457], Figure 2-1.

Figure 6-25. Selected Cross Sections for CRM-21-PWR Waste Package Design

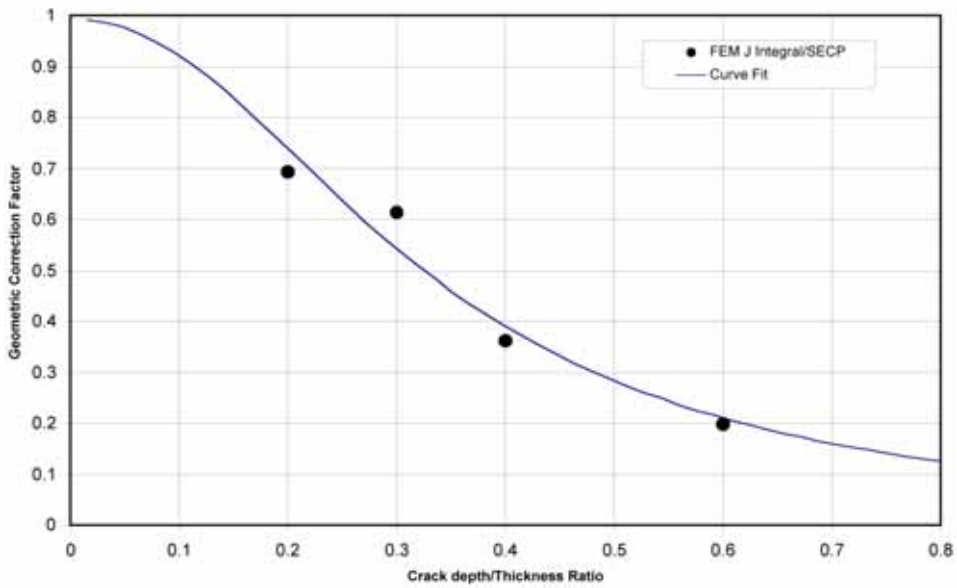

Source: SIA 2003 [DIRS 162457], Figure 3-11.

Figure 6-26. Outer Lid Circumferential Flaw Geometric Correction Factor

To avoid any conceptual confusion regarding the orientations of the flaws (cracks), the relationships between the crack orientations, their driving stresses, and the crack geometries used in this report are summarized below:

- Radially oriented flaws are potentially driven by hoop stress (the "circumferential stress")
- Circumferentially oriented flaws are driven by radial stress
- Circumferential flaws, $(K_I)_{PCCRACK}$, were derived from an infinite SECP with an infinitely long flaw
- Radial flaws, $(K_I)_{PCCRACK}$, were derived from elliptical surface cracks in an infinite plate with a crack aspect ratio of 1 (a semicircular crack)
- Stress distribution was calculated by using a third-order polynomial of the type represented by Equation 22
- The model of a circular crack in an infinite plate is a better representation of a limited-length radial crack in the closure weld than an infinite edge crack in an infinite SECP
- Radial cracks in closure welds do not grow into long semielliptical cracks due to the rapid decay of hoop stress in the radial distance away from the weld and base-metal interface.

6.5.3.4 Numerical Results

As indicated in Section 6.5.3.1, the calculated stress and stress intensity factor profiles for the naval long waste package design are based on the as-welded and plasticity-burnished outer lid for the current waste package closure weld design. As corroborative information, some of the results for the laser-peened waste package closure welds are also presented in this section.

A_0, A_1, A_2, and A_3 in Equation 22 are described by the units ksi, ksi/in, ksi/in^2, and ksi/in^3 using the English unit system and MPa, MPa/mm, MPa/mm^2, and MPa/mm^3 using the metric unit system, respectively. To convert from English to the metric unit system, use the unit conversion factors shown in Table 6-10.

Table 6-10. Unit Conversion Factors from English Units to Metric Units

Parameter	English Units	Metric Units
X	1 in	25.4 mm
A_0	1 ksi	6.894757 MPa
A_1	1 ksi/in	0.271447 MPa/mm
A_2	1 ksi/in^2	0.010687 MPa/mm^2
A_3	1 ksi/in^3	0.000421 MPa/mm^3

Source: Boyer and Gall 1997 [DIRS 155318], p. 1-55 and 1-57.

6.5.3.4.1 Stress and Stress Coefficients for the As-Welded Naval Long Waste Package Outer Lid

The through-wall stress distributions in sections A-A and B-B of the as-welded naval long waste package outer closure lid at normal condition temperature are shown in Figure 6-27 and Figure 6-28, respectively. The stresses are presented as the distance from the outer lid outside surface for S_x (radial stress) and S_z (hoop stress). The directions x, y, and z used in the finite-element model are shown in Figure 6-12.

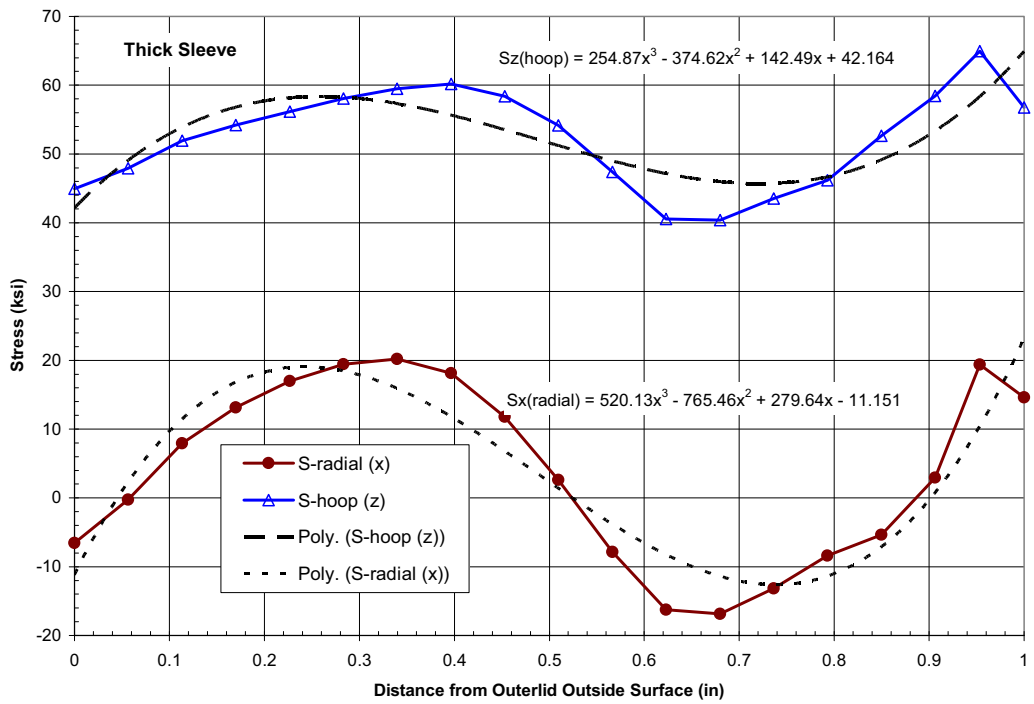

Source: DTN: MO0708RTSWRS06.000 [DIRS 182558], file *NdStrs-R2.xls*, Sheet "AAStrsFit."

Figure 6-27. Through-Wall Stress Distributions in Section A-A of the As-Welded Naval Long Waste Package Outer Closure Lid at Normal Condition Temperature

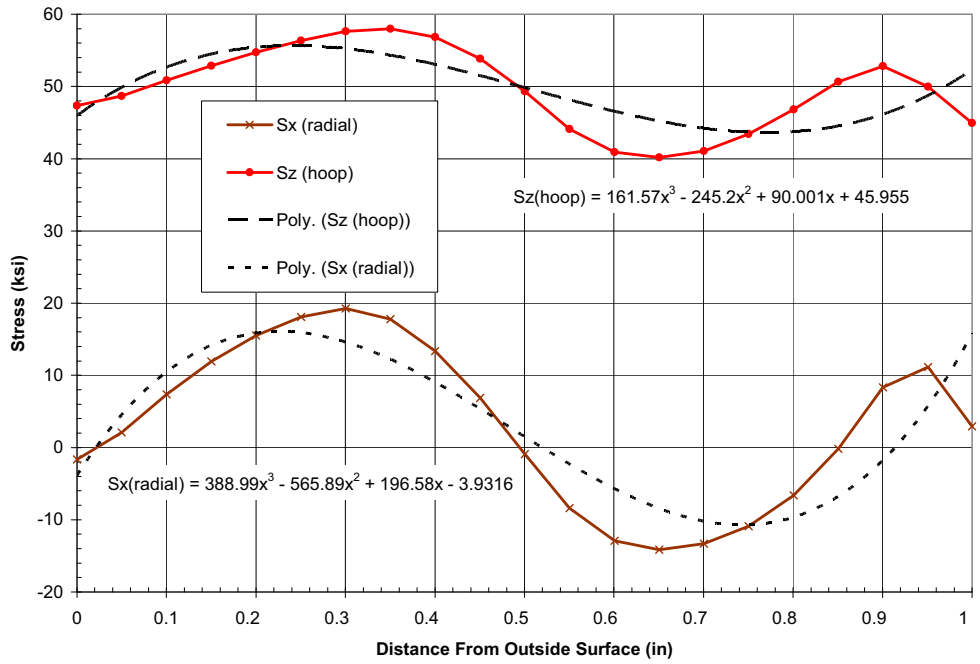

Source: DTN: MO0708RTSWRS06.000 [DIRS 182558], file *NdStrs-R2.xls*, Sheet "BBStrFit."

Figure 6-28. Through-Wall Stress Distributions in Section B-B of the As-Welded Naval Long Waste Package Outer Closure Lid at Normal Condition Temperature

The values of the coefficients in Equation 22 for the as-welded closure-lid welds of naval long waste package designs are obtained by regressing the stress data to a third-order polynomial (Equation 22). These coefficients are listed in the first four rows of Table 4-3 as direct input with the radial stress (S_x) and hoop stress (S_z) in ksi and distance (x) in inches. Table 6-11 shows the converted stress coefficients, A_0, A_1, A_2, and A_3, in the metric unit system by using the conversion factors in Table 6-10.

Table 6-11. Stress Coefficients for the As-Welded Naval Long Waste Package Outer Lid

Stress Coefficient	From First and Second Rows of Table 4-3					Conversion Factors					
	Unit	Section A-A		Section B-B			Unit	Section A-A		Section B-B	
		Radial Stress	Hoop Stress	Radial Stress	Hoop Stress			Radial Stress	Hoop Stress	Radial Stress	Hoop Stress
A_0	ksi	−11.151	42.164	−3.9316	45.955	1 ksi = 6.894757 MPa *	MPa	−76.883	290.711	−27.107	316.849
A_1	ksi/in	279.64	142.49	196.58	90.001	1 ksi/in = 0.271447 MPa/mm	MPa/mm	75.907	38.678	53.361	24.431
A_2	ksi/in^2	−765.46	−374.62	−565.89	−245.2	1 ksi/in^2 = 0.010687 MPa/mm^2	MPa/mm^2	−8.180	−4.004	−6.048	−2.620
A_3	ksi/in^3	520.13	254.87	388.99	161.57	1 ksi/in^3 = 0.000421 MPa/mm^3	MPa/mm^3	0.219	0.107	0.164	0.068

Source: The data in the third, fourth, fifth, and sixth columns are from the first, second, third and fourth rows of Table 4-3 with English units. The last four columns of this table are converted to metric units by using the conversion factors shown in the middle column.
* (Boyer and Gall 1997 [DIRS 155318], p. 1-57)

6.5.3.4.2 Stress and Stress Intensity Factor for the As-Welded Naval Long Waste Package Outer Lid

Figure 6-29 and Figure 6-30 show the calculated stress intensity factor profiles for the as-welded naval long waste package outer lid along the directions of A-A and B-B, respectively (DTN: MO0708RTSWRS06.000 [DIRS 182558], file *NdStrs-R2.xls*, "Sheets A-AWldPlt_new" and "B-BWldPlt_new"). The numerical presentation of the stress intensity factor profiles are shown in Table 6-12 for section A-A with the radial stress and radial stress intensity factor using the SECP crack geometry and with the hoop stress and hoop stress intensity factor using the elliptical crack geometry. As indicated in Section 6.5.3.3.3, for a circumferential flaw, $(K_I)_{PCCRACK}$ was derived from an infinite SECP with an infinitely long flaw and, for a radial flaw, $(K_I)_{PCCRACK}$, was derived from an elliptical surface crack in an infinite plate. Therefore, while all data are shown in Figure 6-29 and Figure 6-30 (i.e., A-A and B-B, SECP, ELL, radial, and hoop) (DTN: MO0708RTSWRS06.000 [DIRS 182558], file *NdStrs-R2.xls*, Sheet: "BBWldPlt_new").

Table 6-12 lists only the data in section A-A that will be used for further analysis, such as the uncertainty and variability analysis in Section 6.5.6. As shown in Figure 6-31, the stress intensity factor distribution along A-A and B-B sections is virtually identical.

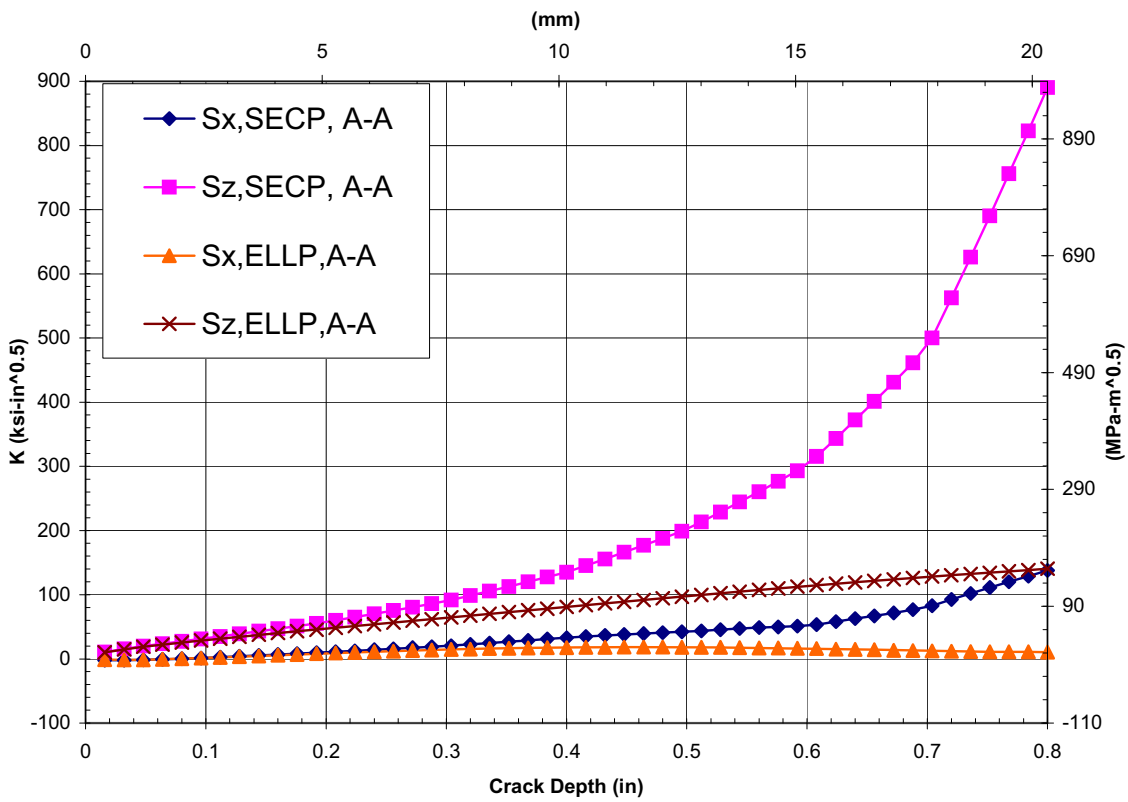

Source: DTN: MO0708RTSWRS06.000 [DIRS 182558], file *NdStrs-R2.xls,* Sheet "A-AWldPlt_new."

Figure 6-29. Through-Wall Stress Intensity Factor Distributions in Section A-A of the As-Welded Naval Long Waste Package Outer Closure Lid at Normal Condition Temperature

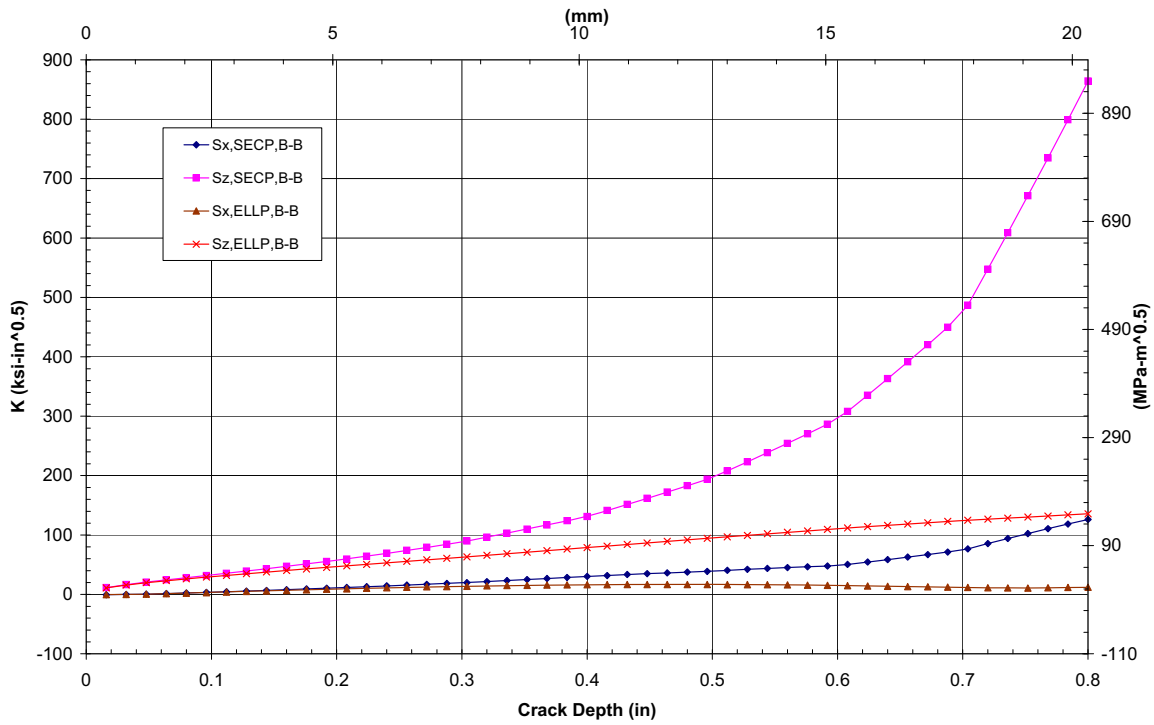

Source: DTN: MO0708RTSWRS06.000 [DIRS 182558], file *NdStrs-R2.xls*, Sheet "B-BWldPlt_new."

Figure 6-30. Through-Wall Stress Intensity Factor Distributions in Section B-B of the As-Welded Naval Long Waste Package Outer Closure Lid at Normal Condition Temperature

Table 6-12. Stress and Stress Intensity Factor Profiles for the As-Welded Naval Long Waste Package Outer Lid

Distance from Outer Surface, mm	Radial Stress (SECP)		Hoop Stress (Elliptical)	
	Sx, MPa	K-Sx, MPa√m	Sz, MPa	K-Sz, MPa√m
0.4064	−6.4090	−2.2678	326.3496	11.2274
0.8128	12.3573	−2.2901	335.0121	16.3747
1.2192	29.2579	−1.7449	342.8640	20.6275
1.6256	44.3589	−0.8637	349.9326	24.4393
2.0320	57.7262	0.2410	356.2453	27.9742
2.4384	69.4260	1.4985	361.8294	31.3100
2.8448	79.5243	2.8147	366.7125	34.6315
3.2512	88.0872	4.2080	370.9218	37.8956
3.6576	95.1806	5.6749	374.4847	41.0731
4.0640	100.8707	7.1989	377.4287	44.1727
4.4704	105.2234	8.7668	379.7810	47.2003
4.8768	108.3049	10.3682	381.5692	50.1595
5.2832	110.1812	12.0423	382.8206	53.1682
5.6896	110.9183	13.7863	383.5625	56.2437

Table 6-12. Stress and Stress Intensity Factor Profiles for the As-Welded Naval Long Waste Package Outer Lid (Continued)

Distance from Outer Surface, mm	Radial Stress (SECP)		Hoop Stress (Elliptical)	
	Sx, MPa	K-Sx, MPa√m	Sz, MPa	K-Sz, MPa√m
6.0960	110.5823	15.5413	383.8224	59.2771
6.5024	109.2392	17.2938	383.6276	62.2685
6.9088	106.9551	19.0311	383.0055	65.2181
7.3152	103.7960	20.7408	381.9836	68.1262
7.7216	99.8280	22.5402	380.5891	71.0425
8.1280	95.1171	24.7409	378.8495	74.0742
8.5344	89.7294	26.9849	376.7922	77.0775
8.9408	83.7308	29.2656	374.4446	80.0523
9.3472	77.1875	31.5760	371.8340	82.9990
9.7536	70.1656	33.9100	368.9878	85.9181
10.1600	62.7310	36.2618	365.9334	88.8104
10.5664	54.9497	38.2561	362.6982	91.8087
10.9728	46.8880	40.1446	359.3096	94.7872
11.3792	38.6117	41.9080	355.7950	97.7469
11.7856	30.1869	43.5280	352.1817	100.6890
12.1920	21.6798	44.9869	348.4971	103.6150
12.5984	13.1563	46.2679	344.7687	106.5266
13.0048	4.6825	48.1026	341.0238	109.3852
13.4112	−3.6756	50.0290	337.2898	112.2171
13.8176	−11.8519	51.7880	333.5940	115.0390
14.2240	−19.7804	53.3637	329.9639	117.8531
14.6304	−27.3950	54.7413	326.4269	120.6618
15.0368	−34.6297	55.9084	323.0103	123.4693
15.4432	−41.4185	58.8299	319.7415	126.1197
15.8496	−47.6952	63.7225	316.6480	128.6086
16.2560	−53.3938	68.6858	313.7570	131.0953
16.6624	−58.4483	73.7252	311.0960	133.5852
17.0688	−62.7927	78.8497	308.6924	136.0818
17.4752	−66.3609	84.0719	306.5735	138.5927
17.8816	−69.0868	90.7634	304.7667	141.0079
18.2880	−70.9044	101.4317	303.2995	143.1078
18.6944	−71.7476	111.8743	302.1992	145.2363
19.1008	−71.5505	122.0826	301.4931	147.4021
19.5072	−70.2469	132.0579	301.2088	149.6130
19.9136	−67.7708	141.8068	301.3735	151.8777
20.3200	−64.0562	151.3480	302.0147	154.2017

Source: The data in the first, third, and fifth columns are from DTN: MO0708RTSWRS06.000 [DIRS 182558], file *NdStrs-R2.xls*, Sheet "Ksolu_As Welded." The data in the second and fourth columns are calculated according to Equation 22 and the stress coefficients in Table 6-11.

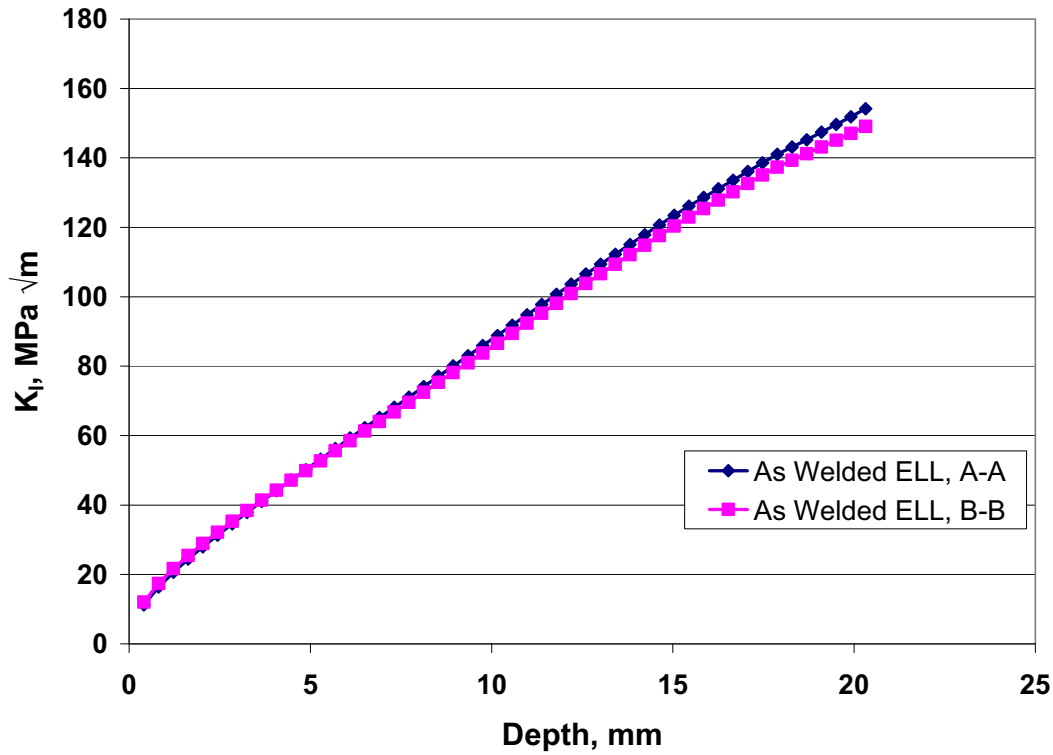

Source: DTN: MO0708RTSWRS06.000 [DIRS 182558], file *NdStrs-R2.xls*, Sheet "Ksolu_As Welded," Column Y (Cells 10 to 59) and Sheet "AA" (Cells 10 to 59), and Column Q (Cells 10 to 59). Output DTN: MO0705CREEPSCC.000, file *KI_AA_BB.xls*.

Figure 6-31. Comparison of the Through-Wall Hoop (Sz) Stress Intensity Factor Distributions Using ELL in Sections A-A and B-B of the As-Welded Naval Long Waste Package Outer Closure Lid at Normal Condition Temperature

A close examination of the data in Table 6-12 and Figure 6-27 to Figure 6-28 for the as-welded naval long waste package closure lid reveals that, without stress mitigation (Section 6.5.5), the tensile hoop stresses well exceed the SCC stress initiation criteria of 0.9 $YS_{(125°C)}$ (316 MPa or 45.8 ksi) in the near-surface region as well as deeper into the plate. The yield strength of Alloy 22 at 125°C is interpolated from the yield strength values shown in Table 4-7 as 351 MPa (50.9 ksi), as shown in Table 6-4.

6.5.4 Impact of Corrosion on Stress and Stress Intensity Factor Profiles

The numerical results presented in Section 6.5.3 were performed for the as-fabricated condition. Thus, the full thickness for all the waste package components was used. Corrosion of the outer surface of the waste package, leading to removal of a layer of the waste package material, causes a redistribution of the stress. Only the effect of general corrosion (or general thinning) of the waste package on stress and stress intensity factor distribution is considered here. Localized corrosion may or may not have an effect on the redistribution of stress and stress intensity factors. However, if localized corrosion occurs, its rate is much faster than SCC crack growth and will penetrate the waste package wall long before the SCC could penetrate the wall. Therefore, only the effect of general corrosion is considered.

To simulate the effect of wall thinning caused by general corrosion, a layer of elements from the outside surface of the outer lid was removed in the finite-element model for the CRM-21-PWR waste package design (SIA 2003 [DIRS 162457]). The thickness of this layer was 12.7% of the thickness of the outer lid based on a 25-mm thickness. The general corrosion rates of Alloy 22 are very low. Based on the mean general corrosion rate of 7.23 nm/yr (Section 6.4.5), the 0.125-in removal is the amount of material that will corrode in 439,140 years, assuming the corrosion rates are constant rather than decreasing with time.

Effect of Corrosion on Stress Redistribution

In a previous analysis conducted by SIA (SIA 2003 [DIRS 162457]), the effect of corrosion on the redistribution of stress is analyzed based on the CRM-21-PWR waste package design. As the consequence of corrosion to the waste package is to remove a thin layer from the outermost surface of the waste package, the difference in the corrosion effect between the naval long and CRM-21-PWR waste package designs is insignificant.

Figure 6-32a shows the removal of a row of elements (3.18 mm) to simulate the effects of general corrosion of the outer lid surface. Figure 6-32b shows the sections for finite-element analysis for the outer lid with a row removed. Figure 6-33 and Figure 6-34 show, respectively, the through-wall radial stress profiles (with and without corrosion effects) and hoop-stress profiles (with and without corrosion effects) at Section 1-1 shown in Figure 6-32b. These results demonstrate the redistribution of the residual stress due to corrosion (removal of an outermost layer of the metal). In general, for the through-wall radial-stress and hoop-stress profiles, the stress distribution does not appear to be sensitive to the effects of corrosion.

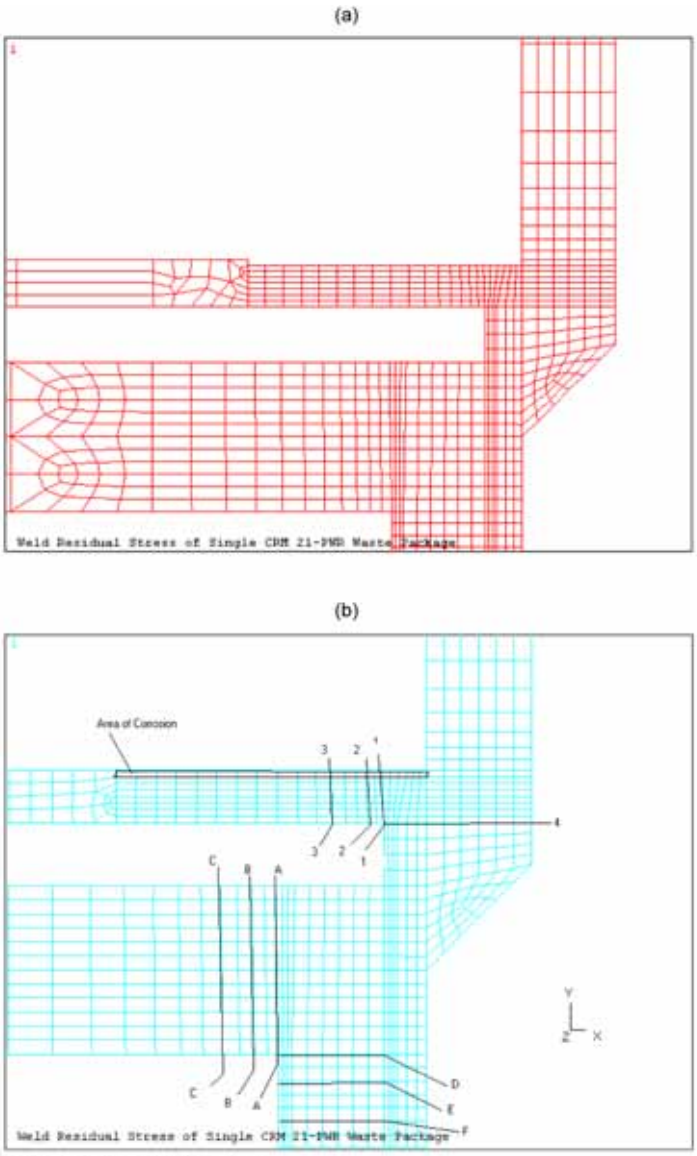

Source: SIA 2003 [DIRS 162457], Figure 4-1.

NOTES: (a) Finite-element model.
(b) Sections for stress profile analysis.

Upper graphic (a) shows the removal of a row of elements (3.18 mm) to simulate the effects of general corrosion of the outer lid surface; lower graphic (b) shows the sections for finite-element analysis for the outer lid with a row removed).

Figure 6-32. Finite-Element Model Used To Evaluate Effect of Corrosion

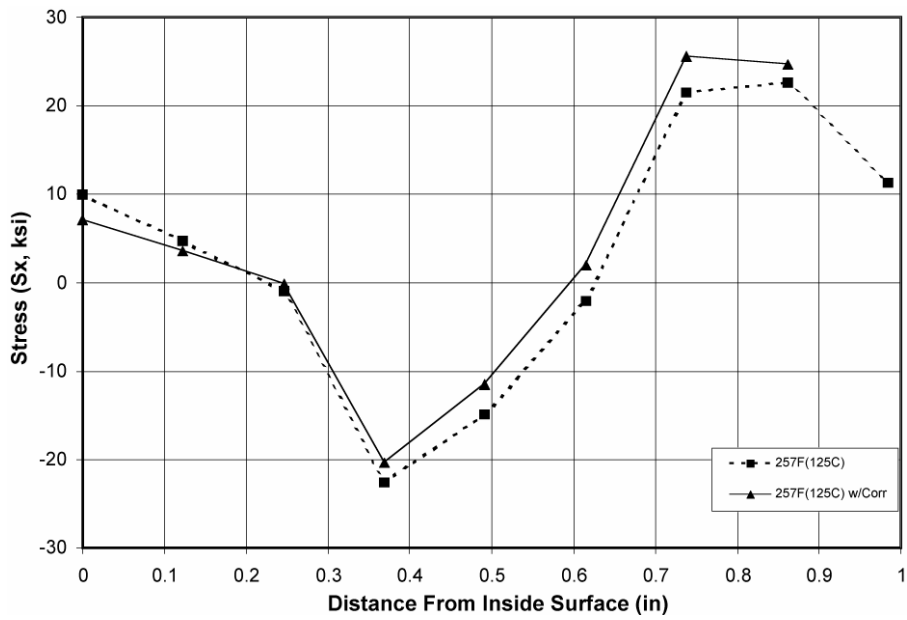

Source: Modified from SIA 2003 [DIRS 162457], Figure 4-2.

Figure 6-33. Effect of Corrosion on Radial Stress in Waste Package Outer Lid

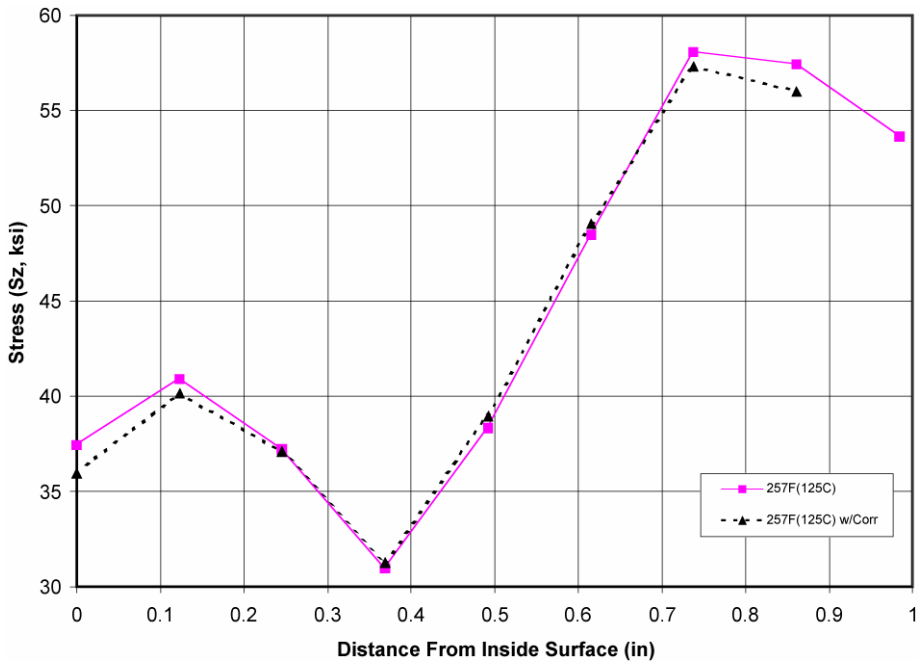

Source: Modified from SIA 2003 [DIRS 162457], Figure 4-4.

Figure 6-34. Effect of Corrosion on Hoop Stress in Waste Package Outer Lid

Effect of Corrosion on Stress Intensity Factor Redistribution

The effect of corrosion on stress intensity factor redistribution was also studied based on the CRM-21-PWR waste package closure design by SIA (2003 [DIRS 162457]). As the stress

intensity factor is a function of stress, the redistribution of stresses will lead to redistribution of stress intensity factors. Figure 6-35 and Figure 6-36 show the stress intensity factor distribution with and without the effects of corrosion for Section 1-1 shown in Figure 6-32 for circumferential and radial cracks as a function of distance from the outside surface and normalized distance from the outside surface. From Figure 6-35 and Figure 6-36, it can be concluded that the overall effect of general corrosion on the distribution of the stress intensity factor is minor.

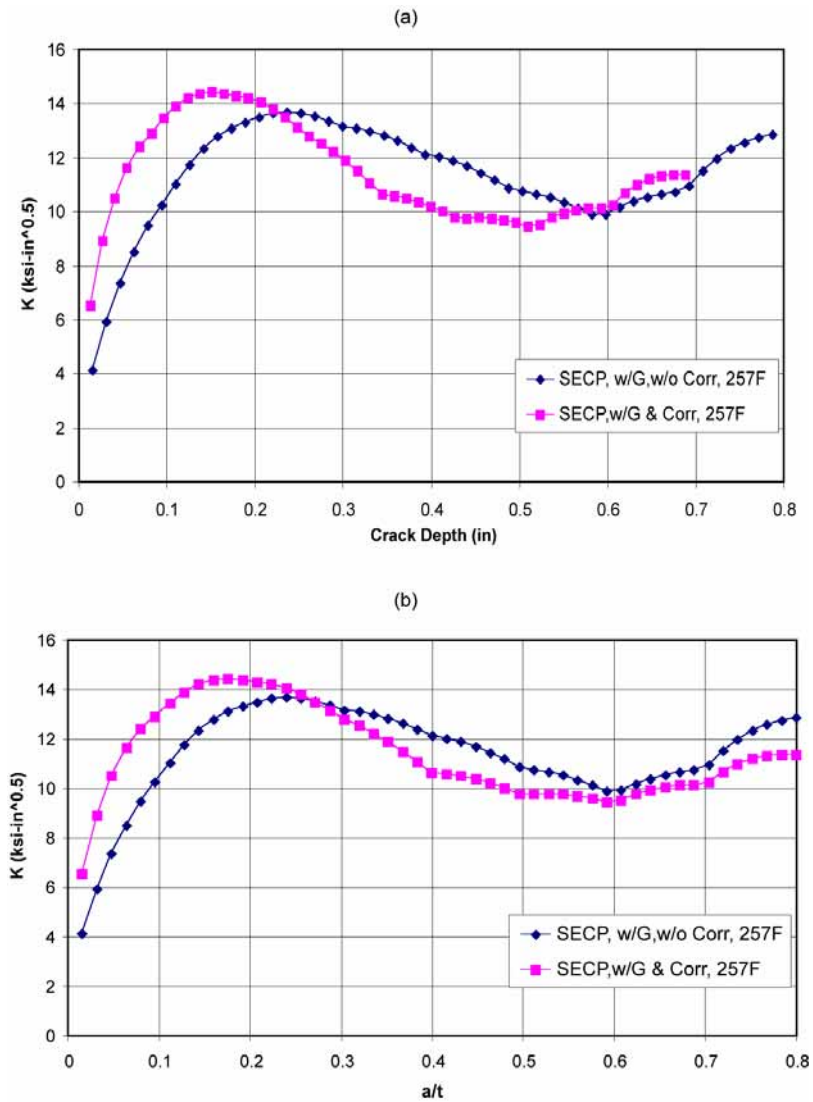

Source: Adapted from SIA 2003 [DIRS 162457], Figure 4-6.

NOTES (a) X-axis is crack depth in inches.
(b) X-axis is shown as the ratio of crack depth (a) versus thickness (t).
(c) "w/G" stands for "with geometric factor (GF).

Figure 6-35. Stress Intensity Factor for Full-Circumference Flaw in the 25-mm Waste Package Outer Lid

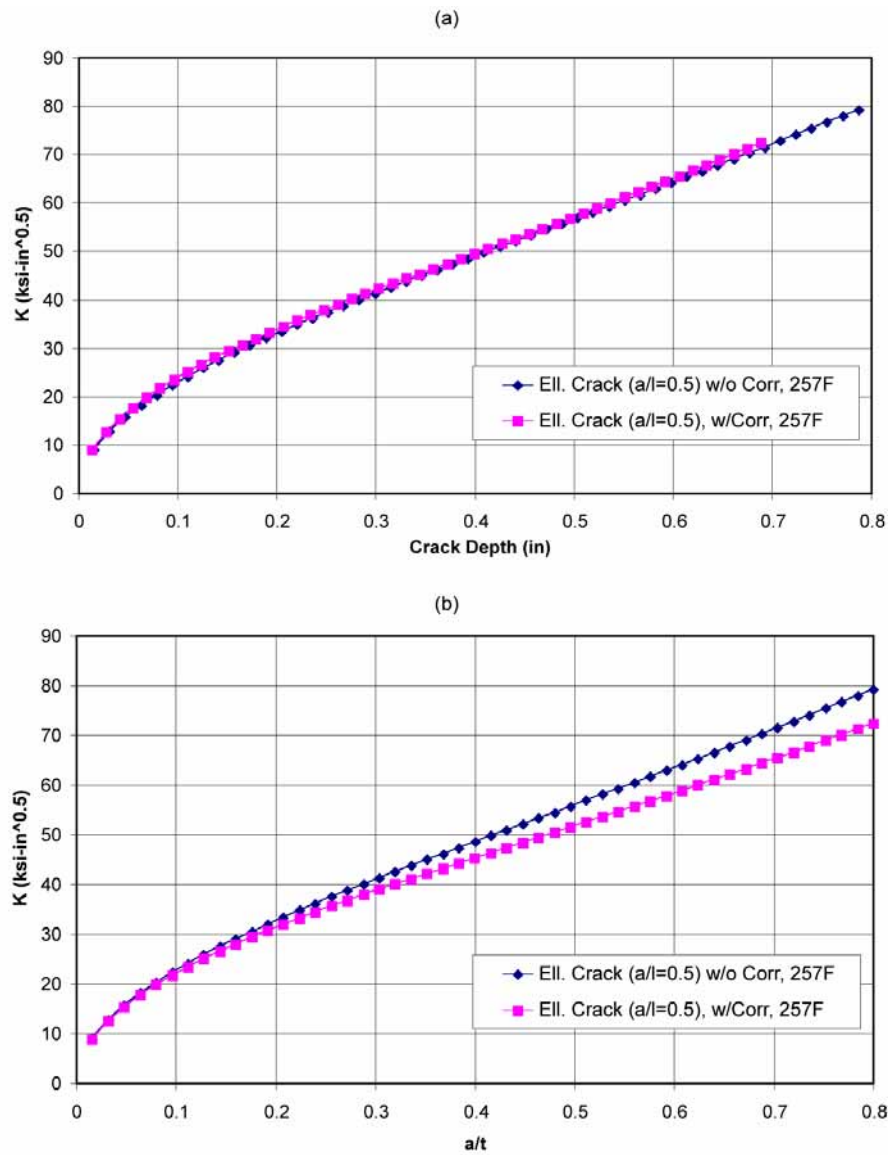

Source: SIA 2003 [DIRS 162457], Figure 4-7.

NOTES: (a) X-axis is crack depth in inches.
(b) X-axis is shown as the ratio of crack depth (a) versus thickness (t).

Figure 6-36. Stress Intensity Factor for Radial Elliptical Crack in the 25-mm Waste Package Outer Lid

6.5.5 Mitigation of Weld Residual Stress

6.5.5.1 Introduction to Laser Peening and Plasticity Burnishing

Stress is one of the three basic factors that cause initiation and propagation of SCC cracks in structural components. The other two factors are metallurgical susceptibility and environmental condition. SCC can be reduced to a manageable state if the weld residual stress in the waste package can be effectively mitigated.

Weld residual stress can be mitigated in several ways. It can be mitigated by optimizing the geometrical configuration of the waste package design. Residual stress can also be mitigated through specially designed weld processes. Processes such as the "narrow-groove" and other low-heat input welding processes, as well as the spray cooling of final weld passes can produce lower magnitude tensile stresses or compressive stresses on the outer surface of the components and thus reduce the detrimental effect of higher residual tensile stresses. Nonthermal stress-mitigation processes, such as laser peening and low-plasticity burnishing, are also effective ways to reduce weld residual stress. A major advantage of implementing a nonthermal stress-mitigation process is it will reduce the performance uncertainty of the waste package due to weld tensile residual stress.

The nonthermal stress-mitigation process, CPB, was selected as the residual stress mitigation method for the final closure welds of the waste package for license application (SNL 2007 [DIRS 179567], Section 4). CPB replaces the previously proposed local induction-annealing process because it eliminates the potential for deterioration of the properties of Alloy 22 due to heat treatment. Both laser peening and CPB are described below.

Laser Peening

The laser-peening treatment, which was previously selected for the 25-mm-thick outer lid of the waste package outer barrier to reduce the weld residual stress, involves using a high-powered laser beam to introduce shock pulses on the material surface. Laser peening is similar to the traditional shot-peening procedure but is better adapted to waste package closure cell remote application. For laser peening, the intense stream of tiny metal or ceramic balls used in the traditional shot peening is replaced by high-energy laser with pulse lengths in the tens of nanoseconds, short enough to generate a rapid, yet energetic shock. This process can produce a uniform layer of highly shocked and compressed material that is extremely resistant to cracks and corrosion.

According to the measured data reported by Hornbach (1999 [DIRS 147757], Figures 18 to 21), laser peening is capable of producing a compressive surface layer of about 60 mils (1.5 mm) with compressive stress in the range of 20 ksi to 60 ksi for a 1-in-thick welded Alloy 22 plate. A typical example is shown in Figure 6-37 (DTN: LL000320005924.145 [DIRS 148482]) for measured stress profiles at the weld centerline before and after laser peening for the 25 mm CRM-21-PWR waste package outer closure lid. In Figure 6-37, the stress component 1, S1, is parallel to the weld centerline, and stress component 3, S3, is perpendicular to the weld centerline. It is evident from Figure 6-37 that compressive stresses on the order of 40 ksi persist to a depth of at least 0.06 in (1.5 mm).

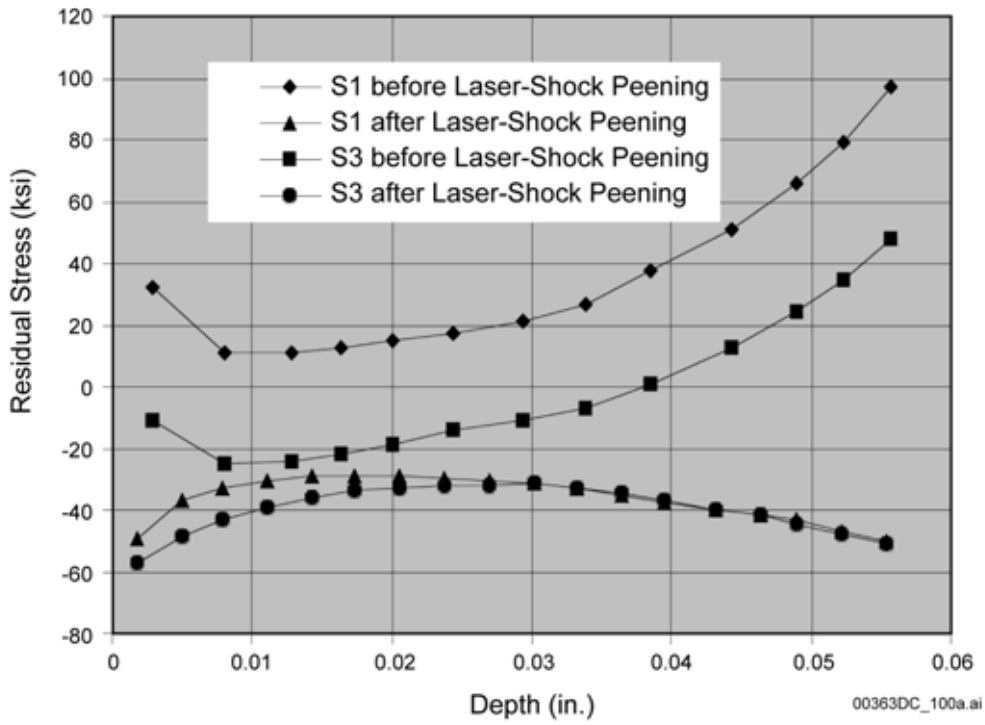

Source: DTN: LL000320005924.145 [DIRS 148482].

Figure 6-37. Mitigation of Weld Stress in Alloy 22 with Laser Peening

In other words, the weld-induced residual stress in the 25-mm outer lid of the CRM–21-PWR design is reduced from tensile stress to 40 ksi compressive stress for a depth of 0.06 in (1.5 mm) at the outside surface as shown in Figure 6-48. In fact, using a depth of compressive stress of 0.06 in (1.5 mm) is conservative. As discussed in Section 6.5.6.5, the measured results from more-recently processed multipass laser-peened 1-in-thick welded Alloy 22 plate (Figure 6-59) and the assessment based on the measured compression depth due to laser peening versus the plate thickness (Chen et al. 2002 [DIRS 165441], Figure 20) both indicate that a compressive stress depth significantly greater than 0.06 in (1.5 mm) is readily obtainable for a 25-mm-thick Alloy 22 weldment.

Controlled Plasticity Burnishing

The current design specifies that the stress mitigation of the outer lid closure weld will be implemented using CPB, which imparts a layer of compressive residual stress to a minimum depth of 1.9 mm (0.0748 in) (BSC 2004 [DIRS 171499]). This process is considered a mitigating process to be applied such that the tensile stress is limited to 90% of yield strength to a minimum depth of 4.6 mm (0.1811 in) (BSC 2004 [DIRS 171499]). As described in *Waste*

Package Closure System Description Document (BSC 2004 [DIRS 171499]), the performance acceptance criterion is:

> Tensile stress from welding in the area near the intersection of the outer lid and outer barrier shall be mitigated by imparting a layer of compressive residual stress to a minimum depth of 1.9 mm (0.0748 in) and limiting tensile stress to 90 percent of yield strength to a minimum depth of 4.6 mm (0.1811 in).

According to the results of CPB in *Controlled Plasticity Burnishing (CPB) for Developing a Very Deep Layer of Compressive Residual Stresses in Rectangular Specimens of Alloy 22 for Yucca Mountain Nuclear Waste Package Closure Weld* (Woolf 2003 [DIRS 178059]) the through-wall stress profile at the closure weld can readily meet the performance acceptance criterion. The approach adopted for representing the laser-peening stress distribution in an earlier version of this document (BSC 2004 [DIRS 172203]) involved adjusting the outer and near-outer surface stress of the original through-wall residual stress profile to a chosen compressive stress (−40 ksi) to a depth of 1.5 mm (0.06 in) without considering the self-equilibrium condition of the residual stress. This approach is also considered acceptable for CPB, as the general impact on the through-wall stress distribution is small compared to the initial as-welded distribution. The CPB stress mitigation process is described in a report by Woolf (2003 [DIRS 178059]).

The effect of stress mitigation by plasticity-burnishing treatment and, for comparison, by the previously adopted laser-peening process (BSC 2004 [DIRS 172203]), on the distributions of outer closure lid weld stress and stress intensity factor for the naval long waste package design is evaluated in this section.

6.5.5.2 Redistribution of Stress and Stress Intensity Factor Due to Laser Peening and Plasticity Burnishing

Although the current license application waste package design utilizes plasticity burnishing as the closure weld stress mitigation process, for comparison purpose, the results for laser peening are also presented here.

6.5.5.2.1 Redistribution of Stress Due to Laser Peening

The through-wall stress distributions in sections A-A and B-B of the laser-peened naval long waste package outer closure lid at normal condition temperature are shown in Figure 6-38 and Figure 6-39, respectively. The stresses are presented as the distance from the outer lid outside surface for S_x (radial stress) and S_z (hoop stress). The directions of x, y, and z used in the finite element model are shown in Figure 6-12.

The values of the stress coefficients in Equation 22 for the laser-peened closure-lid welds of naval long waste package designs are obtained by regressing the stress data to a third-order polynomial (Equation 22). These coefficients are listed in the fifth to eighth rows of Table 4-3 as direct input with the radial stress (S_x) and hoop stress (S_z) in ksi and distance (x) in inches. Table 6-13 shows the converted stress coefficients, A_0, A_1, A_2, and A_3, in the metric unit system by using the conversion factors in Table 6-10.

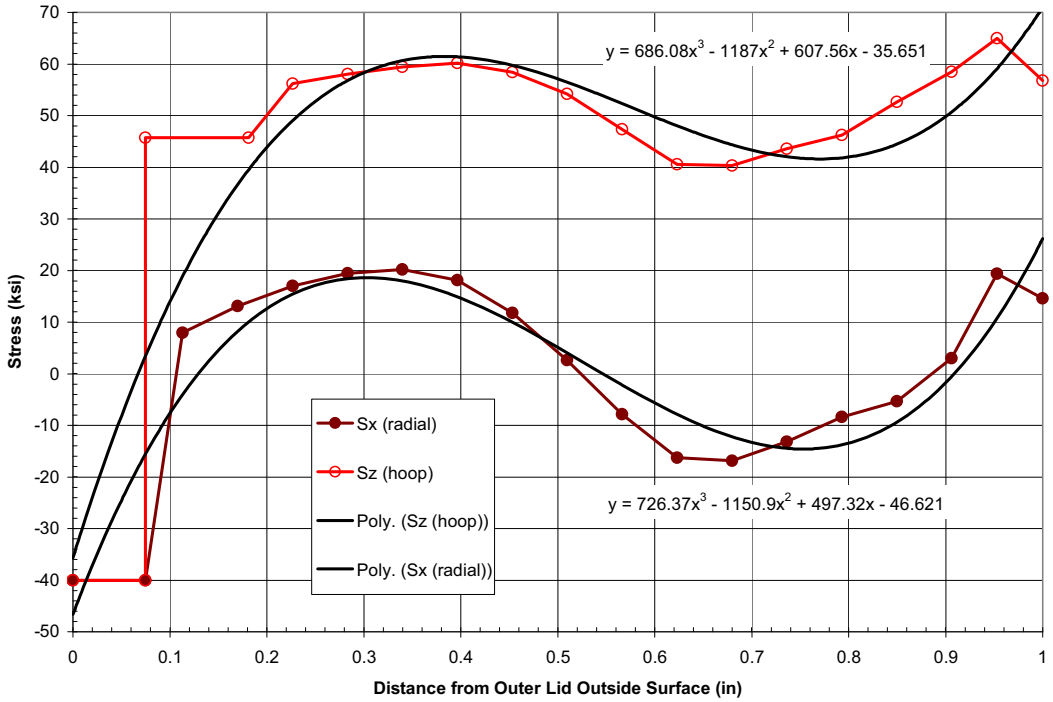

Source: DTN: MO0708RTSWRS06.000 [DIRS 182558], file *NdStrs-R2.xls*, Sheet "A-AThrWLPStrsPlt."

Figure 6-38. Curve-Fitted Through-Wall Stress Profile, Section A-A, Normal Condition Temperature with Laser Peening

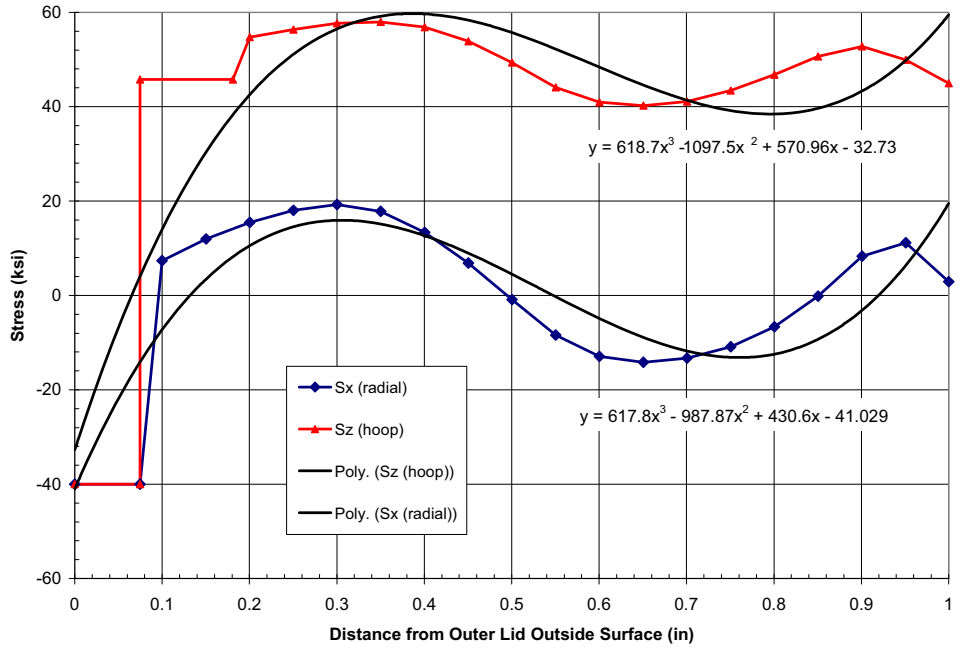

Source: DTN: MO0708RTSWRS06.000 [DIRS 182558], file *NdStrs-R2.xls*, Sheet "B-BLPStrsPlt."

Figure 6-39. Curve-Fitted Through-Wall Stress Profile, Section B-B, Normal Condition Temperature with Laser Peening

Table 6-13. Stress Coefficients for the Laser-Peened Naval Long Waste Package Outer Lid

Stress Coefficient	From Fifth to Eighth Rows of Table 4-3					Conversion Factors					
	Unit	Section A-A		Section B-B			Unit	Section A-A		Section B-B	
		Radial Stress	Hoop Stress	Radial Stress	Hoop Stress			Radial Stress	Hoop Stress	Radial Stress	Hoop Stress
A_0	ksi	−46.621	−35.651	−41.029	−32.73	1 ksi = 6.894757 MPa *	MPa	−321.440	−245.805	−282.885	−225.665
A_1	ksi/in	497.32	607.56	430.6	570.96	1 ksi/in = 0.271447 MPa/mm	MPa/mm	134.996	164.920	116.885	154.985
A_2	ksi/in^2	−1150.9	−1187	−987.87	−1097.5	1 ksi/in^2 = 0.010687 MPa/mm^2	MPa/mm^2	−12.300	−12.685	−10.557	−11.729
A_3	ksi/in^3	726.37	686.08	617.8	618.7	1 ksi/in^3 = 0.000421 MPa/mm^3	MPa/mm^3	0.306	0.289	0.260	0.260

Source: The data in third, fourth, fifth, and sixth columns of this table are from the fifth, sixth, seventh, and eighth rows o f Table 4-3 with English units. The last four columns of this table are converted to metric units by using the conversion factors shown in the middle column.
* (Boyer and Gall 1997 [DIRS 155318], p. 1-57)

6.5.5.2.2 Redistribution of Stress Due to Plasticity Burnishing

The through-wall stress distributions in sections A-A and B-B of the plasticity-burnished naval long waste package outer closure lid at normal condition temperature are shown in Figure 6-40 and Figure 6-41, respectively. The stresses are presented as the distance from the outer lid outside surface for S_x (radial stress) and S_z (hoop stress). The directions of x, y, and z used in the finite element model are shown in Figure 6-12.

The values of the stress coefficients in Equation 22 for the laser-peened closure-lid welds of naval long waste package designs are obtained by regressing the stress data to a third-order polynomial (Equation 22). These coefficients are listed in the last four rows of Table 4-3 as direct input with the radial stress (S_x) and hoop stress (S_z) in ksi and distance (x) in inches. Table 6-14 shows the converted stress coefficients, A_0, A_1, A_2, and A_3, in the metric unit system by using the conversion factors in Table 6-10.

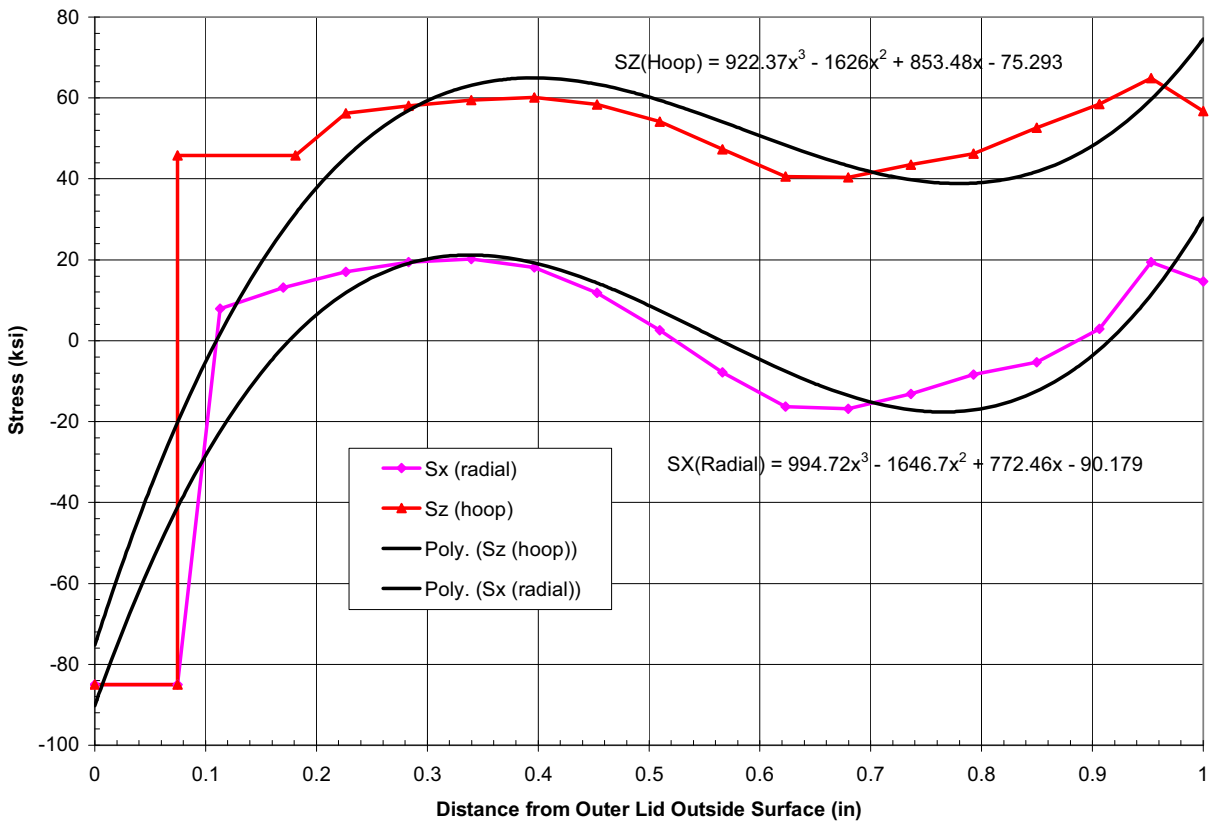

Source: DTN: MO0708RTSWRS06.000 [DIRS 182558], file *NdStrs-R2.xls*, Sheet "A-ACPBPlt."

Figure 6-40. Curve-Fitted Through-Wall Stress Profile, Section A-A, Normal Condition Temperature with Plasticity Burnishing

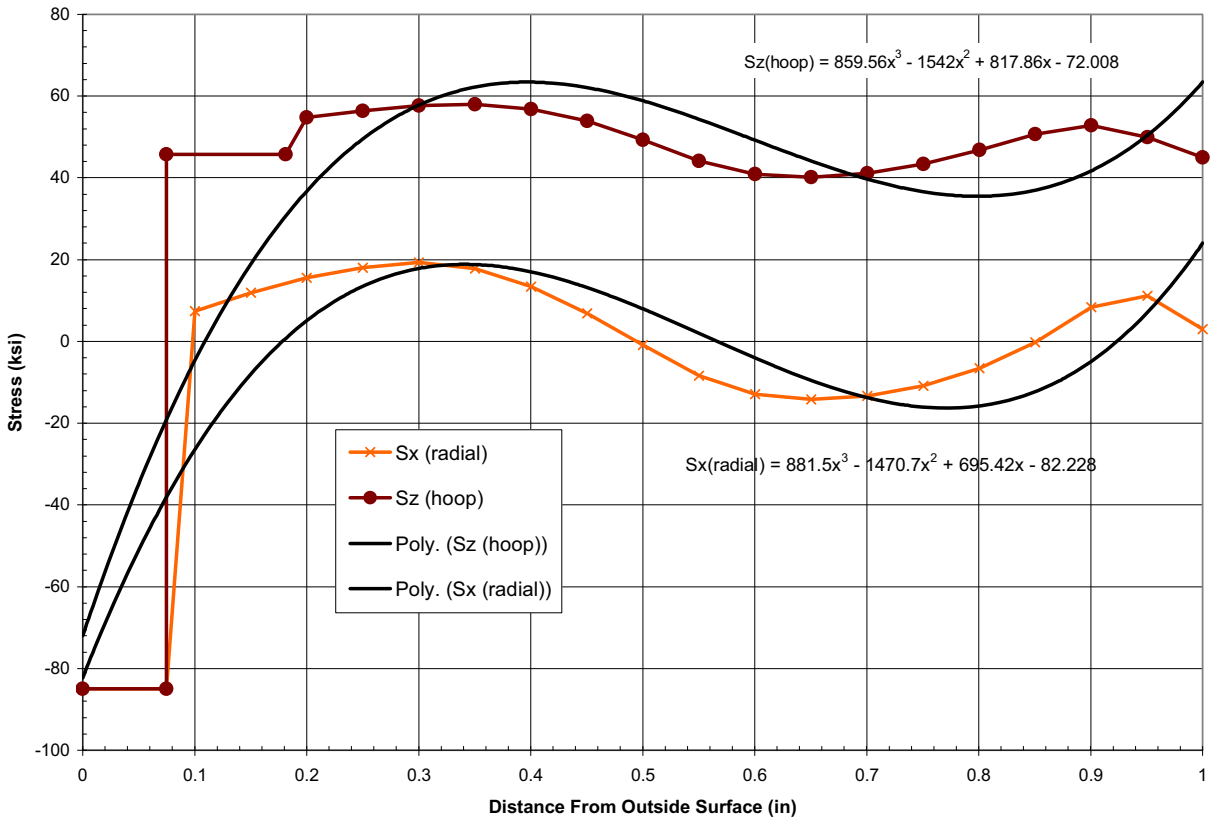

Source: DTN: MO0708RTSWRS06.000 [DIRS 182558], file *NdStrs-R2.xls*, Sheet "B-BCPB."

Figure 6-41. Curve-Fitted Through-Wall Stress Profile, Section B-B, Normal Condition Temperature with Plasticity Burnishing

Table 6-14. Stress Coefficients for the Plasticity-Burnished Naval Long Waste Package Outer Lid

Stress Coefficient	From Last Four Rows of Table 4-3					Conversion Factors					
	Unit	Section A-A		Section B-B			Unit	Section A-A		Section B-B	
		Radial Stress	Hoop Stress	Radial Stress	Hoop Stress			Radial Stress	Hoop Stress	Radial Stress	Hoop Stress
A_0	ksi	−90.179	−75.293	−82.228	−72.008	1 ksi = 6.894757 MPa *	MPa	−621.762	−519.127	−566.942	−496.478
A_1	ksi/in	772.46	853.48	695.42	817.86	1 ksi/in = 0.271447 MPa/mm	MPa/mm	209.682	231.675	188.770	222.006
A_2	ksi/in^2	−1646.7	−1626	−1470.7	−1542	1 ksi/in^2 = 0.010687 MPa/mm^2	MPa/mm^2	−17.598	−17.377	−15.717	−16.479
A_3	ksi/in^3	994.72	922.37	881.5	859.56	1 ksi/in^3 = 0.000421 MPa/mm^3	MPa/mm^3	0.419	0.388	0.371	0.362

Source: The data in third, fourth, fifth and sixth columns are from last four rows of Table 4-3 with English units. The last f our columns of this table are converted to metric units by using the conversion factors shown in the middle column.
* (Boyer and Gall 1997 [DIRS 155318], p. 1-57)

6.5.5.2.3 Redistribution of Stress Intensity Factor Due to Laser Peening

Figure 6-42 and Figure 6-43 show the calculated stress intensity factor profiles for the laser-peened naval long waste package outer lid along the directions of A-A and B-B, respectively (DTN: MO0708RTSWRS06.000 [DIRS 182558], file *NdStrs-R2.xls*, sheets "A-ALPKPlt_new" and "B-BLPKPlt_new"). The numerical presentation of the stress intensity factor profiles is shown in Table 6-15 for section A-A with the radial stress and radial stress intensity factor using the SECP crack geometry and the hoop stress and hoop stress intensity factor using the elliptical crack geometry. As indicated in Section 6.5.3.3.3, for a circumferential flaw, $(K_I)_{PCCRACK}$ was derived from an infinite SECP with an infinitely long flaw, and, for a radial flaw, $(K_I)_{PCCRACK}$ was derived from an elliptical surface crack in an infinite plate. Therefore, while all data are shown in Figure 6-42 and Figure 6-43 (i.e., A-A and B-B, SECP and ELL, and radial and hoop), Table 6-15 only lists the data in section A-A that will be used for further analysis such as uncertainty and variability analysis in Section 6.5.6. The stress intensity factor distributions along A-A and B-B sections are virtually identical as shown in Figure 6-44.

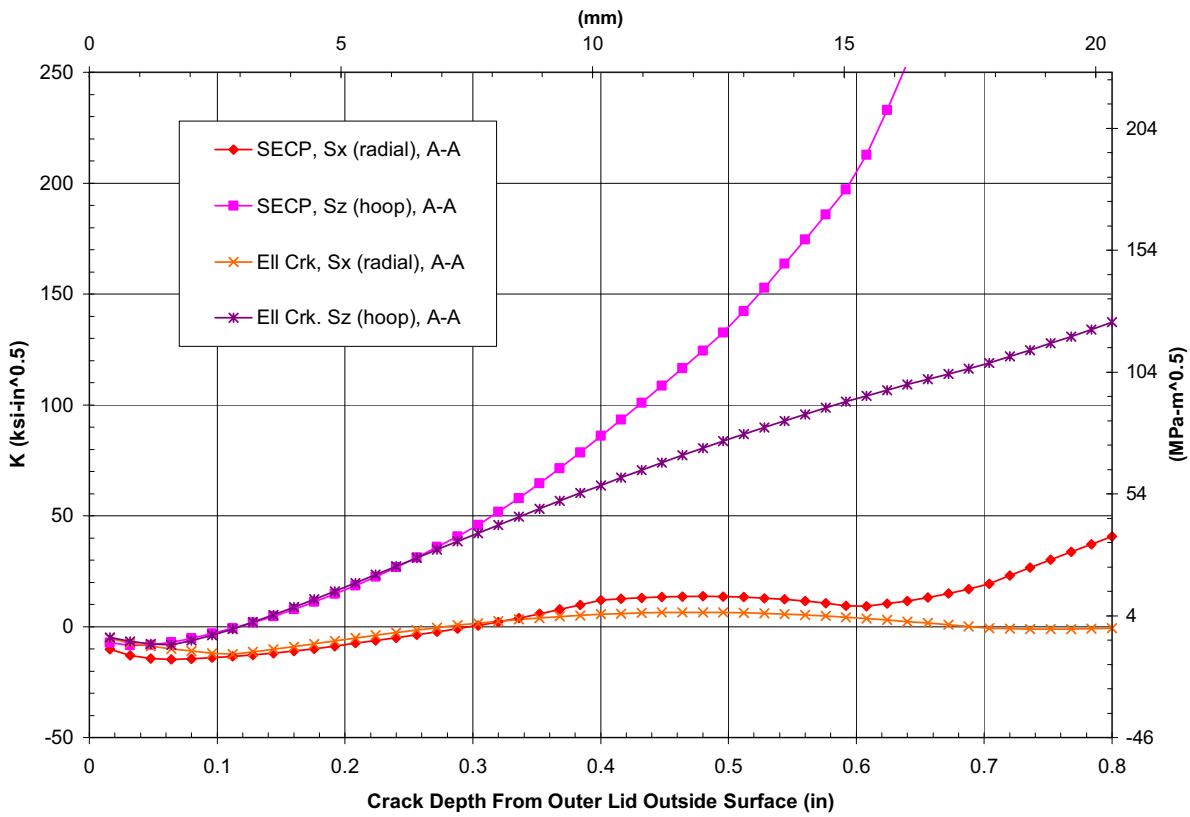

Source: DTN: MO0708RTSWRS06.000 [DIRS 182558], file *NdStrs-R2.xls*, Sheet "A-ALPKPlt_new."

Figure 6-42. Stress Intensity Factor Distribution in Section A-A, Normal Condition Temperature, Laser-Peened

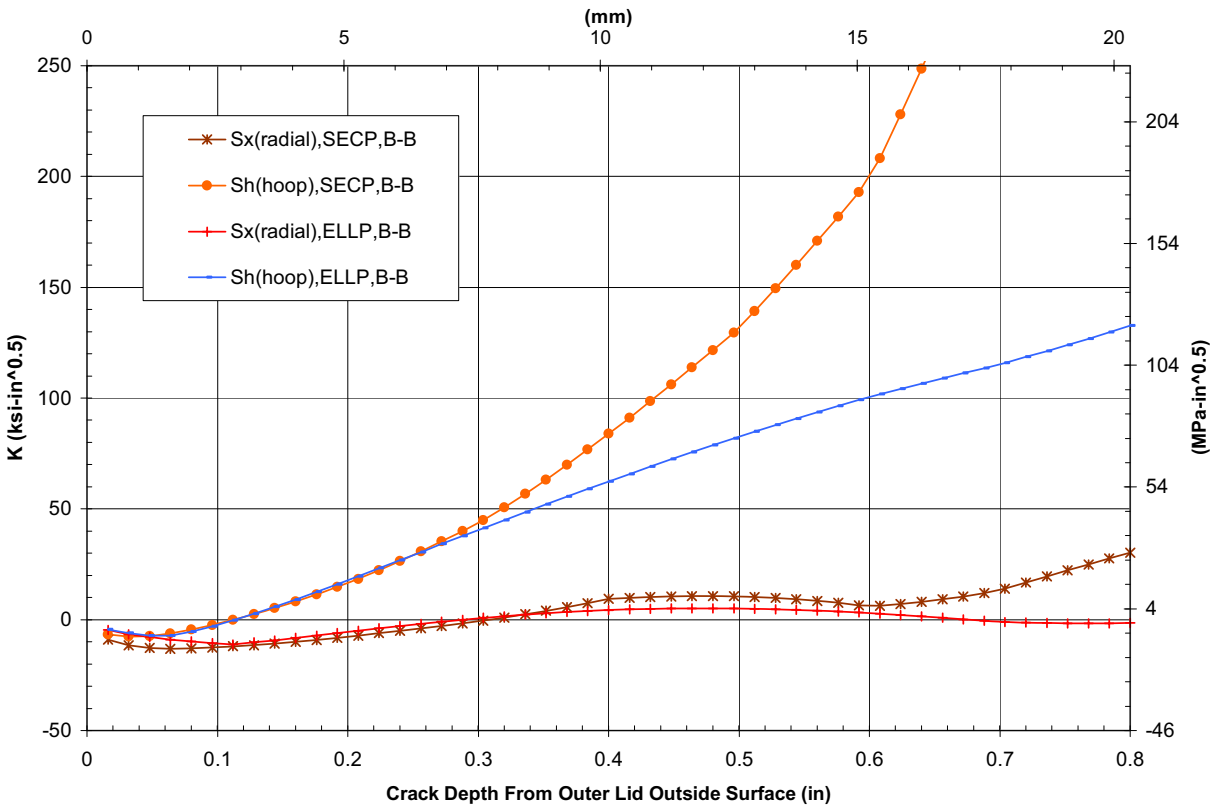

Source: DTN: MO0708RTSWRS06.000 [DIRS 182558], file *NdStrs-R2.xls*, Sheet "B-BLPKPlt_new."

Figure 6-43. Stress Intensity Factor Distribution in Section B-B, Normal Condition Temperature, Laser-Peened

The radial stress intensity factor is compressive up to about 30% (0.3 in or 7.6 mm) of the wall thickness for the circumferential crack (driven by radial stress, S_x), regardless of the crack geometry used. This is due to the combination of significant surface compressive stress and a lower through-wall radial stress. With a radial crack in the weld (i.e., a crack perpendicular to the direction of the closure weld, driven by hoop stress S_z), the compressive hoop stress intensity extends to a depth of about 0.1 in (2.54 mm). Both crack geometries have similar results up to about 0.3 in (7.6 mm) of the wall thickness. Beyond 30% of the thickness, the single-edge crack plate model predicts a higher stress intensity factor because of the conservatism in the model (i.e., the crack is as long as the diameter of the outer lid).

The stress intensity factor results for section B-B are presented in Figure 6-43. The distributions are very similar to those for section A-A. It shows a slightly more compressive stress intensity factor for a circumferential crack using the SECP model (curve Sx(radial) in Figure 6-43).

Table 6-15. Stress and Stress Intensity Factor Profiles for the Laser-Peened Naval Long Waste Package Outer Lid

Distance from Outer Surface (mm)	SECP (Radial Stress)		ELL (Hoop Stress)	
	Sx (MPa)	K-Sx (MPa√m)	Sz (MPa)	K-Sz (MPa√m)
0.4064	−268.5886	−11.2007	−180.8572	−4.4149
0.8128	−219.6769	−14.2933	−119.9831	−6.0412
1.2192	−174.5816	−15.7016	−63.0664	−7.1517
1.6256	−133.1797	−16.1516	−9.9906	−7.4927
2.0320	−95.3477	−15.9606	39.3605	−5.6960
2.4384	−60.9626	−15.3119	85.1035	−3.4512
2.8448	−29.9010	−14.7222	127.3547	−0.9200
3.2512	−2.0397	−14.0206	166.2305	1.8571
3.6576	22.7445	−13.1241	201.8472	4.8365
4.0640	44.5749	−12.0680	234.3213	7.9693
4.4704	63.5747	−10.8798	263.7691	11.2155
4.8768	79.8671	−9.5806	290.3071	14.5414
5.2832	93.5753	−8.2572	314.0517	17.9097
5.6896	104.8226	−6.9171	335.1191	21.3088
6.0960	113.7323	−5.5081	353.6258	24.7318
6.5024	120.4275	−4.0501	369.6883	28.1613
6.9088	125.0316	−2.5622	383.4228	31.5821
7.3152	127.6676	−1.0629	394.9458	34.9809
7.7216	128.4590	0.4953	404.3737	38.3599
8.1280	127.5288	2.3223	411.8228	41.7465
8.5344	125.0004	4.2697	417.4095	45.0972
8.9408	120.9969	6.3293	421.2503	48.4048
9.3472	115.6417	8.4932	423.4614	51.6630
9.7536	109.0579	10.7538	424.1594	54.8667
10.1600	101.3687	13.1039	423.4606	58.0115
10.5664	92.6975	13.7515	421.4814	61.1760
10.9728	83.1675	14.2954	418.3381	64.2839
11.3792	72.9018	14.7097	414.1472	67.3333
11.7856	62.0237	14.9688	409.0250	70.3229
12.1920	50.6565	15.0477	403.0879	73.2522
12.5984	38.9234	14.9221	396.4524	76.1216
13.0048	26.9476	14.6054	389.2348	78.9566
13.4112	14.8524	14.1379	381.5515	81.7403
13.8176	2.7609	13.4958	373.5189	84.4664
14.2240	−9.2035	12.6556	365.2533	87.1381
14.6304	−20.9176	11.5957	356.8713	89.7593
15.0368	−32.2583	10.2965	348.4890	92.3343
15.4432	−43.1022	10.0934	340.2230	94.7842
15.8496	−53.3262	11.3370	332.1897	97.0997
16.2560	−62.8069	12.7956	324.5054	99.3667

Table 6-15 Stress and Stress Intensity Factor Profiles for the Laser-Peened Naval Long Waste Package Outer Lid (Continued)

Distance from Outer Surface (mm)	SECP (Radial Stress)		ELL (Hoop Stress)	
	Sx (MPa)	K−Sx (MPa√m)	Sz (MPa)	K−Sz (MPa√m)
16.6624	−71.4213	14.4752	317.2864	101.5929
17.0688	−79.0459	16.3858	310.6493	103.7866
17.4752	−85.5576	18.5424	304.7103	105.9568
17.8816	−90.8332	21.3185	299.5860	108.2263
18.2880	−94.7495	25.2713	295.3926	110.8524
18.6944	−97.1831	29.2202	292.2465	113.5226
19.1008	−98.0108	33.1436	290.2642	116.2510
19.5072	−97.1095	37.0294	289.5620	119.0541
19.9136	−94.3559	40.8767	290.2563	121.9496
20.3200	−89.6267	44.6951	292.4635	124.9527

Source: The data in the first, third, and fifth columns are from DTN: MO0708RTSWRS06.000 [DIRS 182558], file *NdStrs-R2.xls*, Sheet "Ksolu_Peening." The data in second and fourth columns are calculated according to Equation 22 and the stress coefficients in Table 6-13.

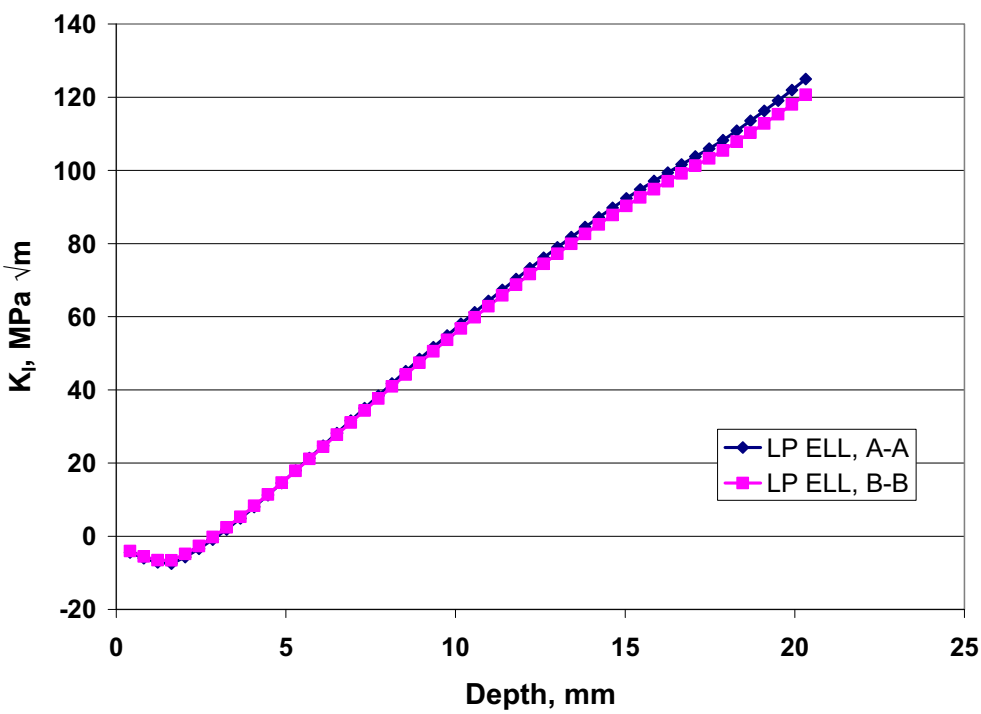

Source: DTN: MO0708RTSWRS06.000 [DIRS 182558], file *NdStrs-R2.xls*, Sheet "Ksolu_Peening," Column X (Cells 10 to 59) and Column Z (Cells 10 to 59) versus Column P (Cells 10 to 59). Output DTN: MO0705CREEPSCC.000, file *KI_AA_BB.xls*.

Figure 6-44. Comparison of the Through-Wall Hoop Stress Intensity Factor Distributions Using Elliptical Crack Geometry in Sections A-A and B-B of the Laser-Peened Naval Long Waste Package Outer Closure Lid at Normal Condition Temperature

6.5.5.2.4 Redistribution of Stress Intensity Factor Due to Plasticity Burnishing

Figure 6-45 and Figure 6-46 show the calculated stress intensity factor profiles for the plasticity-burnished naval long waste package outer lid along the directions of A-A and B-B, respectively. The numerical presentation of the stress intensity factor profiles are shown in Table 6-16 for section A-A with the radial stress and radial stress intensity factor using the SECP crack geometry and the hoop stress and hoop stress intensity factor using elliptical crack geometry. As indicated in Section 6.5.3.3.3, for a circumferential flaw, $(K_I)_{PCCRACK}$ was derived from an infinite SECP with an infinitely long flaw, and, for a radial flaw, $(K_I)_{PCCRACK}$ was derived from an elliptical surface crack in an infinite plate. Therefore, while all data are shown in Figure 6-45 and Figure 6-46 (i.e., A-A and B-B, SECP and ELL, and radial and hoop), Table 6-16 only lists the data in section A-A that will be used for further analysis such as uncertainty and variability analysis in Section 6.5.6. The stress intensity factor distribution along A-A and B-B sections are virtually identical, as shown in Figure 6-47. Therefore, the following discussions use only the section A-A data.

The stress intensity factor results for section A-A are presented in Figure 6-45 for CPB. The stress intensity factor is compressive through the outer lid thickness for the circumferential crack (driven by radial stress, S_x), regardless of the crack geometry used. This is due to the combination of significant surface compressive stress and a lower through-wall radial stress. With a radial crack in the weld (i.e., a crack perpendicular to the direction of the closure weld, subjected to hoop stress, S_z), the compressive stress intensity extends to a depth of at least about 0.2 in (5.08 mm). Both crack models have similar results up to about 30% of the wall thickness. Beyond 30% of the wall thickness, the SECP model predicts a higher stress intensity factor because of the conservatism in the model (i.e., the crack is as long as the diameter of the outer lid).

The stress intensity factor results for section B-B are presented in Figure 6-46 for CPB. The distributions are very similar to those for section A-A. The figure shows a more compressive stress intensity factor for a circumferential crack using the SECP model (curve S_x(radial) in Figure 6-46) due to CPB.

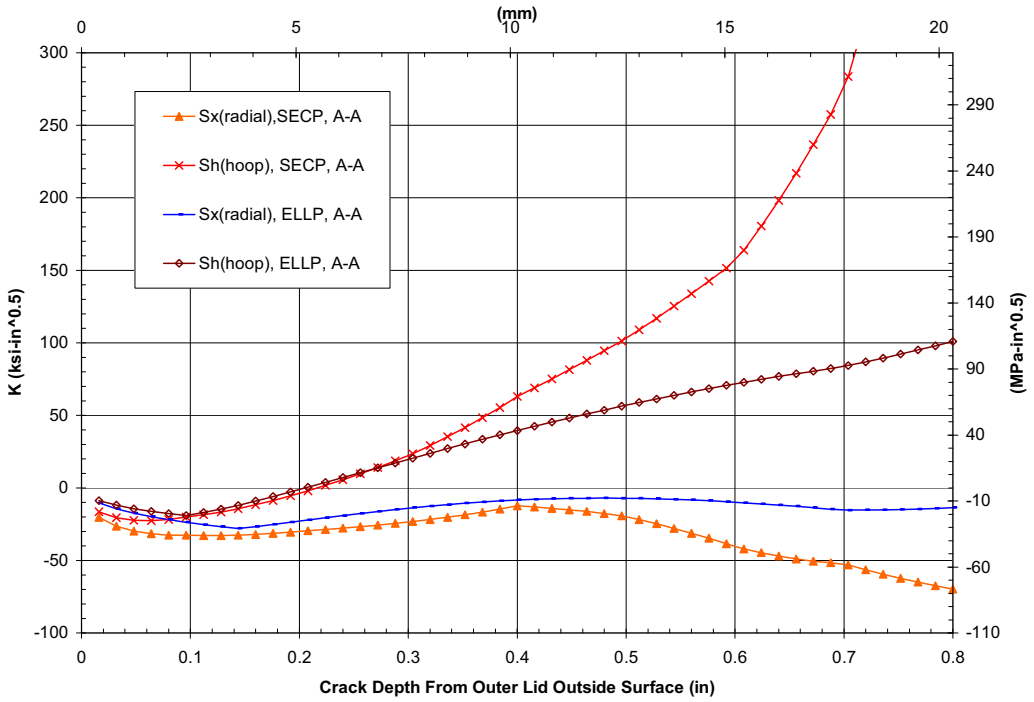

Source: DTN: MO0708RTSWRS06.000 [DIRS 182558], file *NdStrs-R2.xls*, Sheet "A-AKCPBPlt_new."

Figure 6-45. Stress Intensity Factor Distribution in Section A-A, Normal Condition Temperature, Plasticity-Burnished

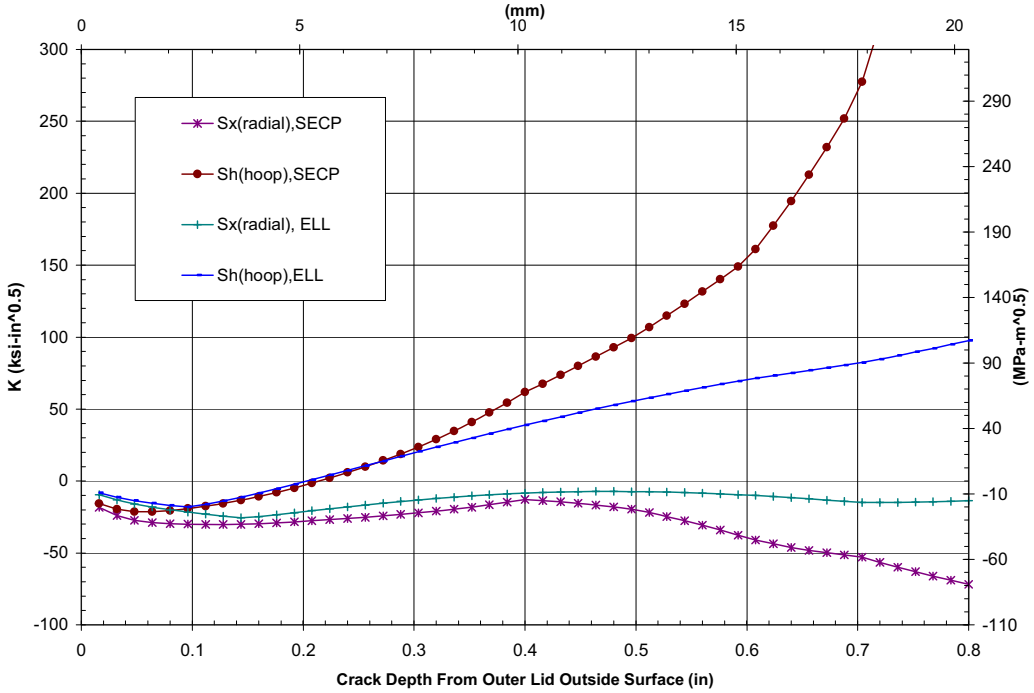

Source: DTN: MO0708RTSWRS06.000 [DIRS 182558], file *NdStrs-R2.xls*, Sheet "B-BCPBKPlt_new."

Figure 6-46. Stress Intensity Factor Distribution in Section B-B, Normal Condition Temperature, Plasticity-Burnished

Table 6-16. Stress and Stress Intensity Factor Profiles for the Plasticity-Burnished Naval Long Waste Package Outer Lid

Distance from Outer Surface (mm)	SECP (Radial Stress)		ELL (Hoop Stress)	
	Sx (MPa)	K-Sx (MPa√m)	Sx (MPa)	K-Sz (MPa√m)
0.4064	−539.4256	−17.9483	−427.8182	−9.4403
0.8128	−462.7335	−22.6622	−342.0932	−13.0870
1.2192	−391.5169	−24.5417	−261.7957	−15.7063
1.6256	−325.6071	−24.7639	−186.7694	−17.7655
2.0320	−264.8353	−23.8426	−116.8581	−19.4500
2.4384	−209.0327	−22.0731	−51.9054	−20.8568
2.8448	−158.0308	−20.2774	8.2447	−18.7051
3.2512	−111.6606	−18.1813	63.7487	−16.1168
3.6576	−69.7535	−15.6533	114.7627	−13.1794
4.0640	−32.1407	−12.7494	161.4431	−9.9714
4.4704	1.3465	−9.5133	203.9461	−6.5568
4.8768	30.8769	−5.9794	242.4278	−2.9886
5.2832	56.6192	−2.2008	277.0447	0.6173
5.6896	78.7421	1.8491	307.9530	4.2344
6.0960	97.4145	6.1848	335.3088	7.9070
6.5024	112.8050	10.7787	359.2686	11.6084
6.9088	125.0823	15.6038	379.9885	15.3153
7.3152	134.4154	20.6344	397.6247	19.0077
7.7216	140.9727	26.0005	412.3336	22.6634
8.1280	144.9232	32.1659	424.2715	26.2705
8.5344	146.4356	38.7572	433.5945	29.8352
8.9408	145.6786	45.7646	440.4589	33.3463
9.3472	142.8209	53.1787	445.0210	36.7941
9.7536	138.0313	60.9899	447.4371	40.1706
10.1600	131.4785	69.1883	447.8633	43.4690
10.5664	123.3313	75.7990	446.4560	46.7415
10.9728	113.7585	82.6202	443.3715	49.9358
11.3792	102.9286	89.6163	438.7659	53.0484
11.7856	91.0106	96.7504	432.7956	56.0768
12.1920	78.1732	103.9864	425.6167	59.0194
12.5984	64.5850	111.2875	417.3856	61.8761
13.0048	50.4149	119.6266	408.2586	64.7048
13.4112	35.8315	128.5514	398.3918	67.4665
13.8176	21.0037	137.7290	387.9415	70.1443
14.2240	6.1001	147.1219	377.0640	72.7415
14.6304	−8.7104	156.6950	365.9156	75.2627
15.0368	−23.2592	166.4143	354.6525	77.7130
15.4432	−37.3775	180.0773	343.4309	80.0499
15.8496	−50.8966	198.4291	332.4072	82.2619
16.2560	−63.6477	217.8863	321.7376	84.3998
16.6624	−75.4621	238.4456	311.5782	86.4731

Table 6-16. Stress and Stress Intensity Factor Profiles for the Plasticity-Burnished Naval Long Waste Package Outer Lid (Continued)

Distance from Outer Surface (mm)	SECP (Radial Stress)		ELL (Hoop Stress)	
	Sx (MPa)	K−Sx (MPa√m)	Sx (MPa)	K−Sz (MPa√m)
17.0688	−86.1710	260.1082	302.0855	88.4922
17.4752	−95.6056	282.8795	293.4157	90.4686
17.8816	−103.5974	311.7154	285.7250	92.6432
18.2880	−109.9774	357.0449	279.1696	95.5196
18.6944	−114.5770	404.2907	273.9059	98.4483
19.1008	−117.2274	453.3914	270.0901	101.4484
19.5072	−117.7599	504.2920	267.8784	104.5400
19.9136	−116.0057	556.9519	267.4272	107.7446
20.3200	−111.7961	611.3402	268.8926	111.0842

Source: The data in the first, third, and fifth columns are from DTN: MO0708RTSWRS06.000 [DIRS 182558], file *NdStrs-R2.xls*, Sheet "Ksolu_CPB." The data in the second and fourth columns are calculated according to Equation 22 and the stress coefficients in Table 6-14.

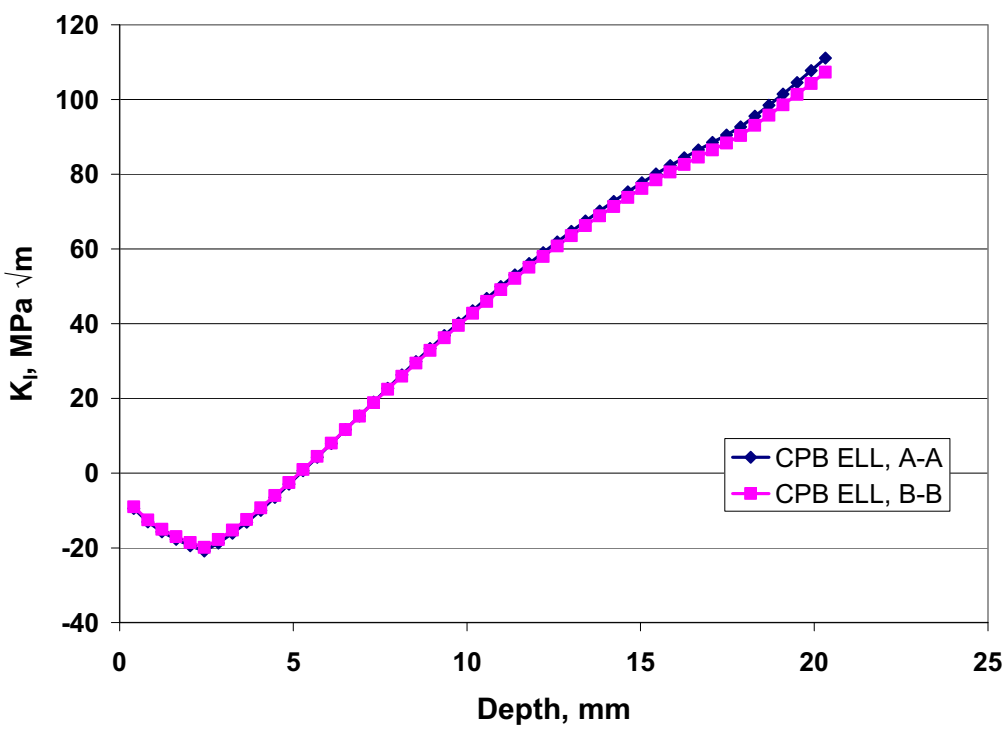

Source: DTN: MO0708RTSWRS06.000 [DIRS 182558], file *NdStrs-R2.xls*, Sheet "Ksolu_CPB," Columns X (Cells 10 to 59) and Z (Cells 10 to 59), and Column p (Cells 10 to 59). Ouput DTN: MO0705CREEPSCC.000, file *KI_AA_BB.xls*.

Figure 6-47. Comparison of the Through-Wall Hoop Stress Intensity Factor Distributions Using Elliptical Crack Geometry in Sections A-A and B-B of the Plasticity-Burnished Naval Long Waste Package Outer Closure Lid at Normal Condition Temperature

6.5.5.2.5 Beneficial Effect of Stress Mitigation

The comparison between the stress distributions for the as-welded and plasticity-burnished naval long waste package closure lid is presented in Figure 6-48. The comparison between the stress intensity factors for the as-welded and plasticity-burnished naval long waste package closure lid is presented in Figure 6-49. In Figure 6-48 and Figure 6-49, the (a) figures present the radial stress and the (b) figures present the hoop stress.

Figure 6-48(a) indicates that the depth to which the waste package outer closure lid–weld radial stress is in compression is about 5 mm. Figure 6-48(b) indicates that the depth to which the waste package outer closure lid–weld hoop stress is in compression is about 3 mm and the depth to which the hoop stress is below the 90% of yield strength criterion ($YS_{(125°C)}$, 316 MPa) is about 6 mm. Clearly the plasticity burnishing provides significant improvement in the situation where the welds are not stress-mitigated.

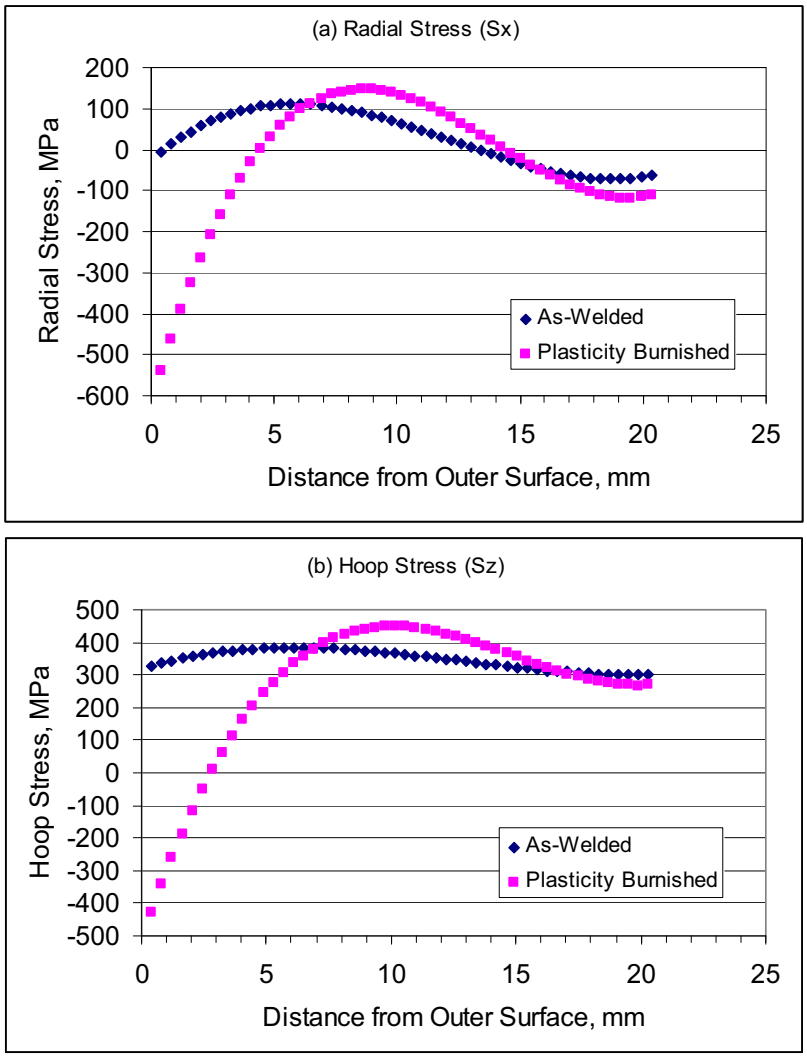

Source: Second (for radial stress) and fourth (for hoop stress) columns of Table 6-12 and Table 6-16. Output DTN: MO0705CREEPSCC.000, file *StressAndIntensityProfiles.xls*.

Figure 6-48. Comparison of Radial Stress, S_x, (a) and Hoop Stress, S_z, (b) in Waste Package Outer Lid with and without Plasticity Burnishing

From Figure 6-49a, it is evident that for the plasticity-burnished waste package outer closure lid, the radial through-wall stress intensity factor is below zero within the whole range of the plate thickness, indicating circumferential cracks will not propagate entirely through the wall thickness. For the hoop stress intensity factor profile, Figure 6-49b shows that the stress intensity factor is below zero within about 5 mm into the outermost burnished waste package closure weld surface.

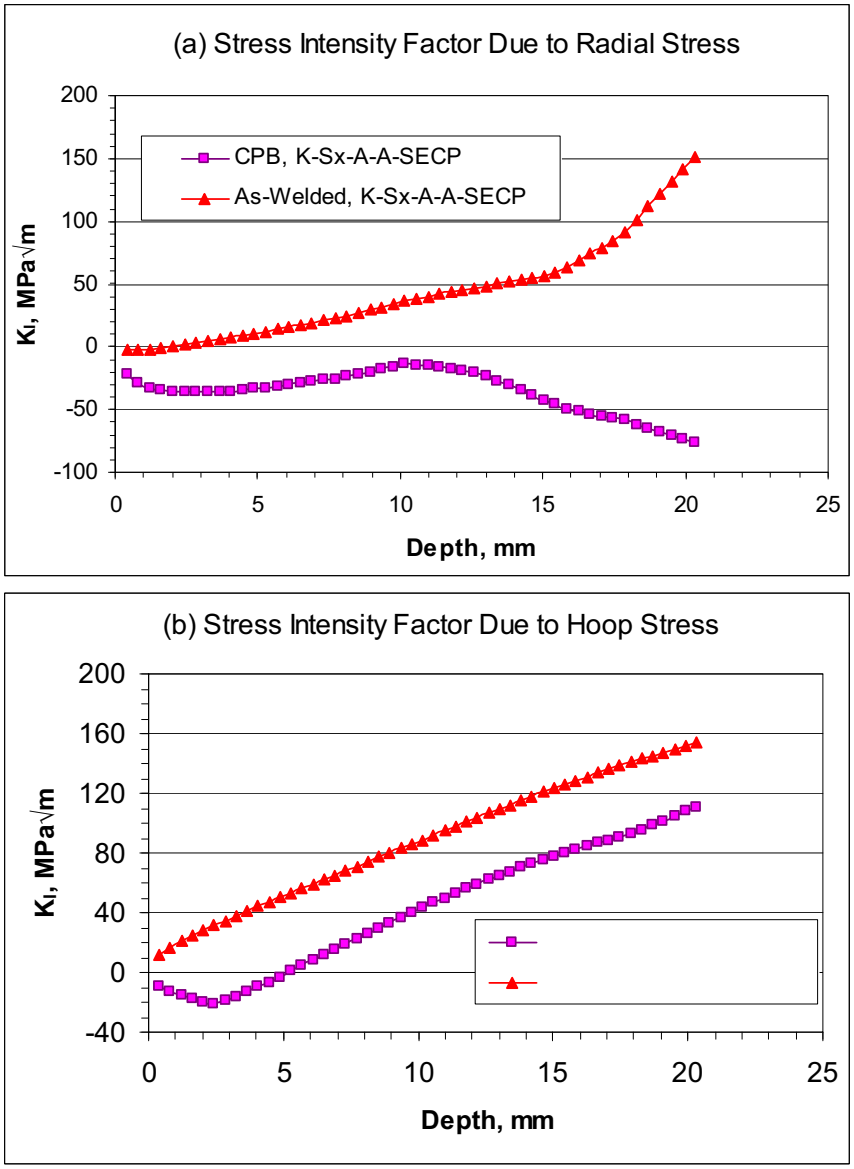

Source: Third (for radial stress) and fifth (for hoop stress) columns of Table 6-12 and Table 6-16. Output DTN: MO0705CREEPSCC.000, *StressAndIntensityProfiles.xls*.

Figure 6-49. Stress Intensity Factors due to (a) Radial Stress and (b) Hoop Stress with and without Plasticity Burnishing

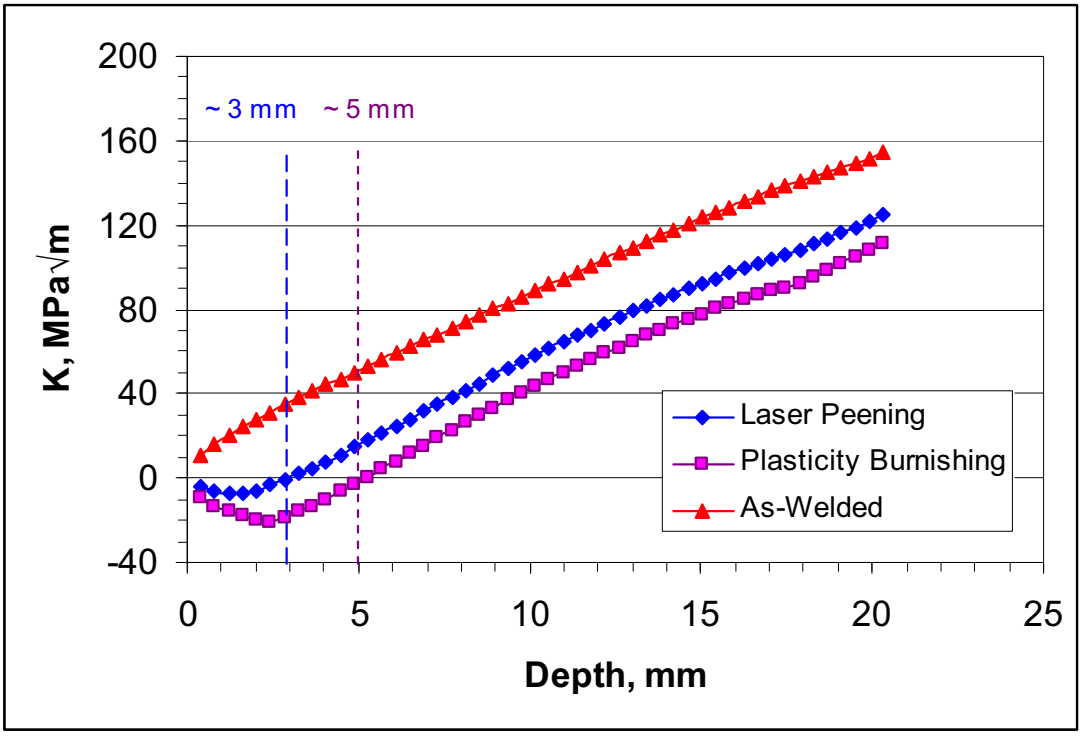

Source: Fifth (for hoop stress) columns of Table 6-12, Table 6-15, and Table 6-16. Output DTN: MO0705CREEPSCC.000, *StressAndIntensityProfiles.xls*.

Figure 6-50. Comparison of Plasticity Burnishing and Laser Peening for Effect of Stress Mitigation

The similarity between CPB and laser peening effects on stress mitigation of the waste package outer closure weld is clearly demonstrated in Figure 6-50, in which the effects on the stress intensity factor in the S_z direction due to the use of elliptical crack geometry in as-weld, laser peened and plasticity-burnished waste package outer closure welds are compared. With stress mitigation, the stress intensity factor in the subsurface region is compressive for 3 mm to 5 mm in these cases. The actual depth in which the stress and stress intensity factor are compressive depends on the methods of applying laser peening and plasticity burnishing.

Any thermally induced stress relaxation of the through-wall stress distribution is expected to be small at waste package temperatures, which are below about 300°C. A small amount of stress relaxation was observed based on measured leg springback in five-year tests of U-bend specimens at 90°C, which were removed from the LLNL LTCTF (Fix et al. 2003 [DIRS 162700], p. 5). Stress relaxation reduces subsurface tensile stresses as well as the outer surface compressive stress, the latter being beneficial. It is unlikely, however, that stress relaxation in a stress-mitigated surface layer will significantly alter the depth where stresses below the threshold stress value for stress corrosion cracking initiation are reached. For instance, as discussed in Section 6.5.4, full removal (e.g., by corrosion) of the outermost approximately 3 mm of surface layer did not significantly change the through-wall stress distribution.

6.5.6 Uncertainty and Variability of Residual Stress and Stress Intensity Factor

Section 6.5.3.3 states that, although the determination of weld residual stress for the waste package closure welds is a three-dimensional problem, a two-dimensional axisymmetric modeling approach has been used for the finite-element analyses. The result is that the stress distribution is axisymmetrical about the waste package axial centerline (i.e., the stress is uniformly distributed along the circumference).

6.5.6.1 Circumferential Variation in Stress and Stress Intensity Factor Profiles

An assessment of circumferential residual stress variation in stainless steel piping welds (DTN: MO0409GGSIACAL.000 [DIRS 171792]) indicates that the residual stress shows a sinusoidal distribution around the circumference with a range of about 5 ksi about the mean stress (i.e., ±2.5 ksi). Based on this assessment, the variability of the mean stress ($S_\theta(x)$) along the circumference (∇S) can be represented by Equation 24:

$$S_\theta(x) = S_0(x) - \nabla S(1 - \cos(\theta)) \qquad \text{(Eq. 24)}$$

where x is the distance from the outermost surface, θ is the angle measured in degrees from a reference location ($\theta = 0°$) on the circumference, and $S_\theta(x)$ is the weld residual stress profile at an angle θ with a distance of x from the outermost surface of the waste package. $S_0(x)$ is the calculated weld residual stress profile at $\theta = 0$ at distance x, and ∇S is taken to be 2.5 ksi or 17.2369 MPa.

Because stress intensity factor is a linear function of stress, the variability in stress intensity factor around the circumference can be similarly treated as:

$$K_\theta(x) = K_0(x)\,(S_\theta(h) / S_0(h)) \qquad \text{(Eq. 25)}$$

where h is the thickness of the closure lid.

6.5.6.2 Uncertainty in Stress and Stress Intensity Factor Profiles

The uncertainty of the weld residual stress calculated by the simplified finite-element analysis can be adequately represented by a normal distribution with the calculated residual stress as the mean ($S_\theta(x)$) and a 3σ bound, which is to be defined.

Mohr (1996 [DIRS 147981], p. 39) indicated that the uncertainty range of the residual stress is a function of the yield strength of the material and varies about the mean by ±35% of the yield strength. The high degree of uncertainty (or variability) associated with Mohr's data (1996 [DIRS 147981]) was related to the large scatter in measured residual stress data. This large scatter resulted from the use of a large number of different welded carbon steel pipes with a range of thickness, different welding processes, weld joint configurations and weld heat inputs, and various yield strengths, etc. In the case of the final closure weld lid, the various parameters contributing to residual stress variation are closely controlled. This includes close automated control of the welding process parameters, the use of a single alloy as the base material and the weld wire, close control of the weld joint configuration and spacing, etc.

In contrast to the large scatter presented by Mohr (1996 [DIRS 147981]), available data on the use of shot-peening (a process analogous to plasticity burnishing) on the nickel alloy Incoloy 908 (Pasupathi 2000 [DIRS 149968]) demonstrated a narrower residual stress scatter range for as-welded and as-welded–plus–shot-peened nickel alloy material with a standard deviation of ±3% of the measured stress value (Pasupathi 2000 [DIRS 149968], Tables II and VI) or an uncertainty range of about ±9% at the 3σ level. An analysis of the residual stresses associated with the shot-peened Incoloy 908 indicates the stress variation is consistent with a normal distribution (Appendix D). In comparison, the residual stresses measured on a peened surface by X-ray diffraction technique showed an average measurement uncertainty of about ±15 MPa, which is about ±5% of the Alloy 22 yield strength (Lu 1996 [DIRS 149957], Table 5-4, p. 103). The Almen strips, which are commonly used to control shot-peening and laser-peening processing, may be used for process stress control. Almen strips are thin rectangular strips that, when peened from one side, deflect with the deflection related to the depth of applied residual compressive stress resulting from the process. If stresses are found to deviate from the specified range, the material should be reprocessed, repaired, or scrapped. It is anticipated that a similar process control method will be implemented for the case of plasticity burnishing for license application.

Thus, based on the above discussion, a 3σ stress uncertainty range of ±15% of the mean at-temperature yield strength (±0.15 $YS_{(T)}$) of the material appears to be a conservative representation of the realistic case that is achievable through appropriate levels of process controls. Therefore, the uncertainty in the stress profiles should be represented by a truncated (at ±3σ) normal distribution with the mean equal to the at-temperature yield strength and the σ equal to 5% of the at-temperature yield strength.

Values of yield strength of Alloy 22 at various temperatures are listed in Table 4-7. The higher yield strength values (i.e., data from Alloy Digest 1985 [DIRS 178194], p. 2, Table 3) in Table 4-7 are used in these finite-element closure weld stress analyses. The use of these higher yield strength values results in higher calculated tensile residual stresses and resultant stress intensity factors. Therefore, for conservative purpose, the higher yield strength values (data from Alloy Digest 1985 [DIRS 178194], p. 2, Table 3) are used in evaluation of stress and stress intensity factor distribution and uncertainties.

6.5.6.3 Determination of Maximum and Minimum Stress and Stress Intensity Factor

The minimum and maximum stresses at the 3σ level, $S_\theta(x)\min$ and $S_\theta(x)\max$ in the weld, can be obtained from the mean stress, $S_\theta(x)$, by Equations 26 and 27:

$$S_\theta(x)\min = S_\theta(x)\left(\frac{S_\theta(h)-\Delta S}{S_\theta(h)}\right) \qquad \text{(Eq. 26)}$$

$$S_\theta(x)\max = S_\theta(x)\left(\frac{S_\theta(h)+\Delta S}{S_\theta(h)}\right) \qquad \text{(Eq. 27)}$$

where $S_\theta(h)$ is the mean residual stress on the inner surface. As this value is not available, the stresses at the deepest depth given in Table 6-12 and Table 6-16 are used. ΔS equals 0.15 $YS_{(125°C)}$ where $YS_{(125°C)}$ is the yield strength at 125°C which can be interpolated from Table 4-7 as shown in Table 6-4 and is used in the analysis performed by SIA (DTN: MO0708RTSWRS06.000 [DIRS 182558]). The stress intensity factor calculated from the mean stress is the mean stress intensity factor $K_\theta(x)$. The minimum and maximum stress intensity factors are calculated similarly to those for stress because stress intensity factor is a linear function of stress, i.e.:

$$K_\theta(x)\min = K_\theta(x)\left(\frac{S_\theta(h)-\Delta S}{S_\theta(h)}\right) \qquad \text{(Eq. 28)}$$

$$K_\theta(x)\max = K_\theta(x)\left(\frac{S_\theta(h)+\Delta S}{S_\theta(h)}\right) \qquad \text{(Eq. 29)}$$

where θ is the angle measured from a reference location (θ = 0°) on the circumference and ΔS = 0.15 $YS_{(125°C)}$ where $YS_{(125°C)}$ is the yield strength at 125°C.

As described in Section 6.3.4, the hoop stress, which promotes radially oriented crack growth, is the dominant component of stress in the waste package outer barrier final closure lid weld regions. Thus, only the hoop stress profiles are considered in calculating the expected range of stress and stress intensity factor through-wall variation. The stress and stress intensity factor profiles in the waste package outer barrier closure weld regions are variable and uncertain. Variability (angular variation) in the hoop stress (σ in MPa) as a function of depth (x in mm) in the closure weld regions of the Alloy 22 waste package outer barrier is given by a third-order polynomial equation, Equation 22, where the values of the coefficients (A_i) are given in Table 6-11 for the as-welded naval long waste package outer lid and in Table 6-14 for the plasticity-burnished naval long waste package outer lid.

6.5.6.4 Angular Variation of Stress and Stress Intensity Factor

The second argument in the stress function is used to represent angular variation (θ = 0, arbitrarily chosen) around the circumference of the Alloy 22 waste package outer and middle closure-lid welds. The angular variation is included using Equation 24′:

$$\sigma(x,\theta) = \sigma(x,0) - (17.236893)\times(1-\cos(\theta)) \qquad \text{Eq. 24}'$$

where $\sigma(x, 0)$ is a function of the stress coefficients (A_i) defined in Equation 22 with x in millimeters (mm) and the stress variability term is defined in Equation 24. Using Equation 24 and θ = 0°, 90°, and 180°, the distribution of the hoop stress along the thickness of the waste package outer closure lid weld with various θ values can be obtained as shown in Figure 6-51 with θ being the angle measured from a reference location (θ = 0°) on the circumference. Figure 6-51 shows the median stress variation with the angle for the waste package outer barrier outer lid weld region without accounting for uncertainty, which is discussed in Section 6.5.6. Figure 6-52 shows the median stress variation, without accounting for the uncertainty, using

Equation 24 and θ = 0°, 90°, and 180°, for the plasticity-burnished waste package outer barrier closure lid weld region. The stress profiles for the waste package outer closure lid, and plasticity-burnished waste package outer closure lid weld regions, calculated using Equation 24 and plotted with angle θ set at 45° and 135° are presented in output DTN: MO0702PASTRESS.002, file *Figure 6-51 (Figure 8-2) Through Figure 6-58 (Figure 8-9).xls*. Also included in Figure 6-51 and Figure 6-52 is the stress threshold for nucleation of incipient flaws (Section 6.2). For the as-welded waste package outer lid, the mean hoop stress exceeds the stress threshold (90% $YS_{(125°C)}$ or 316 MPa) within almost the full range of the lid thickness for the full range of θ. However, in the case of plasticity burnishing, the mean hoop stress does not exceed the stress threshold in the outermost surface region for about 6 mm into the thickness of the plate for the full range of θ. In addition, in the case of plasticity burnishing, the mean hoop stress within about 3 mm of the outermost surface is compressive.

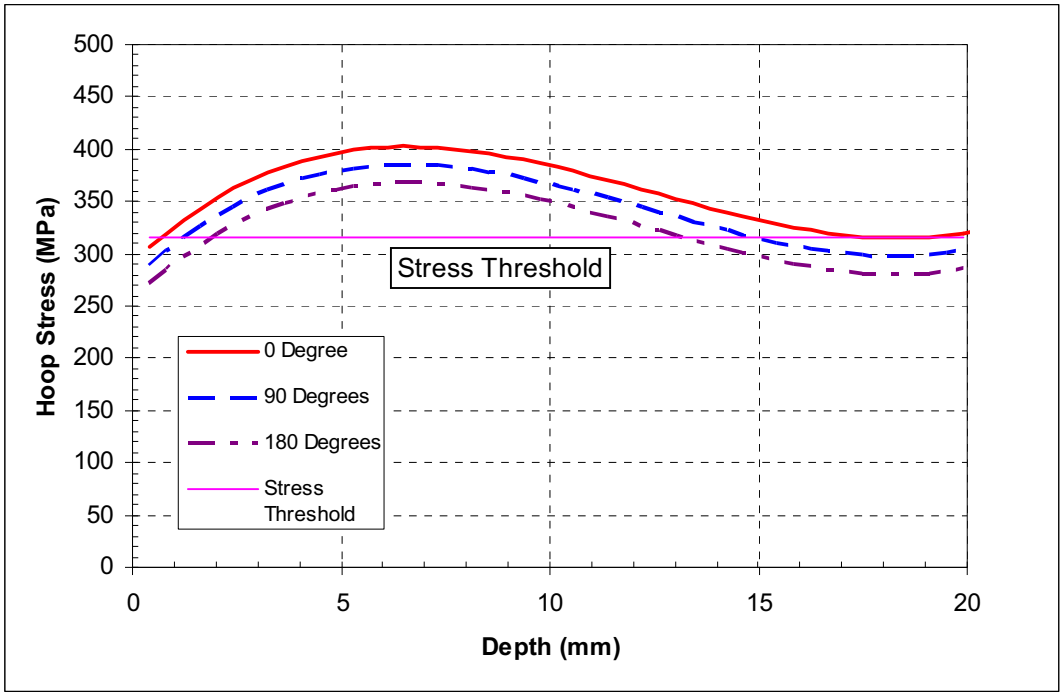

Source: Equation 26 and data from output DTN: MO0702PASTRESS.002, file *Figure 6-51 (Figure 8-2) Through Figure 6-58 (Figure 8-9).xls*, Sheet "Angular S As-Welded."

Figure 6-51. Variation of Hoop Stress versus Depth for As-Welded Waste Package Outer Closure Lid

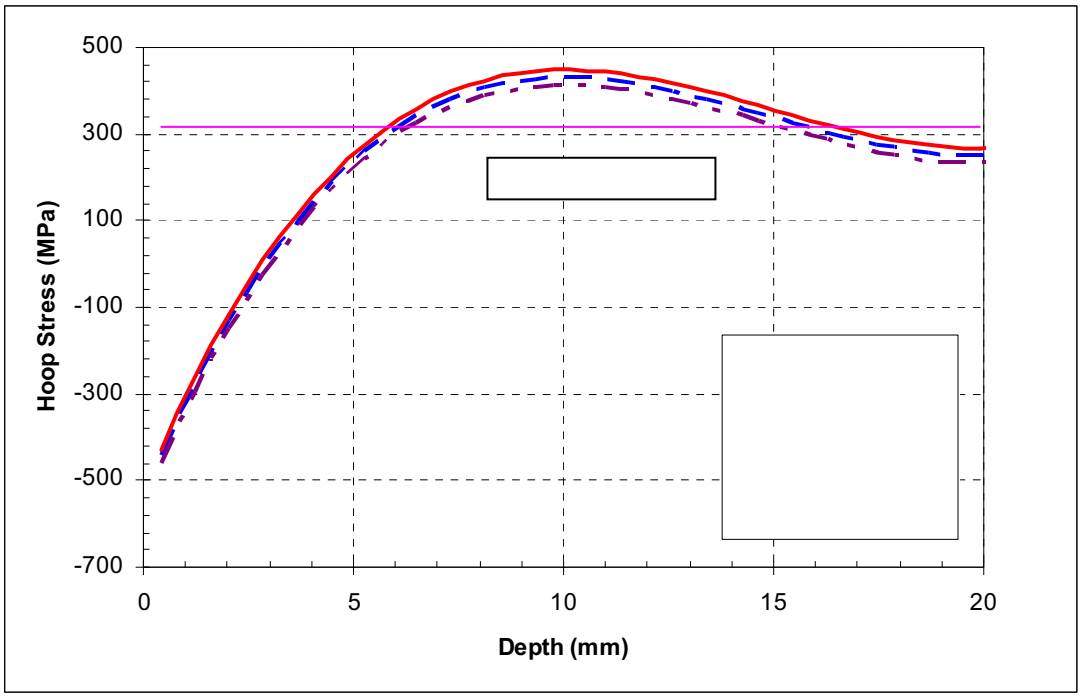

Source: Equation 26 and data from output DTN: MO0702PASTRESS.002, file *Figure 6-51 (Figure 8-2) Through Figure 6-58 (Figure 8-9).xls*, Sheet "Angular S CPB."

Figure 6-52. Hoop Stress versus Depth for Plasticity-Burnished Waste Package Outer Closure Lid with Variability as a Function of Angle

As the stress intensity factor is a linear function of stress, the corresponding stress intensity factor profiles for the as-welded waste package outer closure lid and plasticity-burnished waste package outer closure lid, calculated using Equations 28 and 29 and plotted with angle θ set at 0°, 90°, and 180°, are shown in Figure 6-53 and Figure 6-54, respectively. In the case of plasticity burnishing, the stress intensity factor (K_I) due to hoop stress is below about 20 MPa√m within about 7 mm into the plate thickness. At the same depth from the outermost surface, the stress intensity factor due to hoop stress in the as-welded closure weld is above 60 MPa√m. The stress intensity factor profiles for the as-welded waste package outer closure lid plasticity-burnished waste package outer closure lid calculated using Equations 28 and 29 and plotted with the angle, θ, set at 45° and 135°, are presented in Figure 8-5 of output DTN: MO0702PASTRESS.002.

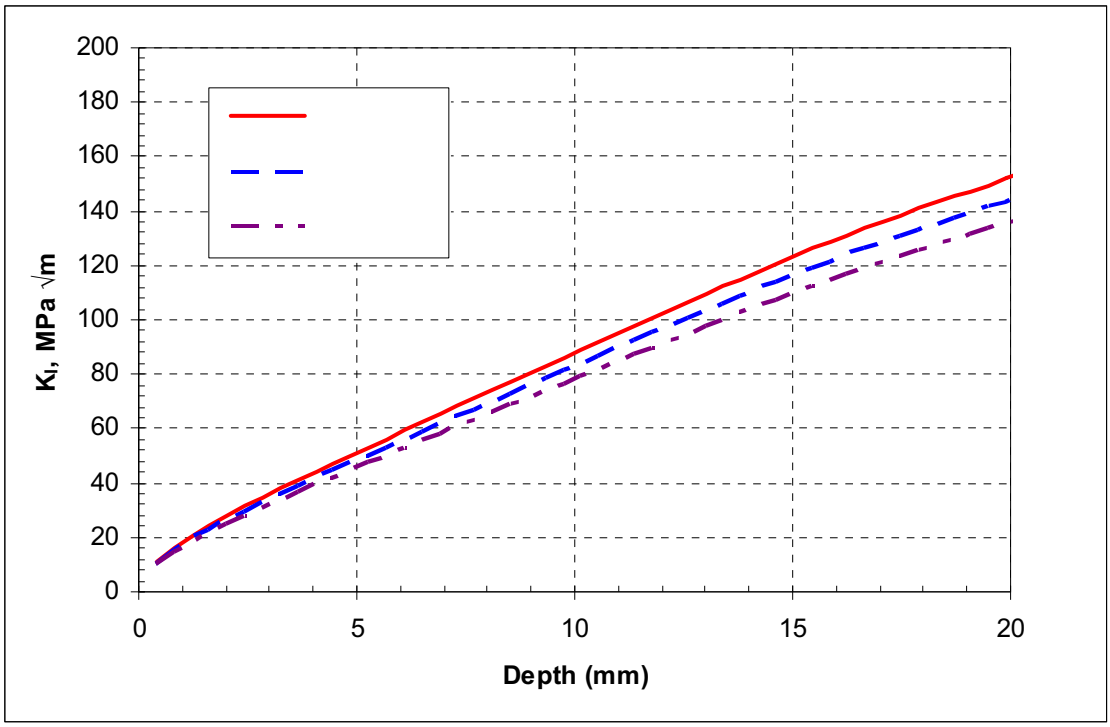

Source: Equation 27 and data from output DTN: MO0702PASTRESS.002, file *Figure 6-51 (Figure 8-2) Through Figure 6-58 (Figure 8-9).xls*, Sheet "Angular S As-Welded."

Figure 6-53. Variation of Stress Intensity Factor versus Depth for As-Welded Waste Package Outer Closure Lid

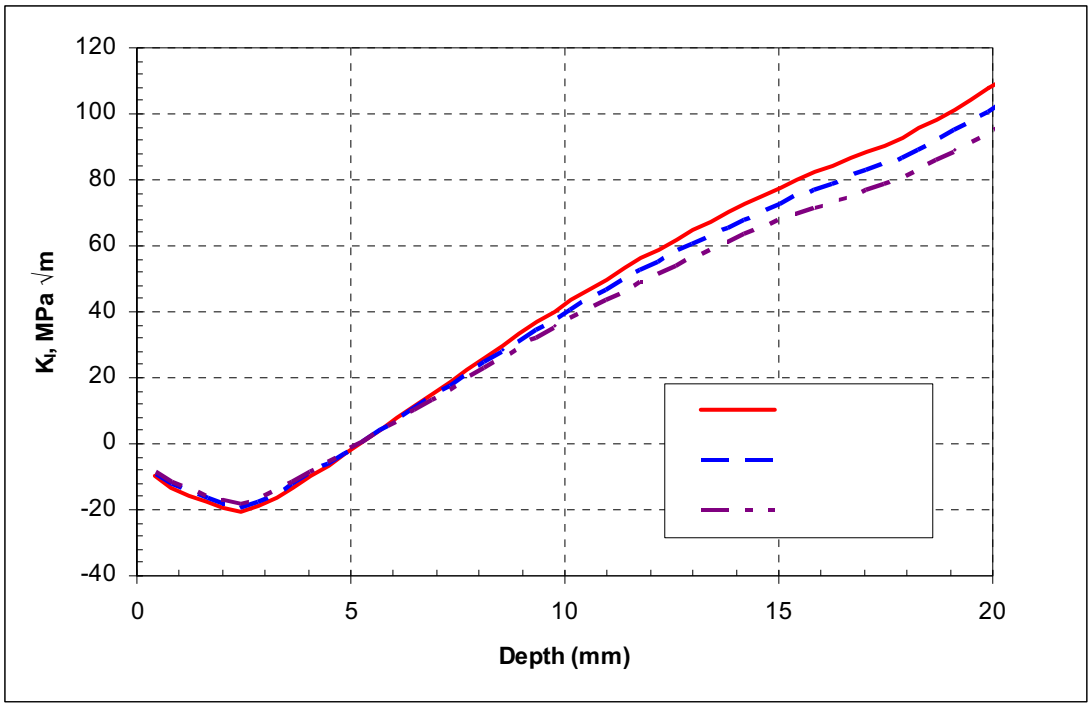

Source: Equation 27 and data from output DTN: MO0702PASTRESS.002, file *Figure 6-51 (Figure 8-2) Through Figure 6-58 (Figure 8-9).xls*, Sheet "Angular S CPB."

Figure 6-54. Stress Intensity Factor versus Depth for Plasticity-Burnished Waste Package Outer Closure Lid with Variability as a Function of Angle

6.5.6.5 Uncertainty in Residual Stress Distribution

Uncertainty in residual stress distributions for the as-welded and plasticity-burnished waste package closure lid weld regions can be calculated based on Equations 26 and 27. Figure 6-55 and Figure 6-56 show the variations of hoop stress at $\theta = 0$ versus depth for as-welded and plasticity-burnished waste package outer lid, respectively, with uncertainty range of ± 5%, ±10% ±15% of the 125°C yield strength ($YS_{(125°C)}$ or 351 MPa).

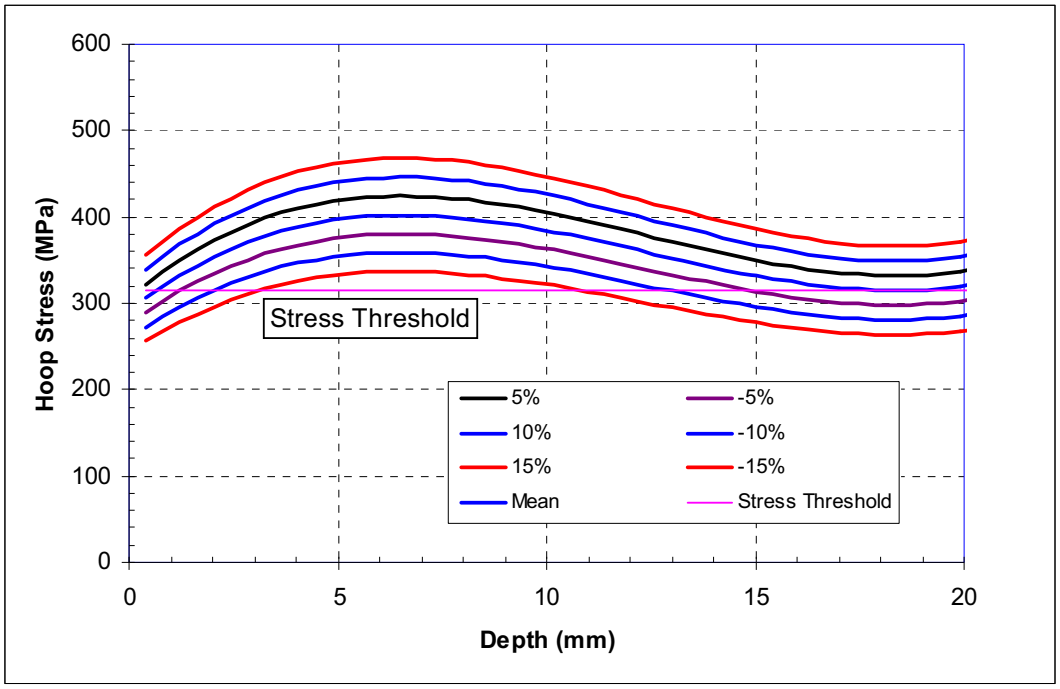

Source: Equation 26 and data from output DTN: MO0702PASTRESS.002, file *Figure 6-51 (Figure 8-2) Through Figure 6-58 (Figure 8-9).xls,* Sheet "Uncertainty As-Welded."

Figure 6-55. Variation and Uncertainty of Hoop Stress (θ = 0) versus Depth for As-Welded Waste Package Outer Closure Lid

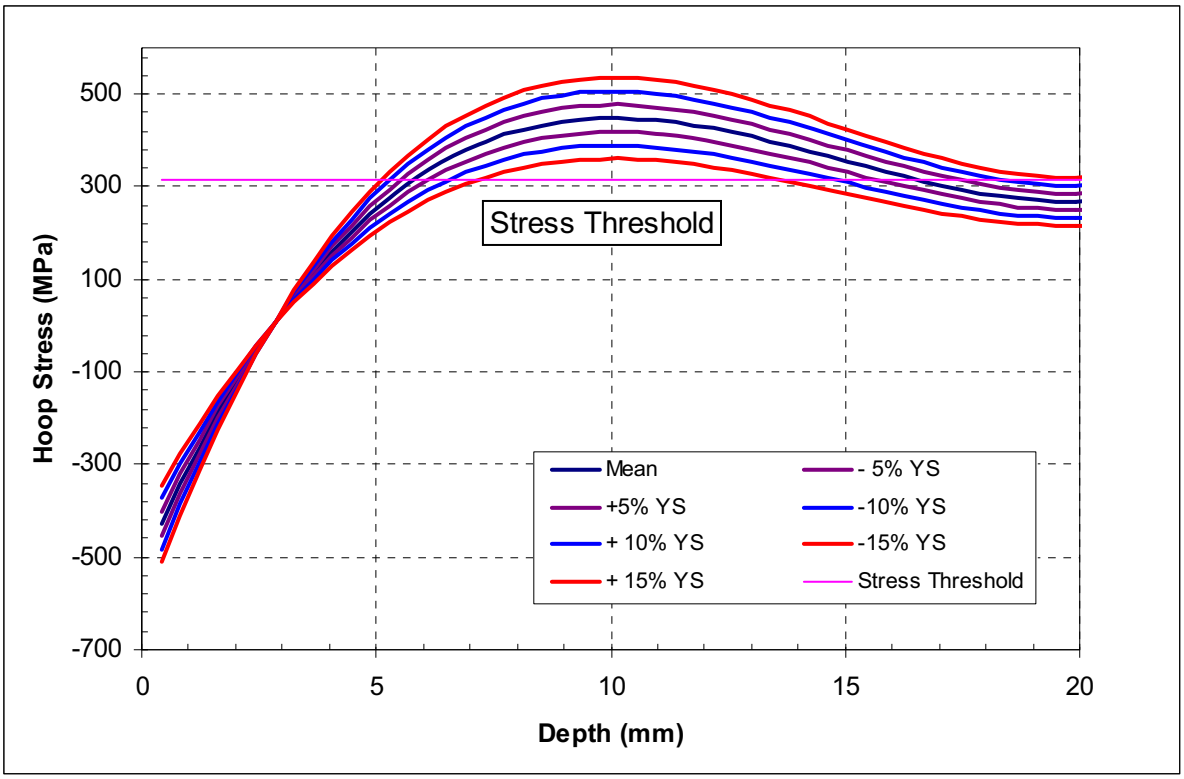

Source: Equation 26 and data from output DTN: MO0702PASTRESS.002, file *Figure 6-51 (Figure 8-2) Through Figure 6-58 (Figure 8-9).xls*, Sheet "Uncertainty CPB."

Figure 6-56. Hoop Stress (θ = 0) versus Depth for Plasticity-Burnished Waste Package Outer Closure Lid with Uncertainty as a Function of Yield Strength

As can be seen from Figure 6-56, the analysis results predict that the minimum threshold stress (90% of $YS_{(125°C)}$) for the plasticity-burnished waste package outer closure lid will not be reached in the outer surface region for about 5 mm into the plate thickness within the entire uncertainty region (±15% YS).

Similarly, uncertainty in the stress intensity factor distributions for the as-welded and plasticity-burnished waste package outer lids can be calculated based on Equations 28 and 29, respectively. Figure 6-57 and Figure 6-58 show the variation of stress intensity factor at θ = 0 versus the depth for as-welded and plasticity-burnished waste package outer lids, respectively.

As can be seen from Figure 6-58, the analysis predicts that, by using upper bound of uncertainty (+15% of $YS_{(125°C)}$, the threshold stress intensity factor due to hoop stress will not exceed approximately 20 MPa√m within about 7 mm of the outer surface region.

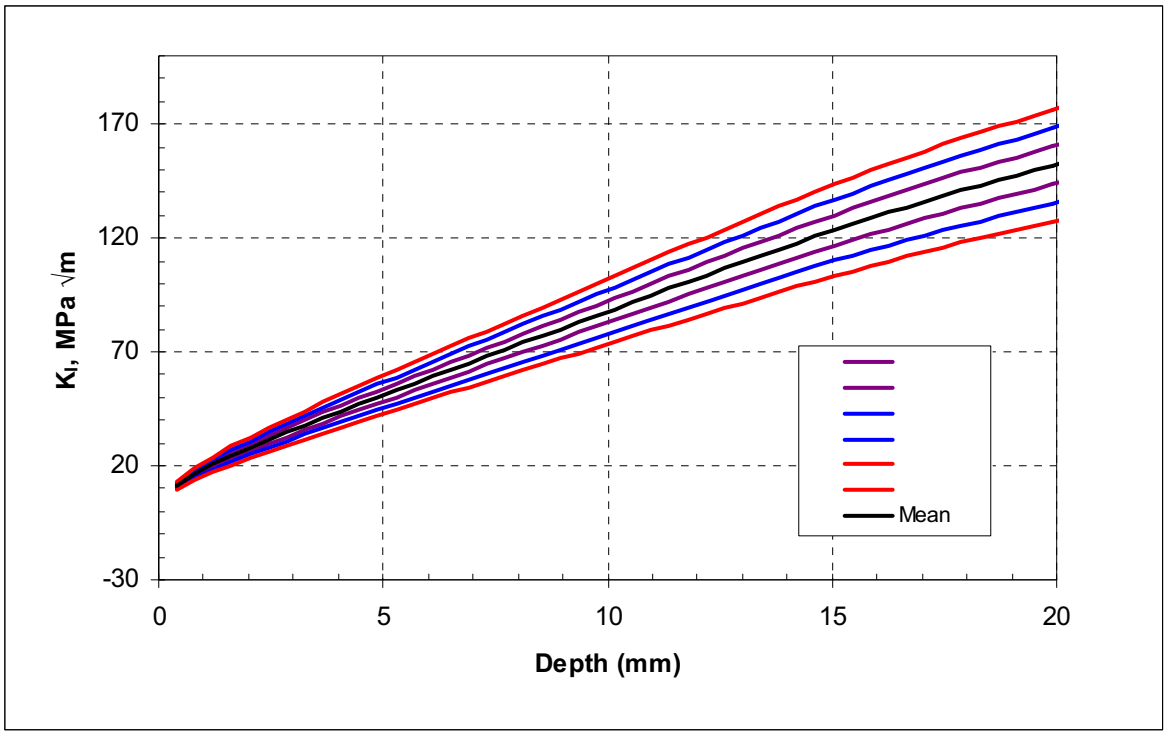

Source: Equation 28 and data from output DTN: MO0702PASTRESS.002, file *Figure 6-51 (Figure 8-2) Through Figure 6-58 (Figure 8-9).xls.* Sheet "Uncertainty As-Welded."

Figure 6-57. Variation of Stress Intensity Factor (θ = 0) versus Depth for As-Welded Waste Package Outer Closure Lid

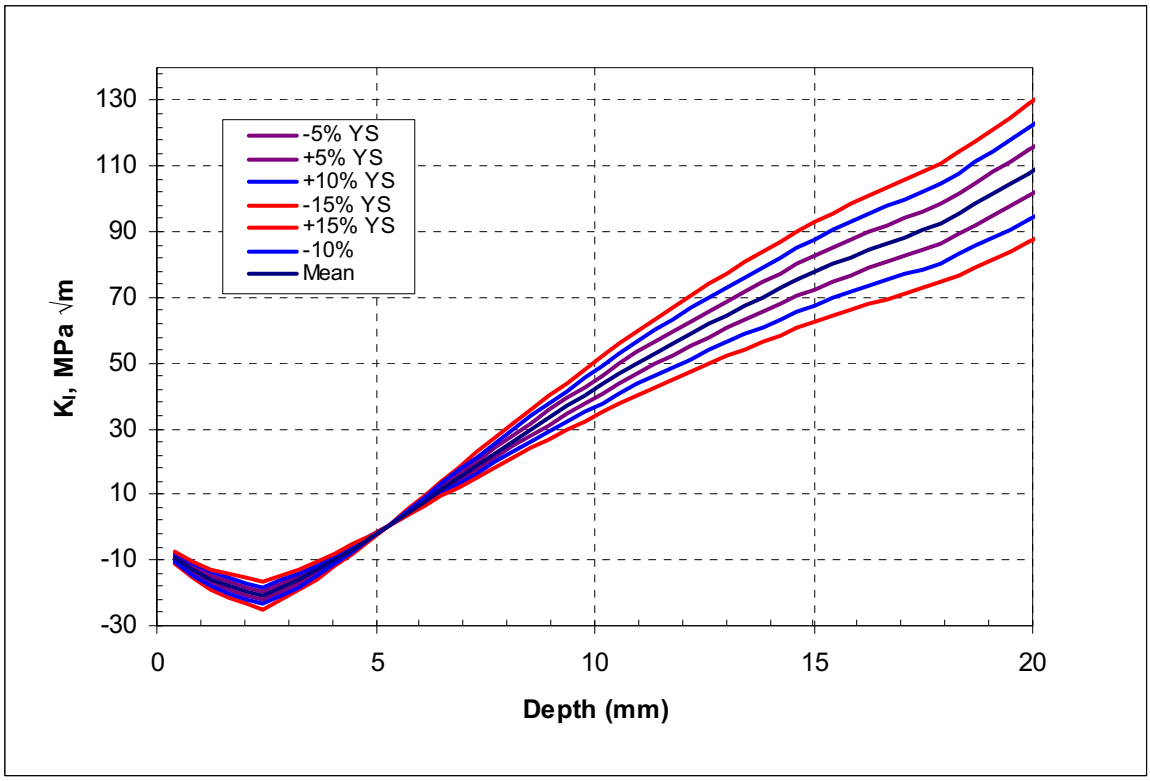

Source: Equation 28 and data from output DTN: MO0702PASTRESS.002, file *Figure 6-51 (Figure 8-2) Through Figure 6-58 (Figure 8-9).xls*, Sheet "Uncertainty CPB."

Figure 6-58. Stress Intensity Factor (θ = 0) versus Depth for Plasticity-Burnished Waste Package Outer Closure Weld Lid with Uncertainty as a Function of Yield Strength

Corroborative measurements of the through-wall residual stress have been made on the 1-in-thick GTAW welded Alloy 22 welds processed with a several-pass laser-shock peening treatment as well as the controlled plasticity-burnishing stress mitigation treatment. These experimental measurements were obtained using 1-in ring-core technique and are reported in DTN: MO0301SPAXRA52.001 [DIRS 165147]. The results of these measurements are shown in Figure 6-59 for the several-pass laser-shock-peened specimen and in Figure 6-60 for plasticity-burnished specimen, respectively. These results, compared with the predicted values shown in Figure 6-52 and Figure 6-54 show that the predicted values are very conservative when evaluating the effect of stress mitigation on stress redistribution. Figure 6-59 and Figure 6-60 refer to the stresses parallel to the weld centerline as the "parallel direction."

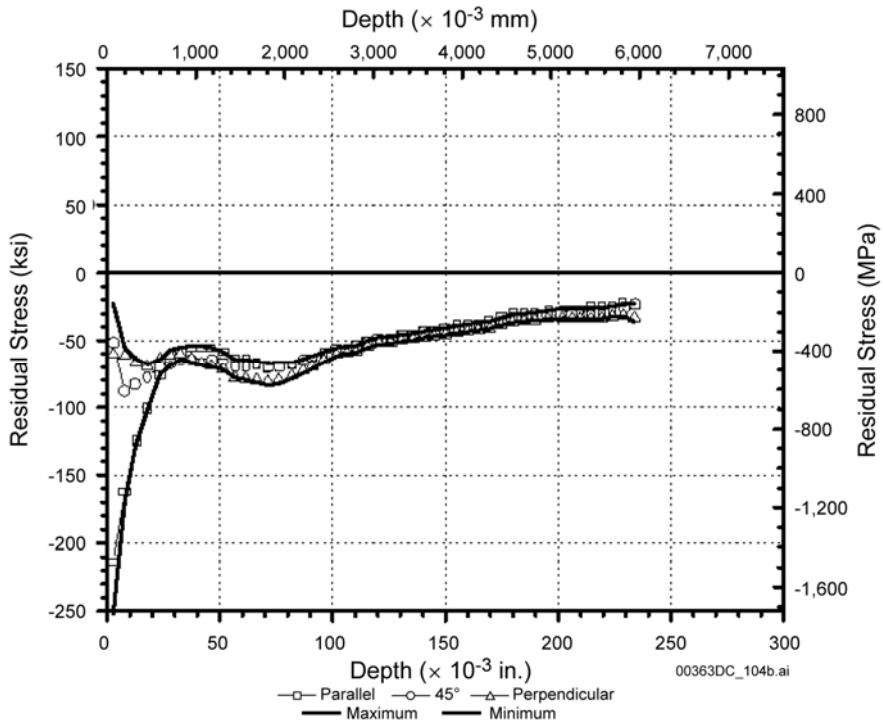

Source: DTN: MO0301SPAXRA52.001 [DIRS 165147], Figure 4.

Figure 6-59. Measured Stress (Using 1-Inch Ring Core Method) versus Depth for Alloy 22 Laser-Peened 1-Inch-Thick Gas Tungsten Arc Welding Welded Plate

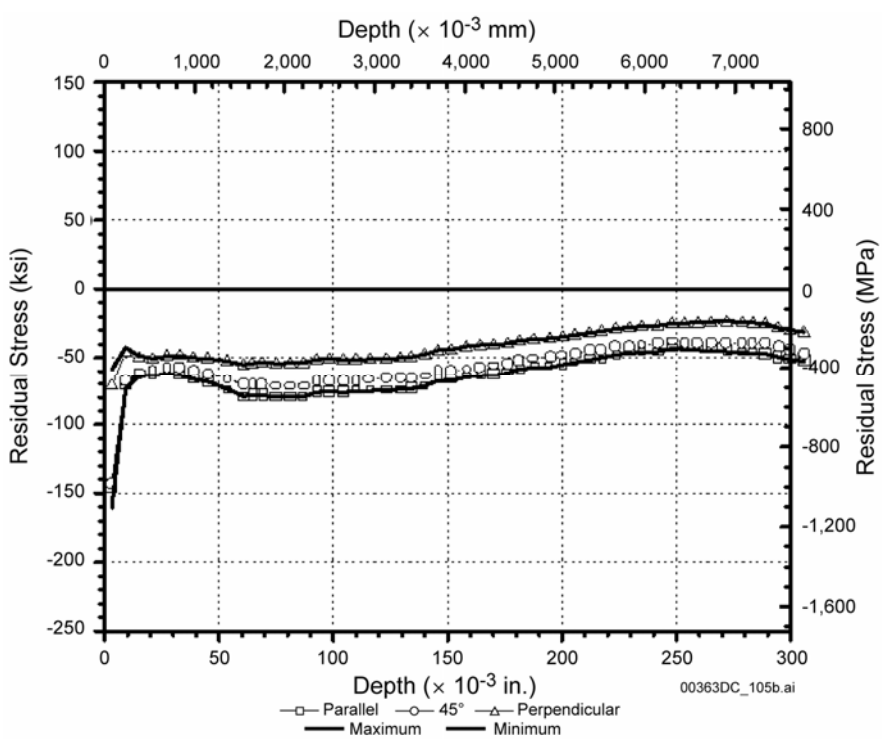

Source: DTN: MO0301SPAXRA52.001 [DIRS 165147], Figure 7.

Figure 6-60. Measured Stress (Using 1-Inch Ring-Core Method) versus Depth for Alloy 22 Plasticity-Burnished 1-in-thick Gas Tungsten Arc Welding Welded Plate

6.6 ESTIMATE OF LENGTH AND INTERCRACK SPACING OF RADIAL THROUGH-WALL CRACKING AND CRACK OPENING

The analysis provided in this section is not directly used in the SDFR model. Rather, it is provided as information that can be used for performance assessment in calculating radionuclide release rates through SCC cracks. Section 6.6.1 provides an estimated length and intercrack spacing of radial through-wall cracks. Section 6.6.2 provides an estimate of the size of crack openings for through-wall cracks. These analyses are based on established engineering practices and, therefore, are not to be considered models which need to be validated.

6.6.1 Estimated Length and Intercrack Spacing of Radial Through-Wall Cracking

As discussed in Section 6.3.4.3, radially oriented flaws are important to SCC of waste packages, as the hoop stress, which drives the growth of the radially oriented cracks, is usually the dominant stress component. The stress intensity factor resulting from the through-wall hoop stress gradient (or profile) can lead to propagation of through-wall SCC for cracks in the radial direction. Based on stress distributions shown in Figure 6-24, the weld residual stress decreases rapidly with increasing distance normal to the weld–metal interface (i.e., in the radial direction). As the tensile stress decreases, the driving force for crack propagation in the radial direction also decreases rapidly and appears to fully attenuate at distances from the weld center line on the order of the thickness of the welded plate. Thus, the expected maximum length of these radial cracks is approximately two times the plate thickness.

With respect to the expected minimum spacing between parallel through-wall radial cracks, detailed analysis (SIA 2002 [DIRS 161933]) indicated that, because of the stress field interactions between closely spaced parallel cracks, for a one-inch-thick plate, the distance between two neighboring through-wall cracks needs to be greater than the plate thickness so that sufficient stress (and resultant stress intensity factor) is available to result in through-wall crack propagation.

6.6.2 Estimate of the Size of Crack Opening

Leaking through a crack can occur if the crack grows into a through-thickness crack. The leak rate depends on the size of the crack opening and other factors. A simplified crack opening size calculation approach is described below.

1. A crack is either circumferential (perpendicular to the radial stress) or radial (perpendicular to the hoop stress) in the outer surface of the waste package closure weld.

2. A circumferential crack is treated as a semi-elliptical crack with depth, a, and length, 2c. The aspect ratio, c/a, for a radial crack is 1 (i.e., a semi-circular crack, c = a).

3. The crack length, 2c, of a circumferential crack remains unchanged but the final length of a through-wall crack is at least twice the wall thickness. Consequently, most cracks will grow in both directions of the minor (depth, a) and major (length, 2c) axes and eventually become semi-circular (i.e., a = c) when they become through-wall cracks. According to fracture mechanics theory (Ewalds and Wanhill 1984 [DIRS 118602],

Section 2.5, p. 43), depth, a, tends to grow faster than length, c, because the stress intensity factor tends to have a maximum value at the end of the minor axis and a minimum value at the end of the major axis. Eventually, a semi-elliptical crack will become a semi-circular crack. The crack length, 2c, will remain unchanged only for very long cracks with initial crack length greater than twice the wall thickness. The probability of the occurrence of such long cracks is very low. The length of a semi-circular crack will always be equal to twice the crack depth.

4. The crack opening has an elliptical shape with length, 2c, and an opening displacement, δ.

Tada et al. (2000 [DIRS 167756], p. 125) showed that the opening displacement of a crack, δ, with length, 2c, in an infinite sheet is given for plane stress condition as:

$$\delta = \frac{(4c)\sigma}{E} \qquad \text{(Eq. 30)}$$

where σ is the stress and E the modulus of elasticity.

The opening area, A_{cr}, for an elliptical crack, therefore, can be estimated by:

$$A_{cr} = \frac{\pi}{4}\delta(2c) = \frac{(2\pi c^2)\sigma}{E} \qquad \text{(Eq. 31)}$$

When Equations 30 and 31 are used to estimate the crack opening displacement and opening area, σ is the maximum stress across the thickness of either the radial stress (for a circumferential crack) or the hoop stress (for a radial crack).

6.7 SEISMIC CRACK DENSITY MODEL FOR WASTE PACKAGE

The requisite conditions for SCC to occur are: (1) residual tensile stress, (2) an environment that supports corrosion, and (3) a material that is susceptible to SCC (e.g., the cold-worked Alloy 22). The conservative modeling assumption is made that, regardless of the actual chemical environment on the waste package surface, the environment is sufficiently severe to support SCC processes.

Seismic activity can lead the waste packages to impact other components in the drift including the emplacement pallets and other waste packages. If the seismically induced impacts are of sufficient magnitude, the impacts could physically dent the waste package outer barrier and potentially the waste package inner vessel. These deformations can result in cold work of the waste package barrier and vessel materials, producing a cold-worked gradient typically highest on the outer surface and lowest on the inner surface. Impacts may also create complex through-wall residual stress profiles. These stress profiles and cold-work gradients may lead to SCC in the seismically affected area of the waste packages.

As discussed in Section 6.8.5, similar damage can be expected for drip shields under seismic loadings as well. However, as in the treatment of SCC due to rockfalls discussed in

Section 6.8.5, stress corrosion cracks in the drip shields are expected to be tight and plugged with corrosion products or mineral deposits, or both, leading to negligible water flow through these openings. The seismic crack density for the drip shield materials is discussed in more detail in Section 6.8.5.

This section evaluates the potential for SCC to occur in the Alloy 22 waste package outer barrier due to the stresses and cold work generated by an unlikely seismic event. After initiation and through-wall propagation of SCC, cracks may provide a path for subsequent radionuclide release from the waste package but, as with the drip shield case, aqueous transport and radionuclide release through SCC-induced crack areas in the waste package are likely to be negligible due to the tight and tortuous nature of the cracks and the potential for plugging by corrosion products or mineral deposits, or both.

6.7.1 Nature of Seismic Deformation and Crack Growth

6.7.1.1 Stress Corrosion Cracking Morphology

The purpose of this section is to present observations of stress corrosion crack morphology relevant to the waste package outer barrier material, Alloy 22. Alloy 22 is potentially susceptible to SCC under repository-relevant environmental conditions. The morphology of SCC is expected to be transgranular, rather than intergranular, a fact commonly observed (e.g., in high-temperature, LWR environments) (Andresen et al. 2001 [DIRS 167840]; Herrera 2004 [DIRS 168133], Section 2.0). Figure 6-61a and b presents typical examples of transgranular stress corrosion cracking and intergranular stress corrosion cracking, respectively.

Depending on the stress distribution, SCC may initiate and propagate through-wall. If several cracks were to initiate in the same general area, coalesce, propagate through-wall while remaining straight (i.e., perpendicular to the surface), and maintain smooth crack faces, a sizeable section of material could “fall out,” leading to a larger area for radionuclide release than would an array of separated stress corrosion cracks (Herrera 2004 [DIRS 168133], Section 2.0). However, the occurrence of all of these events in conjunction is improbable. In the real world, as discussed in Section 6.6.1, only tight and relatively separate through-wall cracks are expected (Herrera 2004 [DIRS 168133], Section 2.0). SCC cracks, unlike a sizable “fall-out” section of the material, would greatly impede radionuclide transport because of their tightness, the tortuous nature of the crack path, and the possibility (similar to cracks in drip shields) of being plugged with corrosion products or mineral deposits, or both. These factors could lead to negligible water flow through these openings.

On the other hand, despite the unlikeliness of through-wall leakage due to SCC cracks, SCC cracks in the waste package, unlike SCC cracks in the drip shield, could lead to the direct release of radionuclides to the environment. For this reason, SCC cracks in the waste package are considered in TSPA.

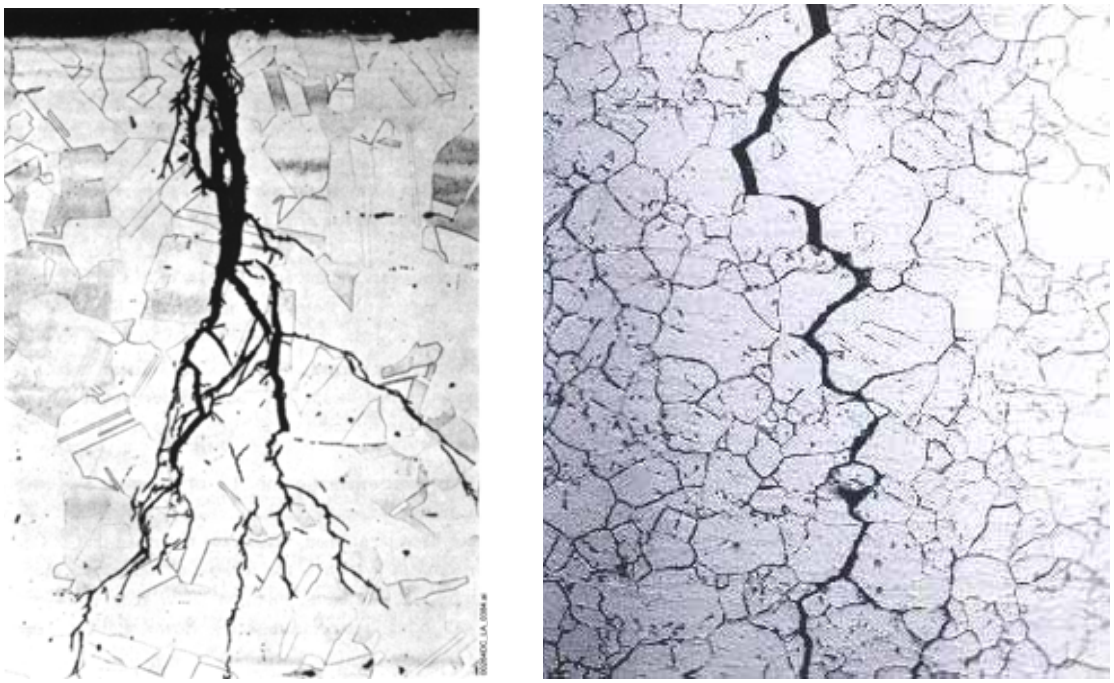

(a) (b)

Sources: (a) Herrera 2004 [DIRS 168133], Figure 2-1.
(b) Herrera 2004 [DIRS 168133], Figure 2-2.

Figure 6-61. Typical Examples of (a) Transgranular Stress Corrosion Cracking and (b) Intergranular SCC in Stainless Steel

6.7.1.2 Decreasing Gradients of Stress and Stress Intensity Factor along Wall Thickness

The nature of most seismically induced deformations in cylindrical vessels is such that it is very unlikely that a residual stress profile would be created that would allow an initiated stress corrosion crack to propagate through-wall and circumscribe the deformed area (Herrera 2004 [DIRS 168133], Section 3.0). Any through-wall residual stress fields resulting from impact loads will be a secondary-type stress (displacement controlled). There is no significant stress from other sources (e.g., due to internal pressure), as sustained, postclosure primary stresses in the waste package outer cylinder, including internal pressure stresses and waste package–pallet contact stresses, are limited by design and are significantly below 90% of the yield strength (the minimum stress threshold for SCC initiation at incipient flaws) (BSC 2004 [DIRS 169766], Tables 2, 21, 22, and 23; SNL 2007 [DIRS 179354], Table 4-1). Further, for such impact-induced residual stress gradients initiated at the outer surface, stresses and strains are of higher magnitude at the outer surface and tend to decrease through the thickness (Herrera 2004 [DIRS 168133], Section 3.0). Thus any SCC that initiates and propagates under such a decreasing driving stress intensity factor gradient may arrest before penetrating the full thickness (Herrera 2004 [DIRS 168133], Section 3.0). Therefore, seismically induced deformation-generated stresses are highly unlikely to lead to a residual stress profile that can result in a sufficiently positive stress intensity factor at which the cracks grow through-wall and around the entire deformed area. Similarly, the stress intensity factor (K_I) will tend to decrease as the crack propagates due to stress relaxation associated with crack growth that relieves stresses normal to the crack faces.

6.7.1.3 Reduction in Driving Force for Neighboring Crack Growth

Herrera (2004 [DIRS 168133], Section 4.0) concluded that cracks that are in close proximity can reduce the overall driving force for crack growth because the stress intensity factor (K_I) for parallel cracks is actually less than that for a single crack. Similarly, as discussed in Section 6.6.1, detailed analysis presented in *Structural Integrity Associates Support of Waste Package Design for Year 2001* (SIA 2002 [DIRS 161933]), indicates that the distance between two neighboring through-wall cracks would need to be greater than the wall thickness for the stress (and resultant stress intensity) to be sufficient to drive a crack penetrating the wall thickness. In addition, neighboring cracks will also reduce the crack driving force by decreasing the overall residual stress state. In the case of a single crack embedded in a secondary stress field (e.g., residual stress), as the crack grows, the through-wall residual stress field will redistribute and can be significantly different from the original distribution. As experience in BWRs has shown (Herrera 2004 [DIRS 168133], Section 5.0 and Appendix A), cracks can actually initiate, grow partly through-wall, and arrest before penetration. The crack arrest is due to the redistribution of the weld residual stress such that the stress intensity factor drops below the threshold value for crack growth.

If two cracks are in close proximity in a residual stress field, this relaxing effect is amplified to the point that one of the cracks may grow significantly deeper than the second crack as the growth of one of the cracks significantly reduces the driving force for the second crack (Herrera 2004 [DIRS 168133], Section 4.0). This has been the experience in many LWR cases (field experience and mockup testing of austenitic stainless steels and nickel-based alloys similar to Alloy 22 (Herrera 2004 [DIRS 168133], Section 4.0) (see Section 6.7.1.4). Through-wall growth of neighboring cracks has not been observed, and it is expected that the stress-relieving effect of neighboring cracks is the cause of this behavior.

Even if through-wall SCC occurs such that it circumscribes the deformed area, the nature of SCC (rough crack face and tortuous crack path) on this scale will preclude the deformed area from falling out (Herrera 2004 [DIRS 168133], Section 3.0). Stress corrosion cracking in Alloy 22 is expected to be transgranular, but, whether transgranular or intergranular, the crack path is complex, with some local areas of branching, and with all areas exhibiting a roughness and tortuosity that make it essentially impossible for the inner "plug" to disengage from the rest of the material in the absence of a superimposed primary load (e.g., significant internal pressure) (Herrera 2004 [DIRS 168133], Section 3.0). Any small internal pressure that develops from the heating up of the waste package or from corrosion due to the small amount of internal water vapor, or both, would not be sufficient to force the deformed area to "fall out" from the wall.

6.7.1.4 Light Water Reactor Case Histories

The previous section concluded that multiple surface cracks will not grow to through-wall cracks when they are in close proximity to each other. Herrera (2004 [DIRS 168133], Appendix A) summarizes several case histories of SCC for LWRs (i.e., BWR and pressurized water reactor (PWR) components). Some of the most significant incidences of cracking discussed included the presence of crevices and did not always occur in areas subjected to the full primary system pressure (i.e., cracking in regions subjected to low differential pressures such as the BWR core shrouds) top guides and steam dryers and in PWR tube sheet and tube support plate creviced

regions and at tube bend areas. Cracking often occurred in regions removed from welds and appeared to be driven by cold work-related residual stresses. In describing the total extent of cracking (i.e., length and depth), it is important to distinguish between cracking driven by a combination of residual stress plus primary pressure stress-induced loads, and that due solely to residual stresses. The seismically loaded waste package is similar to cases when cracking is caused solely by residual stress (in the absence of differential pressure).

Herrera (2004 [DIRS 168133], Appendix A) also reviewed a number of incidents of SCC observed in LWRs, involving austenitic stainless steels and nickel-based alloys (Alloy 22 is also a nickel-based alloy). In many of these cases, the cracking has been extensive, sometimes becoming fully circumferential on the component as driven by weld residual tensile stress plus pressure-induced primary stresses. Even under these severe stress conditions, there has never been a documented case where any section of material dropped out as a result of the observed cracking. Observations in the BWR and PWR industry are consistent with the behavior of cracks that are located in close proximity to one another. For example, the very few SCC-related steam generator tube ruptures observed occurred only under full-system differential pressure. Certainly, no material representing a continuous, through-wall circle has been affected in a manner that would give rise to a through-thickness piece being removed.

Therefore, based on the analyses presented in Sections 6.7.1.1 to 6.7.1.4, seismic activity will not result in large areas separating from the waste package outer barrier. Instead, a network of stress corrosion cracks is expected to form in the waste package outer barrier due to residual stresses induced by seismic activity. The remainder of this section is devoted to modeling the characteristics of such a network of stress corrosion cracks.

6.7.2 General Approach to Modeling Seismic Crack Density

This section outlines the overall approach to obtain an estimate of the crack opening area on a waste package damaged by a seismic event. The cracks within the damaged area are assumed to be caused as a result of stresses induced by a seismic event. In order to assess the damage scenario realistically, it is necessary to assess the possible number of cracks in the damaged area and the opening areas of these cracks. The total crack opening area within the seismic damaged area can be used in an assessment of the radionuclide leakage through the waste package damaged by the seismic events.

These estimates provide the basis for the selection of the effective crack opening area for use in the waste package performance assessment. The expected behavior of flaws that are in close proximity (Section 6.7.1.3), consideration of the stress–strain fields due to deformation (Section 6.7.1.2), and LWR field experience (Section 6.7.1.4) discussed earlier in this section provide the basis for the conclusion that areas of interest will not fall out of the waste package wall. Previous analytical work, supported by field experience, has demonstrated that through-wall flaws will not grow when they are in close proximity. Results of prior analyses indicate that through-wall flaws would not be present if the spacing were less than the thickness of the component (Section 6.6.1). Using this information, the remainder of this section provides an estimate of the crack density and crack opening area for use in the performance assessment of the waste packages.

Based on the previous discussions, the most likely limiting case is that the damaged areas on the waste package are penetrated by a network of tight cracks. This network of cracks will allow diffusive transport, but prevent significant advective flow and advective transport because of the small effective crack opening area and complicated crack path of individual cracks (Section 6.7.1.1).

The seismic scenario requires three inputs to represent the effective area of a network of cracks:

(1) Total damaged area on the waste package, A_D

(2) Crack density in the damaged area on the surface of the barrier, ρ_{SCC}

(3) Crack opening area of an individual crack, A_{SCC}.

The damage abstractions for the seismic scenario will define the total damaged area on the barrier. The total area of the crack network, $A_{SCC,\ NET}$, is then the product of the seismically damaged area, A_D; the crack density, ρ_{SCC} (the number of cracks per unit area); and the crack opening area of an individual crack, A_{SCC} (area/crack), expressed as follows (Herrera 2004 [DIRS 168133], Section 6.1):

$$A_{SCC,\ NET} = A_D\,(\rho_{SCC}\,A_{SCC}) \qquad \text{(Eq. 32)}$$

Not all seismically damaged areas on the waste package are open to radionuclide leakage. The factor ($\rho_{SCC}\,A_{SCC}$) is the crack area density or crack area per unit of seismically damaged area (i.e., the fraction of the seismically damaged area) through which radionuclides can be released. The factor ($\rho_{SCC}\,A_{SCC}$) can be viewed as a scaling factor applied to the seismically damaged area to obtain the total area of the crack network, $A_{SCC,\ NET}$. Section 6.7.3 provides estimates of the crack area density through analysis of networks of cracks arranged in a hexagonal geometry. Section 6.7.4 provides an alternative model for the crack area density by analysis of a damaged area with a circular geometry circumscribed by a single through-wall crack. Because the hexagonal array represents a high effective density (close spacing) of individual cracks, this hexagonal case, with crack center spacings set at the plate thickness, t, (Section 6.7.3) is considered a conservative representation. Section 6.7.4 provides an alternative model for the crack area density by analysis of a damaged area with a circular geometry circumscribed by a single through-wall crack. This is considered a limiting "realistic" case.

6.7.3 Primary Conceptual Model for Crack Area Density: Hexagonal Geometry

This section estimates the crack area density for a network of cracks arranged in a hexagonal geometry. Two crack arrangements are considered (Herrera 2004 [DIRS 168133], Section 6.2):

Case 1—The centers of elliptical cracks form a hexagonal array with major axis of length, $\frac{2t}{\sqrt{3}}$, where t is the wall thickness, with crack centers separated by $\frac{2t}{\sqrt{3}}$ (Figure 6-62). For this case,

the hexagon side length is $\frac{2t}{\sqrt{3}}$, and the perpendicular bisector (the distance from the hexagon center to the midpoint of one of the hexagon sides) is the wall thickness, *t*.

Case 2—The centers of elliptical cracks form a hexagonal array with major axis of length 2t, where t is the wall thickness, with crack centers separated by t (Figure 6-64). For this case, the hexagon side length is *t* and the perpendicular bisector is $\frac{\sqrt{3}t}{2}$. In this case, significant crack overlap is allowed to occur.

As discussed in Section 6.6.1, detailed analysis presented in *Structural Integrity Associates Support of Waste Package Design for Year 2001* (SIA 2002 [DIRS 161933]) indicates that the distance between two neighboring through-wall cracks would need to be greater than the wall thickness for the stress (and resultant stress intensity) to be sufficient to drive a flaw through-wall. This conclusion is based on stress field interactions between closely spaced parallel cracks. Case 1 uses the crack arrangement such that the perpendicular bisector is the wall thickness, *t*, while Case 2 uses the crack arrangement such that the distance between crack centers is equal to the wall thickness.

The results from either of these conceptual models of crack arrangement are considered to be conservative because the crack centers are arranged in a densely packed closely spaced array, which allows for neighboring in-plane stress fields to overlap.

Both conceptual models use the recommendations in Section 6.6 regarding the estimated length, intercrack spacing, and intercrack opening for the weld regions in the waste package lid. While the seismically induced damage to the waste package can occur at any location on the surface of these structures, the generic recommendations provide reasonable guidance for estimating the crack density and crack area in the seismic scenario.

It was shown in Sections 6.6.1 and 6.6.2 that:

1. The minimum distance between two neighboring parallel through-wall cracks is equal to the plate thickness

2. The crack opening area is elliptical

3. The crack width of a single crack, δ, for plane stress conditions in an infinite plate is given as follows (Tada et al. 2000 [DIRS 167756], p. 125):

$$\delta = \frac{(4c)\sigma}{E} \qquad \text{(Eq. 33)}$$

where $2c$ is the crack length, σ is the value of plane stress, and E is the modulus of elasticity. The crack width corresponds to the minor axis of the elliptical cross section of the crack. The crack opening area, A_{SCC}, is equal to the area of the elliptical cross section:

$$A_{SCC} = \pi\left(\frac{\delta}{2}\right)\left(\frac{2c}{2}\right) = \pi\left(\frac{(2c)\sigma}{E}\right)c = \frac{(2\pi c^2)\sigma}{E} \qquad \text{(Eq. 34)}$$

6.7.3.1 Case 1: Hexagonal Array with Side Length and Crack Length of 2t/√3

Consider a hexagonal array with side length $\frac{2t}{\sqrt{3}}$, where t is the plate thickness (Figure 6-62). Each point of the hexagonal array is the center of a crack with length $\frac{2t}{\sqrt{3}}$. This length allows for cracks, if they lie in the same plane, to just touch without overlapping, as shown in Figure 6-62. This crack length is smaller than that used for the waste package closure weld region, as discussed in Section 6.6.1, in which it was concluded that the crack length was equal to twice the thickness. However, that conclusion was based on stress interaction between parallel cracks and, in this case, overlap between neighboring cracks is avoided (this is not true of the next case shown in Figure 6-64).

The crack density, ρ_{SCC}, is the average number of cracks in a hexagon of the array divided by the area of the hexagon. The number of cracks in each hexagonal unit cell is 3 regardless of crack orientation. This is easy to see for Figure 6-62 in which the cracks are aligned in parallel. The crack at the center of the array in Figure 6-62 provides a full crack. The cracks at each of the six corners of the hexagon are shared by two other hexagons, effectively contributing an average of one-third of a crack per corner, regardless of actual crack orientation (in Figure 6-62, the cracks directly adjacent to the center contribute almost one-half of a crack and the other four edge cracks closer to (but not exactly) one-fourth of a crack). It should noted that the same shape is placed on each of the six corners of the hexagon, and each corner is shared by three hexagons. Figure 6-63 shows the cracks in random orientation to aid in visualization. Thus, each hexagon contains three full cracks. The area of the unit hexagon is calculated as the area of six equilateral triangles with side, $\frac{2t}{\sqrt{3}}$, as:

$$6\left(\frac{1}{2}\right)\left(\frac{2t}{\sqrt{3}}\right)(t) = \frac{6t^2}{\sqrt{3}} \qquad \text{(Eq. 35)}$$

It follows that the crack density, ρ_{SCC}, is given by:

$$\rho_{SCC} = \frac{3}{\left(\frac{6t^2}{\sqrt{3}}\right)} = \frac{\sqrt{3}}{2t^2} \qquad \text{(Eq. 36)}$$

Then, using Equations 34 and 36 with 2c = $\frac{2t}{\sqrt{3}}$ (the crack length), the crack area density (crack area per unit of seismically damaged area) can be expressed as:

$$\rho_{SCC} A_{SCC} = \frac{\sqrt{3}}{2t^2} \frac{(2\pi t^2)\sigma}{3E} = \frac{\pi\sigma}{\sqrt{3}E} \cong 1.81 \frac{\sigma}{E} \qquad \text{(Eq. 37)}$$

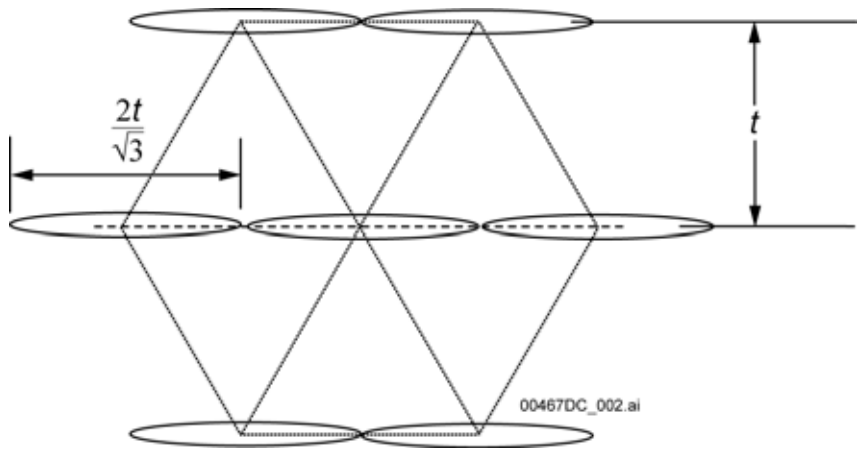

Source: Created for illustrative purposes only.

NOTE: Not to scale.

Figure 6-62. Parallel Rows of Parallel Cracks Whose Centers are Arranged in a Hexagonal Array (with Row Spacing Equal to the Wall Thickness, *t*)

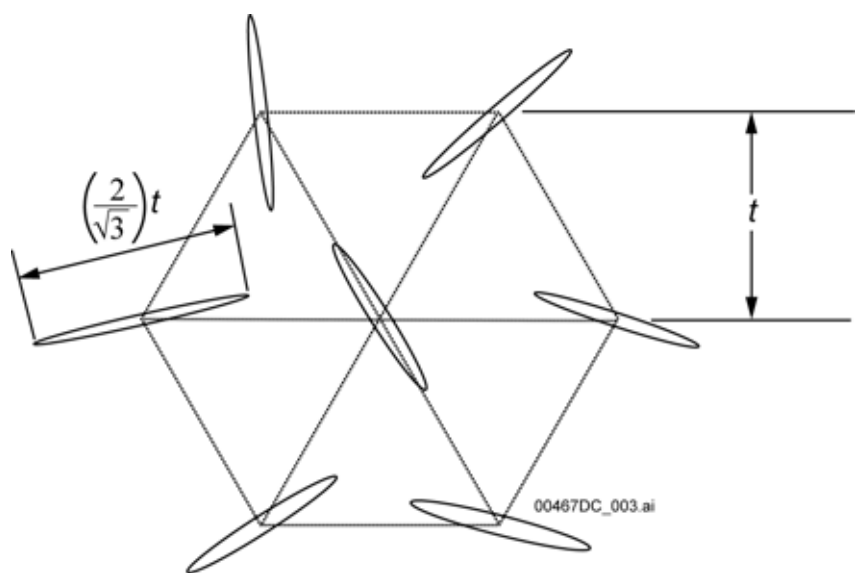

Source: Created for illustrative purposes only.

NOTE: Not to scale.

Figure 6-63. Parallel Rows of Randomly Oriented Cracks with Centers Arranged in a Hexagonal Array (with Row Spacing Equal to Wall Thickness, *t*)

6.7.3.2 Case 2: Hexagonal Array with Side Length, *t,* and Crack Length, *2t*

Consider a hexagonal array with side length *t*, where *t* is the plate thickness (Figure 6-64). Each point of the hexagonal array is the center of a crack with length *2t*. This crack length is the same as that used for the waste package closure weld region, as discussed in Section 6.2.2, in which it was concluded that the crack length was equal to twice the thickness. This geometry allows for cracks, if they lie in the same plane, to overlap significantly (each crack overlaps about half of each of its neighboring cracks) as shown in Figure 6-64. The maximum overlap occurs when the cracks are exactly in line. The overlap will decrease if the crack orientation has some offset from the in-line direction. Conservatively, in calculating the total crack opening area, crack overlap is not considered (i.e., overlapped areas are counted twice) in order to provide an upper bound on the crack area density.

The crack density, ρ_{SCC}, is the average number of cracks in a hexagon of the array divided by the area of the hexagon. As in the previous case, the number of cracks in each hexagonal unit cell is three, regardless of crack orientation. The area of the unit hexagon is calculated as the area of six equilateral triangles with side *t* as:

$$6\left(\frac{\sqrt{3}}{4}\right)(t^2) = \frac{3\sqrt{3}t^2}{2} \qquad \text{(Eq. 38)}$$

It follows that the crack density, ρ_{SCC}, is given by:

$$\rho_{SCC} = \frac{\#\,of\ cracks}{area\,of\ unit\ hexagon} = \frac{3}{\left(\frac{3\sqrt{3}t^2}{2}\right)} = \frac{2}{\sqrt{3}t^2} \qquad \text{(Eq. 39)}$$

Then, using Equations 32 and 37 with $2c = 2t$, the total crack opening area per unit damage area can be expressed as:

$$\rho_{SCC} A_{SCC} = \frac{2}{\sqrt{3}t^2}\frac{(2\pi t^2)\sigma}{E} = \frac{4\pi\sigma}{\sqrt{3}E} \cong 7.26\frac{\sigma}{E} \qquad \text{(Eq. 40)}$$

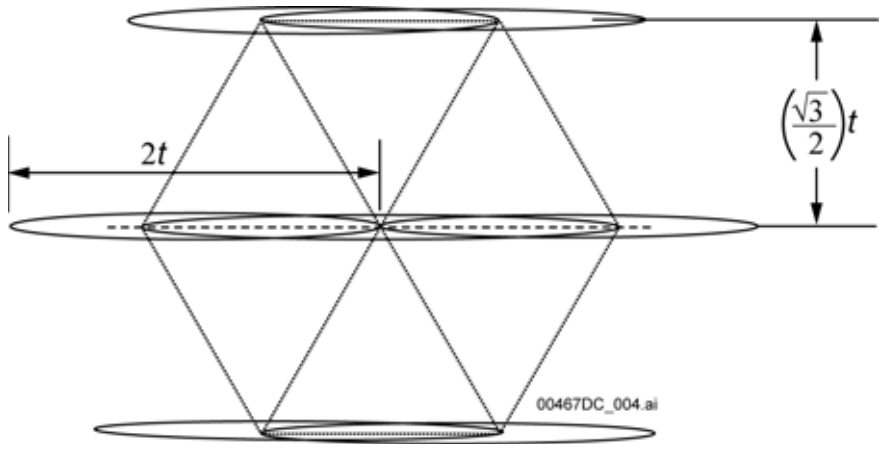

Source: Created for illustrative purposes only.

NOTE: Not to scale.

Figure 6-64. Parallel Rows of Parallel Flaws (with Row Spacing Equal to (√3/2) Wall Thickness)

6.7.3.3 Summary of Primary Conceptual Model for Crack Area Density

The crack area density for Case 1 (where cracks can barely touch) is $\frac{\pi\sigma}{\sqrt{3}E}$, and that for Case 2 (where significant crack overlap is allowed) is $\frac{4\pi\sigma}{\sqrt{3}E}$. The crack area density is shown to be proportional to the applied stress, essentially residual stress due to seismic activity, and inversely proportional to the modulus of elasticity. It does not depend on the wall thickness. Therefore, the crack area density is recommended to be represented as a uniform distribution between $\frac{\pi\sigma}{\sqrt{3}E}$ and $\frac{4\pi\sigma}{\sqrt{3}E}$, i.e.:

$$\text{Crack Area Density} = C\frac{\pi\sigma}{\sqrt{3}E} \qquad \text{(Eq. 41)}$$

where C = epistemic uncertainty factor given by a uniform distribution between 1 and 4.

The use of a uniform distribution is reasonable, as it accurately reflects the lack of knowledge of the exact value of the crack area density. In general, a uniform distribution is appropriate for uncertain quantities where the range can be established by physical arguments or expert knowledge—but not much else is known about the relative likelihood of values within the range (Mishra 2002 [DIRS 163603], Section 2.3). The use of a distribution ranging up to the very conservative upper bound allows for uncertainties, such as the potential for crack overlap and deviations from a regular array of identically shaped cracks, to be appropriately accounted for.

As indicated in Section 6.5.6.2, for conservative purposes, the higher yield strength values (i.e., data from Alloy Digest 1985 [DIRS 178194], p. 2, Table 3, appearing in Table 4-7 of this document) are used in evaluation of stress and stress intensity factor distribution and uncertainties. However, in case of seismic damage analyses, the use of lower yield strength values (i.e., data from Haynes International 1988 [DIRS 101995], p. 15, also appearing in Table 4-7) leads to greater calculated damaged area and, therefore, is a conservative approach.

The yield strength of the material should be used as a very conservative estimate for the stress component in the crack area density calculation. The yield strength is considered conservative because the process of crack initiation and through-wall crack propagation will result in significant reduction in the residual stress. The use of material yield strength will give a conservative estimate of the crack area density appropriate for probabilistic evaluation. Values of the Alloy 22 yield strength and modulus of elasticity at room temperature and at 150°C (the temperature at which the structural calculations of the waste package exposed to ground motion were conducted (SNL 2007 [DIRS 176828])) are shown in the second and third columns of Table 6-17. The linearity of yield strength versus temperature within the temperature range of interest is substantiated by the measured yield strength data listed in Table 4-7. The value of the Alloy 22 yield strength at 150°C (approximately 423 K) was thus determined by linear interpolation between the values for the Alloy 22 yield strength at 366 K(93°C, 200°F) and those at 477 K (204°C, 400°F) (Table 4-7):

$$Yield\ Strength @ 423\,\mathrm{K} = 283\,\mathrm{MPa} - \left(\frac{477\,\mathrm{K} - 423\,\mathrm{K}}{477\,\mathrm{K} - 366\,\mathrm{K}}\right) \cdot \left(283\,\mathrm{MPa} - 338\,\mathrm{MPa}\right) \cong 310\,\mathrm{MPa} \qquad \text{(Eq. 42)}$$

The value of the Alloy 22 modulus of elasticity at 150°C (approximately 423 K) was determined by linear interpolation between the values for the Alloy 22 Young's moduli at 366 K and 477 K (Table 4-7):

$$Young's\ Modulus @ 423\,\mathrm{K} = 196\,\mathrm{GPa} - \left(\frac{477\,\mathrm{K} - 423\,\mathrm{K}}{477\,\mathrm{K} - 366\,\mathrm{K}}\right) \cdot \left(196\,\mathrm{GPa} - 203\,\mathrm{GPa}\right) \cong 199\,\mathrm{GPa} \qquad \text{(Eq. 43)}$$

In Table 6-17, calculations of the crack length (hexagon side length), crack density, crack width, crack opening area, and crack area density are shown for various barrier thicknesses for both hexagonal cases. Table 6-17 shows that the range of the crack area density (crack area per unit of seismically damaged area) ranges from 3.27×10^{-3} to 1.31×10^{-2} at room temperature, and 2.82×10^{-3} to 1.19×10^{-2} at 150°C. It is recommended that the room temperature range of crack area density be used for performance assessment as this choice yields higher (more conservative) crack area densities.

Table 6-17. Crack Characteristics for Hexagonal Geometry

Temperature (°C)	Yield Strength (MPa)	Modulus of Elasticity (GPa)	Case	Barrier Thickness[a] (mm)	Crack Length[b] (mm)	Crack Density[c] (/mm^2)	Crack Width[d] (mm)	Crack Opening Area[e] (mm^2)	Crack Area Density[f]
Room	372	206	1		$\frac{2t}{\sqrt{3}}$	$\frac{\sqrt{3}}{2t^2}$	$\delta = \frac{(4c)\sigma}{E}$	$A_{SCC} = \frac{(2\pi c^2)\sigma}{E}$	$\rho_{SCC} A_{SCC} \cong 1.81 \frac{\sigma}{E}$
				18	20.78	2.67×10^{-3}	0.075	1.23	3.27×10^{-3}
				20	23.09	2.17×10^{-3}	0.083	1.51	3.27×10^{-3}
				23	31.89	1.64×10^{-3}	0.115	2.89	3.27×10^{-3}
				25	34.67	1.39×10^{-3}	0.125	3.41	3.27×10^{-3}
			2		2t	$\frac{2}{\sqrt{3}t^2}$	$\delta = \frac{(4c)\sigma}{E}$	$A_{SCC} = \frac{(2\pi c^2)\sigma}{E}$	$\rho_{SCC} A_{SCC} \cong 7.26 \frac{\sigma}{E}$
				18	36.00	3.56×10^{-3}	0.130	3.68	1.31×10^{-2}
				20	40.00	2.89×10^{-3}	0.144	4.54	1.31×10^{-2}
				23	46.00	2.18×10^{-3}	0.166	6.00	1.31×10^{-2}
				25	50.00	1.85×10^{-3}	0.181	7.09	1.31×10^{-2}
150	310	199	1		$\frac{2t}{\sqrt{3}}$	$\frac{\sqrt{3}}{2t^2}$	$\delta = \frac{(4c)\sigma}{E}$	$A_{SCC} = \frac{(2\pi c^2)\sigma}{E}$	$\rho_{SCC} A_{SCC} \cong 1.81 \frac{\sigma}{E}$
				18	20.78	2.67×10^{-3}	0.065	1.06	2.82×10^{-3}
				20	23.09	2.17×10^{-3}	0.072	1.31	2.82×10^{-3}
				23	26.56	1.64×10^{-3}	0.083	1.73	2.82×10^{-3}
				25	28.87	1.39×10^{-3}	0.090	2.04	2.82×10^{-3}
			2		2t	$\frac{2}{\sqrt{3}t^2}$	$\delta = \frac{(4c)\sigma}{E}$	$A_{SCC} = \frac{(2\pi c^2)\sigma}{E}$	$\rho_{SCC} A_{SCC} \cong 7.26 \frac{\sigma}{E}$
				18	20.78	2.67×10^{-3}	0.065	1.06	1.19×10^{-2}
				20	23.09	2.17×10^{-3}	0.072	1.31	1.19×10^{-2}

Table 6-17. Crack Characteristics for Hexagonal Geometry (Continued)

Temperature (°C)	Yield Strength (MPa)	Modulus of Elasticity (GPa)	Case	Barrier Thickness[a] (mm)	Crack Length[b] (mm)	Crack Density[c] (/mm^2)	Crack Width[d] (mm)	Crack Opening Area[e] (mm^2)	Crack Area Density[f]
				23	26.56	1.64×10^{-3}	0.083	1.73	1.19×10^{-2}
				25	28.87	1.39×10^{-3}	0.090	2.04	1.19×10^{-2}

Source: Output DTN: MO0702PASTRESS.002, file *Model Output DTN.doc*, Table 8-13.

NOTES: [a] The values of the barrier thickness are for illustration purposes only.

[b] The crack length equals $\frac{2t}{\sqrt{3}}$ for Case 1 and $2t$ for Case 2.

[c] The crack density equals $\frac{\sqrt{3}}{2t^2}$ for Case 1 and $\frac{2}{\sqrt{3}t^2}$ for Case 2.

[d] The crack width of a single crack is given by Equation 29 for the given thickness for each case.

[e] The crack opening is calculated from Equation 30 for the two cases.

[f] The crack area density is calculated from Equation 33 for case 1 and Equation 36 for case 2.

6.7.4 Alternative Conceptual Model for Crack Area Density: Circular Geometry

This section considers a conceptual model of a through-wall crack circumscribing a circular damaged area. The main purpose of this model is to provide an alternative mathematical model for crack area density, which can be used in validation of the primary crack area density model. Even though this model leads to a fully circumscribed area, the inner area material would not fall out due to the roughness of crack surfaces. It should be emphasized that this calculation and associated postulated crack morphology are strictly for calculating an alternative crack opening area. They are not meant to imply that this crack morphology is observed.

Timoshenko and Goodier (1970 [DIRS 121096], pp. 68 to 71) present the solution to a hollow cylinder under internal pressure (p_i) and external pressure (p_o) of inner radius (a) and external radius (b) (Figure 6-65) under plane stress conditions. This solution can be easily adapted to determine the displacement about a hole in a two-dimensional infinite body subjected to a radial stress, S. The surface of the hole can be considered as the crack surface for the purposes of this analysis. For this radially symmetric problem, the following is true (Timoshenko and Goodier 1970 [DIRS 121096], p. 70):

$$\varepsilon_\theta = \frac{u}{r} \qquad \text{(Eq. 44)}$$

Further, Hooke's Law can be written for an isotropic material for plane stress as:

$$E\varepsilon_\theta = \sigma_\theta - \nu\sigma_r \qquad \text{(Eq. 45)}$$

where u = radial displacement
r = distance from the origin in a polar coordinate system
E = modulus of elasticity
ν = Poisson's ratio.

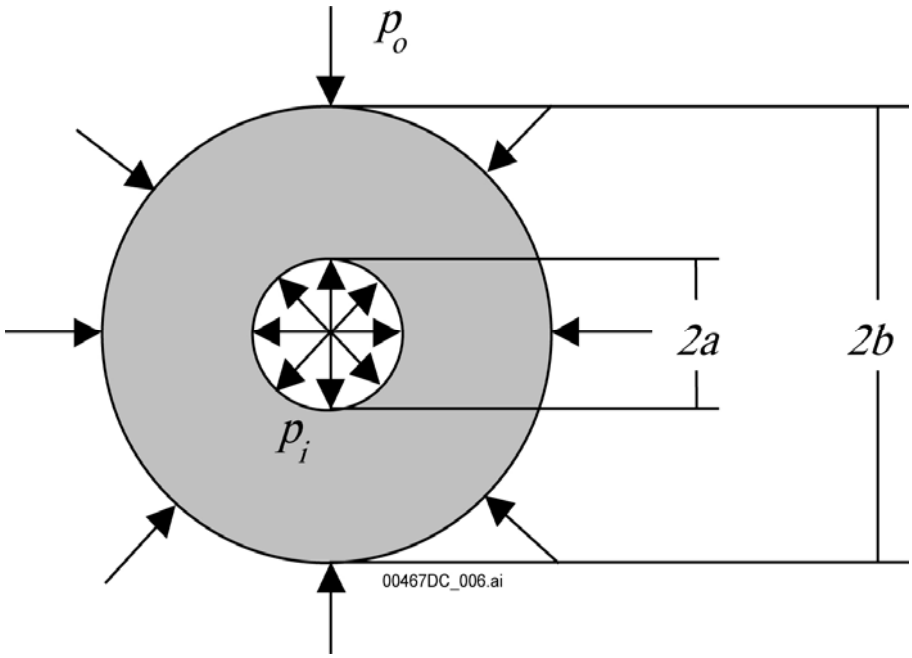

Source: Created for illustrative purposes only.

Figure 6-65. Hollow Cylinder of Inner Radius *a* and Outer Radius *b* Subject to Internal Pressure p_i and External Pressure p_o

The following are expressions for the radial and tangential stress components (Timoshenko and Goodier 1970 [DIRS 121096], p. 70):

$$\sigma_r = \frac{a^2 b^2 (p_o - p_i)}{b^2 - a^2}\frac{1}{r^2} + \frac{p_i a^2 - p_o b^2}{b^2 - a^2}$$
$$\sigma_\theta = -\frac{a^2 b^2 (p_o - p_i)}{b^2 - a^2}\frac{1}{r^2} + \frac{p_i a^2 - p_o b^2}{b^2 - a^2} \qquad \text{(Eq. 46)}$$

For the purposes of this analysis, b approaches infinity (infinite plate), $p_o = -S$, with interest in the radial displacements at $r = a$ (the surface of the hole). With these conditions, at $r = a$, $\sigma_r = 0$, and $\sigma_\theta = 2S$. Using Equations 38 and 39, the radial displacement, u, at $r = a$ is:

$$u = \frac{2aS}{E} \qquad \text{(Eq. 47)}$$

More generally, it has been shown by analysis that the radial displacement (u) at the surface of the hole of radius, r, under the action of a radial stress, σ, could be written as:

$$u = \frac{2r\sigma}{E} \qquad \text{(Eq. 48)}$$

where r is the radius of the hole (i.e., radius of the damaged area) and σ is applied stress.

The radial displacement (u) in Equation 46 can be considered the crack opening for a crack circumscribing a damaged area with a radius of r. This is equivalent to the conservative case where the inner material is detached (i.e., cracked through-wall around the entire circumference) and not subjected to any stress (i.e., not decreasing the displacement particularly by "pulling" on the outer material). The crack opening area of this crack can be expressed as:

$$A_{SCC} = 2\pi r u = 2\pi r \frac{2r\sigma}{E} = \frac{4\pi r^2 \sigma}{E} \qquad \text{(Eq. 49)}$$

The damaged area is πr^2. Therefore, realizing that there is one circular crack in each circular area of radius r, the crack area density can be expressed as:

$$\rho_{SCC} A_{SCC} = \left(\frac{1}{\pi r^2}\right)\left(\frac{4\pi r^2 \sigma}{E}\right) = 4\frac{\sigma}{E} \qquad \text{(Eq. 50)}$$

The crack area density ($\rho_{SCC}\, A_{SCC}$) depends only on the stress state and the modulus of elasticity. Values of the Alloy 22 yield strength and modulus of elasticity at room temperature and at 150°C are shown in the second and third columns of Table 6-18. In Table 6-18, calculations of the crack length, crack density, crack opening area, and crack area density are shown for various radii of the damaged area. The crack area density calculated using values of the Alloy 22 yield strength and modulus of elasticity at room temperature is about 7.22×10^{-3}, while the crack area density calculated at 150°C is about 6.23×10^{-3}.

Table 6-18. Crack Characteristics for Circular Geometry

Temperature (°C)	Yield Strength (MPa)	Modulus of Elasticity (GPa)	Radius[a] (mm)	Crack Length[b] (mm)	Crack Density[c] (/mm^2)	Crack Width[d] (mm)	Crack Opening Area[e] (mm^2)	Crack Area Density[f]
Room	372	206		$2\pi r$	$1/\pi r^2$	$u = \frac{2r\sigma}{E}$	$A_{SCC} = \frac{4\pi r^2 \sigma}{E}$	$\rho_{SCC} A_{SCC} = 4\frac{\sigma}{E}$
			18.0	113.09400	0.00098	0.06501	7.35221	0.00722
			20.0	125.66000	0.00080	0.07223	9.07680	0.00722
			23.0	144.50900	0.00060	0.08307	12.00407	0.00722
			25.0	157.07500	0.00051	0.09029	14.18250	0.00722

Table 6-18. Crack Characteristics for Circular Geometry (Continued)

Temperature (°C)	Yield Strength (MPa)	Modulus of Elasticity (GPa)	Radius[a] (mm)	Crack Length[b] (mm)	Crack Density[c] (/mm^2)	Crack Width[d] (mm)	Crack Opening Area[e] (mm^2)	Crack Area Density[f]
150	310	199		2π r	$1/\pi r^2$	$u = \frac{2r\sigma}{E}$	$A_{SCC} = \frac{4\pi r^2 \sigma}{E}$	$\rho_{SCC} A_{SCC} = 4\frac{\sigma}{E}$
			18.0	113.09400	0.00098	0.05608	6.34236	0.00623
			20.0	125.66000	0.00080	0.06231	7.83007	0.00623
			23.0	144.50900	0.00060	0.07166	10.35527	0.00623
			25.0	157.07500	0.00051	0.07789	12.23448	0.00623

Output DTN: MO0702PASTRESS.002, file *Table 8-13.xls*.

NOTES: [a] Values of the barrier thickness are for illustration purposes only.
[b] Crack length equals $2\pi r$.
[c] Crack density equals $1/\pi r^2$ from Equation 40.
[d] Crack width is given by Equation 44.
[e] Crack opening is calculated from $2\pi r u$ from Equation 45.
[f] Crack area density is calculated from Equation 46.

6.8 SCC OF TITANIUM DRIP SHIELD MATERIALS

This section will discuss a number of topics related to the treatment of stress corrosion cracking of titanium drip shield materials: (1) the SCC initiation threshold stress of Titanium Grade 7 (Section 6.8.3.1), (2) SCC initiation threshold stress of Titanium Grades 28 and 29 (Section 6.8.3.2), (3) the SCC crack growth in drip shield materials (Section 6.8.4), (4) the SCC threshold stress intensity factors for Titanium Grade 7 (Section 6.8.4.2.2), and for Titanium Grades 28 and 29 (Section 6.8.4.2.4), (5) the seismic crack density model for the drip shield (Section 6.8.5), (6) SCC crack "plugging" (Section 6.8.6), and (7) the low-temperature creep of titanium alloys (Section 6.8.7). Weld flaws are not addressed because the drip shield is thermally stress-relieved before emplacement. Several of the subjects discussed in this section are not considered to be "models." For instance, the SCC crack growth rate is a measured parameter only, and the low-temperature creep section only summarizes the literature observations on the subject. The same argument applies to the SCC crack "plugging" section. Therefore, only the seismic crack density is considered as the "model." This model will be validated in Section 7.5.2.

The principal sources of stress that could potentially result in SCC in the Titanium Grades 7 and 29 drip shield are (1) weld-induced residual stress, (2) plastic deformation-induced residual stress caused by seismic events or rockfall, and (3) sustained stresses due to drift-collapse rubble-loading. The fabricated drip shield will be post-weld annealed to mitigate weld-induced residual stresses (SNL 2007 [DIRS 179354]). *Creep Deformation of the Drip Shield* (BSC 2005 [DIRS 174715], Section 5.4) presents an analysis of the consequence of residual stress due to rockfalls and sustained stresses due to drift collapse rubble loading. SCC caused by seismic events is discussed in Section 6.8.5. The threshold stress for crack initiation developed in Section 6.8.3 is used as the through-wall crack penetration (breach) criterion for rockfall, rubble loading, and other seismic-induced stress. However, as described in Section 6.8.3, this criterion is highly conservative.

No model development is conducted in the following activities: (1) the drip shield SCC crack growth rate (Section 6.8.4) is a measured parameter; (2) the low-temperature creep section (Section 6.8.7) summarizes the literature observations on the subject; and (3) the SCC crack initiation threshold stress criteria are experimentally derived parameters. This is also true for the SCC crack "plugging" section (Section 6.8.6). However, for purposes of defensibility, explicit confidence-building activities were conducted. For the drip shield, the SCC initiation threshold stresses (for Titanium Grades 7, 28, and 29) (Section 6.8.3), and threshold stress intensity factors (for Titanium Grades 7, 28, and 29) (Sections 6.8.4.2.2 and 6.8.4.2.4) are discussed in Section 7.4 to provide additional confidence.

Technical Work Plan for Postclosure Engineered Barrier Degradation Modeling (SNL 2007 [DIRS 178849], Section 2.3.2) states that the drip shield SCC modeling warrants a low level of confidence (Level I). This drip shield SCC-related model will be validated in Sections 7.4 and 7.5.2 by using the validation activities specified in *Technical Work Plan for Postclosure Engineered Barrier Degradation Modeling* (SNL 2007 [DIRS 178849], Section 2.3.2).

6.8.1 A Brief Introduction to Titanium Alloys

The current drip shield top and side plates are fabricated from α-phase Titanium Grade 7 (UNS R52400), an alloy analogous to commercial purity Titanium Grade 2 with 0.12% to 0.25% palladium added to increase corrosion resistance. Another Titanium Grade 2 analogue discussed here is Titanium Grade 16 (UNS R52402), a version of Titanium Grade 7 with lower palladium content. Structural support bulkheads and side support beams welded to the plate material are fabricated using a higher-strength material, α+β-phase Titanium Grade 29 (UNS R56404), a ruthenium-containing analog to the extra low interstitial (ELI) grade, Titanium Grade 23 (UNS R56407, also called Ti-6Al-4V ELI). Titanium Grade 29 (UNS R56404) contains 0.08% to 0.14% ruthenium. The weld filler wire will be the near-α- and α-β- phase intermediate strength Titanium Grade 28 (UNS R56323), which is a ruthenium-containing analogue (0.08% to 0.14% ruthenium) of Titanium Grade 9 (UNS R56320). The chemical compositions of the titanium alloys discussed in this section are shown in Table 6-19 (ASTM B 265-02 [DIRS 162726], Table 2).

Table 6-19. ASTM Specifications for Chemical Compositions (wt %) of Relevant Titanium Alloys

ASTM Grade	UNS	N	C	H	O	Fe	Al	V	Pd	Ru	Residual (each)	Residual (total)
12	R53400	0.03	0.08	0.015	0.25	0.30	–	–	–	–	0.2 to 0.4 Molybdenum*	0.6 to 0.9 Nickel*
2	R50400	0.03	0.08	0.015	0.25	0.30	–	–	–	–	0.1	0.4
7	R52400	0.03	0.10	0.015	0.25	0.30	–	–	0.12 to 0.25	–	0.1	0.4
16	R52402	0.03	0.08	0.015	0.25	0.30	–	–	0.04 to 0.08	–	0.1	0.4
5	R56400	0.05	0.08	0.015	0.20	0.40	5.5 to 6.75	3.5 to 4.5	–	–	0.1	0.4

Table 6-19. ASTM Specifications for Chemical Compositions (wt %) of Titanium Alloys (Continued)

ASTM Grade	UNS	N	C	H	O	Fe	Al	V	Pd	Ru	Residual (each)	Residual (total)
23	R56407	0.03	0.08	0.0125	0.13	0.25	5.5 to 6.5	3.5 to 4.5	–	–	0.1	0.4
24	R56405	0.05	0.08	0.015	0.20	0.40	5.5 to 6.75	3.5 to 4.5	0.04 to 0.08	–	0.1	0.4
9	R56320	0.03	0.08	0.015	0.15	0.25	2.5 to 3.5	2.0 to 3.0	–	–	0.1	0.4
28	R56323	0.03	0.08	0.015	0.15	0.25	2.5 to 3.5	2.0 to 3.0	–	0.08 to 0.14	0.1	0.4
29	R56404	0.03	0.08	0.015	0.13	0.25	5.5 to 6.5	3.5 to 4.5	–	0.08 to 0.14	0.1	0.4

Source: Reorganized from ASTM B 265-02 [DIRS 162726], Table 2.

NOTE: Some rows are highlighted to indicate the different categories of the materials for added transparency.

* Residual (each) and residual (total) for Ti Grade 12 are 0.1 and 0.4, respectively.

Table 6-20 shows the mechanical properties of the titanium alloys discussed in this section (ASTM B 265-02 [DIRS 162726], Table 1). As can be seen from Table 6-20, Titanium Grades 7 and 16 have mechanical properties identical to Titanium Grade 2 (their analogue, which does not contain palladium), while Titanium Grades 23 and 29 have mechanical properties similar to Titanium Grade 5. Due to its higher interstitial content than Titanium Grade 23, Titanium Grade 5 has slightly higher mechanical properties but lower notch toughness (Boyer et al. 2003 [DIRS 174636], p. 581). The mechanical properties of wrought annealed Titanium Grade 9 has mechanical properties similar to the Titanium Grade 9 weld metal (Boyer et al. 2003 [DIRS 174636], p. 283), and the presence of the small ruthenium addition in Titanium Grade 28 would not be expected to change the mechanical properties, as indicated in Table 6-20. From Table 6-19 and Table 6-20, it is clear that the slightly lower yield strength of Titanium Grade 29 as compared with its non-ruthenium analogue, Titanium Grade 5, is due to its lower oxygen content (0.13 wt % as compared with 0.20 wt %), rather than to the presence of ruthenium, because the yield strength of Titanium Grade 24 is identical to that of Titanium Grade 5 (both are 0.20 wt % of oxygen), just as the addition of palladium does not alter the mechanical properties of Titanium Grade 7 or 16.

Table 6-20. ASTM Specifications of Mechanical Properties of Relevant Titanium Alloys

Material	UNS Designation	Minimum Tensile Strength		Yield Strength, 0.2 % Offset				Minimum Elongation in 2 in (%)
				Minimum		Maximum		
		ksi	MPa	ksi	MPa	ksi	MPa	
Grade 12	R53400	70	483	50	345	–	–	18
Grade 2	R50400	50	345	40	275	65	450	20
Grade 7	R52400	50	345	40	275	65	450	20
Grade 16	R52402	50	345	40	275	65	450	20
Grade 5	R56400	130	895	120	828	–	–	10
Grade 23	R56407	120	828	110	759	–	–	10
Grade 24	R56405	130	895	120	828	–	–	10
Grade 9	R56320	90	620	70	483	–	–	15
Grade 28	R56323	90	620	70	483	–	–	15
Grade 29	R56404	120	828	110	759	–	–	10

Source: Reorganized from ASTM B 265-02 [DIRS 162726], Table 1.

The relationship between the relevant titanium alloys discussed in this document in light of their chemical compositions and mechanical properties is summarized in Figure 6-66. The alloys grouped by the dashed lines in Figure 6-66 have similar mechanical properties regardless of their chemical compositions (Table 6-19 and Table 6-20).

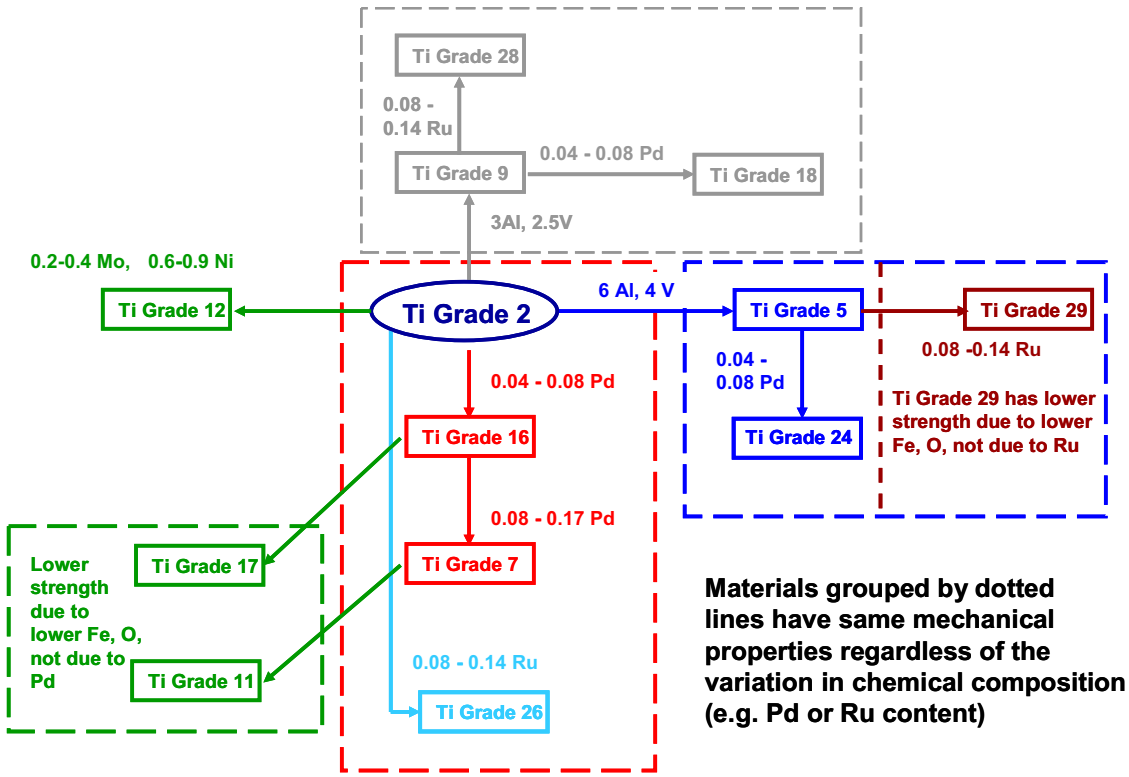

Source: Adapted from Table 6-19 and Table 6-20.

NOTE: Alloys grouped by the dashed lines have similar mechanical properties regardless of their chemical compositions.

Figure 6-66. Relationship between Relevant Titanium Alloys

Heat numbers and compositions of titanium alloy materials employed in various YMP-sponsored SCC-related experimental tests are summarized in Table 6-21 (for GE GRC tests) and Table 6-28 (for LLNL tests).

Table 6-21. Heat and Composition of Materials Tested at GE GRC

Material	Heat	Composition in Wt %
Titanium Grade 7	S-3024, Lot P683	Ti + 0.01N 0.02C 0.007H 0.12Fe 0.14O 0.13Pd
	CN0171	Ti + 0.15Fe 0.16Pd 0.01N 0.045O 0.01C
Titanium Grade 28	870749601	Ti + 2.96Al 2.54V 0.11Fe 0.13Ru 0.006N 0.12O 0.01C
Titanium Grade 29	956205	Ti + 6.05Al 3.83V 0.18Fe 0.112Ru 0.007N 0.116O 0.02C

Source: Reproduced from DTN: MO0707SCCIGMER.000 [DIRS 182202], Table 1-1.

6.8.2 SCC Susceptibility of Relevant Titanium Alloys

Titanium Grades 2, 7, and 16

In general, lower strength, α and near-α titanium alloys such as Titanium Grades 2, 7, and 9 are reported to be immune to SCC except in a few specific environments that include anhydrous

methanol/halide solutions, nitrogen tetroxide, red fuming nitric acid and liquid or solid cadmium (ASM International. 1987 [DIRS 103753], p. 674; Been and Grauman 2000 [DIRS 159767], pp. 874 to 877; Schutz 1992 [DIRS 177345]). As none of these environments are relevant to the repository, SCC is unlikely to occur in the Titanium Grade 7 drip shield plate material, especially under aerated conditions present in the repository where a stable passive film is expected to persist.

This is consistent with published literature evaluating the SCC susceptibility of Titanium Grade 7 and less-SCC-resistant Titanium Grade 2 in repository-relevant environments (Fix et al. 2004 [DIRS 169321]; Pulvirenti et al. 2002 [DIRS 159841], Table 2), as well as in a range of other aggressive chloride brine environments (Smailos et al. 1999 [DIRS 177437]; Pan et al. 2002 [DIRS 165536]; Schutz 1986 [DIRS 151162], pp. 513 to 514; Schutz 1985 [DIRS 162361]).

Although Titanium Grade 7 is highly resistant, it may not always be immune to SCC initiation in nonrelevant aggressive halide environments when fluoride ion is present at high concentration without other beneficial oxyanions such as sulfate and nitrate ions. For example, Pulvirenti et al. (2002 [DIRS 159841], Table 2; 2002 [DIRS 177251], Table II) evaluated Titanium Grade 7 U-bends (with an autogenous spot weld at the specimen apex) exposed in a range of concentrated Yucca Mountain groundwater compositions as well as in accelerated conditions in sealed pressure vessels for 30 days at 250°C. The environments tested included concentrated (approximately 1,000 times) simulated J-13 well water with the pH adjusted to 14, unconcentrated J-13 well water, but with approximately 6,100 ppm chloride added and pH acidified to 1 with HCl and unconcentrated J-13 well water with approximately 1,550 ppm fluoride added and the pH adjusted to approximately 5 with hydrogen fluoride. In spite of the accelerating conditions, evidence of SCC initiation was not detected in any of these tests. In contrast, in the same study, SCC initiated in the U-bend apex spot-welded region in one of two U-bends after about 70 days of exposure to 105°C unconcentrated J-13 groundwater (pH of approximately 6.5) but with 1,900 ppm fluoride and 35,500 ppm chloride added. At 155 days, when the test was terminated, the crack had grown across the entire width and thickness (12.5 mm) of the specimen. The crack initiated and propagated in an intergranular manner through most of the cross section with evidence of tight, branching cracking. Near the midthickness, the cracking propagated in a transgranular mode, which is also typical of α and $\alpha+\beta$ titanium alloys, where the characteristic aqueous SCC process is cleavage of the α phase (Simbi 1996 [DIRS 177262], Section 2.5).

In addition to SCC, extensive intergranular attack and pitting to depths of 150 to 400 microns was observed on the Titanium Grade 7 U-bends as well as on unstressed disc specimens exposed to the same nonrelevant aggressive environment. The attack was very likely due to the presence of the high fluoride-plus-chloride concentrations in the absence of relevant concentrations of other potentially inhibiting anions such as sulfate and nitrate. The beneficial effect of sulfate was described in a subsequent paper (Pulvirenti et al. 2003 [DIRS 162574]). These observations of SCC and intergranular attack are obtained under conditions not relevant to the repository. SCC is neither observed under the conditions simulating the repository environments, nor is it expected under those conditions.

Titanium Grades 5, 23, 28, and 29

In contrast to the extremely high SCC resistance of lower-strength titanium alloys such as Titanium Grades 2, 7, and 9 at temperatures up to about 250°C (Schutz 1992 [DIRS 177345]), higher-strength titanium alloys including Titanium Grades 5 and 23 have the potential to undergo SCC in chloride-containing brines, even at room temperature if defects or other stress risers are present (ASM International. 1987 [DIRS 103753], pp. 674, 690, and 694, Table 27, Figure 42).

In more recent testing, investigators at the Center for Nuclear Waste Regulatory Analyses (Pan et al. 2002 [DIRS 165536], Section 4.2) confirmed this high SCC resistance for Titanium Grade 7 and somewhat lower resistance to environmentally assisted cracking for Titanium Grade 5. Pan et al. (2002 [DIRS 165536]) performed slow strain rate (extension rate of 1.8×10^{-5} mm/s) tests on notched tensile specimens of Titanium Grades 2, 7, and 5 in deaerated 1 M NaCl with and without 0.1 M NaF (no nitrate or sulfate ions were present) at 95°C. With the 0.1 M fluoride present, they found only a slight environmentally assisted transgranular cracking effect (likely accelerated due to HIC) for the Titanium Grades 2 and 7 materials. However, for the higher-strength Titanium Grade 5 material, the investigators found what was described as a significant ductility loss due to environmentally assisted transgranular cracking. As the environment tested was deaerated and reducing, and the specimens contained stress-concentrating notches, it is reasonable to assume that the SCC effect was accelerated due to HIC. In another series of SSRTs on cathodically polarized Titanium Grade 7 and higher-strength Titanium Grade 12 specimens exposed in acidified 5% NaCl (pH of approximately 2.7) brine at 90°C, Roy et al. (2001 [DIRS 177255], pp. 211 to 218) found only shallow transgranular surface cracking in a hydrogen-charged surface layer on Titanium Grade 7. However, Roy et al. (2001 [DIRS 177255], pp. 211 to 218) found no evidence of propagation below the hydrided surface layer and no drop in ductility or time to failure consistent with the lack of SCC or HIC failure observed. In contrast, the higher-strength Titanium Grade 12 alloy (containing no palladium or ruthenium) exhibited a drop in ductility and time to failure at the more negative applied potentials consistent with a contribution from HIC. For both alloys, the extent of secondary surface cracking was only minor at open-circuit potential.

Based on this and other literature observations, Titanium Grade 5 appears to be more susceptible to environmentally assisted cracking than Titanium Grades 7 and 29. However, Titanium Grade 29 and its ruthenium-free analogue, Titanium Grade 23, are ELI versions of Titanium Grade 5, as are Titanium Grade 9 and its ruthenium analogue, Titanium Grade 28. These ELI versions of Titanium Grades 5 and 9 contain less oxygen than Titanium Grade 5 (Table 6-19). Been and Grauman (2000 [DIRS 159767]) and Schutz et al. (2000 [DIRS 177257], pp. 874 to 876) report that the ELI versions of Titanium Grade 5 (including Titanium Grade 23) have substantially lower SCC susceptibility than Titanium Grade 5.

Further, dissolved platinum group metals such as ruthenium have an inhibiting effect on crack propagation, possibly by favoring the recombination of hydrogen atoms as opposed to hydrogen absorption (Schutz et al. 2000 [DIRS 177257]). Thus it is expected that Titanium Grades 28 and 29 will have further improved resistance to environmentally assisted cracking over their non-ruthenium containing analogs. The high resistance of Titanium Grades 28 and 29 to environmentally assisted cracking has been confirmed for a range of brines including acidified sodium chloride, geothermal brines, and “sweet and sour” brines typical of the chemical

processing and petrochemical industries, off-shore oil production, and electric power generation from geothermal sources (Schutz 1995 [DIRS 102790], Table 5; Schutz et al. 2000 [DIRS 177257]).

6.8.3 SCC Crack Initiation for Drip Shield Materials

As described in Section 6.2 for Alloy 22, in the absence of cyclic stresses, SCC will not initiate on a "smooth surface" of an otherwise SCC-susceptible alloy if the surface stress is below a threshold value defined as the threshold stress (ASM International 1987 [DIRS 103753], p. 276). A "smooth" surface is one without sharp defects such as notches and weld flaws. These sharp defects can generate a significant stress intensity factor.

As the yield strength of a material varies in terms of the conditions of the materials and the testing method adopted, the yield strength of Titanium Grade 7 has multiple values in literature. As the yield strength of a material is a function of temperature, for convenience of discussion, it is necessary to present all the yield strength values, both reported earlier and interpolated in this document. The application of various yield strength values for various purposes is also rationalized.

As shown in Table 4-7, several values of the yield strength of Titanium Grade 7 are used in this document. The yield strength of Titanium Grade 7 based on different data sources is summarized in Table 6-22. Table 6-23 lists the yield strength data for Titanium Grades 23, 28, and 29 that are used in Section 6.8.3.2.

Table 6-22. Input Data for Yield Strength of Titanium Grade 7

Data Source	Value of Yield Strength	Note
ASME 2001 [DIRS 158115], Section II, Part D, Table Y-1, pp. 632 to 634	276 MPa at room temperature (21°C) (70°F, 294 K) 176 MPa at 149°C (300°F, 422 K)	Values are used for modeling purposes in Section 6.8.3.1.3
DTN: MO0707SCCIGMER.000 [DIRS 182202], Table 2-4	248 MPa measured in 125°C air.	Value is used in discussion of GE GRC test results in Section 6.8.3.1.1
DTN: MO0003RIB00073.000 [DIRS 152926]*	362 MPa (52.5 ksi) at room temperature (21°C) (70°F, 294 K)* 145 MPa (21 ksi) at 204°C (400°F, 477 K) * 107 MPa (15.5) at 316°C (600°F, 589 K)*	Value is used in discussion of LTCTF test results in Section 6.8.3.1.2.

Source: Table 4-7.

NOTE: * Yield strength values listed are the average of the values listed in DTN: MO0003RIB00073.000 [DIRS 152926]. The room temperature value (362 MPa) is fully consistent with the actual measured yield strength value for the Titanium Grade 7 material tested at LTCTF (Foreman 1998 [DIRS 178278], p. 2).

Table 6-23. Input Data for Yield Strength of Titanium Grades 5, 28, and 29

Material	Data Source	Value of YS	Note
Yield strength for Titanium Grades 23 and 29	ASTM B 265-02 [DIRS 162726]	759 MPa at room temperature (21°C) (70°F, 294 K)	Spec minimum value
Temperature dependence of yield strength for Titanium Grades 23 and 29*	Donachie 2002 [DIRS 178207], Table 7	87% of room temperature YS at 93°C (200°F, 366 K) 70% of room temperature yield strength at 204°C (400°F, 477 K)	Room temperature value is assumed to be 759 MPa in this document
Yield strength for Titanium Grade 29	DTN: MO0705SCCIGM06.000 [DIRS 180869], file *GE-GRC-Final_Sept-2006-Rev3.doc*, Table 8	724 MPa (105 ksi) 125°C	Measured in 125°C air
Yield strength for Titanium Grade 29	DTN: MO0705SCCIGM06.000 [DIRS 180869], file *GE-GRC-Final_Sept-2006-Rev3.doc*, Table 8	123 ksi to 125 ksi (848 MPa to 862 MPa) at room temperature	Measured in air (RTI 2003 [DIRS 178467])
Yield strength for Titanium Grade 28	ASTM B 265-02 [DIRS 162726]	483 MPa at room temperature (21°C) (70°F, 294 K)	Spec minimum value

Source: Table 4-7.

NOTE: *In Donachie (2002 [DIRS 178207], Table 7), only the yield strength values of Ti-6Al-4V (Titanium Grade 5) are listed. However, Titanium Grades 23 and 29 are ELI variants for Titanium Grade 5 (Ti-6Al-4V) that result in a small reduction in room temperature yield strength (10 ksi or 8%). Because of the same alloying element compositions, the reduction in yield strength with temperature should be equivalent.

6.8.3.1 SCC Initiation Response of Titanium Grade 7

6.8.3.1.1 Constant-Load Tests for Titanium Grade 7

The principal test campaign used to establish a threshold stress for stress corrosion crack initiation for the drip shield titanium alloys used constant-load testing. In constant-load testing, a fixed load is applied to each test specimen exposed to the brine environment and the time to failure is recorded. The failure time involves the time to crack initiation plus the time to propagate to specimen overload and failure. However, the large majority of the failure time is involved in crack initiation. Once a crack initiates and starts to propagate, the cross-sectional stress rises rapidly and leads to specimen overload failure.

Using the Keno Test described in DTN: LL021105312251.023 ([DIRS 161253], Section 2.2), GE GRC ran two long-term constant-load test campaigns with the second run currently still going:

- Keno test run 1 was the initial "scoping test," which ran for a total test time of 1,922 hours. Six mill-annealed and six 20% cold-worked Titanium Grade 7

constant-load specimens were tested in 105°C-125°C diluted BSW, along with specimens fabricated from stainless steel and Alloy 22.

- Keno test Run 2 is a larger-scale test, in which 185 constant-load specimens were initially tested in 105°C diluted BSW (DTN: LL021105312251.023 [DIRS 161253], Table 2-2) for a total initial test time of about 25,000 hours (approximately 2.9 years). Among these 185 specimens, 23 were fabricated from as-received, mill-annealed Titanium Grade 7 as indicated in DTN: LL021105312251.023 ([DIRS 161253], Table 2-3).

- Subsequent to the initial 25,000-hour Run 2 test, the failed specimens were removed for examination along with selected unfailed specimens of Alloy 22 and Stainless Steel Type 316NG. The test was restarted and is still underway with the remaining specimens plus new Titanium Grade 7 specimens loaded to lower stresses as well as Titanium Grade 29 specimens. This part of the test is considered as the continuation of Run 2.

The test solution for both test runs was an aerated, concentrated J-13 groundwater-based, carbonate seepage brine with an initial composition given in DTN: LL021105312251.023 ([DIRS 161253], Table 2-2). The target test solution composition was 0.27M Na_2CO_3, 0.35M KCl, 0.41M NaCl, 0.013M NaF, 0.43M $NaNO_3$, 0.03M Na_2SO_4, and 0.04M $Na_2SiO_3.9H_2O$. This composition represents a solution diluted to yield approximately 15% of the concentration of BSW and is used to simulate the chemistry of one of the concentrated Yucca Mountain seepage waters. At 105°C, the pH value of this diluted BSW solution is reported as 10.3 (DTN: LL021105312251.023 [DIRS 161253], Table 2-1, p. 99). Basic pH, carbonate-type brines containing fluoride ions tend to be the most aggressive repository-relevant brines with respect to SCC initiation for Alloy 22 and for titanium alloys. For example, for titanium alloy U-bend specimens (Titanium Grades 7, 12, and 16) exposed in the LLNL LTCTF for up to five years, SCC was observed, but only in Titanium Grade 12 welded specimens exposed to the basic SCW environment (Fix et al. 2004 [DIRS 169321]). This water composition is similar to the diluted BSW brine used in the Keno tests but with a lower pH value between 9 and 10.

Time-to-failure results are plotted as a function of applied stress and often as the ratio of applied stress to yield strength in an attempt to normalize the large differences in yield strength between materials used in the study. Tensile tests were performed in 125°C air to determine applicable yield strength values. Yield strength results (used in ensuing time-to-failure plots) are presented in Table 6-24.

Table 6-24. Yield Strength of Titanium Grade 7 Material Used in GE GRC Keno Test Measured by GE GRC in 125°C Air

Material/Condition	Yield Strength (ksi)	Yield Strength (MPa)
Titanium Grade 7 As-received	36	248
Titanium Grade 7 20% Cold-worked	72.5	500

Source: DTN: MO0707SCCIGMER.000 [DIRS 182202], Table 2-4.

Due to the materials heats and testing methods, the yield strength values of Titanium Grade 7 shown in Table 6-24 are somewhat different from those shown in Table 4-7. In this document, therefore, the values measured by GE GRC (Table 6-24) are used when discussing GE GRC test results, while the other appropriate yield strength values shown in Table 4-7 are used when discussing other sets of data, as well as modeling.

GE GRC Keno Test Run 1 Results

Test results for the initial Keno scoping test run 1, performed in 105°C to 125°C diluted BSW brine are plotted in Figure 6-67 (DTN: LL021105312251.023 [DIRS 161253], Figure 2-5). These constant-load tests were performed in general conformance with ASTM G 49-85 [DIRS 171562] but modified as documented in DTN: LL021105312251.023 ([DIRS 161253], Section 2.2). As can be seen in the referenced plot of maximum applied stress versus time-to-failure (with specimen failure times listed in DTN: LL021105312251.023 ([DIRS 161253], Table 2-2)), reported failure times for mill annealed and for shot-peened Titanium Grade 7 ranged from as little as 0.7 hours to about 50 hours when stressed to about 50 ksi (345 MPa) (i.e., about 139% of the mill annealed yield strength at 125°C ($YS_{(125°C)}$) shown in Table 6-24). As will be shown later in this section (Figure 6-69), the high resistance or immunity of annealed Titanium Grade 7 to SCC is further confirmed by the ductile dimpling-type fractography present in the failed samples exposed to air and brine. In contrast, as also can be seen Figure 6-67, the failure times for 20% cold-worked Titanium Grade 7, a material much more creep-resistant than the mill-annealed Titanium Grade 7, tested at significantly higher applied stress levels of 67 ksi (462 MPa) ranged from about 1,337 hours to 1,922 hours. This stress is about 186 % of the mill-annealed yield strength ($YS_{(125°C)}$) or 92% of the actual higher yield strength of the 20% cold-worked material shown in Table 6-24. Failure times for the more-creep-resistant cold-worked material were much longer (about 1,337 hours to 1,922 hours) than for mill-annealed material tested at lower stress levels (about 0.7 hours to 50 hours). Importantly, the cold-worked material failures were due to ductile overload rather than SCC, as indicated in Figure 6-67 (DTN: LL021105312251.023 [DIRS 161253], Figure 2-5).

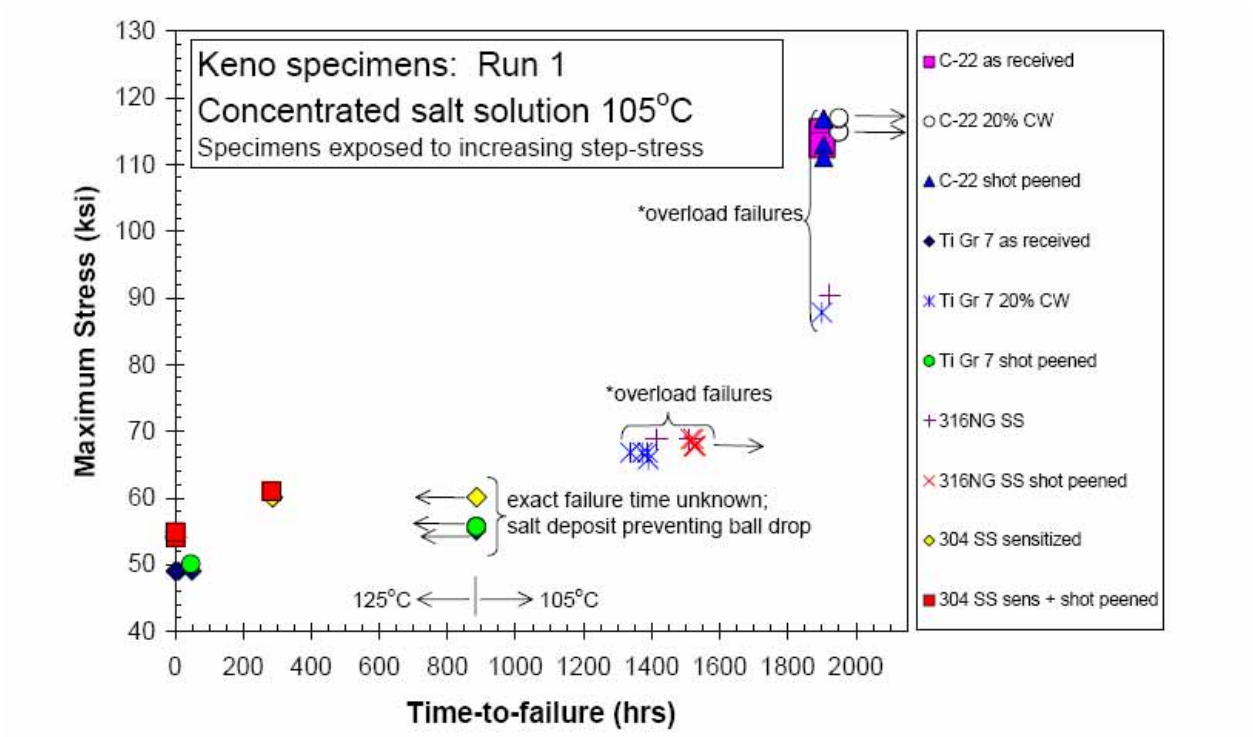

Source: DTN: LL021105312251.023 [DIRS 161253], Figure 2-5.

NOTES: Stress was incrementally increased during testing. The maximum applied stress (which equals the failure stress) is plotted.

Figure 6-67. Failure Stress versus Time to Failure for GE GRC Keno Test Run 1 Specimens

GE GRC Keno Test Run 2 Results

Constant-load Keno test Run 2 results for the initially exposed, as-received (mill-annealed) Titanium Grade 7 specimens (noncreviced and creviced) exposed in 105°C diluted BSW brine are summarized in DTN: MO0707SCCIGMER.000 [DIRS 182202], Table 2-7, and are plotted in Figure 4-1.

Figure 4-1 shows the specimen failure times (or time on test without failure) versus applied stress ratio (the ratio of applied stress to at-temperature yield strength) after about 28,000 total hours (3.2 years) on test. As in Keno test run 1, all the Titanium Grade 7 specimens in Keno test Run 2 failed. At the lowest tested applied stress level of 40 ksi (276 MPa) or 111% $YS_{(125°C)}$, the failure times ranged from 342 hours to 10,182 hours (approximately 1.2 years). At 45 ksi (310.3 MPa) or 125% $YS_{(125°C)}$, failure times ranged from about 20 hours to 220 hours whereas at 50 ksi (344.7 MPa) or 139% $YS_{(125°C)}$ failure times were about 170 hours.

The measured failure times over the range of Keno constant-load aqueous and air environment tests evaluated are summarized in Table 6-25. Table 6-25 also lists the results generated by Atomic Energy of Canada Limited (AECL) on the creep of Titanium Grade 2, which has the same mechanical properties as Titanium Grade 7. As can be seen in Table 6-25, the observed spread in failure times at any reported stress can be fairly large, and is likely due to such factors

as load loss from piston seal ring friction or brine leakage past the piston seal ring and flashing to produce salt deposits (DTN: MO0707SCCIGMER.000 [DIRS 182202], Figures 2-1 and 2-8).

Table 6-25. Comparison of Constant-Load Failure Times for Titanium Grade 7 in Diluted BSW Brine with Those of Titanium Grades 2 and 7 in Air

Test Run	Material Condition*	Applied Stress, MPa (ksi)	% at-temp. Yield Strength	Failure time (hrs)	Specimen Number
Keno 1	20% Cold-Worked	462 (67.0)	92	1,337 to 1,922	GE-6, 16, 26, 36, 46, 49
Keno 1	Annealed	345 (50.0)	139	0.7 to 50	GE-2, 12, 22, 32, 42, 47
Keno 2	Annealed	345 (50.0)	139	170	GE-16, 73, 132, 42, 51
Keno 2	Annealed	310 (45.0)	125	20 to 220	GE-15, 72, 131, 41, 50, 109, 167, 168, 110, 17, 74, 133, 43, 52
Keno 2	Annealed	276 (40.0)	111	342 to 10,182	GE-14, 71, 130, 40, 98, 108
Air -GE	Annealed-GE (long)	310	125	10.1	GE-Creep 1
Air -GE	Annealed-GE (long)	350	141	1.6	GE-Creep 2
Air -GE	Annealed-GE (long)	328	132	6.2	GE-Creep 3
Air -GE	Annealed-GE (long)	276	111	493	GE-Creep 4
Air -GE	Annealed-GE (long)	326	131	1.2	GE-Creep 5
Air -GE	Annealed-GE (short)	285	115	143	GE-Creep 6
Air –AECL	Annealed-AECL (short)	222 (32.2)	95	350**	AECL-C-1
Air –AECL	Annealed-AECL (short)	187 (27.1)	80	24,140	AECL-C-3

Sources: DTN: MO0707SCCIGMER.000 [DIRS 182202], Tables 2-2 to 2-4, and 2-7; Figures 6-3 to 6-6; Dutton et al. 1996 [DIRS 175817], Table 1, Figure 13; DTN: MO0705SCCIGM06.000 [DIRS 180869], file *GE-GRC-Final_Sept-2006-Rev3.doc*, Figures 27 and 29.

NOTES: *Long = GE 105°C longitudinal orientation (yield strength = 248 MPa), short = transverse orientation (yield strength = 262 MPa); AECL short-orientation (yield strength = 234 MPa).

**Failure time estimated from Dutton et al. 1996 [DIRS 175817], Figure 13.

Some rows are highlighted to indicate the different categories of the materials for added transparency.

In the continuation of Keno test Run 2, new specimens of annealed Titanium Grades 7 and 29 were placed on test in June 2006 and have been on test for more than 2,800 hours without failure (DTN: MO0705SCCIGM06.000 [DIRS 180869], file *GE-GRC-Final_Sept-2006-Rev3.doc,* Figure 22 and Table 8). The Titanium Grade 7 specimens are stressed at 180 MPa and 210 MPa (about 73% $YS_{(125°C)}$ (Table 6-24) and 85% $YS_{(125°C)}$(Table 6-24), respectively, to preclude creep rupture. The Titanium Grade 29 Keno results are shown plotted with earlier test results for Titanium Grade 7 in Figure 6-74.

SCC versus Creep

Initially, the failure of the mill-annealed Titanium Grade 7 specimens was assumed to have resulted from SCC. However, subsequent creep testing in the 105°C air of archived Titanium Grade 7 specimens from the same heat of material tested over the same range of stresses indicated failure at times similar to the minimum failure times observed in the Keno tests. This can be seen by examination of air versus brine failure times summarized in Table 6-25. The results generated by the AECL shown in the last two rows of Table 6-25 are for 100°C air exposed Titanium Grade 2 (Dutton et al. 1996 [DIRS 175817], Table 1), which has the same mechanical properties as Titanium Grade 7 (ASTM B 265-02 [DIRS 162726], Table 1). The air test results are compared in Figure 6-68 by using the minimum failures times obtained in the Keno tests performed in the diluted BSW brine (Table 6-25).

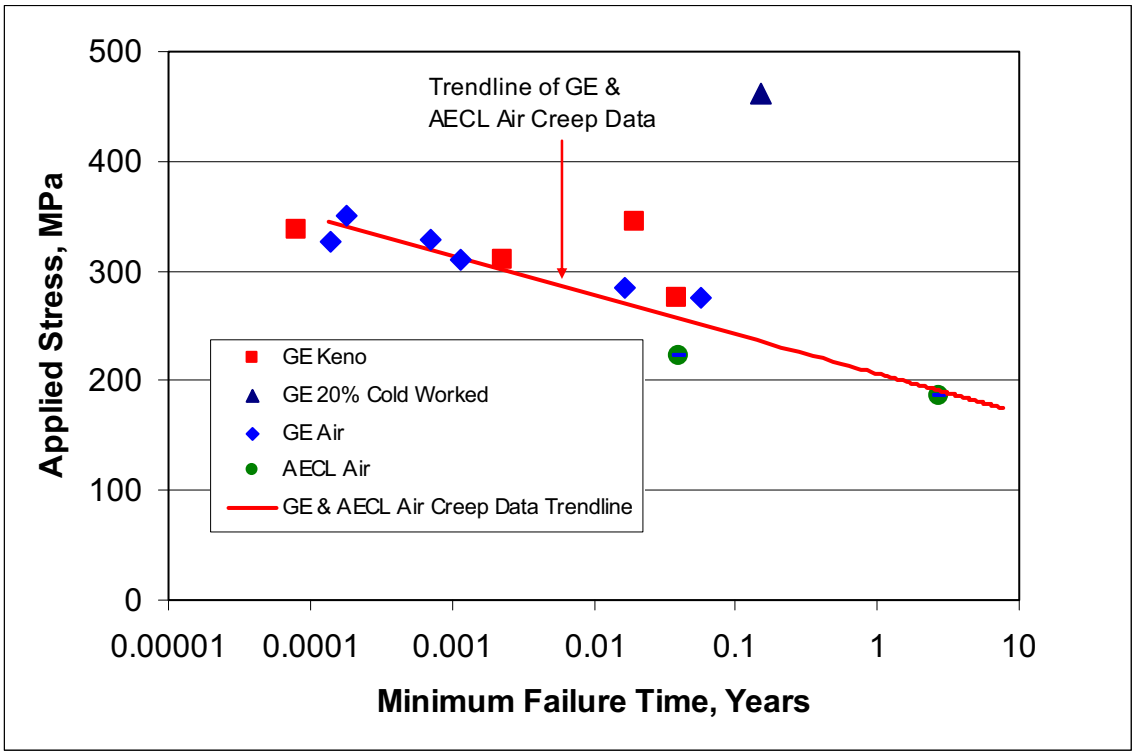

Source: Table 6-25. Ouput DTN: MO0705CREEPSCC.000, file *CreepGraphs.xls,* Sheet *"Applied Stress."*

Figure 6-68. Comparison of Air Creep Rupture Times with Minimum Failure Times in 105°C to 125°C Brine Environments

It is evident from this comparison that the failure times, except those for the 20% cold-worked specimens, which are orders of magnitude more creep-resistant than mill-annealed Titanium Grade 7 (Kiessel and Sinnott 1953 [DIRS 174853], Figure 7), are quite similar in air and brine environments, consistent with the consideration that the annealed constant-load specimen failures in brine are highly likely to have resulted from creep rupture rather than SCC.

In many ductile alloys in aqueous environments, sustained dynamic strain at the crack tip is considered an important contributor to SCC initiation and growth. Therefore, accelerated

environmental cracking is expected in materials that creep readily because these materials have high sustained dynamic strain at the crack tips. Thus, while SCC would be expected if the Titanium Grade 7 were SCC-susceptible in these constant-load tests, the role of creep in cracking may be so dominant that the environmental contribution is negligibly small or absent. This high resistance or immunity of annealed Titanium Grade 7 to SCC is further confirmed by the ductile dimpling-type fracture surfaces present on the specimens exposed to air and brine, as shown in Figure 6-69, which is reproduced from DTN: MO0707SCCIGMER.000 ([DIRS 182202], Figures 2-13(b) and 6-11).

The cold-worked Titanium Grade 7 samples (as well as the Alloy 22 and Stainless Steel Type 316NG samples) are reported to have failed by ductile overload rather than SCC as the autoclave pressure slowly increased after about 1,300 hours to 1,900 hours on test due to a faulty back pressure regulator (DTN: MO0707SCCIGMER.000 [DIRS 182202], Section 2.3).

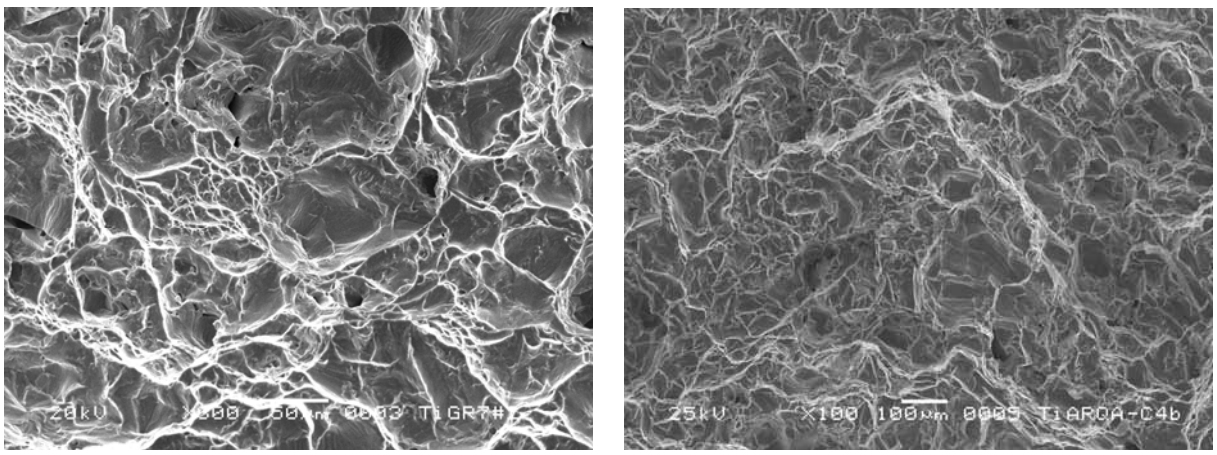

(a) (b)

Sources: (a) DTN: MO0707SCCIGMER.000 [DIRS 182202], Figure 2-13(b) and fracture morphology for as-received Titanium Grade 7 creep specimen fracture surfaces tested at 40 ksi in 105°C air.
(b) DTN: MO0707SCCIGMER.000 [DIRS 182202], Figure 6-11, showing the similarity in fractographic features.

Figure 6-69. Fracture Morphology for As-Received Titanium Grade 7 Keno Specimen Fracture Surfaces at 105°C: (a) Air and (b) Aqueous Exposure

In contrast to the Titanium Grade 7 constant-load creep rupture failures in the Keno test series, the Alloy 22 constant-load specimens did not fail in this test by either creep rupture or SCC, even when the specimens were loaded to about 2.1 times the yield strength (approximately 95% of the at-temperature ultimate tensile strength (DTN: MO0707SCCIGMER.000 [DIRS 182202], Table 2-4).

6.8.3.1.2 U-Bend Tests for Titanium Grade 7

Similar to the Alloy 22 U-bend specimens (Section 6.2.1.2), U-bend specimens fabricated from Titanium Grades 7, 12, and 16 were also exposed at the LLNL LTCTF to a range of relevant naturally aerated brine environments (SDW, SCW, and SAW brines) at 60°C and 90°C for times up to five years (Fix et al. 2004 [DIRS 169321]). The material heat numbers and chemical

compositions (obtained from check analyses) are listed in Table 6-28. The Titanium Grade 7 base metal was received in the annealed condition (10 min at 1,550°F). The room temperature yield strength of the Titanium Grade 7 material, per DTN: MO0003RIB00073.000 [DIRS 152926], is shown in Table 6-26.

Table 6-26. Yield Strength of Titanium Grade 7 Used in LTCTF U-Bend Test

Material	Temperature (°C)	Yield Strength, (ksi)	Average Yield Strength (ksi)	Yield Strength, (MPa)	Average Yield Strength, MPa
Titanium Grade 7	Room Temperature (21)	40 to 65	52.5	275 to 450	362
	204	20 to 22	21	138 to 152	145
	316	13 to 18	15.5	90 to 124	107

Source: DTN: MO0003RIB00073.000 [DIRS 152926].

The Titanium Grade 16 material was also received in the annealed condition (1 hour at 1,400°F), but the measured yield strength is not available and is assumed to be equivalent to the Titanium Grade 7 material.

As no yield strength value was reported at 90°C, the $YS_{(90°C)}$ value is estimated according to the following method. The room temperature yield strength is reported as 362 MPa in Table 6-26. A linear relationship between yield strength and temperature is used for this narrow temperature range. The yield strength values at 60°C and 90°C can, therefore, be interpolated as shown in Table 6-27 and are about 317 MPa and 281 MPa, respectively.

Table 6-27. Estimate by Interpolation of Titanium Grade 7 Yield Strength at 60 °C and 90°C from Yield Strength Values at Other Temperatures

Temperature			Yield Strength (ksi)	Conversion Factor	Yield Strength (MPa)
K	°F	°C			
294	70	21	52.5	1 ksi = 6.894759 MPa *	362
477	400	204	21		145
363	194	90	40.8		281
333	140	60	46		317

Source: Table 4-7, MO0003RIB00073.000 [DIRS 152926].
* Boyer and Gall 1997 [DIRS 155318], p. 1-55 and 1-57.

NOTE: The yield strength at 60°C and 90°C ($YS_{(90°C)}$) are interpolated from the yield strength values at 21°C and 204°C according to the following relationship:

$$YS_{(90°C)} = YS_{(21°C)} + \left[\frac{90°C - 21°C}{204°C - 21°C}\right] \times (YS_{(204°C)} - YS_{(21°C)})$$

$$YS_{(60°C)} = YS_{(21°C)} + \left[\frac{60°C - 21°C}{204°C - 21°C}\right] \times (YS_{(204°C)} - YS_{(21°C)})$$

As in the situation where GE GRC yield-strength values are different from those shown in Table 4-7, due to the material heats and testing methods, the yield strength values of Titanium Grade 7 shown in Table 6-26 are slightly different from the values shown in Table 4-7. In this document, therefore, the yield strength values shown in Table 6-26 and Table 6-27 are used when discussing LTCTF test results, while the other appropriate yield strength values shown in Table 4-7 are used when discussing other sets of data as well as modeling.

Table 6-28. Chemical Composition of Titanium Alloy U-Bend Specimens Test in LTCTF

Chemical Composition	Titanium Grade 7		Titanium Grade 16		Titanium Grade 12	
	Base Metal	Weld Filler	Base Metal	Weld Filler	Base Metal	Weld Filler
	Heat: R3928	Heat: BN4591	Heat: X52020	Heat: 5D3438	Heat: BN2966	Heat: AT7879
	(wt %)					
C	0.07	0.008	0.013	0.008	0.05	0.006
H	0.003	0.002	0.0048	0.0063	0.002	0.0044
Fe	0.18	0.02	0.11	0.04	0.07	0.12
Mo	—	—	—	—	0.36	0.3
N	0.011	0.008	0.006	0.002	0.02	0.004
Ni	—	—	—	—	0.78	0.82
O	0.12	0.037	0.14	0.12	0.14	0.08
Pd	0.16	0.17	0.07	0.19	—	—
Ti	>99	>99	>99	>99	>98	>98

Source: Fix et al. 2004 [DIRS 169321], Table 2.

The titanium alloy U-bend specimens were fabricated, similar to the Alloy 22 U-bend specimens, from sheet materials (3/4-in- (19-mm-) wide and 1/16-in- (approximately 1.6 mm-) thick strips) in the mill-annealed and as-welded (gas metal arc welded using matching filler material) conditions. About half the specimens were exposed in the solution's liquid phase and half in the vapor phase.

In the LLNL tests for Titanium Grade 7, the U-bend specimens were bent to approximately 180 degrees, and then the legs were restrained to give an apex strain (cold-work level) greater than about 12%, resulting in an initial sustained stress level near or somewhat above the yield strength. No SCC initiation was detected in a number of fixed deflection Titanium Grade 7 U-bend test specimens exposed for 2.4 years and Titanium Grade 16 (an analogous titanium–palladium alloy) specimens exposed for five years in a range of relevant environments at 60°C and 90°C (Fix et al. 2004 [DIRS 169321]).

Results of U-Bend SCC Testing

Following the exposure (about 2.4 years for Titanium Grade 7 and about five years for Titanium Grades 12 and 16), a total of 182 specimens (including 72 Titanium Grade 7 specimens, 56 Titanium Grade 16 specimens, and 54 Titanium Grade 12 specimens) were removed from six testing tanks, rinsed in deionized water, and allowed to dry in air. The specimens were then examined optically in a stereomicroscope using up to 100 times magnification. In general, the Titanium Grades 7 and 16 and most of the Titanium Grade 12 specimens were completely featureless; that is, they had a shiny metallic appearance similar to the non-tested condition. No evidence of SCC initiation was observed on any Titanium Grades 7 or 16 specimens. A typical 5-year exposed noncreviced Titanium Grade 12 posttest specimen is shown in Figure 6-70.

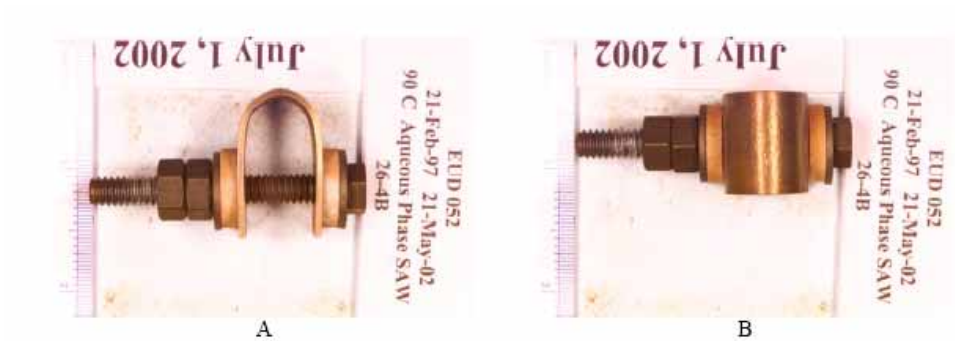

Source: Fix et al. 2004 [DIRS 169321], Figure 2.

Figure 6-70. Welded Titanium Grade 12 U-bend Specimen after Five Years Exposure at LTCTF, (A) Side View Top and (B) Apex View

In contrast to the lack of SCC observed for Titanium Grades 7 and 16 specimens and most of the Titanium Grade 12 specimens, SCC (or possibly HIC) was observed in three of the higher-strength and more-creep-resistant (Boyer et al. 2003 [DIRS 174636], p. 234), welded Titanium Grade 12 specimens exposed in the SCW liquid solution at 90°C. This is consistent with the observations that the near-α, two-phase (α plus β phase) Titanium Grade 12 alloy is generally less resistant to corrosion and SCC than the single-phase (alpha phase) Titanium Grades 7 and 16 (Fix et al. 2004 [DIRS 169321], p. 5).

The initial Titanium Grade 7 outer surface stress expected at room temperature for a U-bend specimen at the maximum apex strain level of about 12% is approximately 500 MPa (Boyer et al. 2003 [DIRS 174636], p. 240), whereas in the region where the specimen legs are tangent to the curved apex region it is approximately at the yield strength. As described earlier, the Titanium Grade 7 base metal was received in the annealed condition (10 min at 1,550°F) and the room temperature yield strength was 52.5 ksi (362 MPa) (Table 6-26). At 60°C and 90°C, it drops to 317 MPa and 281 MPa, respectively, based on the interpolation shown in Table 6-27. As Titanium Grades 7 and 16 exhibit significant creep at room temperature and above as indicated in Section 6.8.3.1.1, the initial U-bend surface stress would be expected to drop with time due to creep-induced stress relaxation. To quantify this time-dependent drop off in stress, X-ray diffraction outer surface residual stress measurements were performed on 12 of the LTCTF U-bend specimens described, as well as four unexposed archive specimens that remained at room temperature for over five years before the measurement was made. Measurement results for different locations (the top apex region and on each leg in the region where the leg is tangent to the U-bend apex) on the still-bolt-restrained U-bend specimen outer surfaces are reported in DTN: MO0708XRAYDRST.000 [DIRS 182572].

Stress Relaxation Due to Creep

Although the stresses would tend to redistribute as creep relaxation slowly occurs at the exposure temperature, values of the maximum remaining U-bend outer surface tensile stresses for each specimen measured as a function of exposure time at 60°C to 90°C are shown plotted in Figure 6-71 based on results listed in Table 6-29. The room-temperature data listed in Table 6-29 are not used in Figure 6-71 because the specimens sat at the room temperature for over five years before the X-Ray stress measurements were obtained. Therefore, stress relaxation from the as-bent state (approximately 500 MPa) had occurred over the five-year period to about 360 MPa to 375 MPa. Since the data used in Figure 6-71 were high-temperature (60°C and 90°C) data, it is inappropriate to include the room temperature data in the same plot. The surface stresses are related to the surface elastic strain and will vary with position (ASM International 1987 [DIRS 103753], pp. 252 to 254). In general, the maximum measured surface stresses were located on the straight portion of the U-bend legs near the location where the legs are tangent to the U-bent portion and therefore are primarily elastically strained (DTN: MO0708XRAYDRST.000 [DIRS 182572]). As the stress is proportional to the elastic strain times the elastic modulus, and as the modulus for Titanium Grades 7 and 16 drops less than about 3% between room temperature and 90°C (CRWMS M&O 1999 [DIRS 102933], p. 45), the at-temperature stresses on these 60°C and 90°C LTCTF exposed specimens would be expected to be similar to those measured at room temperature. Although, as expected (ASTM G30-94 [DIRS 137688], Section 5.1), there is significant scatter in the measured U-bend surface stress results, the trend line indicates a decreasing surface tensile stress with exposure time consistent with creep-related stress relaxation.

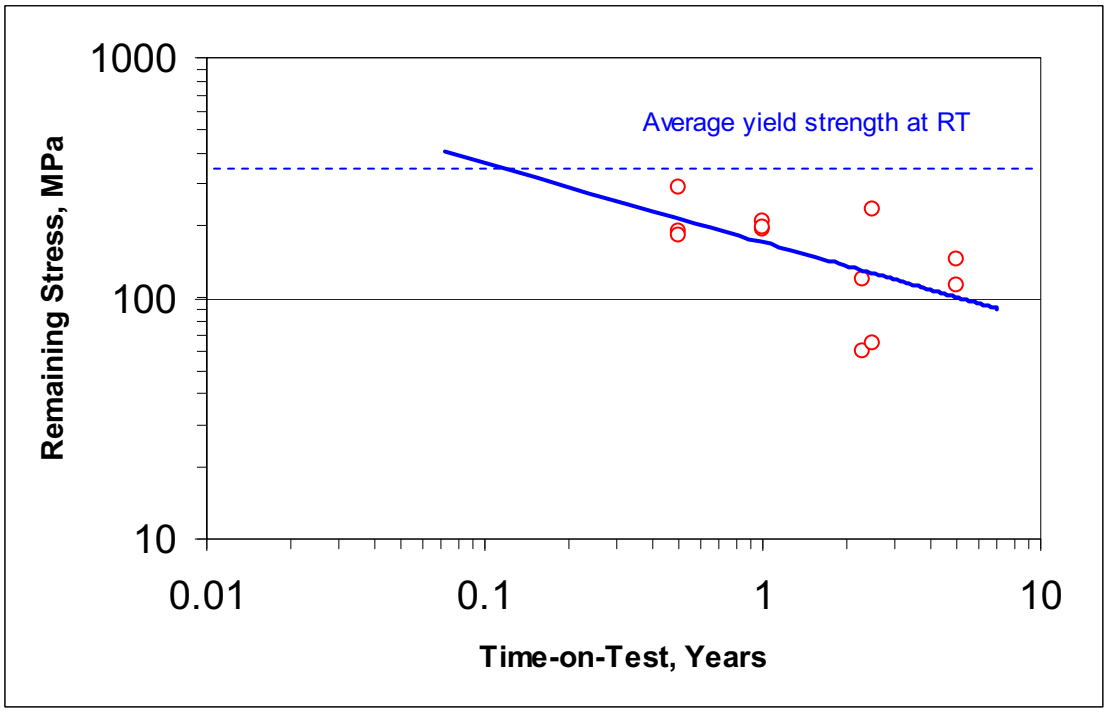

Source: Table 6-29, Output DTN: MO0705CREEPSCC.000, file *CreepGraphs.xls,* Sheet *"RemStress."*

Figure 6-71. Maximum Remaining Tensile Stress versus Exposure Time for Each Titanium Grades 7 and 16 U-Bend Test Specimens Exposed to a Range of Brines without Observed SCC Initiation

Table 6-29. Summary of LTCTF Titanium Grades 7 and 16 U-Bend Specimen Maximum Remaining Stress Levels

Time (yrs)	Test Temperature (°C)	Specimen ID	Maximum Stress (MPa)	Maximum of Maximum Stress (MPa)
5.5	RT	FUA 141	192	—
5.5	RT	FUE 142	360	360
5.5	RT	NUA 181	375	375
5.5	RT	NUE 182	370	370
0.5	60	FUA 122	287	287
0.5	60	NUA 148	188	—
1	60	FUA 124	209	209
2.3	60	FUA 126	60	—
5	60	FUA 128	145	145
0.5	90	FUE 134	181	—
1	90	FUE 136	192	—
1	90	NUE 136	197	—
2.3	90	FUE 138	121	—

Table 6-29. Summary of LTCTF Titanium Grades 7 and 16 U-Bend Specimen Maximum Remaining Stress Levels (Continued)

Time (yrs)	Test Temperature (°C)	Specimen ID	Maximum Stress (MPa)	Maximum of Maximum Stress (MPa)
2.5	90	NUA 178	232	232
2.5	90	NUE 166	65	—
5	90	FUE 140	113	—
0.01	RT	Titanium Grade 7 RT Yield Strength	362	362

Source: DTN: MO0708XRAYDRST.000 [DIRS 182572].

NOTES: The "Maximum of Maximum Stress" in the fifth column is the maximum values from the fourth column under the same exposure time.
RT = room temperature.

As SCC did not initiate in any of the U-bend specimens tested, from a stress corrosion crack initiation standpoint, it is the maximum remaining stress at each exposure time interval that is of most interest. This maximum stress (listed in Table 6-29) is shown plotted versus brine exposure time at 60°C to 90°C in Figure 6-72.

As can be seen from Figure 6-72, the maximum outer surface tensile stress decays from their initial over-yield strength level logarithmically to about 160 MPa (about 44% of the average room temperature yield strength (362 MPa, Table 6-26) or 57% of the average yield strength at 90°C (281 MPa) per estimated value from Table 6-27 after about five years of exposure due to creep-induced stress relaxation. However, SCC initiation did not occur regardless of stress level.

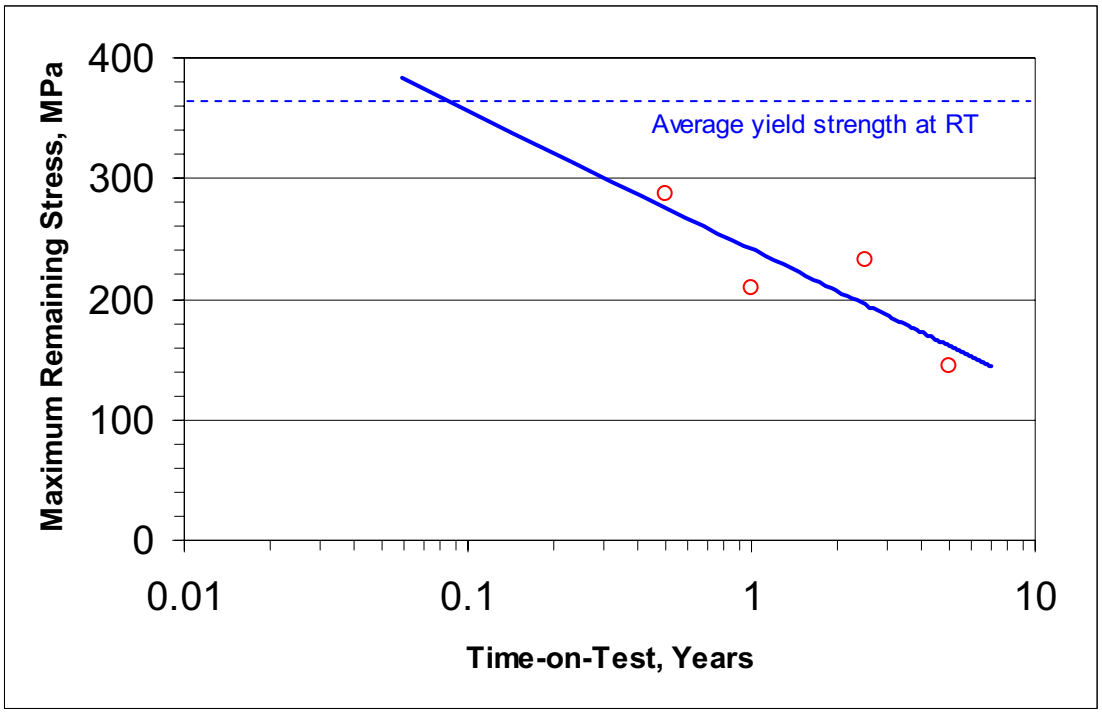

Source: Table 6-29, Output DTN: MO0705CREEPSCC.000, file *CreepGraphs.xls*. Sheet "RemStress."

Figure 6-72. Maximum Remaining U-Bend Tensile Stress at Each Exposure Interval versus Exposure Time

6.8.3.1.3 The SCC Initiation Threshold Stress Criterion for Titanium Grade 7

The constant load and U-bend test results described in Sections 6.8.3.1.1 and 6.8.3.1.2 are for exposure times up to five years. As described in Section 6.8.3.1.1, constant-load Keno test specimen failures of Titanium Grade 7 initially attributed to SCC were later determined to be due to creep rupture based on the fact that no evidence of even incipient SCC initiation was observed and that the fracture surfaces of the as-received Titanium Grade 7 Keno specimen and creep ruptured specimen were nearly identical (Figure 6-69). This is fully consistent with the extremely high SCC initiation resistance or immunity of Titanium Grade 7 described in the literature and reviewed in Section 6.8.3. Therefore, in order to derive a defensible threshold stress criterion value associated with the lifetime of the Titanium Grade 7 drip shield components, an appropriate extrapolation scheme is necessary.

For Titanium Grades 7 and 16, the threshold stress criterion can be derived from an assessment of the maximum stress levels tested without observed SCC initiation. A summary plot comparing the Keno constant-load brine test results without SCC initiation (minimum times from Table 6-25) along with the LTCTF U-bend maximum remaining tensile stress results (without SCC initiation) (Table 6-29) to the experimentally determined air creep rupture behavior is given in Figure 6-73. The data used to construct Figure 6-73 are summarized in Table 6-30. Data summarized in Table 6-30 are abstracted from Table 6-25 and Table 6-29.

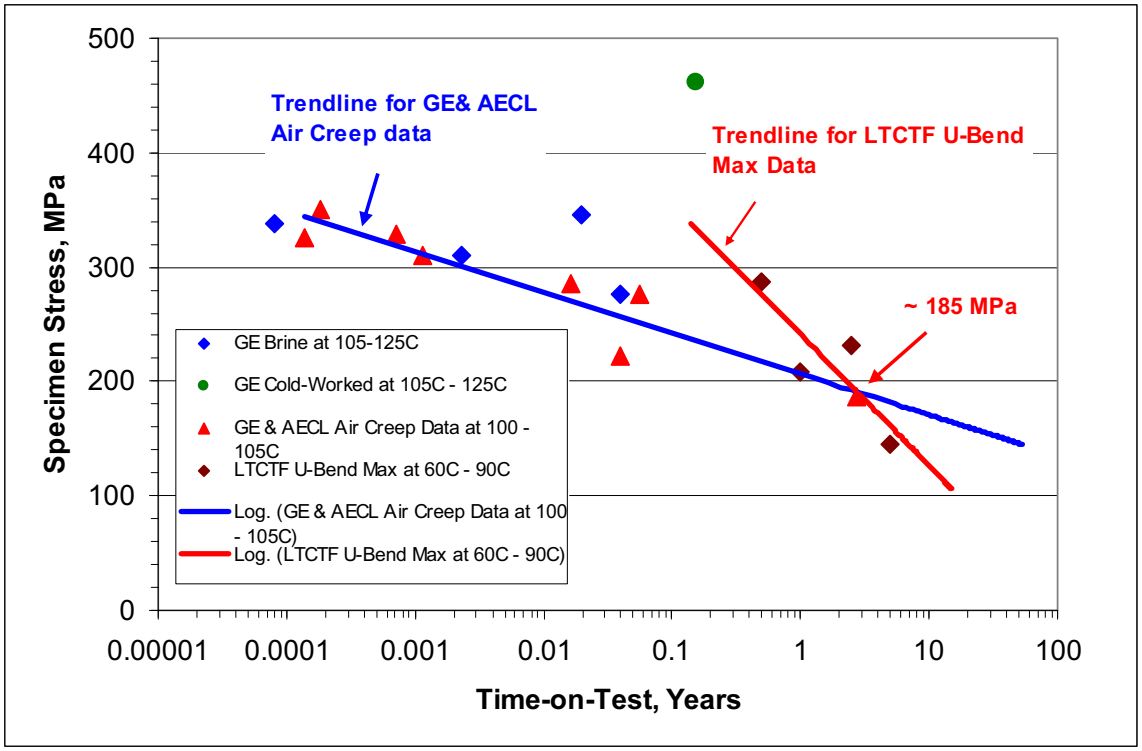

Source: Air Creep Rupture Curve from Figure 6-68. U-Bend Exposure Interval versus Exposure Time from Figure 6-72.

Ouput DTN: MO0702PASTRESS.002, file "*Figure 6-73 Table 6-31.xls*."

Figure 6-73. Comparison of Air Creep Rupture Failure Times with Time-on-Test in 60°C to 125°C Brines Without Stress Corrosion Crack Initiation and Maximum Remaining Tensile Stress at Each U-Bend Exposure Interval versus Exposure Time

Table 6-30. Data Used to Construct Figure 6-73

GE and AECL Data on Load-Failure Times in Diluted BSW Brine and in Air (Abstracted from Table 6-25)				
Legends in Figure 6-73	**Test Temperature (°C)**	**Applied Stress (MPa)**	**Minimum Failure Time (hrs)**	**Corresponding Test ID in Table 6-25**
GE Cold-Worked	105 to 125	462	1,337	Keno 1
GE Brine	125 for Keno 1 105 for Keno 2	345	0.7	Keno 1
		345	170	Keno 2
		310	20	Keno 2
		276	342	Keno 2
GE Air	105	310	10.1	GE-Creep 1
		350	1.6	GE-Creep 2
		328	6.2	GE-Creep 3
		276	493	GE-Creep 4
		326	1.2	GE-Creep 5
		285	143	GE-Creep 6
AECL Air	100	222	350	Air –AECL
		187	24,140	Air –AECL
LTCTF Titanium Grades 7 and 16 U-Bend Specimens (Abstracted from Table 6-29)				
Legends in Figure 6-73	**Test Temperature (°C)**	**Maximum of Maximum Stress (MPa)**	**Time (yrs)**	**Corresponding Test ID in Table 6-29**
LTCTF U-Bend Max at 60°C to 90°C	60	287	0.5	FUA 122
	60	145	5	FUA 128
	90	197	1	NUE 136
	90	232	2.5	NUA 178

Sources: Table 4-8 and Table 4-9.

The Keno specimen failure times used in Figure 6-73 are conservatively taken as the minimum measured values at each applied stress level obtained from Table 6-25. As discussed in Section 6.8.3.1, examination of Figure 6-73 indicates that minimum constant-load failure times in the diluted BSW brine lie essentially on the air creep rupture curve (Figure 6-69), indicating that failure was due to creep rupture rather than SCC. For the U-bend specimens, the LTCTF results used in Figure 6-73 are the maximum of the maximum tensile stress values for each exposure time examined. This is also conservative because no SCC initiation was observed in any of the Titanium Grades 7 and 16 specimens at these stresses. Two trendlines are drawn through the remaining LTCTF maximum U-bend tensile stress data and minimum GE GRC Keno constant-load brine test data, which, as previously analyzed, comprise the air creep data. The intersection of the uncracked U-bend trend line with the air creep rupture trendline at about 185 MPa indicates that SCC is not expected to initiate under constant-load brine exposure conditions at least down to stress of about 185 MPa (approximately 58% and 66% of the 60°C and 90°C yield strengths (317 MPa and 281 MPa, respectively, see Table 6-27), as creep rupture will intervene before SCC can potentially initiate.

The previous Titanium Grade 7 SCC initiation threshold stress criterion (BSC 2004 [DIRS 172203]) was developed analogously to that of Alloy 22 (Section 6.2.2). The approach was based on applying a conservative reduction factor (2.1) to the value of the maximum, long-

term applied stress without SCC failure on a plot of Keno test Run 2 applied stress versus time to failure (BSC 2004 [DIRS 172203], Section 6.2.1). This resulted in a threshold stress criterion of 50% of the Titanium Grade 7 at-temperature yield strength. In the previous work (BSC 2004 [DIRS 172203]), this value was conservatively defined as one half the 140°C yield strength value.

A new threshold stress for potential SCC initiation is developed based on Figure 6-73, which is constructed by using data in Table 6-25 and Table 6-29 and the argument illustrated in Figure 6-73. The new threshold stress for SCC initiation is established as 80% of at-temperature yield strength as discussed below based on considerations of primary and secondary stresses in drip shield design scenarios.

Consideration of Primary Stress

As discussed previously (Section 6.8.3.1), the initially assumed SCC failure stresses in Keno test Run 2, were later found to be due to creep rupture, a mechanical mechanism, rather than the SCC mechanism. It is evident that the previous selection of 50% of yield strength, as well as the concept of using a reduction factor such as 2.1 on the apparent value of the maximum, long-term applied stress without SCC failure (BSC 2004 [DIRS 172203]), was unrealistically conservative for the Titanium Grade 7 drip shield plate material. For drip shield design scenarios where the primary stresses (i.e., sustained load stresses) are present, it is evident from Figure 6-73 and Section 6.8.3.1.1 that creep rupture will occur for brine-exposed specimens before any potential SCC can initiate, at least over the constant-load stress range evaluated for annealed Titanium Grade 7 111% to 139% of the at-temperature yield strength (i.e., between 275 MPa to 345 MPa) (Section 6.8.3.1.1 and Table 6-24) and down to at least approximately 185 MPa (75% of the GE GRC measured yield strength at 125°C $YS_{(125°C)}$, 248 MPa, Table 6-24) after about three years on test.

Consideration of Secondary Stress

For the fixed deflection case (i.e., for the case of secondary design stresses such as deformation-induced residual stresses), it is evident from the drop in measured maximum tensile stress of the U-bend specimens over time (Figure 6-72 and Figure 6-73) that creep-accelerated stress relaxation will lead to continuously decreasing secondary stress levels without SCC initiation. Initially, secondary stresses (i.e., deflection-controlled stresses such as the U-bend stresses) at or above yield strength fell to about 250 MPa after one year, which is about 89% of the yield strength at 90°C based on the yield strength data shown in Table 6-27, and fell to about 145 MPa in about five years, which is about 52% of yield strength at 90°C (281 MPa, Table 6-27), both without SCC initiation.

SCC Initiation Threshold Stress Criterion for Titanium Grade 7

In developing a basis for a threshold stress criterion for Titanium Grade 7, available literature indicates Titanium Grade 7 is extremely resistant or immune to SCC initiation in YMP-relevant brine environments (Section 6.8.2). Consistent with the literature, YMP test results confirm that no SCC initiation is observed over the full range of primary (constant-load) stresses up to 139% of the at-temperature yield strength (Section 6.8.3.1.1) and secondary (U-bend) stresses, up to

89% after one year, evaluated (Section 6.8.3.1.2). However, unlike the situation with Alloy 22, it is inappropriate to select a conservative stress reduction factor such as half the maximum applied stress without SCC initiation, as Titanium Grade 7 undergoes creep rupture rather than SCC at the higher primary stresses and undergoes creep-induced stress relaxation at the higher secondary stresses. Thus, to provide a defensible basis for selection of a potential SCC initiation threshold stress criterion, it is conservative to select the highest stress evaluated without SCC initiation after long-term exposure. As indicated above, under primary stress conditions (i.e., constant-load tests) creep rupture of annealed Titanium Grade 7, rather than SCC failure, will occur after about three years at stresses above about 75% of the at-temperature yield strength. Further, as seen in Figure 6-73 and Table 6-29, no SCC initiation (or creep rupture) was observed for any of the U-bend specimens tested for up to 2.5 years with surface stresses as high as 232 MPa at 90°C, 83% of the at-temperature yield strength (281 MPa, Table 6-27). Thus, these constant-load and U-bend test results provide a reasonable basis for selecting an SCC initiation threshold stress criterion of 80% of at-temperature yield strength. This criterion is conservative because, as can be seen from Section 6.8.3.1.1, no SCC initiation was observed over the full range of primary (constant-load) stresses up to 139% of the at-temperature yield strength (Keno 2 in Table 6-25).

Therefore, the Titanium Grade 7 SCC crack initiation threshold stress is established as 80% of at-temperature yield strength. Although project results and observations in the literature support the lack of SCC initiation potential at this stress level for primary stresses, it is evident from the previous discussions that creep relaxation may occur after about five years of exposure as indicated in Figure 6-68. In other words, it is likely that, in the case of the annealed material, creep relaxation will never allow SCC to occur. However, for the much more creep-resistant cold-worked material (see Figure 6-73), it is not evident that creep rupture will occur before SCC initiation.

In the above discussions, the values of the at-temperature yield strength are based on the actually measured or interpolated yield strength values of the tested materials. For TSPA application, it is recommended that the specification minimum yield strength values from ASME (2001 [DIRS 158115], Section II, Part D, Table Y-1, pp. 632 to 634) be conservatively used to establish the potential SCC crack initiation threshold stress. Since the linearity of yield strength versus temperature within the temperature range of interest is substantiated by the yield strength data listed in Table 4-7, the yield strength can be interpolated to the required temperature. For instance, Table 6-31 shows an example of the interpolation, according to the ASME yield strength values shown in Table 4-7, of the yield strength at 115°C.

Table 6-31. Example of Interpolation of Titanium Grade 7 Yield Strength at 115°C from Yield Strength Values at Other Temperatures.

Temperature			YS, ksi	Conversion Factor	YS, MPa
K	°F	°C			
294	70	21	40.03	1 ksi = 6.894759 MPa	276
422	300	149	25.53		176
388	239	115	29.4		203

Source: Table 4-7, ASME yield strength values.

NOTE: The yield strength at 115°C ($YS_{(115°C)}$) is interpolated from the yield strength values at 21°C and 149°C according to the following relationship:

$$YS_{(115°C)} = YS_{(21°C)} + \left[\frac{115°C - 21°C}{149°C - 21°C}\right] \times (YS_{(149°C)} - YS_{(21°C)})$$

6.8.3.2 SCC Initiation Response for Titanium Grades 28 and 29

6.8.3.2.1 Constant-Load Test Results for Titanium Grades 28 and 29

The literature indicates stressed smooth or notched components fabricated from Titanium Grade 5 are not susceptible to chloride SCC initiation (Schutz 1986 [DIRS 151162], p. 513). However, Titanium Grade 5 is potentially SCC-susceptible in chloride environments when loaded flaws (cracks) already exist (Schutz 1986 [DIRS 151162], p. 513). Limited YMP-generated data currently exist on the stress dependency of time to initiate SCC on a smooth surface versus applied stress (DTN: MO0705SCCIGM06.000 [DIRS 180869]). Recent Keno test Run 2 results in 105°C diluted BSW are available for Titanium Grade 29 (and Titanium Grade 7), as indicated in Section 6.8.3.1.1 and Figure 4-3. The Titanium Grade 29 specimens were put on test at stress levels between 472 MPa (65% of the yield strength shown in Table 6-23) and 684 MPa (94% of the yield strength shown in Table 6-23). The yield strength of Titanium Grade 29 was measured in 105°C air (DTN: MO0705SCCIGM06.000 [DIRS 180869], file *GE-GRC-Final_Sept-2006-Rev3.doc*, Table 8). The composition of the new Titanium Grade 29 material under test is listed in Table 6-21. The material (RTI Energy Systems Ingot Number 956205, Lot No. 50) was procured as 2.5-in-diameter bar material in the annealed and aged condition (solution-annealed 1,740°F (949°C), 30 minutes, air-cooled and then aged 1,150°F (621°C), 2 hours, air-cooled). The measured room temperature yield strength was 123 ksi to 125 ksi (848 MPa to 862 MPa) (RTI 2003 [DIRS 178467]).

The Titanium Grade 29 Keno results are shown plotted with earlier test results for Titanium Grade 7 in Figure 6-74 (DTN: MO0705SCCIGM06.000 [DIRS 180869], file *GE-GRC-Final_Sept-2006-Rev3.doc*, Figure 22). Specimens loaded at about 65% and 94% of at-temperature yield strength have been on test for approximately 2,800 hours without SCC initiation.

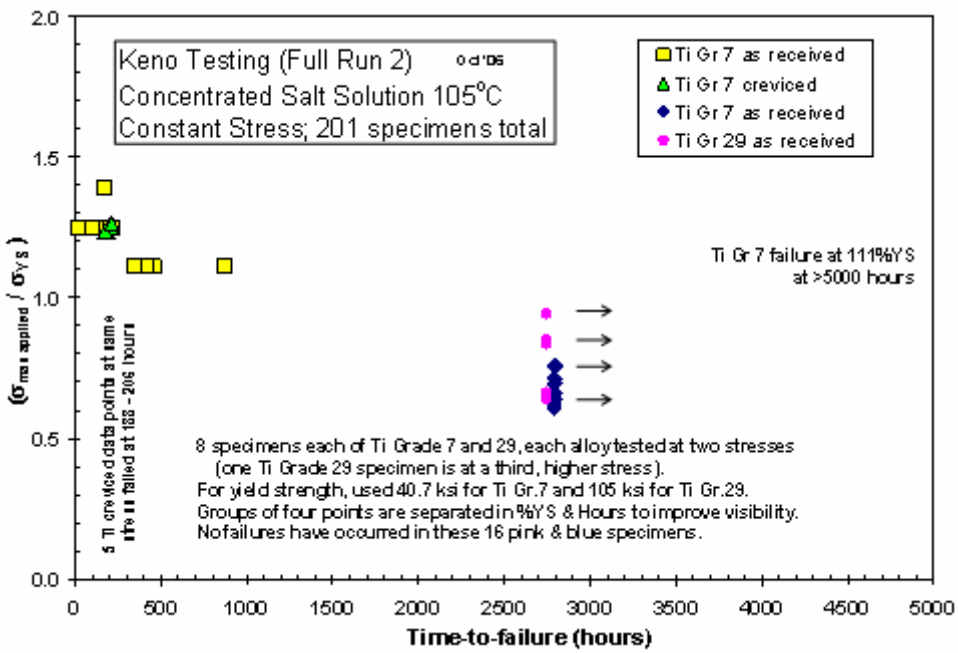

Source: DTN: MO0705SCCIGM06.000 [DIRS 180869], file *GE-GRC-Final_Sept-2006-Rev3.doc*, Figure 22.

Figure 6-74. Time-to-Failure versus Percent Yield Strength for Titanium Specimens in 15% BSW Solution at 105°C

6.8.3.2.2 Fixed Deflection and Slow Strain Rate Test Results for Titanium Grade 29

Titanium Grade 29 U-bend specimens also fabricated from RTI Energy Systems Ingot Number 956205, Lot No. 50, were recently added to the Alloy 22 autoclave test campaign (DTN: MO0705SCCIGM06.000 [DIRS 180869]), using aerated 165°C SCW. Test details are discussed in Section 6.2.1.2.2 (for Alloy 22). These initially over-yield strength stress level specimens have been exposed for 3,185 hours with no evidence of SCC initiation (DTN: MO0705SCCIGM06.000 [DIRS 180869], file *GE-GRC-Final_Sept-2006-Rev3.doc*, Table 6).

In addition to these YMP test results, extensive results from the literature on Titanium Grade 29 corroborate the Keno and U-bend test results, in potentially more aggressive test environments. For example, in one set of tests under very aggressive brine exposure conditions (Schutz et al. 2000 [DIRS 177257]), Titanium Grade 29 SSRTs as well as C-ring tests and were performed in a sour brine environment at 210°C for up to 180 days exposure. This sour brine test environment is deaerated NaCl- and CaF_2-saturated brine also containing $CaCl_2$ and $MgCl_2$ with an H_2S partial pressure of 0.19 MPag and a CO_2 partial pressure of 3.38 MPag. The brine contained about 250,500 ppm chloride and 461 ppm fluoride ions. Under these severe conditions, no SCC initiation was observed on tensile specimens subjected to SSRTs at a strain rate of 4×10^{-6} s^{-1} or on the C-ring specimens stressed using the deflection measurement method (ASTM G 38-01 [DIRS 177289]) at 95% to 105% of yield strength for up to 180 days. Because of the high creep-resistance of Titanium Grade 29 at this test temperature and below, measured creep strains were below the detection limit. Stress relaxation measured at 204°C and 260°C was also very

low, less than 10% of initial applied stresses at 70% to 100% of at-temperature yield strength (Schutz et al. 2000 [DIRS 177257]).

In addition to evaluating the stress dependency of SCC initiation, the critical temperature below which SCC initiation is not observed in various brines under high applied stress conditions is often used as a measurement of SCC resistance. A summary of literature results on threshold temperature below which SCC was not observed for platinum group metal-containing α+β titanium alloys, including Titanium Grades 28 and 29 is presented in Figure 6-75 for a range of brines. These results were obtained using a variety of SCC test methods including C-rings and SSRTs; they confirm the very high SCC-initiation threshold stress for Titanium Grade 28 and 29.

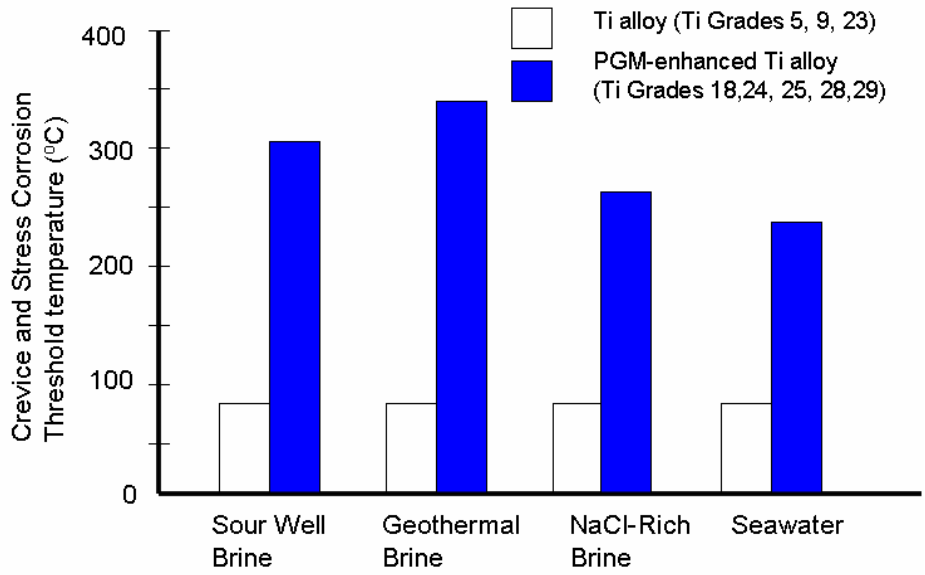

Source: Reproduced from Schutz 2003 [DIRS 168772], Figure 11.

Figure 6-75. Elevation of Crevice and Stress Corrosion Temperature Threshold Limits for Alpha-Beta Titanium Alloys (Including Titanium Grade 29) in Aqueous Chloride Media

6.8.3.2.3 Threshold Stress Criterion for Titanium Grades 28 and 29

Based on the much higher creep strength, on the discussions in Section 6.8.3.2.1 and Section 6.8.3.2.2, and on the precedent established for Alloy 22 as described in Section 6.2.2, it is reasonable and conservative to establish an SCC initiation threshold stress criterion for Titanium Grade 29 by applying a factor of approximately one-half to the maximum applied stress without SCC initiation or creep rupture. Thus, a value of 50% of at-temperature yield strength is appropriate based on the six-month value of the maximum, long-term applied stress without SCC failure, 105% yield strength, for exposure under very aggressive brine conditions in the 210°C sour brine environment described earlier (Schutz et al. 2000 [DIRS 177257]). This 50% yield strength value is also consistent with the lack of SCC initiation observed in the previously described at- or over-yield Titanium Grade 29 U-bends exposed to the relatively aggressive aerated 165°C SCW brine as well as the Keno constant-load specimens tested at stresses up to about 95% yield strength for about 3,185 hours (DTN: MO0705SCCIGM06.000 [DIRS 180869], file *GE-GRC-Final_Sept-2006-Rev3.doc*). Consequently, the SCC initiation

threshold criterion for Titanium Grade 29 is established as 50% of the at-temperature yield strength.

6.8.3.3 Summary of Threshold Stress Criteria for Drip Shield Materials

Based on the discussions in Section 6.8.3.1 and Section 6.8.3.2, a summary of SCC initiation threshold stress criteria is given in Table 6-32.

Table 6-32. Summary of Threshold Stress Criteria for SCC Initiation

Alloy	Threshold Stress Criteria
Titanium Grade 7	$0.8 \times YS_{(T)}$
Titanium Grade 28	$0.5 \times YS_{(T)}$
Titanium Grade 29	$0.5 \times YS_{(T)}$

NOTE: $YS_{(T)}$ = at-temperature yield strength.

6.8.4 SCC Crack Propagation in Drip Shield Materials

6.8.4.1 Potential Crack Propagation Mechanisms in Titanium Grades 7, 28 and 29

Propagation of SCC in titanium alloys from active surface sites, such as by passive film rupture, has been postulated to occur via two basic but highly debated mechanisms (Schutz 1992 [DIRS 177345], pp. 265 to 297). One mechanism, the anodic-assisted cracking, is analogous to the SDFR model concept. The other is based on a hydrogen-assisted cracking phenomenon. As described in Section 6.4.4, the SDFR model initially developed to describe SCC crack growth rates for stainless steels under light water reactor conditions has been demonstrated to be equally relevant for Alloy 22. In the case of titanium alloys, less experimental and modeling effort related to environmentally assisted cracking is available in the published literature. However, titanium alloys are passive metals with corrosion resistant behavior similar to that of stainless steel and nickel-based alloys. Therefore, the concept of time-dependent strain leading to passive film rupture at emerging surface slip steps followed by local anodic dissolution and repassivation occurring in a periodic manner, which constitute the basic mechanisms of the SDFR model, is also likely to reasonably describe SCC crack growth in titanium alloys. For example, this type of behavior has been demonstrated for β titanium alloys (known to be susceptible to SCC in chloride environments) in several brine environments including 0.6 M NaCl using direct measurement of the repassivation slope, n, described in Equation 4. As expected, values of n obtained are quite high, varying from 1.05 to 1.14 (Kolman et al. 1998 [DIRS 177264]). An excellent review of the postulated SCC mechanisms attributed to titanium and its alloys was published by Simbi (1996 [DIRS 177262]).

6.8.4.2 Measured Crack Growth Rates for Drip Shield Materials

6.8.4.2.1 Titanium Grade 7 Crack Growth Rates

Crack growth rate measurements for the drip shield titanium alloys were performed using the same experimental procedure as for Alloy 22 measurements as described by DTN: MO0707SCCIGMER.000 ([DIRS 182202], Section 1). However, because of the propensity of these titanium alloys to undergo low temperature creep, in the case of annealed Titanium Grade 7, subsequent crack growth measurements in air indicated that the crack growth observed was due essentially to creep rather than SCC as described in Section 6.8.3.1. As shown in Figure 6-76, at an applied stress intensity factor, K_I, of 30 MPa√m, the apparent crack growth rate of Titanium Grade 7 in the 110°C BSW brine is 1.3×10^{-8} mm/s (Figure 6-76a; DTN: MO0707SCCIGMER.000 [DIRS 182202], Figure 1-4), as compared to a similar value of 1×10^{-8} mm/s in air after 800 hours on the test (Figure 6-76b; DTN: MO0707SCCIGMER.000 [DIRS 182202], Figure 6-14).

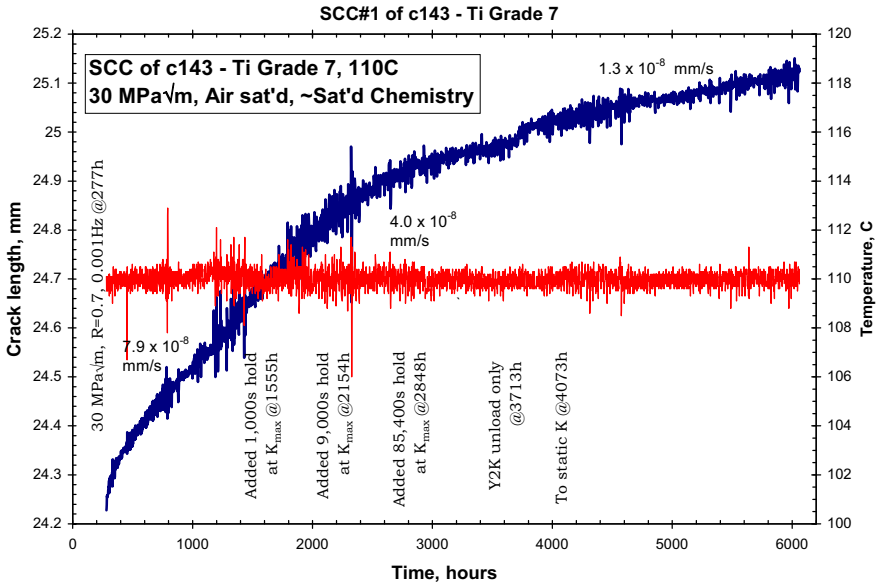

(a)

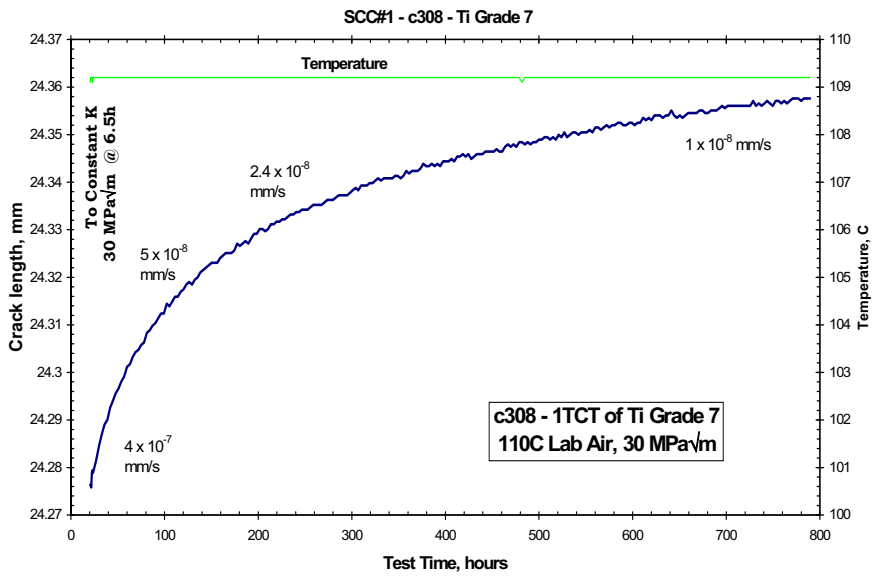

(b)

Sources: (a) DTN: MO0707SCCIGMER.000 [DIRS 182202], Figure 1-4.
(b) DTN: MO0707SCCIGMER.000 [DIRS 182202], Figure 6-14.

Figure 6-76. (a) Crack Length and Temperature versus Time Plot of the Stress Corrosion Crack Length and Temperature versus Time Plot of the Stress Corrosion Cracking Response of Specimen c143 (As-Received Titanium Grade 7) at 110°C in a Concentrated Mixed-Salt Environment with 5 psi Over-Pressure of Laboratory Air and (b) Direct Current Potential Drop Indicated Crack Length versus Time for Titanium Grade 7 Tested in 105°C Air at 30 MPa√m

However, for the case of 20% cold-worked Titanium Grade 7, the creep resistance (creep rate) is at least two orders of magnitude higher than for the annealed material (Kiessel and Sinnott 1953 [DIRS 174853], Figure 7). Therefore, if SCC had occurred in this material, the contribution of creep would be much less significant than that for Titanium Grade 7. Conservatively assuming

the crack growth rate measurement performed on 20% cold-worked Titanium Grade 7 is the result of SCC, rather than creep, the measured crack growth rate for 20% cold-worked Titanium Grade 7 under near-constant-load conditions (i.e., with a maximum-load hold time of 24 hours at an applied stress intensity factor of 30 MPa√m) is extremely low, about 1.4×10^{-10} mm/s (DTN: MO0707SCCIGMER.000 [DIRS 182202], Figure 1-30) as replotted in Figure 6-77.

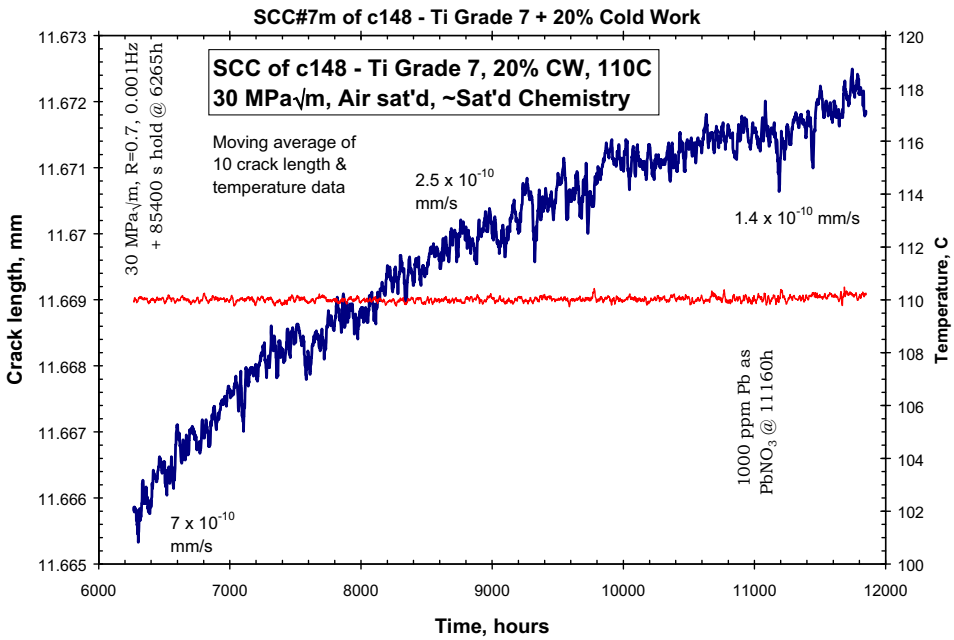

Source: DTN: MO0707SCCIGMER.000 [DIRS 182202], Figure 1-30.

NOTE: Specimen C148 is a half-thickness compact-tension specimen of 20% cold-worked titanium at 110 °C in a concentrated mixed-salt environment with 5 psi over-pressure of laboratory air.

A 10-point moving average was used to smooth the data, which proved quite sensitive to fluctuations in room and test temperatures (110°C).

Figure 6-77. Crack Length and Temperature versus Time Plot of the SCC Response of Specimen c148

This value of crack growth rate is conservative since, if the rate also includes a creep component, the actual SCC growth rate would be less than the measured value. As 20% cold work appears to reduce SCC susceptibility somewhat for commercial purity titanium (Simbi 1997 [DIRS 177263]), it is likely that the 20% cold-worked SCC crack growth rate, if it were SCC rather than creep, is substantially lower than for the annealed Titanium Grade 7 material assuming that annealed Titanium Grade 7 was susceptible to SCC at open-circuit potential in the test environment evaluated. On the other hand, the LTCTF U-bend results, where the apex strain is on the order of 12%, do not indicate susceptibility for annealed, welded, or cold-worked Titanium Grades 7 and 16 materials.

6.8.4.2.2 Threshold Stress Intensity Factor for Titanium Grade 7

As described in Section 6.4.5, the threshold stress intensity factor (K_{ISCC}) is a critical value of stress intensity factor (K_I) below which any preexisting crack either will not grow (by SCC) or is in an arrested state. For the Titanium Grade 7 drip shield material, it is conservatively assumed

that once the SCC initiation threshold criterion is exceeded, SCC initiates and propagates through-wall instantly. Thus, K_{ISCC} is arbitrarily taken as essentially zero and consequently it is not necessary to quantitatively establish an actual K_{ISCC} value for Titanium Grade 7.

6.8.4.2.3 Titanium Grades 28 and 29 Crack Growth Rates

As described in Section 6.8.3, it is to be expected that the higher-strength Titanium Grade 5 and possibly its ruthenium analog, Titanium Grade 29, will have higher SCC susceptibility in chloride brines than the lower-strength Titanium Grade 2 and its palladium analogue, Titanium Grade 7. In addition to potential SCC susceptibility, the literature indicates, for dissimilar metal welds of Titanium Grade 5 to Titanium Grade 2, there is a potential for HIC susceptibility. This potential HIC susceptibility under sustained loading results from an observed propensity for hydrogen present in the alloys to redistribute and concentrate near the Titanium Grade 2 fusion line of the dissimilar metal weld (Waisman et al. 1977 [DIRS 177383]; Gross 2003 [DIRS 177385]; Waisman et al. 1973 [DIRS 177386]; Williams et al. 1970 [DIRS 177387]). Apparently, aluminum in particular, significantly affects hydrogen activity in titanium and, due to weld dilution effects, aluminum concentration can increase near the Titanium Grade 2 fusion line of a dissimilar metal weld between Titanium Grades 5 and 2. As a result, hydrogen in these alloys can redistribute and concentrate near the Titanium Grade 2 fusion line leading to the potential for HIC at the weld region.

Although the presence of palladium and/or ruthenium in a Titanium Grade 29 to Titanium Grade 7 dissimilar metal weld may mitigate this hydrogen concentration effect, in the absence of directly relevant data, it is conservative to assume no credit is taken for the benefit from these precious metal additions. Thus, unlike the initially specified Titanium Grade 7 weld filler metal, the use of an intermediate aluminum content filler metal could decrease or potentially eliminate the tendency for hydrogen redistribution to the Titanium Grade 7 fusion line region. Consequently, Titanium Grade 28 (Ti-3Al-2.5V + ruthenium), which has a lower aluminum content than Titanium Grade 29, is selected as the weld filler metal composition that will be used to weld the drip shield Titanium Grade 29 structural supports to the Titanium Grade 7 plate material. Literature indicates it can potentially reduce any propensity for hydrogen redistribution that could lead to higher-than-expected hydrogen concentrations in the Titanium Grade 2 (or potentially the Titanium Grade 7) weld dilution zone (Kennedy et al. 1993 [DIRS 177388]). Thus, as Titanium Grade 28 welds will help provide structural support for the drip shield, it is important to measure the SCC response of Titanium Grades 28 and 29 alloy composition.

Measurement of Titanium Grades 28 and 29 Crack Growth Rates

Measured crack growth rate results (DTN: MO0705SCCIGM06.000 [DIRS 180869], file *GE-GRC-Final_Sept-2006-Rev3.doc*, Table 3) are listed in Table 6-33 for Titanium Grades 28 and 29 exposed to 150°C aerated SCW brine. Also listed in Table 6-33 are previously developed results obtained for Titanium Grade 7 exposed to 110°C BSW brine (DTN: MO0707SCCIGMER.000 [DIRS 182202], Table 1-7). These results were obtained using fatigued precracked compact tension specimens exposed to the aerated brines. The Titanium Grades 28 and 29 specimens were initially run in series in the same load train with the stress intensity factor controlled on the Titanium Grade 29 specimen as described by DTN: MO0707SCCIGMER.000 ([DIRS 182202], Section 1.2, pp. 16 to 17).

The initial stress intensity factor for both specimens was 27.5 MPa√m. However, the crack growth rate of Titanium Grade 28 was higher than that of Titanium Grade 29. Because the K_I control was maintained with respect to Titanium Grade 29, as the total Titanium Grade 28 crack length, a, increased over time, its stress intensity factor, K_I, also increased since K_I is a function of stress ($\underline{\sigma}$) and crack depth size (a) as shown in Equation 20:

$$K_I(a, \sigma) = \beta\ \sigma\ (\pi a)^{1/2} \qquad \text{(Eq. 20)}$$

where β is a geometry factor dependent on the size and shape of the crack and the configuration of the structural component, σ is the tensile stress distribution through the wall thickness of the structural component, and a is the crack depth size. Because of the increasing K_I on the Titanium Grade 28 specimen, which had the higher crack growth rate, reaching a maximum value of about 37 MPa√m, the test control was switched from Titanium Grade 29 to this Titanium Grade 28 specimen after 3,236 hours, and K_I was subsequently reduced in a stepwise fashion until the Titanium Grade 28 specimen reached its initial value of 27.5 MPa√m (DTNs: MO0707SCCIGMER.000 [DIRS 182202], Figures 1-116 to 1-118; MO0705SCCIGM06.000 [DIRS 180869], file *GE-GRC-Final_Sept-2006-Rev3.doc*, Figure 7). Limited preliminary testing was performed to evaluate the effect of the stress intensity factor on crack growth rate of Titanium Grades 28 and 29. The resulting crack growth rates over the range of stress intensity factors evaluated are listed in Table 6-34 and Table 6-35.

Table 6-33. Measured Crack Growth Rates for Titanium Grades 7, 28, and 29 Compact Tension Specimens

Specimen ID (K)	Material/Solution	Heat Treatment	Loading (R/ν/hold)[a]	Temperature (°C)	Crack Growth Rate (mm/s)
C143 (30 MPa√m)	Titanium Grade 7 in BSW	As-received	0.7, 0.001 Hz, 9,000 s	110	4×10^{-8}
C143 (30 Mpa√m)			0.7, 0.001 Hz, 85,600 s	110	1.3×10^{-8}
C143 (30 Mpa√m)			Constant K	110	1.25×10^{-8}
C148 (30 Mpa√m)	Titanium Grade 7 in BSW	20% Cold-Worked	0.7, 0.001 Hz, 9,000 s	110	1.4×10^{-8}
C148 (30 Mpa√m)			0.7, 0.001 Hz, 9,000 s	110	7.3×10^{-9}
C148 (30 Mpa√m)			0.7, 0.001 Hz, 85,600 s	110	7×10^{-10}
C148 (30 Mpa√m)			0.7, 0.001 Hz, 85,600 s	110	2.5×10^{-10}
C148 (30 Mpa√m)			0.7, 0.001 Hz, 85,600 s	110[b]	1.4×10^{-10}
C287 (27.5 Mpa√m)	Titanium Grade 29 in SCW	As-received	0.7, 0.001 Hz, 0 s	150	2.2×10^{-7}
C287 (27.5 Mpa√m)			0.7, 0.001 Hz, 9,000 s	150	7.5×10^{-8}
C287 (27.5 Mpa√m)			0.7, 0.001 Hz, 85,600 s	150	2×10^{-8}
C287 (20 Mpa√m)			Constant K	150	5×10^{-9}

Table 6-33. Measured Crack Growth Rates for Titanium Grades 7,28, and 29 Contact Tension Specimens (Continued)

Specimen ID (K)	Material/Solution	Heat Treatment	Loading (R/ν/hold)[a]	Temperature (°C)	Crack Growth Rate (mm/s)
C287 (27.5 Mpa√m)			0.7, 0.001 Hz, 0 s	150	2.5×10^{-7}
C287 (27.5 Mpa√m)			0.7, 0.001 Hz, 0 s	100	8.5×10^{-8}
C287 (27.5 Mpa√m)			Constant K	100	3×10^{-9}
C288 (27.5 Mpa√m)	Titanium Grade 28 in SCW	As-received	0.7, 0.001 Hz, 9,000 s	150	2.7×10^{-7}
C288 (30↑ Mpa√m)			0.7, 0.001 Hz, 85,600 s	150	3.7×10^{-7}
C288 (33↑ Mpa√m)			Constant K	150	3.8×10^{-7}
C288 (37↑ Mpa√m)			Constant K	150	4.9×10^{-7}
C288 (34↓ Mpa√m)			Constant K	150	1×10^{-7}
C288 (30↓ Mpa√m)			Constant K	150	6.6×10^{-8}
C288 (≈35 Mpa√m)			Constant K	150	1.1×10^{-7}

Sources: DTNs: MO0707SCCIGMER.000 [DIRS 182202], Table 1-7; MO0705SCCIGM06.000 [DIRS 180869], file *GE-GRC-Final_Sept-2006-Rev3.doc*, Table 3.

NOTES: Specimen C288 grew faster and was removed to permit further evaluation of specimen C287.
Crack growths in as-received Titanium Grade 7 (C143) are consistent with creep crack growth in air.
[a] R/ν/hold = load ratio (K_{max}/K_{min}), frequency in Hz, and hold time at K_{max}.
[b] With $PbNO_3$ added to the environment.

As described above, for the Titanium Grade 28 specimen, Figure 6-78b, a controlled change in K_I was made using $-dK_I/da$. Further, the change was programmed so K_I would change only in proportion to crack advance to allow the material and plastic zone at the crack tip to adjust to the change. The stepwise reduction in the Titanium Grade 28 specimen loading also resulted in a decreasing value for the Titanium Grade 29 specimen as indicated in Figure 6-78a. However, there was a relatively small effect on Titanium Grade 29 growth rate over the range from 25 ksi√in (27.5 Mpa√m) down to 14.2 ksi√in (15.6 Mpa√m) at about 6,000 hours (approximately 0.7 year). The short time steps used (approximately 100 hours) may not have allowed enough time for the crack growth rate to fully readjust to the changing stress intensity factor under the dropping load conditions (i.e., to decrease to a representative steady state rate). Thus, these shorter-term, decreasing K_I results (indicated by an arrow in Table 6-33) are considered as preliminary and are not used to estimate K_{ISCC}. However, they are of interest relative to gaining insight into the underlying crack growth mechanism.

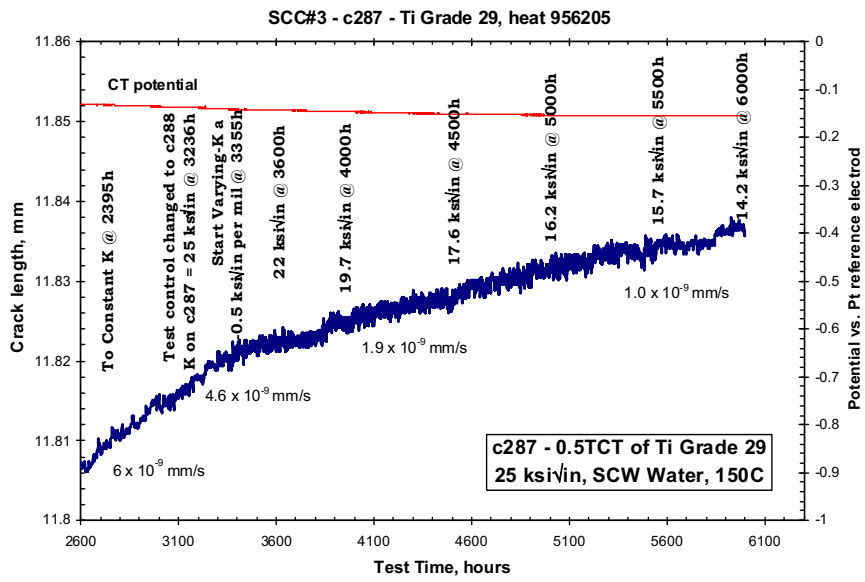

(a)

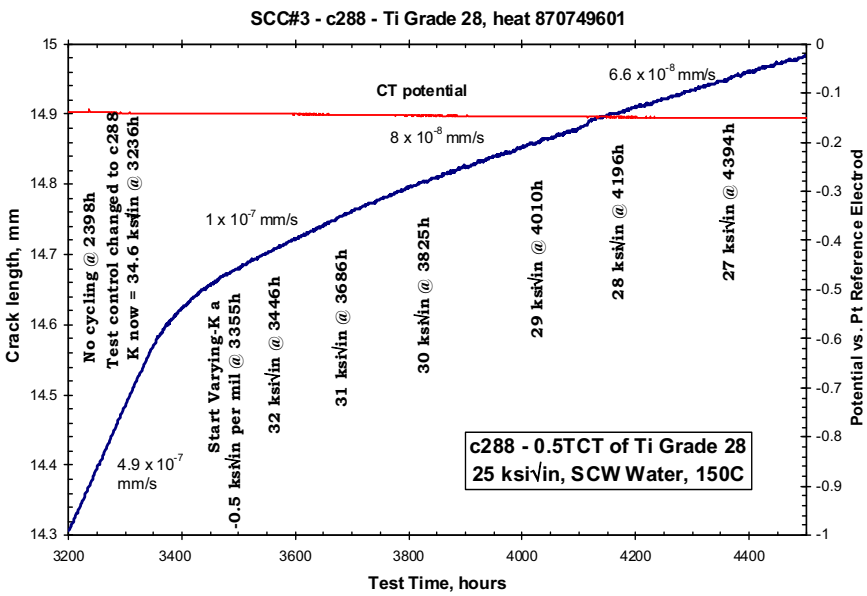

(b)

Source: DTN: MO0705SCCIGM06.000 [DIRS 180869], file *GE-GRC-Final_Sept-2006-Rev3.doc* , Figures 7 and 3, respectively.

Figure 6-78. Crack Length versus Time for Titanium Grades 29 (a) and 28 (b)

Table 6-34. Crack Growth Rate versus Stress Intensity Factor for Titanium Grade 28

K (Mpa√m)	mm/s
36.3	1.50×10^{-7}
35.2	1.14×10^{-7}
34.65	1.12×10^{-7}
33.55	9.30×10^{-8}
33	8.30×10^{-8}
32.45	7.60×10^{-8}

Table 6-34. Crack Growth Rate versus Stress Intensity Factor for Titanium Grade 28 (Continued)

K (Mpa√m)	mm/s
31.57	7.30×10^{-8}
30.8	6.30×10^{-8}
30.25	6.80×10^{-8}
29.7	7.10×10^{-8}

Sources: DTN: MO0708SRSCCIGM.000 [DIRS 182330], folder Crack Growth Rate, file *c288.xls*;
output DTN: MO0705CREEPSCC.000, file *GE_CGRs.xls*.

NOTE: The unit of K was mislabeled as "ksi √in" in DTN: MO0708SRSCCIGM.000 [DIRS 182330], folder Crack Growth Rate, file *c288.xls* and is corrected as "MPa√m."

Table 6-35. Crack Growth Rate versus Stress Intensity Factor for Titanium Grade 29

K (MPa√m)	mm/s
27.5	6.00×10^{-9}
25.3	4.60×10^{-9}
20.35	1.90×10^{-9}
16.5	1.00×10^{-9}

Source: DTN: MO0708SRSCCIGM.000 [DIRS 182330], folder Crack Growth Rate, file *c287.xls*;
output DTN: MO0705CREEPSCC.000, file *GE_CGRs.xls*.

NOTE: The unit K was mislabeled as "ksi √in" in DTN: MO0708SRSCCIGM.000 [DIRS 182330], folder Crack Growth Rate, file c287, and is corrected as "MPa√m" here.

The estimated crack growth rates obtained from the data evaluated over the relatively short 100-hour increments, are plotted versus K_I and shown for Titanium Grade 29 in Figure 6-79a and for Titanium Grade 28 in Figure 6-79b. A comparison of Titanium Grade 28 crack growth rates from Table 6-34 (7.10×10^{-8} mm/s at 29.7 MPa√m) with those of Titanium Grade 29 from Table 6-35 at a similar K_I value (6.00×10^{-9} mm/s at 27.5 MPa√m) indicates that Titanium Grade 28, a lower-strength alloy, has an unexpectedly higher apparent growth rate. However, there may be a creep component to the measured SCC growth rates, and Titanium Grade 28 may have a higher creep rate (see Section 6.8.7.2) than Titanium Grade 29. It is planned to measure the contribution of creep to apparent crack growth rates in the same way as was done for Titanium Grade 7, as described in Section 6.8.3.1. These *n* values are somewhat lower but reasonably consistent with literature values varying from 1.05 to 1.14 obtained on beta titanium alloys exposed to various chloride brines (Kolman et al. 1998 [DIRS 177264], Section 6.8.4.1).

Temperature Effect

To gain insight into the effect of temperature on crack growth rate, the temperature was dropped from 150°C to 100°C after 7,660 hours (approximately 0.9 years) on test, as indicated in Figure 6-80 (DTN: MO0705SCCIGM06.000 [DIRS 180869], file *GE-GRC-Final_Sept-2006-Rev3.doc*, Figures 3 and 5). The Titanium Grade 29 K_I value was transitioned to a constant value at 8,074 hours (approximately one year) resulting in a 100°C sustained-load crack growth rate at

27 MPa√m of 3 × 10^{-9} mm/s as compared with the previous 150°C value of 6 × 10^{-9} mm/s indicated in Figure 6-80 at about 2,600 hours on test. Thus, there was only a small decrease in crack growth rate due to the 50°C drop in temperature.

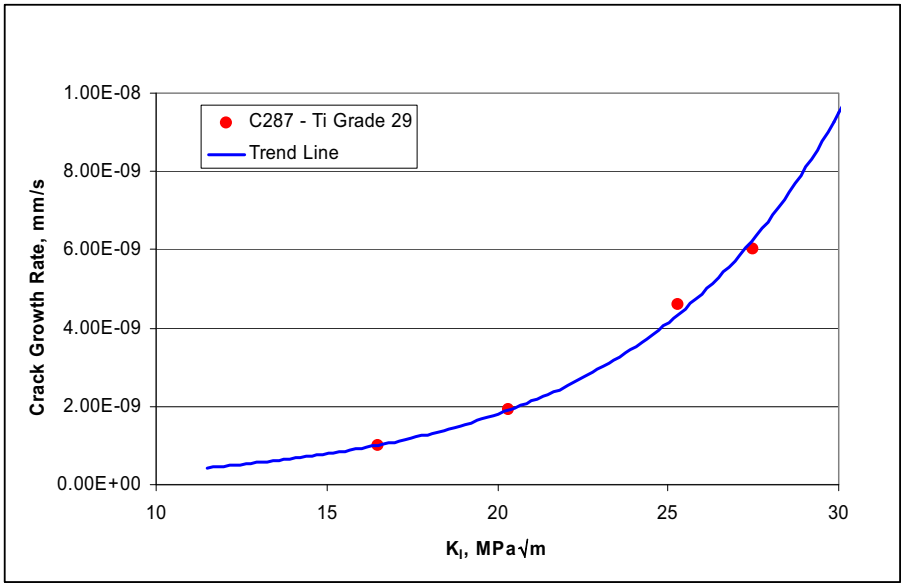

(a)

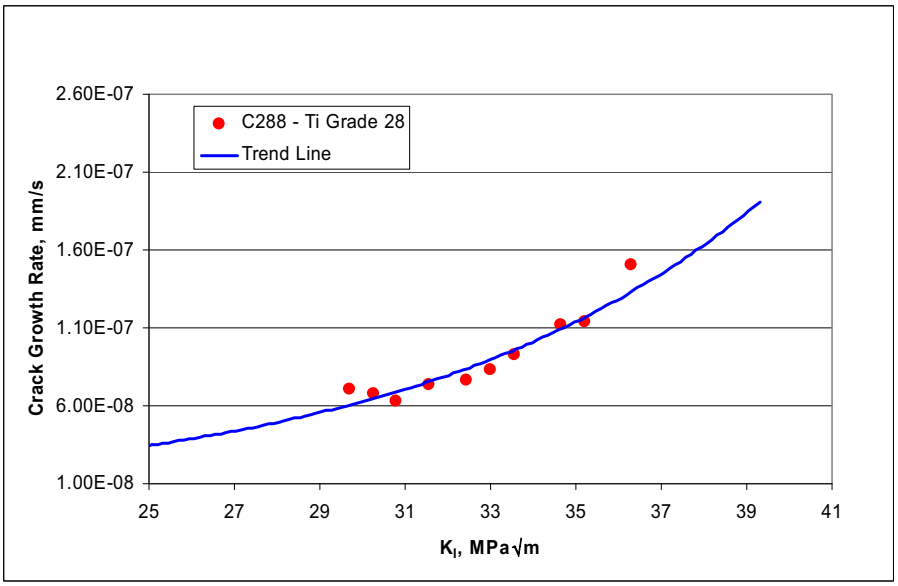

(b)

Sources: Table 6-34 and Table 6-35; Ouput DTN: MO0705CREEPSCC.000, *GE_CGRs.xls*.

Figure 6-79. Measured Crack Growth Rate versus Stress Intensity Factor for Titanium Grades 29 (a) and 28 (b) in SCW Solution at 150°C

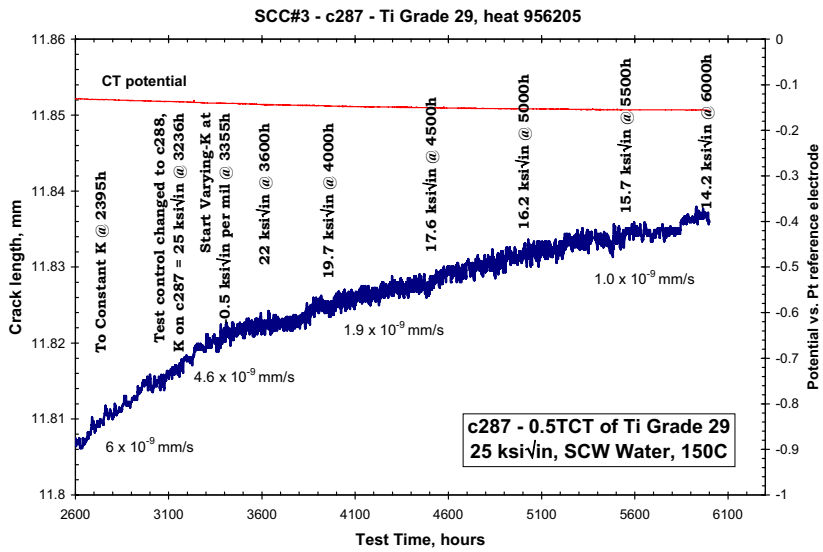

(a)

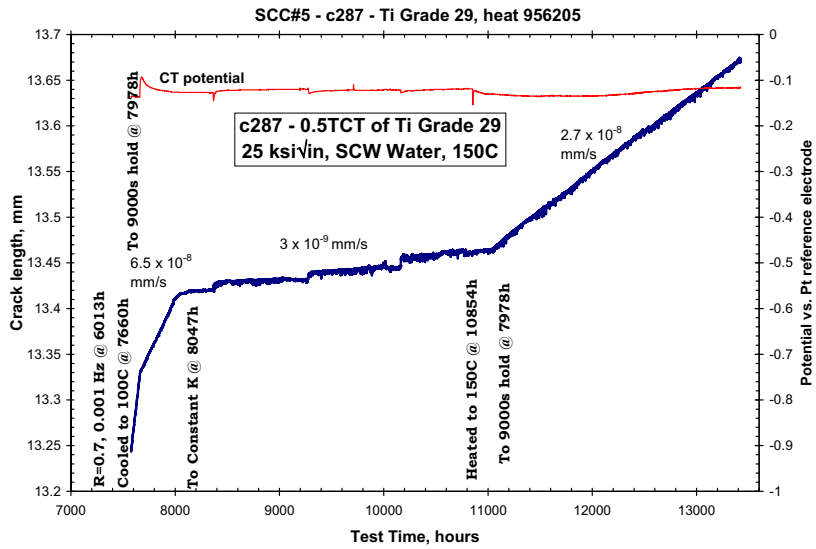

(b)

Sources: (a) DTN: MO0705SCCIGM06.000 [DIRS 180869], file *GE-GRC-Final_Sept-2006-Rev3.doc*, Figure 3, to 100°C
(b) DTN: MO0705SCCIGM06.000 [DIRS 180869], file *GE-GRC-Final_Sept-2006-Rev3.doc*, Figure 5, at 7,660 hours (approximately 0.9 years).

NOTE: Figure (b) is continued from (a) with a temperature drop from 150°C.

Figure 6-80. Crack Length versus Time for Titanium Grade 29

6.8.4.2.4 Threshold Stress Intensity Factor for Titanium Grades 28 and 29

As described in Section 6.8.4.2.2, the threshold stress intensity factor (K_{ISCC}) is a critical value of stress intensity factor (K_I) below which any preexisting crack either will not grow (by SCC) or is in an arrest state. For the Titanium Grade 7 drip shield material, it is conservatively assumed

that, once the SCC initiation threshold criterion is exceeded, SCC initiates and propagates through-wall instantly. Thus, it is not necessary to establish a K_{ISCC} for Titanium Grade 7.

However, for the drip shield structural support material, Titanium Grade 29, and its weld filler metal, Titanium Grade 28, it is advantageous to consider the likely crack growth rates and the threshold stress intensity value, K_{ISCC}, at the propagating crack tip to determine if and at what depth an initiated crack may arrest. In considering the environmentally determined K_{ISCC} parameter, it is also relevant to consider the observation that, for some titanium alloys, crack growth can also occur in air at a stress intensity factor value below the critical plane strain fracture toughness value, K_{IC}, characteristic of brittle fracture (i.e., of unstable fast crack growth) but above the environmentally determined K_{ISCC}. This slow crack growth phenomenon is referred to as sustained load cracking (SLC). SLC is likely aggravated by dissolved hydrogen in the titanium alloy (ASM International 1987 [DIRS 103753], Figure 57, p. 275). SLC is similar to SCC except that it is much slower and occurs in the total absence of a reactive environment. As can be seen, the SLC threshold stress intensity factor, K_{ISLC}, is higher that K_{ISCC} as shown in Figure 6-81 for a higher-strength, near-alpha alloy, Ti-8Al-1Mo-1V (UNS R54810).

A discussion of SLC in Ti-6Al-4V and its potential effect in modifying low-cycle fatigue behavior as well as the effect of dissolved hydrogen is presented by Boyce and Ritchie (2001 [DIRS 177436], pp 129 to 147). The authors found only a transient effect of SLC in air on crack growth in fatigued precracked compact tension specimens at a constant applied stress intensity factor of 36.5 MPa√m. During the first 1,000 seconds, they observed an initial slow crack growth rate of approximately 2×10^{-4} mm/s for about 80 μm of growth followed by growth rate decay to a rate of $\leq 1 \times 10^{-8}$ mm/s, defined by the authors as crack arrest. This room temperature Titanium Grade 5 air crack growth rate ($\leq 1 \times 10^{-8}$ mm/s) is up to a factor of three higher than the rate of 3×10^{-9} mm/s measured for Titanium Grade 29 (Specimen C287) in 100°C aerated SCW brine at 27 MPa√m as indicated in Table 6-33. However, other SLC test results for Titanium Grade 5 performed at a much higher K_I of 60 MPa√m indicate that the extent of transient SLC growth decreases with temperature from about 500 μm at –30°C to about 45 μm at 140°C (Boyce and Ritchie 2001 [DIRS 177436], p. 143) consistent with decreasing SLC tendency at increasing temperatures. In contrast, fracture toughness of Titanium Grade 5 tends to increase with temperature (Boyer et al. 2003 [DIRS 174636] p. 217).

In addition, a comparison of K_I, K_{ISLC}, and K_{ISCC} values for the range of relevant titanium alloys is given in Table 6-36. Most of the reported literature values for K_{ISCC} were measured in 3.5% NaCl or seawater at room temperature (Schutz 1992 [DIRS 177345], p. 277, Table 3; Boyer et al. 2003 [DIRS 174636], p. 217). Also included in Table 6-36 are more-limited literature and project data for specific alloys and for other environments. These results are nominal values and will vary with alloy composition, metallurgical condition, and product form and thickness.

Table 6-36. Summary of Threshold Stress Intensity Factor Results for Relevant Titanium Alloys

Alloy	Fracture Toughness, K_{IC} (MPa√m)	SLC THRESHOLD, K_{ISLC} (MPa√m)	Environmental Threshold, K_{ISCC} (MPa√m)
Titanium Grade 2	58 to 66[a, b]	–	58 to 66[a, b]
Titanium Grade 2	111[c]	<90[c]	–
Titanium Grade 7	≥ Titanium Grade 2		<30[f]
Titanium Grade 5	60 to 90[a, c]	46[c]	27 to 57[b]
Titanium Grade 23	75 to 140[c]	55[c]	53 to 119[b]
Titanium Grade 29	~ 85[d] to 100[e]	–	>60[e]
Titanium Grade 29	–	–	<27.5[f]
Titanium Grade 9	81[a]	75[a]	81[a]
Titanium Grade 9 (weld)	≥ 123[a]	123[a]	123[a]
Titanium Grade 28	≥ Titanium Grade 9	–	<30[f]

Sources:
[a] Boyer et al. 2003 [DIRS 174636] pp. 217, 237, 280, and 581.
[b] Schutz 1992 [DIRS 177345].
[c] Millot 2003 [DIRS 178209], Table 1.
[d] According to DTN: MO0707SCCIGMER.000 [DIRS 182202], Table 1-1, Titanium Grade 29 heat number and vendor cert (RTI 2003 [DIRS 178467]) for the same heat of material.
[e] Titanium Grade 29 environmental results generated in 210°C concentrated NaCl plus CaF_2 saturated brine (Schutz et al. 2000 [DIRS 177257]).
[f] DTN: MO0705SCCIGM06.000 [DIRS 180869], file *GE-GRC-Final_Sept-2006-Rev3.doc*, Table 3 (GE Titanium Grades 28 and 29 results in 150°C SCW).

NOTE: Environmental results for 20°C to 25°C 3.5% NaCl or seawater (Jones 1992 [DIRS 178458], p. 277, Table 3) unless otherwise Indicated.

For Titanium Grade 29, K_{ISCC} values listed in Table 6-36 indicate the lowest "longer hold time," sustained load value of K_I with measurable crack growth (YMP results in 150°C SCW under initially accelerated cyclic loading followed by longer-term, approximately 900-hour, sustained loading conditions) is 27.5 MPa√m (DTN: MO0705SCCIGM06.000 [DIRS 180869], file *GE-GRC-Final_Sept-2006-Rev3.doc*, Table 3 and Figures 2 and 3). It can be observed that under these longer-term hold conditions at 27.5 MPa√m, the crack growth rate drops over time, decreasing significantly from about 7×10^{-8} mm/s at about 2,800 hours to about 6×10^{-9} mm/s at about 3,200 hours. Thus, as described above, while there are apparent further but small growth rate decreases with the short term, (100-hour K_I holds) incremental step decreases in K_I, much of these apparent decreases likely would have occurred over time at the initial 27.5 MPa√m. Thus, as the long-term stresses present on the waste package do not experience cyclic conditions, a reasonable conservative estimate of K_{ISCC} can be obtained by taking a factor of approximately 0.5 times the lowest sustained-load measured value of 27.5 MPa√m or 14 MPa√m. In general, SCC susceptibility increases with increasing alloy strength and, Titanium Grade 28 has a significantly lower yield strength and similar although more dilute alloying element content than Titanium Grade 29. Thus, it is to be expected that Titanium Grade 28 will have a higher K_{ISCC}. However, for Titanium Grade 28, as with Titanium Grade 29, a conservative K_{ISCC} value can be obtained by taking a factor of 0.5 times the lowest sustained-load project-measured value of 30 MPa√m or 15 MPa√m.

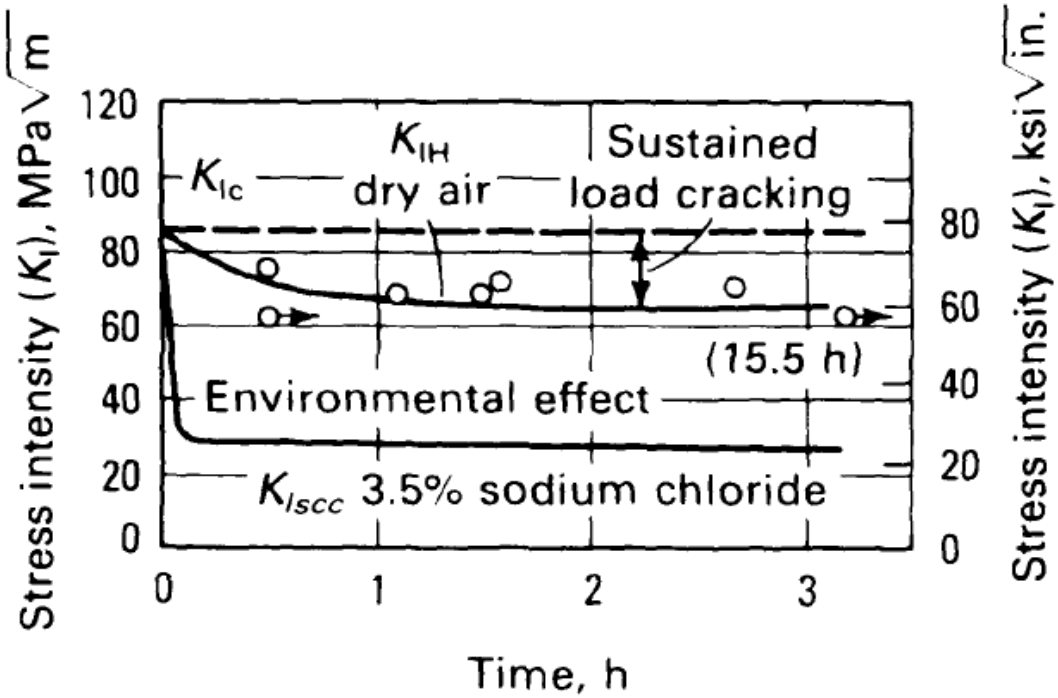

Source: ASM International 1987 [DIRS 103753], Figure 57, p. 275.

Figure 6-81. Effect of Sustained-Load Cracking Compared to SCC on K_I in Ti-8Al-1Mo-1V Mill-Annealed Sheet

6.8.5 Modeling Seismic Crack Density for Drip Shield Materials

6.8.5.1 Drip Shield SCC Due to Rockfall Residual Stress

The Titanium Grade 7 drip shield plates are supported by Titanium Grade 29 drip shield structural support components (SNL 2007 [DIRS 179354], Table 4-2, Parameter 07-01). These support components include the beams (SNL 2007 [DIRS 179354], Table 4-2, Parameter 07-01). The other Titanium Grade 29 components of the drip shield (e.g., the bulkhead longitudinal stiffeners, bulkheads) (SNL 2007 [DIRS 179354]) are in the drip shield interior and are thus not subjected to dripping-water chemistries.

Deformation-induced residual stress resulting from rockfalls can cause stress corrosion crack initiation in the Titanium Grade 7 drip shield plate material and its Titanium Grade 29 structural support beams, if the stress levels exceed the threshold stresses for potential SCC and all other conditions for SCC to occur described in Section 6.1 are met. For conservatism, in this report SCC initiation in drip shield material is assumed to occur immediately once the threshold stress is exceeded.

The stress relaxation effect has been quantified in design calculations for the Titanium Grade 7 drip shield subjected to rockfall impact at room temperature and 150°C (BSC 2005 [DIRS 174715], Section 5.6). Calculation indicates that the bounding residual stresses resulting

from rockfall will relax at room temperature to below 50% of yield strength between one year and 100 years, depending on how conservative a creep law is adopted. At 150°C, stresses relax to below 65% of the 150°C yield strength in less than 10 years and below 50% of yield strength between five years and 1,000 years. In contrast, using the measured assumed SCC crack growth rate for 20% cold-worked Titanium Grade 7 ($<2 \times 10^{-10}$ mm/s at 30 MPa√m (DTN: MO0707SCCIGMER.000 [DIRS 182202], Figure 1-30)) as a reasonable value to represent mechanically damaged drip shield material, it would take about 2,400 years for an initiated crack to grow through-wall. However, as described above, during this long propagation period, the crack tip stresses and resultant stress intensity factor would be continuously decreasing due to stress relaxation and, it would be highly unlikely that through-wall crack growth could occur under these dropping K_I conditions. For example, if the stress level reaches 65% of yield strength stress level normal to the propagating crack after 10 years when the crack depth would nominally be 10/2, 400 × 15 mm, or 0.63 mm, the calculated K_I using Equation 20 with $\beta = 1$ would be about 6.4 MPa√m which would significantly decrease the already low crack growth rate of $<2 \times 10^{-10}$ mm/s at 30 MPa√m.

In contrast to Titanium Grade 7, the stress relaxation rate for Titanium Grade 29, a high-strength titanium alloy equivalent to Titanium Grade 24, is lower because of its higher creep resistance (BSC 2005 [DIRS 174715], Attachment I, Figure I-13). However, the apparent crack growth rate of Titanium Grade 29 is much lower (approximately 4.6×10^{-9} mm/s at 25 ksi√in (27.5 MPa√m) at 150°C, Figure 6-78(a)) than that of Titanium Grade 7 (approximately 1.8×10^{-8} mm/s at 110°C at 30 MPa√m (27.3 ksi√in), Figure 6-76(a)) even through Titanium Grade 29 rate was measured at a higher temperature than that of Titanium Grade 7 (150°C versus 110°C). Thus, crack propagation through the Titanium Grade 29 structural support will take a significantly longer time, compensating for the lower stress relaxation rate. Further, at some stage of its propagation, when the crack becomes sufficiently large, it will affect the overall stiffness (compliance) of the drip shield resulting in additional deformation, or, in the case of a confined drip shield, in load and stress redistribution. This redistribution of stress will reduce stress concentration levels and thus inhibit further crack propagation.

Under primary stresses such as those that result from seismic-induced drift collapse and resultant rock rubble loading, creep will occur and could potentially lead to creep rupture or contact between the drip shield and waste package. However, detailed calculations have been completed (BSC 2005 [DIRS 174715], Section 5.4.3) that take into account the interaction of the drip shield plates and supporting beams with the adjacent contacting rock rubble as the drip shield sides (legs) deform and lean to one side. These calculations indicate that total deformation after, for instance, 10,000 years is limited to less than 5% strain, whereas creep rupture does not occur below a minimum of at least 10% total strain (see Section 6.8.7.1). No contact with the waste package is indicated. The rubble-related reaction forces in the drip shield after, for instance, 10,000 years are relatively low with maximum values of about 75 MPa.

6.8.5.2 Modeling Seismic Crack Density for Drip Shield Materials

Seismic activity can lead the drip shield to impact other components in the drift including the waste packages. If the seismically induced impacts are of sufficient magnitude, the impacts could physically dent the drip shield and potentially the waste package as discussed in Section 6.7. These deformations can result in cold work of the drip shield, producing a

cold-worked gradient typically highest on the outer surface and lowest on the inner surface. Impacts may also create complex through-wall residual stress profiles. These stress profiles and cold-work gradients may lead to SCC in the seismically affected area of the drip shield.

As in the treatment of SCC due to rockfalls (Section 6.8.5.1), stress corrosion cracks in the drip shields due to seismic processes are expected to be tight, tortuous, and potentially plugged with corrosion products or mineral deposits, or both, leading to negligible water flow through these openings.

This section evaluates the potential for SCC that occurs in the drip shield due to the stresses and cold work generated by an unlikely seismic event. After initiation of SCC, cracks may provide a path for subsequent leakage to the waste package but, as in the waste package case, aqueous transport and radionuclide release through SCC-induced crack areas in the drip shield is likely to be negligible due to plugging by corrosion products or mineral deposits, or both. However, conservatively, the seismic crack density model is considered in this section assuming no crack plugging.

The seismic crack density model and analysis developed in Section 6.7 for the waste package generally applies to the drip shield with the exception that the materials properties of titanium alloys, such as yield strength and modulus of elasticity, are different from those of Alloy 22. The crack area density (crack area per unit of seismically damaged area) determined in this section is used as a scaling factor applied to the total seismic damaged area (determined in *Seismic Consequence Abstraction* (SNL 2007 [DIRS 176828])) to obtain the total area of the crack network through which transport can occur. It is expected that the crack area density will serve as input to *Seismic Consequence Abstraction* (SNL 2007 [DIRS 176828]). There are many similarities between Alloy 22 waste package material and titanium alloys including SCC crack morphology (Section 6.7.1.1), decreasing gradients of stress and the stress intensity factor through the wall thickness (Section 6.7.1.2), and reduction in driving force for crack growth in neighboring cracks (Section 6.7.1.3). Therefore, the general approach to development of the seismic crack density model for titanium alloys is similar to that described in Section 6.7.2 for Alloy 22.

6.8.5.2.1 Summary of General Approach to Modeling Seismic Crack Density

Based on the discussions in Section 6.7.2, the most likely limiting case is that the damaged areas on the drip shield are penetrated by a network of tight cracks. This network of cracks has the potential to allow diffusive transport but prevent significant advective flow and advective transport because of the small effective crack opening area and complicated paths of individual cracks (Section 6.7.1.1).

The seismic scenario requires three inputs to represent the effective area of a network of cracks:

(1) Total damaged area on the waste package, A_D
(2) Crack density in the damaged area on the surface of the barrier, ρ_{SCC}
(3) Crack opening area of an individual crack, A_{SCC}.

The damage abstractions for the seismic scenario will define the total damaged area on the barrier. The total area of the crack network, $A_{SCC,\ NET}$, is then the product of the seismically damaged area, A_D; the crack density, ρ_{SCC} (number of cracks per unit area); and the crack opening area of an individual crack, A_{SCC} (area/crack), expressed in Equation 28 (Herrera 2004 [DIRS 168133], Section 6.1) and shown again as Equation 51:

$$A_{SCC,\ NET} = A_D\,(\rho_{SCC}\,A_{SCC}) \qquad \text{(Eq. 51)}$$

All seismically damaged areas on the drip shield are not open. The factor ($\rho_{SCC}\,A_{SCC}$) is the crack area density or crack area per unit of seismically damaged area (i.e., the fraction of the seismically damaged area) through which water can flow. The factor ($\rho_{SCC}\,A_{SCC}$) can be viewed as a scaling factor applied to the seismically damaged area to obtain the total area of the crack network, $A_{SCC,\ NET}$. Section 6.7.3 provides estimates of the crack area density through analysis of networks of cracks arranged in a hexagonal geometry. Section 0 provides an alternative model for the crack area density by analysis of a damaged area with a circular geometry circumscribed by a single through-wall crack. Because the hexagonal array represents a high effective density (close spacing) of individual cracks, this hexagonal case, with crack center spacings set at the plate thickness, t (Section 6.7.3), is considered a conservative representation. Section 6.8.5.2.3 provides an alternative model for the crack area density by analysis of a damaged area with a circular geometry circumscribed by a single through-wall crack. This is considered a limiting "realistic" case.

6.8.5.2.2 Summary of Primary Conceptual Model for Crack Area Density: Hexagonal Geometry

Section 6.7.3 shows that the crack area density for case 1 (where cracks can barely touch) is $\frac{\pi\sigma}{\sqrt{3}E}$ and for case 2 (where significant crack overlap is allowed) is $\frac{4\pi\sigma}{\sqrt{3}E}$. The crack area density is shown to be proportional to the applied stress, essentially residual stress due to seismic activity, and inversely proportional to the modulus of elasticity. It does not depend on the wall thickness. Therefore, the crack area density is recommended to be represented as a uniform distribution between $\frac{\pi\sigma}{\sqrt{3}E}$ (for case 1) and $\frac{4\pi\sigma}{\sqrt{3}E}$ (for case 2), i.e.:

$$\text{Crack Area Density} = C\,\frac{\pi\sigma}{\sqrt{3}E} \qquad \text{(Eq. 52)}$$

where C is the epistemic uncertainty factor given by a uniform distribution between 1 and 4.

The use of a uniform distribution is reasonable as it accurately reflects the lack of knowledge of the exact value of the crack area density. In general, a uniform distribution is appropriate for uncertain quantities where the range can be established by physical arguments or expert knowledge, but not much else is known about the relative likelihood of values within the range (Mishra 2002 [DIRS 163603], Section 2.3). The use of a distribution ranging up to the very conservative upper bound allows for uncertainties, such as the potential for crack overlap and deviations from a regular array of identically shaped cracks, to be appropriately accounted for.

The yield strength of the material should be used as a very conservative estimate for the stress component in the crack area density calculation. The yield strength is considered conservative because the process of crack initiation and through-wall crack propagation as well as creep-induced stress relaxation will result in significant reduction in the residual stress. The use of material yield strength will give a conservative estimate of the crack area density appropriate for probabilistic evaluation. Values of the yield strength of Titanium Grade 7 from room temperature (21°C) to 150°C (the temperature at which the structural calculations of the waste package exposed to ground motion were conducted (SNL 2007 [DIRS 176828])) and the modulus of elasticity from room temperature to 204°C are shown in Table 4-7. Taking the average of values of yield strength, these values are also presented in the second and third columns of Table 6-37.

Table 6-37 shows the crack length, crack density, crack width, crack opening area, and crack area density for cases 1 and 2 at room temperature and 150°C with assumed barrier thickness of 10 mm, 15 mm, and 20 mm. In Table 6-37, the values of the barrier thickness are for illustration purposes only. The crack length equals $\frac{2t}{\sqrt{3}}$ for case 1 and $2t$ for case 2 (Section 6.7.3). The crack density equals $\frac{\sqrt{3}}{2t^2}$ for case 1 and $\frac{2}{\sqrt{3}t^2}$ for case 2 (Section 6.7.3). The crack width of a single crack is calculated by equation 29 ($\delta = \frac{(4c)\sigma}{E}$) for the given thickness for each case. The crack opening is calculated from Equation 30 ($A_{SCC} = \pi\left(\frac{\delta}{2}\right)\left(\frac{2c}{2}\right) = \pi\left(\frac{(2c)\sigma}{E}\right)c = \frac{(2\pi c^2)\sigma}{E}$) for the two cases. The crack area density is calculated from Equation 33 ($\rho_{SCC}A_{SCC} = \frac{\sqrt{3}}{2t^2}\frac{(2\pi t^2)\sigma}{3E} = \frac{\pi\sigma}{\sqrt{3}E} \cong 1.81\frac{\sigma}{E}$) for case 1 and Equation 36 ($\rho_{SCC}A_{SCC} = \frac{2}{\sqrt{3}t^2}\frac{(2\pi t^2)\sigma}{E} = \frac{4\pi\sigma}{\sqrt{3}E} \cong 7.26\frac{\sigma}{E}$) for case 2.

Table 6-37 shows that the crack area density (crack area per unit of seismically damaged area) ranges from 4.67×10^{-3} to 1.88×10^{-2} at room temperature and 3.15×10^{-3} to 1.33×10^{-2} at 149°C. The reason 149°C is chosen instead of 150°C is that the values for yield strength (ASME 2001 [DIRS 158115], Section II, Part D, Table Y-1, pp. 632 to 634) and the modulus of elasticity (DTN: MO0003RIB00073.000 [DIRS 152926]) for Titanium Grade 7 are both listed for 149°C. Using yield strength and modulus of elasticity values at 149°C, therefore, avoids the need to interpolate the values for 1°C difference in temperature. The impact of using values at 149°C, rather than 150°C is insignificant. To be conservative, it is recommended that the room temperature range of crack area density be used for performance assessment as this choice yields higher (more conservative) crack area densities for cases 1 and 2.

Table 6-37. Crack Characteristics for Hexagonal Geometry

Temperature (°C)	Yield Strength (MPa)	Modulus of Elasticity (GPa)	Case	Barrier Thickness[1] (mm)	Crack Length[2] (mm)	Crack Density[3] (/mm^2)	Crack Width[4] (mm)	Crack Opening Area[5] (mm^2)	Crack Area Density[6]
Room	276	107	1		$\frac{2t}{\sqrt{3}}$	$\frac{\sqrt{3}}{2t^2}$	$\delta = \frac{(4c)\sigma}{E}$	$A_{SCC} = \frac{(2\pi c^2)\sigma}{E}$	$\rho_{SCC} A_{SCC} \cong 1.81\frac{\sigma}{E}$
				10	11.54701	0.00866	0.05964	0.54088	0.00467
				15	20.80084	0.00385	0.10744	1.75518	0.00467
				20	27.73445	0.00217	0.14325	3.12032	0.00467
			2		$2t$	$\frac{2}{\sqrt{3}t^2}$	$\delta = \frac{(4c)\sigma}{E}$	$A_{SCC} = \frac{(2\pi c^2)\sigma}{E}$	$\rho_{SCC} A_{SCC} \cong 7.26\frac{\sigma}{E}$
				10	20.00000	0.01155	0.10330	1.62263	0.01875
				15	30.00000	0.00513	0.15495	3.65092	0.01875
				20	40.00000	0.00289	0.20661	6.49053	0.01875
149°C	176	101	1		$\frac{2t}{\sqrt{3}}$	$\frac{\sqrt{3}}{2t^2}$	$\delta = \frac{(4c)\sigma}{E}$	$A_{SCC} = \frac{(2\pi c^2)\sigma}{E}$	$\rho_{SCC} A_{SCC} \cong 1.81\frac{\sigma}{E}$
				10	11.54701	0.00866	0.04038	0.36619	0.00316
				15	17.32051	0.00385	0.06057	0.82392	0.00316
				20	23.09401	0.00217	0.08076	1.46474	0.00316
			2		$2t$	$\frac{2}{\sqrt{3}t^2}$	$\delta = \frac{(4c)\sigma}{E}$	$A_{SCC} = \frac{(2\pi c^2)\sigma}{E}$	$\rho_{SCC} A_{SCC} \cong 7.26\frac{\sigma}{E}$
				10	11.54701	0.00866	0.04038	0.36619	0.01332
				15	17.32051	0.00385	0.06057	0.82392	0.01332
				20	23.09401	0.00217	0.08076	1.46474	0.01332

Source: Output DTN: MO0702PASTRESS.002, *Model Output DTN.doc*, Table 8-14.

NOTES:
1. The values of the barrier thickness are for illustration purposes only.
2. The crack length equals $\frac{2t}{\sqrt{3}}$ for Case 1 and $2t$ for Case 2.
3. The crack density equals $\frac{\sqrt{3}}{2t^2}$ for Case 1 and $\frac{2}{\sqrt{3}t^2}$ for Case 2.
4. The crack width of a single crack is given by Equation 29 for the given thickness for each case.
5. The crack opening is calculated from Equation 30 for the two cases.
6. The crack area density is calculated from Equation 33 for Case 1 and Equation 36 for Case 2.

6.8.5.2.3 Summary of the Alternative Conceptual Model for Crack Area Density: Circular Geometry

A conceptual model of a through-wall crack circumscribing a circular damaged area is considered in Section 6.7.3 for Alloy 22. The main purpose of the conceptual model is to provide an alternative mathematical model for crack area density that can be used to validate the primary crack area density model. A conceptual model for the drip shield material can be established in a way similar to that described in Section 6.8.5.2.2.

Even though this model leads to a fully circumscribed area, the inner area material would not fall out due to the roughness of crack surfaces. It should be emphasized that this calculation and

associated postulated crack morphology are strictly for calculating an alternative crack opening area. It is not meant to imply that this type of crack morphology is observed.

To summarize the approaches described in Section 6.8.5.2.2, for a hollow cylinder under internal pressure (p_i) and external pressure (p_o), of inner radius (a) and external radius (b) (Figure 6-65) under plane stress conditions, Timoshenko and Goodier (1970 [DIRS 121096], pp. 68 to 71) pointed out that (Section 6.7.4):

$$\varepsilon_\theta = \frac{u}{r} \qquad \text{(Eq. 53)}$$

Further, Hooke's Law can be written for an isotropic material for plane stress as:

$$E\varepsilon_\theta = \sigma_\theta - \nu\sigma_r \qquad \text{(Eq. 54)}$$

where u is the radial displacement, r, the distance from the origin in a polar coordinate system, E, the modulus of elasticity, and ν, the Poisson's ratio.

The following are expressions for the radial and tangential stress components (Timoshenko and Goodier 1970 [DIRS 121096], p. 70):

$$\begin{aligned} \sigma_r &= \frac{a^2b^2(p_o - p_i)}{b^2 - a^2}\frac{1}{r^2} + \frac{p_i a^2 - p_o b^2}{b^2 - a^2} \\ \sigma_\theta &= -\frac{a^2b^2(p_o - p_i)}{b^2 - a^2}\frac{1}{r^2} + \frac{p_i a^2 - p_o b^2}{b^2 - a^2} \end{aligned} \qquad \text{(Eq. 55)}$$

For the purposes of this analysis, b approaches infinity (infinite plate), $p_o = -S$, and the focus is on the radial displacements at $r = a$ (the surface of the hole). With these conditions, at $r = a$, $\sigma_r = 0$, and $\sigma_\theta = 2S$. Using Equations 42 and 43, the radial displacement, u, at $r = a$ is:

$$u = \frac{2aS}{E} \qquad \text{(Eq. 56)}$$

More generally, it has been shown by the above analysis that the radial displacement, u, at the surface of the hole of radius, r, under the action of a radial stress, σ, could be written as:

$$u = \frac{2r\sigma}{E} \qquad \text{(Eq. 57)}$$

where r is the radius of the hole (i.e., the radius of the damaged area) and σ is applied stress.

The radial displacement, u, in Equation 55 can be considered the crack opening for a crack circumscribing a damaged area with a radius of r. This is equivalent to the conservative case where the inner material is detached (i.e., cracked through-wall around the entire circumference) and not subjected to any stress (i.e., not decreasing the displacement particularly by "pulling" on the outer material). The crack opening area of this crack can be expressed as:

$$A_{SCC} = 2\pi ru = 2\pi r \frac{2r\sigma}{E} = \frac{4\pi r^2 \sigma}{E} \qquad \text{(Eq. 58)}$$

The damaged area is πr^2. Therefore the crack area density, assuming that there is one circular crack in each circular area of radius r, can be expressed as:

$$\rho_{SCC} A_{SCC} = \left(\frac{1}{\pi r^2}\right)\left(\frac{4\pi r^2 \sigma}{E}\right) = 4\frac{\sigma}{E} \qquad \text{(Eq. 59)}$$

In case of drip shield material (Titanium Grade 7), the crack area density ($\rho_{SCC}\ A_{SCC}$) depends only on the stress state and the modulus of elasticity of Titanium Grade 7. Values of the Titanium Grade 7 yield strength and modulus of elasticity at room temperature and at 149°C are shown in the second and third columns of Table 6-38. In Table 6-38, calculations of the crack length, crack density, crack opening area, and crack area density are shown for various radii of the damaged area. The crack area density, calculated using values of the Titanium Grade 7 yield strength and modulus of elasticity at room temperature, is about 1.03×10^{-2}, while the crack area density calculated at 149°C is about 6.79×10^{-3}. Again, the crack area density is higher at room temperature than at 149°C.

Table 6-38. Crack Characteristics for Circular Geometry

Temperature (°C)	Yield Strength (MPa)	Modulus of Elasticity (GPa)	Radius[a] (mm)	Crack Length[b] (mm)	Crack Density[c] (/mm2)	Crack Width[d] (mm)	Crack Opening Area[e] (mm2)	Crack Area Density[f]
Room	276	107		2π r	1/πr^2	$u = \frac{2r\sigma}{E}$	$A_{SCC} = \frac{4\pi r^2 \sigma}{E}$	$\rho_{SCC} A_{SCC} = 4\frac{\sigma}{E}$
			10	62.83000	0.00318	0.05165	3.24527	0.01033
			15	94.24500	0.00141	0.07748	7.30185	0.01033
			20	125.66000	0.00080	0.10330	12.98106	0.01033
149	176	101		2π r	1/πr^2	$u = \frac{2r\sigma}{E}$	$A_{SCC} = \frac{4\pi r^2 \sigma}{E}$	$\rho_{SCC} A_{SCC} = 4\frac{\sigma}{E}$
			10	62.83000	0.00318	0.03497	2.19712	0.00699
			15	94.24500	0.00141	0.05245	4.94351	0.00699
			20	125.66000	0.00080	0.06994	8.78846	0.00699

Output DTN: MO0702PASTRESS.002, *Table 8-14.xls*.

NOTES: [a] Values of the barrier thickness are for illustration purposes only.
[b] Crack length equals 2πr.
[c] Crack density equals 1/πr^2 from Equation 40.
[d] Crack width is given by Equation 44.
[e] Crack opening is calculated from 2πru from Equation 45.
[f] Crack area density is calculated from Equation 46.

6.8.6 SCC Crack "Plugging"

According to *Plugging of Stress Corrosion Cracks by Precipitates* (BSC 2001 [DIRS 156807], Table 5-13), once a stress corrosion crack develops into a through-wall crack, the crack length,

2c, and the crack gap (or width), δ, are 130 mm and 157 microns, respectively. These values are reasonably consistent with those listed in Table 6-37 and Table 6-38. Thus, the passive oxide film growing normal to each opposing crack face would need to grow until it fills the 157-micron gap. This is equivalent to approximately 103 microns of metal loss per crack side and results in a total oxide thickness per side of approximately 182 microns based on a TiO_2 oxide-to-metal volume ratio of 1.76 (Bradford 1987 [DIRS 151988], Table 2, p. 64). At a corrosion rate of 0.03 microns per year, it will take about 3,400 years for the crack to fill with corrosion product. In the interim, the crack walls are corroding passively. Before the corrosion film grows to a thickness where it will completely fill the crack, there could be a small amount of water transport by surface diffusion (film flow) into the crack and through the drip shield. However, the small heat flux present across the drip shield wall will result in evaporation of the slowly flowing water. A resultant scale deposit (principally calcium carbonate (calcite)) will form over the crack where it intersects the upper drip shield surface, as well as within the crack. This formation of calciferous deposits is well documented (Cowan and Weintritt 1976 [DIRS 105212], pp. 1 to 39 and 376 to 383) in seawater environments and in heat exchangers through which natural brines are forced to flow. This has been observed in desalination plants (carrying approximately 6% NaCl solutions) and in potash plants (carrying greater than 12% brine (NaCl/KCl mixtures) (Cowan and Weintritt 1976 [DIRS 105212], pp. 1 to 39 and 376 to 383). In both cases, titanium surfaces are heat sources at operating temperatures of approximately 100°C. Such deposits form rapidly under flowing conditions and have to be regularly removed to avoid loss of heat exchanger efficiency. Other minerals such as amorphous silica will also precipitate.

A detailed calculation of the expected rate of stress corrosion crack plugging due to calcite precipitation resulting from evaporation of a pore water of typical composition dripping onto a drip shield at the crack location has been performed (BSC 2001 [DIRS 156807]). The calculation conservatively assumes that corrosion products generated on the crack faces, as well as colloids, particles, and any precipitated silica minerals, do not help in plugging the crack opening and that there is a uniform water seepage flow in space and time (BSC 2001 [DIRS 156807], Section 5.3). It was concluded that stress corrosion cracks are sealed in a few hundred years at most when water is allowed to flow through the cracks at a low film flow rate (BSC 2001 [DIRS 156807], Section 6.3). When the cracks are bridged by water, the sealing process may take thousands of years, but no flow occurs as the water is held by capillary forces. In a more realistic case of a nonuniform flow onto the drip shield, more precipitation and faster plugging will occur.

Following plugging of such a drip shield crack, any solution flow through the crack would be dominated by an efficiency factor determined by the ratio of solution runoff on the drip shield surface to through crack flow that in turn is determined by scale porosity and permeability. Because of the expected high density of the calcite deposits (BSC 2001 [DIRS 156807]) and lack of a pressure gradient to drive water through the crack, the quantity of solution flow through the plugged crack would approach zero.

Finally, drip shield structural response to rockfalls induced by seismic events is addressed in *Seismic Consequence Abstraction* (SNL 2007 [DIRS 176828]), where the damaged area of the drip shield is calculated for each of the given rock masses. The damaged area is defined as a region of the drip shield where the calculated stress exceeds the threshold stress. Seismic SCC is discussed further in Section 6.8.5.

6.8.7 Lower-Temperature Creep of Titanium Alloys

As discussed in Section 6.8.3, low-temperature creep leading to creep rupture and to secondary stress relaxation can influence apparent SCC crack initiation results. In this section, the low-temperature creep phenomenon is discussed in more detail. As indicated in Section 1.2, the discussion on low-temperature creep of titanium alloys is not considered as a model in this document.

As has been described, the current drip shield top and side plates are fabricated from Titanium Grade 7 (UNS R52400), an alloy analogous to commercial purity Titanium Grade 2 with 0.12-0.25% palladium added to increase corrosion resistance. Structural support bulkheads and side support beams welded to the plate material are fabricated using a higher-strength material, Titanium Grade 29 (UNS R56404), a ruthenium-containing analogue to Titanium Grade 23 (Ti-6Al-4V ELI) (UNS R56407). Titanium Grades 7 and 29 have mechanical properties identical to their analogues, which do not contain palladium or ruthenium. Titanium Grades 2 and 7, as well as Titanium Grades 23 and 29, have the unusual mechanical response of undergoing creep deformation under load at low temperatures (i.e., at room temperature or above) (McQuillan and McQuillan 1956 [DIRS 177306], pp. 349 to 354; Dutton 1996 [DIRS 174750]) and even at cryogenic temperatures (Dutton 1996 [DIRS 174750], p. 9).

This surprisingly low creep resistance at lower temperatures, compared to other alloy systems with comparable, relatively high melting points (1,660°C for Titanium Grade 7), results from thermally activated dislocation motion overcoming obstacles provided by interstitial impurities such as oxygen and nitrogen. This contrasts with the higher-temperature self-diffusion mechanism, in which atomic diffusion becomes sufficiently rapid such that dislocation climb becomes the rate-controlling creep deformation mechanism. For titanium and its alloys, there is an intermediate temperature range, about 150°C to 500°C, where creep resistance increases or drops less rapidly with temperature due to dynamic strain aging effects (Dutton 1996 [DIRS 174750], pp. 5 to 10).

One of the important aspects of drip shield performance is its creep under the long-term load. Besides its own weight, which is negligibly small compared to the strength of the titanium, the only long-term primary load on the drip shield could be due to pressure (weight) of the caved rock mass covering the drip shield. Collapse of the emplacement drift can occur in cases of strong ground motions (e.g., ground motions with a peak ground velocity greater than 2 m/s in lithophysal rock mass) or time-dependent drift degradation. Total collapse of the emplacement drifts is not likely due to time-dependent strength degradation only. The load of the caved rock on the drip shield structure is a consequence of the interaction between the structure and the surrounding caved rock. The initial loads are calculated to account for that interaction, and analysis of the drip shield stability for short-term loading conditions shows that the drip shield will be stable with a relatively large margin of safety (BSC 2005 [DIRS 174715]). Because of the long duration of the analyzed period, the possibility of early drift collapse after the waste emplacement, and a general impression of the relatively poor resistance of the titanium to creep (Kiessel and Sinnott 1953 [DIRS 174853]), it is important to analyze time-dependent deformation and the stability of the drip shield loaded by the caved rock mass.

As indicated in Section 6.8.1 and earlier in this section, as far as the mechanical properties are concerned, the drip shield-relevant titanium alloys discussed in this report can be divided into two groups, the lower strength alloys such as Titanium Grades 2, 7, and 16 and the higher strength alloys such as Titanium Grades 5, 23, 24, and 29. Also as indicated in Section 6.8.1, from Table 6-19 and Table 6-20, it is clear that the slightly lower yield strength of Titanium Grade 29 as compared with its nonruthenium analogue, Titanium Grade 5, is due to its lower oxygen content (0.13 wt % as compared with 0.20 wt %), rather than to the presence of ruthenium, because the yield strength of Titanium Grade 24 is identical to that of Titanium Grade 5 (both are 0.20 wt % oxygen), just as the addition of palladium does not alter the mechanical properties of Titanium Grade 7 or 16. Based on this, when creep properties are dealt with in this section, Titanium Grades 2, 7, and 16 are reasonably treated as approximately equivalent materials and Titanium Grades 5, 23, 24, and 29 are also reasonably treated as approximately equivalent materials. Similarly, Titanium Grade 28 is considered as identical to Titanium Grade 9. Therefore, these materials are compared and/or discussed in figures and text as two groups of materials in terms of their creep properties. In other words, when original data is obtained for one alloy in a given group, it is considered in this section that the data is applicable to all other alloys in the same group. For instance, data generated for Titanium Grade 5 are considered as applicable to Titanium Grades 23, 24 and 29, and are labeled accordingly.

6.8.7.1 Lower Temperature Creep Behavior of Titanium Alloys

The creep of many metals, including titanium (Dutton 1996 [DIRS 174750]; ASM International 1990 [DIRS 141615], p. 631, Figure 34), can be described by the three stages of observed deformation versus time (i.e., primary, secondary, and tertiary creep). The primary and tertiary stages generally occur over relatively short times and involve larger plastic strains. In contrast, the secondary or steady-state stage generally encompasses the greatest time period before creep rupture occurs and thus is of most interest, especially when extrapolating to very long times.

For commercial purity titanium, Titanium Grades 2 and 5, the strain, ε, accumulated during the primary phase can be represented by a power law expression, i.e.,

$$\varepsilon = A \cdot t^{n} \qquad \text{(Eq. 60)}$$

where A and n are constants (n <1) rather than a logarithmic equation as proposed by some investigators (Dutton 1996 [DIRS 174750], Equations 5 and 6). An expression, Equation 61, proposed specifically to fit experimentally determined Titanium Grade 2 primary creep behavior at 125°C, was developed for stresses approaching the yield strength (Dutton 1996 [DIRS 174750], Equation 5):

$$\varepsilon = 3.1 \times 10^{-30}\, \sigma^{12.6}\, t^{.1125} \qquad \text{(Eq. 61)}$$

where ε is the strain in percent, t is in hours and stress is in MPa. This type of power law (and in some cases logarithmic law) expression appears adequate in describing lower-temperature titanium creep behavior up to about 15% strain (Dutton 1996 [DIRS 174750], Section 5.1), as compared to a total strain to failure for all three creep stages that generally exceeds 40% (Dutton 1996 [DIRS 174750], Figures 11 and 3).

Secondary creep rate measurements for titanium alloys support a secondary creep rate expression of the form (Dutton 1996 [DIRS 174750], Equation 7):

$$d\varepsilon/dt = A\sigma^n \exp\text{-}(H/kT) \qquad \text{(Eq. 62)}$$

where A is a constant, σ is the applied stress, n is a constant characteristic of a given alloy, H is the activation energy (enthalpy), k the Boltzmann constant, and T the temperature. This expression can be converted into the more familiar formulation using the Larson-Miller parameter, K, and presented as Equation 63:

$$K = T(\text{Log } t_r + \text{C}) \qquad \text{(Eq. 63)}$$

where C is a constant. This formulation is derived from the observation that the time to rupture, t_r, is inversely proportional to the minimum creep rate (Dutton 1996 [DIRS 174750], Section 6.0).

These creep laws, as described in the literature, were conservatively bounded and used to calculate the expected response of the drip shield under rockfall and drift collapse/rubble-loading conditions (BSC 2005 [DIRS 174715]).

6.8.7.2 Lower Temperature Creep Rates of Titanium Alloys

Larson Miller plots specifically for commercial purity titanium (Dutton 1996 [DIRS 174750], Figure 22) and for Titanium Grades 5 (Boyer 1997 [DIRS 177440], p. 22.9) and 9 (Boyer et al. 2003 [DIRS 174636], p. 234) are available in the literature. A summary of the expected low temperature, 1,000-hour plastic strains (0.5-1 % strain), and rupture times obtained from these Larson Miller plots for the range of temperatures and stresses of interest is shown in Figure 6-82. The data used to construct these plots is presented in Table 6-39.

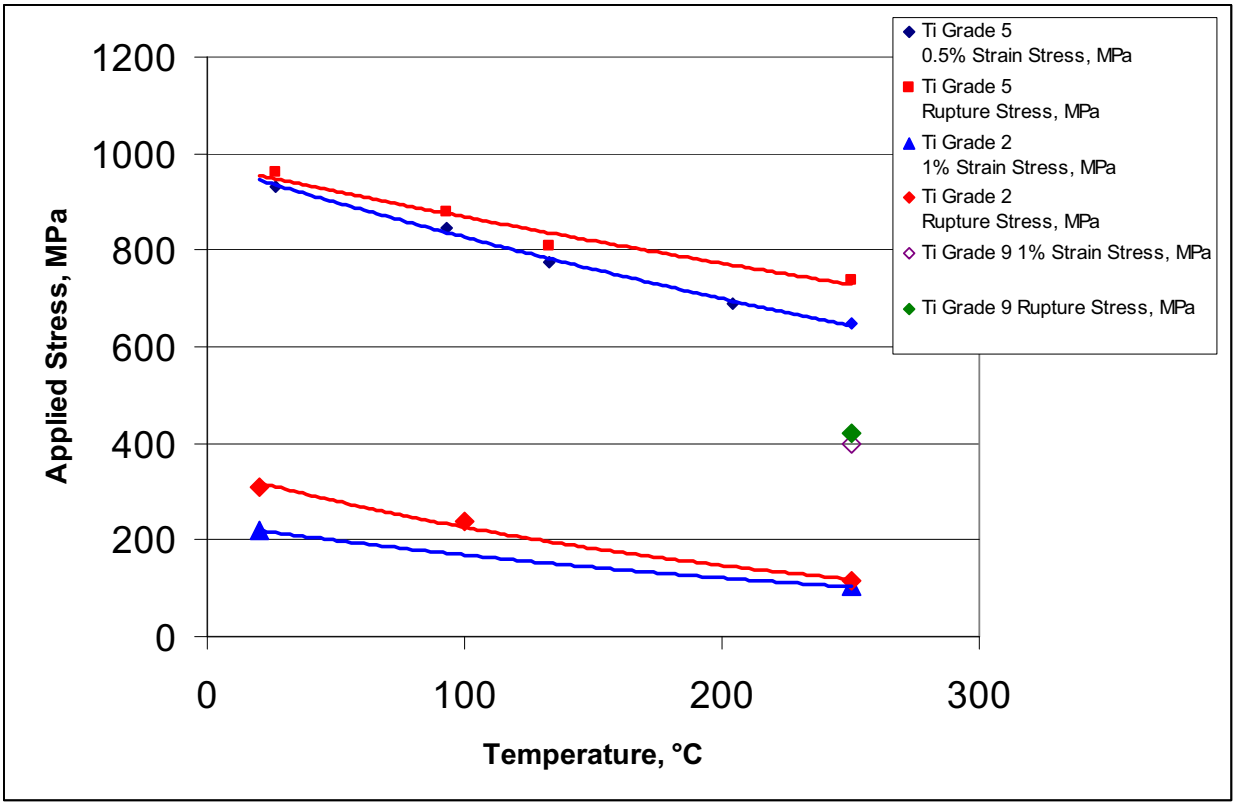

Sources: Dutton 1996 [DIRS 174750], Figures 10 and 11; Boyer 1997[DIRS 177440], p. 22.9 ; Boyer et al. 2003 [DIRS 174636], p. 234. Output DTN: MO0705CREEPSCC.000*, CreepGraphs.xls.*

NOTE: As indicated in the beginning of Section 6.8.7, Titanium Grades 23, 24 and 29 are considered identical to Titanium Grade 5 as far as low temperature creep is concerned and Titanium Grade 28 is considered as identical to Titanium Grade 9.

Figure 6-82. Comparison of 1,000-Hour Creep Response for Titanium Grade 2 with Titanium Grades 5 and 9 Over a Range of Applied Stresses and Temperatures

Table 6-39. Creep Data Used to Construct Figure 6-82

Temperature (°C)	Titanium Grade 5		Titanium Grade 2			Titanium Grade 9		Reference
	0.5% Strain Stress (MPa)	Rupture Stress (MPa)	0.5% Strain Stress (MPa)	1% Strain Stress (MPa)	Rupture Stress (MPa)	1% Strain Stress (MPa)	Rupture Stress (MPa)	
204.4	690	–	–	–	–	–	–	Boyer 1997 [DIRS 177440], p. 22.9
132.8	776	810	–	–	–	–	–	
93.3	847	880	–	–	–	–	–	
26.7	932	960	–	–	–	–	–	
250	647	739	–	–	–	–	–	
20	–	–	210	220	310	–	–	Dutton 1996 [DIRS 174750], Figures 10 and 11
100	–	–	–	–	237	–	–	Figure 6-83*
250	–	–	–	103	117	400	421	Boyer et al. 2003 [DIRS 174636], p. 234

* Estimated from Figure 6-83 at 1,000 hours as indicated in Figure 6-82.

Stress Corrosion Cracking of Waste Package Outer Barrier and Drip Shield Materials

As indicated in the beginning of this section, Titanium Grades 23, 24, and 29 are considered identical to Titanium Grade 5 as far as low temperature creep is concerned and Titanium Grade 28 is considered identical to Titanium Grade 9. Therefore, as shown in Figure 6-82, the creep resistance of the Ti-6Al-4V-type materials, Titanium Grades 5, 23, 24, and 29 is much higher than for the commercial purity Titanium Grades 2 and 7 alloys over the full range of drip shield-relevant temperatures. As might be expected, the intermediate-strength Titanium Grade 9 (Ti-3Al-2.5V) exhibits intermediate creep resistance. It is also apparent that, at 1,000 hours, Titanium Grades 2 and 7 undergo 1% plastic strain in this temperature range at applied stresses down to about 100 MPa. A more-definitive plot of applied stress ratio versus time to failure can be obtained using air creep rupture results by the YMP for Titanium Grade 7 tested at 105°C (DTN: MO0707SCCIGMER.000 [DIRS 182202], Figures 6-3 to 6-6), supplemented with 100°C air results obtained on Titanium Grade 2 at AECL (Dutton et al. 1996 [DIRS 175817], Table 1, specimens C1 and C3). These combined results are summarized in Table 6-25 and are plotted in Figure 6-83 as applied stress versus time to failure (years).

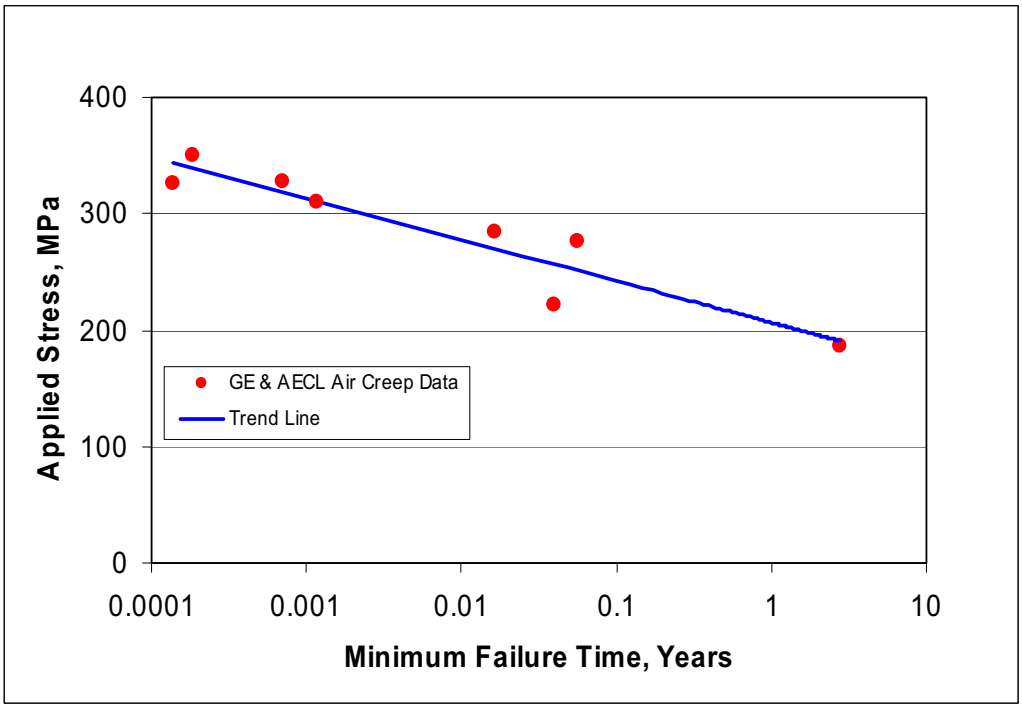

Source: Data are extracted from GE GRC and AECL air creep data in Table 6-25. Output DTN: MO0705CREEPSCC.000, *CreepGraphs.xls.*

Figure 6-83. Time to Failure versus Applied Stress for Titanium Grades 2 and 7 Tested in Air at 100°C to 105°C

It is evident from Figure 6-83 that creep rupture failures can occur in less than 10 years at stresses on the order of 170 MPa (70% of yield strength) and above.

In addition to creep rupture, lower-temperature creep behavior of titanium can be further described in terms of steady state or secondary creep rate. In Figure 6-84, the steady-state creep rates for Titanium Grades 2 and 7 at room temperature (Dutton 1996 [DIRS 174750], Figure 7) and at 100°C to 105°C (Dutton et al. 1996 [DIRS 175817], Table 1 and Figures 1, 13, 14, and 17

to 23; Andresen 2005 [DIRS 173867], Figures 6-3 to 6-6 and 6-13) are plotted versus applied stress ratio (percent of yield strength) for room temperature and 100°C to 105°C. It is evident from Figure 6-84 that significant creep occurs at room temperature even under applied stresses well below room temperature yield strength (i.e., less than 50% yield strength). It is also apparent that the creep rate, when the applied stresses are greater than about 80% of yield strength, is significantly higher at 100°C than at room temperature. This observation is consistent with the creep-rate temperature dependency described in McQuillan and McQuillan (1956 [DIRS 177306], Figure 147). The creep rate reaches a maximum value at about 125°C and then slowly decreases with increasing temperature to about 225°C. Above 225°C, the creep rate again starts to increase rapidly.

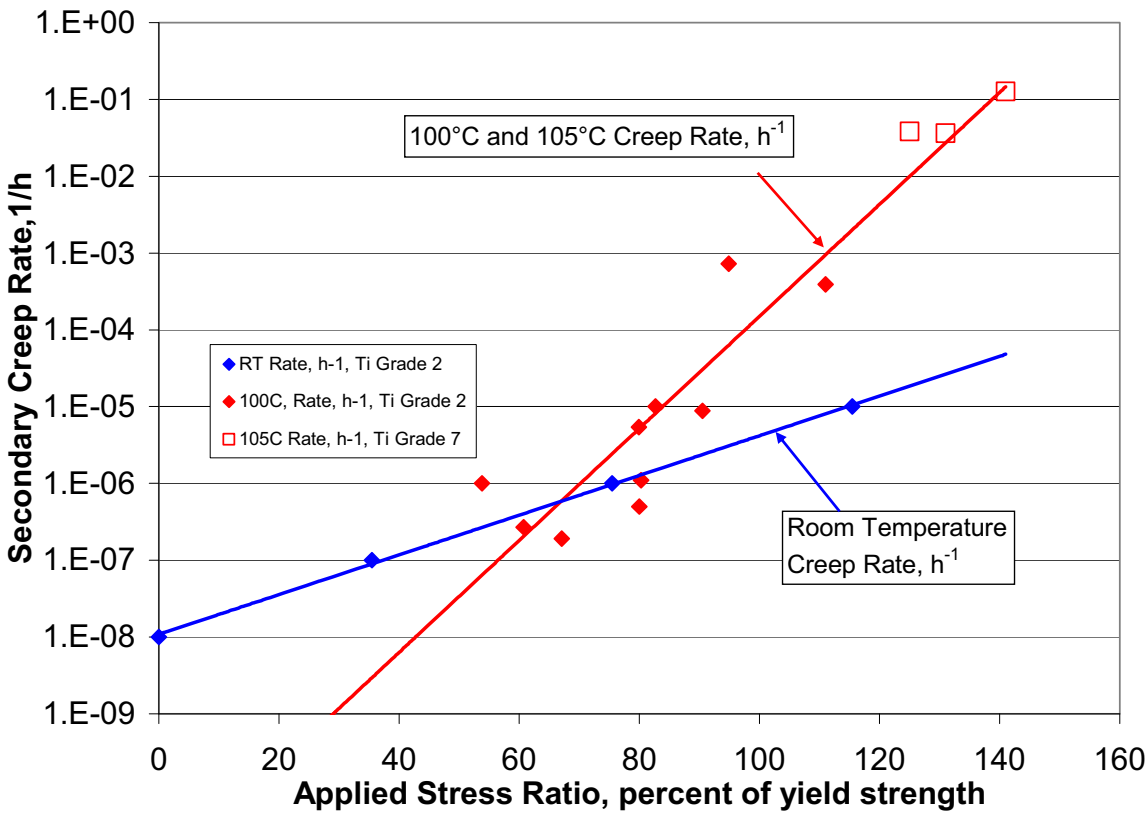

Sources: McQuillan and McQuillan 1956 [DIRS 177306], pp. 349 to 355; Dutton et al. 1996 [DIRS 175817]; DTN: MO0707SCCIGMER.000 [DIRS 182202]. Output DTN: MO0705CREEPSCC.000, file *CreepGraphs2.xls,* sheet *"SCG1."*

Figure 6-84. Steady-State Creep Rate versus Applied Stress Ratio for Titanium Grades 2 and 7 at Room Temperature and 100°C to 105°C

Figure 6-85 compares the lower-temperature behavior of high-strength titanium alloys (Titanium Grades 5 and 24) to that of alloys with lower strength (Titanium Grades 2 and 7). The fact that the higher-strength class of titanium alloys produces lower creep rates is evident in the comparison of room temperature creep rates versus applied stress as shown in Figure 6-85. It is obvious that the rates are several orders of magnitude lower for the higher-strength titanium

alloys (Titanium Grades 5, 24, and 29) at any given applied stress than the creep rates of Titanium Grades 2 and 7.

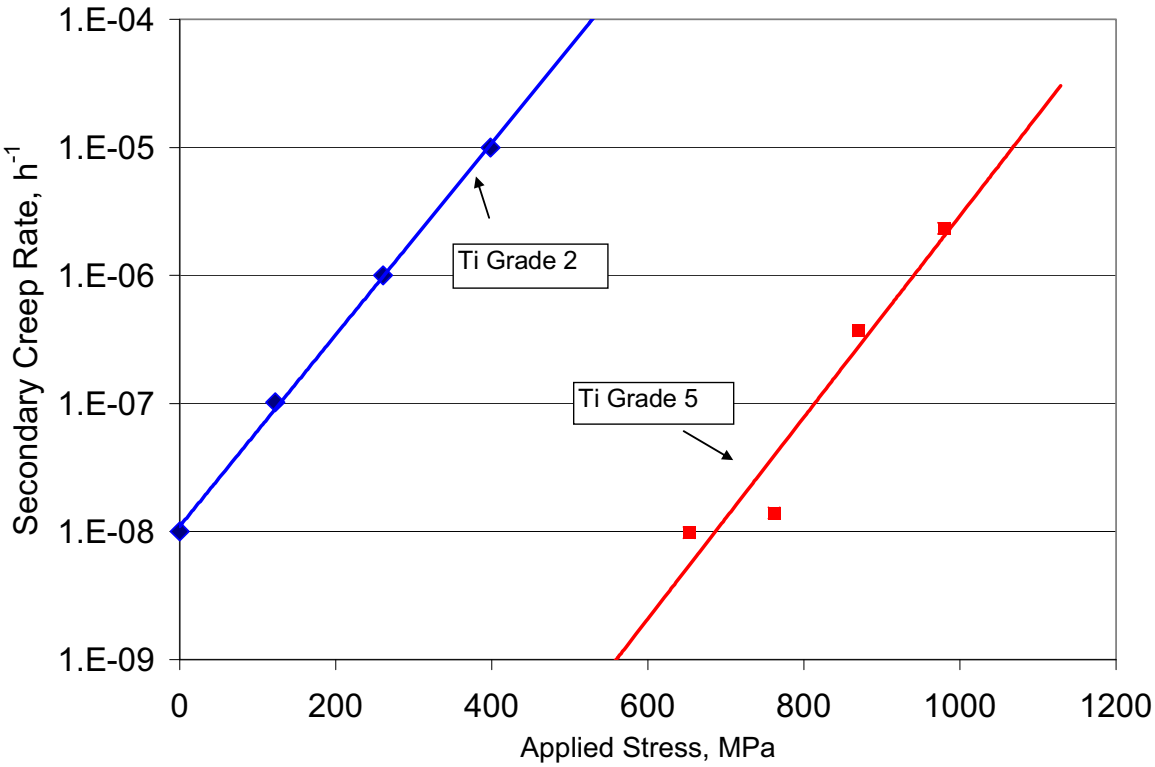

Sources: McQuillan and McQuillan 1956 [DIRS 177306], pp. 349 to 355; Dutton et al. 1996 [DIRS 175817]; DTN: MO0707SCCIGMER.000 [DIRS 182202]; Odegard and Thompson 1974 [DIRS 174818]; Kiessel and Sinnott 1953 [DIRS 174853], pp. 331 to 338. Output DTN: MO0705CREEPSCC.000, *CreepGraphs2.xls.*

NOTE: As indicated in the beginning of Section 6.8.7, Titanium Grades 24 and 29 are considered identical to Titanium Grade 5 as far as low-temperature creep is concerned.

Figure 6-85. Comparison of Secondary Creep Rates versus Applied Stress for Titanium Grades 2 and 7 with Titanium Grades 5 and 24 at Room Temperature

Figure 6-86 compares the secondary creep rates for the two classes of titanium alloys at 100°C to 260°C versus applied stress and again demonstrates the much higher creep resistance of the Ti-6Al-4V class of materials as compared to Titanium Grades 2 and 7. As indicated in Kiessel and Sinnott (1953 [DIRS 174853]), the similarity in creep rates of Titanium Grade 2 at about 100°C and at about 250°C is likely related to strain aging effects. Therefore, the 250°C data point, which falls on the 100°C trendline, is not unexpected.

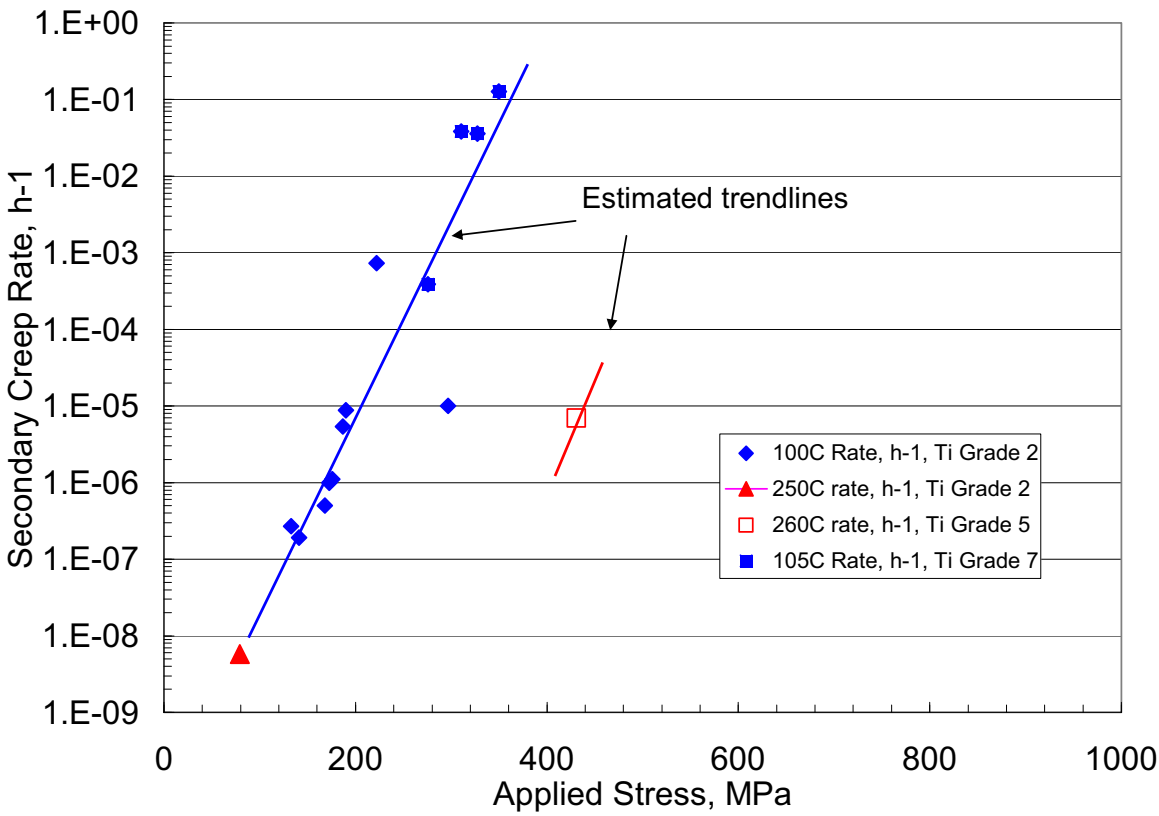

Source: McQuillan and McQuillan 1956 [DIRS 177306], pp. 349 to 354; Dutton et al. 1996 [DIRS 175817]; DTN: MO0707SCCIGMER.000 [DIRS 182202], Figures 6-3 to 6-6 and 6-13; Odegard and Thompson 1974 [DIRS 174818]; ASM International 1990 [DIRS 141615], p. 631, Figure 34; Kiessel and Sinnott 1953 [DIRS 174853], pp. 331 to 338. Output DTN: MO0705CREEPSCC.000, file *CreepGraphs2.xls,* sheet *"SCGG3."*

NOTE: Note that, as indicated in the beginning of Section 6.8.7, Titanium Grades 24 and 29 are considered identical to Titanium Grade 5 as far as low-temperature creep is concerned.

Figure 6-86. Comparison of Steady-State Creep Rates of Titanium Grades 2 and 7 with Titanium Grade 5 versus applied stress at 100°C to 260°C

6.8.7.3 Total Strain for Lower Temperature Creep of Titanium Alloys

In addition to the steady-state creep rates, which can be related to the rate of creep-induced stress relaxation that may occur under fixed deflection conditions such as the case of U-bend specimens, the total time to failure and the relative total strain obtained at any given applied stress value is of interest in an absolute sense and in a comparative sense. The estimated primary creep strains for Titanium Grades 2 and 7 and Titanium Grades 5, 23, 24, and 29 are plotted in Figure 6-87 versus applied stress. These values were estimated from published creep curves given in reports by McQuillan and McQuillan (1956 [DIRS 177306], p. 353, Figure 146), Dutton et al. (1996 [DIRS 175817]), Dutton (1996 [DIRS 174750]), and DTN: MO0707SCCIGMER.000 [DIRS 182202], Figures 6-3 to 6-6). They represent extrapolation of the apparent steady-state creep rate to the approximate one-hour intercept values in McQuillan and McQuillan (1956 [DIRS 177306], p. 353) and to the apparent tangent between the approximate steady state values and the primary creep curves in reports by Dutton et al.

(1996 [DIRS 175817]), Dutton (1996 [DIRS 174750]), Andresen (2005 [DIRS 173867]), and DTN: MO0707SCCIGMER.000 ([DIRS 182202], Figures 6-3 to 6-6).

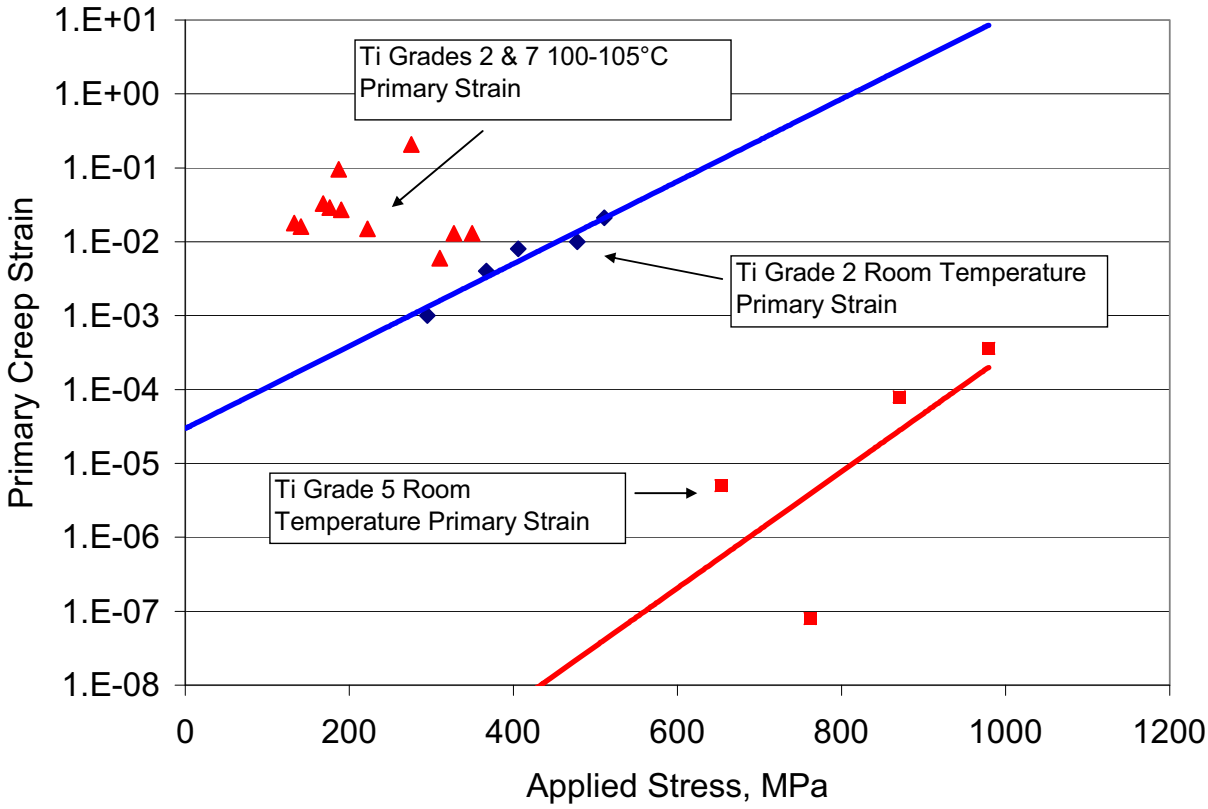

Sources: McQuillan and McQuillan 1956 [DIRS 177306], pp. 349 to 354; Dutton et al. 1996 [DIRS 175817]; DTN: MO0707SCCIGMER.000 [DIRS 182202], Figures 6-3 to 6-6; Odegard and Thompson 1974 [DIRS 174818]; Kiessel and Sinnott 1953 [DIRS 174853], pp. 331 to 338. Output DTN: MO0705CREEPSCC.000, *CreepGraphs2.xls*, file *"SCGG4."*

NOTE: As indicated in the beginning of Section 6.8.7, Titanium Grades 24 and 29 are considered identical to Titanium Grade 5 as far as low-temperature creep is concerned.

Figure 6-87. Comparison of Approximate Primary Creep Strains versus Applied Stress for Titanium Grades 2 and 7 at Room Temperature and at 100°C to 105°C and for Titanium Grades 5, 24, And 29 at Room Temperature

Examination of Figure 6-87 confirms that primary creep strains can be very significant for Titanium Grades 2 and 7, especially at temperatures of about 100°C. Figure 6-87 also shows that the primary strains are orders of magnitude lower for the Titanium Grades 5, 24, and 29, than for Titanium Grades 2 and 7, at least at room temperature.

6.8.7.4 Creep Data in Air for 1-in Thickness Compact Tension Specimen of Titanium Grade 7

Initial data have also been obtained on a 1-in. thickness compact tension specimen of Titanium Grade 7 tested in 110°C air under constant load at 30 MPa√m, as shown in Figure 6-88 (DTN: MO0707SCCIGMER.000 [DIRS 182202], Figure 6-14). These conditions are identical to those of tests described earlier in the BSW environment (Section 6.8.4.1). The crack length data on the Y-axis represents the conversion of direct current potential drop data to crack length using the algorithms used for all compact tension specimens, but it is possible that the potential drop is affected by crack advance as well as by creep alteration of the geometry of the specimen. The initial growth rate is quite high (4×10^{-7} mm/s), and it decays continuously to 10^{-8} mm/s and probably would continue to decay. The growth rate at 700 hours is a bit slower than the constant-load growth rate observed in a 110°C BSW environment of 1.25×10^{-8} mm/s, as discussed later.

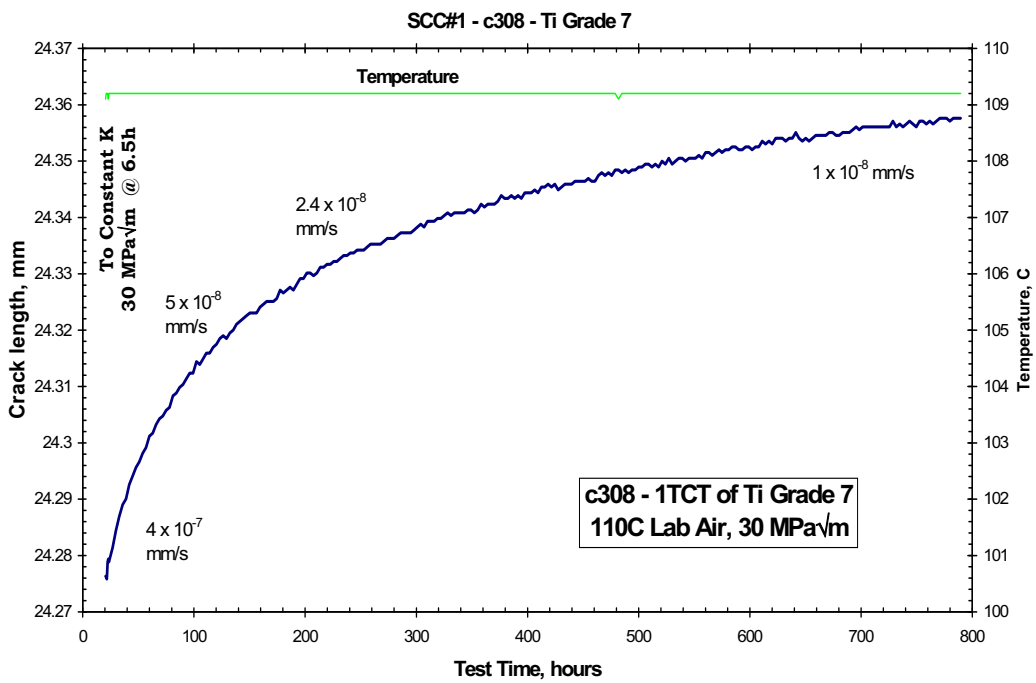

Source: DTN: MO0707SCCIGMER.000 [DIRS 182202], Figure 6-14.

NOTE: 1TCT = 1-in-thickness compact tension specimen.

Figure 6-88. Crack Length (Indicated by Direct Current Potential Drop) versus Time for Titanium Grade 7 Test in 110°C Air at 30 MPa√m

6.8.7.4.1 Creep Response of Titanium Grade 29

Initial data are being obtained on the creep response in 150°C air of Titanium Grade 29 (Figure 6-89; DTN: MO0707SCCIGMER.000 [DIRS 182202], Figure 6-12). The creep rates are very low on this material, and the sensitivity of current measurement techniques is inadequate to provide accurate position measurements (using a linear voltage displacement transducer on the Instron servohydraulic actuator). Thus, a more-direct measurement technique

is needed (e.g., a strain gage that can be clipped on the specimen). However, these data clearly reinforce the dramatic reduction in creep susceptibility of Titanium Grade 29 versus Titanium Grade 7 as illustrated in literature data (Figure 6-85).

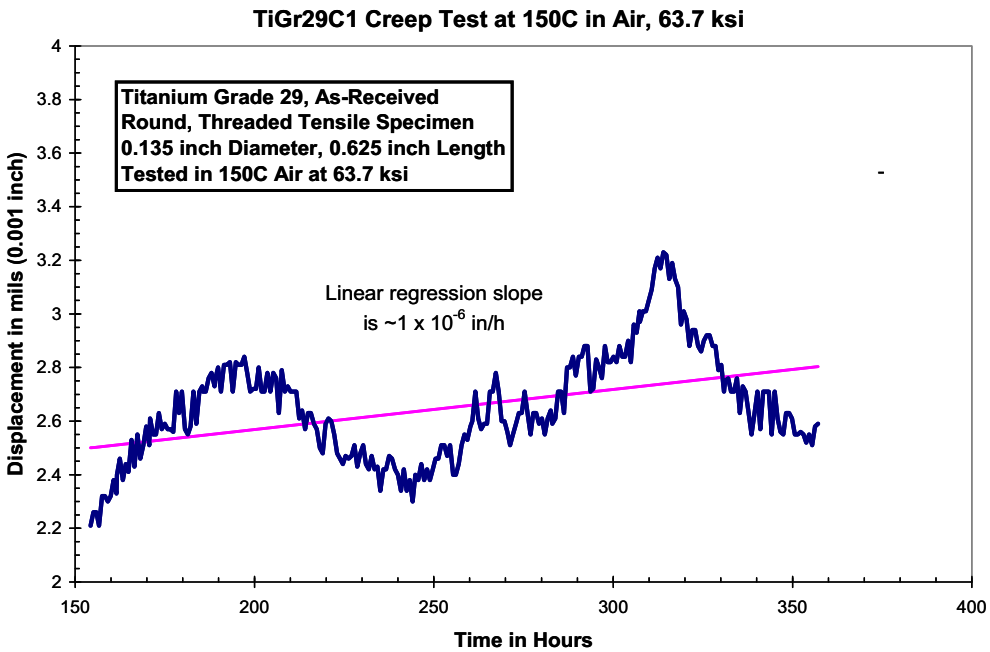

Source: Re-produced from DTN: MO0707SCCIGMER.000 [DIRS 182202], Figure 6-12.

Figure 6-89. Displacement versus Time for a Round Tensile Specimen of Titanium Grade 29 Tested at a Constant Load Of 63.7 ksi in 150°C Air

6.9 FEATURES, EVENTS AND PROCESSES

The development of a comprehensive list of features, events, and processes (FEPs) potentially relevant to postclosure performance of the repository is an ongoing, iterative process based on site-specific information, design, and regulations. Table 6-40 provides a list of FEPs considered in this report and provides specific references to within this report where the FEPs are discussed. A description of these FEPs can be found in DTN: MO0706SPAFEPLA.001 [DIRS 181613].

Table 6-40. FEPs Discussed in this Report

FEP No.	FEP Name	Section Where the FEP Is Described
2.1.03.02.0A	Stress corrosion cracking (SCC) of waste packages	Section 6.2 through Section 6.7
2.1.03.02.0B	Stress corrosion cracking (SCC) of drip shield	Section 6.8
2.1.03.10.0A	Advection of liquids and solids through cracks in the waste package	Section 6.2 through Section 6.7
2.1.03.10.0B	Advection of liquids and solids through cracks in the drip shield	Section 6.8

INTENTIONALLY LEFT BLANK

7. MODEL VALIDATION

Stress corrosion cracking (SCC) is a potential corrosion mode that can result in penetration of the drip shield and waste package outer barrier materials. The purpose of this report is to provide the evaluation of the potential for SCC of the waste package outer barrier and drip shield materials under exposure conditions. As no credit is taken for the SCC resistance of the stainless steel structural material, the SCC of the Stainless Steel Type 316 inner structural vessel is not modeled in this report. For the drip shield and waste package outer barrier, the critical environment is conservatively taken as any aqueous environment contacting the metal surfaces.

It should be noted, however, as described in more detail in Section 6.8, that, even if SCC propagates through-wall, the seepage diversion function of the drip shield will remain intact because of the reasons discussed in Section 6.8.6. The threshold stress intensity factor and the threshold stress for SCC initiation are parameters or criteria that are coupled to the slip dissolution–film rupture (SDFR) model, and it is important to demonstrate a defensible technical basis for each parameter. Consequently, a confidence-building activity (Activity Four, presented in Section 7.2, below) is included for each of these parameters for Titanium Grades 7, 28, and 29, and Alloy 22.

Model validation activities for the Alloy 22 SDFR model are described in Section 7.1 through Section 7.3. Model validation activities for the drip shield SCC model are described in Section 7.4. Model validation activities for the Alloy 22 and drip shield seismic crack density model are described in Section 7.5.

7.1 INTENDED PURPOSE OF THE ALLOY 22 SDFR MODEL

The Alloy 22 SDFR model outputs feed to total system performance assessment (TSPA).

The level of confidence (or validation) for the Alloy 22 SDFR model was determined to be Level II using SCI-PRO-002, *Planning for Science Activities*, Attachment 3, and *Technical Work Plan for Postclosure Engineered Barrier Degradation Modeling* (SNL 2007 [DIRS 178849], Section 2.3.2). The associated level of confidence will be met by following the requirements stated in SCI-PRO-002, Attachment 3; SCI-PRO-006, *Models,* Section 6.3.2*;* and the guidance provided by the technical work plan (TWP) (SNL 2007 [DIRS 178849], Section 2.3.2).

This SCC model directly supports the following TSPA component: Waste Package Stress Corrosion Cracking and Other Corrosion Modes.

7.1.1 Confidence-Building during Model Development to Establish Scientific Basis and Accuracy for Intended Use

All models, per SCI-PRO-006 and SCI-PRO-002 (Attachment 3), are required to, at a minimum, document decisions and activities that are implemented during the model development process that build confidence and verify and justify that an adequate technical approach using scientific and engineering principles was taken.

The following activities were documented during development of the Alloy 22 SDFR SCC crack growth rate model:

> (a) *Document decisions and activities implemented during model development to build confidence and verify a reasonable, corroborative, and credible technical approach using scientific and engineering principles and the approach taken to evaluate and select input parameters and/or data.* (In compliance to SCI-PRO-002 Attachment 3, Level I(1), "Evaluate and select input parameters and/or data that are adequate for the model's intended use").

The bases for selecting the input data that are listed in Section 4.1 and are used to determine and develop the SDFR model for application to the waste package are documented in Section 6.4.4. Detailed discussions about model concepts can be found throughout the Section 6.4. Thus, this requirement can be considered satisfied.

> (b) *Document decisions and activities implemented during model development to build confidence and verify a reasonable, corroborative, and credible technical approach using scientific and engineering principles and the approach taken to formulate defensible assumptions and simplifications.* (In compliance to SCI-PRO-002 Attachment 3, Level I(2), "Formulate defensible assumptions and simplifications that are adequate for the model's intended use").

SCC is assumed to be independent of environmental variables such as chemical compositions and temperature. This assumption is rationalized in Section 5. Per SCI-PRO-006, other model assumptions are discussed throughout the model (or analysis) development in Section 6. A discussion of simplifications and their rationale are provided throughout Section 6.4. Thus, this requirement can be considered satisfied.

> (c) *Document decisions and activities implemented during model development to build confidence and verify a reasonable, corroborative, and credible technical approach using scientific and engineering principles and the approach taken to ensure consistency with physical principles, such as conservation of mass, energy, and momentum.* (In compliance to SCI-PRO-002 Attachment 3, Level I(3), "Ensure consistency with physical principles, such as conservation of mass, energy, and momentum, to an appropriate degree commensurate with the model's intended use").

Relevant physical phenomena and processes are discussed in Section 6.4.2 for the waste package. Thus, this requirement can be considered satisfied.

> (d) *Document decisions and activities implemented during model development to build confidence and verify a reasonable, corroborative, and credible technical approach using scientific and engineering principles and the approach taken to represent important future (aleatoric), parameter, and alternative model uncertainties.* (In compliance to SCI-PRO-002 Attachment 3, Level I(4), "Represent important future state (aleatoric),

parameter (epistemic), and alternative model uncertainties to an appropriate degree commensurate with the model's intended use").

Uncertainties associated with the model analysis are discussed in Section 6.4.4 for the *n* model parameter and in Section 6.5.6 for the through-wall stress and stress intensity factor model parameter. Thus, this requirement can be considered satisfied.

(e) *Document decisions and activities implemented during model development to build confidence and verify a reasonable, corroborative, and credible technical approach using scientific and engineering principles and the approach taken to ensure simulation conditions have been set up to span the range of intended use and avoid inconsistent outputs.* (In compliance to SCI-PRO-002 Attachment 3 (Level I(5), "Ensure simulation conditions have been designed to span the range of intended use and avoid inconsistent outputs or that those inconsistencies can be adequately explained and demonstrated to have little impact on results").

Stress corrosion crack growth rate data were obtained over a range of chemical conditions, and applied stress intensity factor levels (Section 6.4.4). Experimental tests were conducted in a range of concentrated J-13-type brines or other similar composition solutions (Section 6.4.4), as well as accelerated test temperatures. Sets of test specimens were exposed over a range of pH values, test temperatures as well as the presence of potential deleterious impurity elements such as lead. Thus, this requirement can also be considered satisfied.

(f) *Document decisions and activities implemented during model development to build confidence and verify a reasonable, corroborative, and credible technical approach using scientific and engineering principles and the approach taken to ensure model predictions (performance parameters) adequately represent the range of possible outcomes, consistent with important uncertainties*. (In compliance to SCI-PRO-002, Attachment 3, Level I(6), "Ensure that model predictions (performance parameters) adequately represent the range of possible outcomes, consistent with important uncertainties and modeling assumptions, conceptualizations, and implementation").

This requirement is satisfied by the discussion above, particularly the discussion of criteria (d) and (e).

7.1.2 Confidence-Building after Model Development to Support the Scientific Basis of the Model

For confidence building after model development, *Technical Work Plan for Postclosure Engineered Barrier Degradation Modeling* (SNL 2007 [DIRS 178849], Section 2.3.2) specifies the level of confidence for this model as Level II, with two validation activities for the SDFR model:

- Show that crack growth rates predicted by the film rupture/repassivation crack growth model are consistent with observed rates published in literature. This activity will increase confidence if the literature data corroborate model predictions within two standard deviations of the mean of the model prediction.

- Show that the predicted crack growth model is consistent with project experimental data not used to develop the model. This validation will be considered successful if the modeled stress corrosion crack propagation rates are greater than or within two orders of magnitude of the corroborating data.

Validation is described in the following subsections. Corroborating or supporting data and information used to develop and validate the SDFR model parameters are listed in Table 7-1.

Table 7-1. Supporting (Corroborating) Information Used to Validate the SDFR Model

Data/Information	Supporting (Corroborating) Information Source
Corroborative information regarding application of the SDFR model to a range of alloy systems	Andresen and Ford 1994 [DIRS 118581]
Corroborative data supporting use of the SDFR model for other nickel alloys, Inconel 600 and 182	Ford and Andresen 1988 [DIRS 118611], p. 789
Corroborative data supporting use of the SDFR model for a nickel alloy (Alloy 82 (UNS N06082)) with chromium content similar to Alloy 22	Andresen 1991 [DIRS 166965], Figure 37
Model parameter n and A = f(n) for stainless steel	Ford and Andresen 1988 [DIRS 118611], p. 791
Model parameter n and n = f(A) for stainless steel are applicable for nickel alloys 600 and 182	Ford and Andresen 1988 [DIRS 118611], Figure 10
Weld residual stress uncertainty range of ±35%	Mohr 1996 [DIRS 147981]
Uncertainty in shot-peened residual stress in nickel alloy	Pasupathi 2000 [DIRS 149968]
Faraday's Law used to relate SCC crack advance to metal oxidation charge density per film rupture.	Ford and Andresen 1988 [DIRS 118611]
Titanium oxide-to-metal volume ratio used for crack-plugging analysis	Bradford 1987 [DIRS 151988], Table 2, p. 64
Alloy 22 experimental crack growth rates in a range of relevant test environments used to validate SDFR model	DTN : LL030300612251.035 [DIRS 166971] (LLNL)

7.2 VALIDATION ACTIVITIES AND ASSOCIATED CRITERIA USED TO DETERMINE THAT THE REQUIRED LEVEL OF CONFIDENCE HAS BEEN OBTAINED

The SCC model involves the SDFR crack growth model, the threshold stress intensity factor (K_{ISCC}) for crack growth, and the threshold stress for crack initiation. All of these subjects are described in peer-reviewed scientific journals. As described in Section 1.2, the threshold stress intensity factor and the threshold stress for SCC initiation are parameters or criteria that are coupled to the SDFR model. Validation of these parameters is not required per SCI-PRO-006. However, it is important to demonstrate a defensible technical basis for each parameter.

With respect to the SDFR SCC crack growth rate model, validation is accomplished by using the validation activities defined in SCI-PRO-006, Section 6.3.2. Two validation activities were selected, which are consistent with *Technical Work Plan for Postclosure Engineered Barrier Degradation Modeling* (SNL 2007 [DIRS 178849], Section 2.3.2). In addition, a third SDFR validation activity, corroboration of results with an alternative mathematical model (SCI-PRO-006, Section 6.3.2) is implemented. This activity is in addition to the two identified in *Technical Work Plan for Postclosure Engineered Barrier Degradation Modeling* (SNL 2007 [DIRS 178849], Section 2.3.2).

Also, confidence building activities demonstrate the appropriateness of the parameters for the threshold stress intensity factor and the threshold stress for SCC initiation. This fourth activity is applicable to the threshold stress intensity factor parameter (K_{ISCC}) and the threshold stress criterion for SCC initiation on a "smooth" surface (i.e., in the absence of fabrication defects such as weld flaws). This report provides a defensible basis by comparing model output with laboratory test results. Because there is no relevant theoretical basis in the literature to describe these parameters, they are each selected based on a conservative empirical approach. A description of the defensible and conservative basis for selection of the values for each of these parameters is described in Section 7.3 to provide additional confidence.

Activity One: Demonstrate that the crack growth rates, predicted by the film rupture–repassivation crack growth model, are consistent with observed rates published in the peer-reviewed literature (SCI-PRO-006, Section 6.3.2).

Activity Two: Demonstrate that the crack growth rates, predicted for Alloy 22 and Titanium Grade 7 by the film rupture–repassivation crack growth model, are consistent with experimental rates obtained from data not used to develop the model (SCI-PRO-006, Section 6.3.2).

Activity Three: Demonstrate that the crack growth rates, predicted by the film rupture–repassivation crack growth model, are consistent with growth rates predicted by an alternative mathematical model (SCI-PRO-006, Section 6.3.2).

Activity Four: Demonstrate that the establishment of the threshold stress intensity factor (K_{ISCC}) and threshold stress represent an acceptable approach for Alloy 22 and Titanium Grade 7 under environmental conditions relevant to the waste package and drip shield, respectively (SCI-PRO-0006, Section 6.3.2).

To meet the model validation acceptance criterion (corroborating data must match qualitatively) for the SDFR model, it is informative to consider the indicated range of scatter and, based on this, to determine a reasonable match between experimentally generated crack growth rate results and model predictions. Examination of the literature dealing with measured versus predicted SCC growth rates, indicates that, in general, crack growth rates within two or three orders of magnitude may be considered to be in reasonable agreement. For example, see work by Andresen (1991 [DIRS 166965], Figures 2, 37, and 38) and Andresen (2002 [DIRS 166967], Figure 1) for the nickel alloys (Alloys 600, 82, and 182), exposed to 288°C water environments where it is evident that scatter of this magnitude occurs. The issue of reasonable agreement is discussed further in Section 7.3.1. However, considering the spread in measured versus predicted rates observed in the literature, terms such as "consistent" and "reasonable" are used in the model validation section to define a qualitative match.

7.3 COMPARISON OF ACTIVITIES PERFORMED TO GENERATE CONFIDENCE IN THE MODEL WITH MODEL VALIDATION CRITERIA

According to *Technical Work Plan for Postclosure Engineered Barrier Degradation Modeling* (SNL 2007 [DIRS 178849], Section 2.3.2), the developed model is to be validated in accordance with the activities described in the previous section, with specific activities to be performed to generate the desired confidence in the model or model parameter (i.e., to meet the criteria listed in the TWP). This section shows that the required confidence level for the waste package-related SDFR model (Level II) has been achieved, because all activities specified in the TWP, in particular the validation criteria listed in Section 2.3.2 (SNL 2007 [DIRS 178849]) have been fully (or very conservatively) complied with.

7.3.1 Activities Performed for Validating the SDFR Model Using Peer-Reviewed Literature

The applicable activity relating to validation of the SDFR model is Activity One listed in Section 7.2 and repeated here:

> *Show that crack growth rates predicted by the film rupture/repassivation crack growth model are consistent with observed rates published in literature.*

The film rupture–repassivation crack growth model terminology is often used when referring to the SDFR model, and the two are equivalent. The input parameter (exponent n) of this crack growth rate prediction model (Equation 18), used to compare model-predicted rates with corresponding literature values, is that obtained for stainless steel as documented in Section 6.4.3. The model predictions are compared to results already published in peer-reviewed literature, being calculated using the same input parameters. This ensures that the model details and calculation methods described in Sections 6.4.4 and 6.4.5 yield results fully consistent with the peer-reviewed journal-published values. The activities performed to satisfy Activity One and to achieve the desired confidence in the model are discussed below.

As documented in Section 6.4.3, the input parameter (exponent n) obtained for sensitized Stainless Steel Type 304 is 0.55. Figure 6-7 indicates that crack growth rates predicted by the SDFR crack growth model are in reasonable agreement with observed rates published in the

peer-reviewed literature for stainless steel. Figure 7-1 indicates that the range of the prediction error (i.e., the ratio of the difference between the predicted and the observed values divided by the observed value) for the majority of results is –3 to +3. If the extreme results are included, the range of the prediction error is –5 to +7 with a positive ratio indicating overprediction and a negative ratio indicating underprediction. A similar distribution of the ratio of calculated to observed propagation rates is obtained for nickel-base alloys (Alloys 600 and 182) (Ford and Andresen 1988 [DIRS 118611], Figure 10). It is, therefore, concluded that the prediction error, as discussed in the previous statement, is well within two orders of magnitude and, thus, within the required accuracy prescribed in Section 7.2. This has ensured that the model details and calculational methods yield results fully consistent with the peer-reviewed journal-published values and are, therefore, qualitatively corroborated.

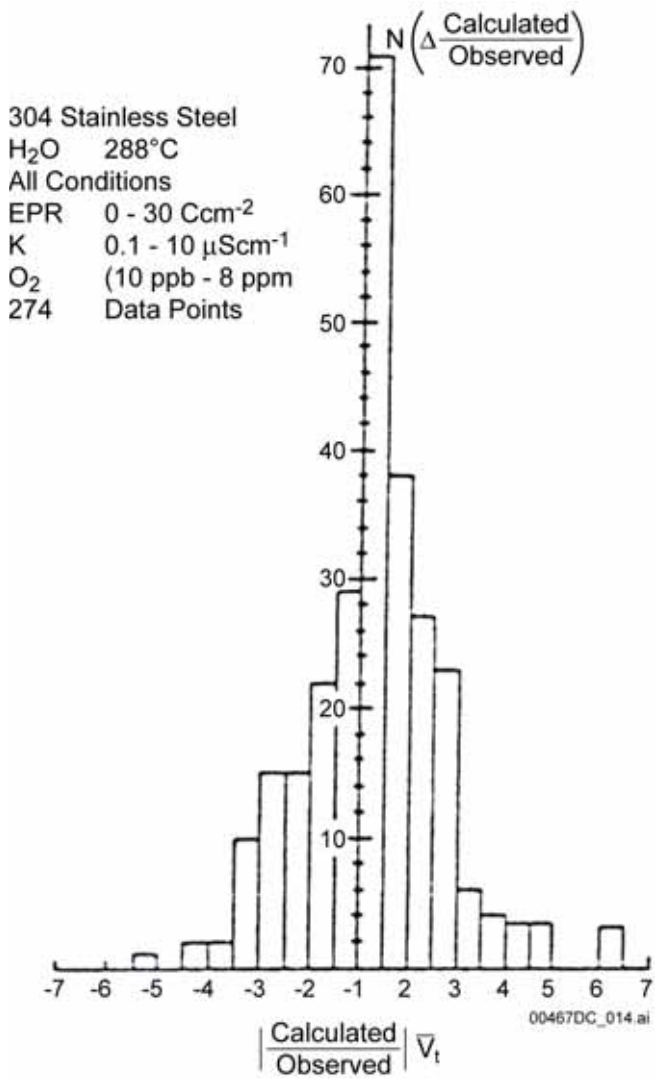

Source: Ford and Andresen 1988 [DIRS 118611], Figure 8.

Figure 7-1. Frequency Distributions of the Ratio of Calculated to Observed Crack Growth Rates for Stainless Steel Type 304

7.3.2 Activity Performed for Validating the SDFR Model Applicable to Alloy 22 Using Independently Obtained Experimental Data

The applicable activity is Activity Two listed in Section 7.2 and repeated here:

> *Show that the predicted crack growth model is consistent with project experimental data*

Having established the validity of the model predictions of crack growth rate versus stress intensity for stainless steel, the model is then utilized to predict selected crack growth rates as a function of stress intensity for Alloy 22 using model input parameters developed specifically for Alloy 22 with qualified experimental data generated under an approved test program at the General Electric Global Research Center (GE GRC).

Validity and predictive capacity of the model developed for Alloy 22 is then established if crack growth rates predicted for this material by the SDFR crack growth model are in reasonable agreement (qualitatively consistent) with growth rates determined independently under an approved test program at Long-Term Corrosion Test Facility (LTCTF) at the Lawrence Livermore National Laboratory (LLNL). The activities performed to satisfy Activity Two and to achieve the desired confidence in the model, in accordance with Section 2.3.2 of the TWP (SNL 2007 [DIRS 178849], Section 2.3.2), are discussed below.

SCC Behavior of Nickel–Chromium-Based Alloys at Temperatures Relevant to the Waste Package

In addition to types of stainless steel, the model has been shown to apply to several nickel-based alloys, including Alloy 600, a nickel-based alloy with lower chromium content than Alloy 22. Table 7-2 lists nominal composition for Alloys 600, 182, and 82 and specified composition for Alloy 22.

Table 7-2. Nominal Chemical Composition of Several Nickel–Chromium-Based Alloys (wt %)

Alloy Composition	Alloy 22 (ASTM B 575-94 [DIRS 100497])	Alloy 600 (UNS N06600)*	Alloy 182 (AWS ERNICRFE-3)*	Alloy 82 (AWS ERNICR-3)*
Element				
C	0.015 max.	0.07	0.04	0.02
Co	2.5 max.	-	-	-
Cr	20 to 22.5	16.1	14.0	19.6
Fe	2.0-6.0	9.4	6.9	1.2
Mn	0.50 max.	0.2	7.9	2.9
Mo	12.5 to 14.5	0.2	-	-
Ni	Balance	73.7	~68.5	73.1
P	0.02 max.	0.01	0.013	0.003

Table 7-2. Nominal Chemical Composition of Several Nickel–Chromium-Based Alloys (wt %) (Continued)

Alloy Composition	Alloy 22 (ASTM B 575-94 [DIRS 100497])	Alloy 600 (UNS N06600)*	Alloy 182 (AWS ERNICRFE-3)*	Alloy 82 (AWS ERNICR-3)*
S	0.02 max	0.002	0.003	0.001
V	0.35 max	0.03	–	–
W	2.5 to 3.5	–	–	–

NOTE: *Heat compositions from Andresen 1991 [DIRS 166965], Table I.

To apply this model to Alloy 22 under relevant conditions, the following discussion shows that (1) results demonstrating that the observation of similar SCC growth behavior of stainless steel and Alloy 600 also applies over the range of temperatures relevant to the waste package (approximately 50°C to 200°C); and (2) results are consistent with the model for other nickel–chromium alloys with higher chromium content than Alloy 600 (similar to Alloy 22). Demonstration of the applicability of the model to these other nickel–chromium alloys supports the applicability of the SDFR model to Alloy 22 with respect to chromium, which is the alloy addition responsible for formation of the protective Cr_2O_3-passive film for stainless steels and chromium-containing nickel-based corrosion-resistant passive alloys including Alloy 22 (DTN: LL021105312251.023 [DIRS 161253], Section 3.3). Specifically, in addition to stainless steel, the SDFR model has been validated for a range of alloys, including irradiated stainless steels; Inconel 600 and 182 nickel–chromium-based alloys; and, subsequently, the higher-chromium-content nickel–chromium-based alloy, Alloy 82 (UNS N06082) (Section 6.4.3), where extensive observations are presented to indicate that there is ample reason to conclude that SCC of nickel–chromium–molybdenum-based Alloy 22 occurs by the same fundamental mechanism characterized by the SDFR stress corrosion cracking model, but with alloy specific values for the *A* and *n* parameters.

Andresen and Ford (1994 [DIRS 118581], p. 62) indicated that the SDFR model has been applied to stainless steels, low alloy and carbon steels, ductile nickel alloys, and irradiated stainless steels. Ford and Andresen (1988 [DIRS 118611], p. 789) also used the SDFR model for the nickel–chromium-based alloys Inconel 600 and 182. Further, as indicated in Section 6.4.3, it was determined that the SDFR model (using the Stainless Steel Type 304 *A* versus *n* relationship in 288°C water) was statistically valid for the chromium-containing, nickel-based Alloys 600 and 182 over a range of anionic impurity concentrations (Ford and Andresen 1988 [DIRS 118611], Figure 10). Subsequently, Andresen (1991 [DIRS 166965], Figure 37) used the SDFR model for comparison of predicted versus measured values of crack growth rate with reasonable agreement for the higher chromium-content nickel-based alloy, Alloy 82 (UNS N06082). Alloy 82 (18% to 22% chromium, UNS N06082) overlaps Alloy 22 (20% to 22.5% chromium) (DTN: MO0003RIB00071.000 [DIRS 148850], p. 2) in chromium content. Analyses indicate that the inner, protective corrosion films that form in the passive potential range on such nickel-based alloys containing more than about 15% chromium include a very thin passive film layer of primarily Cr_2O_3 (with some nickel content) at the oxide–alloy interface (Pensado et al. 2002 [DIRS 166944], p. 2-2). Such a thin, passive Cr_2O_3 film possesses similar repassivation kinetics (depending on actual chromium content) and mechanical properties (e.g., fracture strain) over the range of nickel-chromium-based alloys of interest. This is consistent with the model

having been shown to apply or to give reasonable predictive results for a range of nickel-based alloys with chromium content spanning the Alloy 22 compositional range.

Further, there is general correspondence (reasonable statistical agreement) between the observed SCC growth rate temperature dependencies for sensitized Stainless Steel Type 304 and Alloy 600 over the temperature range of most interest (approximately 50°C to 200°C) when compared under comparable stress intensity factor and environmental conditions (Andresen 1993 [DIRS 166966], Figures 15 and 16). For example, from examination of Figure 6-8 in Section 6.4.4 (Andresen 1993 [DIRS 166966], Figure 15), it is seen that crack growth rates for sensitized Stainless Steel Type 304 and Alloy 600 follow the same temperature dependency with reasonably similar crack growth rates over a temperature range from about 25°C to 275°C, which is broader than the temperature range of most interest (approximately 50°C to 200°C) stated above.

In addition to the similarities in composition and mechanical properties, as indicated earlier in this section, for the passive films present on this class of face-centered cubic crystal structure austenitic alloys, (i.e., austenitic stainless steels and nickel–chromium-based alloys such as Alloys 600, 82, and 22), the expected microdeformation modes of the alloys are also comparable, based on examination of literature values for stacking fault energies (SFE) (Gordon 2004 [DIRS 167027]). A low value of SFE tends to promote coplanar dislocation arrays (promoting local stress buildups that can more easily rupture the passive surface film at slip offsets) whereas high SFE values promote dislocation tangles that tend to diffuse local stress buildups. These alloys possess a face-centered cubic-crystallographic lattice structure and have similar relatively low values of estimated SFE ranging from about 20 to 30 ergs/cm^2 for Stainless Steel Types 304L and 316L to about 80 ergs/cm^2 for Alloy 600 with the estimated value for Alloy 22 being about 65 ergs/cm^2. This range is relatively low compared to published values of about 340 ergs/cm^2 for pure nickel or nickel alloys with much lower chromium contents (Gordon 2004 [DIRS 167027], Table 1). Although lower values of SFE can promote microstress and strain buildups that may accelerate SCC initiation, the relatively high local deformation at a stressed crack or weld flaw tip is likely to lead to relatively high local strains and to overwhelm the effect of SFE on micro-stress or -strain buildups with respect to SCC propagation.

SCC Behavior of Alloy 22 at Higher Temperatures (Approximately 288°C)

Other GE GRC results are described for Alloy 22 tested at higher temperatures (approximately 288°C) illustrating that Alloy 22 follows similar behavior to Stainless Steel Types 304 or 316 and Alloy 600 at similar temperatures (approximately 288°C), further supporting the argument that the initial application of the model to boiling water reactor (BWR) coolant temperatures of approximately 288°C is consistent with the application at lower waste package temperatures. The results were discussed in Section 6.4.4 and are summarized below. It should be noted that these results were not used in Section 6.4.4 for model development but were used for confidence building.

As the SDFR was initially developed for stainless steels and nickel-based alloys Inconel 600 and 182 under higher- temperature (approximately 288°C) light water reactor coolant conditions, additional confidence in the applicability of this model to Alloy 22 can be gained from observation of the response of Alloy 22 under similar conditions. Test results from

DTN: MO0402GEA22SCC.000 [DIRS 167911] indicate the crack growth rate response of Alloy 22 exposed to relatively pure water (2 ppm O_2) at 288°C is broadly consistent with other materials, such as Alloys 600 and 182 (Andresen et al. 2002 [DIRS 166967]) and unsensitized austenitic stainless steel (Andresen et al. 2002 [DIRS 167762]) under these same conditions. The measured crack growth rates show a similar dependency to parameters like corrosion potential and water purity (sulfate). For example, in all test cases, the change in corrosion potential from approximately +0.2 V_{SHE} to approximately –0.5 V_{SHE} (due to a change from 2 ppm O_2 to H_2-deaerated water) causes a drop of at least one order of magnitude in the crack growth rate, as indicated by Figure 6-6 in Section 6.4.4. Also, as expected, Alloy 22 shows crack growth rates under repository-type oxidizing conditions (i.e., at $0.2V_{SHE}$), which are about one order of magnitude lower than those of the other materials under identical test conditions, consistent with the higher *n* parameter values obtained for Alloy 22 using YMP-sponsored testing, Section 6.4.4, and demonstrating its superiority as a structural material under conditions where SCC is a concern.

SCC Behavior of Alloy 22 in Other Relevant Environments

Whereas the initial Alloy 22 crack growth rate data obtained at GE GRC were generated in the basic saturated water (BSW) brine environment at 110°C with a pH of approximately 13, the discussion that follows demonstrates that SCC growth rate results obtained at the LLNL LTCTF in other relevant environments, simulated acidified water (SAW) (pH of approximately 2.8) and simulated concentrated water (SCW) (pH of approximately 9 to 10) at about 95°C, as well as in BSW (pH of approximately 13) at 100°C, fall within or somewhat below the model uncertainty bands predicted by the SDFR model. These results provide further qualitative corroboration of the model applicability to Alloy 22 over the range of repository-relevant environments consistent with the SCC model validation criterion (corroborating data must match qualitatively) cited in Section 7.2. Citing all of these results, strongly supports the use of the SDFR model for Alloy 22.

The satisfactory crack growth rate predictive capability of Equation 18, benchmarked with the experimental results presented in Table 6-6, determined by direct measurements under the accepted Q test program at GE GRC (DTN: LL021105312251.023 [DIRS 161253]), has been validated with a separate set of measured crack growth rates (Table 7-3). These separate results are plotted in Figure 7-2 along with the initial GE GRC crack growth rate measurements. This separate set of measured crack growth rates was collected using the reversing direct-current crack growth measurement technique with compact tension-type fracture-mechanics specimens (loaded per ASTM E 399-90 [DIRS 117480]) tested at LTCTF at 95°C to 100°C (DTN: LL030300612251.035 [DIRS 166971]). Since the temperature difference between 95°C to 100°C and 110°C is small, the comparison is appropriate. As can be seen from Figure 7-2, there is good agreement between the LTCTF data and the predictive curves and statistical limits based on the GE GRC crack growth rate results (i.e., eight data points summarized in Table 6-6). In Figure 7-2, the direct comparison of three LLNL data points listed in Table 7-3 (DCT-13, DCT-14 and DCT-16) and those results obtained in 100°C BSW to the 110°C BSW by GE GRC through the mean curve indicate excellent agreement between the two sets of data. Table 7-4 shows that the prediction error ratio is in the range of −0.60 to 327.45 or −0.60 to 0.41, discounting those rates at or below the measurement limits. While the prediction error ratio is generally within the expected two orders of magnitude, the prediction model has a tendency to

overprediction (with a positive error ratio) (i.e., on the conservative side), rather than underprediction (with a negative error ratio). Also, for specimen DCT-22 from Table 7-4 and very likely also for specimens DCT-18, DCT-19, DCT-20, and DCT-21 for which extremely low reported rates were measured over fairly short test times (<2,000 hours) with a relatively high noise level, the measured growth rates are very likely below the crack growth detection limit, and, thus, the comparison between measured and predicted rates is not directly relevant. Furthermore, it can be seen from Figure 7-2 that the measured data fall mainly within the two bounds representing two standard deviations of the mean value. Further, three data points conservatively fall somewhat below the lower bound, very near the crack growth rate measurement lower limit for longer term tests of 10^{-11} mm/s. The agreement between the predicted and measured data shown in Figure 7-2 provides important input for the validation of the SDFR model for Alloy 22, corroborating the excellent qualitative match between model predictions and independently measured Alloy 22 crack growth rates over a range of environments and pH values.

Table 7-3. Summary of LTCTF Crack Growth Rates in Compact Tension Specimens

Specimen ID	Test Solution	Nominal Test Temperature (°C)	Average Stress Intensity MPa√m	Crack Growth Rate (mm/s)
DCT-13	BSW-13	100	45.13	2.12×10^{-09}
DCT-14	BSW-13	100	44.88	4.23×10^{-09}
DCT-16	BSW-13	100	46.38	1.41×10^{-09}
DCT-18	SAW	94	45.07	2.12×10^{-10}
DCT-19	SAW	94	45.08	1.41×10^{-11}
DCT-20	SCW	95	45.11	4.23×10^{-10}
DCT-21	SCW	95	44.68	2.82×10^{-11}
DCT-22	SCW	95	44.37	4.94×10^{-12}

Source: DTN: LL030300612251.035 [DIRS 166971], Figure 6.

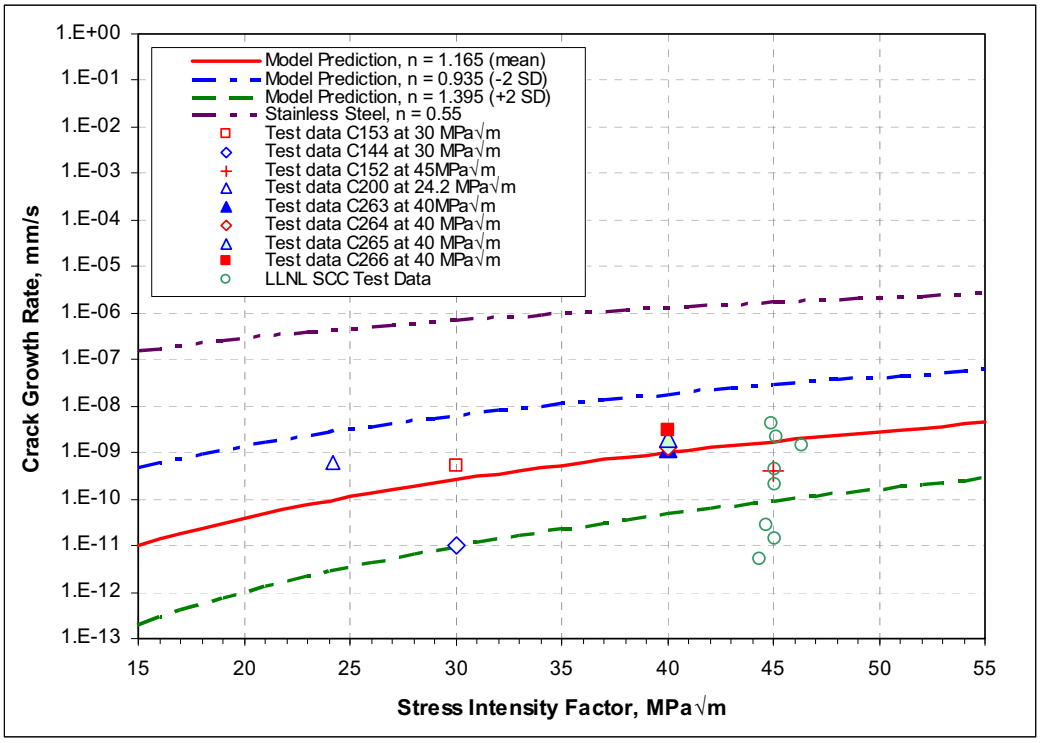

Sources: Plot from Figure 6-9 with initial test data for C144, C152, and C153 from DTN: LL021105312251.023 [DIRS 161253] and LTCTF test data from DTN: LL030300612251.035 [DIRS 166971].

Output DTN: MO0705CREEPSCC.000, *SDFRvData.xls*, file "Graph1."

Figure 7-2. Comparison of the SDFR Prediction Model and Measured Data for Alloy 22

Table 7-4. Comparison of Predicted and Measured Crack Growth Rates for Alloy 22

Specimen ID	Test Solution	Nominal Test Temperature (°C)	Average Stress Intensity MPa√m	Measured Crack Growth Rate (mm/s)	Predicted Crack Growth Rate (mm/s)	Prediction Error Ratio*
DCT-13	BSW-13	100	45.13	2.1276×10^{-09}	1.76×10^{-09}	-0.17
DCT-14	BSW-13	100	44.88	4.2376×10^{-09}	1.71×10^{-09}	-0.60
DCT-16	BSW-13	100	46.38	1.4176×10^{-09}	1.99×10^{-09}	0.41
DCT-18	SAW	94	45.07	2.1276×10^{-10}	1.75×10^{-09}	7.23
DCT-19	SAW	94	45.08	1.4176×10^{-11}	1.75×10^{-09}	122.91
DCT-20	SCW	95	45.11	4.2376×10^{-10}	1.75×10^{-09}	3.14
DCT-21	SCW	95	44.68	2.8276×10^{-11}	1.68×10^{-09}	58.43
DCT-22	SCW	95	44.37	4.9476×10^{-12}	1.62×10^{-09}	327.45

Sources: Columns 1 through 5 are obtained from Table 7-3.
Values in column 6 are obtained from Equation 18 (in Section 6.4.4) with n = 1.165.
Prediction error ratio (column 7) = (column 6 – column 5) / column 5.

NOTE: * As noted in Section 7.3.2, for specimen DCT-22 from Table 7-4 and very likely also for specimens DCT-18, DCT-19, DCT-20, and DCT-21 from Table 7-4, for which extremely low reported rates were measured over fairly short test times (<2,000 hours) with a relatively high noise level, the measured growth rates are below the crack growth detection limit and, thus, the comparison between measured and predicted rates is not directly relevant.

7.3.3 Corroboration of SDFR Model with Available Alternative Conceptual Models

The applicable activity is Activity Three listed in Section 7.2 and repeated here:

> *Demonstrate that the crack growth rates, predicted by the film rupture–repassivation crack growth model, are consistent with growth rates predicted by an alternative mathematical model*

Although not a required model validation activity per *Technical Work Plan for Postclosure Engineered Barrier Degradation Modeling* (SNL 2007 [DIRS 178849], Section 2.3.2), corroboration with available alternative conceptual models (ACMs) such as the coupled environment model, a mathematical model used to predict stress corrosion crack growth rates, can be used to validate the developed model. The ACM is summarized, discussed, and contrasted with the base-case model. The developed base-case model should be comparable or more conservative than the ACMs. More details about ACMs are provided in Section 6.4.6.

Corroboration with available ACMs, such as the coupled environment fracture model for SCC, was considered for the validation of the base-case model. Section 6.4 concludes that the SDFR and the coupled environment fracture (CEF) models are capable of predicting the crack growth rate for SCC. However, the CEF model had a tendency of underestimating the crack growth rate as compared to the SDFR model when both models were applied to predict the crack growth rate for Stainless Steel Type 304 in the BWR environment (Figure 6-10). Comparison with experimental data summarized by Ford and Andresen (1988 [DIRS 118611], Figure 6) for crack propagation rate versus stress intensity factor for sensitized Stainless Steel Type 304 in fully aerated, high-purity water at elevated temperature indicated that the crack growth rate predicted by the CEF model (i.e., 3.2×10^{-9} cm/s at 20 MPa√m) is at the lower end of the range cited by Ford and Andresen (1988 [DIRS 118611]) and Macdonald and Urquidi-Macdonald (1991 [DIRS 162702]). For this reason, the CEF model was not included for evaluation but was only used to further validate the base-case SDFR model.

7.3.4 Activities Performed to Demonstrate the Technical Basis for the Selection of the Threshold Stress Intensity Factor and the Threshold Stress Parameter for SCC Initiation

The applicable activity is Activity Four listed in Section 7.2 and repeated here:

> *Demonstrate that the establishment of the threshold stress intensity factor (K_{ISCC}) and threshold stress represent an acceptable approach for Alloy 22 and Titanium Grade 7 under environmental conditions relevant to the waste package and drip shield, respectively*

This activity is not specified in *Technical Work Plan for Postclosure Engineered Barrier Degradation Modeling* (SNL 2007 [DIRS 178849], Section 2.3.2) as a validation activity. These activities were conducted to provide justification for the approach and basis used for determination of K_{ISCC} and the threshold stress for SCC initiation under environmental conditions relevant to the waste package and drip shield. Thus, to provide additional confidence, a defensible technical basis for selection of each of these parameters is described in Section 7.3.4.1 and Section 7.3.4.2.

7.3.4.1 Activities Performed to Demonstrate the Technical Basis for the Threshold Stress Intensity Factor (K_{ISCC}) for Alloy 22

As described earlier, in Section 6.8.4.2.2, consideration of K_{ISCC} in the Titanium Grade 7 drip shield is not relevant because the value is effectively zero (i.e., once SCC is initiated in the drip shield as a result of rockfall or seismic damage, it is conservatively assumed to propagate through-wall instantly regardless of the through-wall K_{ISCC} values).

For Alloy 22, however, stress corrosion crack growth can generally occur at a rate such as that predicted by the SDFR model only if the calculated stress intensity at any flaw of given dimensions of length and depth exceeds a threshold value known as K_{ISCC}. As there is no accepted theoretical basis for deterministic calculation of K_{ISCC}, this parameter is conservatively determined by selecting a K_I value corresponding to a conservative lower limit value for the crack growth rate, V_t. To accomplish this, the general form of the previously validated SDFR model (see Activities One, Two, and Three) (i.e., Equation 14) is used to calculate the stress intensity factor value corresponding to a crack growth rate equal to the general corrosion rate, V_{gc}, in Section 6.4.5). This calculated value is defined as K_{ISCC}.

The theoretical basis for this approach is that if the crack growth rate equals the rate at which the surface recedes due to general corrosion, then it is not possible to maintain a sharp crack (the crack tip will blunt) and SCC will effectively arrest. Based on this "crack blunting" theory (Andresen and Ford 1994 [DIRS 118581], p. 62), it follows that any existing stress corrosion crack will not continue to grow (i.e., will arrest) if the crack growth rate is equal to or less than the general corrosion rate. If V_{gc} is the mean general corrosion rate, the threshold stress intensity factor K_{ISCC} can be calculated from Equation 19 (a rearrangement of Equation 14) of Section 6.4.5, which represents the SDFR model for the case of constant (noncyclic) stress (i.e., for the waste package sustained-loading conditions):

$$K_{ISCC} = (V_{gc} / \overline{A})^{1/\overline{n}} \qquad \text{(Eq. 20)}$$

The mean general corrosion rate, V_{gc}, based on Section 6.4.5.3, is 7.23 nm/yr. The threshold stress intensity factor for Alloy 22, accordingly, can be calculated, and its distribution is listed in Table 6-8, based on the *n* value distribution shown in Table 6-7. In conclusion, Activity Four is satisfied, since an acceptable, conservative K_{ISCC} value was obtained by setting the crack growth rate in the validated SDFR model to a value equal to the mean general corrosion rate at the alloy surface.

7.3.4.2 Activities Performed to Demonstrate the Technical Basis for the Threshold Stress for Alloy 22

Similar to the previously described establishment of a K_{ISCC} value, the purpose of Activity Four is to demonstrate a defensible technical basis for selecting a threshold-stress parameter for SCC initiation. Thus, this activity specifies the demonstration of an acceptable approach for the establishment of a threshold stress for SCC initiation for Alloy 22 under environmental conditions relevant to the waste package.

Although the threshold stress concept is described in peer-reviewed journal papers, there is no firm accepted basis for calculating a threshold stress value for a given material and environment combination. The threshold stress is that value below which SCC will not initiate on a "smooth" metal surface. Therefore, as described in Section 6.2.2, a conservative, empirical approach is implemented to develop a defensible threshold-stress parameter. For the purpose of lifetime modeling, a "smooth" surface is one that contains microscopic defects associated with incipient environmental crack formation, or metallurgical or mechanical defect sites. The initial defect depth is taken as 0.05 mm, a value qualified for use in Section 6.2.2 using SCI-PRO-006, Section 6.2. Thus, when the metal surface stress exceeds the SCC threshold stress, SCC is initiated at these "smooth" surface microdefects. Once initiated, the crack may reach either the arrest state, or the "propagation" phase, once the crack tip stress intensity factor exceeds the threshold K_{ISCC} value described above. As it is necessary to experimentally establish the threshold stress values, a conservative approach is taken based on qualified experimental data.

As addressed in Section 6.2, long-term SCC initiation stress measurement results have been obtained under constant active applied loading conditions using uniaxial tensile specimens covering a range of metallurgical conditions. These experimental measurements of crack initiation stress are presented in Figure 4-1 as the ratio of applied stress to yield strength versus time on test for specimens exposed in hot concentrated salt solution (pH = 10.3 at 105°C) designed to simulate the chemistry of concentrated Yucca Mountain groundwater. Specimens have been on test for over 28,000 hours (approximately 3.2 years). Sections 6.2.1 and 6.2.2 indicate that Alloy 22 exhibits excellent SCC resistance, since failure was not observed for any of the 120 Alloy 22 specimens under applied stress ratios of about 2.0 (yield strength) for annealed material and 2.1 (yield strength) for welded material. These stress ratios correspond to about 89% to 96% of the ultimate tensile strength. Alloy 22 was also found to be highly resistant to SCC initiation in slow strain rate tests (SSRTs) and U-bend tests covering a broad range of environments.

In establishing a defensible "safety factor," it is appropriate to consider other accepted precedents based on threshold (or maximum long-term applied stress without SCC failure) measurements used in general engineering practice. For example, the ASME code (ASME 1969 [DIRS 162446], p. 20) utilizes a reduction factor of 2 on stress when dealing with high-cycle fatigue (i.e., the code-allowable threshold value is set at half the experimentally measured value of the maximum long-term applied stress without fatigue failure, known as the endurance limit, which is the maximum stress below which a material can presumably endure an infinite number of stress cycles). In dealing with SCC rather than fatigue, it is considered appropriate to also use a conservative "safety factor" on the measured threshold runout stress values (i.e., the maximum long-term applied stress without SCC failure).

Consequently, threshold stress values to be used to develop an initiation criterion for Alloy 22 are based on applying a conservative reduction factor of 2 on the maximum measured threshold or the values of the maximum long-term applied stress ratio without SCC failure obtained from the constant-load tests described above. In addition, it is prudent to select a threshold stress value near the materials yield strength to limit the potential for significant plastic strain to occur. Applying this philosophy and a reduction factor of 2.0, the threshold stress values selected are normally distributed between 0.9 (yield strength) and 1.05 (yield strength) for Alloy 22. Based

on the foregoing discussion, Activity Four, the demonstration of a defensible technical basis for the selection of the threshold stress for SCC initiation for Alloy 22, has been satisfied.

7.4 DISCUSSION OF SCC PARAMETERS FOR DRIP SHIELD MATERIALS

7.4.1 Intended Purpose of the Parameters

Attachment 3 of SCI-PRO-002 states that:

> "Level I validation shall include, at a minimum, discussion of documented decisions and activities that are implemented during the model development process that build confidence and verify and justify that an adequate technical approach using scientific and engineering principles was taken…In addition, for post-development validation of a Level I model, choose a single method (e.g., technical review) described in Section 6.3.2 of SCI-PRO-006, consistent with the model's importance to the TSPA."

However, as indicated in Section 1.2, of the drip shield-related subjects discussed in Section 6.8, only the representation of seismic crack density constitutes model development. The following activities do not develop models: (1) the drip shield SCC crack growth rate (Section 6.8.4) is a measured parameter; (2) the low-temperature creep section (Section 6.8.7) summarizes the literature observations on the subject; and (3) the SCC crack initiation threshold stress criteria are considered experimentally derived parameters. This is also true for the SCC crack "plugging" section (Section 6.8.6). However, since these parameters/analyses are important, additional confidence building activities were conducted to provide defensibility. For the drip shield, the SCC initiation threshold stresses (for Titanium Grades 7, 28, and 29) (Section 6.8.3), and threshold stress intensity factors (for Titanium Grades 7, 28, and 29) (Sections 6.8.4.2.2 and 6.8.4.2.4) are discussed in Section 7.4. The SCDM is validated in Section 7.5.2.

SCC is a potential corrosion mode that can result in penetration of the drip shield, waste package outer barrier, and the stainless steel structural materials. The purpose of this report is to provide the evaluation of the potential for SCC of the drip shield, waste package outer barrier, and stainless steel inner structural cylinder under exposure conditions. As no credit is taken for the SCC resistance of the stainless steel structural material, it is not modeled in this document. For the drip shield and waste package outer barrier, the critical environment is conservatively taken as any aqueous environment contacting the metal surfaces. The model outputs feed to TSPA. This SCC model directly supports the following TSPA components:

- Drip Shield Stress Corrosion Cracking and Other Corrosion Modes.

Technical Work Plan for Postclosure Engineered Barrier Degradation Modeling (SNL 2007 [DIRS 178849], Section 2.3.2) only specifies two validation activities for the drip shield SCDM; these are discussed in Section 7.5. For all other subjects discussed in Section 6.8, *Technical Work Plan for Postclosure Engineered Barrier Degradation Modeling* (SNL 2007 [DIRS 178849], Section 2.3.2), states:

> As a defensibility activity, not validation, this is to show that the approach used is acceptable for Titanium Grade 7 under the relevant environmental

> conditions. This will be deemed useful if the threshold stress intensity (K_{ISCC}) and threshold stress parameters does not underestimate the occurrence of crack initiation and propagation.

This section will discuss the basis for confidence in the SCC representation for the drip shield, developed in Sections 6.8.3, SCC Crack Initiation for Drip Shield Materials, and 6.8.4, SCC Crack Propagation in Drip Shield Materials. The drip shield SCDM will be validated in Section 7.5.2.

7.4.2 Identification and Documentation of Validation Activities and Associated Criteria to be Used to Determine that the Required Level of Confidence Has Been Obtained for the Drip Shield Seismic Crack Density Model

Technical Work Plan for Postclosure Engineered Barrier Degradation Modeling (SNL 2007 [DIRS 178849], Section 2.3.2) only specifies three validation activities for the drip shield SCDM, which is discussed in Section 7.5. For all other subjects discussed in Section 6.8, *Technical Work Plan for Postclosure Engineered Barrier Degradation Modeling* (SNL 2007 [DIRS 178849], Section 2.3.2), states:

> As a defensibility activity, not validation, this is to show that the approach used is acceptable for Titanium Grade 7 under the relevant environmental conditions. This will be deemed useful if the threshold stress intensity (K_{ISCC}) and threshold stress parameters does not underestimate the occurrence of crack initiation and propagation.

Although no specific activities are given in the TWP (SNL 2007 [DIRS 178849]), the following activity is adopted to show that the defensibility purpose specified in the TWP is met.

> **Activity One:** Show that the representations of the SCC initiation threshold stresses for Titanium Grades 7, 28, and 29 are consistent with observations in literature.
>
> **Activity Two:** Demonstrate that the crack growth rates, predicted for drip shield by the film rupture–repassivation crack growth model, are consistent with experimental rates obtained from data not used to develop the model.
>
> **Activity Three:** Demonstrate that the establishment of the threshold stress intensity factor (K_{ISCC}) and threshold stress represent an acceptable approach for drip shield materials under environmental conditions relevant to the waste package and drip shield, respectively.

In particular, the criteria and related activity cited in *Technical Work Plan for Postclosure Engineered Barrier Degradation Modeling* (SNL 2007 [DIRS 178849], Section 2.3.2) are consistent with Section 6.3 of SCI-PRO-006.

7.4.3 Documentation of Activities to be Performed to Generate Confidence in the Model during Model Development

The criteria and related activities to be used to determine that the required level of confidence has been obtained for the drip shield SCC models were listed in Section 7.4.2.

Activity One is satisfied by the following discussion in Section 7.4.3.1 through Section 7.4.3.4 on comparison of the model results with other literature observations.

7.4.3.1 SCC Initiation Stress for Titanium Grade 7

As described in Section 6.8.3.3, the SCC initiation threshold stress for Titanium Grade 7 is 0.8 ($YS_{(T)}$). This criterion is established by using the GE GRC constant-load data shown in Table 6-25 and the LTCTF U-bend test data shown in Table 6-29.

To further strengthen the basis for the new Titanium Grade 7 threshold stress, additional Titanium Grade 7 specimens have been added to the ongoing Keno test Run 2 matrix, as indicated in Table 7-5 (DTN: MO0705SCCIGM06.000 [DIRS 180869], file *GE-GRC-Final_Sept-2006-Rev3.doc*, Table 8). These specimens are loaded to 73% and 85% of the at-temperature yield strength. The upper stress level selected for these new tests is above the SCC initiation threshold criterion (i.e., 80% of at-temperature yield strength) but below the stress levels where rapid creep rupture will occur. Based on the air creep rupture curve in Figure 6-68, expected creep failure times are about 10 years and one year at about 71% and 83% of the at-temperature yield strength, respectively. Thus, assuming Titanium Grade 7 will exhibit SCC susceptibility, there is ample time for SCC to initiate prior to creep rupture.These specimens have been on test for about 2,800 hours without SCC failure.

Moreover, in addition to the noncreviced single U-bend specimens described in Section 6.8.3.1.2, a series of Titanium Grade 7 creviced double U-bend specimens were exposed at LTCTF to 105°C aerated BSW brine. Examination of two of these specimens after 17 months of exposure indicated no evidence of SCC initiation, confirming the LTCTF single U-bend results as shown in Figure 7-3 (DTN: LL030102212251.005 [DIRS 178276]).

The previous Titanium Grade 7 SCC initiation threshold stress criterion was developed in a manner analogous to that of Alloy 22, as described in Section 6.2.2. The approach was based on applying a conservative reduction factor (2.1) to the apparent runout stress (the maximum long-term applied stress without SCC failure) on a plot of Keno Run 2 applied stress versus time-to-failure (BSC 2004 [DIRS 172203], Section 6.2.1). This resulted in a threshold stress criterion of 50% of the Titanium Grade 7 at-temperature yield strength. This value was conservatively defined as one half the 140°C yield strength value of 221 MPa or 110.5 MPa.

Table 7-5. New Titanium Specimens Added to KENO Test on June 8, 2006

Specimen. #	Material	Stress (Mpa)	Yield Strength (%*)
208	Titanium Grade 7	210	85
209	Titanium Grade 7	210	85
210	Titanium Grade 7	210	85
211	Titanium Grade 7	210	85
212	Titanium Grade 7	180	72.5
213	Titanium Grade 7	180	72.5
214	Titanium Grade 7	180	72.5
215	Titanium Grade 7	180	72.5

NOTE: *Yield strength values used are for 105°C. Value for Titanium Grade 7 (248.2 MPa) was measured at 125°C (DTN: MO0705SCCIGM06.000 [DIRS 180869], file *GE-GRC-Final_Sept-2006-Rev3.doc*, Table 8).

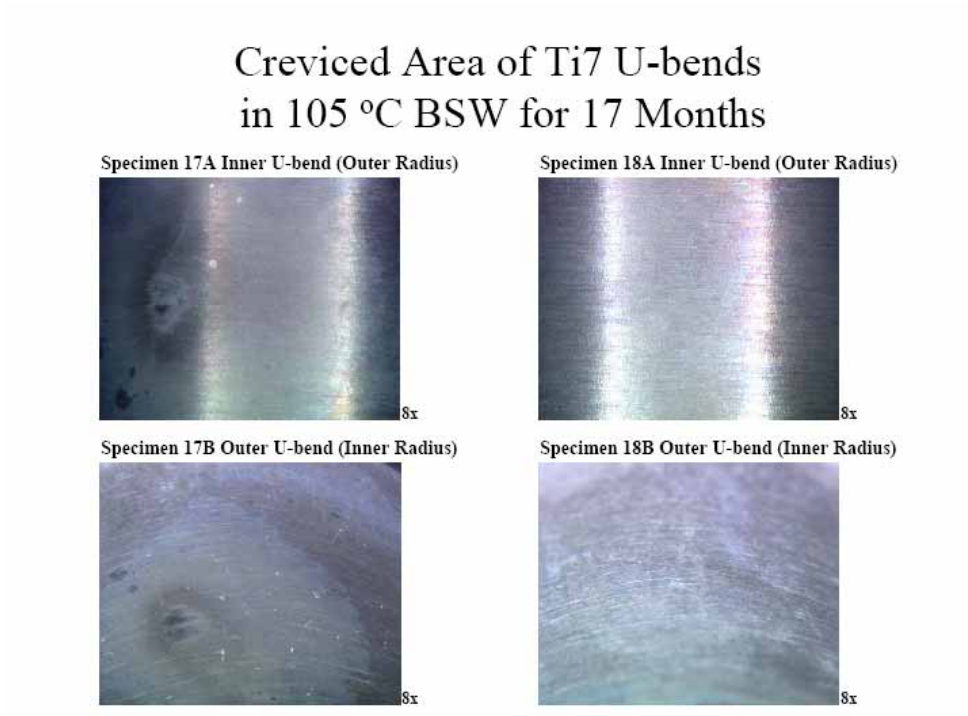

Source: DTN:LL0301022 12251.005 [DIRS 178276].

Figure 7-3. Photomacrographs Showing the Apex Region of Two Double U-bend Specimens Exposed to 105°C BSW for 17 Months

A new threshold stress for SCC initiation is developed based on considerations of the primary and secondary stresses and on Figure 6-73, which is constructed by using data in Table 6-25 and Table 6-29. The new threshold stress for SCC initiation for Titanium Grade 7 is established as 80% of its at-temperature yield strength. This threshold stress criterion can be rationalized by considering the primary and secondary stresses in drip shield design scenarios. The comparison of the criterion developed in Section 6.8.3.1 and other independently obtained observations described in this section (Table 7-5 and Figure 7-3) has improved the confidence of the newly

developed SCC initiation threshold stress criterion for Titanium Grade 7 (i.e., 80% of the at-temperature yield strength) (Table 6-32).

7.4.3.2 SCC Initiation Stress for Titanium Grades 28 and 29

As described in Section 6.8.3.3, the SCC initiation threshold stresses for Titanium Grades 28 and 29 are estimated as 0.5 $YS_{(T)}$. This 50% yield strength value was based on applying a factor of approximately 0.5 to the maximum long-term applied stress without SCC failure obtained in several series of SCC initiation tests (Schutz et al. 2000 [DIRS 177257]; DTN: MO0705SCCIGM06.000 [DIRS 180869]). These experimental results are corroborated by other literature results reported in a range of higher-temperature, aggressive brines. These literature results include:

1. A series of SCC initiation tests on C-ring specimens of Titanium Grades 28 and 29 stressed at 95% and 105% of yield strength and exposed to 260°C, "worst-case" sour gas well brine for 90 days (Schutz 1997 [DIRS 177482]). No SCC initiation was observed on any of these specimens.

2. No SCC initiation was observed in a series of U-bends using Titanium Grades 28 and 29 materials exposed up to 80 days to approximately 300°C sour geothermal brine (Schutz 1997 [DIRS 177482]).

3. A series of SSRTs were performed on Titanium Grades 28 and 29 in acidic sweet and sour brines at temperatures of 230°C to 330°C without SCC initiation (Schutz 1997 [DIRS 177482]).

4. Others reported that U-bend tests on Titanium Grade 9 (Ti-3%Al-2.5%V), an analogue of Titanium Grade 28 not containing ruthenium, were performed for 440 days in boiling seawater with and without 200 ppm $S^{=}$ with no evidence of either SCC or hydriding (Yau 1989 [DIRS 178195]).

5. In addition, more limited literature results were obtained on thin sheet tensile specimens of Ti-6Al-4V exposed under approximate deliquescent conditions with no SCC initiation observed (Boyer et al. 2003 [DIRS 174636], p. 510). A 1.6-mm-thick synthetic sea salt layer was coated on the smooth Ti-6Al-4V specimen surfaces, and the stressed specimens were exposed under humid air conditions over a range of temperatures for 100 hours (Boyer et al. 2003 [DIRS 174636], p. 510). Under these conditions, a threshold stress of about 450 MPa was obtained at approximately 300°C with the threshold stress value increasing rapidly with decreasing temperature (Boyer et al. 2003 [DIRS 174636], p. 510). Although described as SCC results, these salt-coated specimen failures may have been due to hot salt cracking rather than aqueous SCC, although the underlying mechanisms may be similar.

Based on these observations, a reasonable level of confidence has been obtained that the SCC initiation threshold stress developed in Section 6.8.3.2.3 is consistent with the literature results. As discussed in Section 6.8.3, Ti-6Al-4V is more SCC susceptible than Titanium Grade 29.

Therefore, the SCC initiation threshold stress developed in Section 6.8.3.2.3 is considered defensible and conservative.

7.4.3.3 Threshold Stress Intensity Factor for Titanium Grade 7

As described in Section 6.4.5, the threshold stress intensity factor (K_{ISCC}) is a critical value of stress intensity factor (K_I) below which any preexisting crack either will not grow (by SCC) or is in an arrest state. For the Titanium Grade 7 drip shield material, it is conservatively assumed that, once the SCC initiation threshold criterion is exceeded, SCC initiates and propagates through-wall instantly. Thus, it is not necessary to establish a K_{ISCC} for Titanium Grade 7.

7.4.3.4 Threshold Stress Intensity Factor for Titanium Grades 28 and 29

In contrast to the Titanium Grade 28 K_{ISCC} value of 15 MPa√m and Titanium Grade 29 K_{ISCC} value of 14 MPa√m established based on applying a conservative reduction factor for project test results, values obtained from the relevant literature provide a basis for selecting much higher threshold values and thus confirm the conservative nature of the values selected. For example, under fully static sustained loading conditions, Schutz measured a K_{ISCC} value for Titanium Grade 29 of > 60 MPa√m in an aggressive NaCl plus CaF_2 saturated brine at 210°C (Schutz 1992 [DIRS 177345]). Other published test results for Titanium Grade 23, the less-SCC-resistant analogue for Titanium Grade 29 that does not contain palladium, indicate measured K_{ISCC} values from 53 MPa√m to 119 MPa√m in near-room-temperature 3.5% NaCl brines (Table 6-36). Literature data indicates that K_{ISCC} is relatively unaffected by temperatures as high as 93°C in neutral salt solutions, although crack velocity can increase with temperature (Jones 1992 [DIRS 178458], p. 274). Further, SCC threshold temperatures can be raised significantly on alloys including Ti-6Al-4V by minor additions of platinum group metals such as palladium and ruthenium. For example, Ti-6Al-4V plus palladium is resistant to SCC in sour brines to temperatures as high as 260°C (Jones 1992 [DIRS 178458], p. 275).

7.4.4 Other Confidence Building Activities

> **Activity Two:** Demonstrate that the crack growth rates, predicted for drip shield by the film rupture–repassivation crack growth model, are consistent with experimental rates obtained from data not used to develop the model.

As described in Section 6.8, the only SCC breach criterion for the Titanium Grade 7 drip shield is the threshold stress (for SCC initiation). Thus, whether from rockfall or from direct seismic-related residual stresses as described in Section 6.8.5, if the resultant stresses exceed the threshold stress criteria, the crack growth rate is such that "breach" (i.e., through-wall SCC) occurs essentially instantaneously, consistent with a threshold stress intensity factor value of zero. Also, as described in more detail in Section 6.8.5, even if stress corrosion cracking propagates through-wall, the seepage diversion function of the drip shield will remain intact for the reasons discussed in Section 6.8.6.

The confidence-building activities for SCC of drip shield materials are discussed in this section only with respect to establishment of a threshold stress as described in Activity Four. This section shows that the required confidence level for the drip shield-related SCC model has been achieved because all activities specified in the TWP are fully (or very conservatively) complied

with to generate confidence in the parameters and requirements listed in Section 2.3.2 of *Technical Work Plan for Postclosure Engineered Barrier Degradation Modeling* (SNL 2007 [DIRS 178849]).

> **Activity Three:** Demonstrate that the establishment of the threshold stress intensity factor (K_{ISCC}) and threshold stress represent an acceptable approach for drip shield materials under environmental conditions relevant to the waste package and drip shield, respectively.

This activity applies to the threshold stress intensity factor parameter (K_{ISCC}) and the threshold stress criterion for SCC initiation on a "smooth" surface (i.e., in the absence of fabrication defects such as weld flaws). While the TWP states "VA = NA", this report provides a defensible basis consistent with Activity One (SCI-PRO-006, Section 6.3), "compare with laboratory results"). As there is no relevant theoretical basis in the literature to describe these parameters, they are each selected based on a conservative empirical approach.

As described earlier in Section 6.8.4.2.1, consideration of K_{ISCC} in the Titanium Grade 7 drip shield is not relevant, as the value is effectively zero (i.e., once SCC is initiated in the drip shield as a result of rockfall or seismic damage, it is conservatively assumed to propagate through-wall instantly regardless of the through-wall K_{ISCC} values).

Similar to the previously described establishment of a K_{ISCC} value, the purpose of this activity is to demonstrate a defensible technical basis for selecting a threshold-stress parameter for SCC initiation. Thus, Activity Four specifies the demonstration of an acceptable approach for the establishment of a threshold stress for SCC initiation for Alloy 22 under environmental conditions relevant to the waste package.

7.5 VALIDATION OF SEISMIC CRACK DENSITY MODELS FOR WASTE PACKAGE AND DRIP SHIELD MATERIALS

The primary purpose of the seismic crack density models for the waste package outer barrier and drip shield materials is to provide inputs to *Seismic Consequence Abstraction* (SNL 2007 [DIRS 176828]). The developed crack area densities are used as scaling factors applied to the total seismic damaged area to obtain the total area of the crack network through which radionuclide transport could occur, in the case of the waste package, and through which water could flow, in the case of the drip shield. As indicated in Section 6.8.5, both models are identical except that the yield strength and modulus of elasticity values are different for the Alloy 22 waste package outer barrier and the Titanium Grade 7 drip shield plate materials.

The models are validated using the approaches governing this activity described in *Technical Work Plan for Postclosure Engineered Barrier Degradation Modeling* (SNL 2007 [DIRS 178849], Section 2.3.2), and are consistent with SCI-PRO-006. This procedure calls for the determination of the level of confidence required for the model and identification of criteria that can be utilized to show that the level of confidence has been achieved.

Section 7.5.1 discusses the seismic crack density model for Alloy 22. Section 7.5.2 discusses the validation of seismic crack density model for drip shield materials.

7.5.1 Validation Activities for the Waste Package Outer Barrier Seismic Crack Density Model

The current TWP for this report, *Technical Work Plan for Postclosure Engineered Barrier Degradation Modeling* (SNL 2007 [DIRS 178849], Section 2.3.2), states that the Alloy 22 waste package outer barrier SCDM warrants a high level of confidence (Level II). Attachment 3 of SCI-PRO-002 states that Level II validation shall include Level I criteria and documentation that demonstrates model predictions are reasonably corroborated by at least two postdevelopment model validation methods described in Step 6.3.2 of SCI-PRO-006. Therefore, the development of the Alloy 22 SCDM was documented including the following activities that demonstrate the adequacy of the technical approach:

(a) *Evaluate and select input parameters and/or data that are adequate for the model's intended use (SCI-PRO-002, Attachment 3, Level I(1)).*

The bases for selecting the input data listed in Section 4.1 and used to determine and develop the SCDM for application to the waste package are documented in Section 6.7. Detailed discussion about model concepts can be found throughout Section 6.7. Thus, this requirement can be considered satisfied.

(b) *Formulate defensible assumptions and simplifications that are adequate for the model's intended use (SCI-PRO-002, Attachment 3, Level I(2)).*

No assumptions were used for model development. A discussion of simplifications and their rationale are provided throughout the Section 6.7. Thus, this requirement can be considered satisfied.

(c) *Ensure consistency with physical principles, such as conservation of mass, energy, and momentum, to an appropriate degree commensurate with the model's intended use (SCI-PRO-002, Attachment 3, Level I(3)).*

Discussion of relevant physical phenomena and processes are discussed in Section 6.7 for the waste package. Thus, this requirement can be considered satisfied.

(d) *Represent important future state (aleatoric), parameter (epistemic), and alternative model uncertainties to an appropriate degree commensurate with the model's intended use (SCI-PRO-002, Attachment 3, Level I(4)).*

Uncertainties associated with the model analysis are discussed in Section 6.7.3 for the crack area density through the epistemic uncertainty factor, C. Thus, this requirement can be considered satisfied.

(e) *Ensure simulation conditions have been designed to span the range of intended use and avoid inconsistent outputs or that those inconsistencies can be adequately explained and demonstrated to have little impact on results (SCI-PRO-002, Attachment 3, Level I(5)).*

Not applicable because no simulation is used in this report.

(f) Ensure that model predictions (performance parameters) adequately represent the range of possible outcomes, consistent with important uncertainties and modeling assumptions, conceptualizations, and implementation (SCI-PRO-002, Attachment 3, Level I(6)).

This requirement is satisfied by the discussions for items (a) through (d).

In addition, the following lists the postdevelopment model validation methods described in *Technical Work Plan for Postclosure Engineered Barrier Degradation Modeling* (SNL 2007 [DIRS 178849], Section 2.3.2), applied to the Alloy 22 waste package outer barrier SCDM.

Activity One: Show that the representations of the damaged area in the form of a crack network instead of a hole, is consistent with observations in literature. This activity deals with the validity of the use of crack density representations in the seismically damaged areas. It will be considered successful if the model results (such as crack opening area) are corroborated by literature observations, or the model predicts more cracking than is observed.

Activity Two: Show that the model results for crack patterns in the damaged areas are consistent with the results of an alternative model. As [this is] a qualitative criterion, this involves the expert judgment of the principal investigator.

Activity Three: Conduct a technical review by external subject matter experts for the seismic crack density model. The review will answer the following questions:

1. Is the representation of the failure in the form of cracks in the damaged area instead of a hole which is technically appropriate?

2. Does the model consider a variety of crack patterns and distributions?

3. Are the rack networks in the model considered appropriate and reasonable?

4. Do the crack network representations considered in the model represent optimum crack density (i.e., number, size, shape, and distribution of cracks) such that the largest possible crack opening area is included?

5. Do alternative models exist for crack geometry and morphology?

6. In the parameters used to describe the model, has uncertainty been adequately characterized? If not, what additional uncertainties should be added?

7. Are there alternate crack patterns that are more defensible from a technical standpoint?

This activity is considered successfully completed if the external review comments support a conclusion that the model is reasonable.

7.5.1.1 Identification and Documentation of Validation Activities and Associated Criterion to be Used to Determine that the Required Level of Confidence Has Been Obtained for the Waste Package Outer barrier Seismic Crack Density Model

Attachment 3 of SCI-PRO-002 states that Level II validation shall include Level I activities, items (a) through (f) in the previous section (see Section 7.1.1), and documentation that demonstrates model predictions are reasonably corroborated by at least two postdevelopment model validation methods described in Step 6.3.2 of SCI-PRO-006.

The activities and associated criteria are primarily related to confidence building during model development, although they do provide additional confidence in the Alloy 22 waste package outer barrier SCDM results. In particular, the criteria and related activity cited in Section 2.3.2 of the TWP (SNL 2007 [DIRS 178849]) are consistent with Section 6.3.2 of SCI-PRO-006.

7.5.1.2 Documentation of Activities to be Performed to Generate Confidence in the Model during Model Development

The criteria and related activities to be used to determine that the required level of confidence has been obtained for the Alloy 22 waste package outer barrier SCDM were listed in Section 7.5.1.

The criterion established for Activity One is satisfied by the discussions throughout Section 6.7 but particularly in Sections 6.7.1.1 and 6.7.1.2, in which the nature of SCC and analysis of BWR and light water reactor (LWR) SCC case histories are discussed.

Among the observations made in Section 6.7.1.1:

- It is unlikely that the residual stress profile, which would be created by seismic loading, would allow an initiated stress corrosion crack to propagate through-wall and circumscribe the deformed area
- The through-wall residual stress fields resulting from impact loads would be a secondary-type stress (displacement controlled), and there is no source of significant internal pressure
- Stress fields would be expected to be greatest at the outer surface and to decrease with depth
- The magnitude of the stress state will decrease as the crack propagates
- Stress field interactions between adjacent cracks would tend to decrease the driving force for crack growth
- The nature of stress corrosion cracks (crack face roughness, branching, and tortuosity) is such that large sections of material will not “fall out” of the cracked structure.

The primary observation made in Section 6.7.1.2 was that, even under the severe stress conditions experienced in LWRs, there are no documented cases where any section of material dropped out as a result of cracking.

On the basis of these observations, a reasonable level of confidence has been obtained that representations of the damaged area in the form of a crack network instead of a missing portion or hole is consistent with observations in the literature and is a reasonable morphology to use for analysis of waste package through-wall SCC due to seismic loading.

Activity Two is satisfied by Section 0, in which an alternative mathematical model for stress corrosion crack morphology and damaged area shape is presented. The primary model for crack area density was summarized in Section 6.7.3.3. The crack area density based on hexagonal crack arrays was found to be given by a uniform distribution between $\frac{\pi\sigma}{\sqrt{3}E}$ and $\frac{4\pi\sigma}{\sqrt{3}E}$ (approximately $1.81\frac{\sigma}{E}$ and approximately $7.26\frac{\sigma}{E}$). For the alternative model (Section 0), the crack area density based on a circular seismically damaged area with a single circumferential crack was found to be $4\frac{\sigma}{E}$. The crack area density from the alternative mathematical model lies within the bounds of the crack area density resulting from the primary mathematical model. Therefore, the results of the alternative mathematical model corroborate the results of the primary mathematical model. This model validation methodology is consistent with Section 6.3.2 of SCI-PRO-006.

7.5.1.3 Documentation of Postdevelopment Activities Performed By Independent Technical Reviewers

Activity Three is satisfied by a technical review conducted by reviewers independent of the development, checking, and interdisciplinary review of the model documentation. The results of this technical review also serve to satisfy the model validation requirements of SCI-PRO-006, Section 6.3.2.

Technical reviewers were asked to address the following questions (Pasupathi 2004 [DIRS 168350]):

1. Is the representation of failure in the form of cracks in the damaged area technically appropriate?

2. Does the model consider a variety of crack patterns and distributions?

3. Are the crack networks considered in the model appropriate and reasonable?

4. Do the crack network representations considered in the model represent optimum crack density (i.e., number, size, shape, and distribution of cracks) such that the largest possible crack opening area is included?

5. Do alternative models exist for crack geometry morphology?

6. Has uncertainty in the parameters used to describe the model been adequately characterized? If not, what additional uncertainties should be added?

7. Are there alternate crack patterns that are more defensible from a technical standpoint?

The responses to each of these independent technical review questions are considered throughout the remainder of this section.

1. *Is the representation of failure in the form of cracks in the damaged area technically appropriate?*

Generally, the technical reviewers felt that the analysis has done a good job of looking at various crack geometries in the damaged area (Jones 2004 [DIRS 168353]). The representation of the failure in the form of cracks in the damaged area was found to be technically appropriate (Payer 2004 [DIRS 168352]). One technical reviewer (Beavers 2004 [DIRS 168354]) agreed that the damaged area likely failed by "SCC clusters" (arrays of cracks) rather than by the formation of large holes; however, the technical reviewer felt that the report sent for his review did not effectively prove this was the case. This technical reviewer (Beavers 2004 [DIRS 168354]) recommended that additional analysis and discussion be provided. The report in question was revised (Herrera 2004 [DIRS 168133]) in response to these comments, and the revision forms the basis for the model documented in this report.

Conclusion/Response: On this basis, the technical reviewers agreed that the representation of failure in the form of cracks in the damaged area is technically appropriate.

2. *Does the model consider a variety of crack patterns and distributions?*

3. *Are the crack networks considered in the model appropriate and reasonable?*

The technical reviewers generally provided their answers to both of these review questions together. Therefore, their responses are treated together in this summary.

A variety of crack patterns and distributions are considered (Payer 2004 [DIRS 168352]). The technical reviewers felt that the crack networks considered in the model were appropriate and reasonable (Payer 2004 [DIRS 168352]; Jones 2004 [DIRS 168353]). The technical reviewers expressed concerns that a more-relevant geometry might be cracks constrained to an annulus around the deformed area and not cracks distributed throughout the deformed area (Jones 2004 [DIRS 168353]; Beavers 2004 [DIRS 168354]). Additional analysis was recommended for this damaged area geometry (Jones 2004 [DIRS 168353]; Beavers 2004 [DIRS 168354]). One reviewer (Beavers 2004 [DIRS 168354]) suggested that a circular crack circumscribing the damaged area was also a reasonable geometry to consider.

Conclusion/Response: The area damaged by seismic activity is not assigned a specific shape, only an area, A_D. The hexagonal crack density is applied to whatever area is seismically damaged regardless of its specific shape. A circular crack circumscribing the damaged area was considered as an alternative conceptual model in this report. Given the preceding observations, it is concluded, overall, that the report considers a variety of crack patterns and distributions and that the crack networks considered in the model are appropriate and reasonable.

4. *Do the crack network representations considered in the model represent optimum crack density i.e. number, size, shape and distribution of cracks, such that the largest possible crack opening area is included?*

In the context of this review, the wording "the largest possible crack opening area" should be restated as "an appropriate representation of crack area." The technical reviewers generally agreed that the hexagonal array of cracks was the optimum crack density or geometry for analysis; however, additional justification should be provided for the intercrack spacing (t, the wall thickness) (Beavers 2004 [DIRS 168354]; Jones 2004 [DIRS 168353]).

Conclusion/Response: The technical reviewers did not evaluate the documented basis for the intercrack spacing used, *Structural Integrity Associates Support of Waste Package Design for Year 2001* (SIA 2002 [DIRS 161933], Section 6.5.1), which supports the conclusion that the results presented in this report can be considered as the optimum. If the technical reviewers reviewed this detailed minimum crack spacing analysis, they would be more confident in the choice made for intercrack spacing.

On this basis, the crack network representations considered in the model represent the optimum crack density (i.e., the number, size, shape and distribution of cracks), such that an appropriate representation of crack area is included.

5. *Do alternative models exist for crack geometry morphology?*

Two of the reviewers (Jones 2004 [DIRS 168353] and Payer 2004 [DIRS 168352]) were aware of alternative models for crack geometry, although only one (Jones 2004 [DIRS 168353]) could specify what he thought was the most relevant geometry. The third reviewer (Beavers 2004 [DIRS 168354]) was unaware of any alternative models for crack geometry.

Conclusion/Response: The area damaged by seismic activity is not assigned a specific shape, only an area, A_D. The hexagonal crack density is applied to whatever area is seismically damaged regardless of its specific shape. A circular crack circumscribing the damaged area was considered as an alternative conceptual model in this report. Given the preceding observations, overall, the technical reviewers were satisfied that alternative models for crack geometry or morphology were considered.

6. *Has uncertainty in the parameters used to describe the model been adequately characterized? If not, what additional uncertainties should be added?*

One technical reviewer (Payer 2004 [DIRS 168352]) had no response. One reviewer (Beavers 2004 [DIRS 168354]) did not think the report, as supplied for review, adequately addressed uncertainty. Another reviewer (Jones 2004 [DIRS 168353]) pointed out several conservatisms in the analysis:

a) The analysis did not consider the decrease in residual stress as the crack propagates. There is a possibility of crack arrest, although no credit is taken for this process. Also decreased stress states would lead to narrower crack openings.

b) The analysis uses the crack mouth opening to represent the crack opening. The crack tip opening is smaller than the crack mouth opening. The reviewer supplied a crack-mouth-opening equation, which is less conservative than the one used in the analysis.

c) The use of the yield strength as the stress load on the cracks is conservative (the residual stress at penetration should be lower).

Jones (2004 [DIRS 168353]) also pointed out some possible nonconservatisms:

d) The Tada analysis (Tada et al. 2000 [DIRS 167756]) used to determine the crack opening is based on an infinite plate; how much difference would there be for a finite cylinder?

e) Deformation beyond the yield strength could result in work hardening and a higher value of yield strength.

Conclusion/Response: The crack opening results presented in Section 6.7 are based upon plane stress conditions in an infinite plate. The actual structure for the Alloy 22 waste package outer barrier consists of a cylindrical shell of finite length. It would be expected that crack openings in an infinite plate under plane stress would be different than in a finite cylindrical shell in that the membrane stresses and flexural stresses for given loadings in combination with other loads would be different. The analysis is used to determine a crack area density (crack area per unit seismically damaged area) given a seismically damaged area determined elsewhere (SNL 2007 [DIRS 176828]). That is, the spatial stress state is determined elsewhere and is based upon consideration of a cylindrical shell of finite length.

Detailed comparisons between crack openings in infinite plates and finite cylinders were not undertaken in this analysis; however, the results of analyses such as those in *Structural Integrity Associates Support of Waste Package Design for Year 2001* (SIA 2002 [DIRS 161933]) indicate that the presence of multiple cracks will tend to decrease the residual stress state to values well below the yield strength. This would result in crack openings that are smaller than those calculated. Coupling this result to the listed conservatisms outlined in this section (decreasing stress states as the crack propagates, conservative crack opening equations, the use of the yield strength at room temperature), it can be concluded that the current model will provide a reasonably conservative representation of the total crack opening area. On the basis of the discussion in this section, it is concluded that uncertainty in the parameters used to describe the model has been adequately characterized, at least to the extent that the total crack opening area will not be underestimated using the current model.

7. *Are there alternate crack patterns that are more defensible from a technical standpoint?*

This question is similar to questions 2 through 5. As stated in the discussion of question 2, the technical reviewers did express concerns that a more relevant geometry might be cracks constrained to an annulus around the deformed area and not cracks distributed throughout the deformed area (Jones 2004 [DIRS 168353]; Beavers 2004 [DIRS 168354]). One reviewer (Beavers 2004 [DIRS 168354]) indicated that while the "hexagon pattern is a reasonable,

defensible crack pattern for the deformed area of the waste package" …"a combination of this pattern with the circumferential pattern to produce a series of circular cracks around the dents is the most reasonable pattern." Further conversation with this technical reviewer (Pasupathi 2004 [DIRS 168351]) led to the conclusion that what was meant by "circumferential pattern of cracks to produce a series of circular cracks" was actually cracks constrained to an annulus around the deformed area and not cracks distributed throughout the deformed area.

Conclusion/Response: The area damaged by seismic activity is not assigned a specific shape, only an area, A_D. The hexagonal crack density is applied to whatever area is seismically damaged regardless of its specific shape. A circular crack circumscribing the damaged area was considered as an alternative conceptual model in this report. Given the preceding observations, it is concluded that, overall, the technical reviewers were satisfied that alternative models for crack geometry or morphology were considered and the crack patterns analyzed were sufficient from a technical standpoint.

On this basis, the validation criteria from SCI-PRO-006 related to corroboration and those listed in *Technical Work Plan for Postclosure Engineered Barrier Degradation Modeling* (SNL 2007 [DIRS 178849], Section 2.3.2), governing this report have been satisfied and the SCDM is valid for use in the total system performance assessment (TSPA).

7.5.2 Validation Activities for the Drip Shield Seismic Crack Density Model

The TWP for this report, *Technical Work Plan for Postclosure Engineered Barrier Degradation Modeling* (SNL 2007 [DIRS 178849], Section 2.3.2) states that the drip shield SCDM is of lower relative importance and warrants Level 1 validation. Attachment 3 of SCI-PRO-002 states that "Level I validation shall include, at a minimum, discussion of documented decisions and activities that are implemented during the model development process that build confidence and verify and justify that an adequate technical approach using scientific and engineering principles was taken…In addition, for postdevelopment validation of a Level I model, the requirement is to choose a single method (e.g., technical review) described in Section 6.3.2 of SCI-PRO-006, consistent with the model's importance to the TSPA. Therefore, the development of the drip shield SCDM included the following activities:

(a) *Evaluate and select input parameters and/or data that are adequate for the model's intended use (SCI-PRO-002, Attachment 3, Level I(1)).*

The bases for selecting the input data listed in Section 4.1 and used to determine and develop the SCDM for application to the drip shield are documented in Section 6.8.5. Detailed discussion about model concepts can be found throughout Section 6.8.5. Thus, this requirement can be considered satisfied.

(b) *Formulate defensible assumptions and simplifications that are adequate for the model's intended use (SCI-PRO-002, Attachment 3, Level I(2)).*

No assumptions were used for model development. A discussion of simplifications and their rationale are provided throughout the Section 6.8.5. Thus, this requirement can be considered satisfied.

(c) *Ensure consistency with physical principles, such as conservation of mass, energy, and momentum, to an appropriate degree commensurate with the model's intended use (SCI-PRO-002, Attachment 3, Level I(3)).*

Discussion of relevant physical phenomena and processes are discussed in Section 6.8.5 for the drip shield. Thus, this requirement can be considered satisfied.

(d) *Represent important future state (aleatoric), parameter (epistemic), and alternative model uncertainties to an appropriate degree commensurate with the model's intended use (SCI-PRO-002, Attachment 3, Level I(4)).*

Uncertainties associated with the model analysis are discussed in Section 6.8.5.2 for the crack area density through the epistemic uncertainty factor, C. Thus, this requirement can be considered satisfied.

(e) *Ensure simulation conditions have been designed to span the range of intended use and avoid inconsistent outputs or that those inconsistencies can be adequately explained and demonstrated to have little impact on results (SCI-PRO-002, Attachment 3 (Level I(5)).*

Not applicable.

(f) *Ensure that model predictions (performance parameters) adequately represent the range of possible outcomes, consistent with important uncertainties and modeling assumptions, conceptualizations, and implementation (SCI-PRO-002, Attachment 3, Level I(6)).*

This requirement is satisfied by the discussions in items (a) through (d).

In addition, the following lists the postdevelopment model validation methods described in *Technical Work Plan for Postclosure Engineered Barrier Degradation Modeling* (SNL 2007 [DIRS 178849], Section 2.3.2), applied to the drip shield seismic crack density model.

Activity One: Show that the representations of the damaged area in the form of a crack network instead of a hole is consistent with observations in literature. This activity deals with the validity of the use of crack density representations in the seismically damaged areas.

The criterion for this validation activity requires that model results be corroborated by, or conservative with respect to, literature data such as crack morphology or crack width.

Activity Two: Show that the model results for crack patterns in the damaged areas are consistent with the results of an alternative model.

The criterion for this validation is that the alternative model predictions yield similar or less crack damage, that is when the primary model predicts more cracks and/or larger crack opening areas and larger crack area density. The fact that the primary model predicts similar or more crack damage provides additional conservatism in the modeling.

It should be noted that *Technical Work Plan for Postclosure Engineered Barrier Degradation Modeling* (SNL 2007 [DIRS 178849], Section 2.3.2) also indicates:

> This level of validation will be verified as appropriate once the TSPA analyses are completed in accordance with Section 6.3.1 D of SCI-PRO-006. This validation activity will be noted in Section 7 of *Stress Corrosion Cracking of the Drip Shield and the Waste Package Outer Barrier*. A TBV will be assigned to the DTN feed to TSPA containing the seismic damage crack data for drip shields.

The current version of this report, however, does not include the drip shield SCDM feed to TSPA. However, if the level of validation is found as inappropriate once the TSPA analyses are completed, the level of validation of the drip shield SCDM and the corresponding validation activities will be updated in accordance with Section 6.3.1 D of SCI-PRO-006.

7.5.2.1 Identification and Documentation of Validation Activities and Associated Criterion to be Used to Determine that the Required Level of Confidence Has Been Obtained for the Drip Shield Seismic Crack Density Model

Attachment 3 of SCI-PRO-002 states that Level II validation shall include Level I activities, items 1 through 6 in the previous section (see Section 7.1.1) and documentation that demonstrates model predictions are reasonably corroborated by at least two postdevelopment model validation methods described in Step 6.3.2 of SCI-PRO-006.

The activities and associated criteria are primarily related to confidence building during model development although they do provide additional confidence in the drip shields SCDM results. In particular, the criteria and related activity cited in Section 2.3.2 of the TWP (SNL 2007 [DIRS 178849]) are consistent with Section 6.3.2 of SCI-PRO-006.

7.5.2.2 Documentation of Activities to be Performed to Generate Confidence in the Model during Model Development

The criteria and related activities to be used to determine that the required level of confidence has been obtained for the drip shield SCDM were listed in Section 7.5.2.

Activity One is satisfied by the discussions throughout 6.7 but particularly those of Sections 6.7.1.1 and 6.7.1.2, in which the nature of SCC and analysis of BWR and LWR stress corrosion cracking case histories are discussed. It can be reasonably expected that these observations apply to titanium-based alloys also, as the materials discussed are similar in nature to the titanium-based alloys used in drip shield fabrication.

Among the observations made in Section 6.7.1.1:

- It is unlikely that the residual stress profile that would be created by seismic loading would allow an initiated stress corrosion crack to propagate through-wall and circumscribe the deformed area

- The through-wall residual stress fields resulting from impact loads would be a secondary-type stress (displacement controlled), and there is no source of significant internal pressure
- Stress fields would be expected to be greatest at the outer surface and to decrease with depth
- The magnitude of the stress state will decrease as the crack propagates
- Stress field interactions between adjacent cracks would tend to decrease the driving force for crack growth
- The nature of stress corrosion cracks (crack face roughness, branching, and tortuosity) is such that large sections of material will not "fall out" of the cracked structure.

The primary observation made in Section 6.7.1.2 was that, even under the severe stress conditions experienced in LWRs, there are no documented cases where any section of material dropped out as a result of cracking.

On the basis of these observations, a reasonable level of confidence has been obtained that representations of the damaged area in the form of crack network instead of a missing portion or hole is consistent with observations in the literature and is a reasonable morphology to use for analysis of drip shield through-wall SCC due to seismic loading.

Activity Two is satisfied by Section 6.8.5.2.3, in which an alternative mathematical model for stress corrosion crack morphology and damaged area shape is presented. The primary model for crack area density was summarized in Section 6.8.5.2.2. The crack area density based on hexagonal crack arrays was found to be given by a uniform distribution between $\frac{\pi\sigma}{\sqrt{3}E}$ and $\frac{4\pi\sigma}{\sqrt{3}E}$ (approximately $1.81\frac{\sigma}{E}$ and approximately $7.26\frac{\sigma}{E}$). For the alternative model (Section 6.8.5.2.2), the crack area density based on a circular seismically damaged area with a single circumferential crack was found to be $4\frac{\sigma}{E}$. The crack area density from the alternative mathematical model lies between the bounds of the crack area density resulting from the primary mathematical model. Therefore, the results of the alternative mathematical model corroborate the results of the primary mathematical model. This model validation methodology is consistent with Section 6.3.2 of SCI-PRO-006.

7.5.2.3 Documentation of Postdevelopment Activities Performed By Independent Technical Reviewers

There are close similarities in SCC morphologies (tight-branching transgranular or intergranular SCC cracks) between titanium alloys and Alloy 22 and other materials properties (Pulvirenti et al. (2002 [DIRS 159841]; Simbi 1996 [DIRS 177262], Section 2.5). For instance, Pulvirenti et al. (2002 [DIRS 159841]) observed three branching SCC cracks, by using a scanning electron

microscope (SEM) micrograph of the cross section of an exposed Titanium Grade 7 U-bend specimen. As shown in Figure 7-4, at a depth of 0.4 mm, the static stress of the U-bend curve opened the crack by a transgranular mechanism, demonstrated by the linearity of the crack. Within this region, the splitting of individual grains was observed in SEM scans. As the stress was relieved, intergranular crack growth resumed as the dominant mechanism, characterized by the meandering path of attack and by the presence of branching cracks. Therefore, it is reasonable to conclude that the conclusions of the independent technical review team obtained for Alloy 22 described in Section 7.5.1.3 are also applicable to the drip shield titanium alloys.

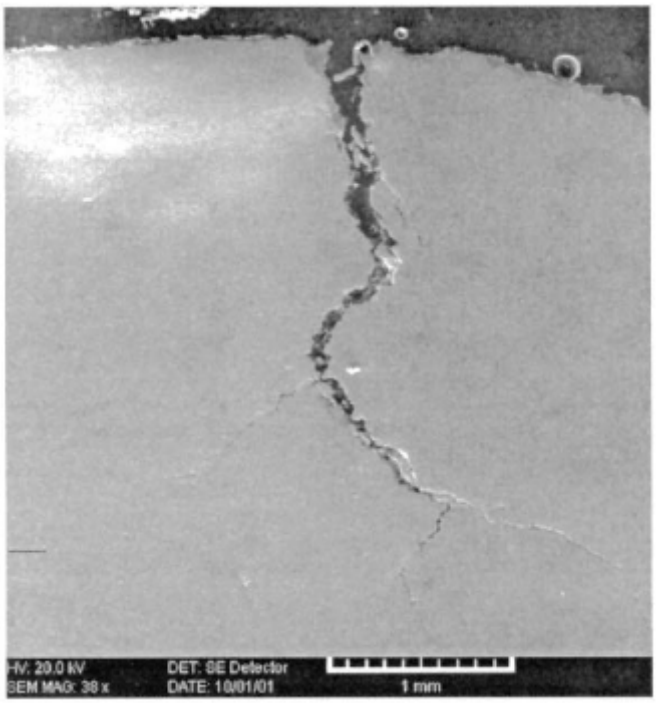

Source: Pulvirenti et al. 2002 [DIRS 159841], Figure 4.

Figure 7-4. SEM Micrograph of a Stress Corrosion Crack, Showing Intergranular Attack and Intragranular Stress Cracking

INTENTIONALLY LEFT BLANK

8. CONCLUSIONS

This section summarizes the modeling work discussed in this document. Conclusions based on the model development are summarized in Section 8.1. Compliance of the modeling work with the Yucca Mountain Project (YMP) acceptance criteria is described in Section 8.2. The outputs of the base-case stress corrosion cracking (SCC) models, the seismic crack density models (SCDMs), and the SCC crack initiation threshold stress criteria for Alloy 22 and titanium alloys are presented in Section 8.3.

8.1 CONCLUSIONS

This document provides detailed descriptions of the process-level models and analyses and the associated outputs developed for use in the performance assessment of the Alloy 22 waste package outer barrier final closure lid welds subjected to SCC due to weld-induced residual stress and analyses of threshold stress for drip shield materials. In addition, the residual stresses generated from rockfall and/or seismic damage are also considered. Table 8-1 summarizes model ouputs.

For waste package outer barrier material, all the welds with the exception of the final closure lid welds are subjected to solution heat treatment to relieve the residual tensile stresses while the entire waste package is heat treated before the loading of spent fuel elements. It is recognized that dynamic loads resulting from unlikely seismic events have the potential of leading to plastic upsets and resultant sustained residual tensile stresses that may initiate cracks and drive them through the wall. Therefore, SCC through-wall propagation criteria governing seismic initiated SCC have also been developed for the waste package material and drip shield materials. The breach criteria are based on a stress threshold as discussed in Section 6.2 for Alloy 22 and Section 6.8.3 for drip shield materials.

8.1.1 Conclusions of the SCC Initiation Threshold Stress for Alloy 22

The SCC initiation threshold stress for Alloy 22 is obtained based on the laboratory results by using the constant-load method at General Electric Global Research Center (GE GRC) (Section 6.2.1.1, Figure 4-1 and Figure 4-2), the U-bend SCC initiation tests at GE GRC and the Long-Term Corrosion Test Facility (LTCTF) at Lawrence Livermore National Laboratory (LLNL) (Section 6.2.1.2), and the slow strain rate test (SSRT) method at LTCTF (Section 6.2.1.3) in the repository-relevant environments.

In the constant-load test, the minimum failure stress (or maximum long-term applied stress without SCC failure) can be obtained from the constant-load test results described in Figure 4-1. Determined from Figure 4-1, the levels of the maximum long-term applied stress without SCC failure have a yield strength ratio of about 2.1 for as-received (mill-annealed) Alloy 22 and about 2.0 for as-welded Alloy 22. The lack of SCC initiation was confirmed using dye penetrant and metallographic examination of an as-received Alloy 22 test specimen after over 25,000 hours (approximately 2.9 years) on test at 93 ksi (641 MPa) as shown in Figure 6-1 (DTN: MO0707SCCIGMER.000 [DIRS 182202], Figure 2-27).

The SCC initiation test results are for exposures up to five years. In order to derive a defensible threshold stress criterion value associated with the lifetime of waste packages, an appropriate extrapolation scheme was developed. For Alloy 22, the threshold stress criterion associated with the lifetime can be derived from the maximum long-term applied stress without failure obtained from the constant-load test results described in Figure 4-1 by applying an appropriate safety factor.

The maximum long-term applied stress without failure obtained from the constant-load test results is 2.1 yield strength, as discussed in Section 6.2.1.1. An acceptable stress safety factor of 2.0 has often been used in general engineering practice. For example, the American Society of Mechanical Engineers (ASME) (ASME 1969 [DIRS 162446], p. 20) uses a reduction factor of 2 on the runout stress (i.e., maximum long-term applied stress without fatigue failure or the endurance limit) for defining fatigue lifetime cycles. Using a similar factor of 2.0, the SCC threshold stress initiation criterion for Alloy 22 can be defined as 1.05 $YS_{(T)}$ (at-temperature yield strength). Further, to conservatively reflect uncertainty, a range from 0.9 $YS_{(T)}$ to 1.05 $YS_{(T)}$ with a uniform distribution between these values is selected for use in TSPA. The nominal yield strength values of Alloy 22 are listed in Table 4-7, and, where appropriate, ASME Code minimum values are used.

For modeling purposes, such as incorporation into total system performance assessment (TSPA) model abstractions, the yield strength value at the normal operating temperature (125°C) is used in Section 6.5 for evaluation of residual stress and stress intensity factor distributions in the waste package closure weld. The interpolated yield strength value at 125°C ($YS_{(125°C)}$) is shown in Table 6-4 as 351 MPa (90% of $YS_{(125°C)}$ is 316 MPa).

8.1.2 Conclusions of the Slip Dissolution-Film Rupture Model for Alloy 22

The base-case slip dissolution–film rupture (SDFR) model relates SCC initiation and subsequent crack advance to the metal oxidation that occurs when the protective film at the crack tip is ruptured. The SDFR model can be applied to assess the breach (or the lack of a breach) of the waste package due to the stress corrosion crack propagation for given manufacturing cracks (e.g., weld flaws) or cracks initiated by the combined effects of stress and environment, or both. The threshold stress intensity factor (SIF) is based on the theory that there exists a threshold value (K_{ISCC}) for the SIF such that there is no growth of a preexisting crack or flaw having a SIF less than the threshold value. The threshold SIF provides a criterion for determining if a stress corrosion crack will reach an arrest state or enter a propagation phase.

The model validation is accomplished by comparing experimental measurements of key model parameters to data measurements and corroborative data available from the open scientific literature and by comparing with another alternative conceptual model. Uncertainty and variability associated with model parameters are assessed.

The SDFR was initially developed for stainless steels and nickel-based alloys Inconel Alloy 600 and Alloy 182 under high-temperature (approximately 288°C) light–water-reactor (LWR) coolant conditions. Confidence in the applicability of this model to Alloy 22 is gained from observation of the response of Alloy 22 under similar LWR coolant conditions based on the test results from GE GRC (DTN: MO0402GEA22SCC.000 [DIRS 167911]) that indicate that the

crack growth rate response of Alloy 22 exposed to 288°C pure water (2 ppm O_2) is broadly consistent with the crack growth rate response of other nickel-based alloys, such as Alloy 600 and Alloy 182 (Andresen et al. 2002 [DIRS 166967]) and austenitic stainless steel (Andresen et al. 2002 [DIRS 167762]) (Section 6.4.4).

Based on the observations, there is ample reason to conclude that SCC of nickel-based Alloy 22 occurs by the same fundamental mechanism characterized by the slip dissolution-film rupture stress corrosion cracking model, *i.e.*, the relationship among V_t, $\dot{\varepsilon}_{ct}$, A and n is described by Equation 5, i.e.

$$V_t = A\,(\dot{\varepsilon}_{ct})^n \qquad \text{(Eq. 5)}$$

The n parameter in the model has been experimentally benchmarked for Alloy 22 based on data obtained in a range of relevant repository brine environments for Yucca Mountain. The relationship between the crack growth rate (V_t), SIF (K_I), and A and n values are described by Equation 18:

$$V_t = 7.8 \times 10^{-2} n^{3.6} (4.1 \times 10^{-14})^n (K_I)^{4n} \qquad \text{(Eq. 18)}$$

where V_t is in mm/s and K_I in MPa√m.

The n value distribution is shown in Table 6-7. The eight data points listed in Table 6-6 were used to obtain a mean value and a range for the n parameter of the model. The model prediction is shown in Figure 6-9 over the range of SIF values (15 to 55 MPa√m), and the individual data points are also included in Figure 6-9 along with ±2σ limits for the n parameter. The ±2σ limits are not for the eight data points.

The threshold SIF (K_{ISCC}) is a critical value of SIF (K_I) below which any preexisting SCC-initiated crack will not grow or is in an arrest state. Preexisting flaws at which SCC may initiate are usually caused by manufacturing processes (especially welding) (Section 6.3.4).

The calculations of SIF for the waste package closure welds in the inner and outer lids of the waste package are described in Section 6.5. The relationship between the K_{ISCC} and corrosion rate (V_{gc}) and $\overline{A}$ and $\overline{n}$ values is shown in Equation 19.

$$K_{ISCC} = (V_{gc} / \overline{A})^{1/\overline{n}} \qquad \text{(Eq. 19)}$$

where $V_{gc} = V_t$ per the crack-blunting criterion.

By using the mean general corrosion rate, 7.23 nm/yr, the distribution of the threshold SIF, K_{ISCC}, is shown in Table 6-8. Table 8-5 and Table 8-6 summarize the distribution of the n value and SIF, respectively.

8.1.3 Conclusions on Evaluation of Stress and Stress Intensity Factor Distributions in As-Welded and Plasticity-Burnished Waste Package Closure Weld Lids

The application of the SCC models to the waste package requires input of weld residual stress profiles and SIF profiles along with uncertainty and variability. These input data have been developed for the naval long waste package outer closure lid (subjected to plasticity burnishing) and are reported in Section 8.3 as output data. This report also provides other outputs needed as input for a complete TSPA for the degradation of the waste package due to SCC effects such as threshold stress for crack initiation and an estimate of crack opening size. In addition, a summary of size, density, and orientation distributions for manufacturing flaws or defects, which are technical product output of *Analysis of Mechanisms for Early Waste Package/Drip Shield Failure* (SNL 2007 [DIRS 178765]), is provided in Section 6.3.4.

Stress and Stress Intensity Factor Distribution

As documented in Section 6.5, the calculated stress and stress intensity factor (SIF) profiles for the naval long waste package outer closure lid (DTN: MO0708RTSWRS06.000 [DIRS 182558], file *BSC-03Q-301-R2.pdf*) are used for the as-welded, laser-peened, and plasticity-burnished Alloy 22 waste package outer lid of the current design. In the finite element model the stress distribution was calculated by using a third-order polynomial of the type represented by Equation 22 below:

$$\sigma = A_0 + A_1x + A_2x^2 + A_3x^3 \qquad \text{(Eq. 22)}$$

where x is the distance from the outer surface of the closure lid and A_0, A_1, A_2, and A_3 are coefficients of the third-order polynomial fit of the through-wall stress distribution (or profile).

The values of the coefficients in Equation 22 for the as-welded waste package outer closure lid welds of waste package are documented in DTN: MO0708RTSWRS06.000 [DIRS 182558], file *NdStrs-R2.xls*, Sheet "AAStrsFit" and Sheet "BBStrFit") and reproduced in Table 6-11 showing the converted stress coefficients, A_0, A_1, A_2, and A_3, in the metric unit system.

The values of the coefficients in Equation 22 for the laser-peened waste package outer closure-lid welds of waste package are documented (DTN: MO0708RTSWRS06.000 [DIRS 182558], file *NdStrs-R2.xls*, Sheet "A-AThrWLPStrsPlt" and Sheet "B-BLPStrsPlt") and reproduced in Table 6-13 showing the converted stress coefficients, A_0, A_1, A_2, and A_3, in the metric unit system.

The values of the coefficients in Equation 22 for the plasticity-burnished waste package outer closure-lid welds of waste package are documented (DTN: MO0708RTSWRS06.000 [DIRS 182558], file *NdStrs-R2.xls*, Sheet "A-ACPBPlt" and "Sheet B-BCPB") and reproduced in Table 6-14 showing the converted stress coefficients, A_0, A_1, A_2, and A_3, in the metric unit system.

The profiles of the stress and SIF in the as-welded, laser-peened, and plasticity-burnished waste package outer lid are shown in Table 6-12, and Table 6-16, respectively.

The effect of corrosion on distribution of stress and SIF is analyzed in Section 6.5.4. It is concluded that the overall effect of general corrosion on distribution of stress and SIF is minor.

A comparison of the stress profiles before and after plasticity burnishing in the lid weld regions demonstrates a marked improvement in profiles with respect to the initiation of SCC, as shown in Figure 6-48 and Figure 6-49. Figure 6-48a indicates that the depth to which the waste package outer closure lid weld radial stress is in compression is about 5 mm, and that the depth to which the waste package outer closure lid weld hoop stress is in compression is about 2 mm (Figure 6-48). The depth to which the hoop stress is below the 90% of yield strength criterion ($YS_{(125°C)}$, 316 MPa) is about 5 mm. Clearly the plasticity burnishing results in a significant improvement.

Uncertainty and Variability of Residual Stress and Stress Intensity Factor

Variability in residual stress magnitude around the perimeter of circumferential welds may result from a number of factors, including stops/starts of the weld torch, variations in heat transfer parameters, power fluctuations, etc. In addition, in multipass welds, the location for the start of each weld pass varies. The results of these variations would be expected to be variations similar to those observed in stainless steel piping and pressure vessel automatic welds.

An assessment of circumferential residual stress variation in stainless steel piping welds (DTN: MO0409GGSIACAL.000 [DIRS 171792]) indicates that the residual stress shows a sinusoidal distribution around the circumference with a range of about 5 ksi about the mean stress (i.e., ±2.5 ksi). Based on this assessment, the variability of the mean stress ($S_\theta(x)$) along the circumference (∇S) can be represented by Equation 24:

$$S_\theta(x) = S_0(x) - \nabla S(1 - \cos(\theta)) \qquad \text{(Eq. 24)}$$

where x is the distance from the outermost surface, θ is the angle measured in degrees from a reference location (θ = 0°) on the circumference, $S_\theta(x)$ is the weld residual stress profiles at an angle θ with a distance of x from the outermost surface of the waste package. $S_0(x)$ is the calculated weld residual stress profile at θ = 0 at distance x, and ∇S is taken to be 2.5 ksi or 17.2369 MPa.

Because the SIF is a linear function of stress, the variability in the SIF around the circumference can be similarly treated as:

$$K_\theta(x) = K_0(x)\,(S_\theta(h) / S_0(h)) \qquad \text{(Eq. 25)}$$

where h is the thickness of the closure lid.

The minimum and maximum stresses at the 3σ level, $S_\theta(x)\min$ and $S_\theta(x)\max$ in the weld can be obtained from the mean stress, $S_\theta(x)$, by Equations 26 and 27:

$$S_\theta(x)\min = S_\theta(x)\left(\frac{S_\theta(h) - \Delta S}{S_\theta(h)}\right) \qquad \text{(Eq. 26)}$$

$$S_\theta(x)\max = S_\theta(x)\left(\frac{S_\theta(h)+\Delta S}{S_\theta(h)}\right) \quad \text{(Eq. 27)}$$

where $S_\theta(h)$ is the mean residual stress on inner surface (i.e., $x = h$, where h is the thickness of the closure lid) and ΔS is the amplitude of variation between the maximum and minimum stresses at the inner surface of the waste package lid. The SIF calculated from the mean stress as described in Section 6.5.3.2 is the mean SIF $K_\theta(x)$. The minimum and maximum SIFs are calculated similarly to those for stress because SIF is a linear function of stress, i.e.:

$$K_\theta(x)\min = K_\theta(x)\left(\frac{S_\theta(h)-\Delta S}{S_\theta(h)}\right) \quad \text{(Eq. 28)}$$

$$K_\theta(x)\max = K_\theta(x)\left(\frac{S_\theta(h)+\Delta S}{S_\theta(h)}\right) \quad \text{(Eq. 29)}$$

where θ is the angle measured from a reference location (θ = 0°) on the circumference and ΔS = 0.15 $YS_{(T)}$ ($YS_{(T)}$ is the mean at-temperature yield strength given in Table 4-7).

The second argument in the stress function is used to represent angular variation (θ = 0, arbitrarily chosen) around the circumference of the Alloy 22 waste package outer closure-lid welds. The angular variation is included using the following functional form, based on Equation 24:

$$\sigma(x,\theta) = \sigma(x,0) - (17.236893)\times(1-\cos(\theta)) \quad \text{(Eq. 24′)}$$

where $\sigma(x, 0)$ is a function of the stress coefficients (A_i) defined in Equation 22 with x in millimeters (mm). Using Equation 24′ and setting θ = 0°, 90°, and 180°, the distribution of the hoop stress along the thickness of the as-welded and plasticity-burnished waste package outer closure lid weld with various θ values can be obtained as shown in Figure 6-51 and Figure 6-52, respectively. In both cases, for the full range of θ the mean stress does not exceed the stress threshold at zero thickness, nor does it extend to the full lid thickness.

As SIF is a linear function of stress, the corresponding SIF profiles for the as-welded and plasticity-burnished waste package outer closure lid, calculated using Equations 28 and 29 and plotted with angle θ set at 0°, 90°, and 180°, are shown in Figure 6-53 and Figure 6-54, respectively.

Uncertainty in residual stress distributions are calculated in Section 6.5.6.2 based on Equations 26 and 27. The results for θ = 0 are shown in Figure 6-55 for as-welded waste package weld closure lid and Figure 6-56 for plasticity-burnished waste package weld closure lid Figure 6-56, respectively, with uncertainty range of ± 5%, ±10% ±15% of the mean at-temperature yield strength (0.15 $YS_{(125°C)}$).

The variation of SIF at $\theta = 0$ versus the depth for as-welded and plasticity-burnished waste package weld closures are shown in Figure 6-57 and Figure 6-58, respectively.

The analysis results predict that the threshold stress (90% of yield strength) for the plasticity-burnished waste package weld closure will be reached at a depth of about 5 mm, based on mean values of the hoop stress. This is a conservative value because this is based on the upper bound of the uncertainty (+15% $YS_{(125°C)}$). The depth at which the residual hoop stress will not reach the stress threshold, based on a mean at-temperature yield strength, is about 6 mm (Figure 6-56).

The time-to-breach due to SCC in the stress-mitigated closure weld will be determined primarily by the time required to corrode through the material to a level where the stress exceeds 90% of the at-temperature yield strength. Added to this is the time required for the initiated crack to propagate through the remaining lid thickness. Any relaxation of the residual-stress gradient tends to reduce the compressive surface-stress magnitude and the subsurface tensile-stress magnitude. This will beneficially increase the depth where 90% of the at-temperature yield strength can be reached. Further, as the outer compressive surface layer is slowly removed by general corrosion, the neutral axis shifts inward.

The scenario for removal of the compressive layer by corrosion is assessed in Section 6.5.4, Figure 6-33 and Figure 6-34). The analysis demonstrates that the stress-mitigated layer on the final closure lid weld is deep enough to significantly extend the lifetime of the waste package after permanent closure even by using conservative values of the mitigated layer depth and upper bound of the uncertainty (i.e., +15% of the at-temperature yield strength, Section 6.5.6.2).

The model output for stress and stress intensity and uncertainties is summarized in Table 8-7 through Table 8-12 in Section 8.3.

8.1.4 Conclusions of Seismic Crack Density Model for Alloy 22

Seismic activity can lead the waste packages to impact other components in the drift including the emplacement pallets, drip shields, and other waste packages. If the seismically induced impacts are of sufficient magnitude, the impacts may physically deform the waste package outer barrier and potentially the waste package inner vessel. These deformations could cause cold work of the waste package barrier and vessel materials, producing a cold-worked gradient typically highest on the outer surface and smallest on the inner surface. Impacts could also create complex through-wall residual stress profiles. These stress profiles and cold-work gradients could lead to SCC in the seismically affected area of the waste packages.

Similar damage can be expected for drip shields under seismic loadings. However, as discussed in the treatment of SCC due to rockfalls discussed in Section 6.8.6, stress corrosion cracks in the drip shields are expected to be tight and plugged with corrosion products or mineral deposits, or both, leading to negligible water flow through these openings. Therefore, as the primary role of the drip shield is to keep water from contacting the waste package, SCC of the drip shield does not compromise its intended design purpose.

A number of incidents of SCC have been observed in LWRs involving austenitic stainless steels and nickel-based alloys. In many of these cases, the cracking has been extensive, sometimes

becoming fully circumferential on the component as driven by weld residual tensile stress plus pressure-induced primary stresses. Even under these severe stress conditions, there has never been a documented case where any section of material dropped out as a result of the observed cracking. Observations in the boiling water reactor (BWR) and pressurized water reactor (PWR) industry are consistent with the expected behavior of flaws that are located in close proximity. For example, the very few SCC-related steam generator tube ruptures observed occurred only under full system differential pressure.

Based on these observations, it is concluded that seismic damage to the waste package outer barrier will not result in portions of the Alloy 22 material becoming wholly separated from the body of the waste package. Instead, a network of stress corrosion cracks is expected to form in the waste package outer barrier due to residual stresses induced by seismic activity.

8.1.5 Conclusions for Potential SCC Analyses for Titanium Alloys

The only issue of concern for SCC associated with the drip shield is the potential for crack initiation due to plastic deformation-induced residual stress caused by unlikely seismic events. Through-wall crack penetration criteria governing seismic initiated residual stress for the drip shield material (i.e., Titanium Grade 7) are based on a stress threshold, which is discussed in Section 6.8. Once initiated, SCC is treated as being through-wall.

<u>SCC Initiation Criterion for Titanium Grade 7</u>

By comparison of the Titanium Grade 7 constant-load test results in brine and in air, it is reasonable to consider that the annealed constant-load specimen failures in brine are highly likely to have resulted from creep rupture rather than SCC (Section 6.8.3).

For Titanium Grades 7 and 16, the threshold stress criterion is derived from an assessment of the maximum stress levels tested without observed SCC initiation. A summary plot comparing the Keno constant-load brine test results (minimum times from Table 6-25) along with the LTCTF U-bend maximum remaining tensile stress results (Figure 6-29) to the experimentally determined air creep rupture behavior is given in Figure 6-73, which indicates that failure was due to creep rupture rather than SCC. The intersection of the uncracked U-bend trend line with the air creep rupture curve at about 185 MPa indicates that SCC is not expected to initiate under constant-load brine exposure conditions at least down to stress levels of about 185 MPa, as creep rupture will intervene before SCC can potentially initiate.

The new threshold stress for SCC initiation is established as 80% of at-temperature yield strength. This threshold stress criterion can be rationalized by considering the primary and secondary stresses in drip shield design scenarios (Section 6.8.3.1.3).

For the TSPA applications, it is recommended that the specified minimum yield strength values from ASME (2001 [DIRS 158115], Section II, Part D, Table Y-1, pp. 632 to 634) be conservatively used to establish the potential SCC crack initiation threshold stress.

SCC Initiation Criterion for Titanium Grades 28 and 29

A value of 50% of at-temperature yield strength is appropriate based on the six-month value of maximum long-term applied stress without SCC failure (i.e. 105% yield strength), for exposure under very aggressive brine conditions in the 210°C sour brine environment described earlier (Schutz et al. 2000 [DIRS 177257]). This 50% yield strength value is also consistent with the absence of SCC initiation observed in the previously described at- or over-yield Titanium Grade 29 U-bends exposed to the relatively aggressive aerated 165°C SCW brine as well as the Keno constant-load specimens tested at stresses up to about 95% yield strength for about 2,800 hours. Consequently, the SCC initiation threshold criterion for Titanium Grade 29 is established as 50% of the at-temperature yield strength ($YS_{(T)}$).

Titanium Grade 7 Crack Growth Rates

Because of the propensity of these titanium alloys to undergo low-temperature creep, in the case of annealed Titanium Grade 7, subsequent crack growth measurements in air indicated that the crack growth observed was due essentially to creep rather than SCC as described in Section 6.8.3.1. As shown in Figure 6-76, at an applied SIF, K_I, of 30 MPa·√m, the apparent crack growth rate in the 110°C basic saturated water (BSW) brine was 1.3×10^{-8} mm/s (DTN: MO0707SCCIGMER.000 [DIRS 182202], Figure 1-4), as compared to a similar value of 1×10^{-8} mm/s in air after 800 hours on test (DTN: MO0707SCCIGMER.000 [DIRS 182202], Figure 6-14).

The measured crack growth rate for 20% cold-worked Titanium Grade 7 under near constant-load conditions (i.e., with a maximum load hold time of 24 hours at an applied SIF of 30 MPa·√m) is extremely low, about 1.4×10^{-10} mm/s (DTN: MO0707SCCIGMER.000 [DIRS 182202], Figure 1-30) as replotted in Figure 6-77.

The assumption that this extremely low value of crack growth rate is due to SCC is conservative because, if the rate also includes a creep component, the actual SCC growth rate will be less than the measured value. This is consistent with the literature, which indicates 20% cold work appears to reduce SCC susceptibility somewhat for commercial purity titanium (Simbi 1997 [DIRS 177263]).

Threshold SIF for Titanium Grade 7

As described in Section 6.4.5, the threshold SIF (K_{ISCC}) is a critical value of SIF K_I below which any preexisting crack either will not grow (by SCC) or is in an arrest state. For the Titanium Grade 7 drip shield material, it is conservatively assumed that, once the SCC initiation threshold criterion is exceeded, SCC initiates and propagates through-wall instantly. Thus, it is not necessary to establish a K_{ISCC} for Titanium Grade 7.

Titanium Grades 28 and 29 Crack Growth Rates

As described in Section 6.8.3, it is to be expected that the higher-strength Titanium Grade 5 and possibly its ruthenium analogue, Titanium Grade 29, will have higher SCC susceptibility in chloride brines than the lower-strength Titanium Grade 2 and its palladium analogue, Titanium Grade 7.

Measured crack growth rate results (DTN: MO0705SCCIGM06.000 [DIRS 180869], file *GE-GRC-Final_Sept-2006-Rev3.doc*) are listed for Titanium Grades 28 and 29 exposed to 150°C SCW brine in Table 6-33. The initial SIF for both specimens was 27.5 MPa√m. However, the crack growth rate of Titanium Grade 28 was higher than Titanium Grade 29, and, as the K_I control was maintained with respect to Titanium Grade 29, as the total Titanium Grade 28 crack length, *a*, increased over time, its SIF, K_I, also increased as K_I is a function of stress (σ) and crack depth size (*a*). Because of the increasing K_I on the higher crack growth rate Titanium Grade 28 specimen which reached a maximum value of about 37 MPa√m, the test control was switched from Titanium Grade 29 to this Titanium Grade 28 specimen after 3,236 hours, and K_I was subsequently reduced in a stepwise fashion until the Titanium Grade 28 specimen reached its initial value of 27.5 MPa√m after 4,800 hours (approximately half a year) on test (DTN: MO0707SCCIGMER.000 [DIRS 182202], Figures 1-116 to 1-118).

Threshold Stress Intensity Factor for Titanium Grades 28 and 29

For the drip shield structural support material, Titanium Grade 29, and its weld filler metal, Titanium Grade 28, it is advantageous to consider the likely crack growth rates and the threshold stress intensity value K_{ISCC} at the propagating crack tip to determine if and at what depth the crack may arrest. In considering the environmentally determined K_{ISCC} parameter, it is also relevant to consider the observation that, for some titanium alloys, crack growth can also occur in air at a SIF value below the critical plane strain fracture toughness value, K_{IC}, characteristic of brittle fracture (i.e., of unstable fast crack growth) but above the environmentally determined K_{ISCC}. This slow crack growth phenomenon is referred to as sustained load cracking (SLC). SLC is likely aggravated by dissolved hydrogen in the titanium alloy (ASM International 1987 [DIRS 103753], Figure 57, p. 275). SLC is similar to SCC except that it is much slower and occurs in the total absence of a reactive environment. As can be seen, the SLC threshold SIF, K_{ISLC}, is higher than K_{ISCC} as shown in Figure 6-81 for a higher-strength, near-alpha alloy, Ti-8Al-1Mo-1V (UNS R54810).

A comparison of K_I, K_{ISLC}, and K_{ISCC} values for the range of relevant titanium alloys is given in Figure 6-81. Also included are more limited literature and YMP data for specific alloys and for other environments. These results are nominal values and will vary with alloy composition, metallurgical condition, and product form and thickness. Although it is indicated in Figure 6-81 that K_{ISCC} for Titanium Grade 7 is less than 30 MPa√m, it is not yet clear whether the measured crack growth rates were due to creep or SCC. As described in Section 6.8.3.2 for annealed Titanium Grade 7, measurements in air indicate that the apparent environmental crack growth in 110°C BSW was due to creep. However, for the 20% cold-worked material, the extremely low measured environmental crack growth rate is more likely due to SCC.

8.1.6 Conclusions of Seismic Crack Density Model for Titanium Alloys

The Titanium Grade 7 drip shield plates are supported by Titanium Grade 29 drip shield structural support components (SNL 2007 [DIRS 179354], Table 4-2, Parameter 07-01). These support components include the beams (SNL 2007 [DIRS 179354], Table 4-2, Parameter 07-01). The other Titanium Grade 29 components of the drip shield (e.g., the bulkhead longitudinal stiffeners, bulkheads) (SNL 2007 [DIRS 179354]) are in the drip shield interior and are, thus, not subjected to dripping-water chemistries.

Seismic activity can lead the drip shield to impact other components in the drift including the waste packages. If the seismically induced impacts are of sufficient magnitude, the impacts may physically deform the drip shield and potentially the waste package. These deformations could cause cold work of the drip shield materials, producing a cold-worked gradient typically highest on the outer surface and smallest on the inner surface. Impacts could also create complex through-wall residual stress profiles. These stress profiles and cold-work gradients could lead to SCC in the seismically affected area of the drip shield.

However, as in the treatment of SCC due to rockfalls discussed in Section 6.8.5.1, stress corrosion cracks in the drip shields are expected to be tight and plugged with corrosion products or mineral deposits, or both, leading to negligible water flow through these openings. Therefore, as the primary role of the drip shield is to keep water from contacting the waste package, SCC of the drip shield does not compromise its intended design purpose.

Based on these results, it is concluded that seismic activity will not result in large areas separating from the drip shield. Instead, a network of stress corrosion cracks is expected to form in the drip shield due to residual stresses induced by seismic activity.

According to *Plugging of Stress Corrosion Cracks by Precipitates* (BSC 2001 [DIRS 156807], Table 5-13), once a stress corrosion crack develops into a through-wall crack, the crack length, *2c*, and the crack gap (or width), δ, are 130 mm and 157 microns, respectively. These values are reasonably consistent with those listed in Table 6-37 and Table 6-38. Thus, the passive oxide film growing normal to each opposing crack face would need to grow until it fills the 157-micron gap. This is equivalent to approximately 103 microns of metal loss per crack side and results in a total per side oxide thickness of approximately 182 microns based on a TiO_2 oxide-to-metal volume ratio of 1.76 (Bradford 1987 [DIRS 151988], Table 2, p. 64). At a corrosion rate of 0.03 microns per year, it will take about 3,400 years for the crack to fill with corrosion product. In the interim, the crack walls are corroding passively. Before the corrosion film grows to a thickness where it will completely fill the crack, there could be a small amount of water transport by surface diffusion (film flow) into the crack and through the drip shield. However, the small heat flux present across the drip shield wall will result in evaporation of the slowly flowing water. A resultant scale deposit (principally calcium carbonate (calcite)) will form over the crack where it intersects the upper drip shield surface, as well as within the crack. This formation of calciferous deposits is well documented (Cowan et al. 1976 [DIRS 105212], pp. 1 to 39 and 376 to 383) in seawater environments and in heat exchangers through which natural brines are forced to flow. This has been observed in desalination plants (carrying approximately 6% NaCl solutions) and in potash plants (carrying greater than 12% brine (NaCl/KCl mixtures) (Cowan et al. 1976 [DIRS 105212], pp. 1 to 39 and 376 to 383). In both cases, titanium surfaces are heat sources at operating temperatures of approximately 100°C. Such deposits form rapidly under flowing conditions and have to be regularly removed to avoid loss of heat exchanger efficiency. Other minerals such as amorphous silica will also precipitate.

A detailed calculation of the expected rate of stress corrosion crack plugging due to calcite precipitation resulting from evaporation of a pore water of typical composition dripping onto a drip shield at the crack location has been performed (BSC 2001 [DIRS 156807]). The calculation conservatively assumes that corrosion products generated on the crack faces, as well as colloids, particles, and any precipitated silica minerals, do not help in plugging the crack

opening and that there is a uniform water seepage flow in space and time (BSC 2001 [DIRS 156807], Section 5.3). It was concluded that stress corrosion cracks are sealed in a few hundred years at most when water is allowed to flow through the cracks at a low film flow rate (BSC 2001 [DIRS 156807], Section 6.3). When the cracks are bridged by water, the sealing process may take thousands of years, but no flow occurs as the water is held by capillary forces. In a more realistic case of a nonuniform flow onto the drip shield, more precipitation and faster plugging will occur.

Following plugging of such a drip shield crack, any solution flow through the crack would be dominated by an efficiency factor determined by the ratio of solution runoff on the drip shield surface compared to through crack flow that in turn is determined by scale porosity and permeability. Because of the expected high density of the calcite deposits (BSC 2001 [DIRS 156807]) and lack of a pressure gradient to drive water through the crack, the quantity of solution flow through the plugged crack would approach zero.

Finally, drip shield structural response to rockfalls induced by seismic events is addressed in *Seismic Consequence Abstraction* (SNL 2007 [DIRS 176828]), where the damaged area of the drip shield is calculated for each of the given rock masses. The damaged area is defined as a region of the drip shield where the calculated stress exceeds the threshold stress.

8.2 COMPLIANCE WITH YMP ACCEPTANCE CRITERIA

Yucca Mountain Review Plan, Final Report (NRC 2003 [DIRS 163274]) contains acceptance criteria intended to establish the basis for the review of the material contained in the license application. As this report serves, in part, as the basis for the license application, it is important the information contained herein conforms to those same acceptance criteria.

This report addresses the degradation of two features of the engineered barriers, the waste package and drip shield. Based on the engineered barrier role of the waste package and the drip shield, on the processes involved with their degradation, and on the potential impact of their degradation, the Yucca Mountain Review Plan (NRC 2003 [DIRS 163274]) acceptance criteria applicable to this report are identified in *Technical Work Plan for Postclosure Engineered Barrier Degradation Modeling* (SNL 2007 [DIRS 178849], Table 3-1) and are delineated below in italics. A discussion of how this report addresses appropriate criteria follows each acceptance criterion, coupled with an indication of where within the report the appropriate information can be found.

8.2.1 System Description and Demonstration of Multiple Barriers

The waste package and the drip shield are features of the Engineered Barrier System, which meets the definition of a barrier in 10 CFR 63.2 [DIRS 180319]. The following acceptance criteria can be found in Section 2.2.1.1.3 of *Yucca Mountain Review Plan, Final Report* (NRC 2003 [DIRS 163274]).

Acceptance Criterion 1 – Identification of Barriers is Adequate

> *Barriers relied upon to achieve compliance with 10 CFR 63.113(b), as demonstrated in the total system performance assessment, are adequately identified and clearly linked to their capability.*

This report addresses the Engineered Barrier System (EBS) and the waste package and the drip shield features. The engineered barrier system features are identified in Section 1.1. The drip shield contributes to waste isolation by keeping seepage waters and falling rocks away from the waste package for its lifetime and, when breached by SCC, by reducing the contact of water with the waste package. The waste package barrier contributes to waste isolation by keeping water away from the waste for its lifetime and, when breached, by reducing both the contact of water with the waste and the rate of radionuclide release from the waste.

Acceptance Criterion 2 – Description of Barrier Capability Is Acceptable

> *The capability of the identified barriers to prevent or substantially reduce the movement of water or radionuclides from the Yucca Mountain repository to the accessible environment or prevent the release or substantially reduce the release rate of radionuclides from the waste is adequately identified and described:*
>
> *(1) The information on the time period over which each barrier performs its intended function, including any changes during the compliance period, is provided;*
>
> *(2) The uncertainty associated with barrier capabilities is adequately described;*
>
> *(3) The described capabilities are consistent with the results from the total system performance assessment;*
>
> *(4) The described capabilities are consistent with the definition of a barrier at 10 CFR 63.2.*

The drip shield contributes to waste isolation by keeping seepage waters and falling rocks away from the waste package for its lifetime and, when breached by SCC, by reducing the contact of water with the waste package. The waste package barrier contributes to waste isolation by keeping water away from the waste for its lifetime and, when breached, by reducing the contact of water with the waste and the rate of radionuclide release from the waste. The drip shield capability is addressed in this report principally in Section 6.8. The waste package function of isolating the waste from water is addressed throughout this document and more specifically in Section 6.2 through Section 6.7. Although SCC can lead to waste package breach at the outer closure lid weld, stress mitigation of this weld (Section 6.5.5) is shown to extend the waste package lifetime beyond the regulatory period.

Acceptance Criterion 3 – Technical Basis for Barrier Capability is Adequately Presented.

> *The technical bases are consistent with the technical basis for the performance assessment. The technical basis for assertions of barrier capability is*

commensurate with the importance of each barrier's capability and the associated uncertainties.

The acceptance criteria delineated above address the overall description and capability of the engineered barriers as a unit. Compliance with these criteria is addressed partially in this report and more fully in other reports. The technical basis for the drip shield capability is documented in Section 7.4 and Section 7.5 and for the waste package capability in Sections 7.2, 7.3, and 7.5.

8.2.2 Degradation of Engineered Barriers

The following acceptance criteria can be found in Section 2.2.1.3.1.3 of *Yucca Mountain Review Plan, Final Report* (NRC 2003 [DIRS 163274]).

Acceptance Criterion 1 – System Description and Model Integration are Adequate

(1) TSPA adequately incorporates important design features, physical phenomena and couplings and uses consistent assumptions throughout the degradation of engineered barriers abstraction process.

The models and analyses addressed in this report accurately reflect the relevant waste package and drip shield design features, physical phenomena, and couplings. These elements of waste package design are discussed in Section 6.2 through Section 6.7 of the main body of the report and of drip shield design in Section 6.8.

(2) Abstraction uses assumptions, technical bases, data and models that are appropriate and consistent with [those used] in other abstractions.

The models, analyses, and assumptions addressed in this report accurately reflect the expected potential SCC responses for the waste package and drip shield under repository conditions and, therefore, they are appropriately used in this report.

(3) The descriptions of the engineered barriers, design features, degradation processes, physical phenomena, and couplings that may affect the degradation of the engineered barriers are adequate.

Detailed descriptions of the processes, phenomena, and couplings that may affect the degradation of the engineered barriers are provided throughout this document as follows: (a) for the relevant design features of the waste package, see Section 6.5, and of the drip shield, see Section 6.8; (b) for the degradation processes affecting both the waste package and the drip shield, see Sections 1.1, 6.1, 6.2, and 6.8.2; (c) for physical phenomena impacting these features, see Section 6.2 through Section 6.7 for the waste package and Section 6.8 for the drip shield; (d) and for couplings, see Sections 1.1 and 6.8. These descriptions are consistent with the information delineated elsewhere in other reports and are adequate for their intended purposes (i.e., to enable the modelers to develop and implement appropriate models and to enable the reviewer to understand the bases for the analytical activities performed by the applicant and the results thereof.).

(4) Initial and boundary conditions are propagated consistently throughout the abstraction process.

Throughout this report, relevant initial and boundary conditions for the performed analyses (i.e., waste package closure configuration, welding process, heat treatments, anticipated temperature, pressure) are used in a manner that is consistent with the data received from other abstractions and models. Examples can be found in Sections 6.4 and 6.5.

(5) Sufficient technical basis for the inclusion [and exclusion] of FEPs are provided.

Four FEPs were identified related to the potential degradation of the waste package and drip shield (Section 6.9). Table 6-40 also provides the location where an explanation related to these decisions is discussed. Sufficient technical bases are provided in Section 6.2 through Section 6.7 for the waste package outer barrier and in Section 6.8 for the drip shield.

(6) Adequate technical bases are provided for selecting the design criteria that mitigate any potential impact of in-package criticality on repository performance, including considering all features, events, and processes that may increase the reactivity of the system inside the waste package.

Not applicable because this report does not address in-package criticality issues.

(7) Guidance in NUREG 1297 and NUREG 1298 [re: Expert Elicitation] are followed.

Not applicable because expert elicitation was not performed.

Acceptance Criterion 2 – Data Are Sufficient for Model Justification

(1) Parameters used to evaluate the SCC degradation of EBS are adequately justified.

The input data and parameters used for the performance of the waste package and drip shield SCC degradation models and model-related parameters came, primarily, from four sources:

- Other analysis models performed for the Yucca Mountain Project
- Laboratory experiments and tests performed for the Yucca Mountain Project
- Industry reviewed and accepted technical or scientific reports and papers
- Industry handbooks.

Justification for the use of specific parameters is typically provided in the section in which the parameter is initially discussed (Section 4.1) and used (Section 6.2 through Section 6.8) or in the source document for the specific parameter. As a result, the parameters used for the analysis have been adequately justified.

(2) Sufficient data have been collected to establish initial and boundary conditions.

Extensive scientific investigations and experiments have been performed to develop the data necessary to support the analyses provided in this report. In those instances where insufficient data were available for the specific materials used for the waste package or drip shield stress corrosion cracking degradation, data on alloys known to be analogous to those anticipated in the waste package were used with conservative assumptions to provide the basis for the performed analyses. Initial and boundary conditions have been adequately and appropriately established and justified.

> *(3) Data on the degradation of the engineered barriers (predominately stress corrosion cracking and to a lesser extent general corrosion and phase stability) are based on laboratory measurements, industrial and/or natural analogs and tests designed to replicate anticipated conditions. As appropriate, sensitivity or uncertainty analyses are provided and are shown to be adequate.*

Data related to the various potential drip shield and waste package degradation modes (in particular for SCC and to a lesser extent for general corrosion and phase stability) are discussed in various subsections throughout this report. Specifically, the data associated with the drip shield is discussed in Sections 4.1 and 6.8 and with the waste package in Sections 4.1 and Section 6.2 through Section 6.7.

> *(4) Degradation models and related parameters for the applicable processes are adequate. For example, the SCC propagation model (SDFR Model), the threshold SCC initiation stress parameter and the threshold stress intensity factor parameter are described in significant detail. The SDFR Model is applied specifically to the waste package outer barrier material and the threshold SCC initiation stress criterion to both the waste package and the drip shield. Effects of general corrosion and phase stability on SCC are given appropriate consideration and treatment relative to their effect on SCC susceptibility.*

The various SCC models (i.e., the SDFR model and the alternative coupled environmental fracture (CEF) model) related to potential waste package and drip shield stress corrosion crack propagation are discussed in Section 6.4 and Section 6.8.4, respectively. Waste package and drip shield stress corrosion crack initiation parameters are discussed in Section 6.2 and Section 6.8.3, respectively. Specifically, the SCC approach associated with breaching of the drip shield is discussed in Sections 6.8.5. The modeling of the potential waste package outer barrier SCC is discussed in Section 6.2 through Section 6.7.

Acceptance Criterion 3 – Data Uncertainty is Characterized and Propagated through the Model Abstraction

> *(1) Models use parameter values, assumed ranges, probability distributions and/or bounding assumptions that are technically defensible, reasonably account for uncertainties and variabilities, and do not result in under-representation of the risk estimate.*

Each of the models and related SCC initiation and crack arrest criteria developed in this report uses parameter values, assumed ranges, and probability distributions or bounding assumptions

(or both of the latter), that are technically defensible, reasonably account for uncertainties and variabilities, and do not result in under-representation of the risk estimate. In each situation, discussion and consideration of the uncertainties associated with specific data are addressed in detail. Examples include the discussion of the range of expected residual stress variation, associated data, and data uncertainty in Section 6.5.6, the development of the threshold SIF, associated data, and data uncertainty in Section 6.4.5, and the modeling of the Alloy 22 stress corrosion cracking growth rate, associated data, and data uncertainty in Section 6.4.4.

(2) Appropriate parameters, based on techniques that may include laboratory experiments, field measurements, and industrial analogs are used.

The SDFR model and related SCC initiation and crack arrest criteria addressed in this report use data and parameters that have been developed based on a variety of techniques including laboratory experiments and industrial analogues. Examples of each category include:

- The use of crack growth rate data for iron and nickel–chromium-based industrial alloys experimentally developed or compiled from the literature for the study of SCC propagation rates in water containing oxygen as a function of temperature in Section 6.4.3

- Review of the stress corrosion crack patterns (morphology) in actual industrial equipment (i.e., LWRs) (Section 6.7)

- Experimental measurement of SCC initiation stress using constant-load specimens, U-bend specimens, and SSRT specimens in a range of brine environments (Section 6.2.1)

- Use of experimentally measured residual stress distributions resulting from the laser-peening stress-mitigation process to benchmark calculated through-wall residual stress distribution conservatively expected in final closure lid weld region (Section 6.5.5).

(3) Assumed range of values and probability distributions for parameters used in conceptual and process-level models are not likely to underestimate the actual degradation and failure of engineered barriers.

In those instances where uncertainties exist regarding the range of values and probability distributions, modelers were careful to choose values that were anticipated to provide either conservative results or a distribution that bounds the expected range of values. Results of such calculated values were compared with values predicted by an alternative model or laboratory experiments, or both, to demonstrate the inherent conservatisms in the analyses. Examples include the comparison of the crack propagation SDFR model-predicted rates with experimentally independently measured rates (Section 7.3.2 and Table 7-4).

(4) Appropriate methods of NDE of fabricated-engineered barriers are used to assess the type, size and location of fabrication defects that may lead to premature failure of engineered barriers.

Nondestructive examinations (NDEs) performed to characterize welding flaws on waste package closure lid weld mockups were verified by destructive metallography and were used to assess the expected type, size, and orientation of welding-related fabrication defects that could lead to premature SCC-related failure of the outer Alloy 22 waste package (Section 6.3).

> *(5) Where sufficient data do not exist, the definition of parameter values and conceptual models is based on appropriate use of other sources, such as expert elicitation.*

In most instances where sufficient data for the exact materials to be used in the repository and processes addressed in this section were not found to be available, data from analogous materials were either found to be or were made available. As a result, the use of expert elicitation in the development and implementation of the SCC-related models was extremely limited, as it was determined that the data and information that were available were adequate to support the required analyses. However, an independent technical review was performed to verify the applicability and conservative nature of the seismic crack density model in Sections 6.7 and 6.8.5.

Acceptance Criterion 4 – Model Uncertainty is Characterized and Propagated Through the Model Abstraction

> *(1) Alternative modeling approaches are considered and are consistent with available data and current scientific understanding.*

An alternative modeling approach for the SDFR model that is consistent with available data and current scientific understanding was considered and evaluated. This model, the CEF SCC propagation-rate model, was considered, and model predictions were compared with available experimental data for stainless steel in the literature. The SDFR model was found to be conservative relative to CEF model (Sections 6.4.6 and 7.3.2) and was therefore selected.

A conservative threshold SIF parameter approach was developed for use because experimental measurement of this parameter was not feasible due to the high resistance of Alloy 22 to stress corrosion cracking propagation (Section 6.4.5).

An alternative seismic crack density model (Sections 6.7.4) was evaluated for its prediction of stress corrosion crack area density and found to be reasonably consistent with the base-case model in Section 6.7.3.

> *(2) Consideration of conceptual model uncertainty is consistent with available site characterization data, laboratory experiments, and the treatment of uncertainty does not result in under-estimation of the risk estimate.*

Consideration of uncertainties in the models used in this report is an integral part of the analyses performed. Conceptual model uncertainty is consistent with the information that has been developed from laboratory experiments. Care has been taken to ensure that the treatment of uncertainty does not result in under-estimation of the risk estimate. Examples of the treatment of such uncertainties are as follows:

- Treatment of residual stress and SIF uncertainty is described in Section 6.5.6
- A conservative approach was used to determine the threshold stress for the SCC initiation parameter for Alloy 22 waste package outer barrier and the Titanium Grade 7 drip shield; this approach is described in Sections 6.2.2 and 6.8.3.3
- Treatment of uncertainty in the threshold SIF parameter is described in Section 6.5.6, and the range of values is listed in Table 6-8.

(3) Alternative modeling approaches, consistent with available data and current scientific understanding, are used and the modeling results are evaluated using tests that are sensitive to the processes modeled.

Wherever it was deemed appropriate (and accepted alternative models were known to exist), alternative modeling approaches consistent with available data and current scientific understanding were considered. In all instances, it was determined that the base-case model provided a similar but more conservative result than would be achieved by using the alternative models. Thus, although due consideration was given to the use of alternative modeling approaches, no alternative models were used.

Acceptance Criterion 5 – Model Abstraction Output Is Supported By Objective Comparisons

(1) Models implemented in this report for input to total system performance assessment abstraction (provide results consistent with output from detailed process-level models and or empirical observations (laboratory and field testing, and/or natural analogs).

The results of model abstractions developed in this report are for use as input to TSPA and thus direct input for use in the TSPA abstraction. Thus, acceptance criterion 5 (1) is not applicable.

(2) Numerical corrosion models used to calculate the lifetime of the engineered barriers are adequate representations, considering the associated uncertainties in long term behavior, range of conditions (including residual stresses) and the variability in fabrication processes.

The numerical stress corrosion models used to calculate the lifetime of the waste package are based on appropriate design considerations and are validated against laboratory results to ensure that they are adequate representations of the processes involved, considering the associated uncertainties in long-term behavior, the range of conditions (including residual stresses) and the variability in fabrication processes (Sections 6.2.2, 6.4.4, 6.8.3, and 6.8.4).

(3) Evidence is sufficient to show that models will not underestimate the actual degradation and failure of engineered barriers.

In those instances where there was doubt about the appropriateness or accuracy of the models, related parameters, or data, modelers were careful to select a conservative approach or conservative data that would result in an overestimation of risk rather than an underestimation

(Sections 6.2.1, 6.3.5, 7.4.3.1, and 7.4.4). The results of analyses were compared against results obtained from laboratory tests or industrial experience to demonstrate the conservatism of the analytical methods. Examples of such instances are provided in Section 7.4.2.

> *(4) Mathematical degradation models are based on the same environmental parameters, material factors, assumptions and approximations shown to be appropriate for closely analogous applications.*

Mathematical degradation models presented in this report are based on environmental parameters, material factors, assumptions, and approximations that have been demonstrated to be appropriate for closely analogous applications. In those instances where it was determined that adequate data did not exist to support the modeling effort, data from testing of analogous materials was used. Examples of such instances can be found in Section 6.2 and Section 6.8.3.

> *(5) Accepted and well documented procedures are used to construct and test the numerical models that simulate the EB chemical environment and degradation of EBS.*

The development and testing of the numerical models and related parameters used to simulate the repository environment and analyze the potential degradation of the Engineered Barrier System features, including the drip shield and waste package, were performed in accordance with previously established well-documented YMP procedures that are based on industry-established norms. These procedures also established the appropriate quality assurance (QA) requirements for such activities, and appropriate checking, auditing, and other activities were performed to ensure the adequacy and appropriateness of the models and data. Examples of compliance with such QA requirements and associated procedures can be found in Sections 2, and 7, respectively.

> *(6) Sensitivity analyses or bounding analyses are provided to support the abstraction of the degradation of engineered barriers.*

Bounding analyses associated with the abstraction of the stress and SIF through-wall gradients driving the potential SCC degradation of the waste package were performed and are documented herein. Examples of such activities can be found in Section 6.5.6.

Objective comparisons with experimental data and relevant literature are described for predicted versus measured Alloy 22 crack growth rates in Sections 6.3.5 and 7.4.2.

The above acceptance criteria (3, 4, and 5) are also addressed by the waste package degradation analysis, which describes the abstracted SCC models and related parameters and the propagation of uncertainties in those models and parameters for the case of nonseismic-related SCC. Acceptance criteria 3 through 5 will also be addressed in the seismic consequence abstraction model report (SNL 2007 [DIRS 176828]), which describes the abstracted SCC models and the propagation of uncertainties in those models for the case of seismic SCC.

8.3 SUMMARY OF MODEL AND ANALYSES OUTPUT AND PARAMETERS USED

Table 8-1 is a summary of the model outputs and the parameters used in development of the models. These outputs and parameters can be used as input for the TSPA with no restrictions if the waste package design, material, and environment are consistent with those considered in the reported modeling activities.

Table 8-1. Summary of Model Outputs

Output Name	Output Value or Equation with Unit	Detailed in This Section	Note
Mechanical Properties of the Materials Studied			
Yield strength (YS) for Alloy 22	403 MPa at room temperature (21°C, 70°F,294 K) 371 MPa at 93°C (200°F, 366 K) 303MPa at 204°C (400°F, 477 K) 351 MPa at 125°C (interpolated)	Table 8-2	Linear between temperatures. Used in this document for conservatism. 351 MPa at 125°C is recommended to be used in TSPA
Yield strength (YS) for Alloy 22	372 MPa at room temperature (21°C) (70°F,294 K) 338 MPa at 93°C (200°F, 366 K) 283 MPa at 204°C (400°F, 477 K)	Table 8-2	Linear between temperatures.
Modulus of elasticity for Alloy 22	206 GPa at room temperature 203 GPa at 366 K (200°F,93°C) 196 GPa at 477 K (400°F, 204°C)	Table 8-2	
Yield strength for Titanium Grade 7	276 MPa at room temperature 176 MPa at 422 K (300°F, 149°C)	Table 8-2	Spec. minimum value. Used for modeling.
Yield strength for Titanium Grade 7	248 MPa measured in 125°C air.	Table 8-2	Measured by GE GRC at 125°C. Used for GE GRC results discussion
Yield strength for Titanium Grade 7	362 MPa (52.5 ksi) at room temperature (21°C) (70°F, 294 K) 145 MPa (21 ksi) at 204°C (400°F, 477 K) 107 MPa (15.5) at 316°C (600°F, 589 K)	Table 8-2	Linear interpolation to 60°C and 90°C
Yield strength for Titanium Grades 23 and 29	759 MPa at room temperature (21°C) (70°F, 294 K)	Table 8-2	
Yield strength for Titanium Grades 23 and 29[b]	87% of 759 MPa at 93°C (200°F, 366 K) 70% of 759 MPa at 204°C (400°F, 477 K)	Table 8-2	
Yield strength for Titanium Grade 29	724 MPa (105 ksi) 105°C	Table 8-2	Measured.
Yield strength for Titanium Grade 28	483 MPa at room temperature (21°C) (70°F, 294 K)	Table 8-2	
Modulus of elasticity for Titanium Grade 7	107 GPa at 294 K (70°F, 21°C) 101 GPa at 422 K (300°F, 149°C) 97 GPa at 477 K (400°F, 204°C)	Table 8-2	
Threshold stress (Alloy 22)	Uniform distribution between 0.9 and 1.05 (at-temperature yield strength), MPa (Section 6.2.2)	Table 8-3	

Table 8-1. Summary of Model Outputs (Continued)

Output Name	Output Value or Equation with Unit	Detailed in This Section	Note
Threshold Stress Criteria for SCC Initiation			
Threshold stress (Titanium Grade 7)	0.8 ($YS_{(T)}$), MPa (Section 6.8.3.1.3)	Table 8-4	
Threshold stress (Titanium Grades 28 and 29)	0.5($YS_{(T)}$), MPa (Section 6.8.3.2.3)	Table 8-4	
Other Metallurgical Parameters			
Initial size of incipient cracks	0.05 mm (Section 6.3.3)		
Depth of plate to be included for embedded flaws	0.25 of plate thickness (25%) (Section 6.3.4.2)		
Fraction of radially oriented flaws	0.005 (0.5%) (Section 6.3.4.3)		
SDFR Model			
Mean of repassivation slope, Alloy 22 SDFR model	1.165 (dimensionless) (Section 6.4.4.4)	Table 8-5	
Standard deviation (SD) of repassivation slope, Alloy 22 SDFR model	0.115 (dimensionless) (Section 6.4.4.4)	Table 8-5	
2 SD; lower bound of repassivation slope, Alloy 22 SDFR model	0.935 (dimensionless) (Section 6.4.4.4)	Table 8-5	
2 SD; upper bound of repassivation slope, Alloy 22 SDFR model	1.395 (dimensionless) (Section 6.4.4.4)	Table 8-5	
Crack growth rate, V_t	$V_t = 7.8\times10^{-2} n^{3.6} \left(4.1\times10^{-14}\right)^n \left(K_I\right)^{4n}$ (mm/s)(Section 6.4.4.2, Equation 18), where K_I is the SIF in MPa√m		*n* is the repassivation slope
Mean general corrosion rate, V_{gc}, Alloy 22	7.23 nm/yr (Section 6.4.5.3)		When used to calculate V_t, V_{gc} should be converted to mm/s
Threshold SIF, K_{ISCC}	KISCC = (Vgc / $\overline{A}$)$^{1/\overline{n}}$ (MPa√m) (Section 6.4.5.3, Equation 19), where $\overline{A} = 7.8\times10^{-2} n^{3.6} \left(4.1\times10^{-14}\right)^n$ (Section 6.4, Equations 15 and 17) and $\overline{n} = 4n$ (Section 6.4, Equation 16)		*n* is the repassivation slope V_{gc} is in mm/s When used to calculate V_t, V_{gc} should be converted to mm/ys
2 SD; lower bound of K_{ISCC} from Alloy 22 SDFR model	1.96 (Table 6-8, Section 6.4.5.3)	Table 8-6	
2 SD; upper bound of K_{ISCC} from Alloy 22 SDFR model	15.38 (Table 6-8, Section 6.4.5.3)	Table 8-6	
Stress and Stress Intensity Factor Distribution and Uncertainties			
Radial stress coefficient A_0 for as-welded naval long waste package weld closure	-76.883 MPa (Section 6.5.3.4.1, Table 6-11)	Table 8-7	
Radial stress coefficient A_1 for as-welded naval long waste package weld closure	75.907 MPa/mm (Section 6.5.3.4.1, Table 6-11)	Table 8-7	

Table 8-1. Summary of Model Outputs (Continued)

Output Name	Output Value or Equation with Unit	Detailed in This Section	Note
Radial stress coefficient A_2 for as-welded naval long waste package weld closure	-8.180 MPa/mm^2 (Section 6.5.3.4.1, Table 6-11)	Table 8-7	
Radial stress coefficient A_3 for as-welded naval long waste package weld closure	0.219 MPa/mm^3 (Section 6.5.3.4.1, Table 6-11)	Table 8-7	
Hoop stress coefficient A_0 for as-welded naval long waste package weld closure	290.711 MPa (Section 6.5.3.4.1, Table 6-11)	Table 8-7	
Hoop stress coefficient A_1, for as-welded naval long waste package weld closure	38.678 MPa/mm (Section 6.5.3.4.1, Table 6-11)	Table 8-7	
Hoop stress coefficient A_2, for as-welded naval long waste package weld closure	-4.004 MPa/mm^2 (Section 6.5.3.4.1, Table 6-11)	Table 8-7	
Hoop stress coefficient A_3, for as-welded naval long waste package weld closure	0.107 MPa/mm^3 (Section 6.5.3.4.1, Table 6-11)	Table 8-7	
Radial stress coefficient A_0 for laser-peened naval long waste package weld closure	-321.440 MPa (Section 6.5.5.2.1, Table 6-13)	Table 8-8	
Radial stress coefficient A_1 for laser-peened naval long waste package weld closure	134.996 MPa/mm (Section 6.5.5.2.1, Table 6-13	Table 8-8	
Radial stress coefficient A_2 for laser-peened naval long waste package weld closure	-12.300 MPa/mm^2 (Section 6.5.5.2.1, Table 6-13)	Table 8-8	
Radial stress coefficient A_3 for laser-peened naval long waste package weld closure	0.306 MPa/mm^3 (Section 6.5.5.2.1, Table 6-13)	Table 8-8	
Hoop stress coefficient A_0 for laser-peened naval long waste package weld closure	−245.805 MPa (Section 6.5.5.2.1, Table 6-13)	Table 8-8	
Hoop stress coefficient A_1 for laser-peened naval long waste package weld closure	164.920 MPa/mm (Section 6.5.5.2.1, Table 6-13)	Table 8-8	
Hoop stress coefficient A_2 for laser-peened naval long waste package weld closure	−12.685 MPa/mm^2 (Section 6.5.5.2.1, Table 6-13)	Table 8-8	
Hoop stress coefficient A_3 for laser-peened naval long waste package weld closure	0.289 MPa/mm^3 (Section 6.5.5.2.1, Table 6-13)	Table 8-8	
Radial stress coefficient A_0 for plasticity-burnished naval long waste package weld closure	−621.762 MPa (Section 6.5.5.2.2, Table 6-14)	Table 8-9	
Radial stress coefficient A_1 for plasticity-burnished naval long waste package weld closure	209.682 MPa/mm (Section 6.5.5.2.2, Table 6-14)	Table 8-9	

Table 8-1. Summary of Model Outputs (Continued)

Output Name	Output Value or Equation with Unit	Detailed in This Section	Note
Radial stress coefficient A_2 for plasticity-burnished naval long waste package weld closure	−17.598 MPa/mm^2 (Section 6.5.5.2.2, Table 6-14)	Table 8-9	
Radial stress coefficient A_3 for plasticity-burnished naval long waste package weld closure	0.419 MPa/mm^3 (Section 6.5.5.2.2, Table 6-14)	Table 8-9	
Hoop stress coefficient A_0 for plasticity-burnished naval long waste package weld closure	−519.127 MPa (Section 6.5.5.2.2, Table 6-14)	Table 8-9	
Hoop stress coefficient A_1 for plasticity-burnished naval long waste package weld closure	231.675 MPa/mm (Section 6.5.5.2.2, Table 6-14)	Table 8-9	
Hoop stress coefficient A_2 for plasticity-burnished naval long waste package weld closure	−17.377 MPa/mm^2 (Section 6.5.5.2.2, Table 6-14)	Table 8-9	
Hoop stress coefficient A_3 for plasticity-burnished naval long waste package weld closure	0.388 MPa/mm^3 (Section 6.5.5.2.2, Table 6-14)	Table 8-9	
S0(x), radial stress, as-welded,	Section 6.5.3.4.2, Table 6-12, second column, MPa	Table 8-10	Calculated from Equation 22
S0(z), hoop stress, as-welded	Section 6.5.3.4.2, Table 6-12, fourth column, MPa	Table 8-10	Calculated from Equation 22
S0(x), radial stress, laser-peened	Section 6.5.5.2.3, Table 6-15, second column, MPa	Table 8-11	Calculated from Equation 22
S0(z), hoop stress, laser-peened	Section 6.5.5.2.3, Table 6-15, fourth column, MPa	Table 8-11	Calculated from Equation 22
S0(x), radial stress, plasticity-burnished	Section 6.5.5.2.4, Table 6-16, second column, MPa	Table 8-12	Calculated from Equation 22
S0(z), hoop stress, plasticity-burnished	Section 6.5.5.2.4, Table 6-16, fourth column, MPa	Table 8-12	Calculated from Equation 22
SIF, K0(x), radial stress, as-welded	MPa√m , Section 6.5.3.4.2, Table 6-12, third column	Table 8-10	
SIF, K0(z), hoop stress, as-welded	MPa√m , Section 6.5.3.4.2, Table 6-12, fifth column	Table 8-10	
SIF, K0(x), radial stress, laser-peened	MPa√m, Section 6.5.5.2.3, Table 6-16, third column	Table 8-11	
SIF, K0(z), hoop stress, laser-peened	MPa√m, Section 6.5.5.2.3, Table 6-15, fifth column	Table 8-11	
SIF, K0(x), radial stress, plasticity-burnished	MPa√m, Section 6.5.5.2.4, Table 6-16, third column	Table 8-12	
SIF, K0(z), hoop stress, plasticity-burnished	MPa√m, Section 6.5.5.2.4, Table 6-16, fifth column	Table 8-12	
Stress variability, ∇S	17.2369, MPa, (Section 6.5.6.1)		Equation 24

Table 8-1. Summary of Model Outputs (Continued)

Output Name	Output Value or Equation with Unit	Detailed in This Section	Note
Stress profile, $S_\theta(x)$, at angle θ from $S_0(x)$	$S_\theta(x)= S_0(x) - \nabla S(1 - \cos(\theta))$, MPa (Section 6.5.6.1)	Figure 8-2 for as-welded, Figure 8-3 for plasticity-burnished	Equation 24
SIF profile, $K_\theta(x)$, at angle θ from $K_0(x)$	$K_\theta(x)= K_0(x)\ (S_\theta(h) / S_0(h))$, MPa√m (Section 6.5.6.1)	Figure 8-4 for as-welded, Figure 8-5 for plasticity-burnished	Equation 25
Variation amplitude of $S_0(x)$, ΔS	0.15 (YS), MPa (Section 6.5.6.2);		Uncertainty for ΔS is represented by a normal distribution truncated at ±3-sigma (±15% YS); use room temperature yield strength value
Lower bound of stress variation	$S_\theta(x)\min = S_\theta(x)\left(\frac{S_\theta(h)-\Delta S}{S_\theta(h)}\right)$, MPa (Section 6.5.6.3)	Figure 8-6 for as-welded, Figure 8-7 for plasticity-burnished	Equation 26
Upper bound of stress variation	$S_\theta(x)\max = S_\theta(x)\left(\frac{S_\theta(h)+\Delta S}{S_\theta(h)}\right)$, MPa (Section 6.5.6.3)	Figure 8-6 for as-welded, Figure 8-7 for plasticity-burnished	Equation 27
Lower bound of SIF variation	$K_\theta(x)\min = K_\theta(x)\left(\frac{S_\theta(h)-\Delta S}{S_\theta(h)}\right)$, MPa√m (Section 6.5.6.3)	Figure 8-8 for as-welded, Figure 8-9 for plasticity-burnished	Equation 28
Upper bound of SIF variation	$K_\theta(x)\max = K_\theta(x)\left(\frac{S_\theta(h)+\Delta S}{S_\theta(h)}\right)$, MPa√m (Section 6.5.6.3)	Figure 8-8 for as-welded, Figure 8-9 for plasticity-burnished	Equation 29

Table 8-1. Summary of Model Outputs (Continued)

Output Name	Output Value or Equation with Unit	Detailed in This Section	Note
Seismic Crack Density Models			
WP_Crack_Area_Density_a	Uncertainty uniformly distributed between $\frac{\pi\sigma}{\sqrt{3}E}$ and $\frac{4\pi\sigma}{\sqrt{3}E}$ (Section 6.7.3.3)	Table 8-13	
DS_Crack_Area_Density_a	Uncertainty uniformly distributed between $\frac{\pi\sigma}{\sqrt{3}E}$ and $\frac{4\pi\sigma}{\sqrt{3}E}$ (Section 6.8.5.2.2)	Table 8-14	
TSPA Parameter Feeds			
TSPA parameter feeds are summarized in Table 8-15.			

Source: Output DTN: MO0702PASTRESS.002, *Model Output DTN.doc*.

Mechanical Properties

The details of the mechanical properties, including yield strength and modulus of elasticity data, of Alloy 22 and titanium alloys are listed in Table 8-2. Table 8-2 is included in output DTN: MO0702PASTRESS.002, *Model Output DTN.doc*, Table 8-2.

Table 8-2. Output Data for Yield Strength and Modulus of Elasticity for Alloy 22 and Titanium Grade 7

Input Name	Input Source	DTN	Input Value or Equation
Yield Strength for Alloy 22*	Physical and Chemical Characteristics of Alloy 22. Submittal date: 03/13/2000 [DIRS 148850]	MO0003RIB00071.000 [DIRS 148850] (Data from Alloy Digest 1985 [DIRS 178194], p. 2, Table 3)	403 MPa at room temperature (21°C) (70°F, 294 K) 371 MPa at 93°C (200°F, 366 K) 303MPa at 204°C (400°F, 477 K) 351 MPa at 125°C (interpolated). 351 MPa at 125°C is recommended to be used in TSPA
Yield Strength for Alloy 22	Physical and Chemical Characteristics of Alloy 22. Submittal date: 03/13/2000 [DIRS 148850]	MO0003RIB00071.000 [DIRS 148850] (Data from Haynes International 1988 [DIRS 101995], p. 15)	372 MPa at room temperature (21°C) (70°F, 294 K) 338 MPa at 93°C (200°F, 366 K) 283 MPa at 204°C (400°F, 477 K)

Table 8-2. Output Data for Yield Strength and Modulus of Elasticity for Alloy 22 and Titanium Grade 7 (Continued)

Input Name	Input Source	DTN	Input Value or Equation
Modulus of elasticity for Alloy 22	Physical and Chemical Characteristics of Alloy 22. Submittal date: 03/13/2000 [DIRS 148850]	MO0003RIB00071.000[DIRS 148850] (Data from Haynes International 1988 [DIRS 101995], p. 15)	206 GPa at room temperature 203 GPa at 366 K (200°F, 93°C) 196 GPa at 477 K (400°F, 204°C)
Yield Strength for Titanium Grade 7*	ASME 2001 [DIRS 158115], Section II, Part D, Table Y-1, pp. 632 to 634	N/A	276 MPa at room temperature (21°C) (70°F, 294 K) 176 MPa at 149°C (300°F, 422 K)
Yield Strength for Titanium Grade 7	DTN: MO0707SCCIGMER.000 [DIRS 182202], Table 2-4	MO0707SCCIGMER.000 [DIRS 182202]	248 MPa measured in 125°C air
Yield Strength for Titanium Grade 7	Physical and Chemical Characteristics of Titanium Grades 7 and 16. Submittal date: 03/13/2000 [DIRS 152926]	MO0003RIB00073.000 [DIRS 152926]	281 MPa at 90°C 317 MPa at 60°C
Modulus of elasticity for Titanium Grade 7	Physical and Chemical Characteristics of Titanium Grades 7 and 16. Submittal date: 03/13/2000 [DIRS 152926]	MO0003RIB00073.000 [DIRS 152926]	107 GPa at 294 K (70°F, 21°C) 101 GPa at 422 K (300°F, 149°C) 97 GPa at 477 K (400°F, 204°C)
Yield Strength for Titanium Grade 23 and Grade 29	ASTM B 265-02 [DIRS 162726]	N/A	759 MPa at room temperature (21°C) (70°F, 294 K)
Yield Strength for Titanium Grade 23 and Grade 29**	Donachie 2002 [DIRS 178207], Table 7		87% of 759 MPa at 93°C (200°F, 366 K) 70% of 759 MPa at 204°C (400°F, 477 K)
Yield Strength for Titanium Grade 29	DTN: MO0705SCCIGM06.000 [DIRS 180869], file *GE-GRC-Final_Sept-2006-Rev3.doc*	MO0705SCCIGM06.000 [DIRS 180869]	724 MPa (105 ksi) 105°C
Yield Strength for Titanium Grade 28	ASTM B 265-02 [DIRS 162726]	N/A	483 MPa at room temperature (21°C) (70°F, 294 K)

Source: Output DTN: MO0702PASTRESS.002, *Model Output DTN.doc*, Table 8-2.

NOTE: * Yield strength values recommended to be used in TSPA. Some of the yield strength input data are given with English units in the input sources. The English unit, ksi, has been converted to the metric unit, MPa, according to 1 ksi = 6.894757 MPa (Boyer and Gall 1997 [DIRS 155318], p. 1-57).
** In Donachie 2002 [DIRS 178207], Table 7, only the yield strength values of Ti-6Al-4V (Titanium Grade 5) are listed. However, Titanium Grades 23 and 29 are extra-low interstitial variants for Titanium Grade 5 (Ti-6Al-4V) that result in a small reduction in room temperature yield strength (10 ksi or 8%). Because of the similarity in alloying element compositions, the reduction in yield strength with temperature should be equivalent.

SCC Crack Initiation Stress Threshold Criteria

Figure 8-1 demonstrates the technical basis for evaluating Titanium Grade 7 SCC initiation criterion (0.8 yield strength) by comparison of air creep rupture failure times with time on test in 60°C to 125°C brines without stress corrosion crack initiation. Figure 8-1 is included in output DTN: MO0702PASTRESS.002, *Figure 6-73 Table 6-30.xls*.

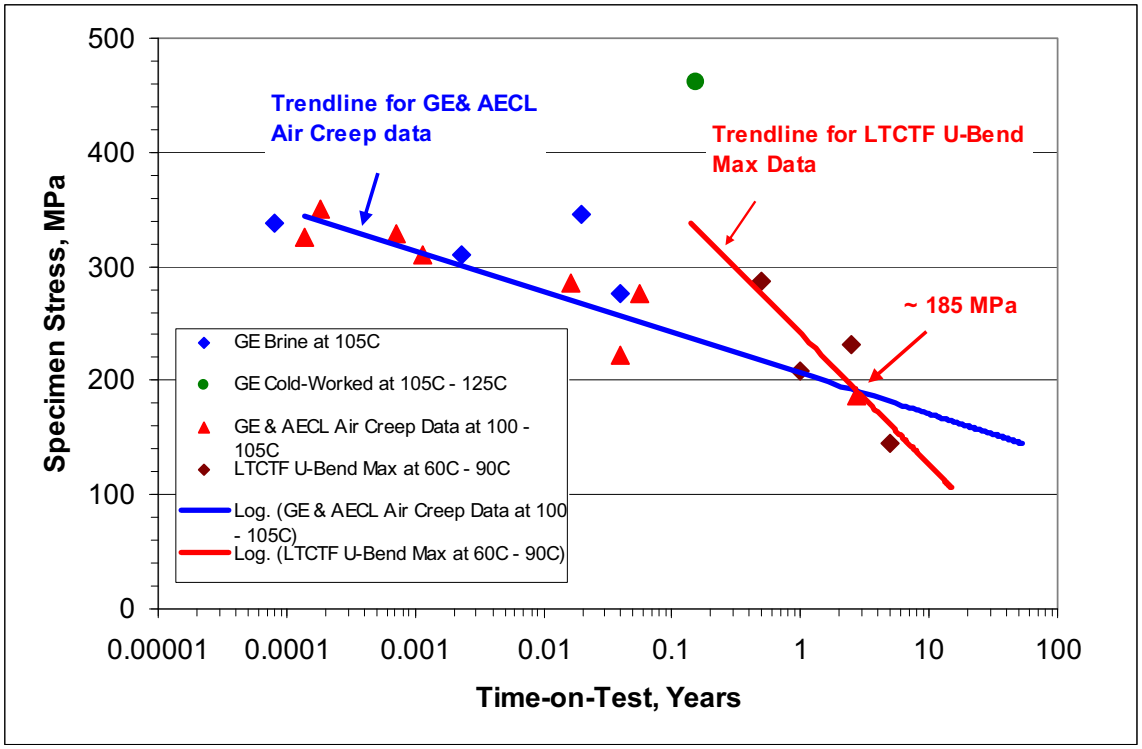

Source: Air creep rupture curve from Figure 6-68 and the maximum remaining tensile stress at each U-bend exposure interval versus exposure time from Figure 6-72.

Figure 8-1. Comparison of Air Creep Rupture Failure Times with Time on Test in 60°C to 125°C Brines Without Stress Corrosion Crack Initiation

The SCC crack initiation stress threshold criterion for Alloy 22 is shown in Table 8-3. The SCC crack initiation stress threshold criteria for Titanium Grades 7, 28, and 29 are shown in Table 8-4. Table 8-3 and Table 8-4 are included in output DTN: MO0702PASTRESS.002, *Model Output DTN.doc*, Tables 8-3 and 8-4.

Table 8-3. SCC Initiation Threshold Stress Criteria of Alloy 22

Material	Threshold Stress Criteria
Alloy 22	Uniform distribution between 0.9 x $YS_{(T)}$ and 1.05 × $YS_{(T)}$

Source: Output DTN: MO0702PASTRESS.002, *Model Output DTN.doc*, Table 8-3.

NOTE: $YS_{(T)}$= at-temperature yield strength.

Table 8-4. SCC Initiation Threshold Stress Criteria of Titanium Alloys

Alloy	Threshold Stress Criteria
Titanium Grade 7	0.8 × $YS_{(T)}$
Titanium Grade 28	0.5 × $YS_{(T)}$
Titanium Grade 29	0.5 × $YS_{(T)}$

Source: Output DTN: MO0702PASTRESS.002, *Model Output DTN.doc*, Table 8-4.

NOTE: $YS_{(T)}$= at-temperature yield strength.

SDFR Model of Alloy 22 SCC

The details on distribution of the parameter *n*, the repassivation slope, and on distribution of K_{ISCC}, the threshold SIF, for Alloy 22 are listed in Table 8-5 and Table 8-6, respectively. Table 8-5 and Table 8-6 are included in output DTN: MO0702PASTRESS.002, *Model Output DTN.doc*, Tables 8-5 and 8-6.

Table 8-5. Distribution of the Parameter *n*

	Standard Deviation	*n* Value (n_{MEAN} ± *i*SD, *i* = 1 and 2)	Cumulative Probability
n_{MEAN} = 1.165 n_{SD} = 0.115	−2	0.935	0.000
	−1	1.050	0.142
	0	1.165	0.500
	1	1.280	0.858
	2	1.395	1.000

Source: Output DTN: MO0702PASTRESS.002, *Model Output DTN.doc*, Table 8-5.

NOTE: Generated using Excel function NORMDIST; mean, upper bound, lower bound, standard deviation.

Table 8-6. Distribution of the Threshold Stress Intensity Factor, K_{ISCC}, for Alloy 22

	Standard Deviation (SD)	*n* Value (n_{Mean} ± I SD, i = 0, 1 and 2)	'K_{ISCC}' Value (MPa√m)
n_{Mean} = 1.165 n_{SD} = 0.115 V_{gcMean} = 7.23 nm/yr	−2	0.935	1.96
	−1	1.050	3.83
	0	1.165	6.62
	1	1.280	10.45
	2	1.395	15.38

Source: Output DTN: MO0702PASTRESS.002, *Model Output DTN.doc*, Table 8-6.

NOTE: Generated using Excel function NORMDIST; mean, upper bound, lower bound, standard deviation.

Residual Stress and Stress Intensity Factor Distributions

Table 8-7, Table 8-8, and Table 8-9 list the stress coefficients (A_i) for the as-welded, laser-peened, and plasticity-burnished waste package closure weld lids, respectively. The data shown in Table 8-7, Table 8-8, and Table 8-9 are from the original data in Table 4-3. Table 8-7, Table 8-8, and Table 8-9 are included in output DTN: MO0702PASTRESS.002, *Model Output DTN.doc*, Tables 8-7, 8-8, and 8-9.

Table 8-7. Stress Coefficients for the As-Welded Naval Long Waste Package Outer Lid

Stress Coefficient	From First and Second Rows of Table 4-3					Conversion Factors					
	Unit	Section A-A		Section B-B			Unit	Section A-A		Section B-B	
		Radial Stress	Hoop Stress	Radial Stress	Hoop Stress			Radial Stress	Hoop Stress	Radial Stress	Hoop Stress
A_0	ksi	−11.151	42.164	−3.9316	45.955	1 ksi = 6.894757 MPa *	MPa	−76.883	290.711	−27.107	316.849
A_1	ksi/in	279.64	142.49	196.58	90.001	1 ksi/in = 0.271447 MPa/mm	MPa/mm	75.907	38.678	53.361	24.431
A_2	ksi/in^2	−765.46	−374.62	−565.89	−245.2	1 ksi/in^2 = 0.010687 MPa/mm^2	MPa/mm^2	−8.180	−4.004	−6.048	−2.620
A_3	ksi/in^3	520.13	254.87	388.99	161.57	1 ksi/in^3 = 0.000421 MPa/mm^3	MPa/mm^3	0.219	0.107	0.164	0.068

Source: Output DTN: MO0702PASTRESS.002, *Model Output DTN.doc*, Table 8-7.

NOTE: The data in third, fourth, fifth and sixth columns are from the first, second, third and fourth rows of Table 4-3 with En glish units. The last four columns are converted to metric units by using the conversion factors shown in the middle column.
* Boyer and Gall 1997 [DIRS 155318], p. 1-57.

Table 8-8. Stress Coefficients for the Laser-Peened Naval Long Waste Package Outer Lid

Stress Coefficient	From Fifth to Eighth Rows of Table 4-3					Conversion Factors					
	Unit	Section A-A		Section B-B			Unit	Section A-A		Section B-B	
		Radial Stress	Hoop Stress	Radial Stress	Hoop Stress			Radial Stress	Hoop Stress	Radial Stress	Hoop Stress
A_0	ksi	−46.621	−35.651	−41.029	−32.73	1 ksi = 6.894757 MPa *	MPa	−321.440	−245.805	−282.885	−225.665
A_1	ksi/in	497.32	607.56	430.6	570.96	1 ksi/in = 0.271447 MPa/mm	MPa/mm	134.996	164.920	116.885	154.985
A_2	ksi/in^2	−1,150.9	−1,187.0	−987.87	−1,097.5	1 ksi/in^2 = 0.010687 MPa/mm^2	MPa/mm^2	−12.300	−12.685	−10.557	−11.729
A_3	ksi/in^3	726.37	686.08	617.8	618.7	1 ksi/in^3 = 0.000421 MPa/mm^3	MPa/mm^3	0.306	0.289	0.260	0.260

Source: Output DTN: MO0702PASTRESS.002, *Model Output DTN.doc*, Table 8-8.

NOTE: The data in third, fourth, fifth and sixth columns are from the fifth, sixth, seventh and eighth rows of Table 4-3 with E nglish units. The last four columns are converted to metric units by using the conversion factors shown in the middle column.
* Boyer and Gall 1997 [DIRS 155318], p. 1-57.

Table 8-9. Stress Coefficients for the Plasticity-Burnished Naval Long Waste Package Outer Lid

Stress Coefficient	From Last Four Rows of Table 4-3					Conversion Factors					
	Unit	Section A-A		Section B-B			Unit	Section A-A		Section B-B	
		Radial Stress	Hoop Stress	Radial Stress	Hoop Stress			Radial Stress	Hoop Stress	Radial Stress	Hoop Stress
A_0	ksi	−90.179	−75.293	−82.228	−72.008	1 ksi = 6.894757 MPa *	MPa	−621.762	−519.127	−566.942	−496.478
A_1	ksi/in	772.46	853.48	695.42	817.86	1 ksi/in = 0.271447 MPa/mm	MPa/mm	209.682	231.675	188.770	222.006
A_2	ksi/in^2	−1,646.7	−1,626	−1,470.7	−1,542	1 ksi/in^2 = 0.010687 MPa/mm^2	MPa/mm^2	−17.598	−17.377	−15.717	−16.479
A_3	ksi/in^3	994.72	922.37	881.5	859.56	1 ksi/in^3 = 0.000421 MPa/mm^3	MPa/mm^3	0.419	0.388	0.371	0.362

Source: Output DTN: MO0702PASTRESS.002, *Model Output DTN.doc*, Table 8-9.

NOTE: The data in third, fourth, fifth and sixth columns are from last four rows of Table 4-3 with English units. The last fou r columns are converted to metric units by using the conversion factors shown in the middle column.
* Boyer and Gall 1997 [DIRS 155318], p. 1-57.

Stress and SIF Profile of Alloy 22 Closure Lids

Table 8-10, Table 8-11 and Table 8-12 provide the stresses and SIF data for as-welded, laser-peened, and plasticity-burnished naval long waste package closure weld lids, respectively. Table 8-10, Table 8-11 and Table 8-12 (directly duplicated from Table 6-12, Table 6-15, and Table 6-16, respectively) explain how data are obtained from Section 4. For the plasticity-burnished waste package closure weld, it is clear from Table 8-12 that the hoop stress and corresponding SIFs are the predominant stress and SIF components. The original data shown in Table 8-10, Table 8-11 and Table 8-12 are abstracted from Table 4-4, Table 4-5, and Table 4-6 , respectively. Table 8-10, Table 8-11 and Table 8-12 are included in output DTN: MO0702PASTRESS.002, *Model Output DTN.doc*, Tables 8-10 to 8-12.

Table 8-10. Stress and SIF Profiles for the As-Welded Naval Long Waste Package Outer Lid

Distance from Outer Surface (mm)	Radial Stress (SECP)		Hoop Stress (Elliptical)	
	Sx (MPa)	K−Sx (MPa√m)	Sz (MPa)	K−Sz (MPa√m)
0.4064	−6.4090	−2.2678	305.7754	11.2274
0.8128	12.3573	−2.2901	319.5611	16.3747
1.2192	29.2579	−1.7449	332.1107	20.6275
1.6256	44.3589	−0.8637	343.4673	24.4393
2.0320	57.7262	0.2410	353.6743	27.9742
2.4384	69.4260	1.4985	362.7748	31.3100
2.8448	79.5243	2.8147	370.8119	34.6315
3.2512	88.0872	4.2080	377.8289	37.8956
3.6576	95.1806	5.6749	383.8689	41.0731
4.0640	100.8707	7.1989	388.9751	44.1727
4.4704	105.2234	8.7668	393.1908	47.2003
4.8768	108.3049	10.3682	396.5590	50.1595
5.2832	110.1812	12.0423	399.1231	53.1682
5.6896	110.9183	13.7863	400.9261	56.2437
6.0960	110.5823	15.5413	402.0113	59.2771
6.5024	109.2392	17.2938	402.4218	62.2685
6.9088	106.9551	19.0311	402.2009	65.2181
7.3152	103.7960	20.7408	401.3917	68.1262
7.7216	99.8280	22.5402	400.0373	71.0425
8.1280	95.1171	24.7409	398.1811	74.0742
8.5344	89.7294	26.9849	395.8662	77.0775
8.9408	83.7308	29.2656	393.1357	80.0523
9.3472	77.1875	31.5760	390.0329	82.9990
9.7536	70.1656	33.9100	386.6009	85.9181
10.1600	62.7310	36.2618	382.8830	88.8104
10.5664	54.9497	38.2561	378.9222	91.8087
10.9728	46.8880	40.1446	374.7619	94.7872
11.3792	38.6117	41.9080	370.4451	97.7469
11.7856	30.1869	43.5280	366.0151	100.6890

Table 8-10. Stress and SIF Profiles for the As-Welded Naval Long Waste Package Outer Lid (Continued)

Distance from Outer Surface (mm)	Radial Stress (SECP)		Hoop Stress (Elliptical)	
	Sx (MPa)	K−Sx (MPa√m)	Sz (MPa)	K−Sz (MPa√m)
12.1920	21.6798	44.9869	361.5151	103.6150
12.5984	13.1563	46.2679	356.9882	106.5266
13.0048	4.6825	48.1026	352.4777	109.3852
13.4112	−3.6756	50.0290	348.0266	112.2171
13.8176	−11.8519	51.7880	343.6783	115.0390
14.2240	−19.7804	53.3637	339.4759	117.8531
14.6304	−27.3950	54.7413	335.4625	120.6618
15.0368	−34.6297	55.9084	331.6815	123.4693
15.4432	−41.4185	58.8299	328.1758	126.1197
15.8496	−47.6952	63.7225	324.9888	128.6086
16.2560	−53.3938	68.6858	322.1637	131.0953
16.6624	−58.4483	73.7252	319.7435	133.5852
17.0688	−62.7927	78.8497	317.7715	136.0818
17.4752	−66.3609	84.0719	316.2910	138.5927
17.8816	−69.0868	90.7634	315.3449	141.0079
18.2880	−70.9044	101.4317	314.9767	143.1078
18.6944	−71.7476	111.8743	315.2294	145.2363
19.1008	−71.5505	122.0826	316.1462	147.4021
19.5072	−70.2469	132.0579	317.7704	149.6130
19.9136	−67.7708	141.8068	320.1450	151.8777
20.3200	−64.0562	151.3480	323.3134	154.2017

Source: Output DTN: MO0702PASTRESS.002, file *Model Output DTN.doc*, Table 8-10.

Table 8-11. Stress and SIF Profiles for the Laser-Peened Naval Long Waste Package Outer Lid

Distance from Outer Surface (mm)	SECP (Radial Stress)		ELL (Hoop Stress)	
	Sx (MPa)	K−Sx (MPa√m)	Sz (MPa)	K−Sz (MPa√m)
0.4064	−268.5886	−11.2007	−180.8572	−4.4149
0.8128	−219.6769	−14.2933	−119.9831	−6.0412
1.2192	−174.5816	−15.7016	−63.0664	−7.1517
1.6256	−133.1797	−16.1516	−9.9906	−7.4927
2.0320	−95.3477	−15.9606	39.3605	−5.6960
2.4384	−60.9626	−15.3119	85.1035	−3.4512
2.8448	−29.9010	−14.7222	127.3547	−0.9200
3.2512	−2.0397	−14.0206	166.2305	1.8571
3.6576	22.7445	−13.1241	201.8472	4.8365
4.0640	44.5749	−12.0680	234.3213	7.9693
4.4704	63.5747	−10.8798	263.7691	11.2155
4.8768	79.8671	−9.5806	290.3071	14.5414

Table 8-11. Stress and SIF Profiles for the Laser-Peened Naval Long Waste Package Outer Lid (Continued)

Distance from Outer Surface (mm)	SECP (Radial Stress)		ELL (Hoop Stress)	
	Sx (MPa)	K−Sx (MPa√m)	Sz (MPa)	K−Sz (MPa√m)
5.2832	93.5753	−8.2572	314.0517	17.9097
5.6896	104.8226	−6.9171	335.1191	21.3088
6.0960	113.7323	−5.5081	353.6258	24.7318
6.5024	120.4275	−4.0501	369.6883	28.1613
6.9088	125.0316	−2.5622	383.4228	31.5821
7.3152	127.6676	−1.0629	394.9458	34.9809
7.7216	128.4590	0.4953	404.3737	38.3599
8.1280	127.5288	2.3223	411.8228	41.7465
8.5344	125.0004	4.2697	417.4095	45.0972
8.9408	120.9969	6.3293	421.2503	48.4048
9.3472	115.6417	8.4932	423.4614	51.6630
9.7536	109.0579	10.7538	424.1594	54.8667
10.1600	101.3687	13.1039	423.4606	58.0115
10.5664	92.6975	13.7515	421.4814	61.1760
10.9728	83.1675	14.2954	418.3381	64.2839
11.3792	72.9018	14.7097	414.1472	67.3333
11.7856	62.0237	14.9688	409.0250	70.3229
12.1920	50.6565	15.0477	403.0879	73.2522
12.5984	38.9234	14.9221	396.4524	76.1216
13.0048	26.9476	14.6054	389.2348	78.9566
13.4112	14.8524	14.1379	381.5515	81.7403
13.8176	2.7609	13.4958	373.5189	84.4664
14.2240	−9.2035	12.6556	365.2533	87.1381
14.6304	−20.9176	11.5957	356.8713	89.7593
15.0368	−32.2583	10.2965	348.4890	92.3343
15.4432	−43.1022	10.0934	340.2230	94.7842
15.8496	−53.3262	11.3370	332.1897	97.0997
16.2560	−62.8069	12.7956	324.5054	99.3667
16.6624	−71.4213	14.4752	317.2864	101.5929
17.0688	−79.0459	16.3858	310.6493	103.7866
17.4752	−85.5576	18.5424	304.7103	105.9568
17.8816	−90.8332	21.3185	299.5860	108.2263
18.2880	−94.7495	25.2713	295.3926	110.8524
18.6944	−97.1831	29.2202	292.2465	113.5226
19.1008	−98.0108	33.1436	290.2642	116.2510
19.5072	−97.1095	37.0294	289.5620	119.0541
19.9136	−94.3559	40.8767	290.2563	121.9496
20.3200	−89.6267	44.6951	292.4635	124.9527

Source: Output DTN: MO0702PASTRESS.002, file *Model Output DTN.doc*, Table 8-11.

Table 8-12. Stress and SIF Profiles for the Plasticity-Burnished Naval Long Waste Package Outer Lid

Distance from Outer Surface(mm)	SECP (Radial Stress)		ELL (Hoop Stress)	
	Sx (MPa)	K−Sx (MPa√m)	Sx (MPa)	K−Sx (MPa√m)
0.4064	−539.4256	−17.9483	−427.8182	−9.4403
0.8128	−462.7335	−22.6622	−342.0932	−13.0870
1.2192	−391.5169	−24.5417	−261.7957	−15.7063
1.6256	−325.6071	−24.7639	−186.7694	−17.7655
2.0320	−264.8353	−23.8426	−116.8581	−19.4500
2.4384	−209.0327	−22.0731	−51.9054	−20.8568
2.8448	−158.0308	−20.2774	8.2447	−18.7051
3.2512	−111.6606	−18.1813	63.7487	−16.1168
3.6576	−69.7535	−15.6533	114.7627	−13.1794
4.0640	−32.1407	−12.7494	161.4431	−9.9714
4.4704	1.3465	−9.5133	203.9461	−6.5568
4.8768	30.8769	−5.9794	242.4278	−2.9886
5.2832	56.6192	−2.2008	277.0447	0.6173
5.6896	78.7421	1.8491	307.9530	4.2344
6.0960	97.4145	6.1848	335.3088	7.9070
6.5024	112.8050	10.7787	359.2686	11.6084
6.9088	125.0823	15.6038	379.9885	15.3153
7.3152	134.4154	20.6344	397.6247	19.0077
7.7216	140.9727	26.0005	412.3336	22.6634
8.1280	144.9232	32.1659	424.2715	26.2705
8.5344	146.4356	38.7572	433.5945	29.8352
8.9408	145.6786	45.7646	440.4589	33.3463
9.3472	142.8209	53.1787	445.0210	36.7941
9.7536	138.0313	60.9899	447.4371	40.1706
10.1600	131.4785	69.1883	447.8633	43.4690
10.5664	123.3313	75.7990	446.4560	46.7415
10.9728	113.7585	82.6202	443.3715	49.9358
11.3792	102.9286	89.6163	438.7659	53.0484
11.7856	91.0106	96.7504	432.7956	56.0768
12.1920	78.1732	103.9864	425.6167	59.0194
12.5984	64.5850	111.2875	417.3856	61.8761
13.0048	50.4149	119.6266	408.2586	64.7048
13.4112	35.8315	128.5514	398.3918	67.4665
13.8176	21.0037	137.7290	387.9415	70.1443
14.2240	6.1001	147.1219	377.0640	72.7415
14.6304	−8.7104	156.6950	365.9156	75.2627
15.0368	−23.2592	166.4143	354.6525	77.7130
15.4432	−37.3775	180.0773	343.4309	80.0499
15.8496	−50.8966	198.4291	332.4072	82.2619
16.2560	−63.6477	217.8863	321.7376	84.3998
16.6624	−75.4621	238.4456	311.5782	86.4731
17.0688	−86.1710	260.1082	302.0855	88.4922

Table 8-12. Stress and SIF Profiles for the Plasticity-Burnished Naval Long Waste Package Outer Lid (Continued)

Distance from Outer Surface(mm)	SECP (Radial Stress)		ELL (Hoop Stress)	
	Sx (MPa)	K−Sx (MPa√m)	Sx (MPa)	K−Sx (MPa√m)
17.4752	−95.6056	282.8795	293.4157	90.4686
17.8816	−103.5974	311.7154	285.7250	92.6432
18.2880	−109.9774	357.0449	279.1696	95.5196
18.6944	−114.5770	404.2907	273.9059	98.4483
19.1008	−117.2274	453.3914	270.0901	101.4484
19.5072	−117.7599	504.2920	267.8784	104.5400
19.9136	−116.0057	556.9519	267.4272	107.7446
20.3200	−111.7961	611.3402	268.8926	111.0842

Source: Output DTN: MO0702PASTRESS.002, file *Model Output DTN.doc*, Table 8-12.

Figure 8-2 and Figure 8-3 present the variation of hoop stress versus depth for the as-welded and plasticity-burnished waste package outer closure weld lid, respectively. Figure 8-4 and Figure 8-5 present variations of SIF versus depth for the as-welded and plasticity-burnished waste package closure weld lid, respectively. Figure 8-2 through Figure 8-5 are included in output DTN: MO0702PASTRESS.002, *Model Output DTN.doc*, Figures 8-2 through 8-5.

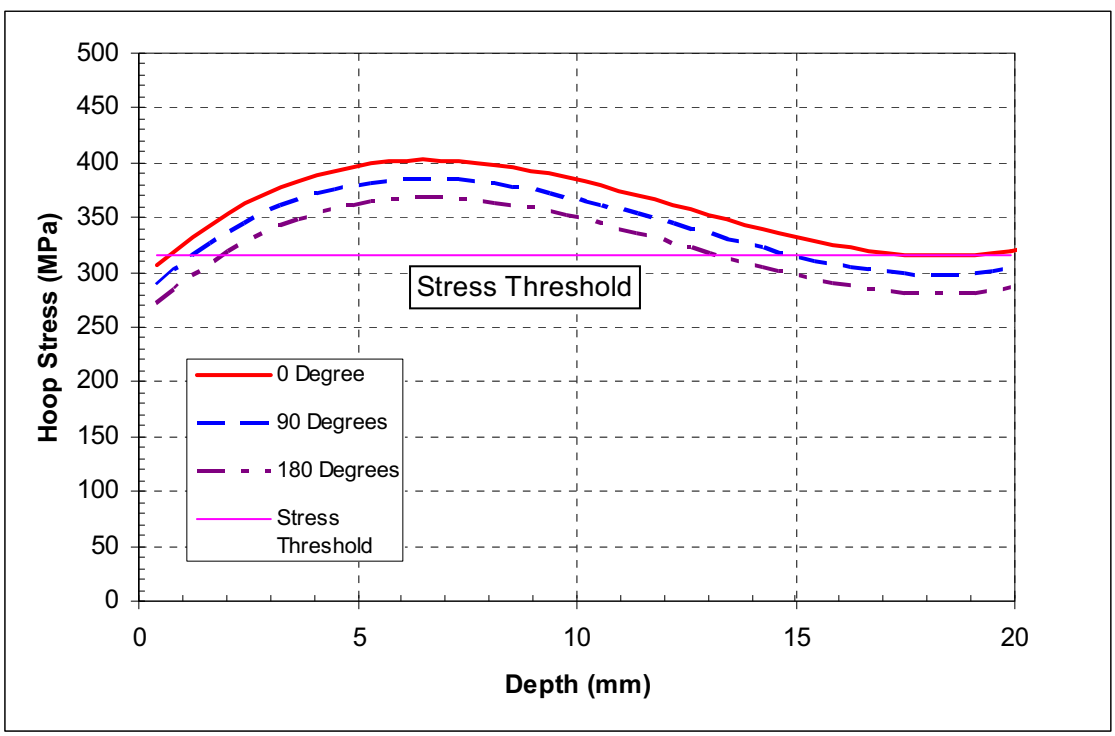

Source: Output DTN: MO0702PASTRESS.002, file *Figure 6-51 (Figure 8-2) Through Figure 6-58 (Figure 8-9).xls*, sheet "Angular S As-Welded."

Figure 8-2. Variation of Hoop Stress versus Depth for As-Welded Waste Package Closure Weld Lid

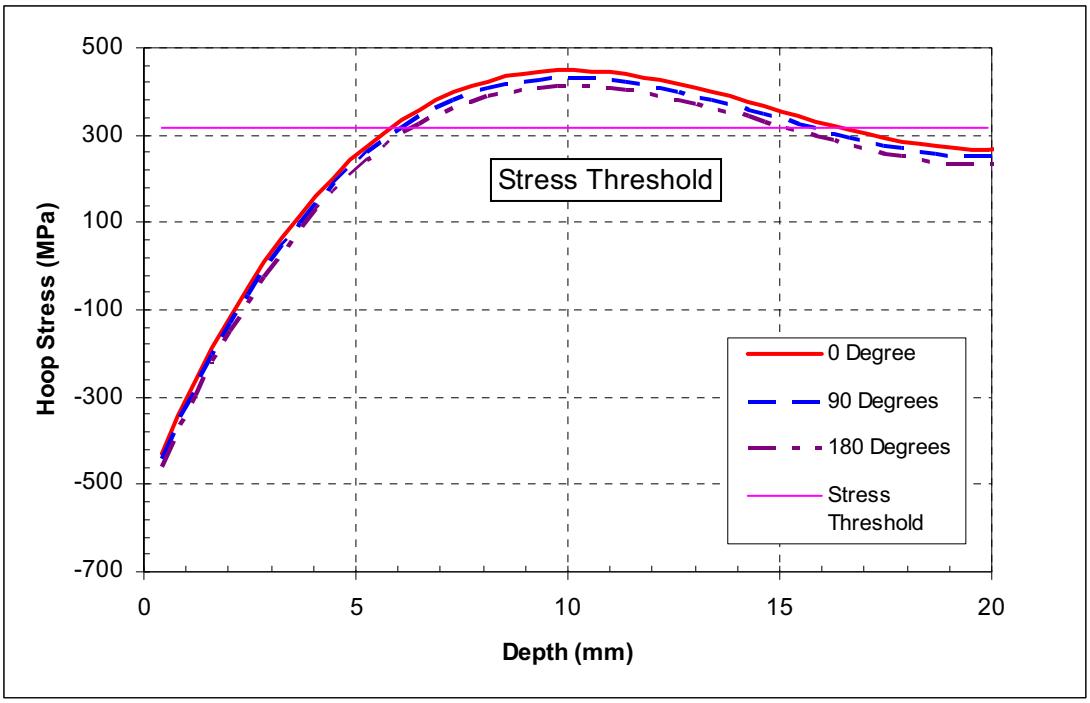

Source: Output DTN: MO0702PASTRESS.002, file *Figure 6-51 (Figure 8-2) Through Figure 6-58 (Figure 8-9).xls*, sheet "Angular S CPB."

Figure 8-3. Hoop Stress versus Depth for Plasticity-Burnished Waste Package Outer Closure Lid with Variability as Function of Angle

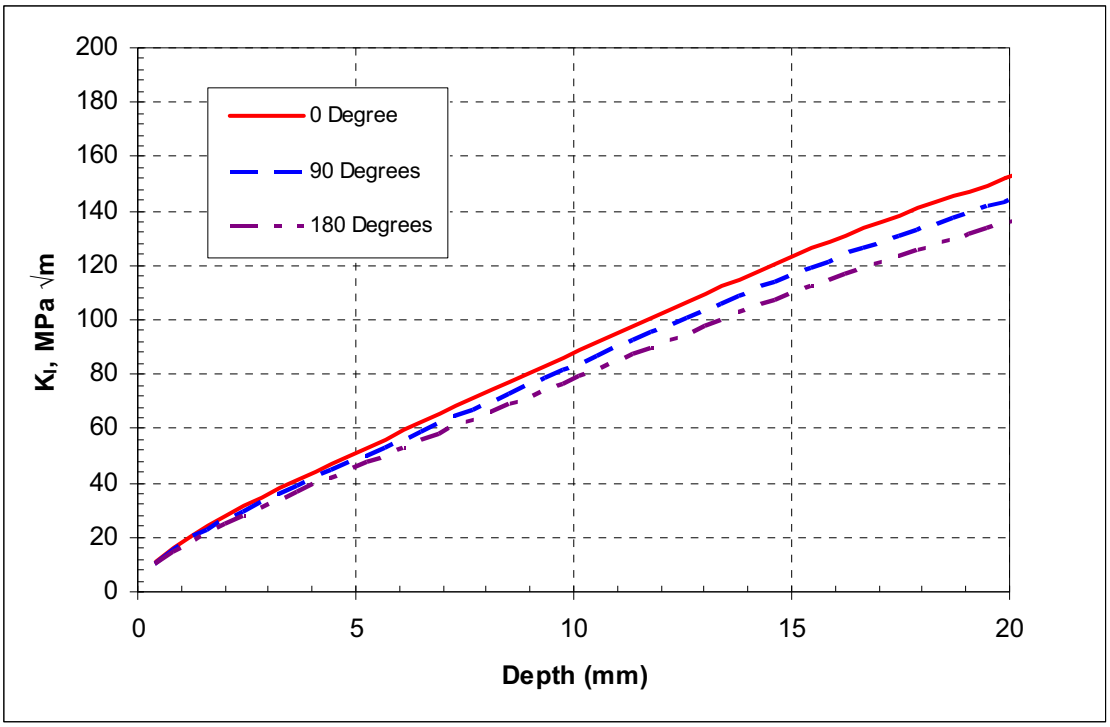

Source: Output DTN: MO0702PASTRESS.002, *Figure 6-51 (Figure 8-2) Through Figure 6-58 (Figure 8-9).xls*, file *"Angular S As-Welded."*

Figure 8-4. Variation of SIF versus Depth for As-Welded Waste Package Outer Closure Weld Lid

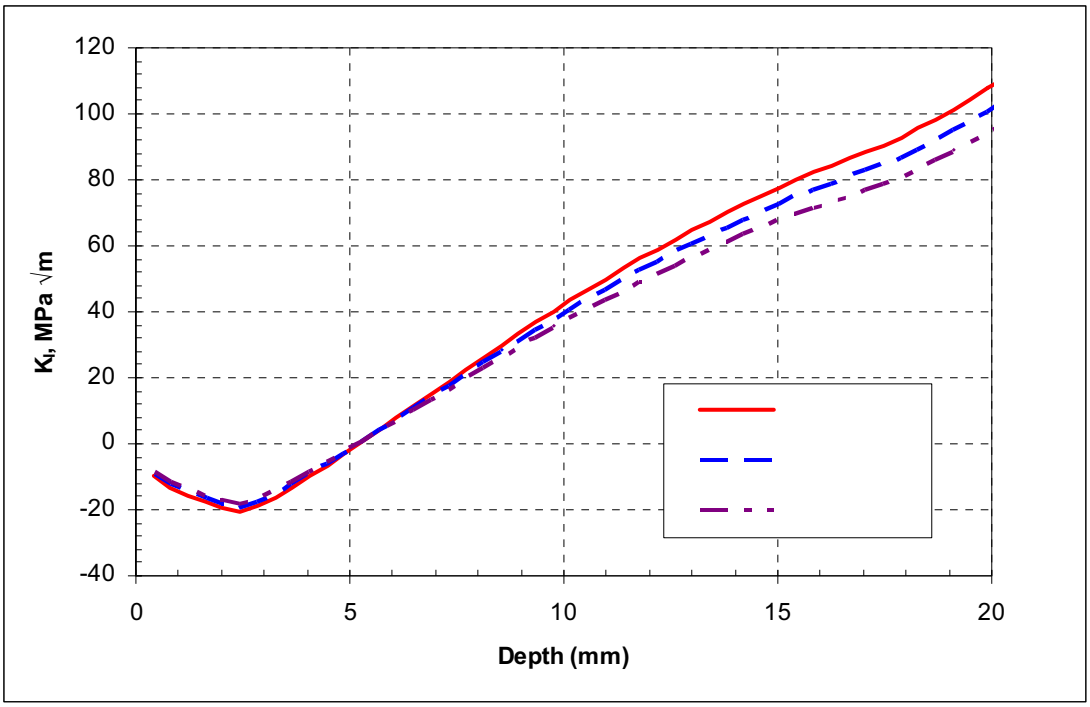

Source: Output DTN: MO0702PASTRESS.002, *Figure 6-51 (Figure 8-2) Through Figure 6-58 (Figure 8-9).xls,* file *"Angular S CPB."*

Figure 8-5. Stress Intensity Factor versus Depth for Plasticity-Burnished Waste Package Outer Closure Lid with Variability as Function of Angle

Uncertainty and Variability of Residual Stress and SIF

igure 8-6 and Figure 8-7 present the uncertainty and variability in hoop stress (θ = 0) versus depth with an uncertainty range of ± 5%, ±10%, and ±15% of the mean yield strength (0.15 yield strength) for as-welded and plasticity-burnished waste package closure weld lids, respectively. Figure 8-8 and Figure 8-9 present the variation of SIF (θ = 0) versus depth with an uncertainty range of ±5%, ±10%, and ±15% of the mean yield strength (0.15 yield strength) for as-welded and plasticity-burnished waste package closure weld lids, respectively. Figure 8-6 through Figure 8-9 are included in output DTN: MO0702PASTRESS.002, *Model Output DTN.doc*, Figures 8-6 through 8-9.

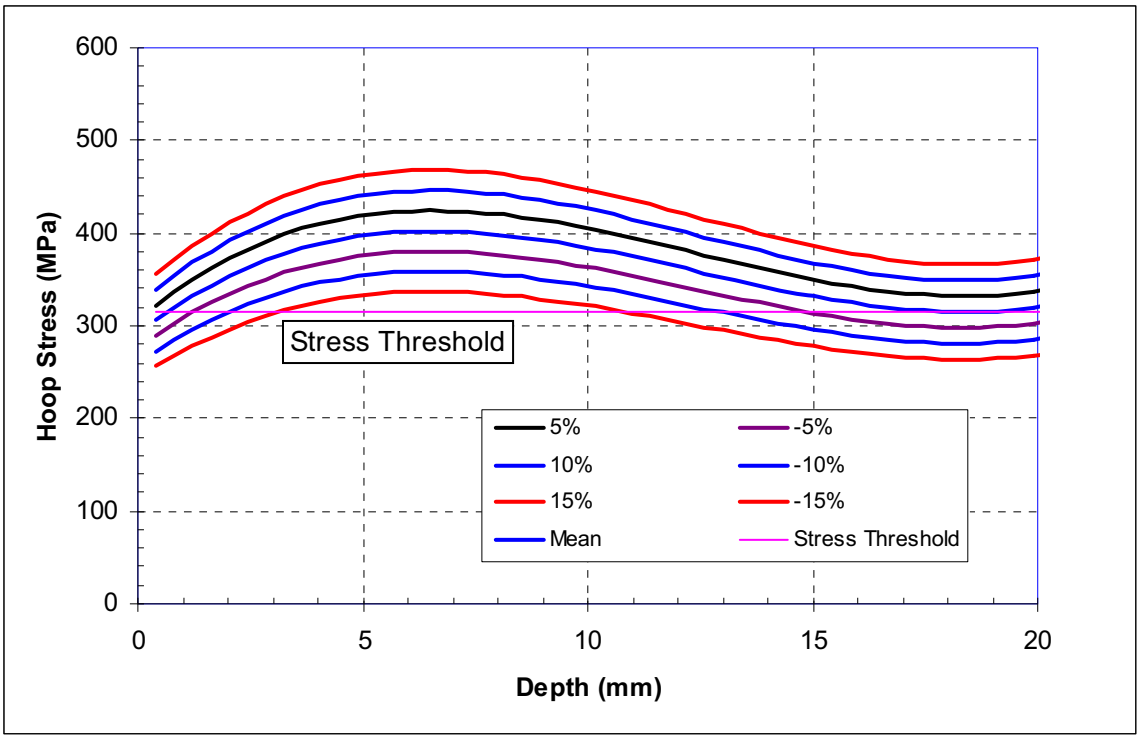

Source: Output DTN: MO0702PASTRESS.002, file *Figure 6-51 (Figure 8-2) Through Figure 6-58 (Figure 8-9).xls,* sheet "Uncertainty As-Welded."

Figure 8-6. Variation of Hoop Stress (θ = 0) versus Depth for As-Welded Waste Package Outer Closure Weld Lid

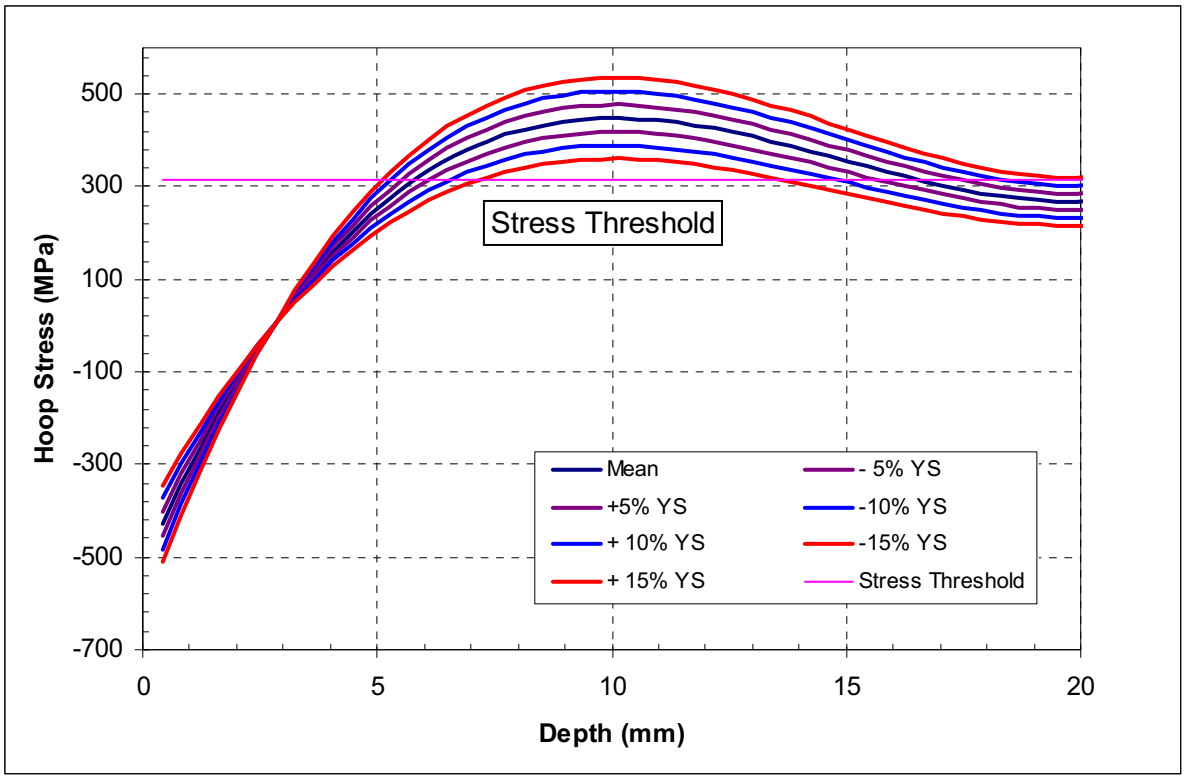

Source: Output DTN: MO0702PASTRESS.002, file *Figure 6-51 (Figure 8-2) Through Figure 6-58 (Figure 8-9).xls*, sheet "Uncertainty CPB."

Figure 8-7. Hoop Stress (θ = 0) versus Depth for Plasticity-Burnished Waste Package Outer Closure Lid with Uncertainty as Function of Yield Strength

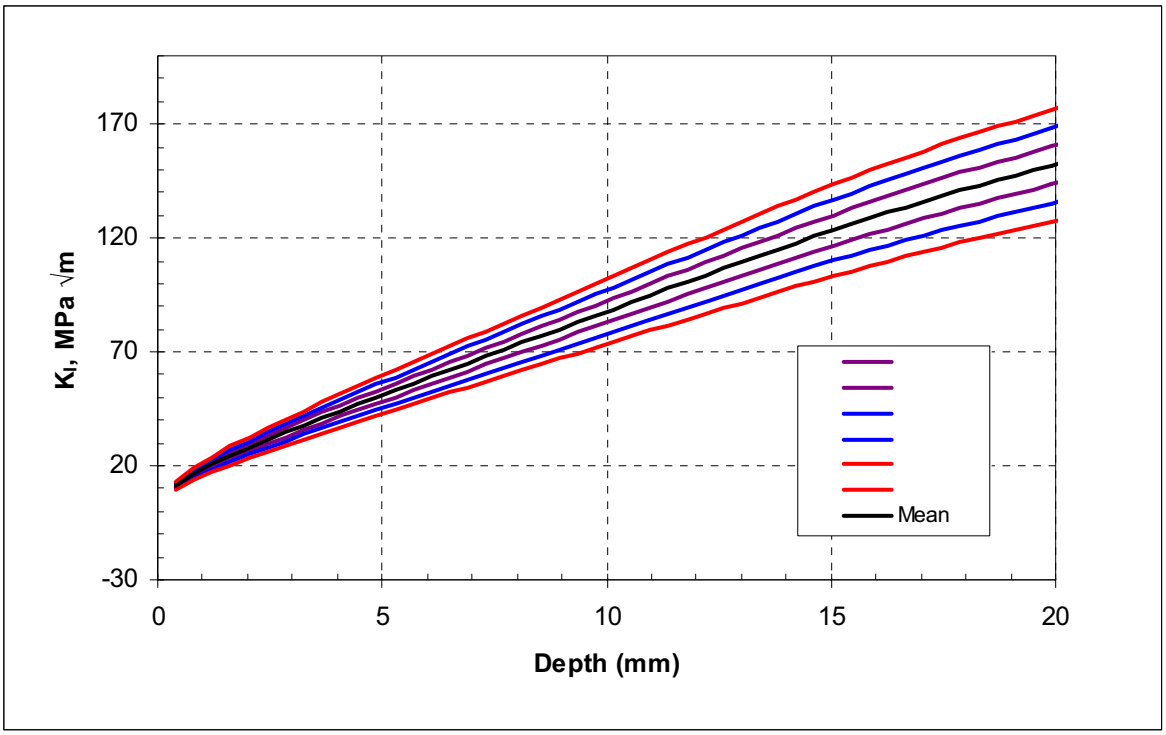

Source: Output DTN: MO0702PASTRESS.002, file *Figure 6-51 (Figure 8-2) Through Figure 6-58 (Figure 8-9).xls*, sheet "Uncertainty As-Welded."

Figure 8-8. Variation of SIF (θ = 0) versus Depth for As-Welded Waste Package Outer Closure Weld Lid

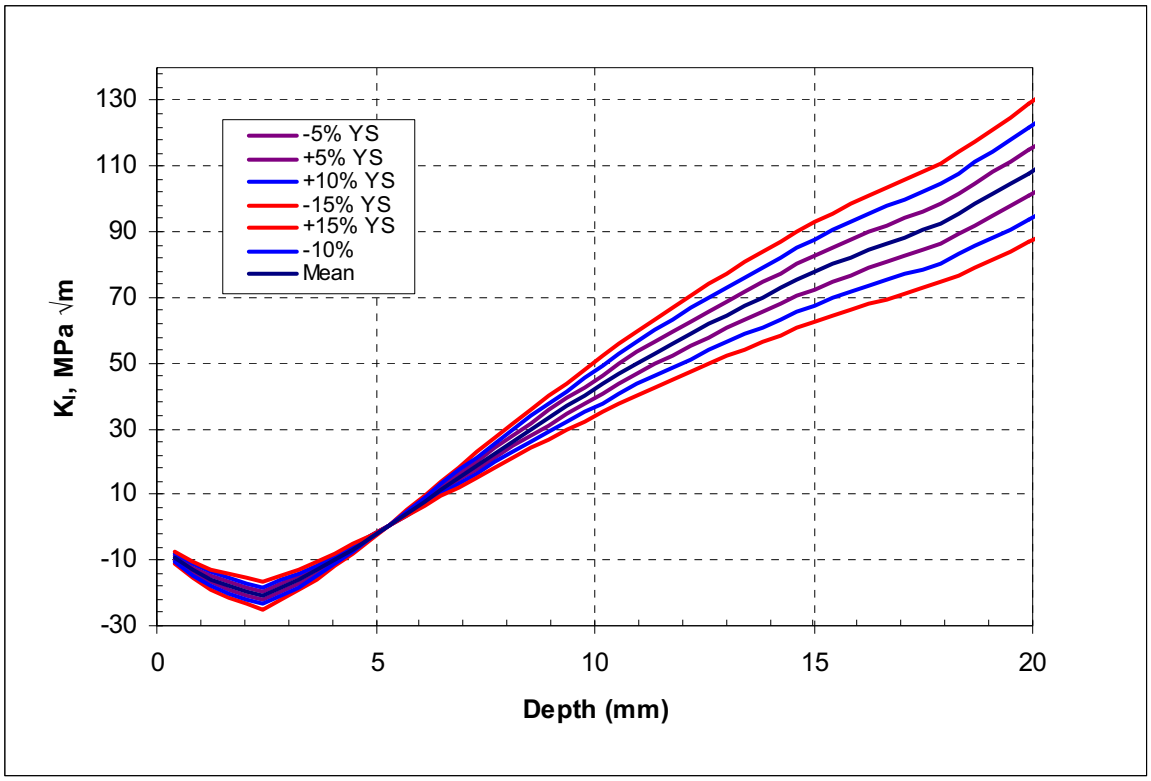

Source: Output DTN: MO0702PASTRESS.002, file *Figure 6-51 (Figure 8-2) Through Figure 6-58 (Figure 8-9).xls*. sheet "Uncertainty CPB."

Figure 8-9. Stress Intensity Factor (θ = 0) versus Depth for Plasticity-Burnished Waste Package Outer Closure Weld Lid with Uncertainty as a Function of Yield Strength

Seismic Crack Density Model for Alloy 22

Table 8-13 summarizes the crack characteristics for hexagonal geometry for seismic crack density model of Alloy 22. Table 8-13 is included in output DTN: MO0702PASTRESS.002, *Model Output DTN.doc*, Table 8-13.

Table 8-13. Crack Characteristics for Alloy 22 for Hexagonal Geometry

Temperature (°C)	Yield Strength (MPa)	Modulus of Elasticity (GPa)	Case	Barrier Thickness[1] (mm)	Crack Length[2] (mm)	Crack Density[3] (/mm^2)	Crack Width[4] (mm)	Crack Opening Area[5] (mm^2)	Crack Area Density[6]
Room	372	206	1		$\frac{2t}{\sqrt{3}}$	$\frac{\sqrt{3}}{2t^2}$	$\delta = \frac{(4c)\sigma}{E}$	$A_{SCC} = \frac{(2\pi c^2)\sigma}{E}$	$\rho_{SCC} A_{SCC} \cong 1.81\frac{\sigma}{E}$
				18	20.78	2.67×10^{-3}	0.075	1.23	3.27×10^{-3}
				20	23.09	2.17×10^{-3}	0.083	1.51	3.27×10^{-3}
				23	31.89	1.64×10^{-3}	0.115	2.89	3.27×10^{-3}
				25	34.67	1.39×10^{-3}	0.125	3.41	3.27×10^{-3}
			2		2t	$\frac{2}{\sqrt{3}t^2}$	$\delta = \frac{(4c)\sigma}{E}$	$A_{SCC} = \frac{(2\pi c^2)\sigma}{E}$	$\rho_{SCC} A_{SCC} \cong 7.26\frac{\sigma}{E}$
				18	36.00	3.56×10^{-3}	0.130	3.68	1.31×10^{-2}
				20	40.00	2.89×10^{-3}	0.144	4.54	1.31×10^{-2}
				23	46.00	2.18×10^{-3}	0.166	6.00	1.31×10^{-2}
				25	50.00	1.85×10^{-3}	0.181	7.09	1.31×10^{-2}
150	310	199	1		$\frac{2t}{\sqrt{3}}$	$\frac{\sqrt{3}}{2t^2}$	$\delta = \frac{(4c)\sigma}{E}$	$A_{SCC} = \frac{(2\pi c^2)\sigma}{E}$	$\rho_{SCC} A_{SCC} \cong 1.81\frac{\sigma}{E}$
				18	20.78	2.67×10^{-3}	0.065	1.06	2.82×10^{-3}
				20	23.09	2.17×10^{-3}	0.072	1.31	2.82×10^{-3}
				23	26.56	1.64×10^{-3}	0.083	1.73	2.82×10^{-3}
				25	28.87	1.39×10^{-3}	0.090	2.04	2.82×10^{-3}
			2		2t	$\frac{2}{\sqrt{3}t^2}$	$\delta = \frac{(4c)\sigma}{E}$	$A_{SCC} = \frac{(2\pi c^2)\sigma}{E}$	$\rho_{SCC} A_{SCC} \cong 7.26\frac{\sigma}{E}$
				18	20.78	2.67×10^{-3}	0.065	1.06	1.19×10^{-2}
				20	23.09	2.17×10^{-3}	0.072	1.31	1.19×10^{-2}
				23	26.56	1.64×10^{-3}	0.083	1.73	1.19×10^{-2}
				25	28.87	1.39×10^{-3}	0.090	2.04	1.19×10^{-2}

Source: Output DTN: MO0702PASTRESS.002, *Model Output DTN.doc*, Table 8-13.

NOTES: [1]Barrier thickness values are for illustration purposes only.

[2]Crack length equals $\frac{2t}{\sqrt{3}}$ for case 1 and *2t* for case 2.

[3]Crack density equals $\frac{\sqrt{3}}{2t^2}$ for case 1 and $\frac{2}{\sqrt{3}t^2}$ for case 2.

[4]Crack width of a single crack is given by Equation 29 for the given thickness for each case.

[5]Crack opening is calculated from Equation 30 for the two cases.

[6]Crack area density is calculated from Equation 33 for case 1 and Equation 36 for case 2.

Seismic Crack Density Model for Drip Shield

Table 8-14 summarizes the crack characteristics for hexagonal geometry for seismic crack density model of drip shield, respectively, and is included in output DTN: MO0702PASTRESS.002, file *Model Output DTN.doc*, Table 8-14.

Table 8-14. Crack Characteristics for Drip Shield for Hexagonal Geometry

Temperature (°C)	Yield Strength (MPa)	Modulus of Elasticity (GPa)	Case	Barrier Thickness[1] (mm)	Crack Length[2] (mm)	Crack Density[3] (/mm^2)	Crack Width[4] (mm)	Crack Opening Area[5] (mm^2)	Crack Area Density[6]
Room	276	107	1		$\frac{2t}{\sqrt{3}}$	$\frac{\sqrt{3}}{2t^2}$	$\delta = \frac{(4c)\sigma}{E}$	$A_{SCC} = \frac{(2\pi c^2)\sigma}{E}$	$\rho_{SCC} A_{SCC} \cong 1.81\frac{\sigma}{E}$
				10	11.54701	0.00866	0.05964	0.54088	0.00467
				15	20.80084	0.00385	0.10744	1.75518	0.00467
				20	27.73445	0.00217	0.14325	3.12032	0.00467
			2		*2t*	$\frac{2}{\sqrt{3}t^2}$	$\delta = \frac{(4c)\sigma}{E}$	$A_{SCC} = \frac{(2\pi c^2)\sigma}{E}$	$\rho_{SCC} A_{SCC} \cong 7.26\frac{\sigma}{E}$
				10	20.00000	0.01155	0.10330	1.62263	0.01875
				15	30.00000	0.00513	0.15495	3.65092	0.01875
				20	40.00000	0.00289	0.20661	6.49053	0.01875
149	176	107	1		$\frac{2t}{\sqrt{3}}$	$\frac{\sqrt{3}}{2t^2}$	$\delta = \frac{(4c)\sigma}{E}$	$A_{SCC} = \frac{(2\pi c^2)\sigma}{E}$	$\rho_{SCC} A_{SCC} \cong 1.81\frac{\sigma}{E}$
				10	11.54701	0.00866	0.04038	0.36619	0.00316
				15	17.32051	0.00385	0.06057	0.82392	0.00316
				20	23.09401	0.00217	0.08076	1.46474	0.00316
			2		*2t*	$\frac{2}{\sqrt{3}t^2}$	$\delta = \frac{(4c)\sigma}{E}$	$A_{SCC} = \frac{(2\pi c^2)\sigma}{E}$	$\rho_{SCC} A_{SCC} \cong 7.26\frac{\sigma}{E}$
				10	11.54701	0.00866	0.04038	0.36619	0.01332
				15	17.32051	0.00385	0.06057	0.82392	0.01332
				20	23.09401	0.00217	0.08076	1.46474	0.01332

Source: Output DTN: MO0702PASTRESS.002, *Model Output DTN.doc*, Table 8-14.

NOTES: [1]Barrier thickness values are for illustration purposes only.
[2]Crack length equals $\frac{2t}{\sqrt{3}}$ for case 1 and *2t* for case 2.
[3]Crack density equals $\frac{\sqrt{3}}{2t^2}$ for case 1 and $\frac{2}{\sqrt{3}t^2}$ for case 2.
[4]Crack width of a single crack is given by Equation 29 for the given thickness for each case.
[5]Crack opening is calculated from Equation 30 for the two cases.
[6]Crack area density is calculated from Equation 33 for case 1 and Equation 36 for case 2.

8.4 TSPA DATA INPUT PACKAGE FOR SCC OF WASTE PACKAGE OUTER BARRIER AND DRIP SHIELD MATERIALS

Not all of the outputs from this report are considered as models. For the TSPA, this report feeds parameters related to: (1) SCC initiation for the waste package; (2) stress and SIF profiles of the waste package, and (3) the slip dissolution-film rupture model for the waste package.

8.4.1 TSPA Parameter(s) Identification and Description

Table 8-15 lists the parameter name, its definition or description, its type, its value and uncertainty or variability, and the source DTN name and number for each TSPA parameter.

8.4.1.1 TSPA Parameter Names

TSPA parameter names are listed in the first column of Table 8-15.

Table 8-15. TSPA Parameter Information/Specification

Parameter Name	Parameter Definition/Description	Parameter Type	Parameter Value and Uncertainty/Variability	Parameter Source DTN
Yield_Strength_A22	Yield strength of Alloy 22 in MPa	Constant	351 MPa at 125°C	MO0702PASTRES S.002. Output DTN of Model Report, *Stress Corrosion Cracking of Waste Package Outer Barrier and Drip Shield Materials*
Defect_Frac_Embedded	Fraction of embedded manufacturing defect flaws able to propagate	Constant	0.25	
Incipient_Crack_Size_OL	Flaw size parameter	Constant	0.05 mm	
WDKIinO	File of stress intensity versus depth for outer lid	Table	4th column of Table 8-12	
Mean_GC_A22	Mean general corrosion rate of Alloy 22	Constant	7.23 nm/yr	
A0_OL	Outer lid stress coefficient	Constant	−519.127	
A1_OL	Outer lid stress coefficient	Constant	231.675	
A2_OL	Outer lid stress coefficient	Constant	−17.377	
A3_OL	Outer lid stress coefficient	Constant	0.388	
fys_OL	Outer lid yield strength scaling factor	Constant	0.15	
z_OL_a	Uncertainty variation in the yield strength of the outer closure lid	Stochastic	Normal distribution (truncated at ±3 SD) Mean = 0; SD = 1; Uncertainty	
Num_Angles_OL	Number of angles at which SIF will be evaluated by SCCD, for the outer lid	Constant	5	
amp_OL	Amplitude of the stress variation with angle, for the outer lid	Constant	17.2369	
n_SCC_a	SCC growth rate exponent (repassivation rate)	Stochastic	Normal distribution (truncated at ±2 SD) Mean = 1.165 SD = 0.115 Uncertainty	
Stress_Thresh_A22	Stress threshold for SCC nucleation	Stochastic	Uncertainty uniformly distributed between 0.9 and 1.05 of yield strength (MPa)	
WP_Crack_Area_Density_a	Ratio of SCC crack area to unit of seismic damaged area for waste packages (“the crack area density”)	Stochastic	Uncertainty uniformly distributed between 3.27×10^{-3} and 1.31×10^{-2} at room temperature	

Table 8-15. TSPA Parameter Information/Specification (Continued)

Parameter Name	Parameter Definition/Description	Parameter Type	Parameter Value and Uncertainty/Variability	Parameter Source DTN
DS_Crack_Area _Density_a	Ratio of SCC crack area to unit of seismic damaged area for drip shields ("the crack area density")	Stochastic	Uncertainty uniformly distributed between 4.67×10^{-3} and 1.875×10^{-2} at room temperature	

Sources: This report, Section 8; Output DTN: MO0702PASTRESS.002.

NOTES: SCCD = the TSPA model, SCCD V. 2.01 ([DIRS 161757]; STN: 10343-2.01-00); SD = standard deviation.

8.4.1.2 TSPA Parameter Definition/Description

TSPA parameter definitions are given in the second column of Table 8-15.

8.4.1.3 TSPA Parameter Type

TSPA parameter types are identified in the third column of Table 8-15.

8.4.1.4 TSPA Parameter Value(s)

Value(s) for the TSPA parameters are provided in column 4 of Table 8-15. If the parameter is treated with uncertainty, uncertainty in the parameter values or their distribution characteristics is also presented in column 4 of Table 8-15. Values for files and tables are not included in Table 8-15 but can be found in the reference provided in column 5 (the output DTN of this report).

8.4.1.5 DTN/Name or Other Reference

The source for all of the TSPA input parameters listed in Table 8-15 is Section 8 of this report and its output DTN: MO0702PASTRESS.002.

8.4.2 TSPA Implementation

This section presents a description of how the parameters defined in Table 8-15 are to be used in the TSPA model.

8.4.2.1 SCC Initiation Implementation

All regions of the Alloy 22 waste package outer barrier, except the outer-closure lid welds, are solution-annealed before the waste packages are loaded with waste. Thus, they do not develop residual stress or SIFs high enough for SCC to occur. The outer closure lid weld is plasticity burnished to produce a layer of compressive stress that prevents SCC initiation until general corrosion removes this layer. Stress and SIF profiles due to weld residual stress in the outer lid subject to plasticity burnishing are used by the SCC initiation and growth abstraction.

SCC can be initiated on a smooth weld surface (with incipient cracks) or at an existing weld flaw. Incipient cracks are considered to be 50-µm (0.05-mm) deep (TSPA parameter Incipient_Crack_Size_OL) at the time of their nucleation and will be initiated on smooth surfaces when general corrosion has penetrated to the depth at which the stress profile exceeds the threshold stress. Stress profiles reflect any stress mitigation performed, so stress mitigation is implicitly incorporated in the TSPA model. The threshold stress (TSPA parameter Stress_Thresh_A22) is taken to be 90% to 105% of the yield strength (TSPA parameter Yield_Strength_A22). Because weld flaws are already formed, they do not require a stress threshold to nucleate. However, most of the weld flaws are embedded within the material and are not exposed to the environment. As general corrosion proceeds, some initially embedded weld flaws may be exposed to the environment while others are corroded away. The evolution of the number of weld flaws is not considered in detail. Instead, a conservative approach is used. Only the fraction of weld flaws embedded within the outer one-fourth (0.25) of the weld thickness (TSPA parameter Defect_Frac_Embedded) is considered capable of propagation.

8.4.2.2 Stress and Stress-Intensity Factor Profile Implementation

The dominant component of stress in the waste package outer barrier closure lid weld regions has been determined to be hoop stress, which promotes radially oriented crack growth on the lid. The hoop stress (σ in MPa) as a function of depth (x in mm) in the closure weld regions of the Alloy 22 waste package outer barrier is given by a third-order polynomial equation of the form:

$$\sigma(x,0) = A_0 + A_1 \times x + A_2 \times x^2 + A_3 \times x^3 \qquad \text{(Eq. 64)}$$

where the values of the coefficients (A_i) are given in Table 8-15 by TSPA parameters A0_OL, A1_OL, A2_OL, and A3_OL.

The second argument in the stress function is used to represent angular variation (θ = 0, arbitrarily chosen) around the circumference of the Alloy 22 waste package outer closure lid weld region. The angular variation is included using the following functional form:

$$\sigma(x,\theta) = \left(\sigma(x,0) - (\text{Amp}) \times (1-\cos(\theta))\right)\left(\frac{\sigma(Thck,\theta)+z}{\sigma(Thck,\theta)}\right) \qquad \text{(Eq.65)}$$

where Amp (TSPA parameter amp_OL) is the amplitude of the stress variation with angle, *Thck* is the lid thickness, and z is the uncertain scaling factor defined in Equation 67.

The calculation is carried out for a discrete number of angles (TSPA parameter Num_Angles_OL). It should be noted that $\sigma(x, 0)$ (defined in Equation 65) uses the stress coefficients (A_i) defined in Table 8-15 with x in units of mm. Based on the angular stress variation in Equation 2, the SIF variation with angle is given by:

$$K_I(x,\theta) = K_I(x) \times \left(\frac{\sigma(Thck,\theta)+z}{\sigma(Thck,0)}\right) \qquad \text{(Eq. 66)}$$

where $K_I(x)$ is given by the values in the table of stress intensity versus depth (TSPA parameter WDKIinO), $\sigma(Thck, \theta)$ is defined in Equation 65, and z is the uncertain scaling factor defined in Equation 67.

The variation of the stress and SIF profiles with angle is due to variability. The uncertainty in the stress and SIF profiles is introduced through a scaling factor, z, defined as:

$$z = \left(\frac{z_OL_a \times Yield_Strength_A22 \times fys_OL}{3} \right) \qquad \text{(Eq. 67)}$$

The parameter z_OL_a is sampled from a standard normal distribution; its use in Equation 67 results in a scaling factor, z, that follows a normal distribution with a mean of zero and a standard deviation of 5% of the yield strength (TSPA parameter Yield_Strength_A22) and has an upper-bound of 15% of the yield strength and a lower-bound of −15% of the yield strength (TSPA parameter fys_OL).

In the TSPA model, SCCD V. 2.01 ([DIRS 161757]; STN: 10343-2.01-00) calculates the variation in stress and stress-intensity factor versus depth and angle. The details of this calculation are given in Section 2 of *SCCD Software Routine Report* (CRWMS M&O 2000 [DIRS 152499]). These input parameters are defined in Table 8-15.

8.4.2.3 Slip Dissolution-Film Rupture Model Implementation

The abstraction of SCC initiation and growth, due to both incipient cracks and weld flaws, uses the SDFR mechanism. Inputs to the SDFR mechanism include threshold stress, threshold SIF, an incipient crack size, and crack-growth-rate parameters. The threshold SIF is a function of the repassivation slope and the mean general corrosion rate. Crack growth velocity is a function of the SIF and repassivation slope.

If the calculated SIF at the incipient crack or weld flaw tip is greater than the calculated threshold SIF, then the crack or flaw will grow.

The threshold SIF, K_{ISCC}, is given in Equation 68 as a function of the repassivation slope, n, and V_{gc} (TSPA parameter Mean_GC_A22, which equals 7.23 nm/yr and is expressed in units of mm/sec for use in Equation 68):

$$K_{ISCC} = \left(\frac{V_{gc}}{\overline{A}} \right)^{1/\overline{n}} \qquad \text{(Eq. 68)}$$

where $\overline{A}$ and $\overline{n}$ are functions of n as defined in Equation 69 and Equation 70. Although TSPA treats the Alloy 22 general corrosion rate as uncertain, for this analysis it is treated as a constant value (i.e., the mean value (V_{gc})), because of the minimal impact on K_{ISCC}, which is already treated with uncertainty. The threshold SIF is applied to both incipient cracks and weld flaws. The variations in the threshold stress and SIF distributions are entirely due to epistemic uncertainty. The thresholds are sampled once per realization of the TSPA model (i.e., the same value of these thresholds is used for each lid in a given realization).

The depth of the crack or weld flaw tip is the sum of the general corrosion depth and the crack or weld flaw length. If the depth of the tip exceeds the weld thickness, then failure occurs.

Cracks, once initiated, grow at a rate given by:

$$V = \overline{A}\left(K_I\left(x,\theta\right)\right)^{\overline{n}} \qquad \text{(Eq. 69)}$$

where V is the crack velocity in mm/yr, K_I is the SIF defined in Equation 66, $\overline{A}$ is defined by Equation 70, and $\overline{n}$ is defined by Equation 71.

The crack growth parameters ($\overline{A}$ and $\overline{n}$) are defined by Equations 15, 16, and 17 (Section 6.4.3) and by the repassivation slope (TSPA parameter n_SCC_a) in this report (Section 6.4.4). Equations 15 and 16 are reproduced below as Equations 70 and 71:

$$\overline{A} = 7.8\times10^{-2} n^{3.6}\left(4.1\times10^{-14}\right)^{n} \qquad \text{(Eq. 70)}$$

$$\overline{n} = 4n \qquad \text{(Eq. 71)}$$

where n is the repassivation slope. Equation 70 must be multiplied by the number of s/yr to obtain the crack velocity in mm/yr.

SCC initiation and growth is implemented in TSPA by the use of a slip dissolution-film rupture event in the WAPDEG software (BSC 2002 [DIRS 162606], Sections 3.3.2.1.1 and 4.2.7.5). Stress corrosion cracking due to both incipient cracks and weld flaws is analyzed using the slip dissolution-film rupture event. When a slip dissolution-film rupture event includes weld flaws (defects), the weld flaw density, and size distribution are defined by a manufacturing defect event in the WAPDEG software (BSC 2002 [DIRS 162606], Sections 3.3.2.1 and 4.2.7.2). The incipient crack size is given by the parameter Incipient_CrackSize_OL. The density of incipient cracks is determined by the plate thickness, as discussed in Section 6.3.2, because the minimum spacing between parallel through-wall radial cracks must be greater than the plate thickness to ensure the stress (and resultant SIF) will be sufficient to drive a crack through-wall.

The slip dissolution-film rupture event also requires a stress threshold or a SIF threshold, or both, for crack growth initiation. These thresholds are defined separately for incipient cracks and weld flaws. The values of stress threshold and SIF threshold are defined in Section 6.2.

Uncertainty in the crack growth and in the SIF threshold is represented by the uncertainty in the repassivation slope. The repassivation slope is sampled once for every realization in the TSPA model. The stress and SIF tables, produced by the SCCD Dynamic Link Library, also include uncertainty due to the use of a scaling factor that describes the deviation from the median stress/SIF. This scaling factor is sampled once every realization.

8.4.2.4 SCC Seismic Damage Implementation

As indicated in Section 6.7, the seismic scenario requires three inputs to represent the effective area of a network of cracks:

(1) Total damaged area on the waste package, A_D

(2) Crack density in the damaged area on the surface of the barrier, ρ_{SCC}

(3) Crack opening area of an individual crack, A_{SCC}.

The damage abstractions for the seismic scenario will define the total damaged area on the barrier (SNL 2007 [DIRS 176828]). The total area of the crack network, $A_{SCC,\ NET}$, is then the product of the seismically damaged area, A_D; the crack density, ρ_{SCC} (# cracks per unit area); and the crack opening area of an individual crack, A_{SCC} (area/crack), expressed as (Herrera 2004 [DIRS 168133], Section 6.1):

$$A_{SCC,\ NET} = A_D\ (\rho_{SCC}\ A_{SCC}) \qquad \text{(Eq. 72)}$$

Not all seismically damaged areas on the waste package are open to radionuclide leakage. The factor ($\rho_{SCC}\ A_{SCC}$) is the crack area density or crack area per unit of seismically damaged area (i.e., the fraction of the seismically damaged area) through which radionuclides can be released. The factor ($\rho_{SCC}\ A_{SCC}$) can be viewed as a scaling factor applied to the seismically damaged area to obtain the total area of the crack network, $A_{SCC,\ NET}$. Sections 6.7.3 and 6.7.4 provide estimates of the crack area density ($\rho_{SCC}\ A_{SCC}$) through analysis of networks of cracks arranged in hexagonal and circular geometries, respectively, circumscribed by a single through-wall crack. Because the hexagonal array represents a high effective density (close spacing) of individual cracks, this hexagonal case, with crack center spacings set at the plate thickness, t, (Section 6.7.3) is considered a conservative representation.

A similar approach is adopted for the seismic crack density model outputs as discussed in Sections 6.8.5.2.2 and 6.8.5.2.3 for drip shield based on hexagonal and circular geometries, respectively.

TSPA requires the effective area for transport through the waste package and drip shield, rather than the damaged area that exceeds the residual stress threshold for the material. The effective area is determined by the density of SCC cracks and the area of individual cracks in the regions where the residual stress exceeds the residual stress threshold. The product of the crack density per unit surface area and the area per crack defines the effective area of the SCC network per unit area of damaged surface.

Seismically damaged areas are represented in the TSPA model as a dense network of SCC cracks. The effective area for transport through the crack network is determined by the product of two random parameters. The first parameter is the factor defining the ratio of effective area for transport to damaged area on the material and is given by the product of the crack density per unit surface area and the gap area per crack. The second parameter is the damaged area. The product of these two parameters determines the effective area for transport.

8.4.3 Statement and Justification of Uncertainty Treatment

To the extent that uncertainties are treated, a discussion of uncertainties and their justifications is included in this report. The information presented in this section is reproduced from earlier sections. In summary:

- The uncertainty of SCC initiation threshold stress for Alloy 22 is treated as uniformly distributed between 0.9 and 1.05 of the yield strength of Alloy 22 (Section 6.2.2)

- The uncertainty of the repassivation slope, *n*, is treated as a normal distribution (truncated at ±2 SD) with mean = 1.165 and SD = 0.115 (Section 6.4.4)

- The uncertainty and variability of residual stress and SIF are discussed in Section 6.5.6

- Stress variation and SIF variation with angle are discussed in Section 6.5.6.1 (Equations 24 and 25, respectively)

- The crack area density is recommended to be represented as a uniform distribution between $\frac{\pi\sigma}{\sqrt{3}E}$ and $\frac{4\pi\sigma}{\sqrt{3}E}$, i.e.:

$$\text{Crack Area Density} = C\frac{\pi\sigma}{\sqrt{3}E} \qquad \text{(Eq. 73)}$$

  where C is the epistemic uncertainty factor given by a uniform distribution between 1 and 4

- The use of a uniform distribution is reasonable as it accurately reflects the lack of knowledge of the exact value of the crack area density. In general, a uniform distribution is appropriate for uncertain quantities where the range can be established by physical arguments or expert knowledge but where not much else is known about the relative likelihood of values within the range (Mishra 2002 [DIRS 163603], Section 2.3). The use of a distribution ranging up to the very conservative upper bound allows for uncertainties, such as the potential for crack overlap and deviations from a regular array of identically shaped cracks, to be appropriately accounted for.

In addition, for TSPA purposes, the following uncertainty treatments are adopted:

- Uncertainty in the stress and SIF profiles is included via an uncertainty scaling factor, *z*, given by Equation 65

- Uncertainty in the probability of occurrence and the density and size distributions for weld flaws is included via the stochastic elements (Defect_Count_a and Defect_Size_a)

- Spatial variability is included in the crack growth analysis via the stress factor-versus-depth and SIF-versus-depth tables. A new set of tables is calculated for every realization due to the epistemic uncertainty in *z*.

INTENTIONALLY LEFT BLANK

9. INPUTS AND REFERENCES

9.1 DOCUMENTS CITED

178194 Alloy Digest 1985. Hastelloy Alloy C-22. Filing Code: Ni-317. Orange, New Jersey: Alloy Digest. TIC: 239931.

166965 Andresen, P.L. 1991. "Fracture Mechanics Data and Modeling of Environmental Cracking of Nickel-Base Alloys in High Temperature Water." *Corrosion 91, The NACE Annual Conference and Corrosion Show, March 11-15, 1991, Cincinnati, Ohio.* Paper No. 44. Houston, Texas: National Association of Corrosion Engineers. TIC: 255507.

166966 Andresen, P.L. 1993. "Effects of Temperature on Crack Growth Rate in Sensitized Type 304 Stainless Steel and Alloy 600." *Corrosion, 49,* (9), 714-725. Houston, Texas: NACE International. TIC: 255500.

173867 Andresen, P.L. 2005. *Stress Corrosion Crack Initiation & Growth Measurements in Environments Relevant to High Level Nuclear Waste Packages*. Schenectady, New York: General Electric Global Research Center. ACC: MOL.20050608.0317.

162528 Andresen, P.L. and Ford, F.L. 1985. "Modeling and Life Prediction of Stress Corrosion Cracking in Sensitized Stainless Steel in High-Temperature Water." *Predictive Capabilities in Environmentally Assisted Cracking, Presented at the Winter Annual Meeting of the American Society of Mechanical Engineers, Miami Beach, Florida, November 17-22, 1985.* Rungta, R., ed. PVP-Vol. 99. Pages 17-38. New York, New York: American Society of Mechanical Engineers. TIC: 254383.

118581 Andresen, P.L. and Ford, F.P. 1994. "Fundamental Modeling of Environment Cracking for Improved Design and Lifetime Evaluation in BWRs." *International Journal of Pressure Vessels and Piping, 59 (1-3),* 61-70. New York, New York: Elsevier. TIC: 247388.

167762 Andresen, P.L.; Angeliu, T.M.; Young, L.M.; Catlin, W.R.; and Horn, R.M. 2002. "Mechanisms and Kinetics of SCC in Stainless Steels." *Tenth International Conference on Environmental Degradation of Materials in Nuclear Power Systems–Water Reactors, August 5 to 9, 2001, Lake Tahoe, Nevada.* Houston, Texas: NACE International. TIC: 252999.

167840 Andresen, P.L.; Emigh, P.W.; Young, L.M.; and Gordon, G.M. 2001. "Stress Corrosion Cracking of Annealed and Cold Worked Titanium Grade 7 and Alloy 22 in 110°C Concentrated Salt Environments." *Corrosion/2001, 56th Annual Conference & Exposition, March 11-16, 2001, Houston, Texas, USA.* Paper No. 01130. Houston, Texas: NACE International. TIC: 255671.

178449 Andresen, P.L.; Morra, M.M.; and Catlin, W.R. 2004. "Effects of Yield Strength, Corrosion Potential, Composition and Stress Intensity Factor in SCC of Stainless Steels." *Corrosion/2004, 59th Annual Conference & Exposition, March 28-April 1, 2004, New Orleans.* Paper No. 04678. Houston, Texas: NACE International. TIC: 255943.

166967 Andresen, P.L.; Young, L.M.; Emigh, P.W.; and Horn, R.M. 2002. "Stress Corrosion Crack Growth Rate Behavior of Ni Alloys 182 and 600 in High Temperature Water." *Corrosion/2002, 57th Annual Conference & Exposition, April 7-11, 2002, Denver, Colorado.* Paper No. 02510. Houston, Texas: NACE International. TIC: 255502.

103753 ASM International 1987. *Corrosion.* Volume 13 of *Metals Handbook.* 9th Edition. Metals Park, Ohio: ASM International. TIC: 209807.

141615 ASM International 1990. *Properties and Selection: Nonferrous Alloys and Special-Purpose Materials.* Volume 2 of *ASM Handbook.* Formerly Tenth Edition, Metals Handbook. 5th Printing 1998. Materials Park, Ohio: ASM International. TIC: 241059.

162446 ASME (American Society of Mechanical Engineers) 1969. *Criteria of the ASME Boiler and Pressure Vessel Code for Design by Analysis in Sections III and VIII, Division 2.* New York, New York: American Society of Mechanical Engineers. TIC: 254727.

158115 ASME 2001. *2001 ASME Boiler and Pressure Vessel Code (includes 2002 addenda).* New York, New York: American Society of Mechanical Engineers. TIC: 251425.

164859 Averbach, B.L. 1968. "Microcrack Formation." Section III of Chapter 7 of *Fracture, An Advanced Treatise.* Liebowitz, H., ed. Pages 449-455. New York, New York: Academic Press. TIC: 254807.

154496 Barkatt, A. and Gorman, J.A. 2000. *Tests to Explore Specific Aspects of the Corrosion Resistance of C-22.* Presentation to the Nuclear Waste Technical Review Board on August 1, 2000, Carson City, Nevada. Washington, D.C.: Catholic University of America. TIC: 249714.

168354 Beavers, J. 2004. "Report Review." E-mail from J. Beavers to P. Pasupathi, February 24, 2004, with attachment. ACC: MOL.20040311.0147.

159767 Been, J. and Grauman, J.S. 2000. "Titanium and Titanium Alloys." Chapter 47 of *Uhlig's Corrosion Handbook.* 2nd Edition. Revie, R.W., ed. New York, New York: John Wiley & Sons. TIC: 248360.

164860 Bernstein, M.D. 1988. "Design Criteria for Boilers and Pressure Vessels in the U.S.A." *Journal of Pressure Vessel Technology, 110,* 430-443. New York, New York: American Society of Mechanical Engineers. TIC: 254806.

162429 Bokhari, S.A. 2003. "Approved Baseline Change Proposal (BCP) YMP-2003-005, Design Changes to Site Recommendation (SR) Waste Package." Memorandum from S.A. Bokhari (DOE) to W.J. Arthur, III (OCRWM/CCB), R.A. Milner (OCRWM/CCB), and R.D. Brown (OCRWM/CCB), January 30, 2003, with attachments. ACC: MOL.20030508.0040.

177436 Boyce, B.L. and Ritchie, R.O. 2001. "Effect of Load Ratio and Maximum Stress Intensity on the Fatigue Threshold in Ti-6Al-4V." *Engineering Fracture Mechanics, 68,* 129-147. New York, New York: Pergamon. TIC: 258528.

177440 Boyer, H.E., ed. 1997. *Atlas of Creep and Stress-Rupture Curves.* 2nd Printing. Metals Park, Ohio: ASM International. TIC: 258538.

155318 Boyer, H.E. and Gall, T.L., eds. 1984. *Metals Handbook*. Desk Edition. 10th Printing 1997. Metals Park, Ohio: American Society for Metals. TIC: 250192.

174636 Boyer, R.; Welsch, G.; and Collings, E.W. 2003. *Materials Properties Handbook: Titanium Alloys.* Materials Park, Ohio: ASM International. TIC: 257276.

151988 Bradford, S.A. 1987. "Fundamentals of Corrosion in Gases." In *Corrosion,* Volume 13, Pages 61-76 of *Metals Handbook.* 9th Edition. Metals Park, Ohio: ASM International. TIC: 209807.

156807 BSC (Bechtel SAIC Company) 2001. *Plugging of Stress Corrosion Cracks by Precipitates.* CAL-EBS-MD-000017 REV 00. Las Vegas, Nevada: Bechtel SAIC Company. ACC: MOL.20011010.0168.

162606 BSC 2002. *Users' Manual for WAPDEG 4.07.* SDN: 10000-UM-4.07-00. Las Vegas, Nevada: Bechtel SAIC Company. ACC: MOL.20030409.0233; MOL.20040427.0343.

171924 BSC 2004. *Aging and Phase Stability of Waste Package Outer Barrier.* ANL-EBS-MD-000002 REV 02. Las Vegas, Nevada: Bechtel SAIC Company. ACC: DOC.20041005.0003.

169766 BSC 2004. *Commercial SNF Waste Package Design Report.* 000-00C-DSU0-02800-000-00B. Las Vegas, Nevada: Bechtel SAIC Company. ACC: ENG.20040709.0001; ENG.20050817.0021.

166894 BSC 2004. *Naval Waste Package Design Report.* 000-00C-DNF0-00800-000-00A. Las Vegas, Nevada: Bechtel SAIC Company. ACC: ENG.20040316.0010; ENG.20050817.0012.

172203 BSC 2004. *Stress Corrosion Cracking of the Drip Shield, the Waste Package Outer Barrier, and the Stainless Steel Structural Material.* ANL-EBS-MD-000005 REV 02. Las Vegas, Nevada: Bechtel SAIC Company. ACC: DOC.20041028.0008; DOC.20050621.0003.

171499 BSC 2004. *Waste Package Closure System Description Document.* 100-3YD-HW00-00100-000-003. Las Vegas, Nevada: Bechtel SAIC Company. ACC: ENG.20040927.0003.

174715 BSC 2005. *Creep Deformation of the Drip Shield.* CAL-WIS-AC-000004 REV 0A. Las Vegas, Nevada: Bechtel SAIC Company. ACC: DOC.20050830.0007.

175539 BSC 2005. *Q-List.* 000-30R-MGR0-00500-000-003. Las Vegas, Nevada: Bechtel SAIC Company. ACC: ENG.20050929.0008.

174836 BSC 2005. *Safety Classification of SSCs and Barriers.* 000-00C-MGR0-03000-000 REV 00A. Las Vegas, Nevada: Bechtel SAIC Company. ACC: ENG.20050805.0004; ENG.20050929.0004.

173492 BSC 2005. *Waste Package Behavior in Magma.* 000-00C-SSE0-00600-000-00A. Las Vegas, Nevada: Bechtel SAIC Company. ACC: ENG.20050502.0005; ENG.20050817.0027.

174922 BSC 2006. *Naval Long Waste Package Configuration.* 000-MW0-DNF0-00102-000 REV 00B. Las Vegas, Nevada: Bechtel SAIC Company. ACC: ENG.20061120.0003.

174923 BSC 2006. *Naval Long Waste Package Configuration.* 000-MW0-DNF0-00103-000 REV 00B. Las Vegas, Nevada: Bechtel SAIC Company. ACC: ENG.20061120.0004.

178479 BSC 2006. *TMRB Decision Proposal, Delete Inner Alloy 22 Waste Package Closure Lid (Middle Lid).* TMRB-2006-16. Las Vegas, Nevada: Bechtel SAIC Company. ACC: MOL.20061028.0242.

118597 Buchalet, C.B. and Bamford, W.H. 1976. "Stress Intensity Factor Solutions for Continuous Surface Flaws in Reactor Pressure Vessels." *Mechanics of Crack Growth, Proceedings of the Eighth National Symposium on Fracture Mechanics, Providence, Rhode Island, 26-28 August 1974.* ASTM Special Technical Publication 590. Pages 385-402. Philadelphia, Pennsylvania: American Society for Testing and Materials. TIC: 247548.

147968 Chan, S.K.; Tuba, I.S.; and Wilson, W.K. 1970. "On Finite Element Method in Linear Fracture Mechanics." *Engineering Fracture Mechanics,* 1-17. Oxford, United Kingdom: Pergamon Press. TIC: 247507.

165441 Chen, H.-L.; Evans, K.J.; Hackel, L.A.; Rankin, J.E.; Yamamoto, R.M.; Demma, A.G.; Dewald, A.T.; Lee, M.J.; and Hill, M.R. 2002. *Mitigation of Tensile Weld Stresses in Alloy 22 Using Laser Peening.* UCRL-ID-151055. Livermore, California: Lawrence Livermore National Laboratory. ACC: MOL.20030911.0252.

178444 Chiang, K.T.; Dunn, D.S.; and Cragnolino, G.A. 2005. "Effect of Simulated Groundwater Chemistry on Stress Corrosion Cracking of Alloy 22." *Corrosion/2005, 60th Annual Conference & Exposition, 1945-2005, April 3-7, 2005, George R. Brown Convention Center, Houston, Texas.* Paper No. 05463. Houston, Texas: NACE International. TIC: 257165.

105212 Cowan, J.C. and Weintritt, D.J. 1976. *Water-Formed Scale Deposits.* Houston, Texas: Gulf Publishing Company. TIC: 245620.

102933 CRWMS M&O 1999. *Waste Package Materials Properties.* BBA000000-01717-0210-00017 REV 00. Las Vegas, Nevada: CRWMS M&O. ACC: MOL.19990407.0172.

152499 CRWMS M&O 2000. *SCCD Software Routine Report.* SDN: 10343-SRR-2.01-00. Las Vegas, Nevada: CRWMS M&O. ACC: MOL.20010205.0113.

160320 D'Agostino, R.B. and Stephens, M.A., eds. 1986. *Goodness-Of-Fit Techniques.* Statistics, Textbooks and Monographs Volume 68. New York, New York: Marcel Dekker. TIC: 253256.

182051 DOE (U.S. Department of Energy) 2007. *Quality Assurance Requirements and Description*. DOE/RW-0333P, Rev. 19. Washington, D. C.: U.S. Department of Energy, Office of Civilian Radioactive Waste Management. ACC: DOC.20070717.0006.

178207 Donachie, M.J. 2002. "Selection of Titanium Alloys for Design." Chapter 6 of *Handbook of Materials Selection.* Kutz, M., ed. New York, New York: John Wiley & Sons. TIC: 258794.

154481 Dunn, D.S.; Pan, Y-M.; and Cragnolino, G.A. 1999. *Effects of Environmental Factors on the Aqueous Corrosion of High-Level Radioactive Waste Containers—Experimental Results and Models.* CNWRA 99-004. San Antonio, Texas: Center for Nuclear Waste Regulatory Analyses. TIC: 246615.

177469 Dunn, D.S.; Pan, Y.-M.; Chiang, K.T.; and Cragnolino, G.A. 2006. "Surface Analysis of Alloy 22 Under Conditions that Promote Stress Corrosion Cracking." *Corrosion 2006, 61st Annual Conference & Exposition, San Diego Convention Center, March 12-16, 2006.* Paper No. 06509. Houston, Texas: NACE International. TIC: 258178.

178104 Dunn, D.S.; Pensado, O.; Pan, Y.-M; Pabalan, R.T.; Yang, L.; He, X.; and Chiang, K.T. 2005. *Passive and Localized Corrosion of Alloy 22 - Modeling and Experiments.* CNWRA 2005-02. San Antonio, Texas: Center for Nuclear Waste Regulatory Analyses. ACC: LLR.20070305.0002.

174750 Dutton, R. 1996. *A Review of the Low-Temperature Creep Behaviour of Titanium.* AECL-11544. Pinawa, Manitoba, Canada: Whiteshell Laboratories, Atomic Energy of Canada Limited. TIC: 231204.

175817 Dutton, R.; Leitch, B.W.; Crosthwaite, J.L.; and Kasprick, G.R. 1996. *Preliminary Analysis of the Creep Behaviour of Nuclear Fuel-Waste Container Materials.* AECL-11495. Pinawa, Manitoba, Canada: Atomic Energy of Canada Limited. TIC: 232683.

167274 Estill, J.C.; King, K.J.; Fix, D.V.; Spurlock, D.G.; Hust, G.A.; Gordon, S.R.; McCright, R.D.; Rebak, R.B.; and Gordon, G.M. 2002. "Susceptibility of Alloy 22 to Environmentally Assisted Cracking in Yucca Mountain Relevant Environments." *Corrosion/2002, 57th Annual Conference & Exposition, April 7-11, 2002, Denver, Colorado.* Paper No. 02535. Houston, Texas: NACE International. TIC: 252066.

118602 Ewalds, H.L. and Wanhill, R.J.H. 1984. *Fracture Mechanics.* New York, New York: Edward Arnold. TIC: 247389.

162700 Fix, D.V.; Estill, J.C.; Hust, G.A.; King, K.J.; Day, S.D.; and Rebak, R.B. 2003. "Influence of Environmental Variables on the Susceptibility of Alloy 22 to Environmentally Assisted Cracking." *Corrosion/2003, 58th Annual Conference & Exposition, March 16-20, 2003, San Diego, California.* Paper No. 03542. Houston, Texas: NACE International. TIC: 254387.

169321 Fix, D.V.; Estill, J.C.; Wong, L.L.; and Rebak, R.B. 2004. "Susceptibility of Welded and Non-Welded Titanium Alloys to Environmentally Assisted Cracking in Simulated Concentrated Ground Waters." *Corrosion/2004, 59th Annual Conference & Exposition, March 28-April 1, 2004, New Orleans.* Paper No. 04551. Houston, Texas: NACE International. TIC: 255943.

167203 Ford, F.P. 1996. "Quantitative Prediction of Environmentally Assisted Cracking." *Corrosion, 52,* (5), 375-395. Houston, Texas: NACE International. TIC: 255526.

118611 Ford, F.P. and Andresen, P.L. 1988. "Development and Use of a Predictive Model of Crack Propagation in 304/316L, A533B/A508 and Inconel 600/182 Alloys in 288°C Water." *Environmental Degradation of Materials in Nuclear Power Systems—Water Reactors, Proceedings of the Third International Symposium, Traverse City, Michigan, August 30-September 3, 1987.* Theus, G.J. and Weeks, J.R., eds. Pages 789-800. Warrendale, Pennsylvania: Metallurgical Society. TIC: 247505.

178278 Foreman, E.A. 1998. *Laboratory Certificate, Two Coupons were Submitted for Chemical Analysis with one for Mechanical Testing. The samples were Identified as Weld Wire, AWS A5.16, ER Ti-7, Lot P150, Ref. P.O. #JRM 198024 and Coupon, Alloy Ti-7 NCA 182, Ref. P.O. #B501535.* Laboratory Number: 5003.135. Hayward, California: FTI Anamet. ACC: MOL.20061109.0092.

178480 Galvele, J.R. 1987. "A Stress Corrosion Cracking Mechanism Based on Surface Mobility." *Corrosion Science, 27,* (1), 1-33. New York, New York: Pergamon Journals. TIC: 245395.

167027 Gordon, B. 2004. "Effect of Stacking Fault Energy on the Modeling of Stress Corrosion Cracking in Alloy 22, SIR-04-009, Rev. 0." Letter from B. Gordon (Structural Integrity Associates) to G.M. Gordon (BSC), January 26, 2004, with attachment. ACC: MOL.20040301.0287.

178145 Gordon, B.M. 1999. *Literature Survey of the Threshold Stress for Stress Corrosion Cracking.* Report No. SIR-99-100. San Jose, California: Structural Integrity Associates. ACC: MOL.20060925.0017.

177385 Gross, P.M. 2003. "Dissimilar Titanium Alloy Welds." *6th International Trends in Welding Research Conference Proceedings, 15-19 April 2002, Pine Mountain, Georgia.* Pages 778-781. Materials Park, Ohio: ASM International. TIC: 258523.

168053 Harris, D.O.; Dedhia, D.D.; and Lu, S.C. 1992. *Theoretical and User's Manual for pc–PRAISE, a Probabilistic Fracture Mechanics Computer Code for Piping Reliability Analysis.* NUREG/CR-5864. Washington, D.C.: U.S. Nuclear Regulatory Commission. ACC: MOL.20040310.0038.

118624 Harris, D.O.; Lim, E.Y.; and Dedhia, D.D. 1981. *Probabilistic Fracture Mechanics Analysis.* Volume 5 of *Probability of Pipe Fracture in the Primary Coolant Loop of a PWR Plant.* NUREG/CR-2189. Washington, D.C.: U.S. Nuclear Regulatory Commission. TIC: 247333.

101995 Haynes International 1988. Hastelloy Alloy C-22. Kokomo, Indiana: Haynes International. TIC: 239938.

168133 Herrera, M.L. 2004. *Evaluation of the Potential Impact of Seismic Induced Deformation on the Stress Corrosion Cracking of the YMP Waste Packages.* SIR-04-015, Rev. 1. San Jose, California: Structural Integrity Associates. ACC: MOL.20040311.0149.

147757 Hornbach, D.J. 1999. *X-Ray Diffraction and Ring-Core Determination of the Residual Stress Distributions in One (1) Alloy C22 Welded Plate and One (1) Alloy C22 Test Bar.* Report 1034-8520. Cincinnati, Ohio: Lambda Research. TIC: 247252.

169906 Jones, D.A. 1992. *Principles and Prevention of Corrosion.* 1st Edition. New York, New York: Macmillan. TIC: 242631.

168353 Jones, R.H. 2004. "RE: Independent Technical Review of the Seismic Crack Density Model." E-mail from R.H. Jones to J. Payer, J. Beavers, and P. Pasupathi, February 20, 2004, with attachment. ACC: MOL.20040311.0145.

118672 Jones, R.H. and Ricker, R.E. 1987. "Stress-Corrosion Cracking." In *Corrosion,* Volume 13, Pages 145-163 of *Metals Handbook.* 9th Edition. Metals Park, Ohio: ASM International. TIC: 209807.

178458 Jones, R.H., ed. 1992. *Stress-Corrosion Cracking.* Materials Park, Ohio: ASM International. TIC: 9221.

177388 Kennedy, J.R.; Adler, P.N.; and Margolin, H. 1993. "Effect of Activity Differences on Hydrogen Migration in Dissimilar Titanium Alloy Welds." *Metallurgical Transactions A, 24A,* (12), 2763-2771. New York, New York: Metallurgical Society of AIME. TIC: 258524.

174853 Kiessel, W.R. and Sinnott, M.J. 1953. "Creep Properties of Commercially Pure Titanium." *Journal of Metals, 5,* (2), 331-338. New York, New York: American Institute of Mining and Metallurgial Engineers. TIC: 257556.

170981 King, K.J.; Wong, L.L.; Estill, J.C.; and Rebak, R.B. 2004. "Slow Strain Rate Testing of Alloy 22 in Simulated Concentrated Ground Waters." *Corrosion/2004, 59th Annual Conference & Exposition, March 28-April 1, 2004, New Orleans.* Paper No. 04548. Houston, Texas: NACE International. TIC: 255943.

177264 Kolman, D.G.; Gaudett, M.A.; and Scully, J.R. 1998. "Modeling of Anodic Current Transients Resulting from Oxide Rupture of Plastically Strained {Beta + Alpha} Titanium." *Journal of the Electrochemical Society, 145,* (6), 1829-1840. New York, New York: Electrochemical Society. TIC: 258496.

149957 Lu, J., ed. 1996. *Handbook of Measurement of Residual Stresses.* Lilburn, Georgia: Fairmont Press. TIC: 247903.

161780 Lundin, C.D. 2002. "Re: Welding Process Considerations for Waste Package Fabrication." Letter from C.D. Lundin to J.A. Cogar (BSC), September 11, 2002, with attachment. ACC: MOL.20021015.0209.

162702 Macdonald, D.D. and Urquidi-Macdonald, M. 1991. "A Coupled Environment Model for Stress Corrosion Cracking in Sensitized Type 304 Stainless Steel in LWR Environments." *Corrosion Science, 32,* (1), 51-81. New York, New York: Pergamon Press. TIC: 254386.

162701 Macdonald, D.D.; Urquidi-Macdonald, M.; and Lu, P-C. 1994. "The Coupled Environmental Fractural Model - A Deterministic Method for Calculating Crack Growth Rates." *Corrosion 94, The Annual Conference and Corrosion Show.* Paper No. 246. Houston, Texas: NACE International. TIC: 254388.

177306 McQuillan, A.D. and McQuillan, M.K. 1956. *Titanium.* Metallurgy of the Rarer Metals-4. London, England: Butterworths Scientific Publications. TIC: 259164.

178209 Millot, T. 2003. "Creep and Creep Cracking of a Heat Exchanger Component of Submarine Made of ASTM Pure Titanium Grade 4 and Grade 2." *Advanced Marine Materials: Technology & Applications*. London, United Kingdom: Royal Institution of Naval Architects. TIC: 258810.

163603 Mishra, S. 2002. *Assigning Probability Distributions to Input Parameters of Performance Assessment Models.* SKB TR-02-11. Stockholm, Sweden: Svensk Kärnbränsleförsörjning A.B. TIC: 252794.

147981 Mohr, W.C. 1996. "Internal Surface Residual Stresses in Girth Butt-Welded Steel Pipes." *Residual Stresses in Design, Fabrication, Assessment and Repair, PVP-Vol. 321,* 37-44. New York, New York: American Society of Mechanical Engineers. TIC: 247502.

163274 NRC (U.S. Nuclear Regulatory Commission) 2003. *Yucca Mountain Review Plan, Final Report.* NUREG-1804, Rev. 2. Washington, D.C.: U.S. Nuclear Regulatory Commission, Office of Nuclear Material Safety and Safeguards. TIC: 254568.

174818 Odegard, B.C. and Thompson, A.W. 1974. "Low Temperature Creep of Ti-6 Al-4 V." *Metallurgical Transactions, 5,* (5), 1207-1213. New York, New York: Metallurgical Society of American Institute of Mining, Metallurgical, and Petroleum Engineers. TIC: 251481.

165536 Pan, Y.-M.; Brossia, C.S.; Cragnolino, G.A.; Dunn, D.S.; Gute, G.D.; and Yang, L. 2002. *Stress Corrosion Cracking and Hydrogen Embrittlement of Container and Drip Shield Materials.* CNWRA 2003-02. San Antonio, Texas: Center for Nuclear Waste Regulatory Analyses. TIC: 254055.

168351 Pasupathi, P. 2004. "Additional Clarification Provided by the Independent Technical Reviewer on the Seismic Crack Density." E-mail from P. Pasupathi to K. Mon and G. Gordon, March 11, 2004. ACC: MOL.20040311.0148.

168350 Pasupathi, P. 2004. "Independent Technical Review of the Seismic Crack Density Model." E-mail from P. Pasupathi to J. Payer, R.H. Jones, and J. Beavers, February 13, 2004, with attachment. ACC: MOL.20040311.0141.

149968 Pasupathi, V. 2000. "Documentation of Literature on Residual Stress Measurements." Interoffice correspondence from V. Pasupathi (CRWMS M&O) to G.M. Gordon, May 19, 2000, LV.WP.VP.05/00-070, with enclosures. ACC: MOL.20000522.0146.

168352 Payer, J.H. 2004. "Independent Technical Reviews." E-mail from J.H. Payer to P. Pasupathi, February 29, 2004, with attachment. ACC: MOL.20040311.0143.

166944 Pensado, O.; Dunn, D.S.; Cragnolino, G.A.; and Jain, V. 2002. *Passive Dissolution of Container Materials—Modeling and Experiments.* CNWRA 2003-01. San Antonio, Texas: Center for Nuclear Waste Regulatory Analyses. TIC: 254056.

177251 Pulvirenti, A.L.; Needham, K.M.; Adel-Hadadi, M.A.; Barkatt, A.; Marks, C.; and Gorman, J. 2002. "Effects of Fluoride and Chloride Ions on Corrosion of Titanium Grade 7 in Concentrated Groundwaters." *Scientific Basis for Nuclear Waste Management XXV, Symposium held November 26-29, 2001, Boston, Massachusetts.* McGrail, B.P. and Cragnolino, G.A., eds. *713,* 77-82. Warrendale, Pennsylvania: Materials Research Society. TIC: 248663.

159841 Pulvirenti, A.L.; Needham, K.M.; Adel-Hadadi, M.A.; Barkatt, A.; Marks, C.R.; and Gorman, J.A. 2002. "Corrosion of Titanium Grade 7 in Solutions Containing Fluoride and Chloride Salts." *Corrosion/2002, 57th Annual Conference & Exposition, April 7-11, 2002, Denver, Colorado.* Paper No. 02552. Houston, Texas: NACE International. TIC: 253169.

162574 Pulvirenti, A.L.; Needham, K.M.; Wong, D.S.; Adel-Hadadi, M.A.; Barkatt, A.; Marks, C.R.; and Gorman, J.A. 2003. "Fluoride Corrosion of Ti-Grade 7: Effects of Other Ions." *Corrosion/2003, 58th Annual Conference & Exposition, March 16-20, 2003, San Diego, California.* Paper No. 03686. Houston, Texas: NACE International. TIC: 254029.

147983 Rice, J.R. 1968. "A Path Independent Integral and the Approximate Analysis of Strain Concentration by Notches and Cracks." *Journal of Applied Mechanics, Transactions of the ASME, 35,* 379-386. New York, New York: American Society of Mechanical Engineers. TIC: 247487.

118696 Roy, A.K.; Fleming, D.L.; Freeman, D.C.; and Lum, B.Y. 1998. *Stress Corrosion Cracking of Alloy C-22 and Ti GR-12 Using Double-Cantilever-Beam Technique.* UCRL-JC-132145. Livermore, California: Lawrence Livermore National Laboratory. ACC: MOL.19990420.0114.

177255 Roy, A.K.; Spragge, M.K.; Fleming, D.L.; and Lum, B.Y. 2001. "Cracking of Titanium Alloys Under Cathodic Applied Potential." *Micron, 32,* 211-218. New York, New York: Pergamon. TIC: 258492.

178467 RTI Energy Systems 2003. *Test Report - Alpha/Beta Processed, Solution Annealed & Aged.* Customer Order No. 600118335. Niles, Ohio: RTI International. ACC: MOL.20070214.0006.

178214 Rybicki, E.F.; Groom, J.J.; Lemcoe, M.M.; Mishler, H.W.; Rodabaugh, E.C.; Schmuester, D.W.; Stonesifer, R.B.; and Strenkowski, J.S. 1977. *Residual Stresses at Girth-Butt Welds in Pipes and Pressure Vessels*. NUREG-0376, Rev. 5. Washington, D.C.: U.S. Nuclear Regulatory Commission. ACC: LLR.20070305.0001.

178216 Rybicki, E.F. and Stonesifer, R.B. 1979. "Computation of Residual Stresses Due to Multipass Welds in Piping Systems." *Journal of Pressure Vessel Technology, 101,* 149-154. New York, New York: American Society of Mechanical Engineers. TIC: 258771.

151162 Schutz, R.W. 1986. "Titanium." *Process Industries Corrosion.* Pages 503-527. Houston, Texas: National Association of Corrosion Engineers. TIC: 226189.

177345 Schutz, R.W. 1992. "Stress-Corrosion Cracking of Titanium Alloys." Chapter 10 of *Stress-Corrosion Cracking.* Jones, R.H., ed. Materials Park, Ohio: ASM International. TIC: 258498.

177482 Schutz, R.W. 1997. "Performance of Ruthenium-Enhanced Alpha-Beta Titanium Alloys in Aggressive Sour Gas and Geothermal Well Produced-Fluid Brines." *Corrosion 97, The NACE International Annual Conference and Exposition, March 9-14, 1997, New Orleans, Louisiana.* Paper No. 32. Houston, Texas: NACE International. TIC: 245216.

162361 Schutz, R.W. 1985. "Performance and Application of Titanium Alloys in Geothermal Brine Service." *Materials Performance, 24,* (1), 39-47. Houston, Texas: National Association of Corrosion Engineers. TIC: 226195.

102790 Schutz, R.W. 1995. "Recent Titanium Alloy and Product Developments for Corrosive Industrial Service." *Corrosion 95, The NACE International Annual Conference and Corrosion Show, March 26-31, 1995, Orlando, Florida.* Paper No. 244. Pages 244/1-244/20. Houston, Texas: NACE International. TIC: 245067.

168772 Schutz, R.W. 2003. "2003 F.N. Speller Award Lecture: Platinum Group Metal Additions to Titanium: A Highly Effective Strategy for Enhancing Corrosion Resistance." *Corrosion, 59,* (12), 1043-1057. Houston, Texas: NACE International. TIC: 255969.

177257 Schutz, R.W.; Porter, R.L.; and Horrigan, J.M. 2000. "Qualifications of Ti-6%Al-4%V-Ru Alloy Production Tubulars for Aggressive Fluoride-Containing Mobile Bay Well Service." *Corrosion, 56,* (11), 1170-1179. Houston, Texas: NACE International. TIC: 258489.

149953 Shcherbinskii, V.G. and Myakishev, V.M. 1970. "Statistical Distribution of Welding Defects with Respect to Azimuth." *Translated from Defektoskopiya, No. 4,* 143-144. New York, New York: Plenum Publishing. TIC: 247890.

177461 Shukla, P.K.; Dunn, D.S.; Chiang, K.-T.; and Pensado, O. 2006. "Stress Corrosion Cracking Model for Alloy 22 in the Potential Yucca Mountain Repository Environment." *Corrosion 2006, 61st Annual Conference & Exposition, San Diego Convention Center, March 12-16, 2006.* Paper No. 06502. Houston, Texas: NACE International. TIC: 258178.

161933 SIA (Structural Integrity Associates) 2002. *Structural Integrity Associates Support of Waste Package Design for Year 2001.* SIR-02-073. San Jose, California: Structural Integrity Associates. ACC: MOL.20020709.0389.

162457 SIA 2003. *Evaluation of the CRM-21 PWR and Viability Availability Waste Package.* Report No. SIR-99-094, Rev. 1. San Jose, California: Structural Integrity Associates. ACC: MOL.20030327.0004.

178078 SIA 2003. *Evaluation of the Effect of Removal of Strong Backs on the Residual Stress Distributions in the Unmitigated and Mitigated Alloy 22 Plates.* File No. BSC-01Q-304. San Jose, California: Structural Integrity Associates. ACC: MOL.20040408.0175.

177262 Simbi, D.J. 1996. "Stress Corrosion Cracking of Titanium and its Alloys in Halide Containing Environments – A Mechanistic Review." *Corrosion Reviews, 14,* (3-4), 343-374. Tel Aviv, Israel: Freund Publishing House. TIC: 258541.

177263 Simbi, D.J. 1997. "Effect of Prior Cold Plastic Deformation on Mechanical Properties and Susceptibility to Stress Corrosion Cracking and Hydrogen Embrittlement of Titanium." *Journal of Applied Science in Southern Africa, 3,* (1 & 2), 79-88. Mount Pleasant, Harare, Zimbabwe: University of Zimbabwe Publications. TIC: 258360.

177437 Smailos, E.; Martínez-Esparza, A.; Kursten, B.; Marx, G.; and Azkarate, I. 1999. *Corrosion Evaluation of Metallic Materials for Long-Lived HLW/Spent Fuel Disposal Containers.* FZKA 6285. Karlsruhe, Germany: Forschungszentrum Karlsruhe GmbH. TIC: 258525.

163114 Smith, D. 2003. *Weld Flaw Evaluation and Nondestructive Examination Process Comparison Results for High-Level Radioactive Waste Package Manufacturing Program.* TDR-EBS-ND-000007 REV 01. Las Vegas, Nevada: Bechtel SAIC Company. ACC: ENG.20030515.0003.

178765 SNL (Sandia National Laboratories) 2007. *Analysis of Mechanisms for Early Waste Package/Drip Shield Failure.* ANL-EBS-MD-000076 REV 00. Las Vegas, Nevada: Sandia National Laboratories. ACC: DOC.20070629.0002.

176828 SNL 2007. *Seismic Consequence Abstraction.* MDL-WIS-PA-000003 REV 03. Las Vegas, Nevada: Sandia National Laboratories.

178849 SNL 2007. *Technical Work Plan for Postclosure Engineered Barrier Degradation Modeling.* TWP-EBS-MD-000020 REV 00. Las Vegas, Nevada: Sandia National Laboratories. ACC: DOC.20070216.0001.

179354 SNL 2007. *Total System Performance Assessment Data Input Package for Requirements Analysis for EBS In-Drift Configuration.* TDR-TDIP-ES-000010 REV 00. Las Vegas, Nevada: Sandia National Laboratories.

179567 SNL 2007. *Total System Performance Assessment Data Input Package for Requirements Analysis for DOE SNF/HLW and Navy SNF Waste Package Overpack Physical Attributes Basis for Performance Assessment.* TDR-TDIP-ES-000009 REV 00. Las Vegas, Nevada: Sandia National Laboratories.

118702 Sprowls, D.O. 1987. "Evaluation of Stress-Corrosion Cracking." In *Corrosion,* Volume 13, Pages 245-282 of *Metals Handbook.* 9th Edition. Metals Park, Ohio: ASM International. TIC: 209807.

167756 Tada, H.; Paris, P.C.; and Irwin, G.R. 2000. *The Stress Analysis of Cracks Handbook.* 3rd Edition. New York, New York: American Society of Mechanical Engineers. TIC: 255547.

122064 Timoshenko, S. and Goodier, J.N. 1951. *Theory of Elasticity.* 2nd Edition. New York, New York: McGraw-Hill. TIC: 224221.

121096 Timoshenko, S.P. and Goodier, J.N. 1970. *Theory of Elasticity.* 3rd Edition. New York, New York: McGraw-Hill. TIC: 245469.

177386 Waisman, J.L.; Sines, G.; and Robinson, L.B. 1973. "Diffusion of Hydrogen in Titanium Alloys Due to Composition, Temperature, and Stress Gradients." *Metallurgical Transactions, 4,* 291-302. New York, New York: Metallurgical Society of AIME and American Society for Metals. TIC: 258532.

177383 Waisman, J.L.; Toosky, R.; and Sines, G. 1977. "Uphill Diffusion and Progressive Embrittlement: Hydrogen in Titanium." *Metallurgical Transactions A, 8A,* 1249-1256. Metals Park, Ohio: Metallurgical Society of AIME and American Society for Metals. TIC: 258531.

177387 Williams, D.N.; Koehl, B.G.; and Mueller, R.A. 1970. "Hydrogen Segregation in Ti-6 Al-4V Weldments Made with Unalloyed Titanium Filler Metal." *Welding Journal, 49,* (5), 207-212. Baltimore, Maryland: American Welding Society. TIC: 258530.

178059 Woolf, R. 2003. *Controlled Plasticity Burnishing (CPB) for Developing a Very Deep Layer of Compressive Residual Stresses in Rectangular Specimens of Alloy 22 for Yucca Mountain Nuclear Waste Package Closure Weld.* SET Job No. 37. Cincinnati, Ohio: Surface Enhancement Technologies. ACC: ENG.20030729.0002.

178195 Yau, T-L. 1989. "Ti-3Al-2.5V: An Emerging Alloy for Seawater Service." *International Conference on Evaluation of Materials Performance in Severe Environments, EVALMAT 89, November 20-23, 1989, International Conference Center, Kobe, Japan.* Pages 975-984. Tokyo, Japan: Iron and Steel Institute of Japan. TIC: 258506.

9.2 CODES, STANDARDS, REGULATIONS, AND PROCEDURES

180319 10 CFR 63. 2007. Energy: Disposal of High-Level Radioactive Wastes in a Geologic Repository at Yucca Mountain, Nevada. Internet Accessible.

169771 ASME (American Society of Mechanical Engineers) 1977. "Risk-Informed Requirements for Class 1, 2, and 3 Piping, Method B, Section XI, Division 1." *Supplement 10, Case N-578 of 1995 Code Cases, Nuclear Components. 1995 ASME Boiler & Pressure Vessel Code*. New York, New York: American Society of Mechanical Engineers. TIC: 245287.

162726 ASTM B 265-02. 2002. *Standard Specification for Titanium and Titanium Alloy Strip, Sheet, and Plate*. West Conshohocken, Pennsylvania: American Society for Testing and Materials. TIC: 254000.

100497 ASTM B 575-94. 1994. *Standard Specification for Low-Carbon Nickel-Molybdenum-Chromium and Low-Carbon Nickel-Chromium-Molybdenum Steel Alloy Plate, Sheet, and Strip*. Philadelphia, Pennsylvania: American Society for Testing and Materials. TIC: 237683.

117480 ASTM E 399-90 (Reapproved 1997). 1991. *Standard Test Method for Plane-Strain Fracture Toughness of Metallic Materials*. West Conshohocken, Pennsylvania: American Society for Testing and Materials. TIC: 246299.

137688 ASTM G 30-94. 1994. *Standard Practice for Making and Using U-Bend Stress-Corrosion Test Specimens*. Philadelphia, Pennsylvania: American Society for Testing and Materials. TIC: 246890.

177289 ASTM G 38-01. 2001. *Standard Practice for Making and Using C-Ring Stress-Corrosion Test Specimens*. Conshohocken, Pennsylvania: American Society for Testing and Materials. TIC: 259162.

171562 ASTM G 49-85 (Reapproved 2000). 2000. *Standard Practice for Preparation and Use of Direct Tension Stress-Corrosion Test Specimens*. West Conshohocken, Pennsylvania: American Society for Testing and Materials. TIC: 249897.

171563 ASTM G 129-00. 2000. *Standard Practice for Slow Strain Rate Testing to Evaluate the Susceptibility of Metallic Materials to Environmentally Assisted Cracking*. West Conshohocken, Pennsylvania: American Society for Testing and Materials. TIC: 256501.

IM-PRO-002, *Control of the Electronic Management of Information*.

IM-PRO-003, *Software Management.*

SCI-PRO-001, *Qualification of Unqualified Data*.

SCI-PRO-002, *Planning for Science Activities*.

SCI-PRO-004, *Managing Technical Product Inputs*.

SCI-PRO-006, *Models*.

9.3 SOURCE DATA, LISTED BY DATA TRACKING NUMBER

General Electric Global Research Center (GE GRC)

161253 LL021105312251.023. Stress Corrosion Crack Growth and Initiation Measurements for C-22 and Ti-7, GE GRC 121202. Submittal date: 01/08/2003.

167911 MO0402GEA22SCC.000. Alloy 22 Stress Corrosion Crack Growth Rate Data in 288°C Water. Submittal date: 02/25/2004.

171564 MO0409GE835924.000. Stress Corrosion Crack Initiation & Growth Measurements for C-22 and Ti-7 in Environments Relevant to High Level Nuclear Waste Packages. Submittal date: 09/07/2004.

180869 MO0705SCCIGM06.000. Final Report for FY06: Stress Corrosion Crack Initiation & Growth Measurements in Environments Relevant to High Level Nuclear Waste Packages. Submittal date: 05/14/2007.

182202 MO0707SCCIGMER.000. Final Report for FY05: Stress Corrosion Crack Initiation & Growth Measurements in Environments Relevant to High Level Nuclear Waste Packages. Submittal date: 07/27/2007.

182558 MO0708RTSWRS06.000. FY06 Reports on Technical Services of Weld Residual Stress. Submittal date: 08/20/2007.

182330 MO0708SRSCCIGM.000. Supporting Files for Final Report for FY06: Stress Crack Initiation & Growth Measurements in Environments Relevant to High Level Nuclear Waste Packages. Submittal date: 08/07/2007.

182572 MO0708XRAYDRST.000. X-Ray Diffraction Determination of the Residual Stress Distributions in Ten Titanium Grade 16 and Six Titanium Grade 7 U-Bend Specimens. Submittal date: 08/21/2007.

Lawrence Livermore National Laboratory Long-Term Corrosion Test Facility (LTCTF)

178276 LL030102212251.005. Stress Corrosion Cracking. Submittal date: 01/29/2003.

166971 LL030300612251.035. Reversing DC Test Generated Fatigue Crack Growth Data. Submittal Date: 07/09/2003.

163712 LL030412512251.057. LTCTF Corrosion Rate Calculations for Five-Year Exposed Alloy C22 Specimens Cleaned Under TIP-CM-51. Submittal date: 05/28/2003.

171362 LL040803112251.117. Target Compositions of Aqueous Solutions Used for Corrosion Testing. Submittal date: 08/14/2004.

SIA

148482 LL000320005924.145. Corrosion Cracking of the Drip Shield, the Waste Package Outer Barrier and the Stainless Steel Structural Material. Submittal date: 03/22/2000.

171792 MO0409GGSIACAL.000. Structural Integrity Associates Calculation Files 2004. Submittal date: 09/20/2004.

Lambda

165147 MO0301SPAXRA52.001. X-Ray Diffraction and Ring Core Determination of the Subsurface Residual Stress Distributions in Two Alloy 22 Welded Plates. Submittal date: 01/30/2003.

Other

148850 MO0003RIB00071.000. Physical and Chemical Characteristics of Alloy 22. Submittal date: 03/13/2000.

152926 MO0003RIB00073.000. Physical and Chemical Characteristics of Ti Grades 7 and 16. Submittal date: 03/13/2000.

181613 MO0706SPAFEPLA.001. FY 2007 LA FEP List and Screening. Submittal date: 06/20/2007.

9.4 OUTPUT DATA

MO0702PASTRESS.002. Output DTN of Model Report, “Stress Corrosion Cracking of Waste Package Outer Barrier and Drip Shield Materials,” ANL-EBS-MD-000005. Submittal date: 04/24/2007.

MO0705CREEPSCC.000. Supplementary Output DTN of Model Report, "Stress Corrosion Cracking of Waste Package Outer Barrier and Drip Shield Materials," ANL-EBS-MD-000005. Submittal date: 05/14/2007.

9.5 SOFTWARE CODES

161757 SCCD V. 2.01. 2000. WINDOWS NT. STN: 10343-2.01-00.

INTENTIONALLY LEFT BLANK

APPENDIX A
DATA QUALIFICATION PLAN

A. DATA QUALIFICATION PLAN

Sandia National Laboratories

Data Qualification Plan

Complete only applicable items.

QA: QA
Page 1 of 1

Section I. Organizational Information

Qualification Title
Qualification of Incipient Crack Size

Requesting Organization
Waste Package Modeling and Testing

Section II. Process Planning Requirements

1. List of Unqualified Data to be Evaluated
1. Incipient crack size for use with the stress corrosion cracking model.

2. Type of Data Qualification Method(s) [Including rationale for selection of method(s) (Attachment 3) and qualification attributes (Attachment 4)]
Technical Assessment.

This method was chosen because of the determination that confidence in the data acquisition or development is warranted and the confirmation that the data have been used in similar application.

3. Data Qualification Team and Additional Support Staff Required
Chairperson: Fred Hua
Team member: Gerald Gordon

4. Data Evaluation Criteria
The following qualification criteria will be used:

Method 1: Equivalent QA Program.
Method 2: Corroborating Data.
Method 5: Technical Assessment.

5. Identification of Procedures Used
SCI-PRO-001

Section III. Approval

Qualification Chairperson Printed Name	Qualification Chairperson Signature	Date
Fred Hua		01/24/2007
Responsible Manager Printed Name	**Responsible Manager Signature**	**Date**
Cliff Howard	Cliff Howard	1-24-07

SCI-PRO-001.1-R0

INTENTIONALLY LEFT BLANK

APPENDIX B
MATHCAD CALCULATION FOR *n* VALUES IN TABLE 6-6

APPENDIX B. MATHCAD CALCULATION FOR *N* VALUES IN TABLE 6-6

Evaluation of *n* values from measured crack growth rates (output DTN: MO0705CREEPSCC.000, *B SDFR n-values Calculation.xmcd*):

$$TOL := 1 \times 10^{-5}$$

$$V_t(n, K_I) := \left(7.8 \times 10^{-2}\right) \cdot n^{3.6} \cdot \left(4.1 \times 10^{-14}\right)^{n} \cdot K_I^{4 \cdot n}$$

$$KI := (30 \;\; 30 \;\; 45 \;\; 24.2 \;\; 40 \;\; 40 \;\; 40 \;\; 40)^T$$

$$vt := (5.0 \;\; 0.1 \;\; 4.0 \;\; 6.0 \;\; 12 \;\; 13 \;\; 20 \;\; 30)^T \cdot \left(1 \times 10^{-10}\right)$$

$$ii := 0 .. last(vt)$$

$$n_{ii} := root\left(V_t\left(n, KI_{ii}\right) - vt_{ii}, n, 1.0, 1.4\right)$$

$$augment(KI, vt, n) = \begin{pmatrix} 30 & 5 \times 10^{-10} & 1.119 \\ 30 & 1 \times 10^{-11} & 1.392 \\ 45 & 4 \times 10^{-10} & 1.281 \\ 24.2 & 6 \times 10^{-10} & 1.041 \\ 40 & 1.2 \times 10^{-9} & 1.151 \\ 40 & 1.3 \times 10^{-9} & 1.145 \\ 40 & 2 \times 10^{-9} & 1.111 \\ 40 & 3 \times 10^{-9} & 1.08 \end{pmatrix}$$

INTENTIONALLY LEFT BLANK

APPENDIX C
NORMAL DISTRIBUTION HYPOTHESIS TEST FOR *n* VALUES

APPENDIX C: NORMAL DISTRIBUTION HYPOTHESIS TEST FOR *n* VALUES

Output DTN: MO0705CREEPSCC.000, *Normal-n-values.xmcd*.

Normal Distribution Hypothesis Test for n values

The n values are asserted to follow a Normal (Gaussian) distribution. This is validated qualitatively by observing the values graphically on a Quantile-Normal plot where they appear linear. A quantitative evaluation is applied in an Anderson-Darling Goodness-of-Fit test. The p-value calculated is consistent with the Normal Distribution.

$ORIGIN := 1$

Number of data points: $N_d := 8$

n values from eight sources:

$n := (1.119\ \ 1.391\ \ 1.281\ \ 1.041\ \ 1.151\ \ 1.145\ \ 1.111\ \ 1.080)^T$

Null Hypothesis: Slopes are from a Normal distribution with mean and standard deviation:

$m_0 := mean(n)$ $\quad s_0 := Stdev(n)$

$m_0 = 1.165$ $\quad s_0 = 0.115$

$ii := 1..N_d$

$p_{ii} := \dfrac{ii - \frac{3}{8}}{N_d + 1 - 2\cdot\frac{3}{8}}$ Blom plotting positions, Stedinger et al. 1993 [DIRS 105941], Table 18.3.1

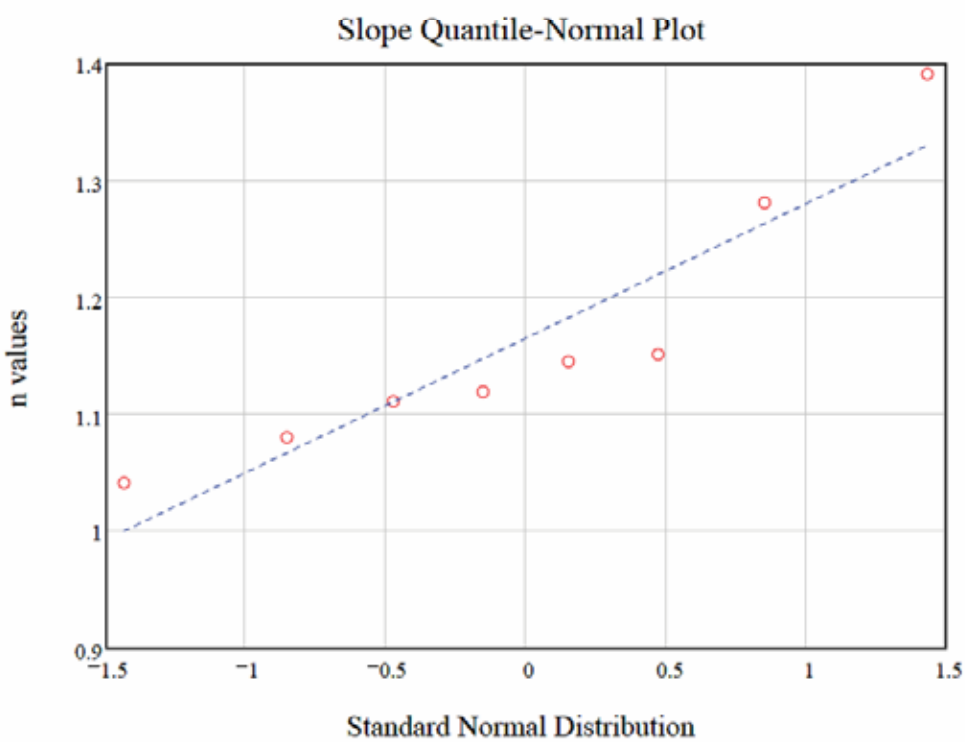

Anderson-Darling Goodness of Fit Statistic

$$Z := \mathrm{pnorm}\left(\mathrm{sort}(n), m_0, s_0\right)$$

$$A2 := \left[-N_d - \frac{1}{N_d}\cdot\sum_{i=1}^{N_d}\left[(2\cdot i - 1)\cdot\left(\ln\left(Z_i\right) + \ln\left(1 - Z_{N_d - i + 1}\right)\right)\right]\right]\cdot\left(1 + \frac{0.75}{N_d} + \frac{2.25}{N_d^{\,2}}\right)$$

$$A2 = 0.614$$

p-value by table interpolation, (D'Agostino and Stephens 1986 [DIRS 160320], Table 4.7)

$$0.10 + \left(\frac{A2 - 0.631}{0.561 - 0.631}\right)\cdot(0.15 - 0.10) = 0.11$$

Accept the null hypothesis that the slopes are from the specified normal distribution.
The p-value is the probability that the test statistic will take a value at least as extreme as that actually observed (Pr[A2 > Observed]). Small p-values (e.g., less than 0.05) suggest evidence against the null hypothesis, indicating that the data set is unlikely to have been drawn from the specified distribution. Large p-values indicate the data set is consistent with the null hypothesis.

APPENDIX D
UNCERTAINTY ANALYSIS OF PEENED STRESS DATA

APPENDIX D: UNCERTAINTY ANALYSIS OF PEENED STRESS DATA

A statistical analysis of residual surface stresses from shot-peening of a nickel alloy was preformed to characterize uncertainty. Seventeen measurements from a shot-peened sample, along with their estimated reading error, were used to estimate the observed fractional uncertainty for the data. The residual surface stresses are centered on a value consistent with the reference value of the materials' yield strength. It is concluded that the uncertainty in the values is consistent with a normal distribution.

The stress measurements are from Table VI of a report from the Plasma Fusion Center, Massachusetts Institute of Technology (Pasupathi 2000 [DIRS 149968], Table VI). X-ray diffraction residual stress measurements were made at the surface of a shot-peened Incoloy 908 sample. A measurement error was estimated for each measurement resulting from the random error in the determination of the diffraction peak angular position and the empirically determined value of the x-ray elastic constant, required for calculating stress from strain measurements. This measurement error is used to weight the values for estimating the mean and standard deviation of the stress values. The observed trend in the errors is that lower (more negative) stress values have more error associated with them. The consequence of this is that the weighted estimated mean is higher in value than the unweighted estimate.

The W test, developed by Shapiro and Wilk (D'Agostino and Stephens 1986 [DIRS 160320], Section 5.10.3), was performed to test whether the data set was drawn from a normal distribution. This resulted in a W-value of 0.97 with a p-value of 0.83. This is very strong evidence that the data can be treated as coming from a normal distribution. This may also be seen qualitatively from the fractile and probability graphs in Figures D-1 and D-2.

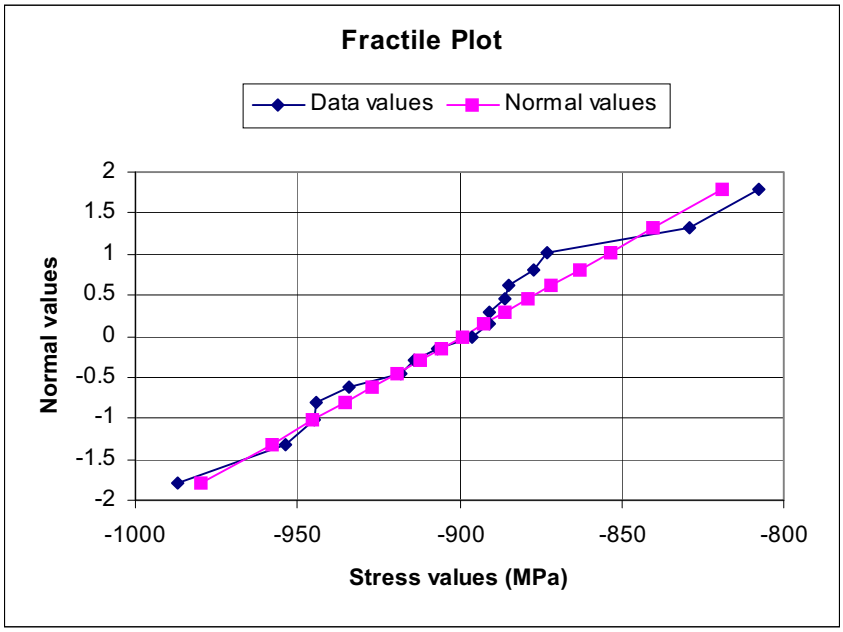

Source: Output DTN: MO0705CREEPSCC.000, *SCC_Normal.xls*.

Figure D-1. Fractile Plot of Stress Values

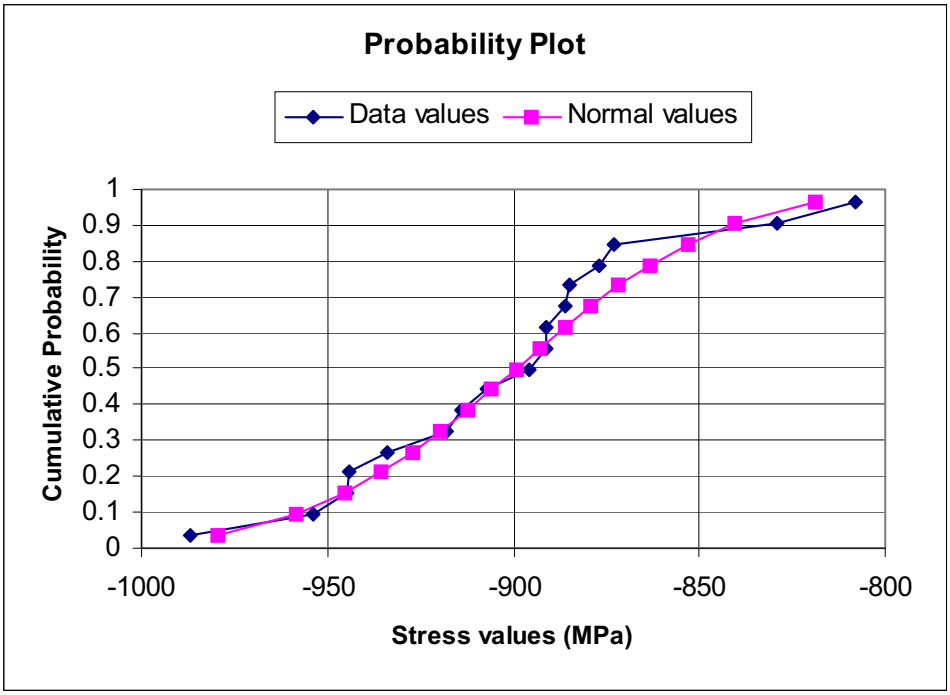

Source: Output DTN: MO0705CREEPSCC.000, *SCC_Normal.xls*.

Figure D-2. Probability Plot of Stress Values

The descriptive statistics of the sample are found in Table D-1. The weighted mean is calculated to be –899 MPa. This is consistent in magnitude to the reference yield strength for this material, 896 MPa. The weighted standard deviation of the data is calculated to be 45 MPa. With these values, the fractional uncertainty, defined as the ratio of the standard deviation to the absolute value of the mean, is 5%.

Table D-1. Descriptive Statistics of Data

Estimator	Unweighted	Weighted
Mean	−902.3	−899.2
Standard Error	10.8	10.9
Median	−896	
Mode	−891	
Standard Deviation	44.3	44.8
Sample Variance	1,965.2	2,006.7
Fraction Uncertain	0.049	0.050
Kurtosis	0.5	
Skewness	0.3	
Range	179	
Minimum	−987	
Maximum	−808	
Count	17	

Source: Output DTN: MO0705CREEPSCC.000, *SCC_Normal.xls*.

The approach outlined in this appendix resulted in a best estimate of the fractional uncertainty of five percent. Assuming that the bounding values on the uncertainty distribution for the stress state (±F) are given by ±3 times the fractional uncertainty, it is concluded that the stress state uncertainty distribution can be represented as a truncated normal distribution with a mean of zero and $\pm 3\sigma$ bounds at ±15%.

INTENTIONALLY LEFT BLANK